Oxidation and reduction properties of iron-containing oxides

Thesis

UNRESTRICTED.

Oxidation and Reduction Properties of Iron-Containing Oxides

Ibrar Ayub

Thesis Submitted for the Degree of Doctor of Philosophy

The Open University

Department of Chemistry

October 2001

To my family

Declaration

I declare that the work presented in this thesis is the result of my own investigations, and where the work of others is cited, it is fully acknowledged. The material embodied in the thesis has not been submitted, nor is currently being submitted for any other degree.

.....

Ibrar Ayub

.....

Prof. Frank J. Berry

Abstract

Iron oxides and their metal- doped variants of formulation M/Fe_3O_4, $M/\gamma–Fe_2O_3$, M/α-Fe_2O_3 have been prepared by the calcination of solids formed by the boiling of precipitates under reflux and by hydrothermal processing.

Titanium-, tin-, ruthenium- and magnesium- doped variants of $\gamma–Fe_2O_3$ have been subjected to special investigation and the influence of the dopants on the surface area, particle size, reduction properties, stability to conversion to α-Fe_2O_3- related structures, and oxidation- reduction cycling has been examined. Titanium- doped $\gamma–Fe_2O_3$ prepared by the calcination of a solid formed by the addition of base to salt and boiling the precipitate under reflux was formed with a smaller particle size and higher surface area than the other counterparts. These properties remained superior to those of the other materials when $Ti/\gamma–Fe_2O_3$ was subjected to a three-fold reduction-oxidation cycle. The stabilisation of a spinel- related $\gamma–Fe_2O_3$ structure with respect to thermally induced conversion to a corundum- related α-Fe_2O_3 phase was related to the presence of titanium as opposed to particle size or surface area effects.

Impregnation of $Ti/\gamma–Fe_2O_3$ with palladium lowered the temperatures at which the iron oxide was reduced as a result of the adsorption and dissociation of hydrogen on palladium which facilitates more facile reduction of iron in iron oxide. The oxygen storage capacity and the performance of palladium- impregnated $Ti/\gamma–Fe_2O_3$ for the oxidation of carbon monoxide to carbon dioxide was good. Although generally similar behaviour was observed in $\gamma–Fe_2O_3$ doped with tin, ruthenium and magnesium, and in palladium impregnated variants, $Ti/\gamma–Fe_2O_3$ and palladium impregnated $Ti/\gamma–Fe_2O_3$ showed the most favourable properties in terms of their potential use as oxygen-storage components in automobile exhaust catalysts.

A comparison of the results with those recorded from materials derived from Fe_3O_4 and α-Fe_2O_3 confirmed the superior properties of $Ti/\gamma–Fe_2O_3$ and palladium impregnated $Ti/\gamma–Fe_2O_3$ for use as catalysts in automobile exhaust systems.

Acknowledgement

I would like to thank:

My supervisors, Professor Frank J. Berry and Dr Eleanor M. Crabb for many useful discussions and for their advise throughout this work.

Professor Örn Helgason, Science Institute, University of Iceland, for providing facilities and assistance with *in situ* high temperature ^{57}Fe Mössbauer spectroscopy.

Kristjan Jónsson, Science Institute, University of Iceland, for helping with the Mössbauer software.

Mr Gordon Oates for his help with TPR and Mössbauer apparatus. The technical staff of the Chemistry Department – Messrs. Cook, Gibbs, Jeffs, Leslie and Patel for their technical expertise.

Mrs Naomi Williams, Electron Microscope Suite, The Open University, for instruction and assistance with TEM and EDX.

Finally I would like to thank Johnson Matthey for their financial support and Drs D. Thompsett, T.I. Hyde and J.M. Fisher, for helpful discussions and for OSC measurements.

Contents

Chapter 1

INTRODUCTION

Chapter 1

INTRODUCTION

1.1 Introduction

The work reported in this thesis concerns an investigation of some of the properties of iron- containing oxides relevant to their potential use as oxygen storage and release components in automobile exhaust catalysts. The main areas of work have been:

i. the preparation and characterisation of materials of composition :

Fe_3O_4, γ-Fe_2O_3, α-Fe_2O_3,

M/Fe_3O_4, (M = Ti, Sn, Ru and Mg),

M/γ-Fe_2O_3 (M = Ti, Sn, Ru, and Mg),

M/α-Fe_2O_3 (M = Ti, Sn, Ru, and Mg);

ii. the investigation of the effects of different synthesis routes on the properties of some of these materials;

iii. the investigation of the influence of the dopants on the surface area, particle size, reduction properties, thermal stability and oxidation- reduction cycling of selected oxides;

iv. the investigation of the oxygen storage capacity of some of the solids.

1.2 Background

1.2.1 Oxygen Storage for Automobile Exhaust Catalyst

Vehicle emission and engine characteristics

Concerns about the emission of pollutants such as carbon monoxide (CO), unburnt hydrocarbons (HC), and nitrogen oxides (NO_x) from motor vehicles on the quality of the atmosphere have existed for some time. Unburnt hydrocarbons, especially aromatic compounds such as benzene and polycyclic aromatic hydrocarbons, are carcinogens. Carbon monoxide is a poisonous gas. Oxides of nitrogen are toxic and are a source of acid rain. The combination of unburnt hydrocarbons and oxides of nitrogen when irradiated by sunlight can result in a chemical fog or smog.

To understand the origin of these emissions it is necessary to consider the working of the internal combustion engine[1,2]. Petrol driven cars typically run on four cylinders. The conventional cylinder employs a four-stroke cycle. As the piston descends (Figure 1.1), it draws in a mixture of air and fuel vapour through the inlet valve. The inlet valve then closes and the piston ascends to the top of its stroke, compressing the air and fuel mixture. Just before the moment of maximum compression, a spark from the plug ignites the mixture; the exothermic reaction causes a sudden temperature rise, accompanied by rapid expansion of the gases in the cylinder, which propels the piston downwards. This provides the energy to turn the crankshaft, which in turn drives the wheels of the car. Gas temperatures during combustion are typically in excess of 1500 °C. Finally, the exhaust valve opens as the piston returns to the top of its stroke, and the combustion products carbon dioxide (CO_2), water (H_2O), carbon

monoxide (CO), unburnt hydrocarbons (HC), and nitrogen oxides (NO_x) are driven into the exhaust system at temperatures of 900- 1000 °C. The gases cool down as they pass through the exhaust and enter the atmosphere at about 200 °C.

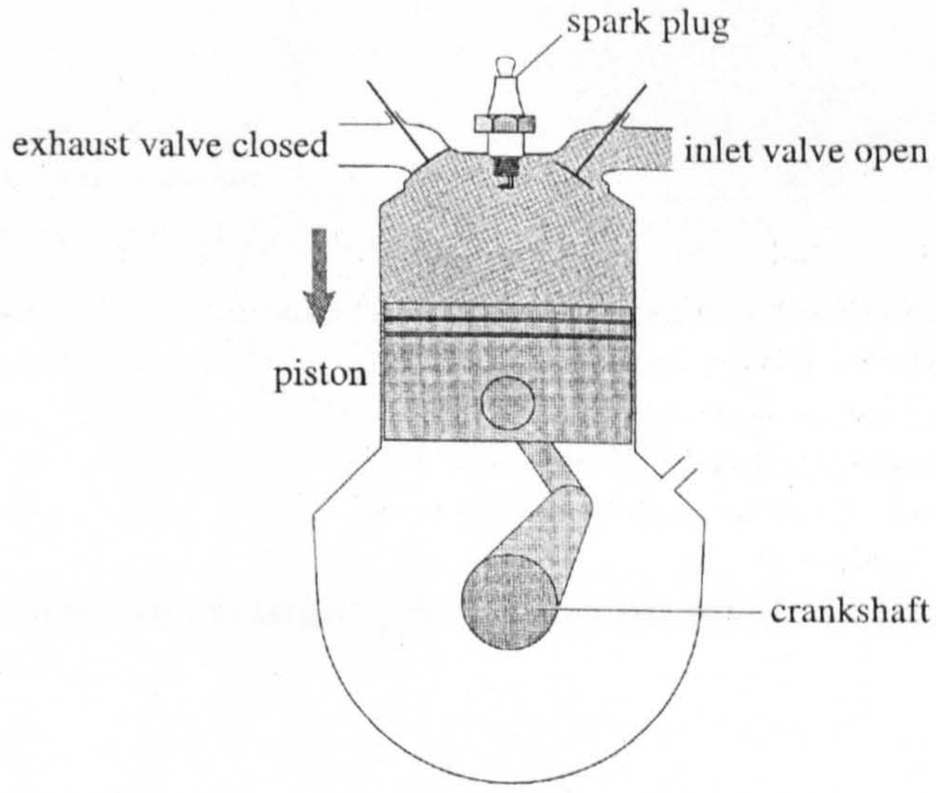

Figure 1.1. One cylinder of an internal combustion engine

A general relationship exists between levels of CO, HC, and NO_x released from the engine and the air/fuel (A/F) ratio and is shown in Figure 1.2. At A/F ratios somewhat above stoichiometric (14.7:1) – that is when the engine is operating under fuel-lean (excess air) net oxidising conditions – low levels of HC and CO are produced in the engine, and there is a peak in NO_x concentration. Eventually the HC concentration increases whilst the CO and NO_x levels fall to a minimum. At lower A/F values, fuel rich (excess fuel), net reducing conditions – NO_x falls, but the HC and CO concentration increases.

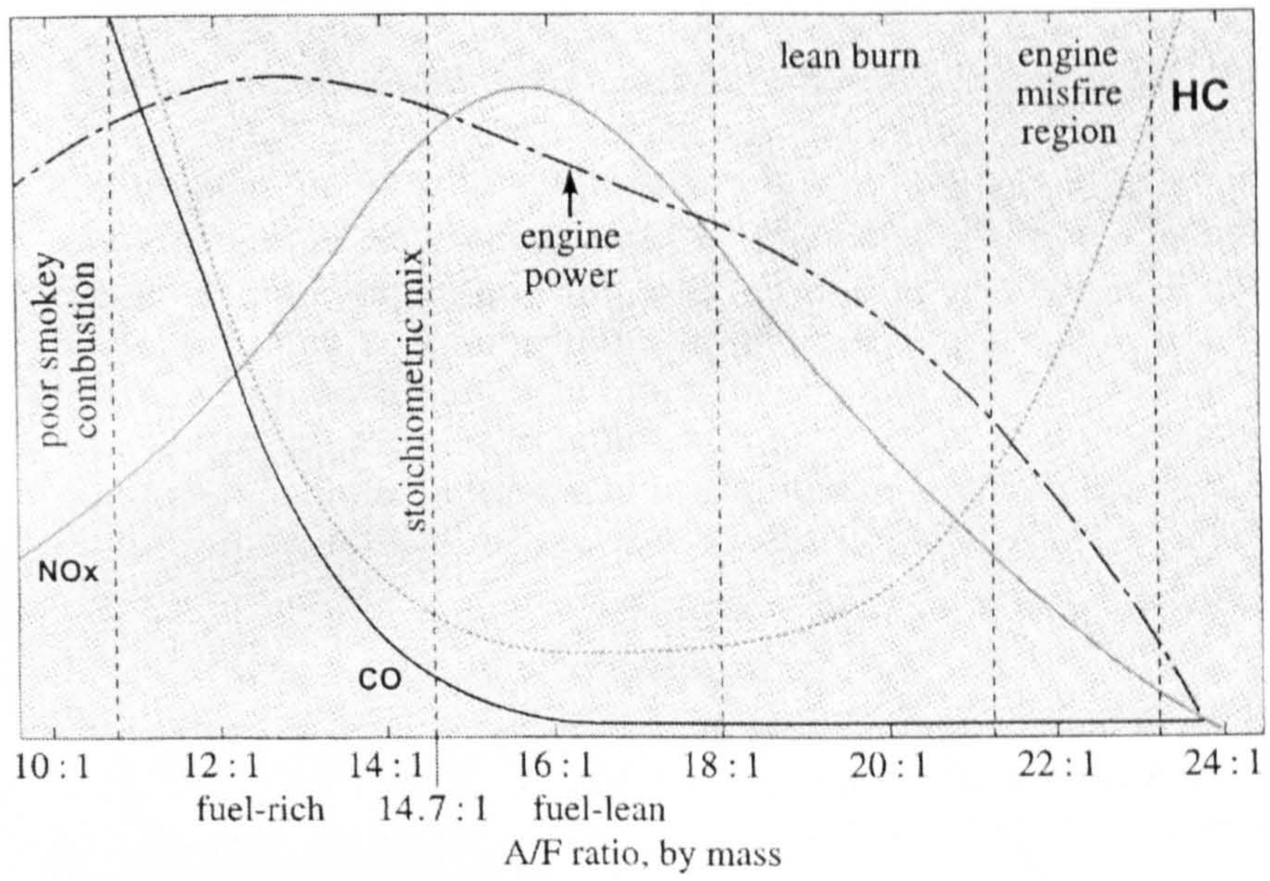

Figure 1.2. The effect of changing A/F ratio on levels of NO_x, CO and HC

Three Way Catalyst

Exhaust catalysts systems are used to reduce pollutants in the exhaust gases of vehicles. The three-way catalyst (TWC)[1-5] (Figure 1.3) is currently used in petrol driven vehicles to reduce CO, HC and NO_x emissions. The current TWC is a multicomponent material, containing rhodium, platinum, palladium, ceria (CeO_2), γ-alumina (Al_2O_3) and other metal oxides.

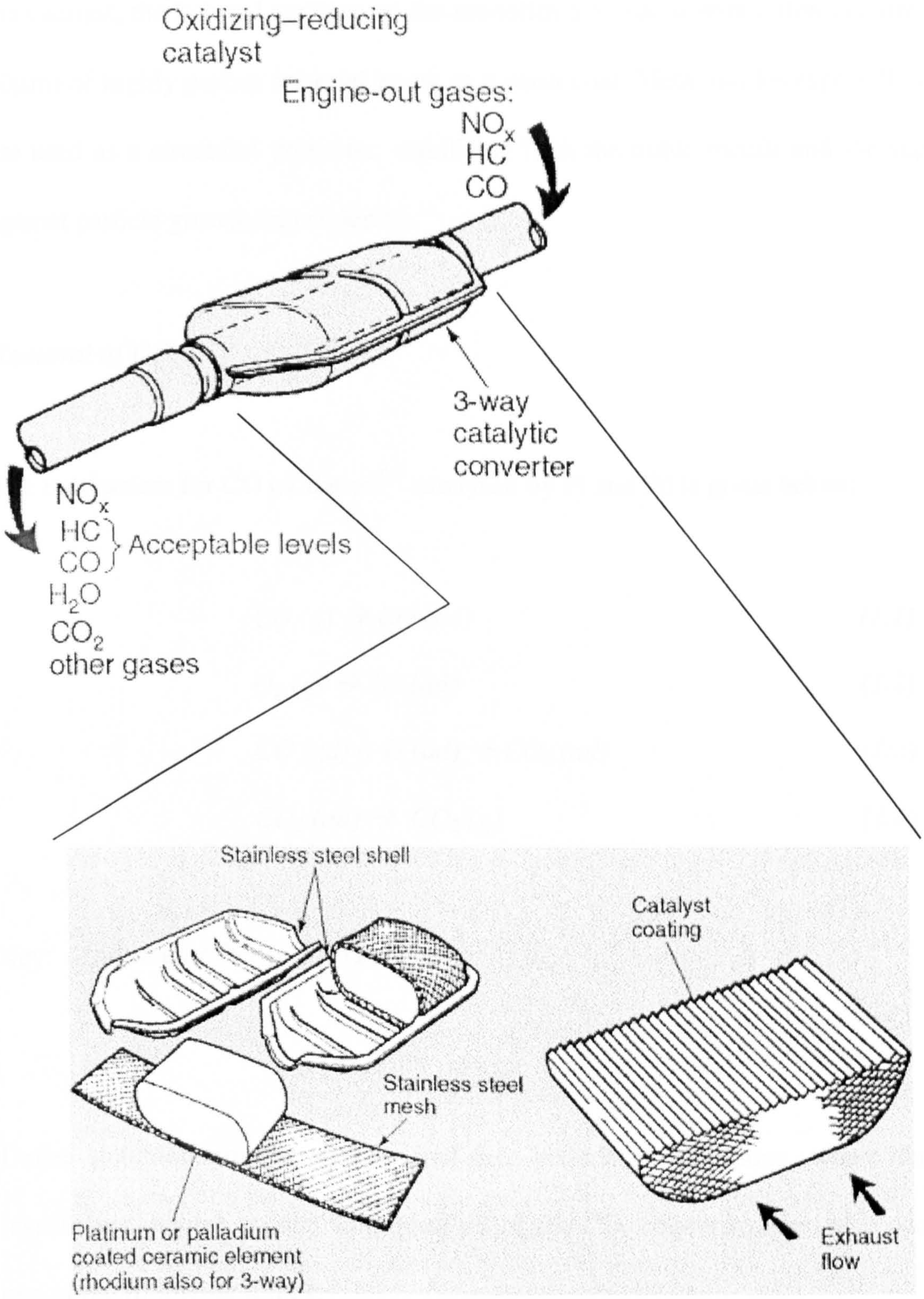

Figure 1.3. Three-way catalytic converter

The noble metals platinum (Pt), palladium (Pd) and rhodium (Rh) are supported on fine particles of high surface area γ-alumina (*ca.* 180 m^2g^{-1}), which is coated onto a porous monolith (extruded ceramic honeycomb). To achieve a large surface area for

the catalyst, the internal surfaces of the monolith are coated with a thin coating (30-50μm) of highly porous material know as a wash coat. Metal oxides especially ceria are used as a structural promoter, stabilising both the noble metals and the support against particle growth and sintering.

Removal of CO

The mechanism for CO oxidation[6,7] catalysed by Pt and Pd is given below:

$$CO\ (g) \rightarrow CO\ (ad) \qquad (1.1)$$

$$O_2\ (g) \rightarrow 2O\ (ad) \qquad (1.2)$$

$$CO\ (ad) + O\ (ad) \rightarrow CO_2\ (ad) \qquad (1.3)$$

$$CO_2\ (ad) \rightarrow CO_2\ (g) \qquad (1.4)$$

Key: (*ad*) = adsorbed; (*g*) = gas

Under stoichiometric or slightly fuel-rich (reducing) conditions, where there is insufficient oxygen present to oxidise all of the CO, conversion can also occur by one of the following routes:

via CO + NO redox reaction:

$$2CO\ (g) + 2NO\ (g) = 2CO_2\ (g) + N_2\ (g) \qquad (1.5)$$

via the water-gas shift (WGS) reaction:

$$CO\ (g) + H_2O\ (g) = CO_2\ (g) + H_2\ (g) \qquad (1.6)$$

The water-gas shift reaction has been reported[8] to be catalysed by Pt and /or Rh, with ceria acting as an excellent promoter. Pt/CeO_2-Al_2O_3 and Pt-Rh/ CeO_2-Al_2O_3 are particularly active combinations for the removal of CO under slightly fuel-rich conditions. The hydrogen produced in this reaction will react, in preference to CO, with any oxygen present. Hence, although the water-gas shift reaction removes CO, it also inhibits CO oxidation by producing hydrogen, which will remove any O_2 present:

$$H_2\,(g) + \tfrac{1}{2}O_2\,(g) = H_2O\,(g) \qquad (1.7)$$

Removal of HC

HC oxidation:

$$HC\,(g) + O_2\,(g) \rightarrow CO_2\,(g) + H_2O\,(g) \qquad (1.8)$$

(not balanced)

Pt is the main component responsible for oxidation of the hydrocarbons.

When the engine exhaust gas composition is reducing (fuel-rich), hydrocarbons compete effectively with CO for oxygen, and they can also react with water vapour to produce CO and H_2 – a reaction known as steam reforming:

$$C_nH_m\,(g) + nH_2O\,(g) = nCO\,(g) + (n + m/2)H_2\,(g) \qquad (1.9)$$

This is catalysed by Rh and/or Pt with ceria and, as in the case of water-gas shift reaction, the combination Pt-Rh/CeO_2-Al_2O_3 is particularly active. The H_2 produced may react preferentially with any O_2 present, thus reducing the amount of oxygen available to react with the HC and CO. In addition, the CO produced adds to the amount of carbon monoxide to be removed.

Removal of NO

Under the conditions of the catalytic converter, the decomposition of NO to O_2 and N_2 over noble metal catalysts is too slow to be significant. When the A/F ratio is stoichiometric (or below stoichiometric), NO can be removed by reduction with CO and/or HC.

In principle a variety of products can be formed, especially:

$$2NO\,(g) + 2CO\,(g) = N_2\,(g) + 2CO_2\,(g) \qquad (1.10)$$

$$2NO\,(g) + CO\,(g) = N_2O\,(g) + CO_2\,(g) \qquad (1.11)$$

In addition, H_2 produced from the water-gas shift or steam reforming reactions can reduce NO to N_2, N_2O or NH_3:

$$2NO\,(g) + 2H_2\,(g) = N_2\,(g) + 2H_2O\,(g) \qquad (1.12)$$

$$2NO\,(g) + H_2\,(g) = N_2O\,(g) + H_2O\,(g) \qquad (1.13)$$

$$2NO\,(g) + 5H_2\,(g) = 2NH_3\,(g) + 2H_2O\,(g) \qquad (1.14)$$

The aim of the catalyst is to selectively promote production of N_2, rather than N_2O (a greenhouse gas) or NH_3 (a general pollutant). Any number of these reactions may be occurring simultaneously as the A/F ratio goes through its cycle about the stoichiometric composition.

When the exhaust gas is close to its stoichiometric balanced composition, at an A/F ratio of about 14.7:1, the concentration of oxidising gases (NO and CO_2) and reducing gases (HC and CO) are matched and in theory it should be possible to achieve complete conversion to produce only CO_2, H_2O and N_2. This is the objective of the TWC and so, ideally, it should be operated in a narrow band or window close to the stoichiometric ratio, within which it will promote simultaneously the nearly complete reduction of NO_x to N_2 and the nearly complete oxidation of CO and HC to CO_2 and H_2O. In practice however this can be hard to control and an oxygen-storage component[8-12] can be added to dampen the effect of the oscillations of the engine between reducing and oxidation conditions.

Oxygen Storage Components

Oxygen storage is the ability of the catalyst to store excess oxygen during fuel-lean conditions (net oxidising conditions) and then release it during fuel-rich conditions (net reducing conditions) where there is limited oxygen to oxidise HC and CO. One of the functions of ceria added to the washcoat in the TWC is as an oxygen- storage component. This is due to the activity of the redox couple Ce^{IV}-Ce^{III} with its ability to form Ce^{IV} (CeO_2) under oxidising conditions and Ce^{III} (Ce_2O_3) under net reducing conditions.

1.2.2 Iron Oxides

The overall objective of this project has been to study iron- containing oxides, their reduction and reoxidation properties, their stability as a function of temperature and other properties relevant to their use as potential oxygen-storage components for automobile exhaust catalysts. Iron oxide was chosen as previous studies have shown[13] that iron- containing materials exhibit some properties suitable for this application. Iron oxides[14] are also some of the cheapest and most abundant of all metal oxides. Iron- containing oxides derived from Fe_3O_4, γ-Fe_2O_3 and α-Fe_2O_3 were therefore examined. The conversion of Fe_3O_4, γ–Fe_2O_3 and α-Fe_2O_3 arises because of the similarity in structure of Fe_3O_4 and γ–Fe_2O_3 and the phase conversion to α-Fe_2O_3 when heated to higher temperatures. Fe_3O_4 is oxidised to γ-Fe_2O_3 and undergoes phase transition to α-Fe_2O_3 at higher temperatures.

Fe_3O_4

Fe_3O_4 (magnetite) is a mixed Fe^{II}/Fe^{III} oxide. It has an inverse spinel- related structure. Spinel- related materials take the form $M^{II}M_2^{III}O_4$ and in the normal spinel the oxide ions form a cubic close packed (ccp) lattice with the M^{II} ions occupying tetrahedral *A* sites and M^{III} ions octahedral *B* sites (Figure 1.4). In the inverse spinel structure half the M^{III} ions occupy tetrahedral sites, with the M^{II} and the other half of the M^{III} occupying octahedral sites.

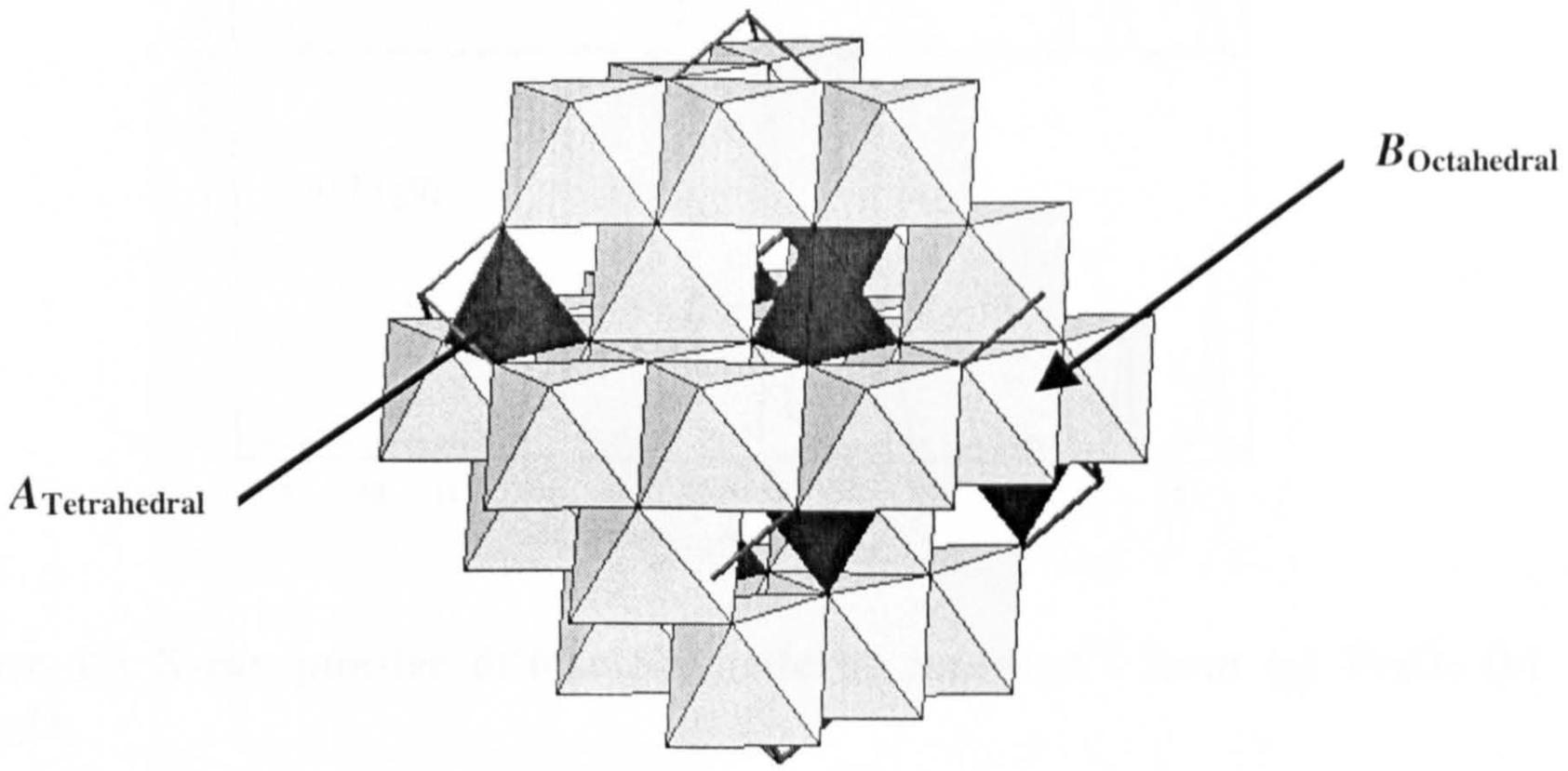

Figure 1.4 Spinel structure

Fe_3O_4 occurs naturally as the mineral magnetite or Lodestone. It is a black, ferrimagnetic substance, insoluble in water and acid. The X-ray powder diffraction pattern[15,16] for Fe_3O_4 is shown in Figure 1.5a, showing the main peak at *ca.* 36° 2θ.

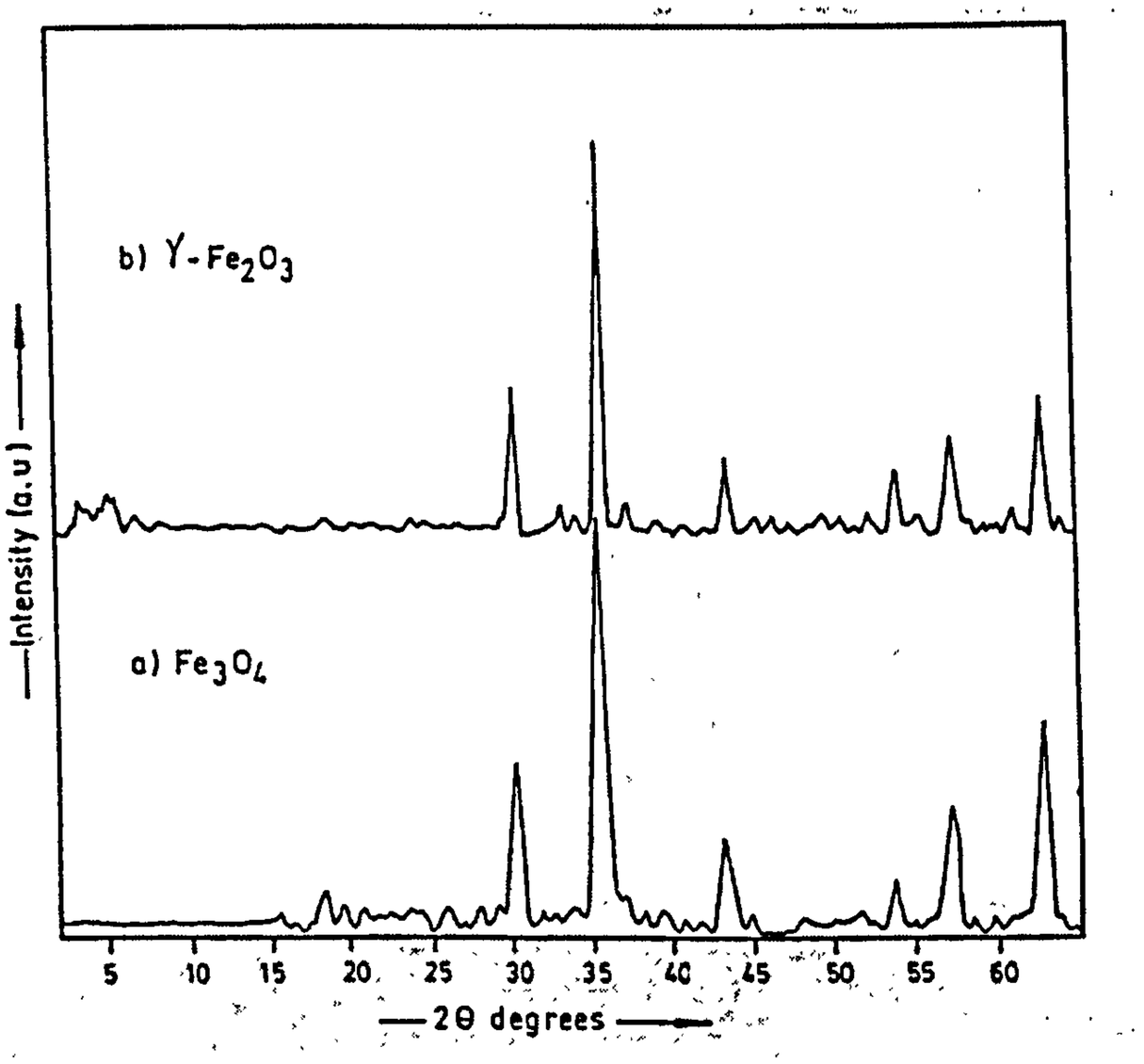

Figure 1.5 X-ray powder diffraction patterns recorded[16] from (a) Fe_3O_4 (b) γ–Fe_2O_3

The structure of magnetite has been investigated by ^{57}Fe Mössbauer spectroscopy over a variety of temperature ranges[17-23]. The ^{57}Fe Mössbauer spectrum of Fe_3O_4 at 298 K is composed of two components. One, with a magnetic hyperfine field of 49 T is associated with iron on the tetrahedral *A* sites and the other, with a magnetic hyperfine field of 46 T, is associated with iron on the octahedral *B* sites (Figure 1.6). Table 1.1 shows the ^{57}Fe Mössbauer parameters of some iron oxides.

Table 1.1 Literature Mössbauer parameters of some iron oxides[17,23]

Sample	δ (+/- 0.02) mms^{-1}	Δ (+/- 0.02) mms^{-1}	H (+/- 1) T
Fe_3O_4	0.67	0.03	46
	0.27	-0.05	49
α-Fe_2O_3	0.37	-0.09	51
γ-Fe_2O_3	0.32	-0.01	49

The magnetic hyperfine field (H) is somewhat diminished when the particles are small. When the particle size is less than *ca.* 100 Å then a doublet (Δ *ca.* 0.7 mms^{-1}) characterises the small particles.

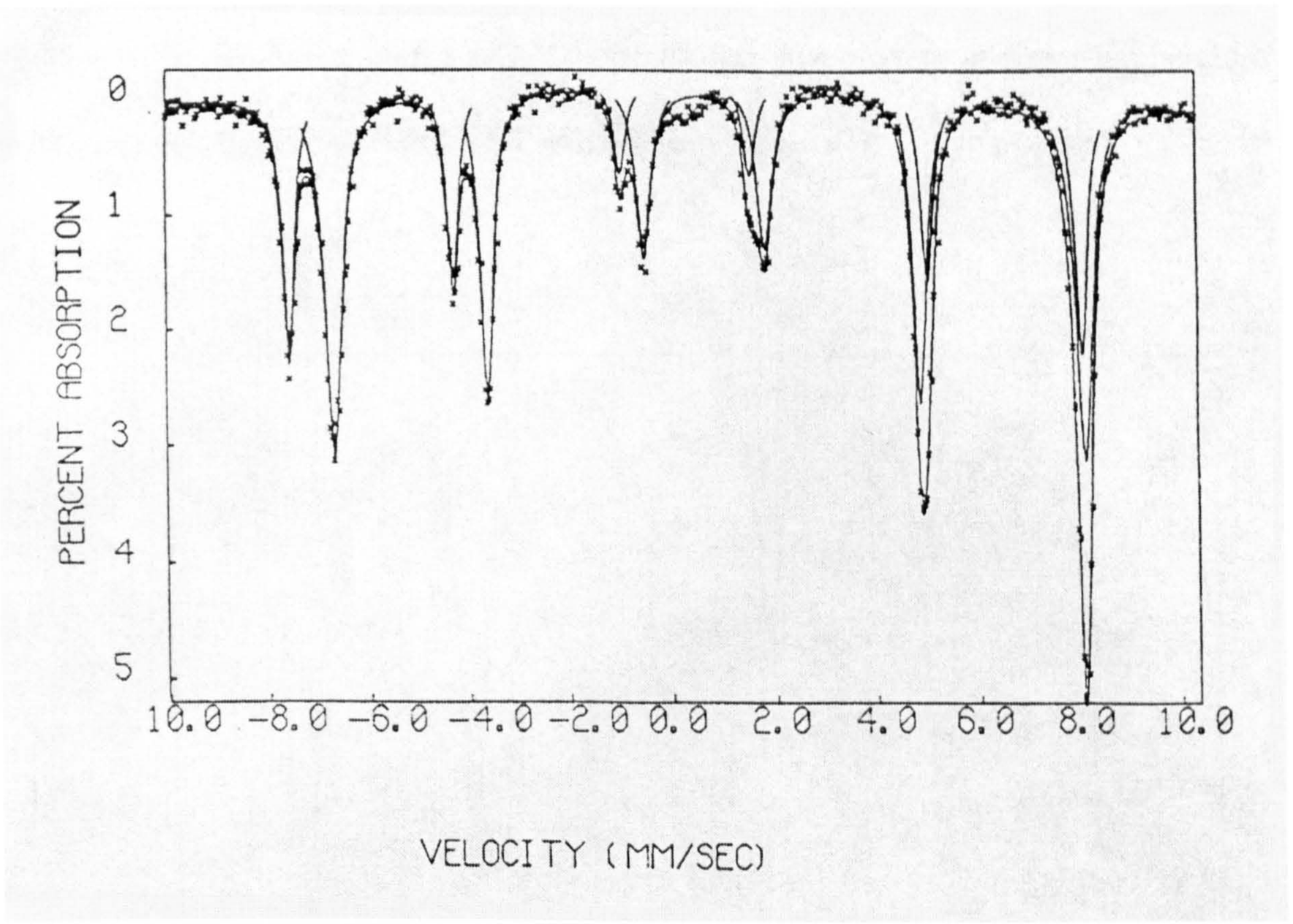

Figure 1.6 ^{57}Fe Mössbauer spectrum recorded from Fe_3O_4[23] at 298 K

γ-Fe_2O_3

γ-Fe_2O_3 (maghemite) is obtained by controlled oxidation of Fe_3O_4. Like Fe_3O_4 it is cubic close packed (ccp). γ-Fe_2O_3 has a defect spinel structure. There are insufficient Fe^{3+} cations to fill all the *A* and *B* sites so that the stoichiometry corresponds to $Fe_{8/3}\square_{1/3}O_4$ where □ represents a cation vacancy. Antiparallel alignment of the *A* and *B* sublattices makes γ–Fe_2O_3 ferrimagnetic. The X-ray powder diffraction pattern from γ–Fe_2O_3[16,24] is shown in Figure 1.5b. γ–Fe_2O_3 has a similar structure to that of

Fe_3O_4 so their X-ray powder diffraction patterns are very similar and the technique is not a satisfactory one for distinguishing between Fe_3O_4 and γ–Fe_2O_3. However, the ^{57}Fe Mössbauer spectrum of γ–Fe_2O_3 is different from that of Fe_3O_4. At room temperature γ–Fe_2O_3[17,23] shows one sextet with a magnetic hyperfine field of 49 T (Figure 1.7), compared with Fe_3O_4[17,23] which has two sextets at room temperature with magnetic hyperfine fields 46 T and 49 T.

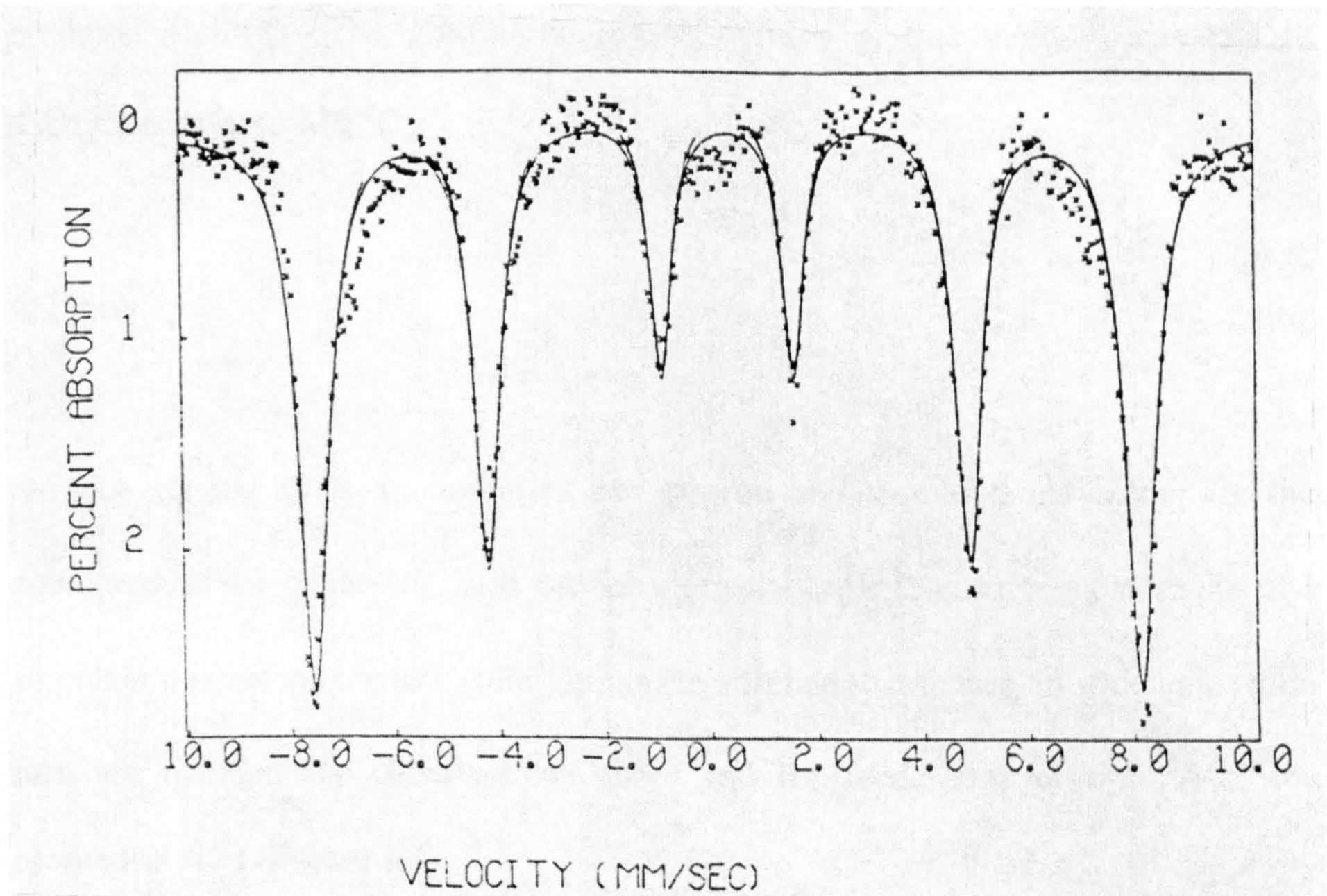

Figure 1.7 ^{57}Fe Mössbauer spectrum recorded from γ–Fe_2O_3[23] at 298 K

The preparation of γ–Fe_2O_3 with different morphologies and particle sizes[16,25-29] is of special interest in various applications e.g. as catalysts, magnetic solids and pigments. Small magnetic particles are of special interest since they show different properties from those of the bulk materials. Such magnetic materials lead to technological applications in ferrofluids, catalysts and magnetic recording materials.

Numerous methods for the synthesis of metal oxide nanoparticles have been reported. γ–Fe_2O_3 is normally made by oxidation of Fe_3O_4. Other methods, which have been used to synthesise γ–Fe_2O_3, are hydrolysis and pyrosol methods[25], inert gas condensation[26] and microwave plasma techniques[27].

The phase transition from γ–Fe_2O_3 to α-Fe_2O_3 has been studied by a number of workers[26,28,30-34]. The transition temperature depends on particle size, impurities and synthesis methods. The general consensus opinion is that γ–Fe_2O_3 converts to α-Fe_2O_3 at around 350 °C.

α-Fe_2O_3

α-Fe_2O_3 (hematite) is an important ore of iron and its blood red colour (in the powdered form) renders it as a useful pigment. α-Fe_2O_3 is the most stable and abundant polymorph of iron. α-Fe_2O_3 has the corundum structure, in which the oxide ions are hexagonally close packed (hcp) and the ferric ions occupy $^2/_3$ of the octahedral sites (Figure 1.8).

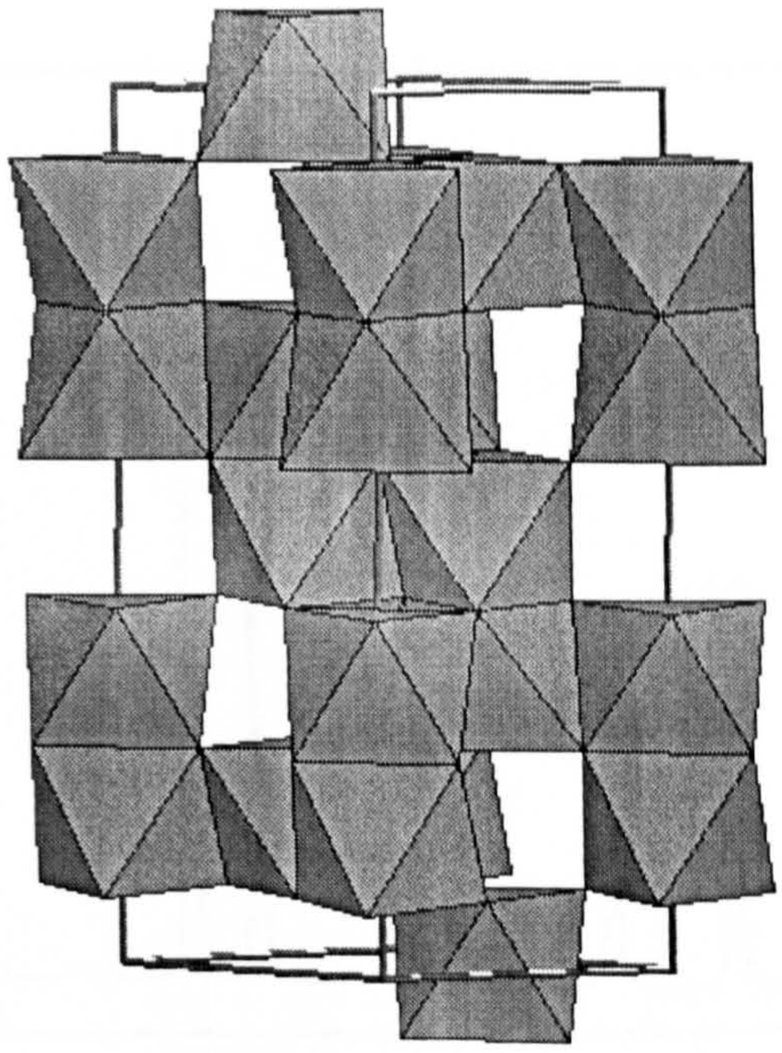

Figure 1.8 Corundum structure

The X-ray powder diffraction pattern from α–Fe_2O_3[32,35] is shown in Figure 1.9. The ^{57}Fe Mössbauer spectrum recorded from α-Fe_2O_3[17,23] at 298 K is shown in Figure 1.10, which shows a sextet with magnetic hyperfine field 51 T and quadrupole splitting of *ca.* –0.1 mms^{-1}.

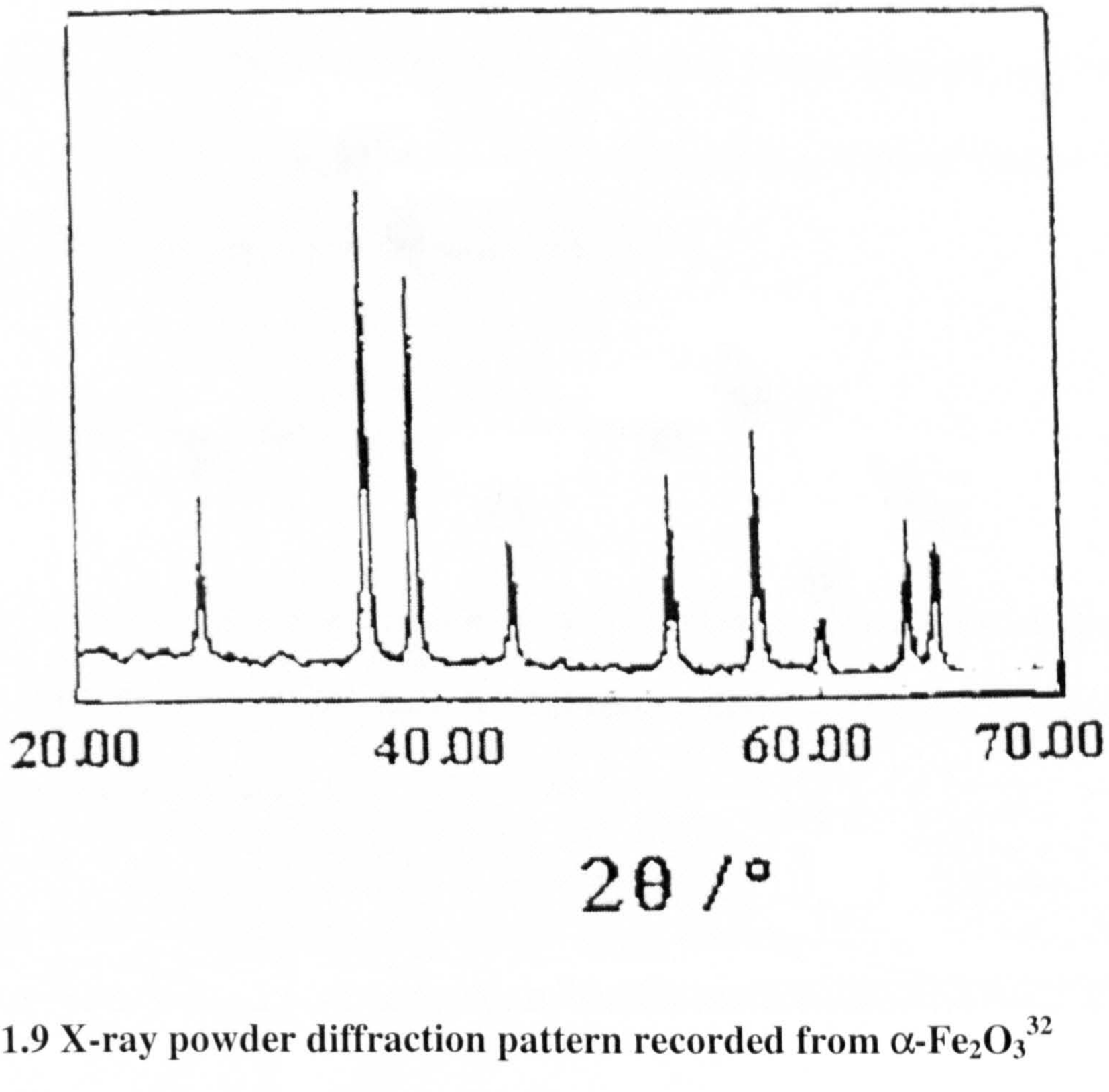

Figure 1.9 X-ray powder diffraction pattern recorded from α-Fe_2O_3[32]

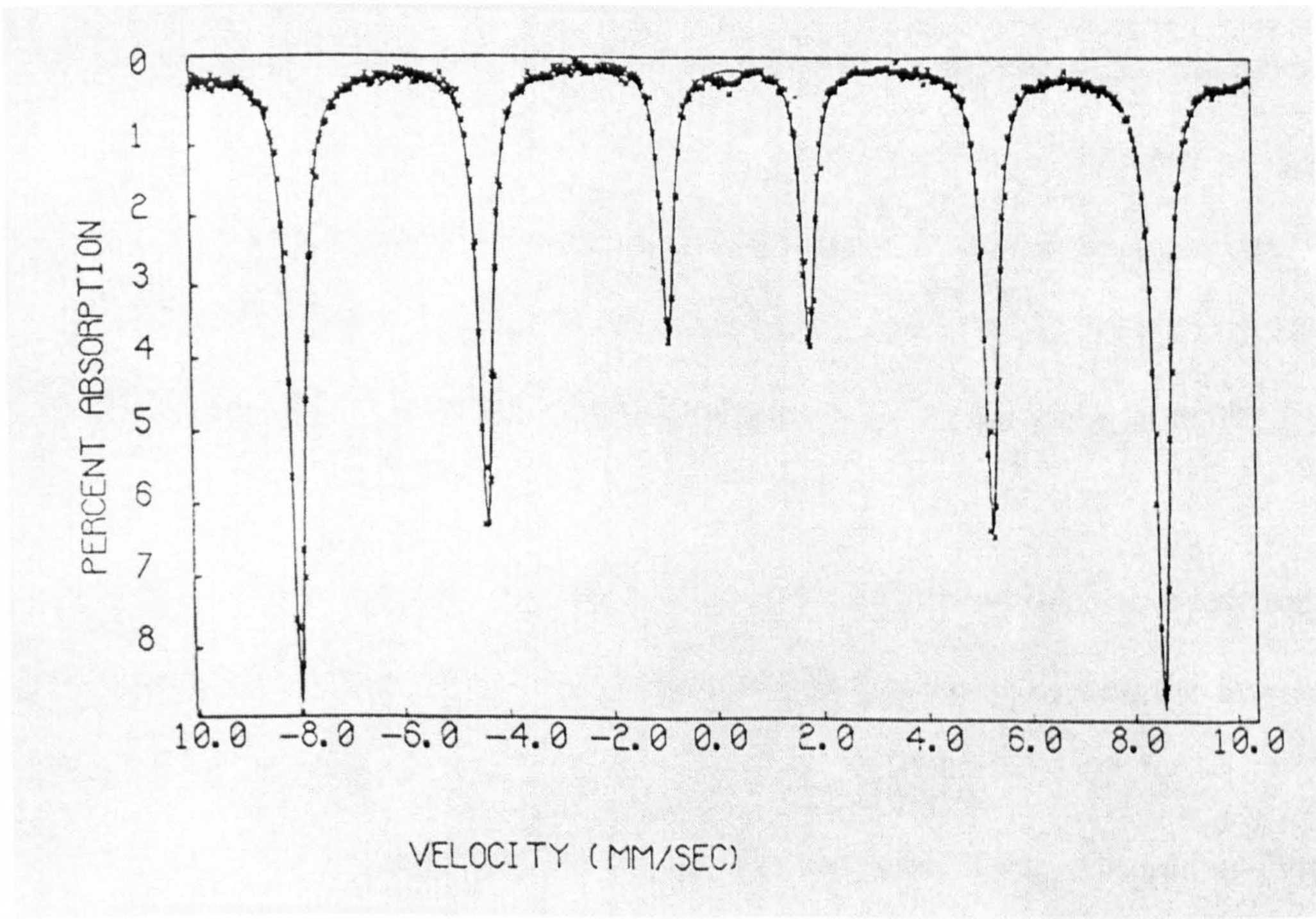

Figure 1.10 ^{57}Fe Mössbauer spectrum recorded from α-Fe_2O_3[23] at 298 K

α-Fe_2O_3 has complex magnetic properties being antiferromagnetic at low temperature, then undergoing a transition above the Morin temperature (260 K) to a weak ferrimagnetic state as a result of spin canting, before finally becoming paramagnetic at temperatures exceeding 948 K.

1.2.3 Doped Iron Oxides

Metal doped iron oxides have found a number of uses in a variety of applications. These include high frequency transformer cores, magnetic memories, and heterogeneous catalysts.

Doped Fe_3O_4

The minerals titanomagnetite, $Fe_{3-x}Ti_xO_4$, may be considered as a solid solution series between Fe_3O_4 (magnetite) and Fe_2TiO_4 (ulvospinel). Materials of composition $Fe_{3-x}Sn_xO_4$ have been considered to adopt the same inverse spinel structure as that observed in titanomagnetite[34]. $Fe_{3-x}Ti_xO_4$ and $Fe_{3-x}Sn_xO_4$ have both been prepared[34] by heating stoichiometric quantities of powdered titanium (IV)- or tin (IV)- oxide, iron (III) oxide and metallic iron in sealed evacuated quartz ampoules at 900°C for 24 hours.

Rietveld structure refinement[30] of the X-ray powder diffraction data recorded from tin-doped Fe_3O_4 showed the tin to substitute on the octahedral sites of the inverse spinel-related structure.

Berry et al also reported[36] that the tin K-edge Extended X-ray Absorption Fine Structure (EXAFS) of compound of composition $Fe_{3-x}Sn_xO_4$ ($x < 0.3$) showed the tin

to be co-ordinated by six oxygen atoms and thereby demonstrated that tin adopts the octahedral, as opposed to the tetrahedral, sites of the inverse spinel-related structure. X-ray photoelectron spectroscopy (XPS) showed that the incorporation of tin was accompanied by the partial reduction of Fe^{3+} to Fe^{2+}.

Results[37] from atomistic simulation calculations were used to refine the defect structures of Fe_3O_4 with tetravalent ions. The calculations confirmed that occupation by Sn^{4+} and Ti^{4+} of octahedral sites in Fe_3O_4 is more favourable than occupation of tetrahedral sites and indicated that the M^{4+} ions substitute on iron sites rather than occupy interstitial sites. The results suggested that charge balance is achieved by reduction of Fe^{3+} to Fe^{2+} on a site adjacent to M^{4+}.

^{119}Sn Mössbauer spectroscopy has shown[34] the existence of a magnetic hyperfine field on the tin site demonstrating an interaction between Fe^{3+} ions on the tetrahedral *A* sites and Sn^{4+} ions on the octahedral *B* sites of Fe_3O_4[34]. ^{57}Fe Mössbauer spectroscopy showed the Curie temperatures of the materials to be lower than those of magnetite and related titanomagnetites[34]. The ^{57}Fe Mössbauer and ^{119}Sn Mössbauer spectra also showed the exsolution of tin from the tin-doped magnetite after prolonged treatment at elevated temperatures[34].

Doped γ–Fe_2O_3

Tin K- edge Extended X-ray Absorption Fine Structure (EXAFS)[30,31] recorded from tin-doped γ-Fe_2O_3 prepared by boiling a precipitate derived from iron (III), iron (II) and tin (II) under reflux, showed that the material adopts an inverse spinel-related structure containing tin on the octahedral sites. The material was converted to α-Fe_2O_3 at 527 °C, as compared to pure γ-Fe_2O_3 which converts to α-Fe_2O_3 at *ca.* 377 °C[30].

X-ray photoelectron spectroscopy[37] (XPS) recorded from tin- doped γ–Fe_2O_3 provided no evidence for the reduction of Fe^{3+} to Fe^{2+} to have occurred in contrast to tin- doped Fe_3O_4. The authors[37] described vacancy formation as a balancing defect.

Doped α-Fe_2O_3

The structural characteristics of tin- and titanium- doped α-Fe_2O_3 prepared by hydrothermal methods have been investigated[30,31, 38-40] by Rietveld structure refinement of the X-ray powder diffraction data. The analysis revealed that the dopant ions adopt two distinct sites: in addition to partially substituting at the octahedral iron sites, they also occupy the interstitial octahedral sites which are vacant in the α-Fe_2O_3 structure. The defect structures can be related to the lines of octahedral Fe^{3+} ions, which are directed along [001] in the structure of α-Fe_2O_3. In the parent phase, pairs of face-sharing FeO_6 octahedra exist due to ordered octahedral vacancies: the chain can be represented -Fe-Fe-□-Fe-Fe-□- and is shown in Figure 1.11(a). For M^{4+} (M = Sn, Ti) the occupancy of interstitial and substitutional sites is shown in Figure 1.11(b) where local charge balance in the -Fe-Fe-□-M-□-M-□-M-□-Fe-Fe- chains arises from three M^{4+} ions replacing four Fe^{3+} ions. The result was endorsed by interatomic potential calculations[41]. The model contrasted with that proposed[39] for M^{2+} incorporation in which charge balance was achieved via the formation of MMM triplets: -Fe-Fe-□-Fe-M-M-M-Fe-□-Fe-Fe- in which three M^{2+} ions replaced two Fe^{3+} ions (Figure 1.11(c)).

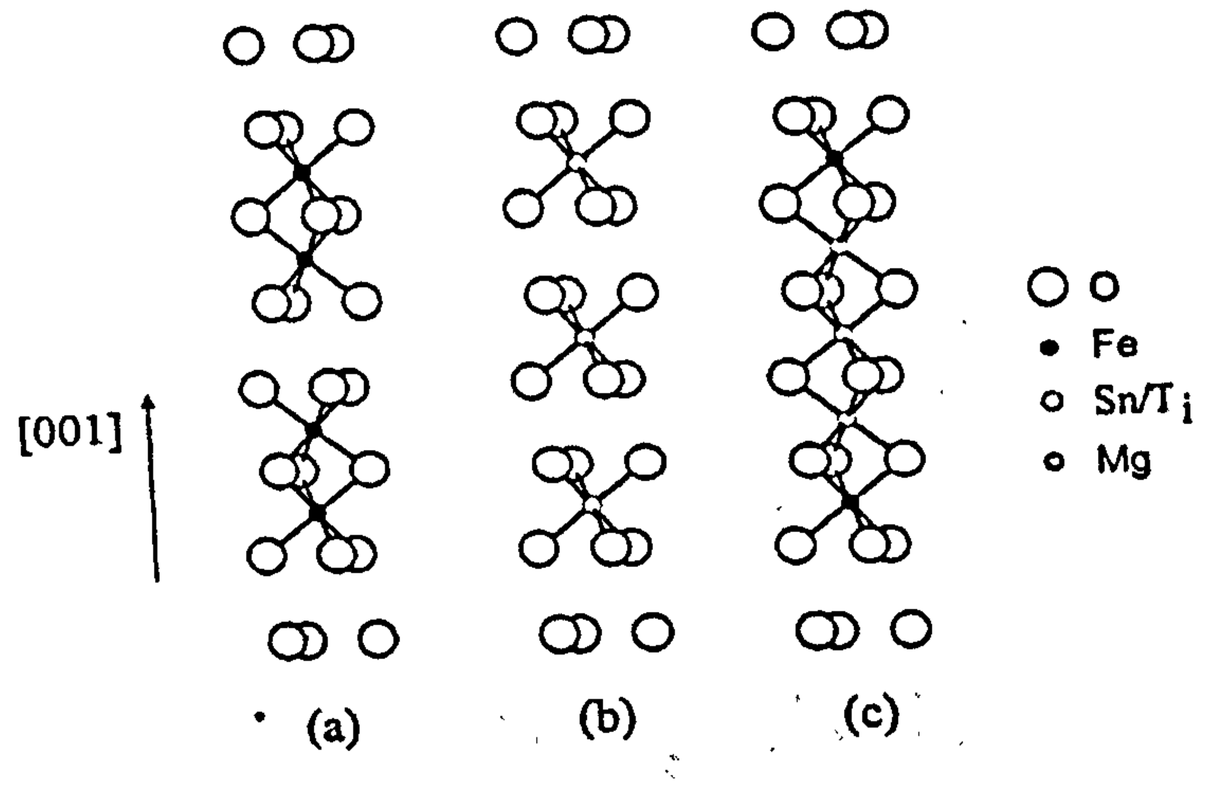

Figure 1.11 (a) Linking of FeO_6 octahedra in α-Fe_2O_3, (b) structural model involving the substitution of $4Fe^{3+}$ ions by $3M^{4+}$ ions, (c) structural model involving the substitution of $2Fe^{3+}$ ions by $3M^{2+}$ ions

References

1. J.C. Guilbet, "Fuels and Engines: Technology · Energy · Environment", Vol 1, Editions Technip, Paris, 1999.
2. J.C. Guilbet, "Fuels and Engines: Technology · Energy · Environment", Vol 2, Editions Technip, Paris, 1999.
3. K.C. Taylor, "Automobile Catalytic Converters", Catalyst and Automotive Pollution Control, Elsevier Science Publishers B.V. Amsterdam, 1987.
4. M. Shelef and G.W. Graham, *Catal. Rev.-Sci. Eng.*, 1994, 36, 433.
5. H.S. Gandi and M. Shelef, "The Role of Research in the Development of New Generation Automotive Catalyst", Catalyst and Automotive Pollution Control, Elsevier Science Publishers B.V. Amsterdam, 1987.
6. T. Engel and G. Ertl, *J. Chem. Phys.*, 1978, 69, 1267.
7. T. Engel and G. Ertl, *Adv. Catal.*, 1979, 28, 1.

8. A. Trovarelli, *Catal. Rev. Sci. Eng.*, 1996, 38, 439.

9. A.F. Diwell, R.R. Rajaram, H.A. Shaw and T.J. Truex, "The Role of Ceria in Three-Way Catalyst", Catalyst and Automotive Pollution Control II, Elsevier Science Publishers B.V. Amsterdam, 1991.

10. H.C. Yao and Y.F. Yu Yao, *J.Catal.*, 1984, 86, 254.

11. J.G. Nunan, H.J. Robota, M.J. Cohn and S.A. Bradley, "Physico-Chemical Properties of Ce-Containing Three-Way Catalyst and the Effect of Ce on Catalyst Activity", Catalyst and Automotive Pollution Control II, Elsevier Science Publishers B.V. Amsterdam, 1991.

12. D.Terribile, J. Llorca, M. Boaro, Carla de Leitenburg, G. Dolcetti and A. Trovarelli, *Chem. Commun.*, 1998, 1897.

13. J.M. Fisher, T.I. Hyde and D. Thompsett, U.K. Patent PCT/GB98/00325, 1998.

14. N.N. Greenwood and A. Earnshaw, "Chemistry of the Elements", Pergamon Press, Oxford, 1984.

15. JCPDS Index Card No. 19-0629 Fe_3O_4.

16. C.V.Gopal Reddy, K. Kalyana Seela and S.V. Manorama, , *International J. Inorg. Mater.*, 2000, 2, 301.

17. N.N. Greenwood and T.C. Gibb, "Mössbauer Spectroscopy", Chapman and Hall Ltd, London, 1971.

18. A. Ito, K. Ono and Y. Ishikawa, *J. Phys. Soc. Jpn.*, 1963, 18, 1465.

19. W. Kundig and R.S. Hargrove, *Solid State Commun.*, 1969, 7, 223.

20. R.S. Hargrove and W. Kündig, *Solid. State Commun.*, 1970, 8, 303.

21. L. Häggström, H. Annerstein, T. Erricsson, R. Wäppling, W.Karner and S. Bjarman, *Hyp. Int.*, 1978, 5, 201.

22. F.J. Berry, S. Skinner and M.F. Thomas, *J. Phys. Condens. Matter.*, 1998, 10, 215.

23. C.W. Childs and J.G. Baker-Sherman, "Mössbauer Spectra and Parameters of standard samples.1", New Zealand Scientific Report 66, 1984.

24. JCPDS Index Card No. 39-1346 γ–Fe_2O_3.

25. E. Herrero, M.V. Cabañas, M. Vallet-Regí, J.L. Martínez and J.M. González-Calbet, *Solid State Ionics*, 1997, 101-103, 213.

26. G. Schimanke, M.Martin, *Solid State Ionics*, 2000, 136-137, 1235.

27. E. Pellegrin, M. Hagelstein, S. Doyle, H.O. Moser, J. Fuchs, D. Vollath, S. Schuppler, M.A. James, S.S. Saxena, L. Niesen, O. Rogojanu, G. A. Swatzky, C. Ferrero, M. Borowski, O. Tjernberg and N.B. Brookes, *Phys. Stat. Sol.*, 1999, 215, 797.

28. C. Pascal, J.L. Pascal, F. Favier, M.L.E. Moubtassim and C. Payen, *Chem. Mater.*, 1999, 11, 141.

29. D. Chen and R. Xu, *J. Solid State Chem.*, 1998, 137, 185.

30. F. J. Berry, C. Greaves, Ö. Helgason and J. McManus. *J. Mater. Chem.*, 1999, 9, 223.

31. F.J. Berry, C. Greaves, Ö. Helgason, K. Jonsson, J. McManus and S. Skinner, "Structure and Properties of Tin-Doped Metal Oxides", Mössbauer Spectroscopy in Materials Science, Ed. M. Miglierini and D. Petridis, 1999.

32. X.S. Ye, D.S. Lin, Z.K. Jiao and L.D. Zhang. *J. Phys.D-Applied Phys.*, 1998, 31, 2739.

33. S. Grimm, T. Stelzner, J. LeuthauBer, S. Barth and K. Heide, *Thermochimica Acta*, 1997, 300, 141.

34. F.J. Berry, Ö. Helgason, K. Jonsson and S.J. Skinner, *J. Solid State Chem.*, 1996, 122, 353.

35. JCPDS Index Card No. 33-0664 α-Fe_2O_3.

36. F.J. Berry, S.J. Skinner, Ö. Helgason, R. Bilsborrow and J.F. Marco, *Polyhedron*, 1998, 17, 149.

37. E.A. Moore, A. Bohórquez, F.J. Berry, Ö. Helgason and J.F. Marco, *J. Phys. Chem. Solids*, 2001, 62, 1277.

38. F.J. Berry, C. Greaves, J. McManus, M. Mortimer and G. Oates. *J. Solid State Chem.*, 1997, 130, 272.

39. F.J. Berry, A. Bohórquez, C. Greaves, J. McManus, E.A. Moore, and M. Mortimer, *J. Solid State Chem.*, 1998, 140, 428.

40. F.J. Berry, C. Greaves, Ö. Helgason, J. McManus, H.M. Palmer and R.T. Williams, *J. Solid State Chem.*, 2000, 151, 157.

41. F.J. Berry, A. Bohórquez and E.A. Moore, *Solid State Commun.*, 1999, 109, 207.

Chapter 2

THEORY OF EXPERIMENTAL TECHNIQUES

Chapter 2

THEORY OF EXPERIMENTAL TECHNIQUES

2.1 X-ray Powder Diffraction (XRD)

XRD has been used routinely for the characterisation of crystalline solids for many years. The theory of X-ray diffraction has been understood since the early part of the 20th century. The use of X-ray diffraction as a structural technique has been explained in detail in standard textbooks[1-3].

2.1.1 Theory of XRD

When an X-ray beam strikes an atom the interaction between the X-radiation and the electrons in the atom results in a scattering of X-rays in all directions. If the diffracted X-rays are in phase then constructive interference can occur and if they are out of phase then destructive interference will occur. An incident X-ray beam will be diffracted by a crystal and the diffraction is described by Bragg's Law.

Bragg's approach was to consider the crystals as being built in layers, or planes, such that each acts as a semi-transparent mirror. The planes allow some of the X-ray beams to be reflected at the same angle as the angle of incidence (Figure 2.1).

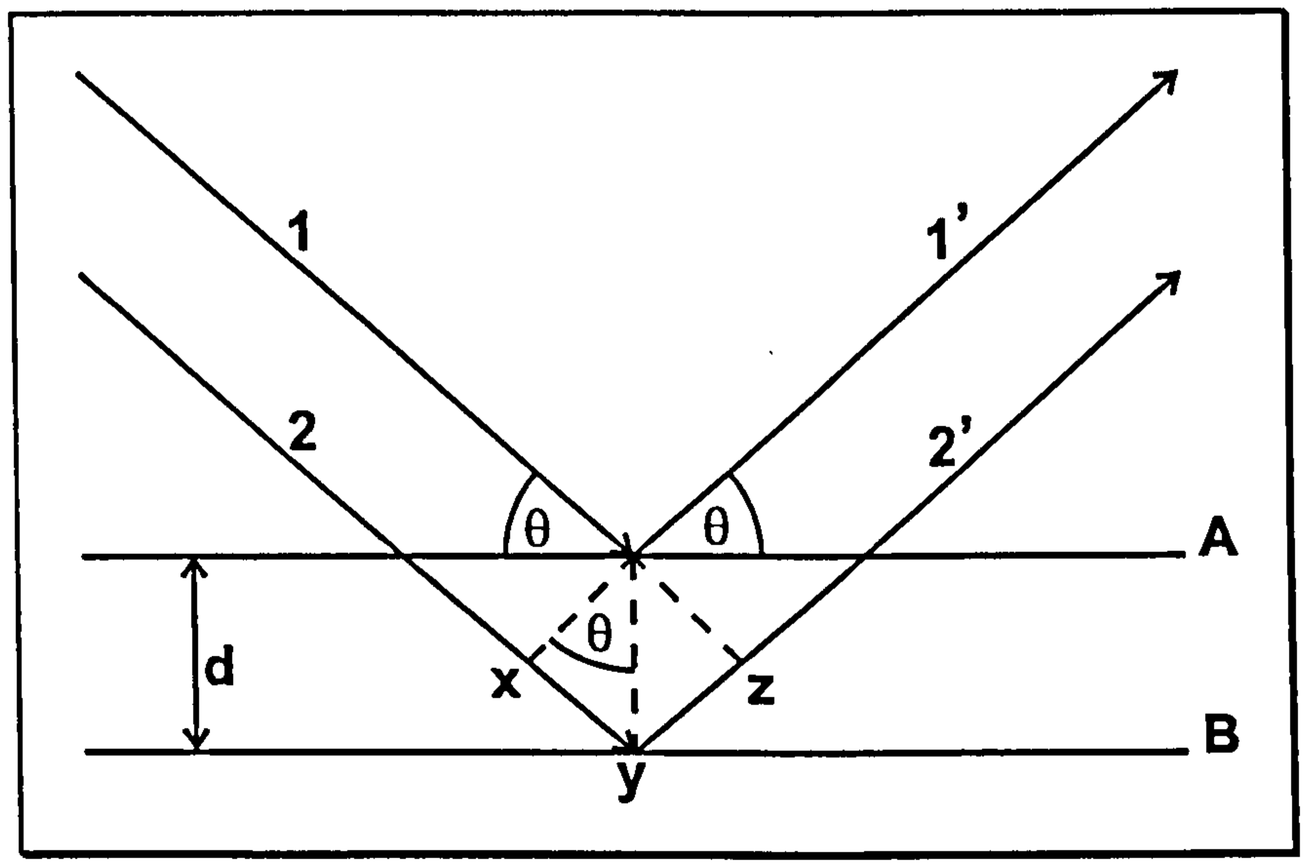

Figure 2.1 Schematic representation of derivation of Bragg's law.

The incident beams 1 and 2 are reflected by planes A and B to form beams 1' and 2', the condition under which these beams are in phase with each other is approached as follows. Beam 2 2', shown in Figure 2.1, has to travel a further distance, xyz, as compared to beam 1 1'. For 1'and 2' to be in phase with each other, xyz must equal n, where n is an integer and is equivalent to the number of wavelengths. The perpendicular spacing, d, and angle of incidence, θ, called the Bragg angle, are related by :

$$xy = yz = d \sin \theta \qquad (2.1)$$

$$\Rightarrow \quad xyz = 2\, d \sin \theta \qquad (2.2)$$

$$\text{Since} \quad xyz = n\lambda \qquad (2.3)$$

$$\Rightarrow \quad n\lambda = 2\, d \sin \theta \qquad (2.4)$$

When the above equation, (2.4) Bragg's Law, is satisfied the reflected beams are in phase and thus constructively interfere. If the angle is not correct then usually

interference of a destructive nature will occur. It can be seen that many solutions are possible i.e. $n = 1,2,3$.

2.1.2 The Powder Method.

The basic principle of the powder method is shown in Figure 2.2. A powder sample is a random assembly of crystallites, a monochromatic beam of X-rays strike the powdered sample such that every orientation is possible. As a result, for every diffraction plane there are some crystals correctly oriented at the Bragg angle and hence some diffraction occurs.

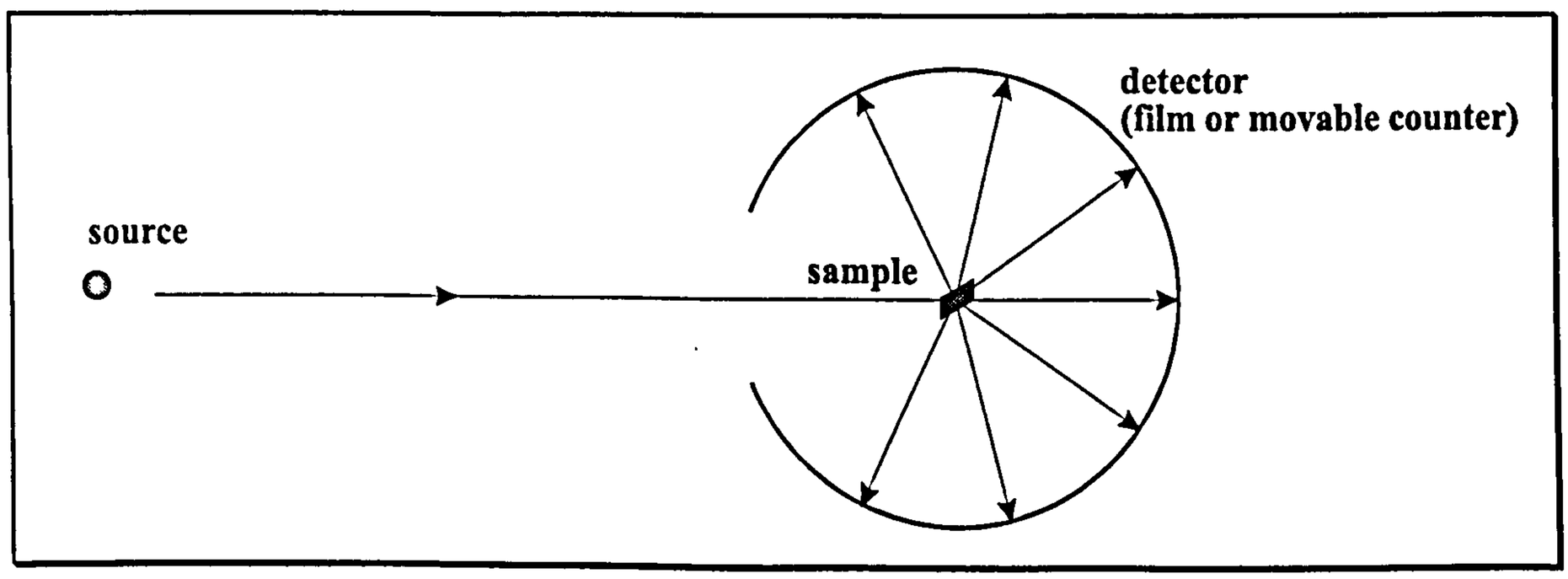

Figure 2.2 A schematic representation of the powder method.

The diffracted beam can be detected by one of two means, a photographic plate surrounding the sample, or a movable detector, connected to a computer. The original photographic method, called the Debye-Scherrer method, is little used in modern X-ray diffraction practices. A modern diffractometer can collect accurate positional and intensity data both quickly and easily. This enables the phase composition to be determined in less than an hour, with the recorded pattern being matched against standard patterns.

2.1.3 Diffractometer

The collection of X-ray powder diffraction data is routinely carried out on a diffractometer, such as shown in Figure 2.3:

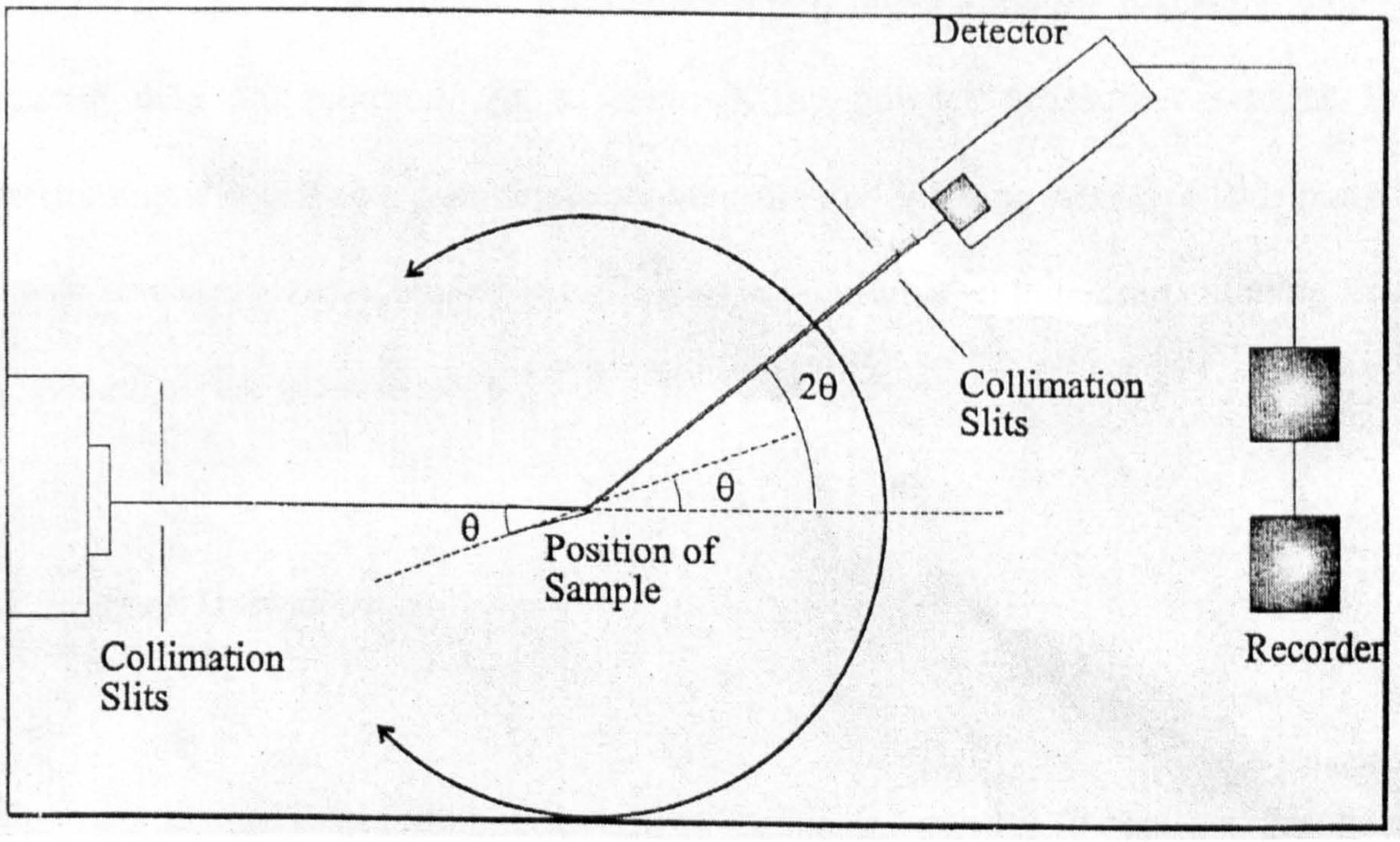

Figure 2.3 Schematic representation of a standard X-ray diffractometer.

The X-rays are generated in an X-ray tube, where electrons are bombarded against a metal target, usually copper. This bombardment results in the evolution of X-rays. The X-rays are then collimated into a pencil like beam. The beam then passes through the sample, which is rotating around a central axis, and is diffracted. This diffracted beam is then passed through a further set of collimation slits to remove X-ray scattering. The X-rays are then counted in a detector moving around the central axis, at an angle of rotation twice that of the sample.

2.1.4 Unit Cell Sizes.

The calculation of unit cell parameters is usually carried out using computer modelling techniques using one of a variety of programs, an example of such a program is PowderCell[4].

Since the calculation of unit cell parameters is dependent upon the d-spacing, highly accurate data are required. As a result, X-ray powder diffraction patterns for determining unit cell size parameters are measured over a long period of time (*ca.* 12 h) with fine step sizes. Coupled to the higher resolution is an increased counting time to increase signal to noise ratio.

2.1.5 Peak Intensities

There are many factors which can affect the peak intensity, a few are described below.

i) Structure Factor.

The peak intensity is influenced by the position of the atom in the unit cell and the atom type. If an atom has a high atomic number then it will scatter X-rays better than an element with a low atomic number, e.g. Cs scatters better than Li giving greater intensity.

ii) Multiplicity Factor.

For a cubic system, lattice planes such as (013), (031), (103), (130), all have the same d-spacing where a = b = c. In a powder XRD pattern the variable co-ordinate is

d-spacing, therefore reflections which give rise to the same d-spacing will be superimposed. As a result a more intense peak will be observed.

iii) Preferred orientation.

This occurs if the powder is poorly ground or if the powder is not completely oriented randomly. This effect can cause some intensities to be increased while others are decreased.

iv) Temperature factor.

Thermal vibrations of atoms cause a decrease in the observed peak intensity with an increase in background scatter. This effect is usually only important for experiments performed at high temperature.

2.1.6 Crystallite Size Measurement

It is possible to measure the crystallite size from X-ray powder diffraction patterns using the effect of line broadening on the diffraction pattern. The relationship between the mean dimension of the crystallites in a powder, D, and the pure X-ray diffraction broadening, β, was first determined by Scherrer, and is discussed in detail by Klug and Alexander[5].

Scherrer related the mean dimension, D, to the pure diffraction broadening, β, by the equation;

$$D = \frac{K\lambda}{\beta \cos\theta} \qquad (2.5)$$

where K is a constant approximately equal to unity, θ is the diffraction angle and λ is the wavelength of the X-radiation.

2.2 Mössbauer Spectroscopy

2.2.1 Theory of Mössbauer Spectroscopy

Mössbauer spectroscopy is a technique which involves the resonant absorption and emission of gamma rays by nuclei. This phenomenon was first observed by Rudolf Mössbauer in ^{191}Ir in 1958, and led to the development of the technique which now bears his name. Many detailed accounts of the theory and instrumentation of Mössbauer spectroscopy can be found in the literature[6-8].

In Mössbauer spectroscopy the γ-ray source consists of a solid matrix in which a radioactive isotope is embedded which then decays into the Mössbauer isotope in an excited state which subsequently relaxes with the emission of a γ-ray. For resonant absorption the energy of the γ-ray must not be influenced by nuclear recoil, to achieve this the Mössbauer nuclei are held in a rigid crystal lattice. If the energy of the nuclear recoil associated with the absorption and emission of γ-rays is small in comparison to the lowest quantised lattice vibration, recoil free transitions suitable for a Mössbauer experiment can occur. In the case of ^{57}Fe the γ-ray energy is small (14.4 keV), and thus recoil effects are small.

The energy of the transition between the excited and ground state of the Mössbauer nucleus is usually different in the source and absorber. Therefore, rarely does the

energy of the incident γ-ray correspond to the energy transition of the absorber Mössbauer nucleus. The γ-ray energy is therefore modified by the Doppler effect and is achieved by vibration of the source at a velocity of millimetres per second. Thus, a Mössbauer spectrum consists of a plot of γ-ray counts against γ-ray energy. The γ-ray energy is presented in terms of the velocity of the source. A typical Mössbauer spectrum obtained from a sample in which the Mössbauer atoms are in the same cubic environment in both source and absorber is presented in Figure 2.4.

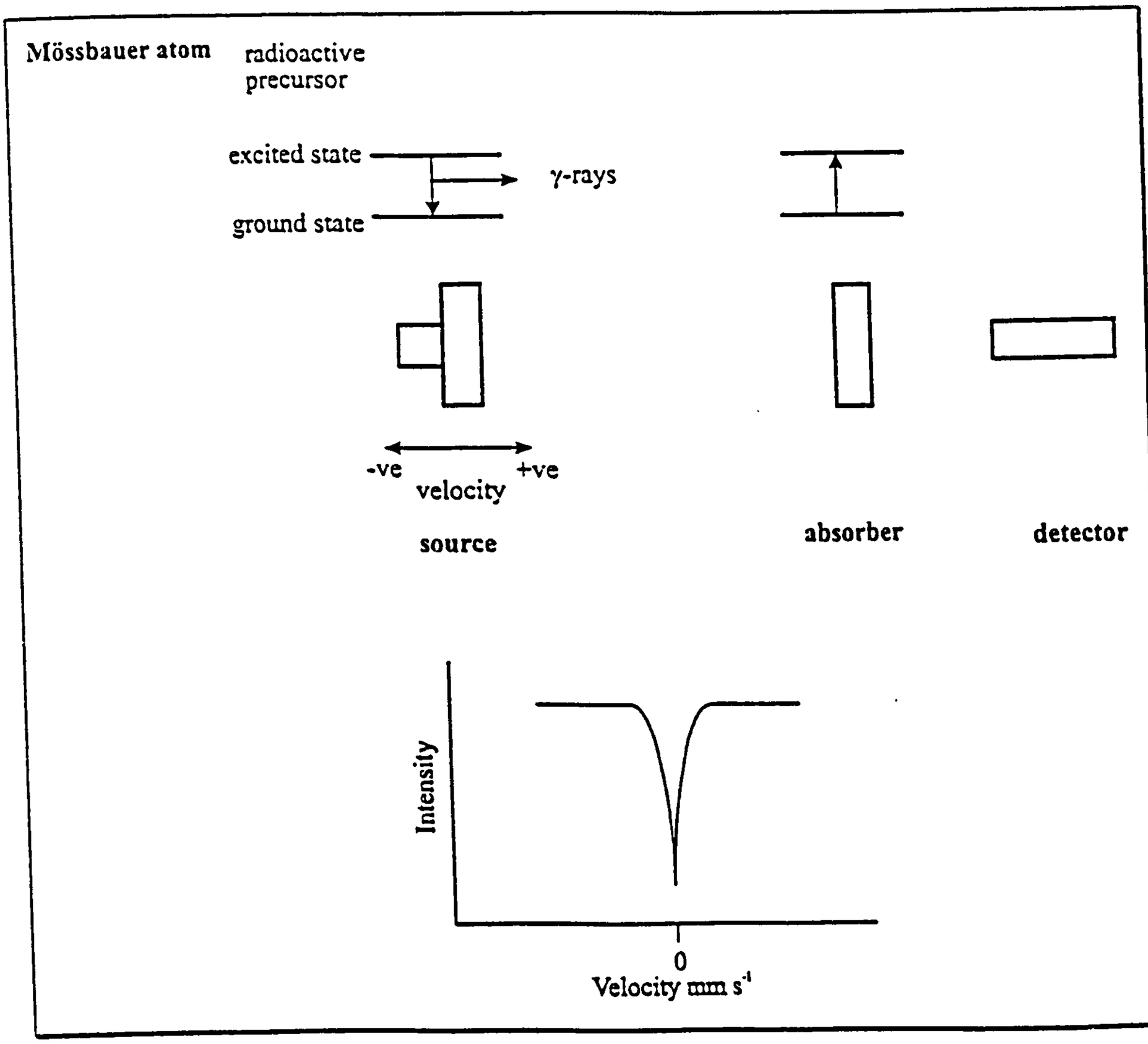

Figure 2.4 Schematic representation of a Mössbauer spectroscopy experiment.

Differing environments about the nucleus in the absorber atom give rise to hyperfine interactions which give the Mössbauer parameters known as isomer shift, quadrupole splitting and magnetic hyperfine splitting. These arise because of the electric monopole interaction, electric quadrupole interaction and magnetic dipole interaction respectively.

2.2.2 Isomer Shift

To understand the origin of the isomer shift it is useful to consider a nucleus stripped of its electrons. In such a nucleus the energy of the transition between ground and excited states may be represented as E, in the Figure 2.5(a).

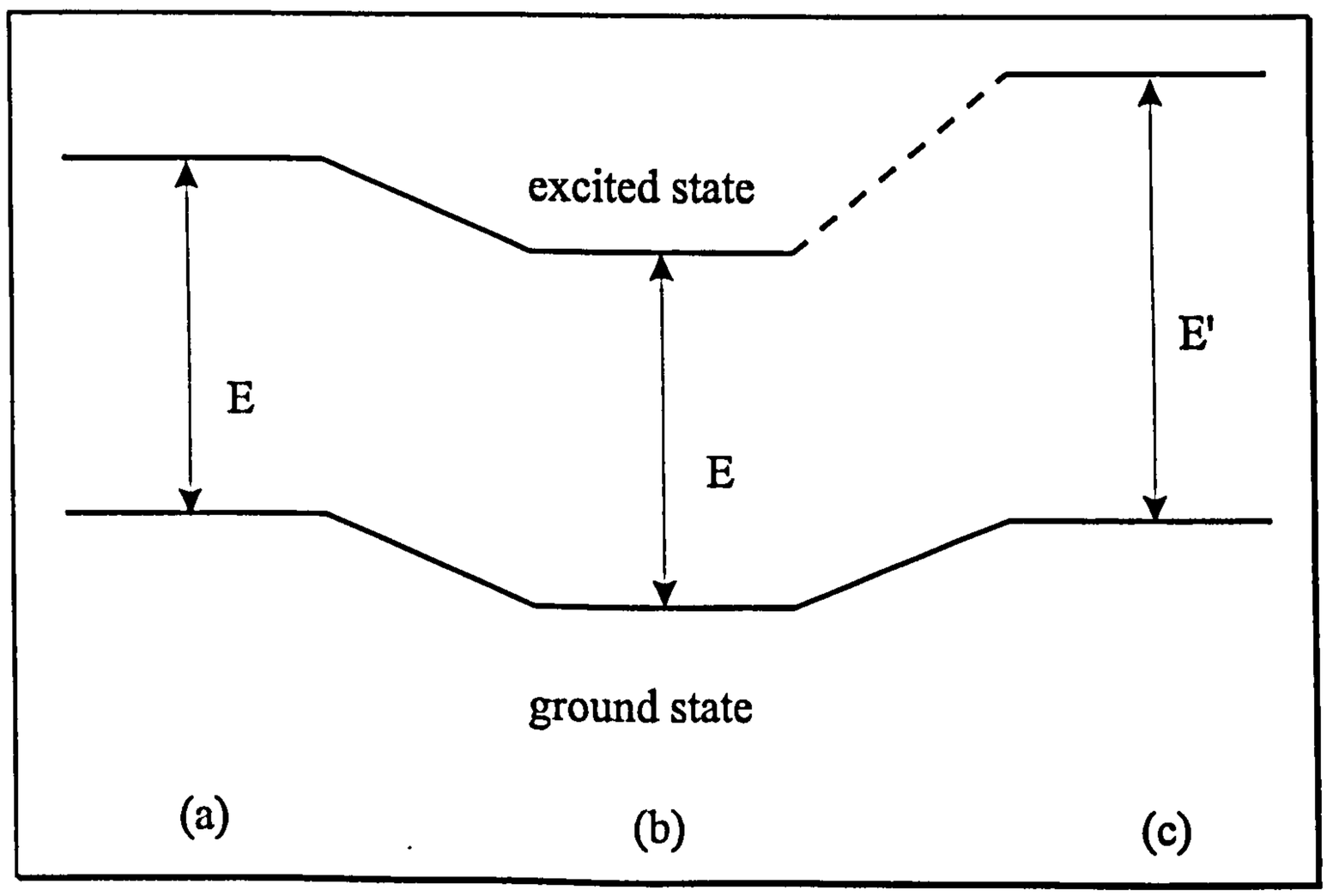

Figure 2.5 Nuclear energy level of (a) bare nucleus, and a nucleus where the excited and ground states are (b) the same size and (c) differing sizes.

If the nucleus is surrounded by electrons a Coulombic attraction between the nuclear and the electronic charges occurs which modifies the nuclear energy levels. If in both

the excited and ground states the size of the nuclei is the same, then the interaction of these states with the electrons will be the same. Hence the energy levels will be changed by the same amount, as will the energy of the transition E, in Figure 2.5(b). If, alternately, the size of the nuclei in the two states is different, as usually arises, the energies of the ground and excited states will be modified to a different extent, consequently the energy of the transition will be modified to a new value E', Figure 2.5(c).

The nuclear energy levels depend upon the electronic environment. Therefore if the source and absorber nuclei are in different electronic environments then the nuclear energy levels will be modified to differing degrees, Figure 2.6(a). The energy of the emitted γ-ray is then modified by the Doppler effect and the Mössbauer spectrum will exhibit a resonant absorption shifted from zero velocity, Figure 2.6(b). This is known as the isomer or chemical isomer shift, δ.

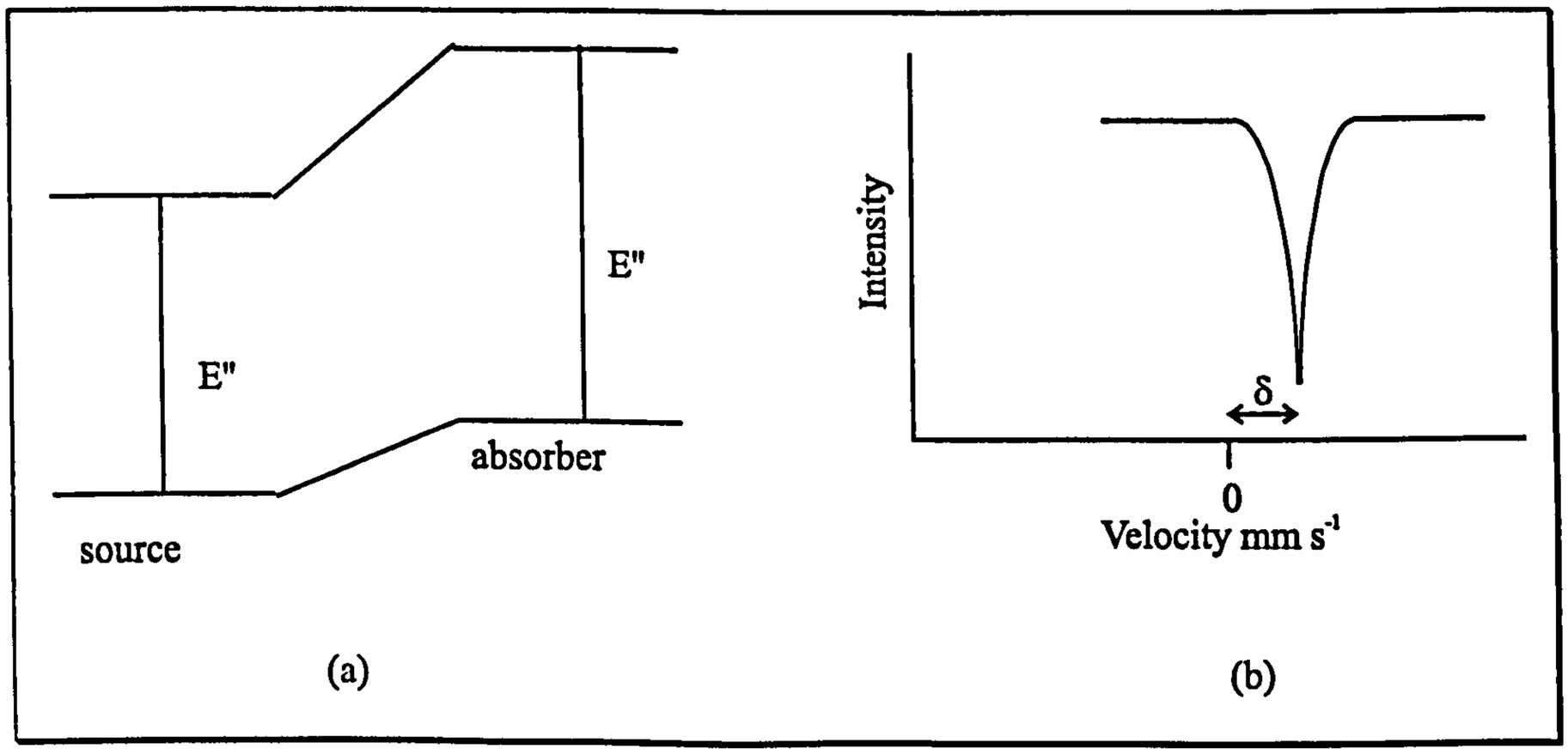

Figure 2.6 (a) Nuclear energy levels of source and absorber atoms in different electronic environments, (b) the resultant spectrum.

The isomer shift can be related to the electronic properties by the equation

$$\delta = constant\ \Delta R/R\ (\Psi^2_s(o)_A - \Psi^2_s(o)_S) \qquad (2.6)$$

where $\Delta R/R$ is $(R_e - R_g)/R_g$ and R_e and R_g are the radii of the excited and ground state nuclei respectively and $\Psi^2_s(o)_A$ and $\Psi^2_s(o)_S$ are the s-electron densities at the absorber and source respectively. $\Psi^2_s(o)$ is dependent primarily on the population of the s-orbitals, but will also be influenced by the occupation of other types of orbitals. This is due to the outer electrons shielding the interaction of the s-electrons from the nucleus. For any particular source the value of $\Psi^2_s(o)_S$ will be constant, and therefore any change in the isomer shift will reflect changes in $\Psi^2_s(o)_A$. Hence information about the electronic environment of the absorber is obtained, which can then be used as a probe of oxidation state.

For ^{57}Fe Mössbauer spectroscopy the value of $\Delta R/R$ is negative. Hence higher s-electron densities at iron nuclei are reflected by a decrease in isomer shift. Another influence on the isomer shift in iron compounds is the effect of shielding. As d-electron removal effectively increases the s-electron density at the iron nuclei, iron(II) species with a d^6 configuration have a more positive isomer shift than iron(III) species with a d^5 configuration. In ^{57}Fe nuclei the magnitude of $\Delta R/R$ is sufficiently large for a range of isomer shifts to exist.

2.2.3 Quadrupole Splitting

If a nucleus has a spin *I* greater than ½ then it will have an asymmetric charge distribution, which gives rise to a nuclear quadrupole moment. It is then possible for the nuclear quadrupole moment to interact with an asymmetric electric field

represented by an electric field gradient. This results in the partial or complete splitting of the nuclear energy levels. As more than one nuclear transition may occur, a multi-line Mössbauer spectrum results. For nuclear transitions the selection rule is $\Delta m = 0, \pm 1$. ^{57}Fe has excited and ground state spins of $^{3}/_{2}$ and $^{1}/_{2}$ respectively, which for this isotope means that the presence of an electric field gradient gives rise to a two line spectrum, shown in Figure 2.7. The distance between the peaks is the quadrupole splitting, Δ.

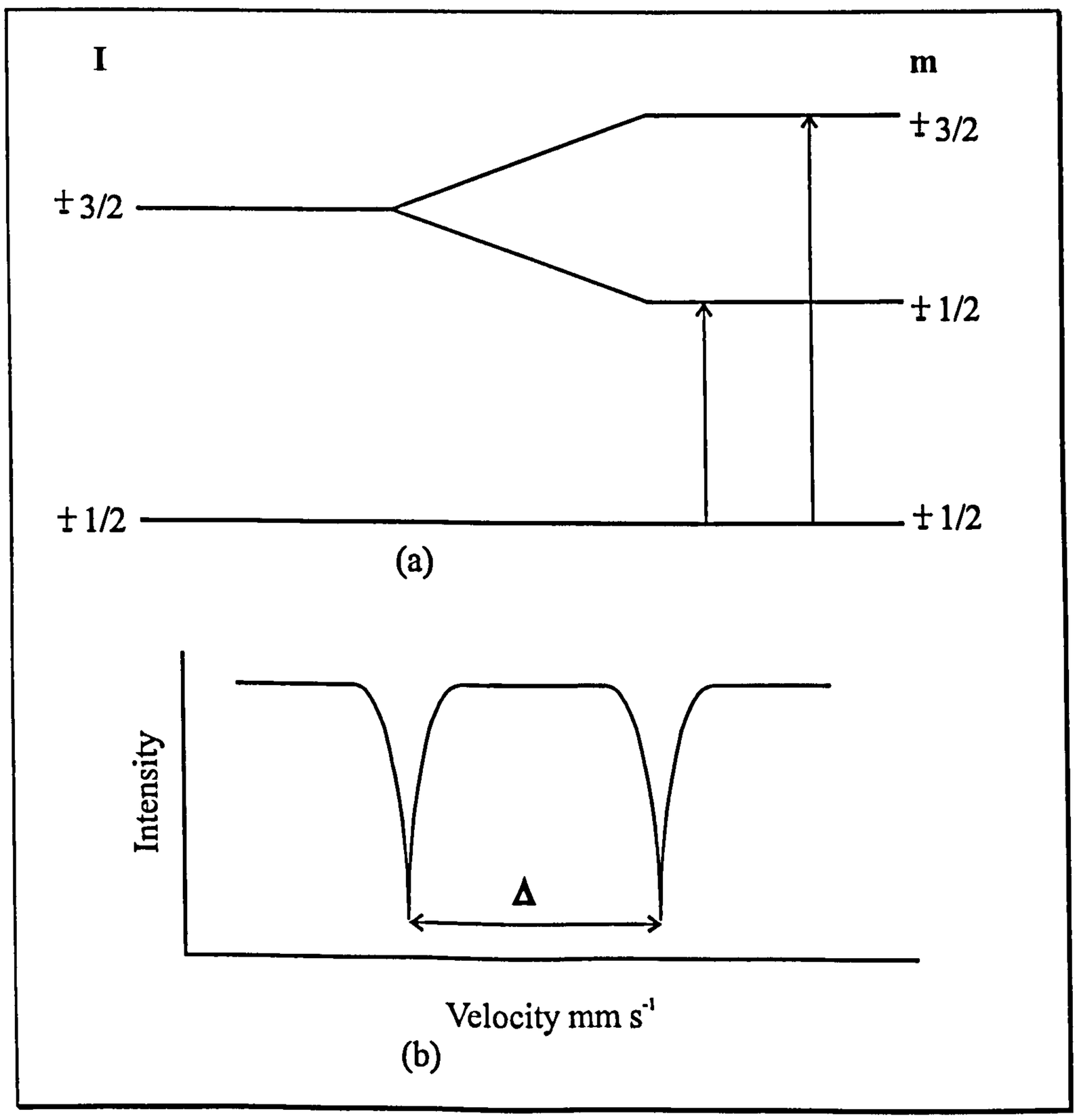

Figure 2.7 (a) Splitting of nuclear energy levels for ^{57}Fe nuclei in the presence of an electric field gradient and (b) resultant spectrum.

Several different components contribute to the electric field gradient. One is from the electronic environment about the nucleus, called the valence term. The valence term can be envisaged as arising from the valence electrons of the Mössbauer atom and originates from asymmetry in the electronic structure which derives from the unfilled or partially filled electron shells occupied by the valence electrons. The main contribution to the valence term is the asymmetric p- and d- electron populations, as the s-electron density is principally symmetric about the nuclear volume. A lattice contribution, arising from surrounding charged entities, also contributes to the electric field gradient. This arises from asymmetry in the arrangement of atoms around the Mössbauer nuclei. Further contributions to the electric field gradient include the effects of molecular orbitals and any polarisation of the core electrons of the Mössbauer atom.

Hence, quadrupole splitting reflects the symmetry of the bonding environment and local structure in the vicinity of the Mössbauer atom. Used in conjunction with chemical isomer shift data, the quadrupole splitting can be used to elucidate the oxidation states, electronic configurations and ligand arrays.

2.2.4 Magnetic Splitting

A nucleus of spin $I > 0$ has a magnetic moment which may interact with a magnetic field via a magnetic dipole interaction. Such a magnetic interaction induces splitting of the nuclear energy levels. Degeneracy of the nuclear states is removed by interaction of the nucleus with the magnetic field, and the levels subsequently split into $2I + 1$ substates. In ^{57}Fe the ground state with $I = ½$ splits into two substates, and the excited state with $I = {}^{3}/_{2}$ splits into four substates. For these spin states the

selection rules $\Delta m = 0, \pm 1$, give rise to a symmetric six line Mössbauer spectrum. In such a spectrum the isomer shift is given as the centroid of the six peaks. The magnetic splitting of the ground and excited states for ^{57}Fe and the resultant spectrum is illustrated in Figure 2.8.

The total magnetic field experienced by the nucleus is a vector sum of the magnetic hyperfine field and any external applied field. The magnetic hyperfine field arises from the spin of any unpaired electrons and is dependent upon oxidation- and spin-state of that atom. Hence, interpretation of the magnetically split Mössbauer spectrum can give information about electronic structure and magnetic properties in a system. It is also possible to modify the hyperfine field by application of an externally applied magnetic field, which distinguishes the hyperfine field from the other Mössbauer hyperfine interactions. Altering the applied field can change the appearance of the spectrum and aid interpretation. The occurrence of magnetically split ^{57}Fe Mössbauer spectra is common among ferro- and antiferro- magnetic materials. Paramagnetic materials cooled to below their Curie temperatures also exhibit a magnetically split Mössbauer spectrum.

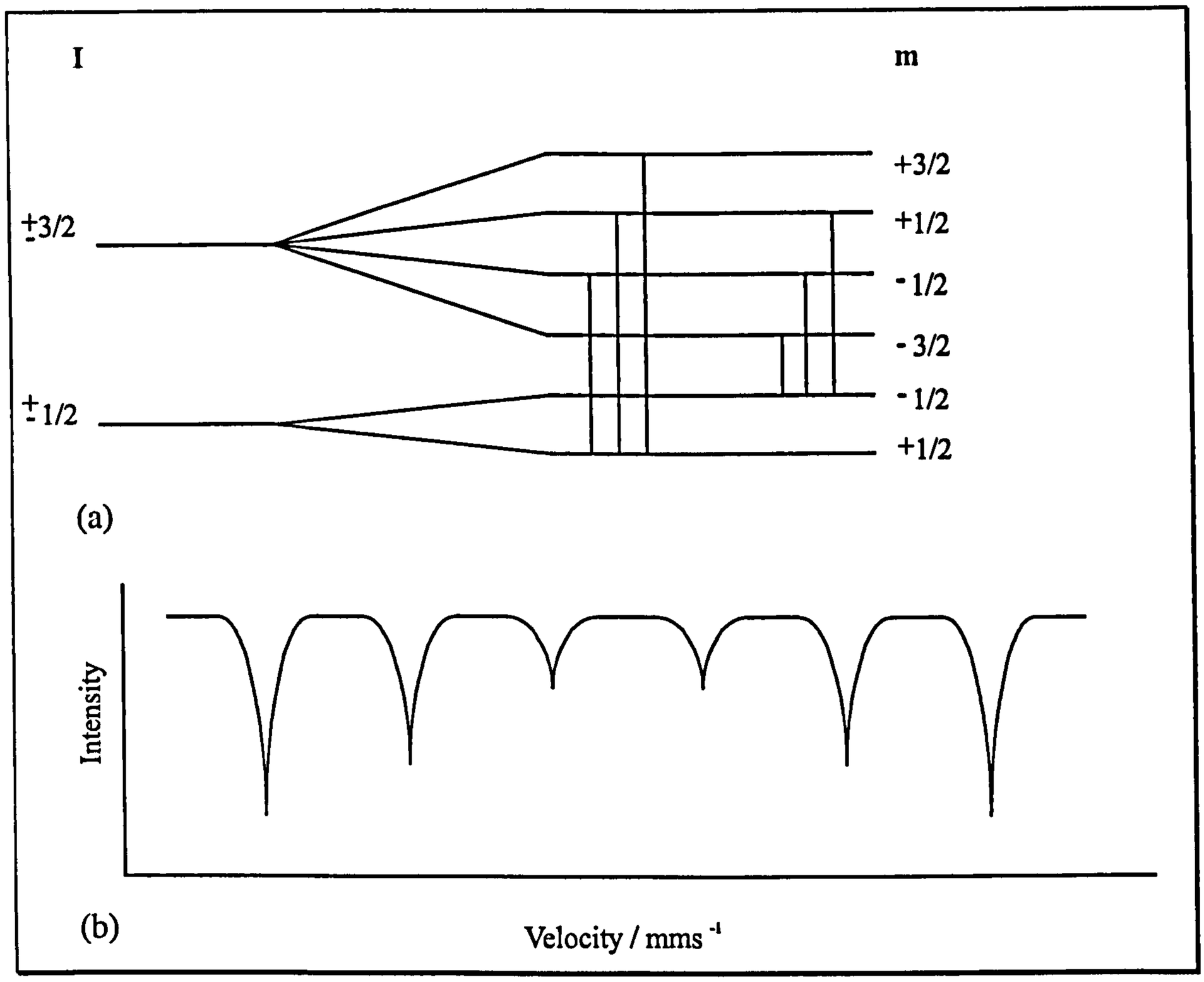

Figure 2.8 (a) Splitting of nuclear energy levels by a magnetic field (b) and resultant spectrum.

2.3 Temperature Programmed Reduction (TPR)

2.3.1 Theory of TPR

Temperature Programmed Reduction (TPR)[9,10] is a thermal-analytical technique used to probe the reducibility of solid compounds. Typically a dilute hydrogen mixture is passed over a sample and the uptake of hydrogen is monitored as the temperature is raised linearly.

2.3.2 Instrumentation

The procedure involves flowing a gas mixture through the reference arm of a kathrometer detector of a gas chromatograph and then over the sample under investigation with the gas mixture returning via a drying tube to the other arm of the kathrometer. Consumption of hydrogen (and therefore reduction) is detected as a voltage imbalance between the two arms of the kathrometer. This is displayed schematically in Figure 2.9.

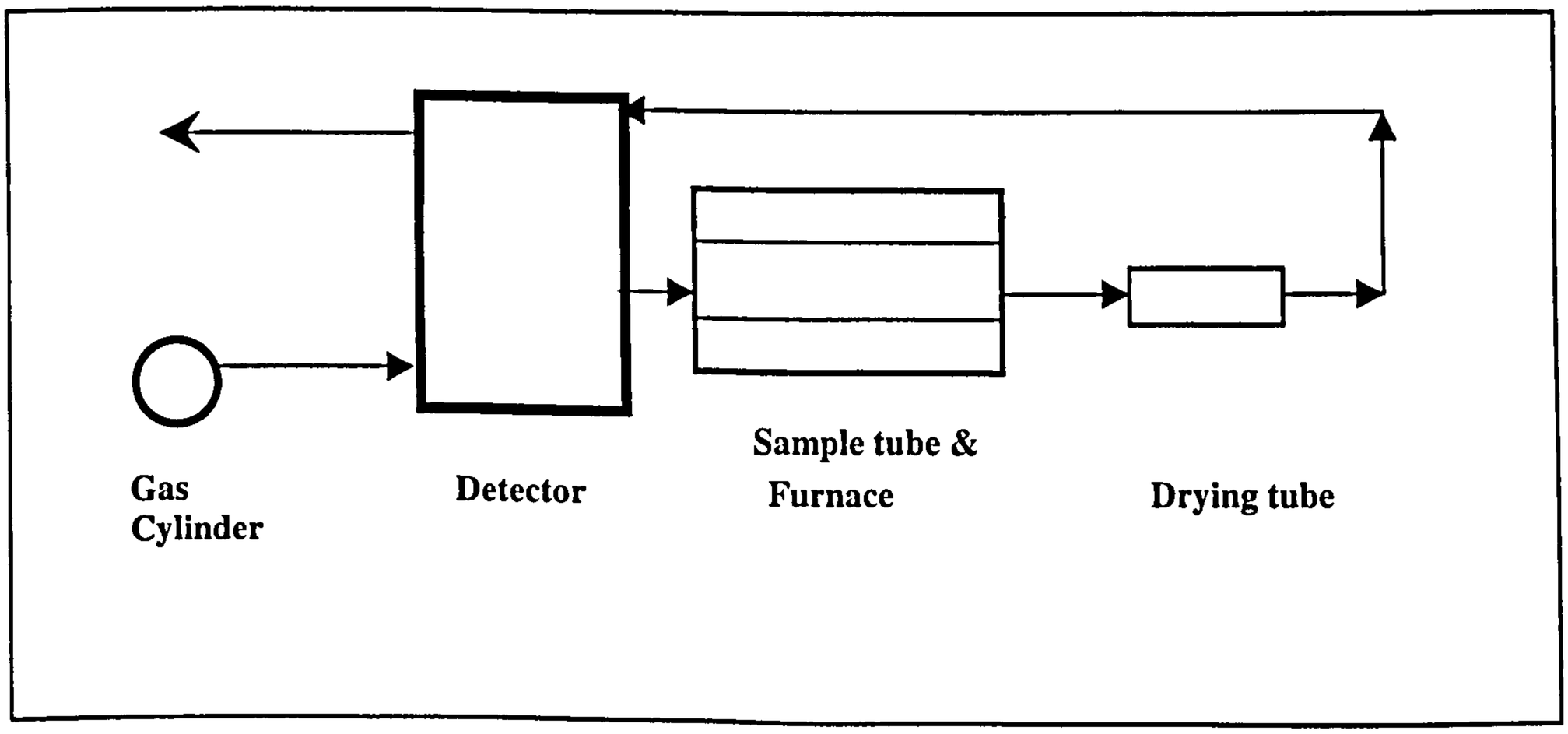

Figure 2.9 Schematic diagram of apparatus used for TPR experiment

2.4 Surface Area Measurements

2.4.1 Theory of Physisorption and Chemisorption

Surface area measurement involves the principles of physical adsorption of a gas onto the surface at low temperatures. If conditions under which a complete monolayer of gas, averaging one molecule thick, can be established and the area per molecule is known, then the quantity of adsorbed gas gives the surface area. A gas will be adsorbed on a solid surface due to the forces acting between the solid and gas. Depending on the nature of the interaction between the solid (adsorbent) and gas (adsorbate) the adsorption can be described as either physisorption or chemisorption. Physisorption involves weak interactions - similar to Van Der Waals forces - with low heats of adsorption, usually at the boiling point of the adsorbate, and can lead to multilayer adsorption. Chemisorption, with much higher heats of adsorption, involves the formation of a chemical bond between the gas and solid and is, therefore, necessarily limited to a monolayer coverage of adsorbate.

The adsorption of gas by a solid is proportional to the mass of the solid sample, the temperature of adsorption, the pressure of the gas and the nature of both the solid and the gas. If constant temperature is assumed then an isotherm can be constructed depicting the relationship between the quantity of gas adsorbed by the solid surface and the relative pressure of the gas. The isotherm that derives from the adsorption of a gas by a non-porous material is commonly referred to as a type II isotherm after the original classification by Brunauer, L.Deming, W.Deming and Teller[11]. From this type II isotherm depicted by a non-porous solid it is possible to calculate the

monolayer capacity, defined as the amount of adsorbate which can be accommodated in a completely filled molecular layer on the surface of unit mass (1 g) of the solid, from which the total surface area of the solid can be calculated using the following relationship:

$$A = n_m A_m L \qquad (2.7)$$

where:

A	=	total surface area
n_m	=	moles of adsorbate per gram of adsorbent
A_m	=	average area occupied by a molecule of adsorbate in the completed monolayer
L	=	Avogadro constant

The most common model used for determining the value for the monolayer capacity and hence, the total surface area was proposed by Brunauer, Emmett and Teller (BET) in 1938.

The method depends upon physisorption of an adsorbate gas on the surface of the solid. The adsorbate used is usually nitrogen at its boiling point (77 K). It is assumed that A_m, the average area occupied by one nitrogen molecule in the completed monolayer, is 1.62×10^{-19} m^2.

The BET theory is based on the kinetic model of adsorption presented by Langmuir[12]. In essence the adsorption of a gas is extended to multilayer adsorption, where less strongly adsorbed layers tend to develop on top of the initial adsorbed monolayer. The monolayer coverage can be calculated from the BET equation derived from their theoretical model. The most conventional form is given below; details of the derivation are given elsewhere[13].

$$\frac{n}{n_m} = \frac{c(p/p^o)}{(1 - p/p^o)\{1 - (1 - c)\, p/p^o\}} \qquad (2.8)$$

where:

n	=	amount adsorbed on 1g of adsorbent
n_m	=	monolayer capacity
p^o	=	saturation vapour presssure
p	=	pressure of adsorbate gas over solid
c	=	constant related to the net heat of adsorption

Rearranging this equation gives:

$$\frac{p}{n\left(p^o - p\right)} = \frac{1}{n_m c} + \frac{c-1}{n_m c}\left(\frac{p}{p^0}\right) \qquad (2.9)$$

If the solid is a non-porous material then n/n_m plotted against p/p^o gives a type II isotherm. Plotting $p/n(p^o-p)$ against p/p^o gives a straight line with gradient $s=(c-1)/n_m c$ and intercept $i=1/n_m c$ and by solving these two equations simultaneously the value of n_m can be obtained.

Knowing n_m, A_m and L then A, the total surface area, can be calculated. Depending upon the surface studied the BET equation plot is found to be linear in the region with p/p^o values of 0.05 to 0.3.

It has to be noted, however, that the BET model does rely on a number of critical assumptions. Firstly, it is assumed that each adsorption site on the solid has an equal probability of adsorbing a gas molecule. However, it is known that most surfaces have energetically different sites which have different probabilities of adsorption i.e. the surface is heterogeneous. Secondly, the model neglects the interaction between neighbouring adsorbed molecules instead it concentrates on the interactions between the gas and solid surface.

2.4.2 Apparatus

The procedure for determining the total surface area of a solid is carried out under high vacuum conditions in a calibrated vacuum system. The experimental details of the apparatus used in the work reported here are contained in Chapter 3.

References

1. A.R West, "Solid State Chemistry and Its Applications", John Wiley & Sons, Chichester, 1992.
2. C Kittel, "Introduction to Solid State Physics", John Wiley & Sons, New York, 7th Ed., 1996.
3. M.J Buerger, "X-ray Crystallography", John Wiley & Sons, New York, 1942.
4. W. Kraus and G. Nolze, PowderCell for Windows v2.3, 1999.
5. H.P Klug and L.E Alexander, "X-ray Diffraction Procedures for Polycrystalline and Amorphous Materials", Wiley, 1974.
6. N.N Greenwood and T.C Gibb, "Mössbauer Spectroscopy", Chapman and Hall, London, 1971.
7. D.P.E Dickson and F.J Berry, "Mössbauer Spectroscopy", Cambridge University Press, Great Britain, 1986.
8. F.J. Berry "The Mössbauer Effect in Supported Microcrystallites", Advances in Inorganic Chemistry and Radichemistry, vol. 21, Ed. H.J. Emeleus and A.G. Sharpe, Academic Press, 1978.
9. N.W. Hurst, S.J. Gentry, A. Jones and B.D. McNicol, *Catal. Rev. Sci. Eng.*, 1982, 24, 233.
10. D.A.M. Monti and A. Baiker, *J. Catal.*, 1983, 83, 323.
11. S.J. Gregg and K.S.W. Sing "Adsorption, Surface Area and Porosity", Academic Press Inc. Ltd., 2nd Ed., 1982.
12. I. Langmuir, J. Amer. Chem. Soc., 1916, 38, 2221.
13. P.W. Atkins, "Physical Chemistry", Oxford University Press, 5th Ed., 1994.

Chapter 3

EXPERIMENTAL

Chapter 3

EXPERIMENTAL

A. Preparation of Samples

3.1 γ-Fe_2O_3

3.1.1 γ–Fe_2O_3 (addition of base to salt and boiling under reflux) gel point studies

Iron (III) chloride hexahydrate (Aldrich, 98 %) [$FeCl_3.6H_2O$] (16.41 g) and iron (II) chloride tetrahydrate (Aldrich, 99 %) [$FeCl_2.4H_2O$] (6.03 g) were dissolved separately in distilled water (100 ml and 50 ml respectively). The Fe (II)- containing solution was added to the Fe (III)- containing solution, in a molar ratio of Fe (II) to Fe (III) of 1:2. To the mixed iron- containing solution aqueous ammonia (Fisher) (5 ml) was added. (Additional samples were prepared with 10 and 15 ml aqueous ammonia). The precipitate was boiled under reflux for 3 h. The precipitate was then filtered, washed with 95 % ethanol (Hayman) (200 ml), and dried under an infrared lamp. Half of the resulting solid was calcined in air at 250 °C for 12 h and the remaining half left uncalcined.

3.1.2 γ–Fe_2O_3 (addition of base to salt, boiling under reflux, and calcination at 250 °C/12 h)

A similar procedure as that described in section 3.1.1 was used, but involving addition of excess aqueous ammonia (40 ml) and heating at 250 °C (12 h).

3.1.3 γ-Fe_2O_3 (addition of salt to base, boiling under reflux, and calcination at 250 °C/12 h)

A similar procedure as that described in 3.1.1 was used, but adding the iron-containing solution to excess aqueous ammonia solution (40 ml) and heating at 250 °C (12 h).

3.1.4 γ-Fe_2O_3 (addition of base to salt, heated hydrothermally and dried under an infrared lamp)

Iron (III) chloride hexahydrate (Aldrich, 98 %) [$FeCl_3.6H_2O$] (16.41 g) and iron (II) chloride tetrahydrate (Aldrich, 99 %) [$FeCl_2.4H_2O$] (6.03 g) were dissolved separately in distilled water (100 ml and 50 ml respectively). The Fe (II)- containing solution was added to the Fe (III)- containing solution. Aqueous ammonia (Fisher) (40 ml) was added. The solution was treated in a Teflon-lined autoclave at 150 °C for 5 h at *ca.* 10atm. The precipitate was removed by filtration, washed with 95 % ethanol (Hayman) (200 ml), and dried under an infrared lamp.

3.1.5 γ-Fe_2O_3 (addition of salt to base, heated hydrothermally and dried under an infrared lamp)

A similar procedure as that described in 3.1.4 was used, but adding the iron-containing solution to aqueous ammonia solution (40 ml).

3.2 Metal- Doped γ-Fe_2O_3

3.2.1 Titanium- doped γ–Fe_2O_3 (addition of base to salt, boiling under reflux, and calcination at 250 °C/12 h)

An identical procedure to that described in 3.1.1 was used but with the addition of aqueous suspension of titanium tetrachloride (Aldrich, 99.9) [$TiCl_4$] (0.87 ml) to the iron- containing solution and precipitated with excess aqueous ammonia (40 ml) and heating at 250 °C (12 h).

3.2.2 Tin- doped γ–Fe_2O_3 (addition of base to salt, boiling under reflux, and calcination at 250 °C/12 h)

An identical procedure to that described in 3.1.1 was used but with the addition of aqueous tin dichloride (Acros, 98 %) [$SnCl_2$] (1.51 g) to the iron- containing solution and precipitated with excess aqueous ammonia (40 ml) and heating at 250 °C (12 h).

3.2.3 Ruthenium- doped γ–Fe_2O_3 (addition of base to salt, boiling under reflux, and calcination at 250 °C/12 h)

An identical procedure to that described in 3.1.1 was used but with the addition of aqueous ruthenium trichloride (Johnson Matthey chemicals) [$RuCl_3$] (1.6 g) to the iron- containing solution and precipitated with excess aqueous ammonia (40 ml) and heating at 250 °C (12 h).

3.2.4 Magnesium- doped γ–Fe_2O_3 (addition of base to salt, boiling under reflux, and calcination at 250 °C/12 h)

An identical procedure to that described in 3.1.1 was used but with the addition of aqueous magnesium dichloride (BDH, 97 %) [$MgCl_2.6H_2O$] (1.63 g) to the iron-containing solution and precipitated with excess aqueous ammonia (40 ml) and heating at 250 °C (12 h).

3.3 γ–Fe_2O_3 doped with two metals (addition of base to salt, boiling under reflux, and calcination at 250 °C/12 h)

An identical procedure to that described in 3.1.1 was used but with aqueous solutions containing two different metal salts (Table 3.1) being added to the iron-containing solution and precipitated with excess aqueous ammonia (40 ml) and heating at 250 °C (12 h).

Table 3.1 Metals used for the preparation of MM'/Fe_2O_3

Metal 1 (M)	Metal 2 (M')
Ti	Mg
Sn	Mg
Sn	Ti

3.4 Palladium impregnated γ–Fe_2O_3 and metal- doped variants

γ-Fe_2O_3 prepared by addition of base to salt and boiling under reflux (2 g) and its metal- doped variants were impregnated using the incipient wetness technique with 2 wt % palladium using palladium nitrate in nitric acid solution (Johnson Matthey Chemicals) [$Pd(NO_3)_2$] (0.150 ml), or dinitrodiammine palladium (II) in nitric acid solution (Johnson Matthey Chemicals) [Pd(DNDA)] (1.55 ml), or bis-(acetylacetonato) palladium (II) (Johnson Matthey Chemicals) [$Pd(acac)_2$] (0.118 g). The palladium-containing solutions were made up to the pore volume of the iron oxide in distilled water (1.6 g) with the exception of $Pd(acac)_2$ which was diluted in slightly excess toluene. (Pore volume was estimated by the addition of water to 2 g of iron oxide dropwise until the oxide appeared wet. The weight of water added corresponded to the pore volume). The iron oxide was slurried with the palladium solution and allowed to dry in air under an infrared lamp for *ca.* 1 h. The samples were calcined at 300 °C for 2 h.

3.5 Fe_3O_4

3.5.1 Fe_3O_4 (addition of base to salt, heated hydrothermally and dried under an infrared lamp)

Iron (III) chloride hexahydrate (Aldrich, 98 %) [$FeCl_3.6H_2O$] (16.41 g) and iron (II) chloride tetrahydrate (Aldrich, 99 %) [$FeCl_2.4H_2O$] (6.03 g) were dissolved separately in distilled water (100 ml and 50 ml respectively). The Fe (II) -containing solution was added to the Fe (III)-containing solution, in a molar ratio of Fe (II) to Fe (III) of 1:2. Aqueous ammonia (Fisher) (40 ml) was added. The suspension was hydrothermally processed in a Teflon lined autoclave at 150 °C for 3 h at *ca.* 10 atm pressure. The product was removed by filtration, washed with 95 % ethanol (Hayman) (200 ml), and dried under an infrared lamp.

3.5.2 Fe_3O_4 (addition of salt to base, heated hydrothermally and dried under an infrared lamp)

A similar procedure as that described in 3.5.1 was used, but adding the iron-containing solution to aqueous ammonia solution (40 ml).

3.6 Metal- Doped Fe_3O_4

3.6.1 Titanium- doped Fe_3O_4 (addition of base to salt, heated hydrothermally and dried under an infrared lamp)

A similar procedure to that described in 3.5.1 was adopted but with an aqueous suspension of titanium (IV) chloride (Aldrich, 99.9 %) [$TiCl_4$] (0.87 ml) being added to the iron- containing solution.

3.6.2 Tin- doped Fe_3O_4 (addition of base to salt, heated hydrothermally and dried under an infrared lamp)

A similar procedure to that described in 3.5.1 was adopted but with aqueous tin (II) chloride (Acros, 98 %) [$SnCl_2$] (1.51 g) being added to the iron- containing solution.

3.6.3 Ruthenium- doped Fe_3O_4 (addition of base to salt, heated hydrothermally and dried under an infrared lamp)

A similar procedure to that described in 3.5.1 was adopted but with aqueous ruthenium (III) chloride (Johnson Matthey Chemicals) [$RuCl_3$] (1.6 g) being added to the iron- containing solution.

3.6.4 Magnesium- doped Fe_3O_4 (addition of base to salt, heated hydrothermally and dried under an infrared lamp)

An identical procedure to that described in 3.5.1 was used but with aqueous magnesium dichloride (BDH, 97 %) [$MgCl_2.6H_2O$] (1.63 g) being added to the iron-containing solution.

3.7 Palladium impregnated Fe_3O_4

Fe_3O_4 prepared by addition of base to salt and heated hydrothermally (2 g) was impregnated with 2 wt% palladium using ($Pd(NO_3)_2$) (Johnson Matthey Chemicals) in nitric acid solution by the incipient wetness technique. The $Pd(NO_3)_2$ (0.150 ml) solution was made up to the pore volume of the iron oxide in distilled water (1.7 g). (Pore volume was estimated by the addition of water to 2g of iron oxide dropwise until the oxide appeared wet. The weight of water added corresponded to the pore volume). The iron oxide was slurried with the $Pd(NO_3)_2$ solution and allowed to dry in air under an infrared lamp for *ca.* 1 h. The sample was calcined at 300 °C for 2 h.

3.8 α-Fe_2O_3

3.8.1 α-Fe_2O_3 (addition of base to salt, boiling under reflux, and calcination at 600 °C/12 h)

Iron (III) chloride hexahydrate (Aldrich, 98 %) [$FeCl_3.6H_2O$] (16.41 g) was dissolved in distilled water (100 ml). Aqueous ammonia (Fisher) (40 ml) was added.

The precipitate was boiled under reflux for 3 h. The precipitate was filtered, washed with 95 % ethanol (Hayman) (200 ml), and dried under an infrared lamp. The resulting solid was calcined in air at 600 °C for 12 h.

3.8.2 α-Fe_2O_3 (addition of salt to base, boiling under reflux, and calcination at 600 °C/12 h)

An identical procedure to that described in 3.8.1 was used, but with the iron-containing solution added to aqueous ammonia (40 ml).

3.8.3 α-Fe_2O_3 (addition of base to salt, heated hydrothermally and dried under an infrared lamp)

Iron (III) chloride hexahydrate (Aldrich, 98 %) [$FeCl_3.6H_2O$] (16.41 g) was dissolved in distilled water (100 ml). Aqueous ammonia (Fisher) (40 ml) was added. The suspension was hydrothermally processed in a Teflon lined autoclave at 200 °C for 3 h at *ca.* 15 atm pressure. The precipitate was filtered, washed with 95 % ethanol (Hayman) (200 ml) and dried under an infrared lamp.

3.8.4 α-Fe_2O_3 (addition of salt to base, heated hydrothermally and dried under an infrared lamp)

A similar procedure as described in 3.8.3 was used, but adding the iron- containing solution to aqueous ammonia solution (40 ml).

3.9 Metal- Doped α-Fe_2O_3

3.9.1 Titanium- doped α–Fe_2O_3 (addition of base to salt, boiling under reflux, and calcination at 600 °C/12 h)

An identical procedure to that described in 3.8.1 was used but with an aqueous suspension of titanium tetrachloride (Aldrich, 99.9) [$TiCl_4$] (0.87 ml) solution added to the iron- containing solution.

3.9.2 Tin- doped α-Fe_2O_3 (addition of base to salt, boiling under reflux, and calcination at 600 °C/12 h)

An identical procedure to that described in 3.8.1 was used but with aqueous tin dichloride (Acros, 98 %) [$SnCl_2$] (1.51 g) solution added to the iron- containing solution.

3.9.3.1 Ruthenium- doped α-Fe_2O_3 (addition of base to salt or salt to base, boiling under reflux, and calcination at 600 °C/12 h)

An identical procedure to that described in 3.8.1 was used but with aqueous ruthenium trichloride (Acros, 98 %) [$RuCl_3$] (1.6 g) solution added to the iron- containing solution, with aqueous ammonia added to the ion- containing solution or the ion- containing solution added to the aqueous ammonia.

3.9.3.2 Ruthenium- doped α–Fe_2O_3 (addition of base to salt, heated hydrothermally and dried under an infrared lamp)

An identical procedure to that described in 3.8.3 was used but with aqueous ruthenium trichloride (Johnson Matthey chemicals) [$RuCl_3$] (1.6 g) solution added to the iron- containing solution.

3.9.4 Magnesium- doped α–Fe_2O_3 (addition of base to salt, boiling under reflux, and calcination at 600 °C/12 h)

An identical procedure to that described in 3.8.1 was used but with aqueous magnesium dichloride (BDH, 97 %) [$MgCl_2.6H_2O$] (1.63 g) solution added to the iron- containing solution.

3.10 α-Fe_2O_3 doped with two metals (addition of base to salt, boiling under reflux, and calcination at 600 °C/12 h)

An identical procedure to that described in 3.8.1 was used but with aqueous solutions containing two different metal salts (Table 3.1) being added to the iron-containing solution and precipitated with excess aqueous ammonia (40 ml).

3.11 Palladium impregnated α-Fe_2O_3 and metal- doped variants

α-Fe_2O_3 prepared by addition of base to salt and boiling under reflux (2 g) and its metal- doped variants were impregnated by the incipient wetness technique with

2 wt% palladium using a palladium nitrate in nitric acid solution (Johnson Matthey Chemicals) [$Pd(NO_3)_2$] (0.150 ml), or dinitrodiammine palladium (II) in nitric acid solution (Johnson Matthey Chemicals) [Pd(DNDA)] (0.155 ml), or bis-(acetylacetonato) palladium (II) (Johnson Matthey Chemicals) [$Pd(acac)_2$] (0.118 g). The palladium-containing solutions were made up to the pore volume of the iron oxide in distilled water (1.4 g) with the exception of $Pd(acac)_2$ which was diluted in slightly excess toluene. (Pore volume was estimated by the addition of water to 2 g of iron oxide dropwise until the oxide appeared wet. The weight of water added corresponded to the pore volume). The iron oxide was slurried with the palladium solution and allowed to dry in air under an infrared lamp for *ca.* 1 h. The samples were calcined at 500 °C for 2 h.

B. Instrumental Techniques

3.12 X-ray Powder Diffraction (XRD)

X-ray powder diffraction patterns were recorded with a Siemens D5000 diffractometer using CuKα radiation of wavelength $\lambda = 0.15418$ nm. The instrument was calibrated using a quartz standard. The samples were ground to a fine powder and, depending on the amount of sample, either pressed into a sample holder or smeared onto a mirror holder with Vaseline grease. The samples were scanned in the range $10° < 2\theta < 80°$ over 1 h or 12 h period. Lattice parameters were calculated using Powdercell for Windows version 2.3 (1999)[1].

3.13 Temperature Programmed Reduction (TPR)

A 10 % H_2 in N_2 gas mixture (flow rate 20 cm^3min^{-1}) was passed over the sample at ambient temperature. The temperature was increased linearly with time (5 $^oCmin^{-1}$) and the consumption of hydrogen monitored with a kathrometer detector.

3.14 Surface Area Measurement

The surface areas were determined by nitrogen gas adsorption at 77 K by the Brunauer-Emmett-Teller (BET) method using high vacuum conditions in a calibrated vacuum system (Figure 3.1).

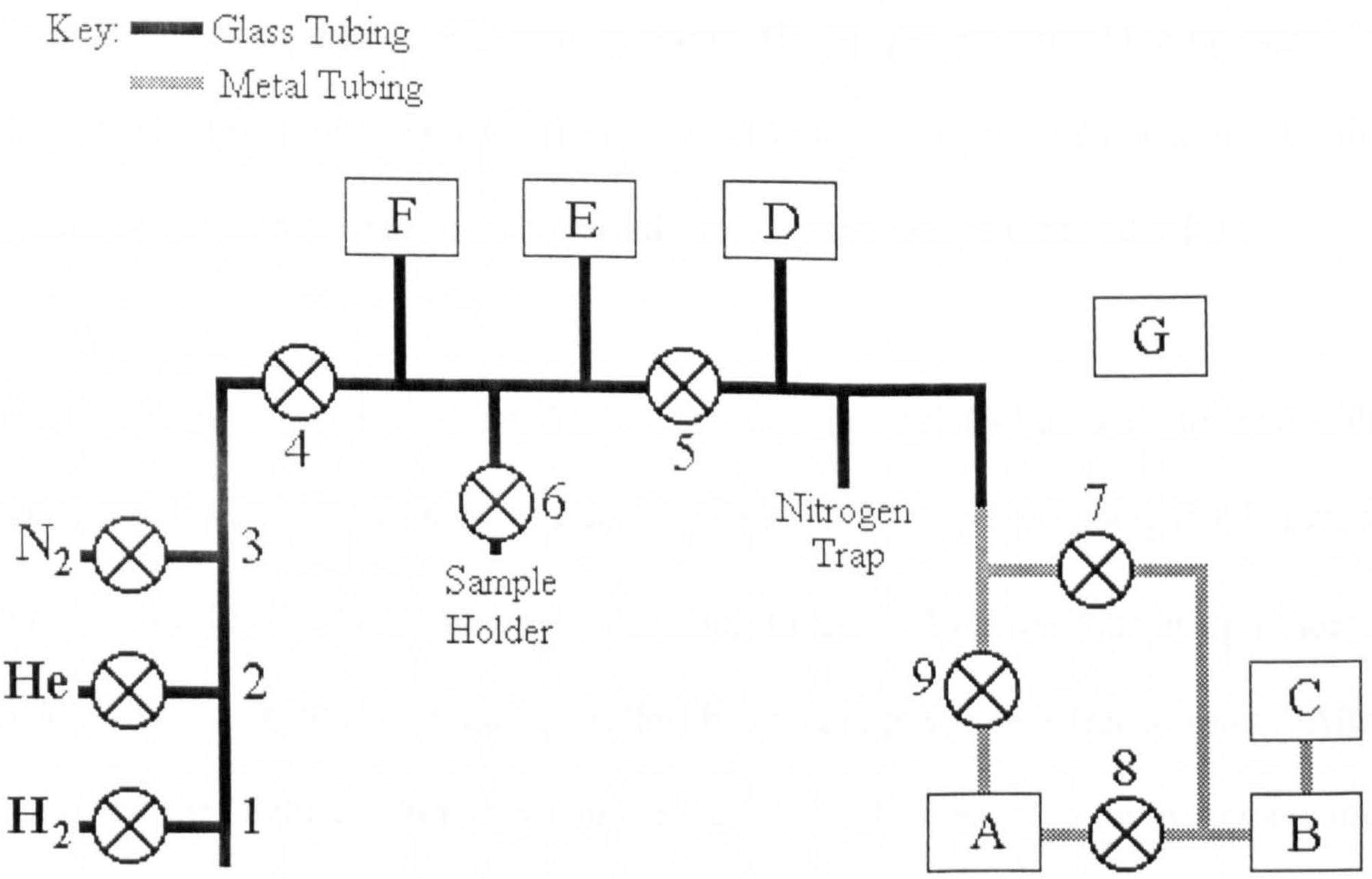

Figure 3.1 Diagram of apparatus used for the determination of surface area

This consists of a glass vacuum line approximately 10 mm in diameter. The vacuum was maintained by an Edwards Two Way Rotary Pump [B] and an Edwards Air Cooled Diffusion pump [A]. A trap containing liquid nitrogen was situated on the line leading to the pumps to prevent any unwanted products from contaminating the pumps. The pressure in the vacuum line was measured by pressure gauges attached to the line. An Edwards Active Pirani Gauge [C] read the pressure in the range 100 to 10^{-3} mbar and an Edwards Active Inverted Magnetron [D] gauge read the pressure in the 10^{-3} to 10^{-8} mbar range.

With the two pumps on and the liquid nitrogen trap in place a dynamic vacuum of $10^{-5}/10^{-6}$ mbar can be achieved. High purity hydrogen gas, helium gas and nitrogen gas cylinders were attached to the line via taps 1, 2 and 3 respectively. These were prevented from over pressuring the line by means of mini-pressure regulators. The pressure of the gases in the vacuum line were measured by two Edward Barocel Capacitance Barometers positioned as shown [E, F]. [E] measured the pressures in the range 0-1000 mbar and [F] in the range 0-10 mbar. All pressures measured by the pressure gauges were displayed by an Edwards Active Gauge Controller [G].

The sample (*ca.* 0.1 g) was loaded into a dry, clean sample holder and attached, with the sinter in place, to the vacuum line. Typically each sample was outgassed at room temperature for *ca.* 17 h followed by heating to 250 ^{o}C for an hour using a home-made vertical heating column controlled by a Zenith variable transformer. After removing the heating column the sample was allowed to return to room temperature. Particular attention was taken to maintain a standard outgassing routine, with respect to duration, temperature and final pressure, in order to be able to legitimately compare results from separate experiments.

With taps 4, 5 and 6 closed, the sample holder was immersed in liquid nitrogen up to the pre-etched mark on the sample holder. This level of nitrogen was kept constant by continually topping up the flask. Nitrogen gas was then admitted to the vacuum line by opening tap 3. By opening tap 4 a certain volume of nitrogen was allowed into the dosing volume and this pressure of nitrogen was noted (P_d^1) and the temperature of the dosing volume recorded (T_1) using the thermocouple attached to the vacuum line for this purpose. Tap 6 would then be opened a pre-determined amount and the nitrogen allowed to expand into the sample holder and adsorb onto the sample. On attainment of equilibrium (indicated by constant pressure) tap 6 would be closed and the pressure noted again (P_e^1). Another quantity of nitrogen was then admitted to the dosing volume and noted (P_d^2) along with the temperature (T_2) and P_e^2 was recorded in the same manner as above. The procedure was repeated until seven or eight values of P_d^n, T_n and P_e^n (n=1 to 7 or 8) were recorded.

The pressure of nitrogen must necessarily be in the range of relative pressure (P_d^n / P^o) 0.05 to 0.3 to give linear BET plots where P^o is the saturation vapour pressure of liquid nitrogen at its boiling point. For our purposes this was assumed to be 1000 mbar. Therefore, the pressures of nitrogen taken as the initial pressure (P_d^n) in the dosing volume are typically 50, 75, 100, 150, 200, 250 and 300 mbar.

3.15 ^{57}Fe Mössbauer Spectroscopy

^{57}Fe Mössbauer spectra were recorded at 298 K with a microprocessor controlled Mössbauer spectrometer using a *ca.* 25 mCi ^{57}Co/Rh source. The instrument was calibrated using a natural iron standard. Chemical isomer shift data are referred to metallic iron.

3.16 In situ ^{57}Fe Mössbauer Spectroscopy

In situ ^{57}Fe Mössbauer spectra were recorded at elevated temperatures using a furnace as shown in Figure 3.2 and described elsewhere[2]. The central part of the furnace consists of a highly polished aluminium elliptical cylinder. The heat source is a 250 W halogen Osram lamp placed at one focal point of the ellipse with a cylindrical black painted quartz tube, the heat absorber, at the other focal point. The sample is placed between two berylium oxide disks of 0.5 mm thickness and held in the quartz tube. Aluminised mylar windows allow the gamma rays to enter and leave the chamber. The temperature of the tube is monitored by a thermocouple. The signal from the thermocouple controls the temperature by modulating the power of the lamp and maintains the sample at a temperature within +/- 0.5 K over 24 h.

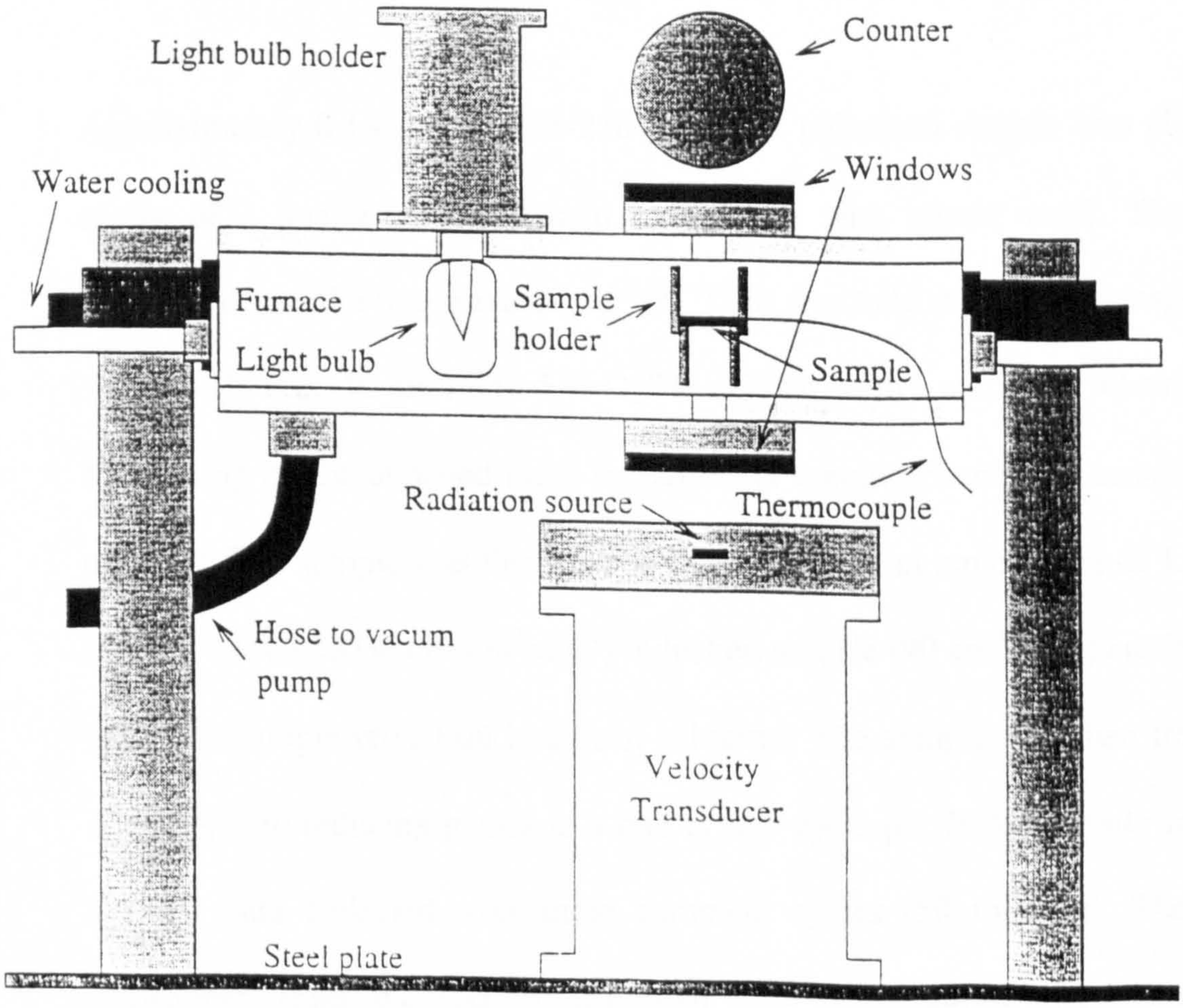

Figure 3.2 Schematic representation of the furnace used for *in situ* Mössbauer spectroscopy

3.17 Transmission Electron Microscopy (TEM)

Materials were examined with a JEOL electron microscope (JEOL JEM 2000fx) operating at 200 kV. The samples were placed on a copper grid.

3.18 Carbon Monoxide Oxidation

The sample (0.1 g) was placed in a glass tube and heated under 1 % CO in air (flow rate 100 cm^3min^{-1}) from *ca.* 50 °C to 200 °C at a ramp rate of 5 $°Cmin^{-1}$. The conversion of CO to CO_2 was recorded using a CO_2 analyser.

3.19 Oxygen Storage Capacity (OSC)

Approximately 0.1-0.2 g of 355-250 μm thick pelletised sample was placed in the centre of a quartz tube and held in position with quartz wool. The tube was introduced into the micro reactor at 200 °C. It was held under an atmosphere of 0.5 % O_2 in He (i.e., 10 cm^3min^{-1} 5 % O_2/He oxidant, with a carrier of 90 cm^3min^{-1} He). Monitoring by the attached mass spectrometer continued until the sample was fully oxidised. The sample was then manually switched to an atmosphere of 1.0 % CO in He, (ie, 10 % CO/He (10 cm^3min^{-1}) reductant and He (90 cm^3min^{-1}) carrier gas) until complete sample reduction had been achieved. The sample was then treated in the oxidising and reducing gasses at a rate of one cycle per 1000 seconds and the mass spectral data collected over three complete cycles (50 minutes). The OSC was determined from the CO breakthrough time (time during the cycle when the oxidation to CO_2 is complete) and expressed in μmol [O]/g sample.

$$OSC\ (\mu mol\ [O]/g) = 0.694 * T/wt \qquad (3.1)$$

where T = CO breakthrough time in seconds, wt = sample weight in grams.

Variable temperature OSC measurements were carried out on samples within the temperature range 200 – 500 °C.

References

1. W. Kraus and G. Nolze, Powdercell for Windows version 2.3, 1999.
2. Ö. Helgason, H.P. Gunnlaugsson, K. Jonsson and S. Steinthorsson, *Hyperfine Int.*, 1994, 91, 595.

Chapter 4

RESULTS AND DISCUSSION: γ–Fe_2O_3 AND RELATED PHASES

Chapter 4

RESULTS AND DISCUSSION:

γ–Fe_2O_3 AND RELATED PHASES

4.1. γ-Fe_2O_3

4.1.1 γ–Fe_2O_3 (addition of base to salt and boiling under reflux) gel point studies

γ–Fe_2O_3 was prepared by the separate addition of the base of 5, 10 and 15 ml aqueous ammonia to the iron- containing salt solution, yielding three samples. The samples were dried under an infrared lamp. Half of each sample was subsequently calcined at 250 °C in air for 12 h.

Materials dried under an infrared lamp

The XRD pattern recorded from the uncalcined material formed by addition of 5 ml of aqueous ammonia and dried under an infrared lamp (Figure 4.1(a)) showed a broad peak at *ca.* 36 ° 2θ. The pattern was generally characteristic of a poorly crystalline material. The ^{57}Fe Mössbauer spectrum (Figure 4.2(a), Table 4.1) showed a sextet pattern (δ 0.37(2) mms^{-1}, Δ -0.10(2) mms^{-1}, H 50(1) T) corresponding to α-Fe_2O_3[1,2], and a paramagnetic doublet (δ 0.36(2) mms^{-1}, Δ 0.72(2) mms^{-1}), corresponding to small particle iron oxide[3] and accounting for *ca.* 62 % of the spectral area.

Figure 4.1 XRD patterns recorded from materials prepared by addition of (a) 5, (b) 10 and (c) 15 ml aqueous ammonia and dried under an infrared lamp

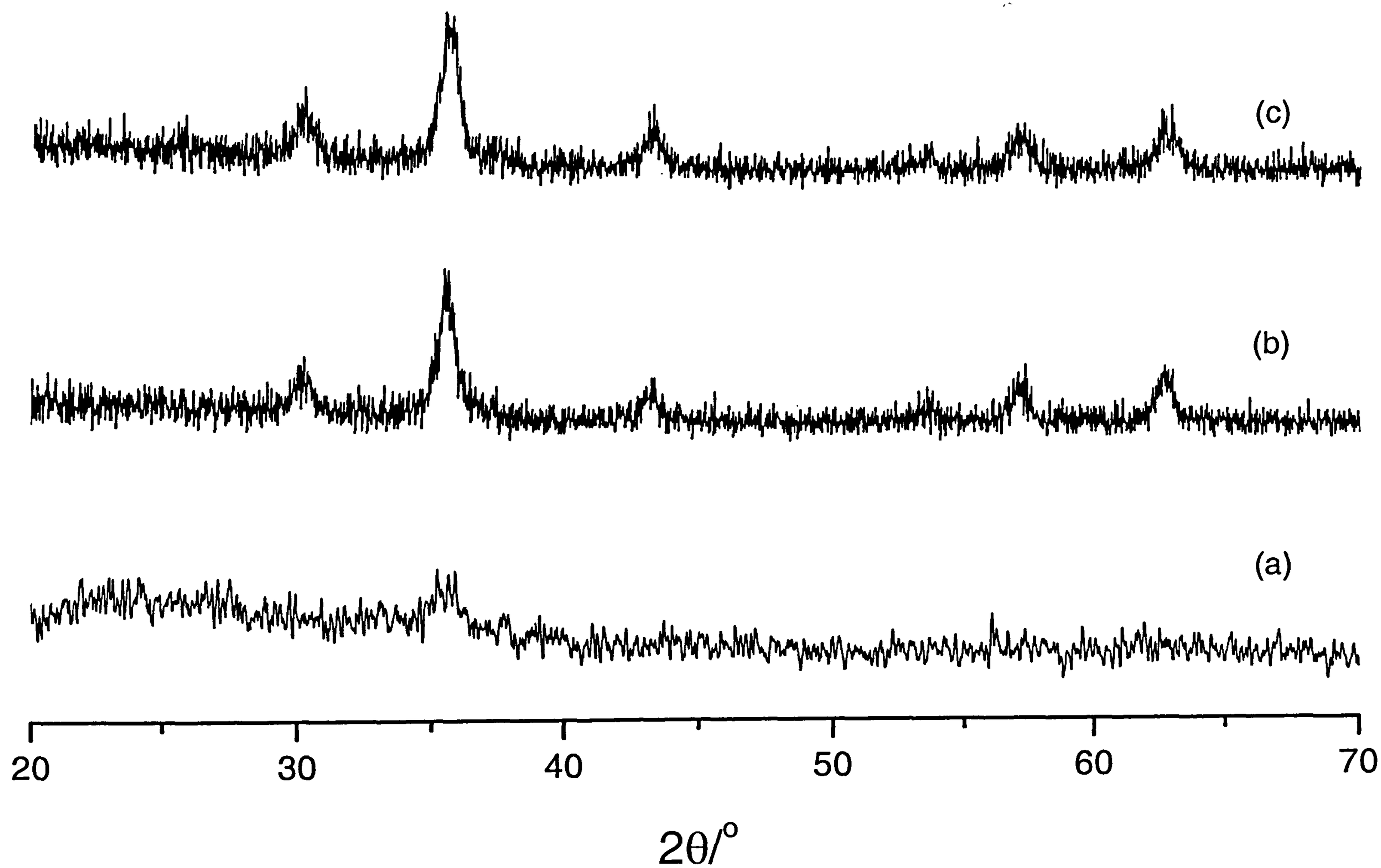

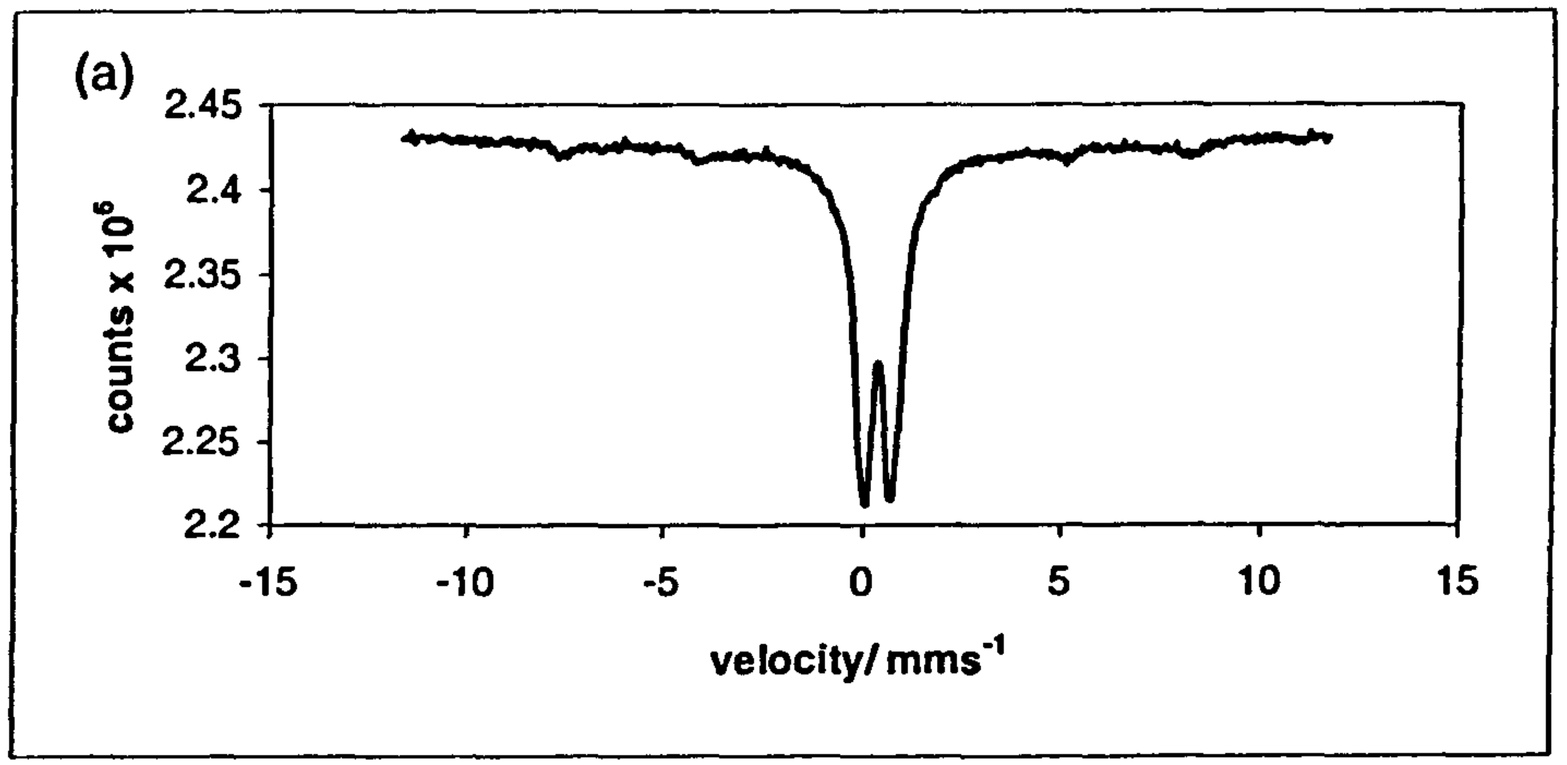

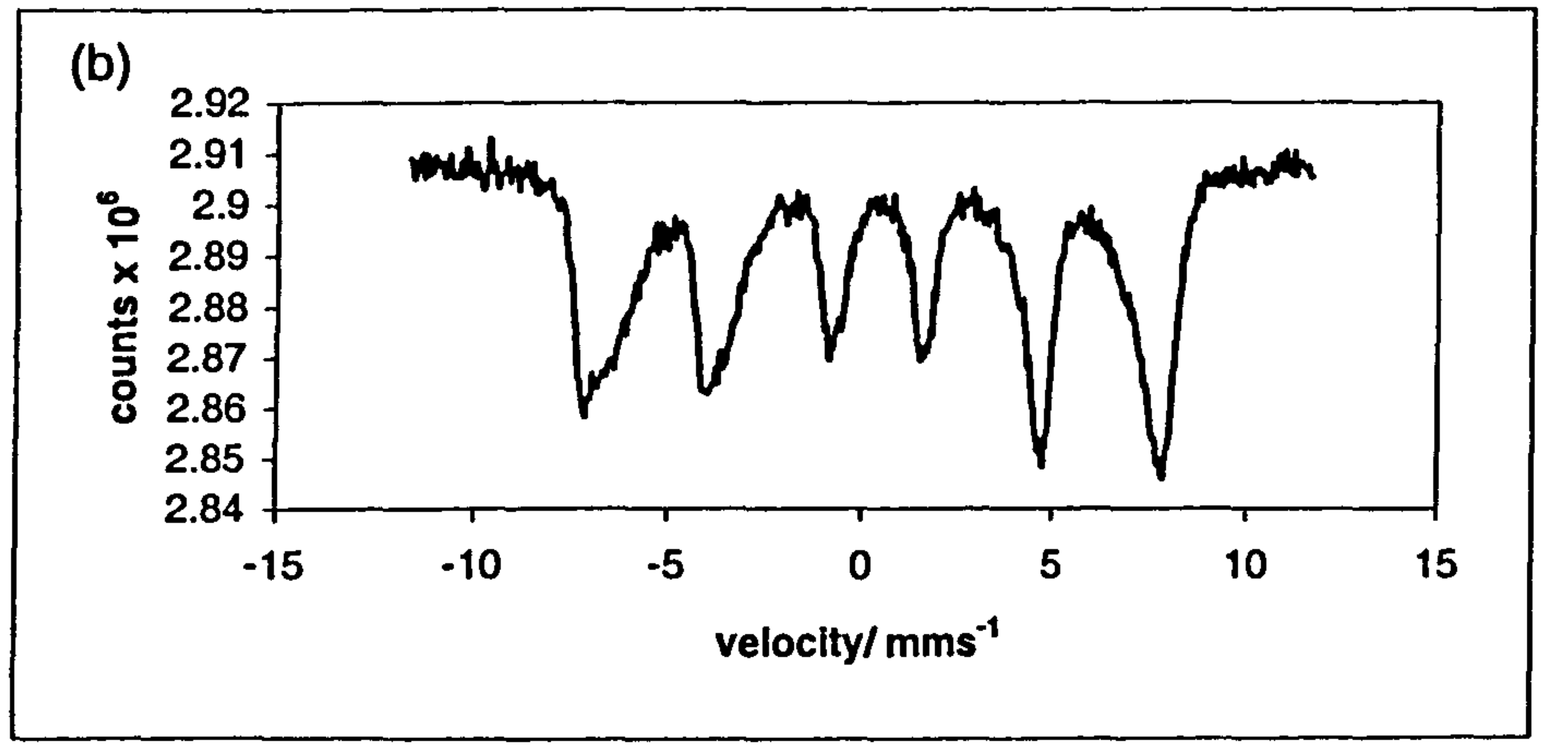

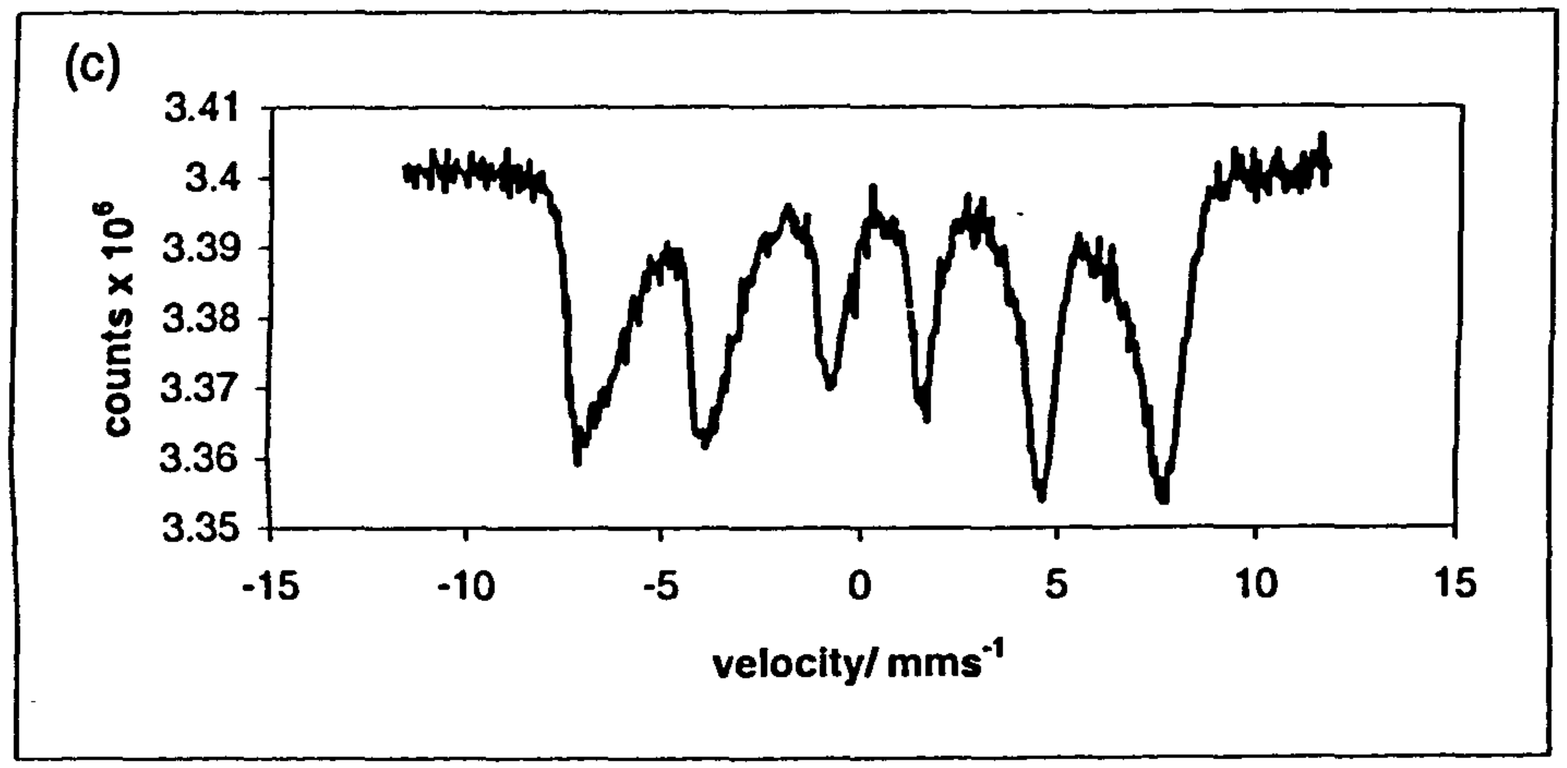

Figure 4.2 ^{57}Fe Mössbauer spectra recorded from materials prepared by addition of (a) 5, (b) 10 and (c) 15 ml aqueous ammonia and dried under an infrared lamp

The XRD patterns recorded from the uncalcined materials formed by addition of 10 and 15 ml of aqueous ammonia to the iron- containing solutions and dried under an infrared lamp (Figure 4.1(b and c)) corresponded to a spinel-related structure and were not dissimilar to that reported for Fe_3O_4[4]. The lattice parameters from the samples prepared by the addition of 10 and 15 ml aqueous ammonia were a = 8.377(2) Å, and a = 8.376(2) Å, respectively. The X-ray powder diffraction patterns of spinel-related γ–Fe_2O_3[5] and Fe_3O_4[4] are very similar. ^{57}Fe Mössbauer spectroscopy is a more sensitive method of distinguishing between γ–Fe_2O_3 and Fe_3O_4 since the spectra are significantly different[1,2] (see Chapter 1.). The ^{57}Fe Mössbauer spectra showed two sextet patterns characteristic of Fe_3O_4[1,2] (Figures 4.2(b and c), Table 4.1).

Table 4.1 ^{57}Fe Mössbauer parameters recorded from uncalcined materials formed by addition of aqueous ammonia to iron-containing solutions

Sample: addition of *X* ml aqueous ammonia	**δ (± 0.02) mms^{-1}**	**Δ (± 0.02) mms^{-1}**	**H (± 1) T**	**Interpretation**	**Area (± 5) %**
***X* = 5**	0.36	0.72	---	Small particle iron oxide	62
	0.37	-0.10	50	α-Fe_2O_3	38
***X* = 10**	0.50	0.00	43	Fe_3O_4	100
	0.33	0.00	47	Fe_3O_4	
***X* = 15**	0.47	-0.01	42	Fe_3O_4	100
	0.34	0.01	46	Fe_3O_4	

Materials calcined at 250 °C/12 h

The XRD pattern recorded from the calcined material formed by addition of 5 ml of aqueous ammonia to the iron- containing solution corresponded to α-Fe_2O_3[6] (Figure

4.3(a)), with lattice parameters a = 5.035(2) Å, c = 13.751(2) Å. The ^{57}Fe Mössbauer spectrum showed a sextet pattern (δ 0.38(2) mms^{-1}, Δ -0.09(2) mms^{-1}, H 50(1) T) confirming it to be α-Fe_2O_3[1,2] (Figure 4.4(a), Table 4.2). The XRD patterns recorded from calcined materials formed by addition of 10 and 15 ml of aqueous ammonia corresponded to a spinel-related structure[5], Figure 4.3(b and c), with lattice parameters a = 8.364(2) Å and a = 8.363(2) Å respectively. The ^{57}Fe Mössbauer spectra showed sextet patterns corresponding to γ–Fe_2O_3[1,2] (Figures 4.4(b and c), Table 4.2).

Table 4.2 ^{57}Fe Mössbauer parameters recorded from calcined materials formed by addition of aqueous ammonia to iron-containing solutions

Sample: addition of *X* ml aqueous ammonia	**δ (± 0.02) mms^{-1}**	**Δ (± 0.02) mms^{-1}**	**H (± 1) T**	**Interpretation**
***X* = 5**	0.38	-0.09	50	α-Fe_2O_3
***X* = 10**	0.33	0.01	46	γ-Fe_2O_3
***X* = 15**	0.33	0.01	46	γ-Fe_2O_3

Conclusion

The results showed that Fe_3O_4 is formed by the addition of 10 and 15 ml of aqueous ammonia to a 1:2 mixture of iron (II) and iron (III) salts in aqueous solution and subsequent drying of the resulting precipitate under an infrared lamp. Calcination at 250 °C converts the Fe_3O_4 to γ–Fe_2O_3. The solid formed by the addition of only 5 ml of aqueous ammonia to the mixture of iron- containing solution was α-Fe_2O_3. Given that Fe^{3+} precipitates in ammonia before Fe^{2+} it is likely that 5 ml aqueous ammonia is insufficient to precipitate the iron (II) in the solution[7]. The result led to all

Figure 4.3 XRD patterns recorded from materials prepared by addition of (a) 5, (b) 10 and (c) 15 ml aqueous ammonia and calcined at 250 °C/12 h

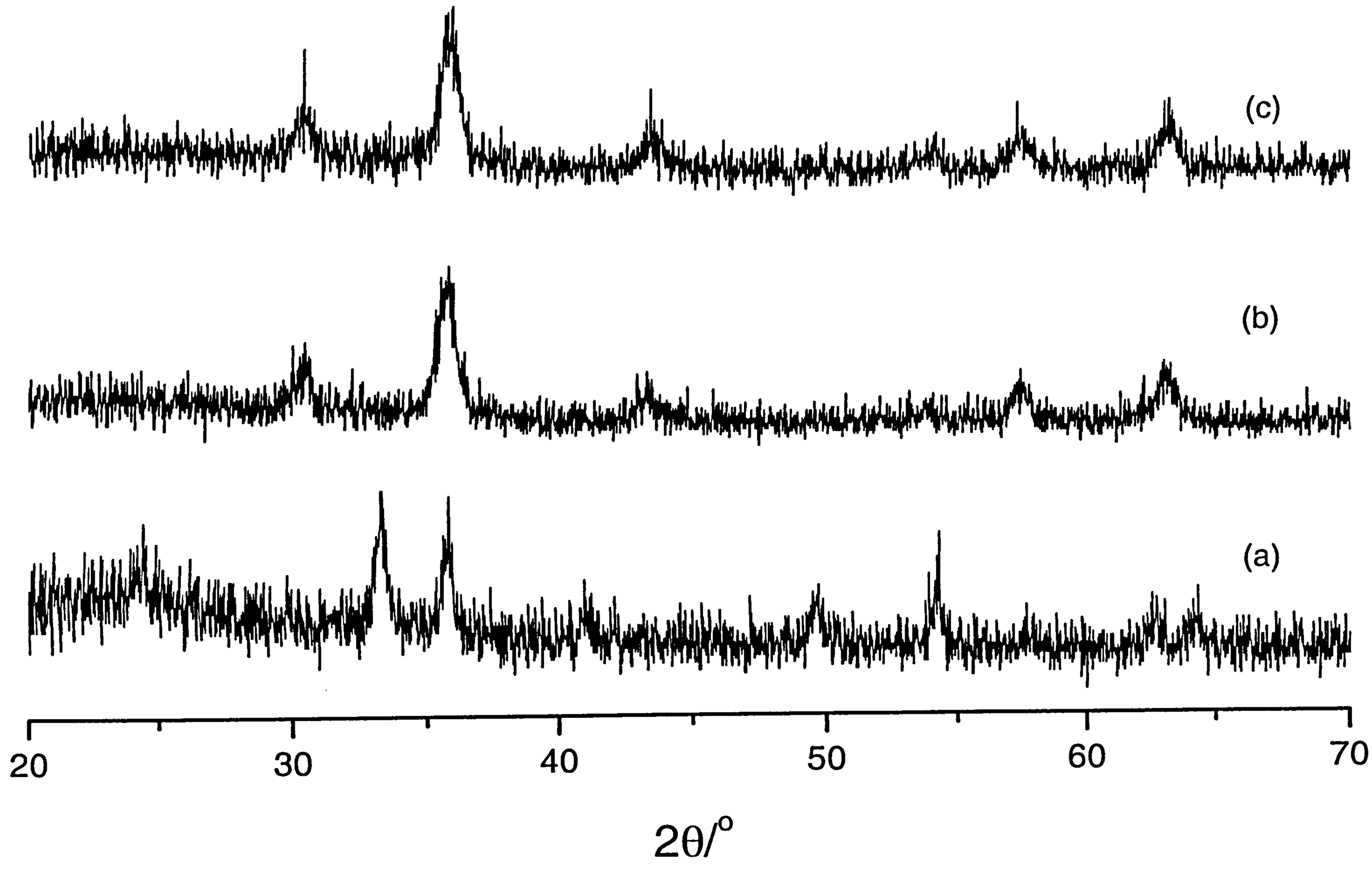

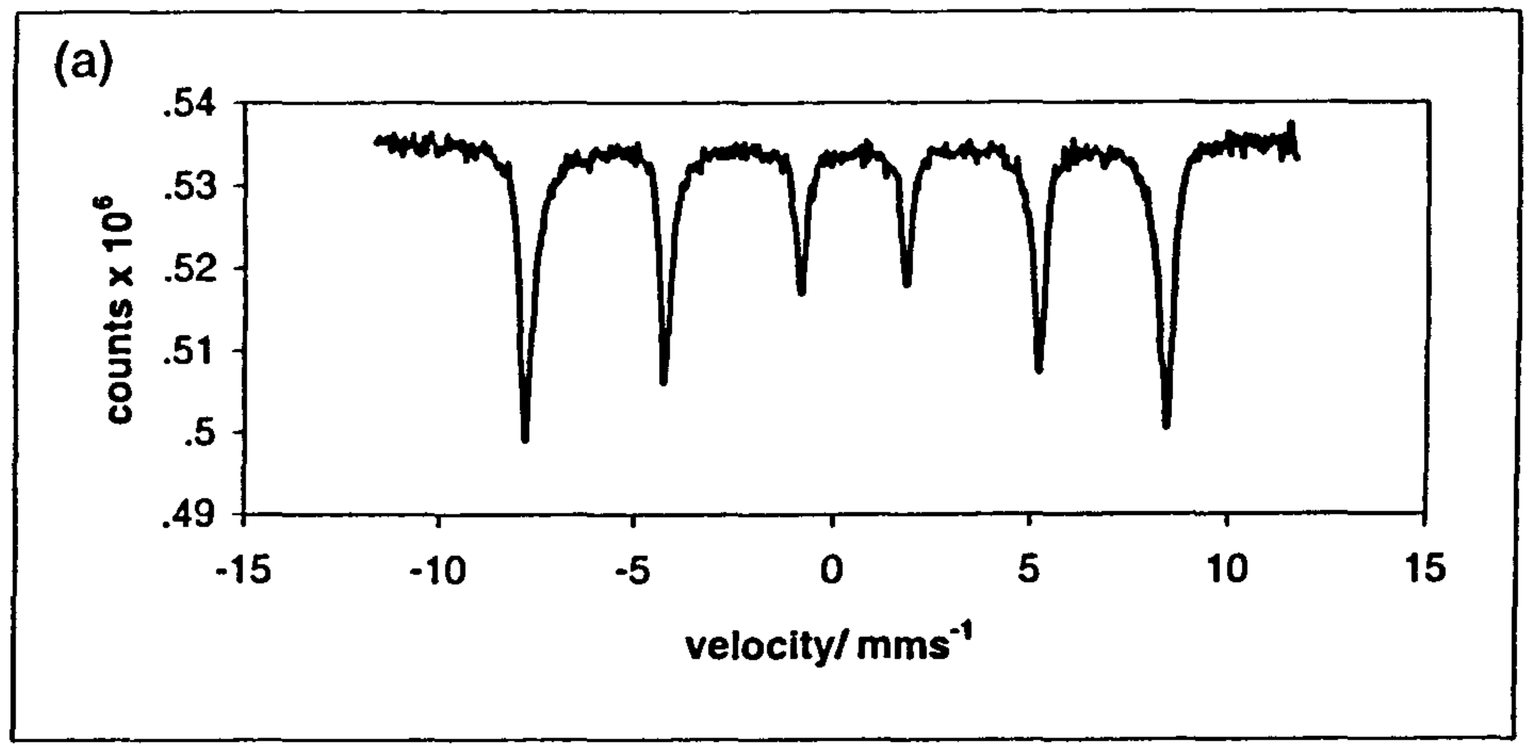

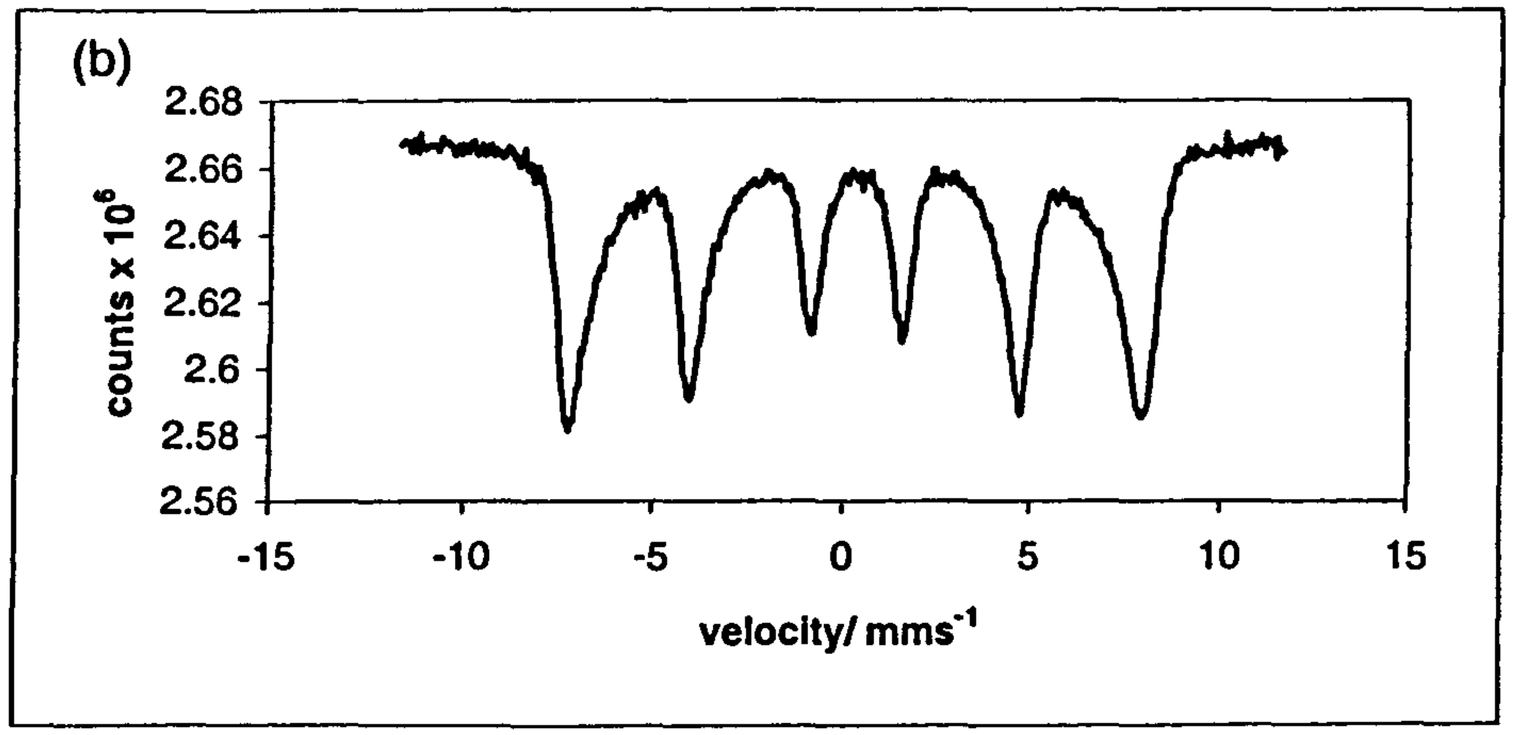

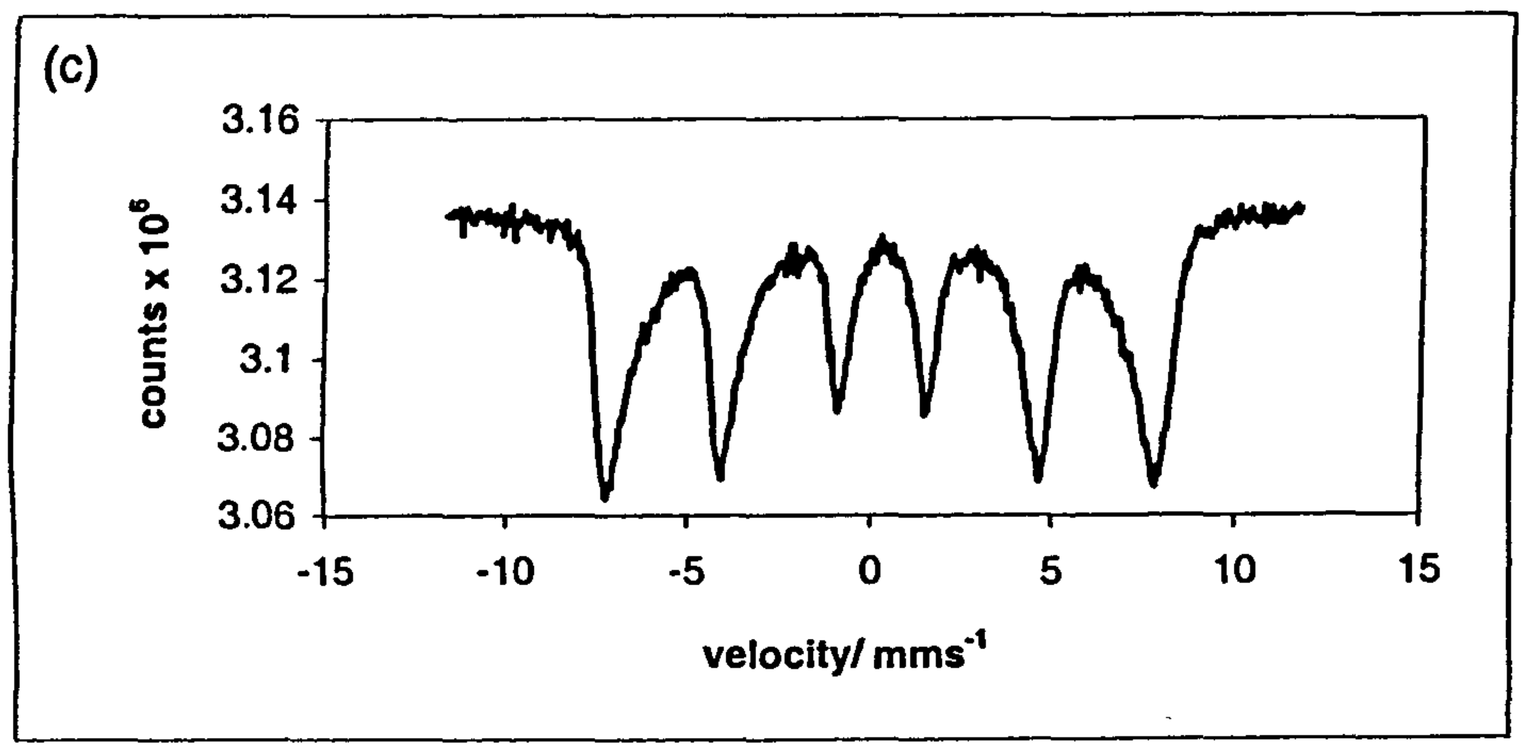

Figure 4.4 ^{57}**Fe Mössbauer spectra recorded from materials prepared by addition of (a) 5, (b) 10 and (c) 15 ml aqueous ammonia and calcined at 250 °C/12 h**

subsequent materials reported here being formed by the use of excess aqueous ammonia (40 ml).

4.1.2 γ–Fe_2O_3 (addition of base to salt, boiling under reflux, and calcination at 250 °C/12 h)

The ^{57}Fe Mössbauer spectrum recorded at 298 K (Figure 4.5) showed a sextet pattern (δ 0.34(2) mms^{-1}, Δ 0.01(2) mms^{-1}, H 47(1) T) characteristic[1,2] of γ–Fe_2O_3. The ^{57}Fe Mössbauer parameters are shown in Table 4.3.

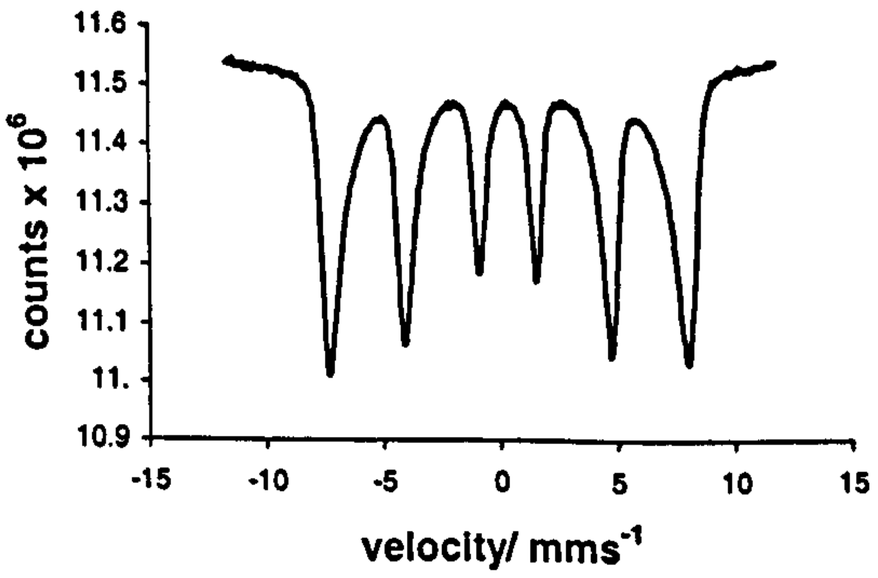

Figure 4.5 ^{57}Fe Mössbauer spectrum recorded from γ-Fe_2O_3 formed by addition of aqueous ammonia to a 1:2 mixture of iron (II)- and iron (III)- containing solution, boiling under reflux, and calcination at 250 °C

Table 4.3 ^{57}Fe Mössbauer parameters recorded from γ-Fe_2O_3 prepared by addition of base to salt or salt to base and boiling under reflux and calcination at 250 °C or heating hydrothermally

Sample	δ (± 0.02) mms^{-1}	Δ (± 0.02) mms^{-1}	H (± 1) T	Interpretation	Area (± 5) %
γ-Fe_2O_3 (base to salt, boiling under reflux and calcination at 250 °C)	0.34	0.01	47	γ-Fe_2O_3	100
γ-Fe_2O_3 (salt to base, boiling under reflux and calcination at 250 °C)	0.36	0.05	---	Small particle iron oxide	42
	0.35	0.01	43	γ-Fe_2O_3	58
γ-Fe_2O_3 (base to salt and heated hydrothermally)	0.35	0.00	48	γ-Fe_2O_3	100
γ-Fe_2O_3 (salt to base and heated hydrothermally)	0.35	0.01	47	γ-Fe_2O_3	100

The X-ray powder diffraction pattern (Figure 4.6) recorded from the material prepared from the iron (III)- and iron (II)- salts showed a single spinel-related phase with lattice parameter a = 8.354(2) Å which compares with the reported[8] value for γ–Fe_2O_3 of a = 8.334 Å.

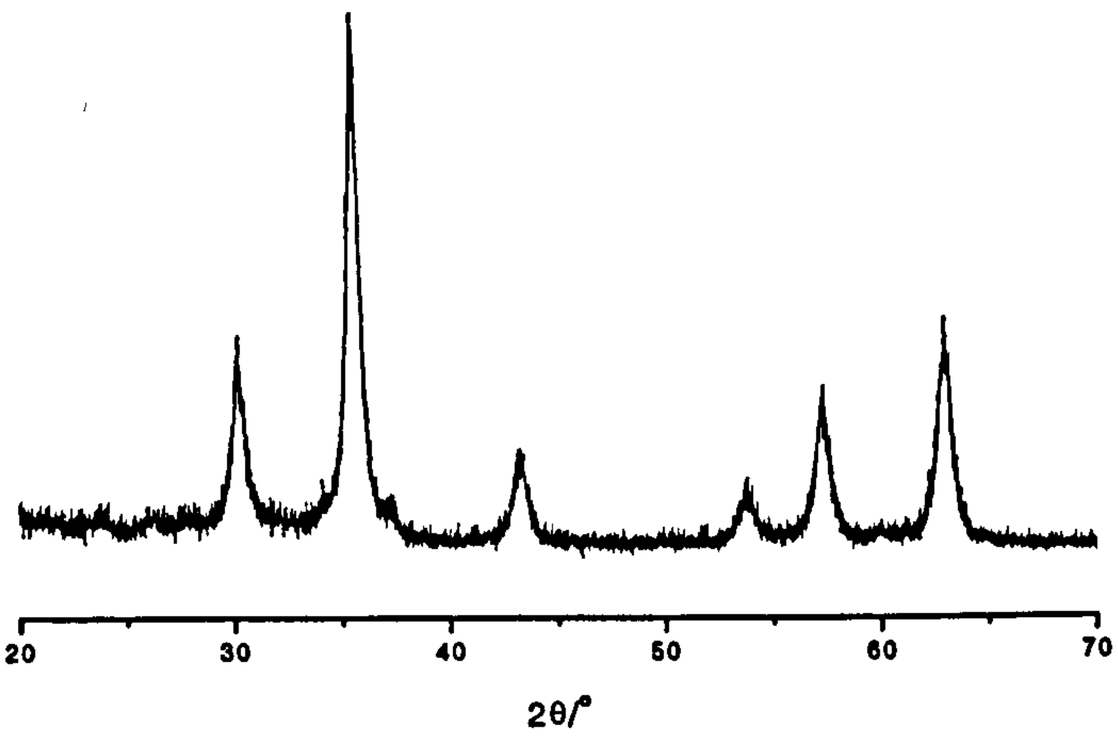

Figure 4.6 XRD pattern recorded from γ-Fe_2O_3 formed by addition of aqueous ammonia to a 1:2 mixture of iron (II)- and iron (III)- containing solution, boiling under reflux, and calcination at 250 °C

The particle size and surface area measurements are contained in Table 4.4. γ–Fe_2O_3 prepared by the addition of base to salt, boiling under reflux and calcination at 250 °C/12 h was formed with a particle size of *ca.* 13 nm as deduced from the X-ray powder diffraction linewidth data. The results agree well with data obtained from electron microscopy (*ca.* 14 nm) and the surface area of *ca.* 69 m^2g^{-1} which was determined by nitrogen adsorption measurements.

Table 4.4 Particle size and surface area measurements for γ-Fe_2O_3 prepared by addition of base to salt or salt to base and boiling under reflux and calcination at 250 °C or heating hydrothermally

Sample	Average particle size Scherrer method / nm (± 10 %)	Average particle size TEM / nm (± 10 %)	Surface Area / m^2g^{-1} (± 10 %)
γ-Fe_2O_3 (base to salt, boiling under reflux and calcination at 250 °C)	13	14	69
γ-Fe_2O_3 (salt to base, boiling under reflux and calcination at 250 °C)	8	7	150
γ-Fe_2O_3 (base to salt and heated hydrothermally)	15	13	72
γ-Fe_2O_3 (salt to base and heated hydrothermally)	14	15	71

The temperature programmed reduction profile recorded from γ–Fe_2O_3 formed by addition of base to salt and boiling under reflux (Figure 4.7) showed three reduction peaks. The reduction peak temperatures are shown in Table 4.5.

Table 4.5 TPR reduction peaks recorded from γ-Fe_2O_3 prepared by addition of base to salt or salt to base and boiling under reflux and calcination at 250 °C or heating hydrothermally

Sample	Reduction Peaks /°C (± 50 °C)			
	Peak 1	Peak 2	Peak 3	Additional Peaks
γ-Fe_2O_3 (base to salt, boiling under reflux and calcination at 250 °C)	350	720	1013	
γ-Fe_2O_3 (salt to base, boiling under reflux and calcination at 250 °C)	360	740	990	430-440
γ-Fe_2O_3 (base to salt and heated hydrothermally)	340	760	950	*690 (shoulder)*
γ-Fe_2O_3 (salt to base and heated hydrothermally)	325	718	910	*547 (shoulder)*

XRD and ^{57}Fe Mössbauer spectroscopy were recorded *ex situ* from the samples retrieved after each reduction peak from the TPR experiment to elucidate the nature of the reduced phases (Figures 4.7 and 4.8). Table 4.6 contains the ^{57}Fe Mössbauer parameters recorded from γ-Fe_2O_3 after each reduction step.

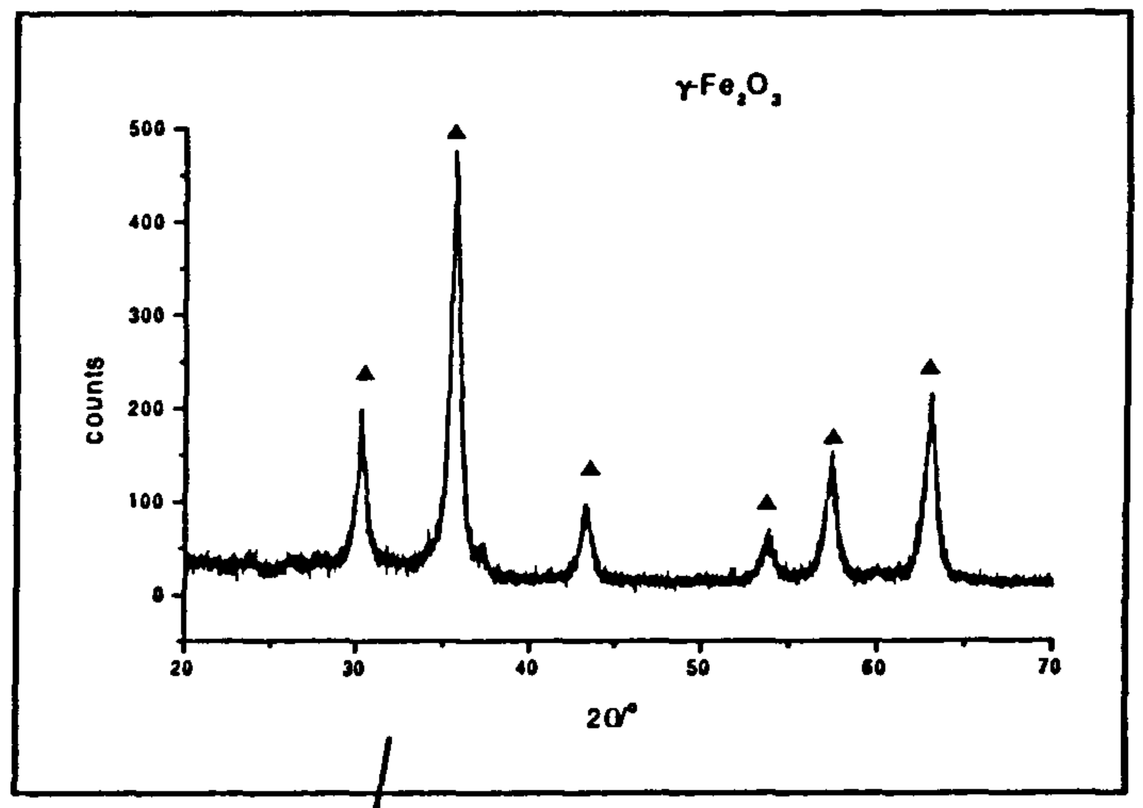

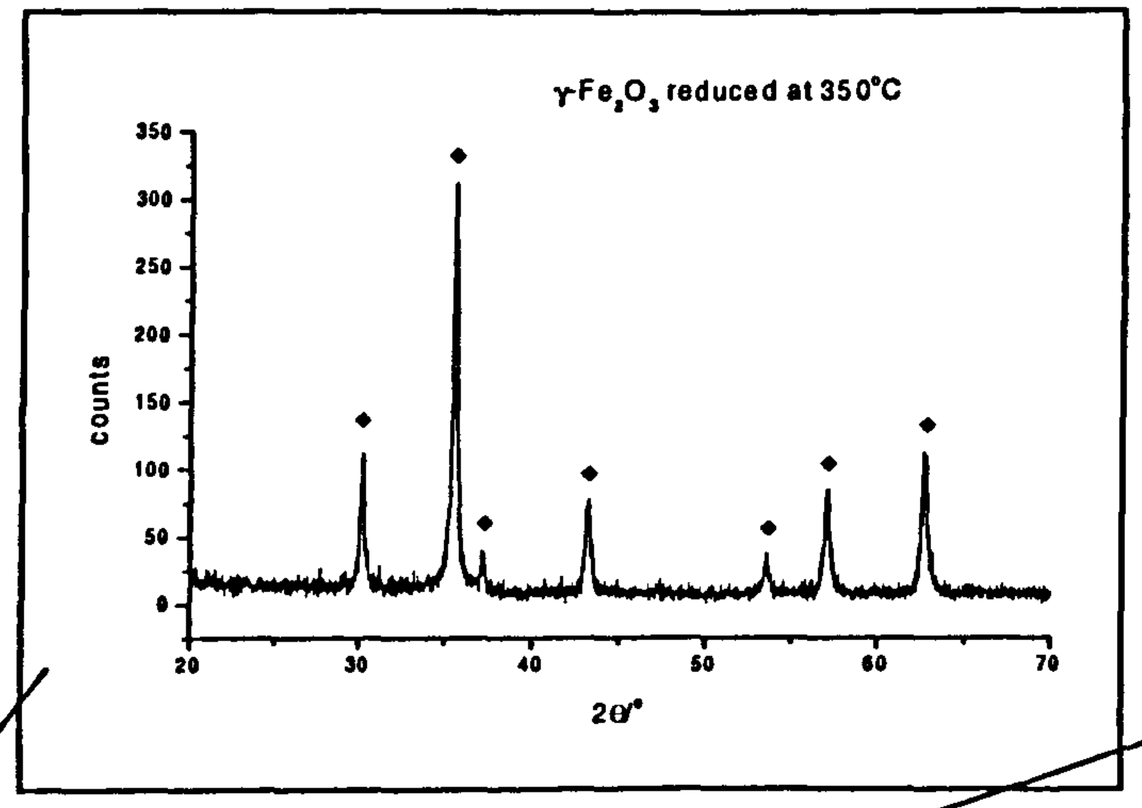

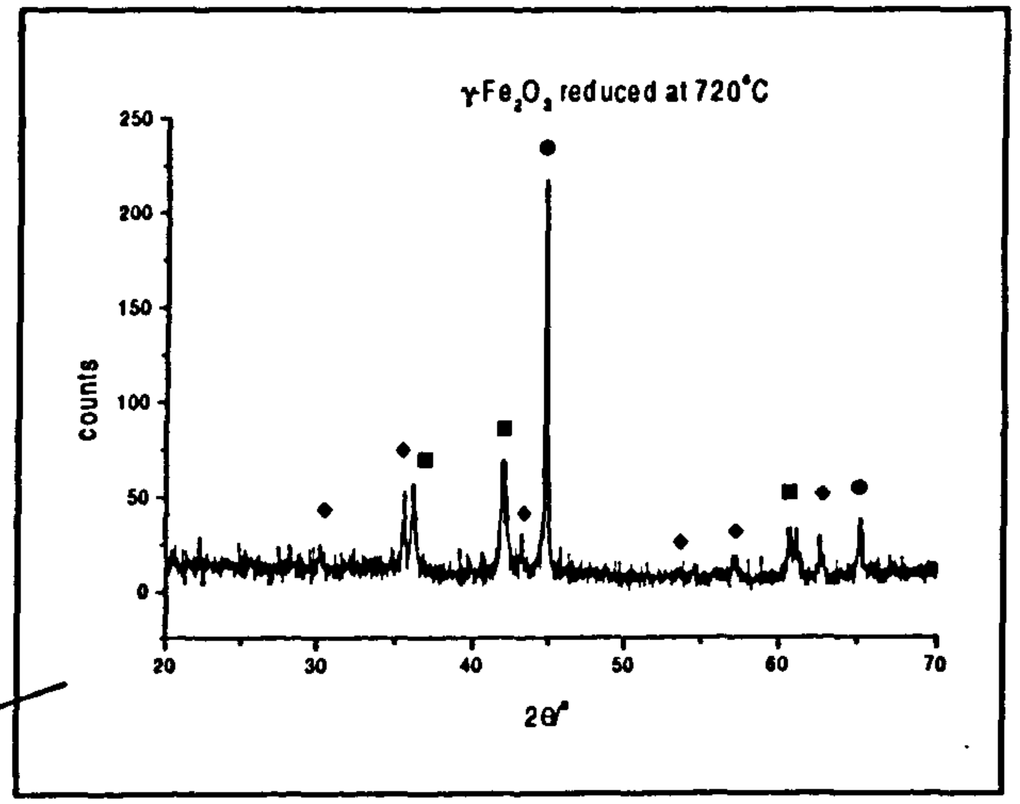

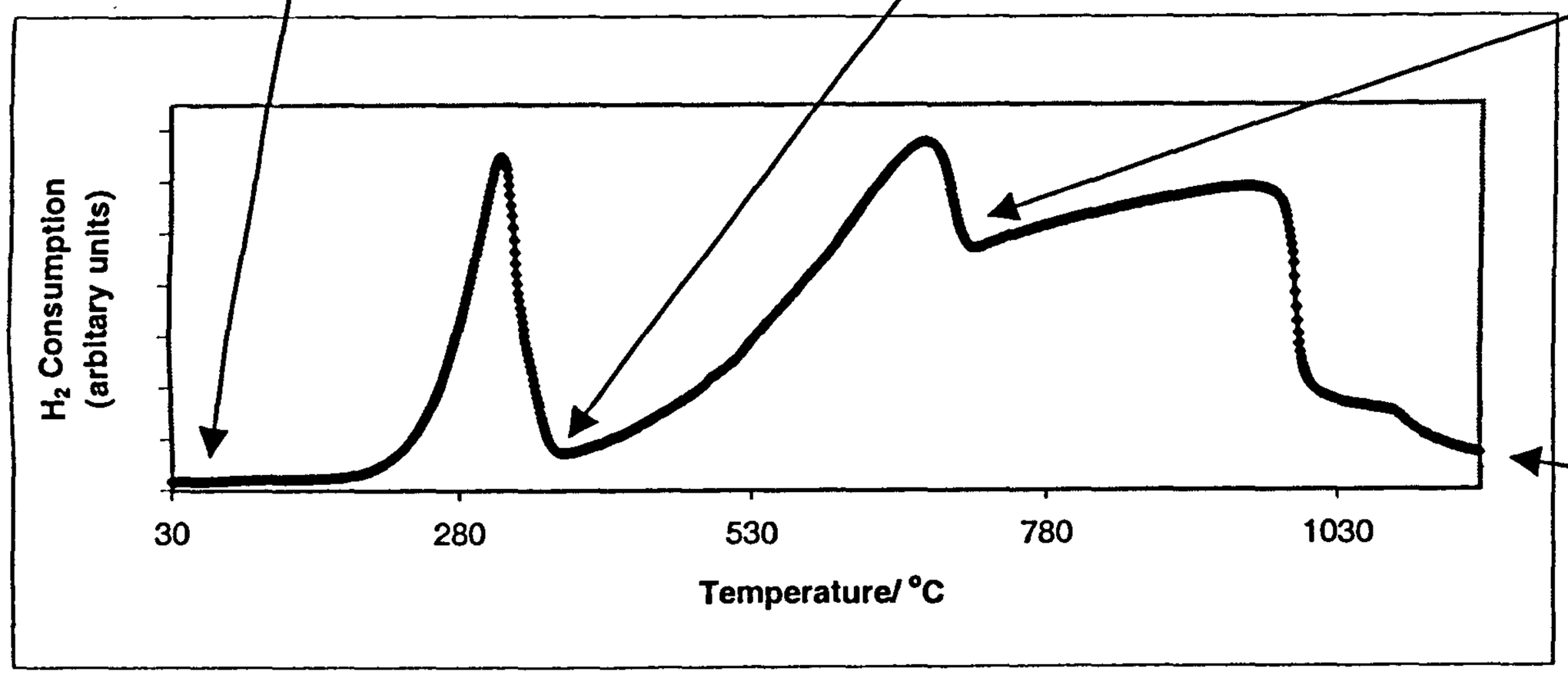

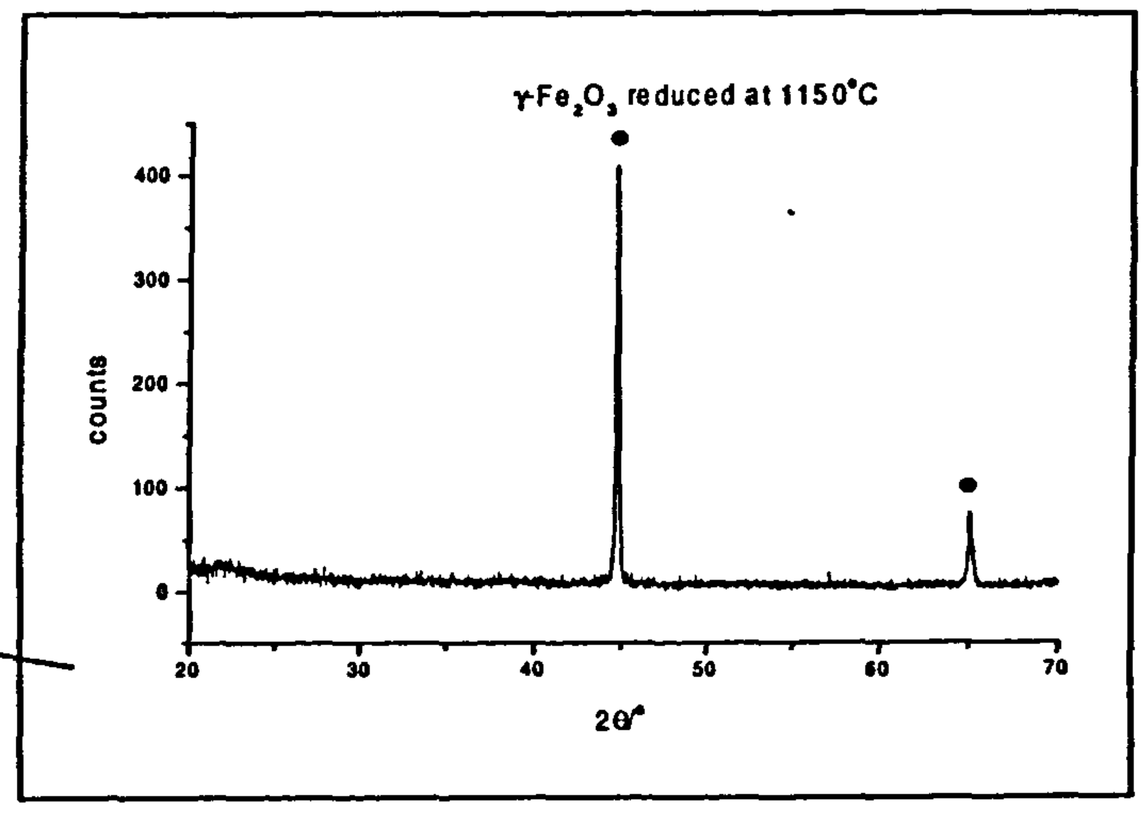

▲ = γ-Fe_2O_3
◆ = Fe_3O_4
■ = FeO
● = Fe

Figure 4.7 TPR profile recorded from γ-Fe_2O_3 and XRD patterns recorded following each reduction peak

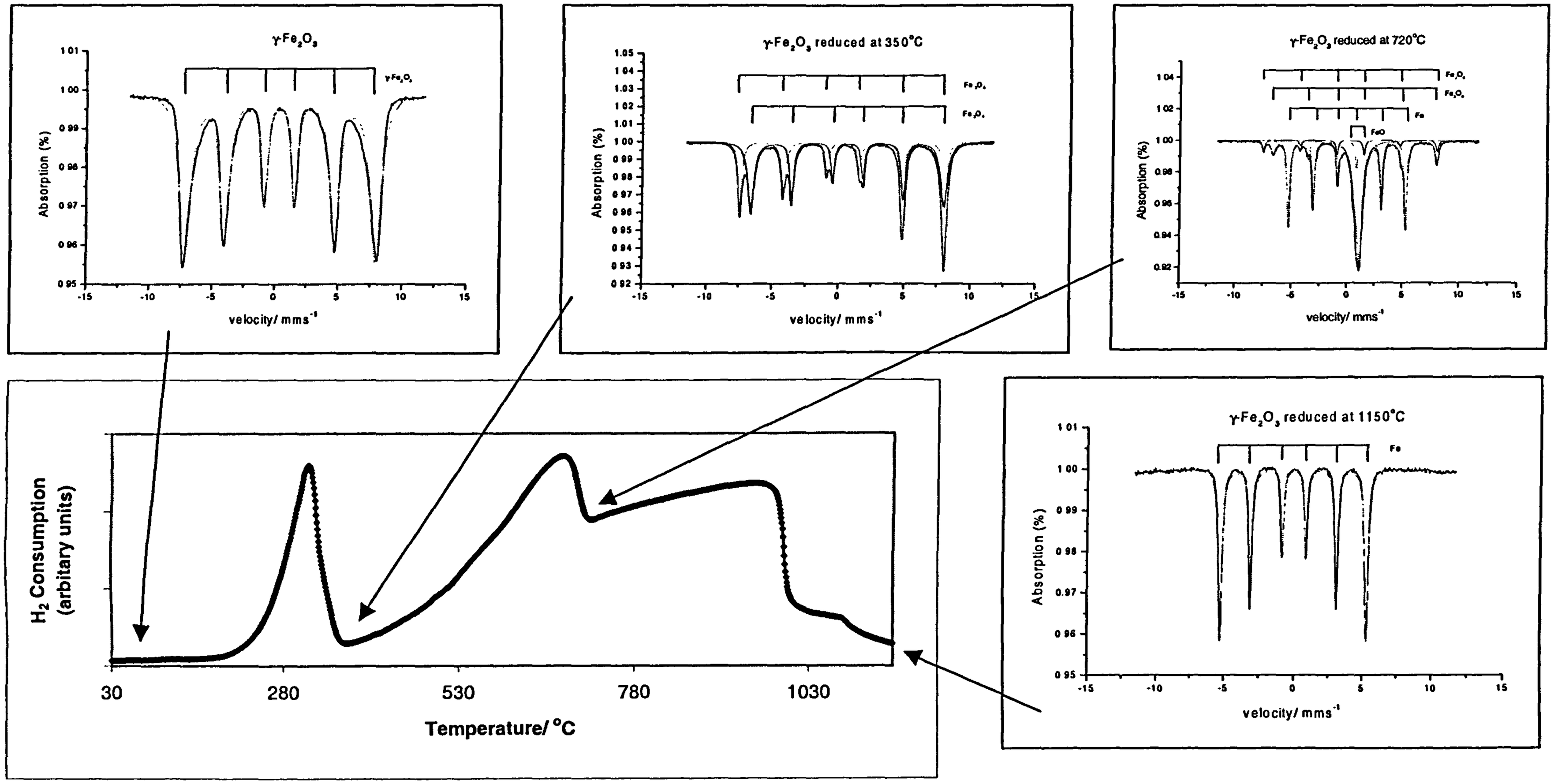

Figure 4.8 TPR profile recorded from γ-Fe_2O_3 and ^{57}Fe Mössbauer spectra recorded following each reduction peak

Table 4.6 ^{57}Fe Mössbauer parameters recorded from γ-Fe_2O_3 prepared by addition of base to salt, boiling under reflux, and calcination at 250 °C/12 h, following reduction in TPR experiment

Sample	δ (± 0.02) mms^{-1}	Δ (± 0.02) mms^{-1}	H (± 1) T	Interpretation	Area (± 5) %
γ-Fe_2O_3	0.34	0.01	47	γ-Fe_2O_3	100
γ-Fe_2O_3 reduced at 350 °C	0.68	0.01	45	Fe_3O_4	100
	0.30	0.01	48	Fe_3O_4	
γ-Fe_2O_3 reduced at 720 °C	0.70	0.0	45	Fe_3O_4	16
	0.29	0.0	48	Fe_3O_4	
	1.05	0.29	---	FeO	40
	0.02	0.0	33	Fe	44
γ-Fe_2O_3 reduced at 1150 °C	0.02	0.01	33	Fe	100

The ^{57}Fe Mössbauer spectra recorded *ex situ* after each reduction step (Figure 4.8) showed the initial reduction of γ–Fe_2O_3 to Fe_3O_4 at 350 °C followed by partial reduction to wüstite (FeO) and metallic iron (Fe) at *ca.* 720 °C. The identification of wüstite, which is generally agreed to be nonstoichiometric when formed at low pressures and is always cation deficient with a formula corresponding to $Fe(II)_{1-3x}Fe(III)_{2x}O$[9] is interesting. The presence of Fe^{3+} and vacancies in nonstoichiometric wüstite result in complex ^{57}Fe Mössbauer spectra which generally appear as an asymmetric broadened doublet[10] and unequivocal characterisation by Mössbauer spectroscopy is difficult especially in a multiphasic sample. However, the X-ray powder diffraction pattern recorded *ex situ* from the γ–Fe_2O_3 after the second reduction peak at *ca.* 720 °C (Figure 4.7) showed the three peaks at *ca.* 37°, 42° and 61° 2θ, characteristic[11] of wüstite together with those at *ca.* 30°, 35°, 43°, 57° and 62°

2θ, characteristic of magnetite[4] and *ca.* 45°, and 65° 2θ, characteristic of metallic iron[12].

The ^{57}Fe Mössbauer spectrum recorded *ex situ* after the final reduction peak in the TPR profile (Figure 4.8) was characteristic of metallic iron. This was endorsed by the X-ray powder diffraction pattern recorded from the reduced phase (Figure 4.7).

The results show that the reduction of γ–Fe_2O_3 follows three steps:

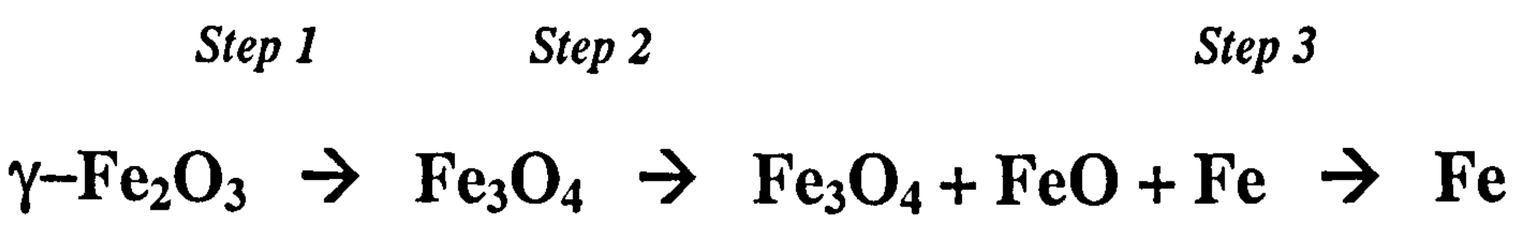

Reduction-reoxidation properties

γ–Fe_2O_3 was subjected to reduction at 350 °C in the 10 % hydrogen- 90 % nitrogen mixture (R1) and reoxidation by heating at 400 °C for 1 h in air (O1). The cycle of reduction and reoxidation was repeated twice (samples R2, O2, R3 and O3). X-ray powder diffraction (Figure 4.9) and ^{57}Fe Mössbauer spectroscopy (Figure 4.10, Table 4.7) were used to identify the materials after each reduction/oxidation step.

Figure 4.9 XRD patterns recorded *ex situ* from γ-Fe_2O_3 following reduction and reoxidation cycles

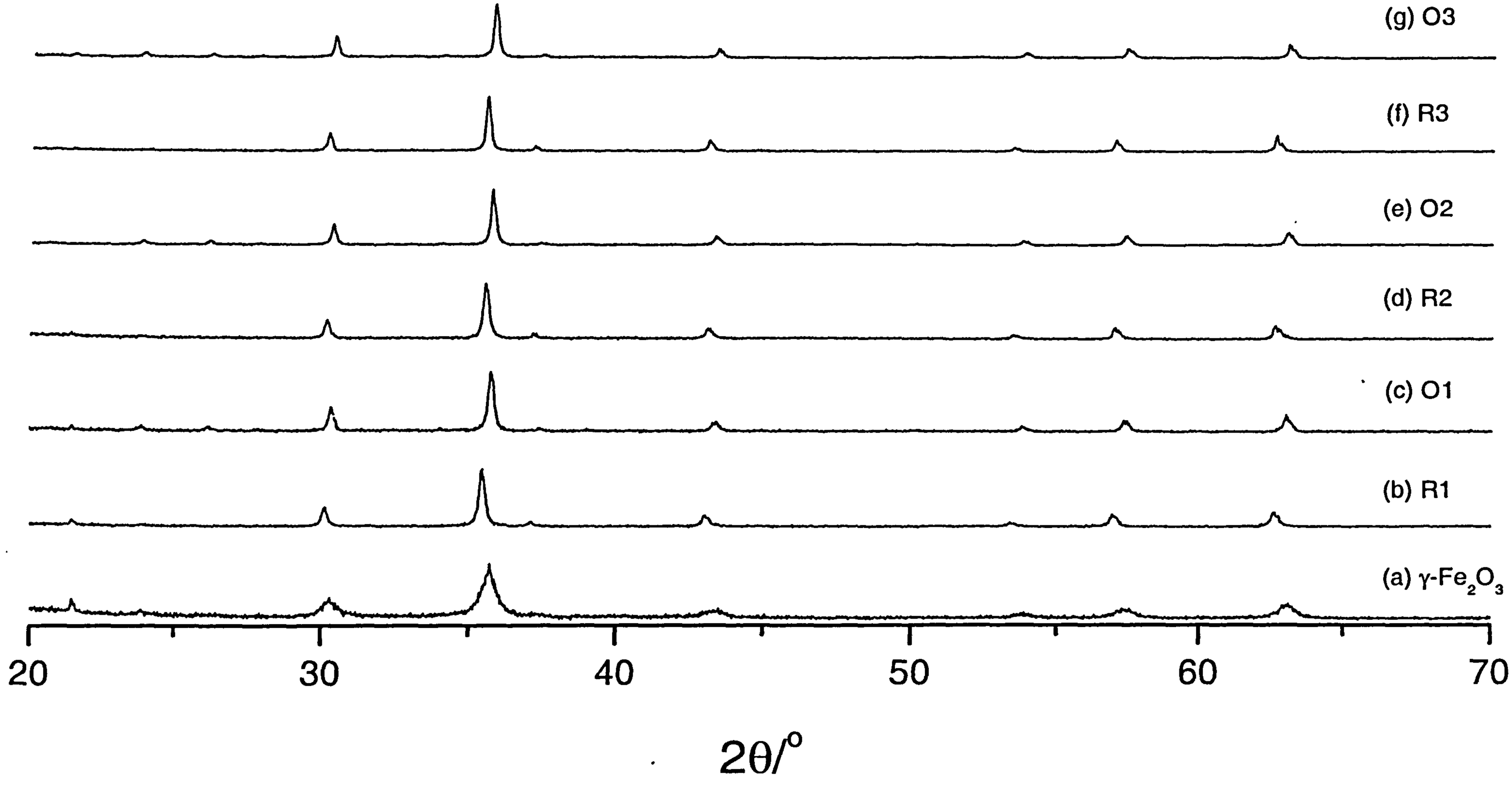

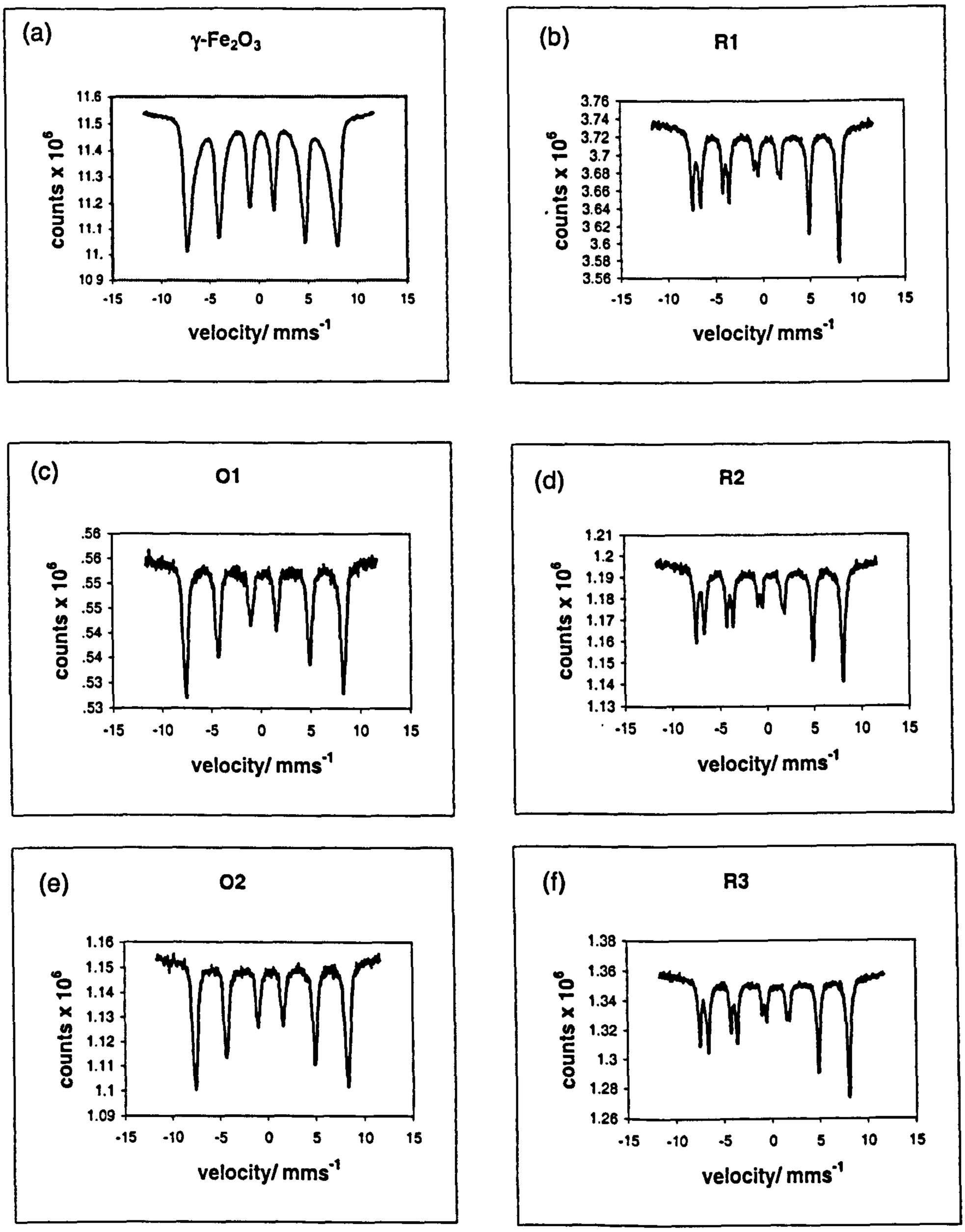

Figure 4.10 ^{57}Fe Mössbauer spectra recorded from γ-Fe_2O_3 following reduction and reoxidation cycles

Table 4.7 ^{57}Fe Mössbauer parameters recorded from γ-Fe_2O_3 following treatment in reducing and oxidising environments

Sample	δ (± 0.02) mms^{-1}	Δ (± 0.02) mms^{-1}	H (± 1) T	Interpretation
γ-Fe_2O_3	0.34	0.01	47	γ-Fe_2O_3
R1	0.68	0.02	45	Fe_3O_4
	0.32	-0.01	48	Fe_3O_4
O1	0.35	0.02	49	γ-Fe_2O_3
R2	0.68	0.02	45	Fe_3O_4
	0.32	0.0	49	Fe_3O_4
O2	0.34	0.02	49	γ-Fe_2O_3
R3	0.68	0.01	45	Fe_3O_4
	0.32	-0.01	48	Fe_3O_4
O3	0.35	0.02	49	γ-Fe_2O_3

The results show that γ–Fe_2O_3 can be reduced to Fe_3O_4 and reoxidised to γ–Fe_2O_3 and the reduction and reoxidation cycle repeated.

The particle size of γ–Fe_2O_3 of *ca.* 13 nm as determined by the Scherrer method from the X-ray powder diffraction data was found to increase to 44 nm when Fe_3O_4 was formed by initial reduction (R1). The surface area decreased from *ca.* 69 m^2g^{-1} for γ–Fe_2O_3 to *ca.* 29 m^2g^{-1} for Fe_3O_4 (R1). This was followed by reoxidation to γ–Fe_2O_3 (O1) with slightly higher particle size (*ca.* 48 nm), and lower surface area (15 m^2g^{-1}). The reduction-reoxidation process was repeated on the same sample for a further two cycles with further gradual increases in particle size, with the finally regenerated γ–Fe_2O_3 (O3) with particle size of *ca.* 55 nm and surface area *ca.* 15 m^2g^{-1}. The major changes in particle size of γ–Fe_2O_3 was induced by the initial reduction to Fe_3O_4 (R1).

In situ ^{57}*Fe Mössbauer spectroscopy studies*

The ^{57}Fe Mössbauer spectra recorded *in situ* from Fe_3O_4 formed by reduction of γ–Fe_2O_3 and subsequent heating in air in the specially designed furnace[13] under a partial pressure of *ca.* 1 Pa are collected in Figure 4.11. Fe_3O_4 (H = 45(1) T, 48(1) T) (Figure 4.11(a)) was initially converted to γ–Fe_2O_3 at 200 °C, which appeared as a broad lined spectrum (Figure 4.11(b)). Cooling the sample to room temperature confirmed the identity of the material as γ–Fe_2O_3 (H = 50(1) T) (Figure 4.11(c)). Heating to 300 °C (Figure 4.11(d)) showed the onset of α-Fe_2O_3 formation. The spectrum recorded after cooling to room temperature (Figure 4.11(e)) showed the superposition of sextets corresponding to γ–Fe_2O_3 (H = 50(1) T and α-Fe_2O_3 H = 52(1) T). Further heating increased the intensity of the peaks corresponding to α-Fe_2O_3 until at 427 °C (Figure 4.11(i and j)) the material was completely converted to α-Fe_2O_3 (H = 52(1) T).

Ex situ studies on the conversion of γ–Fe_2O_3 to α-Fe_2O_3

The X-ray powder diffraction patterns recorded *ex situ* from γ–Fe_2O_3 following heating at various temperatures in air are shown in Figure 4.12. The temperatures of the appearance of α-Fe_2O_3 and the disappearance of γ–Fe_2O_3 are shown in Table 4.8. The results showed the onset of conversion to α-Fe_2O_3 at *ca.* 450 °C and its virtual completion at *ca.* 550 °C. The results are similar to those recorded previously[14] from synthetic γ–Fe_2O_3 of poor crystallinity. The results also show that ^{57}Fe Mössbauer spectroscopy is more sensitive to the detection of the early stages of α-Fe_2O_3 formation.

Figure 4.11 ***In situ*** **Mössbauer spectra recorded from Fe_3O_4 reduced from γ-Fe_2O_3**

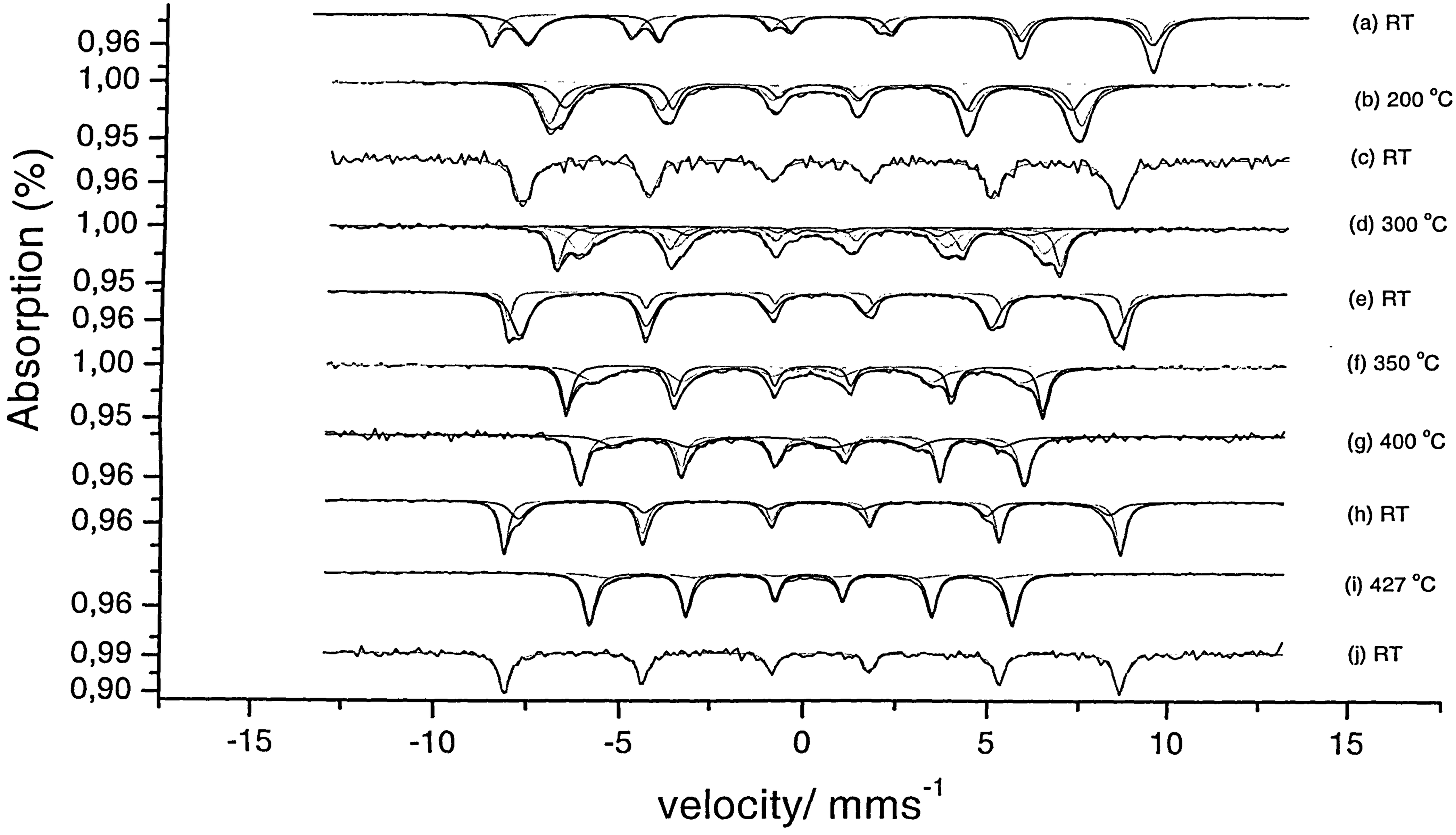

Figure 4.12 XRD patterns recorded *ex situ* from γ-Fe_2O_3 prepared by addition of base to salt, boiling under reflux, heating to 250 °C and then heated from 350 to 700 °C

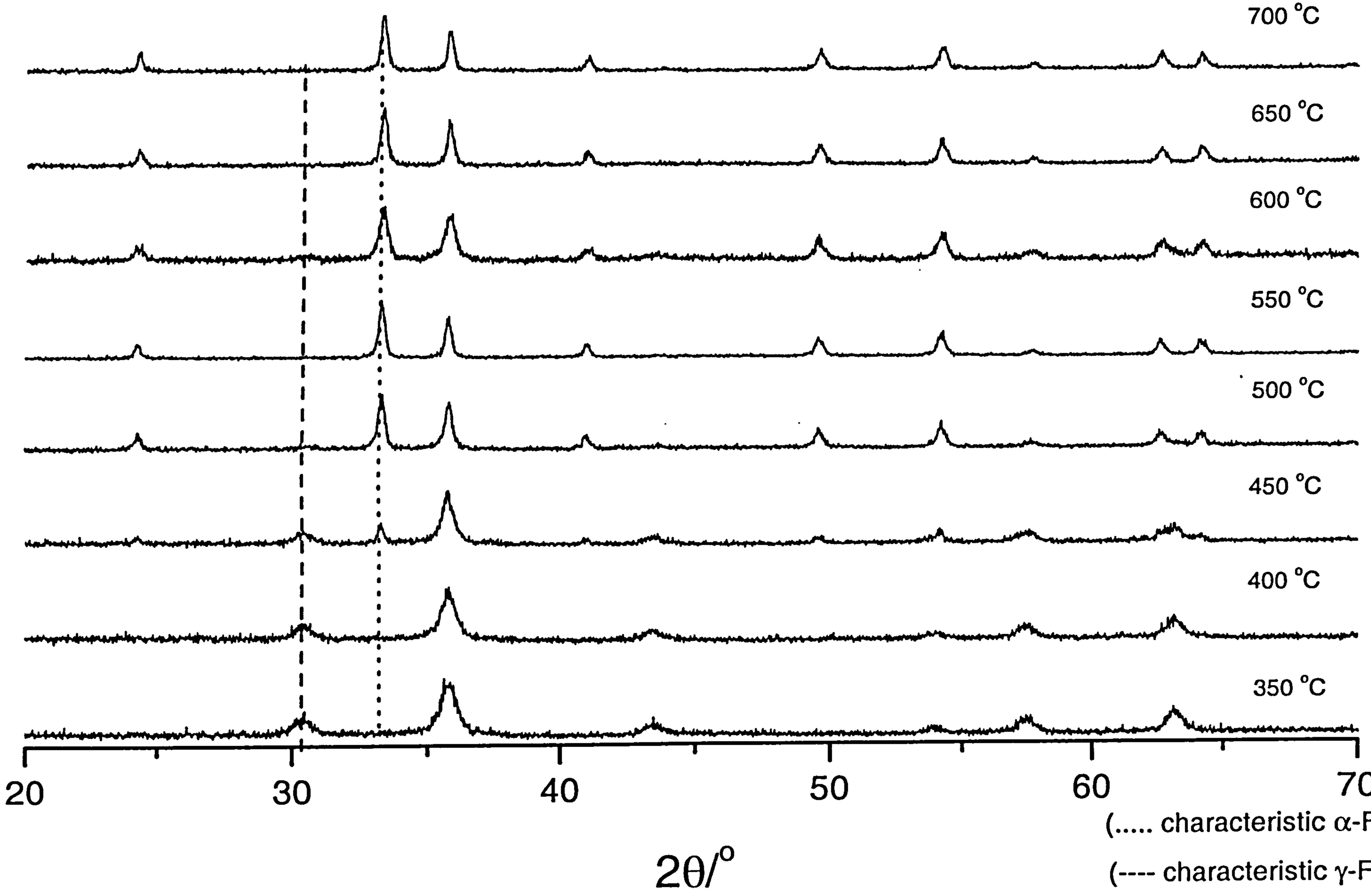

Table 4.8 Temperature of conversion of γ–Fe_2O_3 (prepared by addition of base to salt or salt to base and boiling under reflux and calcination at 250 °C or heating hydrothermally) to α-Fe_2O_3

Sample	Temperature/ °C (± 25 °C)	
	α-Fe_2O_3 formation	γ-Fe_2O_3 disappearance
γ-Fe_2O_3 (base to salt, boiling under reflux, and calcination at 250 °C)	450	550
γ-Fe_2O_3 (salt to base, boiling under reflux, and calcination at 250 °C)	400	500
γ-Fe_2O_3 (base to salt and heated hydrothermally)	400	500
γ-Fe_2O_3 (salt to base and heated hydrothermally)	450	500

Conclusion

γ-Fe_2O_3 prepared by addition of base to salt, boiling the precipitate under reflux, and heating the resulting solid at 250 °C/12 h has a surface area of 69 m^2g^{-1}. The TPR profile showed three reduction peaks. From the study of the reduced phases, γ–Fe_2O_3 was found to initially reduce to Fe_3O_4, followed by partial reduction to FeO and Fe and then finally to metallic iron. The reduction-reoxidation cycle showed that γ–Fe_2O_3 can be reduced to Fe_3O_4 and reoxidised back to γ–Fe_2O_3 with the greatest difference in the particle size and surface area being due to the initial reduction step over a three fold reduction- oxidation cycle. *In situ* high temperature Mössbauer spectroscopy studies on Fe_3O_4 reduced from γ–Fe_2O_3 prepared by addition of base to salt and boiling under reflux showed oxidation to γ–Fe_2O_3 at *ca.* 200 °C and the onset of conversion to α-Fe_2O_3 at *ca.* 300 °C with complete conversion at *ca.* 427 °C. *Ex situ* XRD studies showed the onset of α-Fe_2O_3 formation at *ca.* 450 °C.

4.1.3 γ-Fe_2O_3 (addition of salt to base, boiling under reflux, and calcination at 250 °C/12 h)

The ^{57}Fe Mössbauer spectrum recorded from γ–Fe_2O_3 prepared by addition of salt to base, boiling under reflux, and calcination at 250 °C/12 h showed a broad sextet pattern (δ 0.35(2) mms^{-1}, Δ 0.01(2) mms^{-1}, H 43(1) T) corresponding to γ–Fe_2O_3[1,2] (Figure 4.13, Table 4.3). The spectrum was different from that recorded from the sample prepared by addition of base to salt in that it was broader and contained a doublet characteristic of small particles of iron oxide[3] accounting for *ca.* 42 % of the spectral area. The magnetic hyperfine field was lower than that reported in the literature[1,2] and is consistent with the presence of small particle.

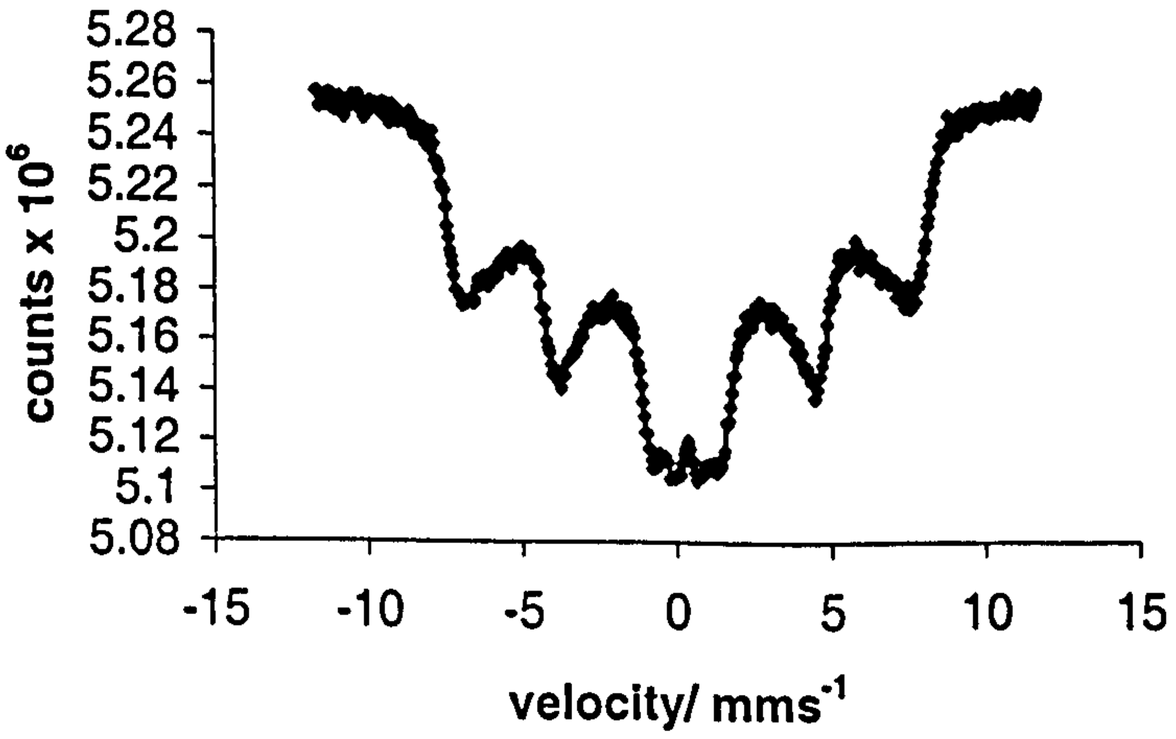

Figure 4.13 ^{57}Fe Mössbauer spectrum recorded from γ-Fe_2O_3 formed by addition of a 1:2 mixture of iron (II)- and iron (III)- containing solution to aqueous ammonia, boiling under reflux, and calcination at 250 °C

The XRD pattern shown in Figure 4.14 corresponded to a spinel-related structure[5] with lattice parameter a = 8.353(2) Å compared to a = 8.334 Å for γ–Fe_2O_3[8], and to a = 8.354(2) Å for γ–Fe_2O_3 formed here by addition of base to salt, boiling under reflux, and calcination at 250 °C/12 h, (see Section 4.1.2).

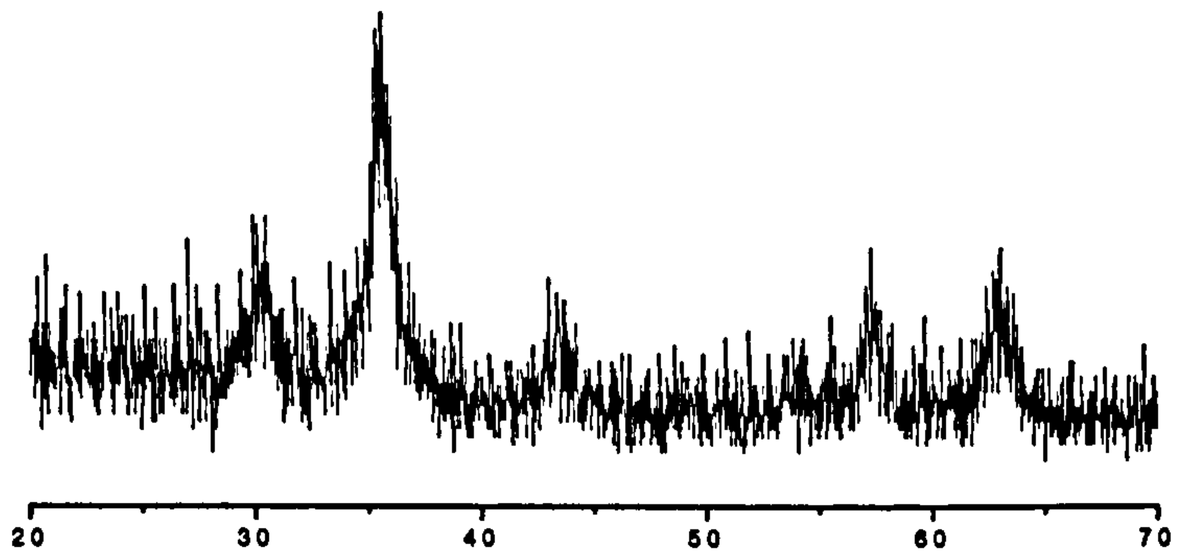

Figure 4.14 XRD pattern recorded from γ-Fe_2O_3 formed by addition of a 1:2 mixture of iron (II)- and iron (III)- containing solution to aqueous ammonia, boiling under reflux, and calcination at 250 °C

The BET surface area of γ-Fe_2O_3 prepared by calcinating at 250 °C of the solid formed by addition of salt to base and boiling under reflux was calculated to be 150 m^2g^{-1}, Table 4.4. This is significantly higher than the surface area of γ-Fe_2O_3 prepared by addition of base to salt and boiling under reflux (69 m^2g^{-1}). The particle size of 8 nm derived from the X-ray powder diffraction linewidth data (Table 4.4) is in agreement with the higher surface area and is smaller than the particle size of γ–Fe_2O_3 prepared by addition of base to salt, boiling under reflux, and calcination at 250 °C/12 h (13 nm).

The TPR profile recorded from γ-Fe_2O_3 prepared by addition of salt to base, boiling under reflux, and calcination at 250 °C/12 h (Figure 4.15) showed the material to follow a similar reduction pathway as γ-Fe_2O_3 prepared by addition of base to salt. The reduction peak temperatures are shown in Table 4.5. The initial reduction peak corresponded to the reduction of γ-Fe_2O_3 to Fe_3O_4. It was of low intensity compared with that recorded from γ-Fe_2O_3 prepared by addition of base to salt and boiling under reflux. An additional broad peak at *ca.* 430-440 °C was observed. The peaks at

ca. 740 and 990 °C correspond to the partial reduction of Fe_3O_4 (Fe^{3+} to Fe^{2+}) followed by complete reduction to metallic iron.

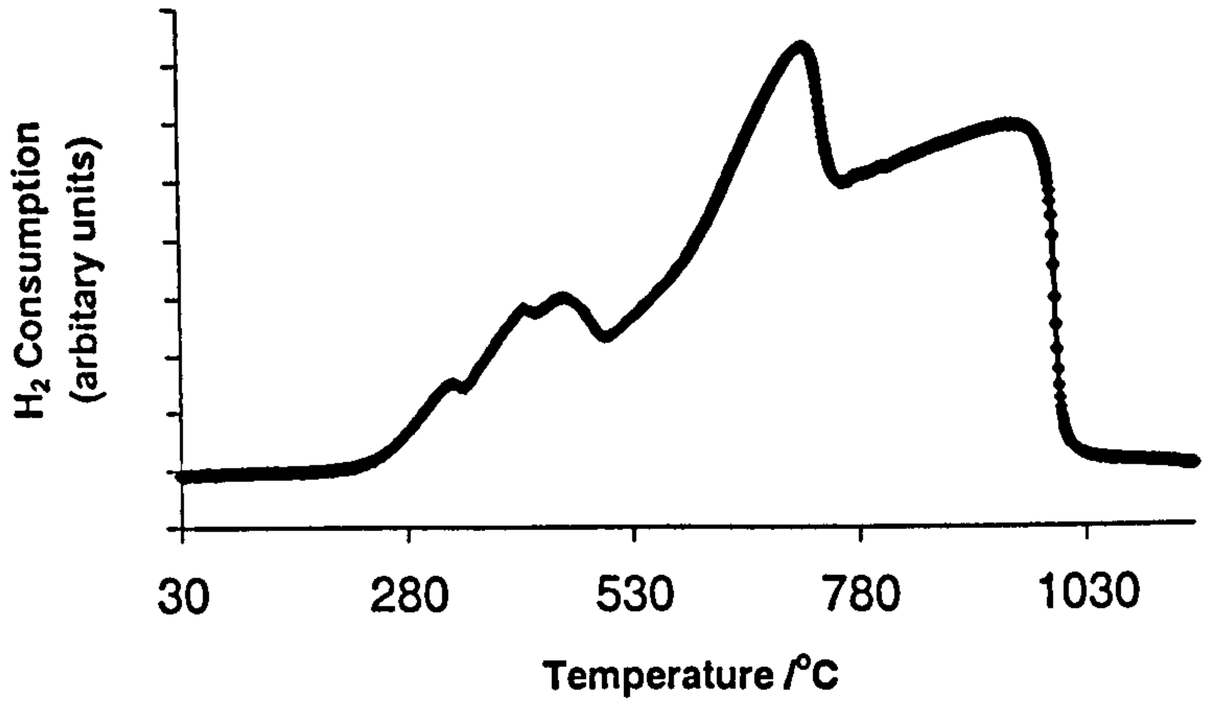

Figure 4.15 TPR profile recorded from γ-Fe_2O_3 formed by addition of a 1:2 mixture of iron (II)- and iron (III)- containing solution to aqueous ammonia, boiling under reflux, and calcination at 250 °C

The sample prepared by addition of salt to base was subjected to heat treatment at various temperatures and XRD patterns recorded *ex situ*, Figure 4.16. Table 4.8 shows the temperature of α-Fe_2O_3 appearance and γ–Fe_2O_3 disappearance. The disappearance of γ-Fe_2O_3 (prepared by addition of salt to base, boiling under reflux, and calcination at 250 °C/12 h) was observed at *ca.* 500 °C compared to 550 °C for γ–Fe_2O_3 prepared by addition of base to salt (Figure 4.12) although the temperatures are probably within the errors. γ–Fe_2O_3 formed by addition of salt to base shows similar stability to conversion to α-Fe_2O_3 as compared with γ–Fe_2O_3 formed by addition of base to salt.

Figure 4.16 XRD patterns recorded *ex situ* from γ-Fe_2O_3 prepared by addition of salt to base, boiling under reflux, heated to 250 °C and then heated from 300 to 600 °C

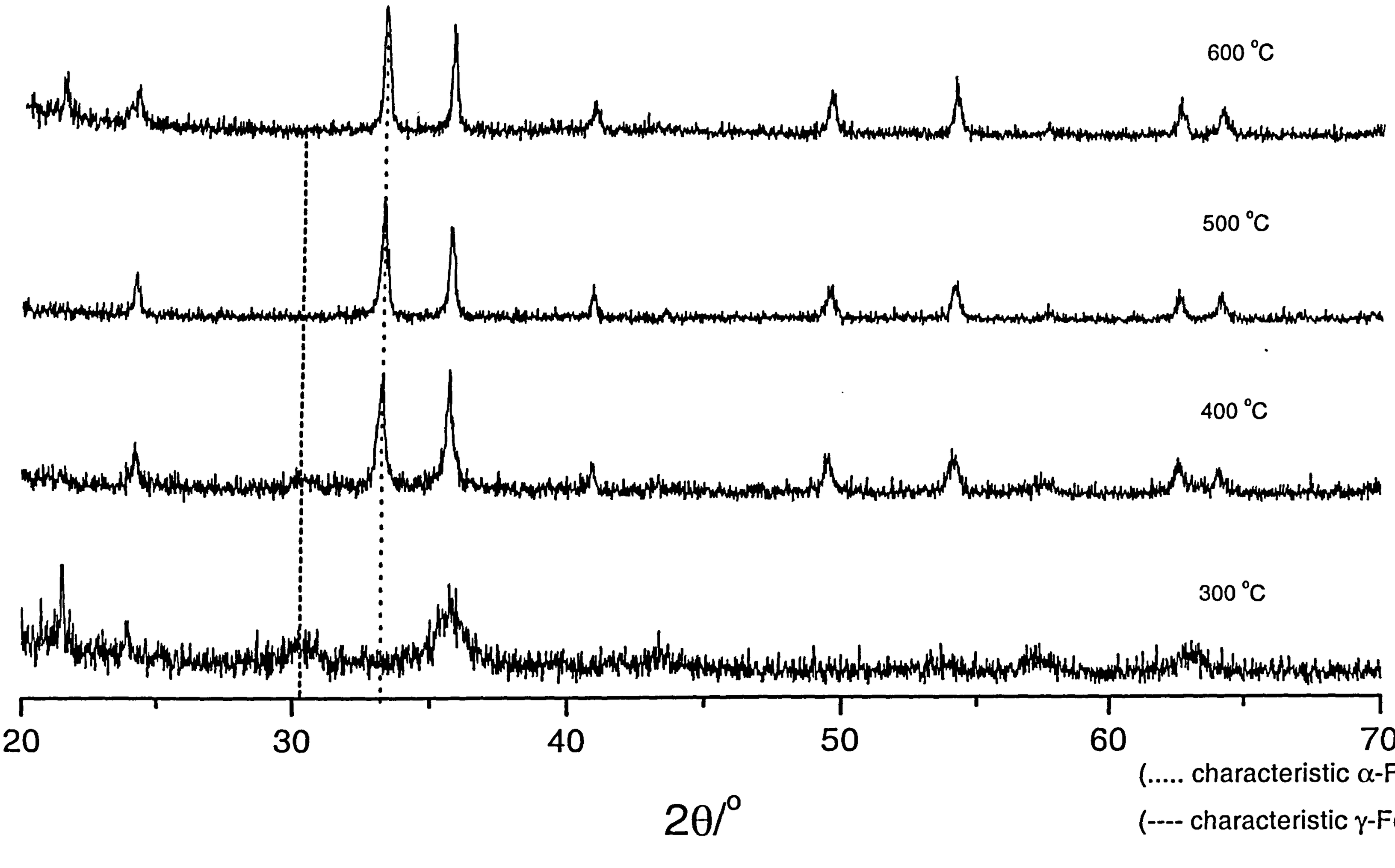

Conclusion

The Mössbauer spectrum recorded from γ–Fe_2O_3 prepared by addition of salt to base showed it to have a smaller particle size, higher surface area and smaller magnetic hyperfine field as compared to γ–Fe_2O_3 prepared by addition of base to salt, boiling under reflux, and calcination at 250 °C/12 h. The material prepared by addition of salt to base showed similar stability with respect to the thermal conversion to α-Fe_2O_3 as compared with γ–Fe_2O_3 prepared by addition of base to salt. The TPR profile recorded from γ–Fe_2O_3 prepared by addition of salt to base showed three main reduction peaks similar to γ–Fe_2O_3 prepared by addition of base to salt.

4.1.4 γ-Fe_2O_3 (addition of base to salt, heated hydrothermally and dried under an infrared lamp)

^{57}Fe Mössbauer spectrum recorded from γ–Fe_2O_3 prepared by addition of base to salt and heated hydrothermally (Table 4.3) showed a sextet pattern (δ 0.35(2) mms^{-1}, Δ 0.00(2) mms^{-1}, H 48(1) T) which is similar to the literature values reported for γ–Fe_2O_3[1,2]. The XRD pattern recorded from the hydrothermally prepared sample corresponded to a spinel-related structure[5], with lattice parameter a = 8.373(2) Å compared to a = 8.334 Å for reported γ–Fe_2O_3[8], and a = 8.354(2) Å for γ–Fe_2O_3 formed here by addition of base to salt and boiling under reflux (see Section 4.1.2).

The BET surface area data is shown in Table 4.4. The surface area for γ-Fe_2O_3 prepared by addition of base to salt and heated hydrothermally was calculated to be 72 m^{2}g^{-1} and is similar to the surface area of γ-Fe_2O_3 formed by addition of base to salt, boiling under reflux, and calcination at 250 °C/12 h (69 m^{2}g^{-1}).

The particle size calculated from the XRD linewidth data was found to be *ca.* 15 nm in agreement with particle size calculated from electron microscopy (*ca.* 13 nm).

The TPR profile recorded from γ-Fe_2O_3 prepared by addition of base to salt and heated hydrothermally showed three reduction peaks, similar to that of γ–Fe_2O_3 prepared by addition of base to salt, boiling under reflux, and calcination at 250 °C/12 h. The reduction peak temperatures are shown in Table 4.5. A shoulder at *ca.* 690 °C was also observed.

γ–Fe_2O_3 prepared by addition of base to salt and heated hydrothermally was subjected to heat treatment and XRD patterns recorded *ex situ* (Figure 4.17, Table 4.8). The complete conversion of γ–Fe_2O_3 to α-Fe_2O_3 was observed at *ca.* 500 °C.

Conclusion

γ-Fe_2O_3 prepared by addition of base to salt and heated hydrothermally had a similar surface area, similar thermal stability and gave a similar TPR profile to that of γ–Fe_2O_3 prepared by addition of base to salt, boiling under reflux, and calcination at 250 °C/12 h.

4.1.5 γ-Fe_2O_3 (addition of salt to base, heated hydrothermally and dried under an infrared lamp)

The ^{57}Fe Mössbauer spectrum recorded from the sample prepared by addition of salt to base and heated hydrothermally showed a sextet pattern (δ 0.35(2) mms^{-1}, Δ

Figure 4.17 XRD patterns recorded *ex situ* from γ-Fe_2O_3 prepared by addition of base to salt and heated hydrothermally, heated from 400 to 600 °C

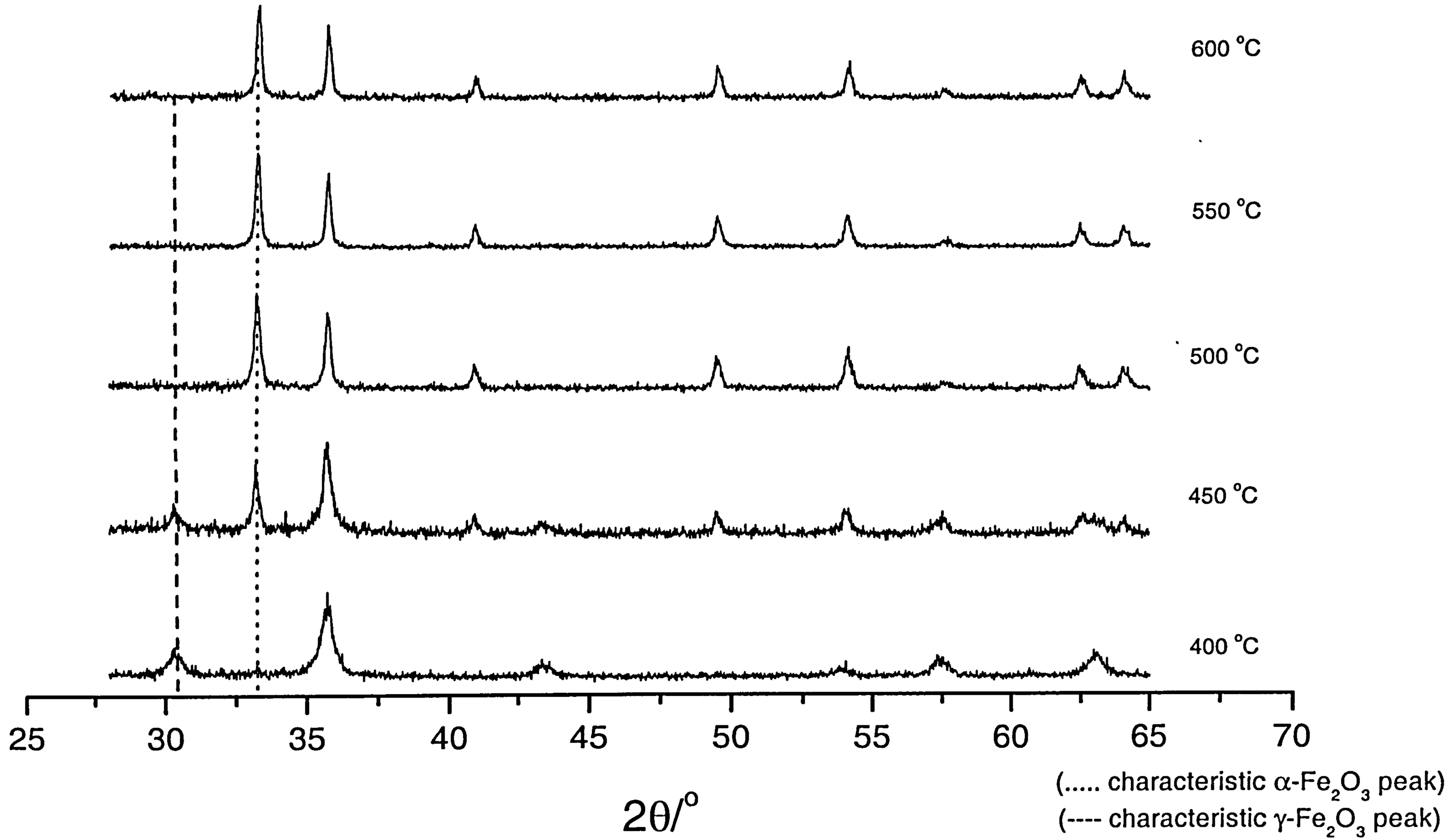

0.01(2) mms^{-1}, *H* 47(1) T) corresponding to γ-Fe_2O_3[1,2] (Table 4.3), and similar to that recorded from γ–Fe_2O_3 prepared hydrothermally by addition of base to salt and γ–Fe_2O_3 prepared by addition of base to salt, boiling under reflux, and calcination at 250 °C/12 h. The reduction of the magnetic hyperfine field observed when γ–Fe_2O_3 was prepared by addition of salt to base, boiling under reflux and calcination at 250 °C was not observed. The result implies that both hydrothermally prepared samples (base to salt and salt to base) have similar particle sizes. The XRD pattern recorded from the sample prepared by the addition of salt to base and heated hydrothermally corresponded to a spinel-related structure[5], with lattice parameter a = 8.383(2) Å compared to a = 8.334 Å for reported γ–Fe_2O_3[8], and a = 8.373(2) Å for γ–Fe_2O_3 formed here by addition of base to salt and heated hydrothermally (Section 4.1.4).

The surface area and particle size data are shown in Table 4.4. The BET surface area of γ-Fe_2O_3 prepared hydrothermally by the addition of salt to base was calculated to be 71 m^2g^{-1}. This was similar to the surface area of γ-Fe_2O_3 prepared hydrothermally by the addition of base to salt and γ–Fe_2O_3 prepared by addition of base to salt, boiling under reflux, and calcination at 250 °C/12 h, but was significantly smaller than the surface area of γ–Fe_2O_3 formed by addition of salt to base, boiling under reflux, and calcination at 250 °C/12 h (Section 4.1.3).

The TPR profile recorded from γ-Fe_2O_3 formed hydrothermally by addition of salt to base showed three reduction peaks similar to that of γ-Fe_2O_3 formed hydrothermally by addition of base to salt and γ–Fe_2O_3 prepared by addition of base to salt, boiling

under reflux, and calcination at 250 °C/12 h. The reduction peak temperatures are collected in Table 4.5.

γ–Fe_2O_3 prepared by addition of salt to base and heated hydrothermally was subjected to heat treatment and the XRD patterns recorded *ex situ* (Figure 4.18, Table 4.8). The results were similar to those recorded from the material prepared by addition of base to salt and heated hydrothermally and materials prepared by addition of base to salt or salt to base, boiling under reflux, and calcination at 250 °C/12 h and showed the onset of α-Fe_2O_3 at *ca.* 450 °C and its virtual completion at *ca.* 500 °C.

Conclusion

γ-Fe_2O_3 prepared by addition of salt to base and heated hydrothermally had a similar surface area to γ–Fe_2O_3 prepared by addition of base to salt and heated hydrothermally but lower than that of γ–Fe_2O_3 prepared by addition of salt to base, boiling under reflux, and calcination at 250 °C/12 h. The TPR profiles recorded from γ–Fe_2O_3 prepared by addition of salt to base or base to salt and heated hydrothermally were similar. Both samples of γ-Fe_2O_3 prepared by hydrothermal processing showed the onset of conversion to α-Fe_2O_3 between *ca.* 400 and 450 °C.

Taken together the results recorded in this Section (Section 4.1) show that the preparation of γ–Fe_2O_3 by addition of base to salt, boiling under reflux, and heating the solid at 250 °C/12 h gave a material with small particle size (*ca.* 13 nm) and high surface area (69 m^2g^{-1}). The material also gave a six peak Mössbauer spectrum and three reduction peaks in the TPR profile. The material was also suitable for studies of

Figure 4.18 XRD patterns recorded *ex situ* from γ-Fe_2O_3 prepared by addition of salt to base and heated hydrothermally, heated from 400 to 600 °C

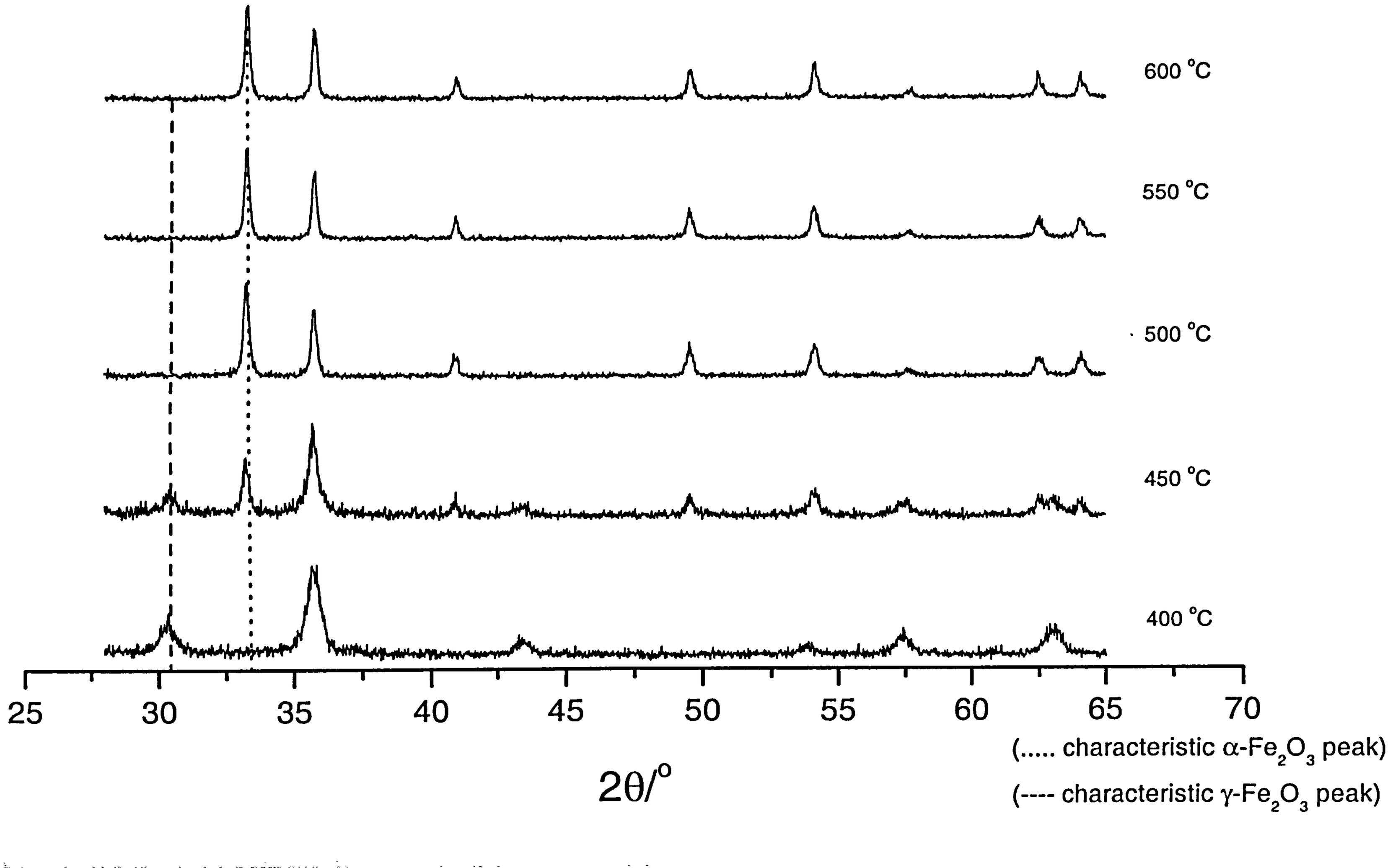

reduction-oxidation cycling. Such a solid was deemed satisfactory for studies by diffraction, spectroscopic and other physical techniques and to have suitable properties for potential uses as a catalyst in automobile exhaust systems. Hence, all metal- doped variants of γ–Fe_2O_3 were prepared by addition of base to salt, boiling the precipitate under reflux, and heating the solid at 250 °C/12 h.

4.2 Metal- Doped γ–Fe_2O_3

γ–Fe_2O_3 was nominally doped with 8 mass % titanium, tin, ruthenium and magnesium all prepared by addition of base to salt, boiling under reflux, and calcination of the solid at 250 °C/12 h.

4.2.1 Titanium- doped γ–Fe_2O_3 (addition of base to salt, boiling under reflux, and calcination at 250 °C/12 h)

The X-ray powder diffraction pattern (Figure 4.19) recorded from the material which inductive coupled plasma (ICP) analysis showed to contain 4.04 mass % Ti was characteristic of a single phase spinel-related structure. The lattice parameter a = 8.368(2) Å may be compared to a = 8.334 Å reported for γ–Fe_2O_3[8] and the γ–Fe_2O_3 formed here by addition of base to salt, boiling under reflux, and calcination at 250 °C (a = 8.354(2) Å). Recent studies[15] by EXAFS of Ti- doped γ–Fe_2O_3 have indicated that titanium adopts the octahedral site in the spinel-related structure. Ti^{4+} in octahedral co-ordination has a radius of 0.61 Å compared to Fe^{3+} which has a radius of 0.65 Å in six fold co-ordination[16]. The small increase in lattice parameter is therefore unexpected.

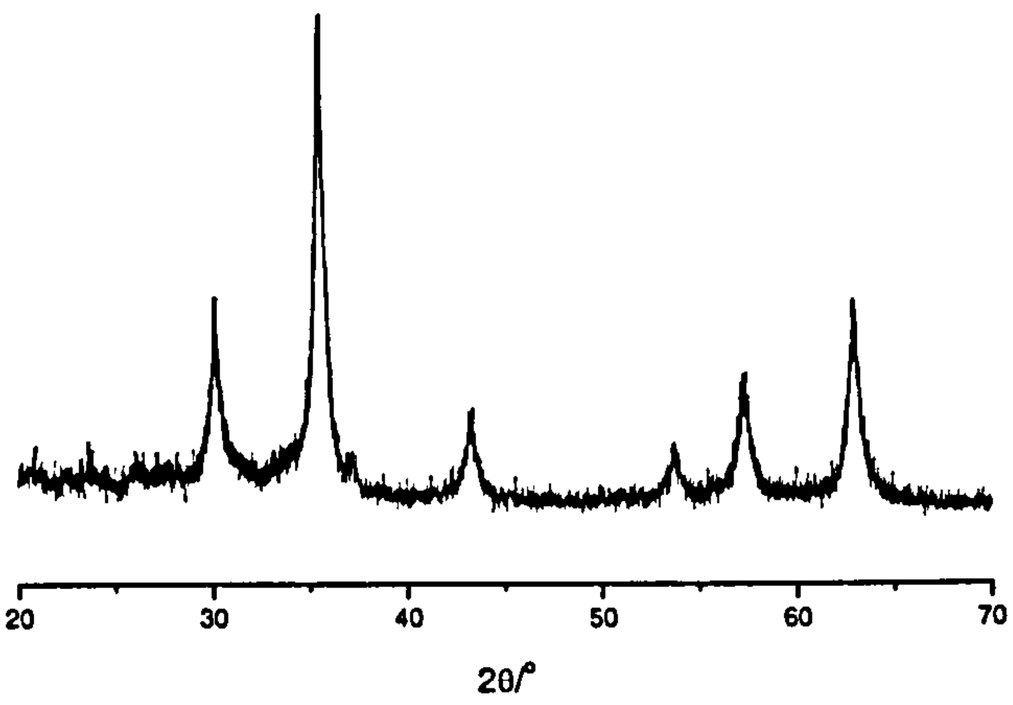

Figure 4.19 XRD pattern recorded from Ti/γ–Fe_2O_3 prepared by addition of base to salt, boiling under reflux, and calcination at 250 °C

The ^{57}Fe Mössbauer spectrum (Figure 4.20) recorded at 298 K showed a sextet pattern (δ 0.35(2) mms^{-1}, Δ 0.01(2) mms^{-1}, H 48(1) T) characteristic[1,2] of a γ–Fe_2O_3-related phase together with a broadened doublet (δ 0.35(2) mms^{-1}, Δ 0.17(2) mms^{-1}) characteristic of the additional presence of paramagnetic Fe^{3+} in small particle iron oxide[3]. The particle size of *ca.* 12 nm obtained from the X-ray powder diffraction linewidth data was similar to that of undoped γ–Fe_2O_3 prepared by addition of excess aqueous ammonia to a 1:2 mixture of iron (II)- and iron (III)- containing solution, boiling under reflux, and calcination at 250 °C (Section 4.1.2). The surface area recorded from Ti/γ–Fe_2O_3 of *ca.* 139 m^{2}g^{-1} was significantly greater than that of undoped γ–Fe_2O_3, prepared by the addition of base to salt and boiling under reflux (Section 4.1.2) but similar to γ–Fe_2O_3 prepared by addition of salt to base and boiling under reflux (Section 4.1.3). The results endorse the observation in the ^{57}Fe Mössbauer spectrum of a significant (*ca.* 42 %) amount of small particle iron oxide.

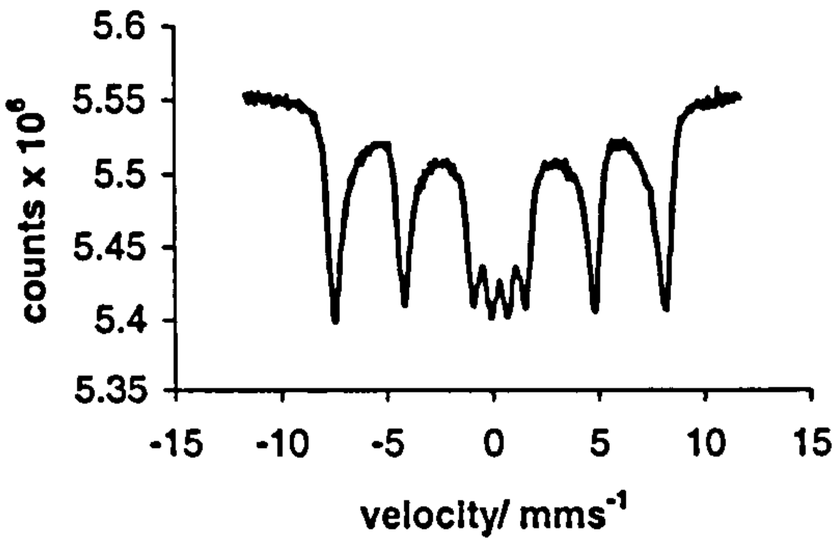

Figure 4.20 ^{57}Fe Mössbauer spectrum recorded from Ti/γ–Fe_2O_3 prepared by addition of base to salt, boiling under reflux, and calcination at 250 °C

The temperature programmed reduction profile recorded from titanium- doped γ–Fe_2O_3 showed three reduction peaks, with the latter two peaks merging together (Figure 4.21). *Ex situ* XRD and *ex situ* ^{57}Fe Mössbauer spectroscopy examination of samples retrieved after each reduction peak from the TPR experiment were used to reveal the identity of the reduced phases (Figures 4.21 and 4.22 respectively). Table 4.9 shows the ^{57}Fe Mössbauer parameters of Ti/γ-Fe_2O_3 after each reduction step.

The first reduction step at *ca.* 350 °C can, as in the case of undoped γ–Fe_2O_3 prepared by a similar method (Figure 4.7), be associated with the reduction of titanium- doped γ–Fe_2O_3 to titanium- doped Fe_3O_4. The ^{57}Fe Mössbauer spectrum also showed that *ca.* 33 % of the material remained in small particle form following the initial reduction step. In contrast to the results recorded from undoped γ–Fe_2O_3 prepared by a similar method (Figure 4.7) subsequent reduction proceeded over a large temperature range being completed at *ca.* 1030 °C where the ^{57}Fe Mössbauer spectrum recorded after reduction at 1150 °C showed the formation of metallic iron. It is interesting that no evidence for a reduced form of titanium was observed in the Mössbauer spectrum or XRD pattern recorded following reduction at 1150 °C. This may reflect the difficulty in titanium dioxide reduction to the metallic phase at these

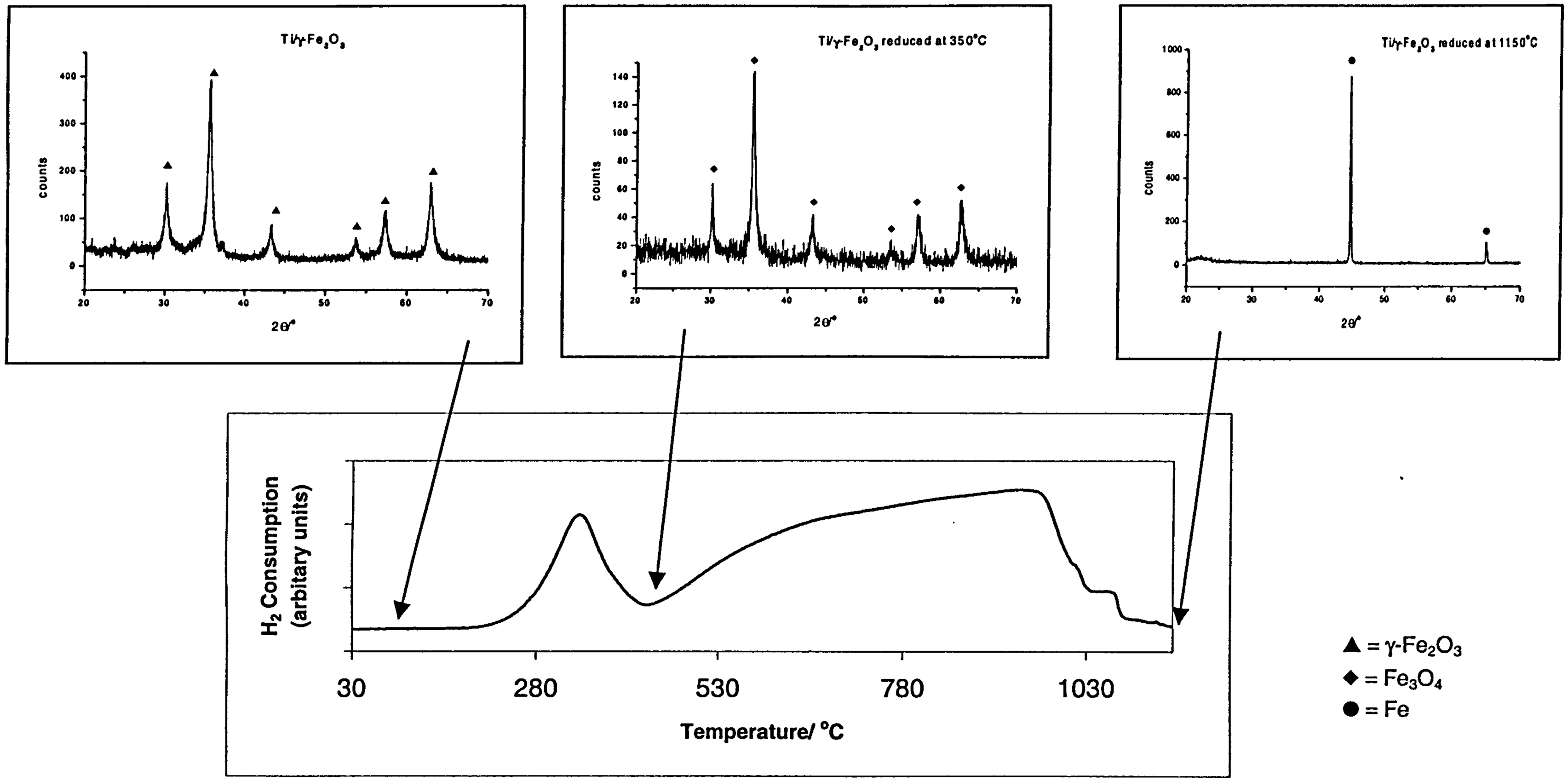

Figure 4.21 TPR profile recorded from Ti/γ-Fe_2O_3 and XRD patterns recorded following each reduction peak

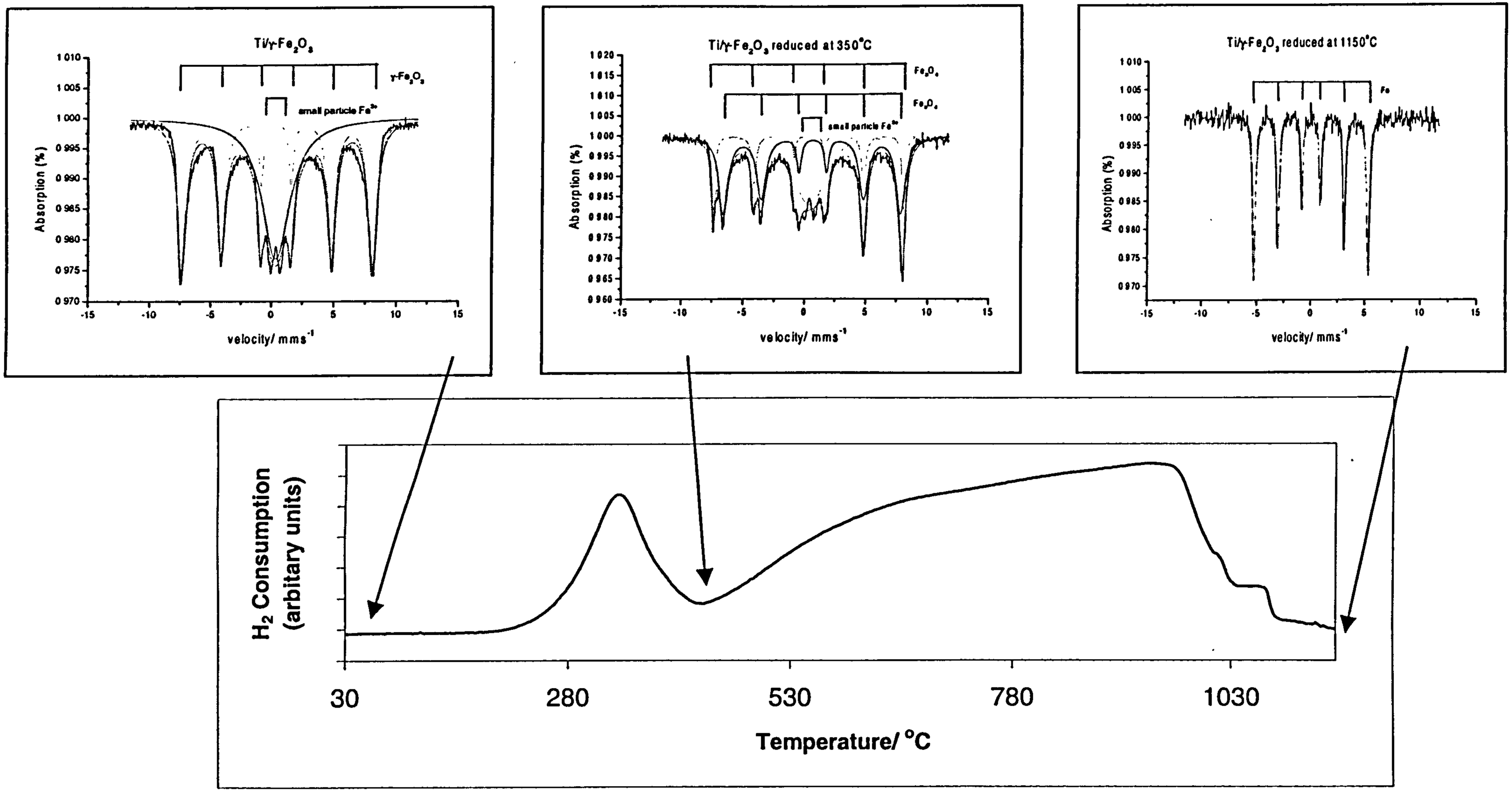

Figure 4.22 TPR profile recorded from Ti/γ-Fe_2O_3 and ^{57}Fe Mössbauer spectra recorded following each reduction peak

conditions. No evidence for the formation of wüstite was observed. The nature of the reduction products were confirmed by the X-ray powder diffraction patterns (Figure 4.21) recorded *ex situ* from the reduced phases.

Table 4.9 ^{57}Fe Mössbauer parameters recorded from Ti/γ-Fe_2O_3 following reduction in TPR experiment

Sample	δ (± 0.02) mms^{-1}	Δ (± 0.02) mms^{-1}	H (± 1) T	Interpretation	Area (± 5) %
Ti/γ-Fe_2O_3	0.35	0.17	---	Small particle iron oxide	42
	0.35	0.01	48	γ-Fe_2O_3	58
Ti/γ-Fe_2O_3 reduced at 350 °C	0.38	1.04	---	Small particle iron oxide	33
	0.61	-0.01	45	Fe_3O_4	67
	0.32	0.0	48	Fe_3O_4	
Ti/γ-Fe_2O_3 reduced at 1150 °C	0.02	0.01	33	Fe	100

Reduction-reoxidation properties

Ti/γ–Fe_2O_3 was subjected to reduction at 350 °C in the 10 % hydrogen- 90 % nitrogen mixture (R1) and reoxidation by heating at 400 °C for 1 h in air (O1). The cycle of reduction and reoxidation was repeated twice (samples R2, O2, R3 and O3). X-ray powder diffraction (Figure 4.23) and ^{57}Fe Mössbauer spectroscopy (Figure 4.24, Table 4.10) were used to identify the materials after each reduction- reoxidation step.

Figure 4.23 XRD patterns recorded *ex situ* from Ti/γ-Fe_2O_3 following reduction and reoxidation cycles

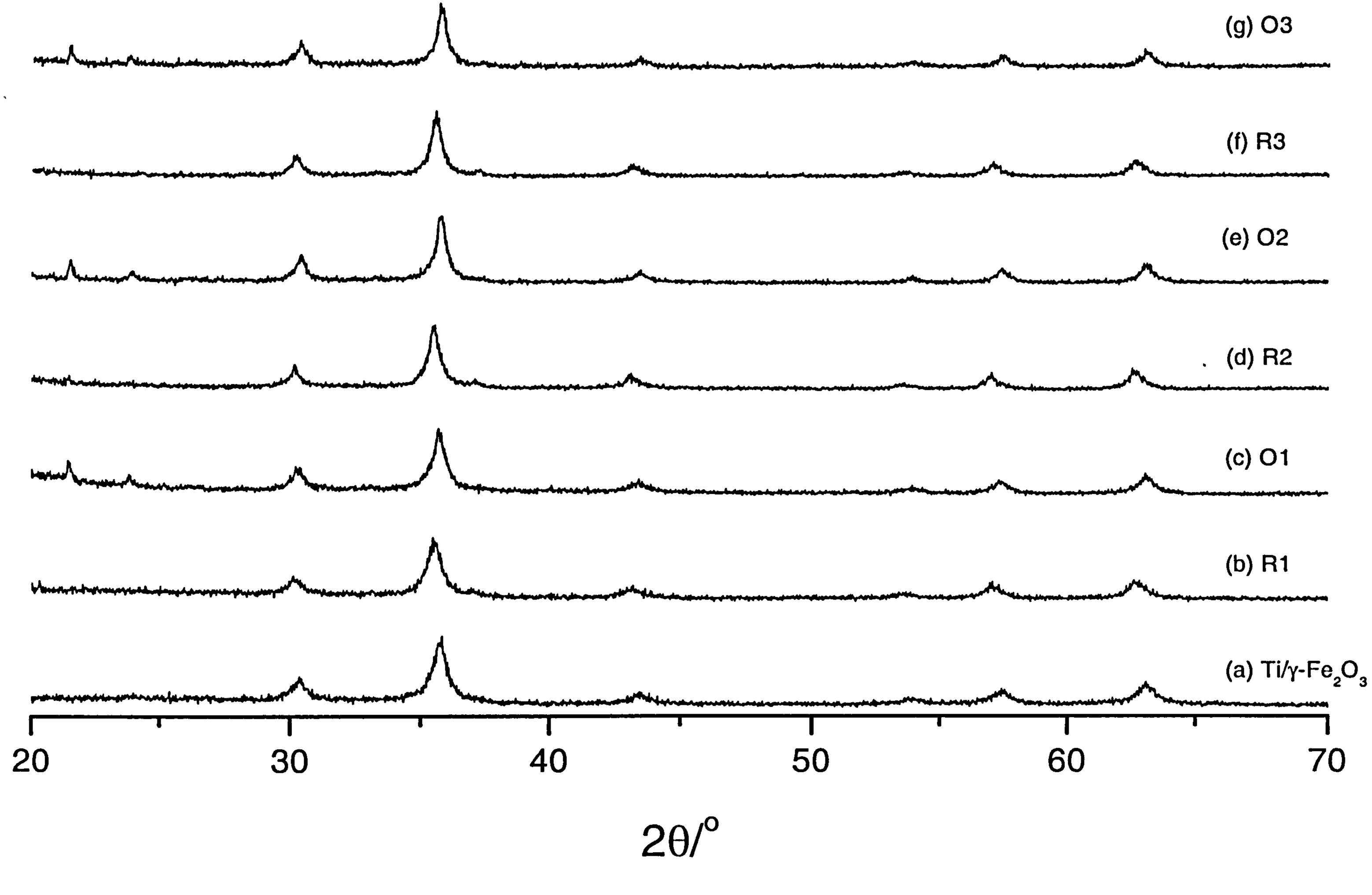

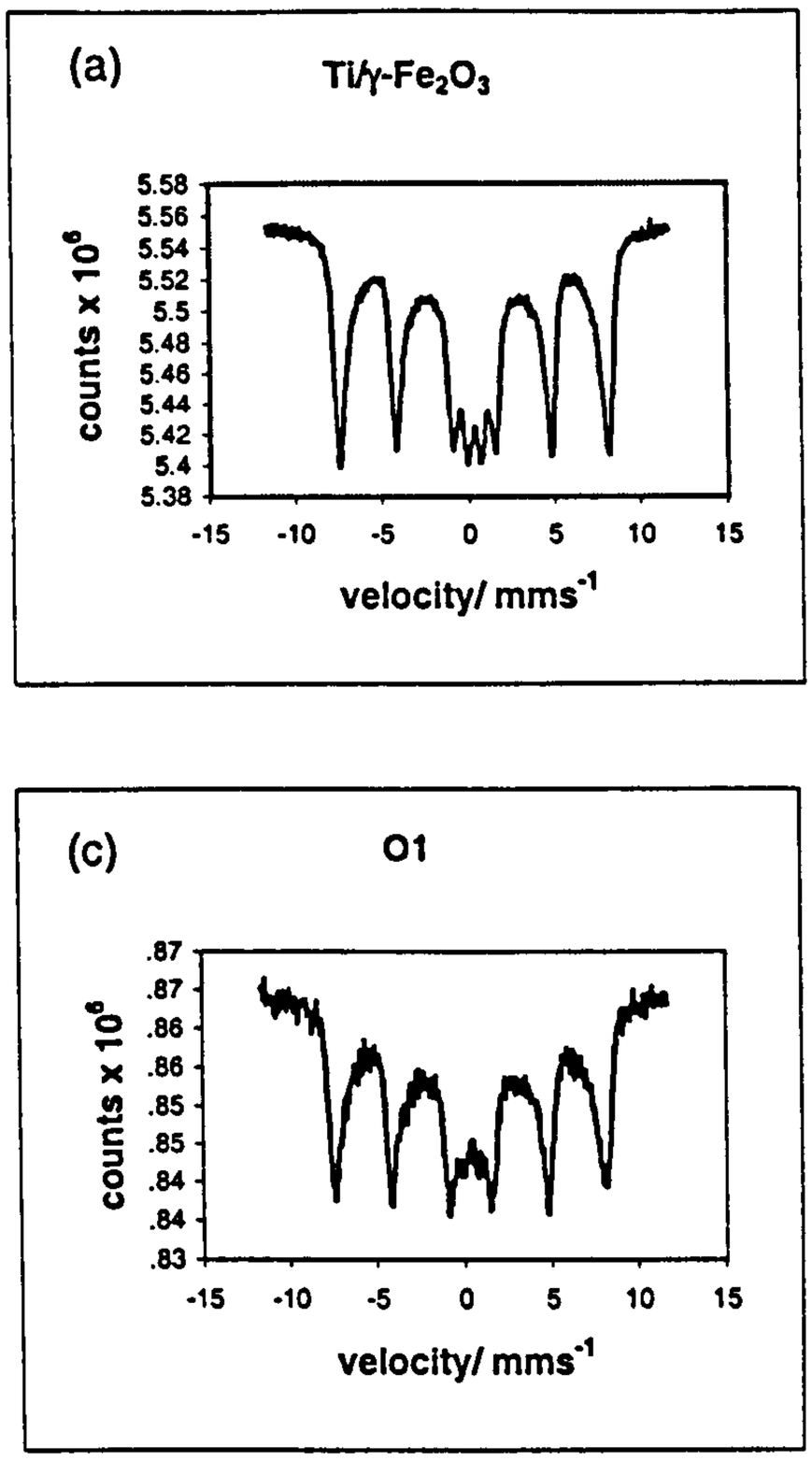

Figure 4.24 ^{57}Fe Mössbauer spectra recorded from Ti/γ-Fe_2O_3 following reduction and reoxidation cycles

Table 4.10 ^{57}Fe Mössbauer parameters recorded from Ti/γ-Fe_2O_3 following treatment in reducing and oxidising environments

Sample	δ (± 0.02) mms^{-1}	Δ (± 0.02) mms^{-1}	H (± 1) T	Interpretation	Area (± 5) %
Ti/γ-Fe_2O_3	0.35	0.17	---	Small particle iron oxide	42
	0.35	0.01	48	γ-Fe_2O_3	58
R1	0.31	0.88	---	Small particle iron oxide	12
	0.54	0.02	44	Fe_3O_4	88
	0.36	-0.04	48	Fe_3O_4	
O1	0.34	0.79	---	Small particle iron oxide	8
	0.35	0.00	47	γ-Fe_2O_3	92
R2	0.31	0.86	---	Small particle iron oxide	6
	0.59	0.01	44	Fe_3O_4	94
	0.36	-0.05	48	Fe_3O_4	
O2	0.34	0.94	---	Small particle iron oxide	8
	0.35	0.01	48	γ-Fe_2O_3	92
R3	0.13	1.16	---	Small particle iron oxide	5
	0.57	0.02	44	Fe_3O_4	95
	0.32	-0.01	48	Fe_3O_4	
O3	0.35	0.92	---	Small particle iron oxide	8
	0.35	0.01	48	γ-Fe_2O_3	92

The results show that Ti/γ–Fe_2O_3 can be reduced to Ti/Fe_3O_4 and reoxidised to Ti/γ–Fe_2O_3 and the reduction and reoxidation cycle repeated twice.

The particle size of titanium- doped Fe_3O_4 (R1) (*ca.* 19 nm) formed by initial reduction of titanium- doped γ–Fe_2O_3 was only slightly larger than that of the precursor titanium- doped γ–Fe_2O_3 (*ca.* 12 nm). The surface area of the titanium-doped Fe_3O_4 (R1) (*ca.* 99 m^2g^{-1}) was also slightly lower than titanium- doped

γ–Fe_2O_3 (*ca.* 139 m^2g^{-1}). Reoxidation by heating at 400 °C for 1 h in air followed by reduction and reoxidation for a further two cycles produced small variations in particle size and surface area but with the finally regenerated titanium- doped γ–Fe_2O_3 (O3) having a size of *ca.* 18 nm and surface area of *ca.* 67 m^2g^{-1}. The significant features of these results are that titanium- doped -γ–Fe_2O_3 and -Fe_3O_4 are of smaller particle size and higher surface area than their undoped counterparts. The material suffers the greatest change in particle size and surface area during initial reduction, but the high surface area is maintained through a three fold reduction-reoxidation cycle.

In situ ^{57}Fe Mössbauer spectroscopy studies

The ^{57}Fe Mössbauer spectra recorded *in situ* from titanium- doped Fe_3O_4 formed by reduction of titanium- doped γ–Fe_2O_3 and subsequently heated in the furnace[13] in an oxygen partial pressure of *ca.* 1 Pa are shown in Figure 4.25. The material heated between 300 and 400 °C (Figure 4.25 (b), (c) and (d)) showed broad-lined spectra best fitted to a distribution of sextet patterns and demonstrating conversion to titanium- doped γ–Fe_2O_3 together with a doublet characteristic of small particle iron oxide which accounted for *ca.* 16 % of the spectrum in each case. The spectrum recorded from the material following cooling to room temperature (Figure 4.25 (e)) confirmed conversion to a γ–Fe_2O_3-related phase (H = 50(1) T) and the absence of α-Fe_2O_3. Further heating at 450 and 500 °C gave spectra (Figure 4.25 (f) and (g)) which showed the superposition of the broadened sextet pattern together with a doublet, which increases in magnitude with increasing temperature. After treatment at *ca.* 550 °C, *ca.* 40 % of the material corresponded to a paramagnetic species. The

Figure 4.25 *In situ* Mössbauer spectra recorded from Ti/Fe_3O_4 reduced from Ti/γ-Fe_2O_3

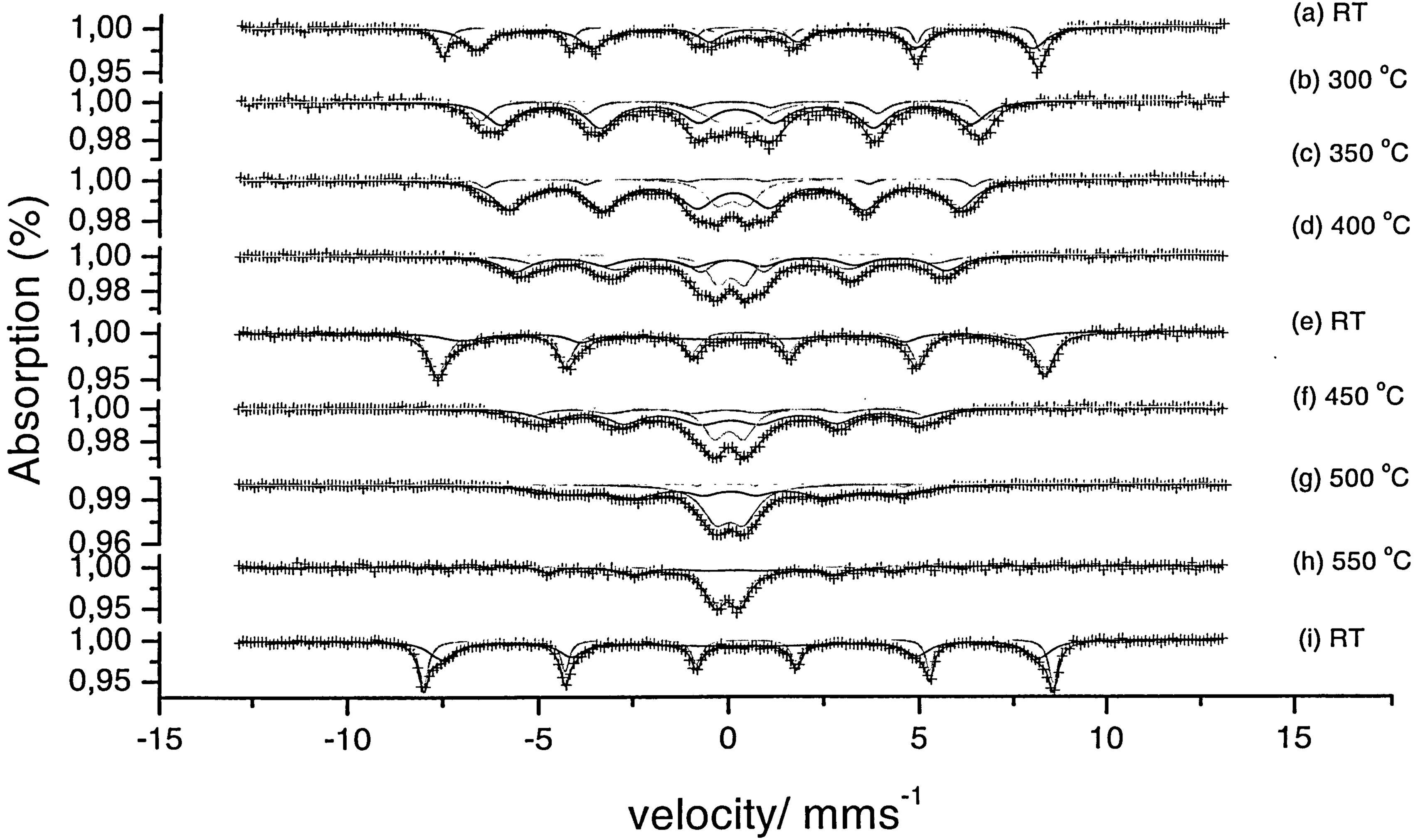

appearance of a component typical of an α-Fe_2O_3-related phase was only observed after heating at *ca.* 550 °C (Figure 4.25 (h)) and cooling to room temperature (Figure 4.25 (i)) where the sextet characteristic of α-Fe_2O_3 (H = 51(1) T) accounted for *ca.* 40 % of the spectrum. X-ray powder diffraction confirmed that titanium had not segregated from the iron oxide during the thermal treatment. A comparison of these results with those recorded from undoped γ–Fe_2O_3 subjected to similar treatment (Figure 4.11) suggests that titanium stabilises the conversion of spinel-related γ–Fe_2O_3 to its corundum-related polymorph.

Effect of metal loading

γ-Fe_2O_3 was nominally doped with 5, 8, 10 and 20 mass % titanium. Energy dispersive X-ray analysis (EDX) data and lattice parameters recorded from Ti- doped samples are shown in Table 4.11. The XRD patterns recorded from the materials are shown in Figure 4.26 (a-d) and corresponded to γ–Fe_2O_3[5]. All the materials appeared to be single phase from the X-ray powder diffraction patterns. No evidence for the formation of TiO_2 in its anatase form (most intense peak at *ca.* 25 ° 2θ) or in its rutile form (most intense peak at *ca.* 27 ° 2θ) was observed. It must be recognised however that the low calcination temperature (250 °C) may have been insufficient to crystallise any titanium which could not be accommodated in the γ–Fe_2O_3 structure and hence the presence of amorphous material cannot be excluded.

Figure 4.26 XRD patterns recorded from Ti/γ-Fe_2O_3 with nominal loadings of (a) 5, (b) 8, (c) 10 and (d) 20 mass % titanium

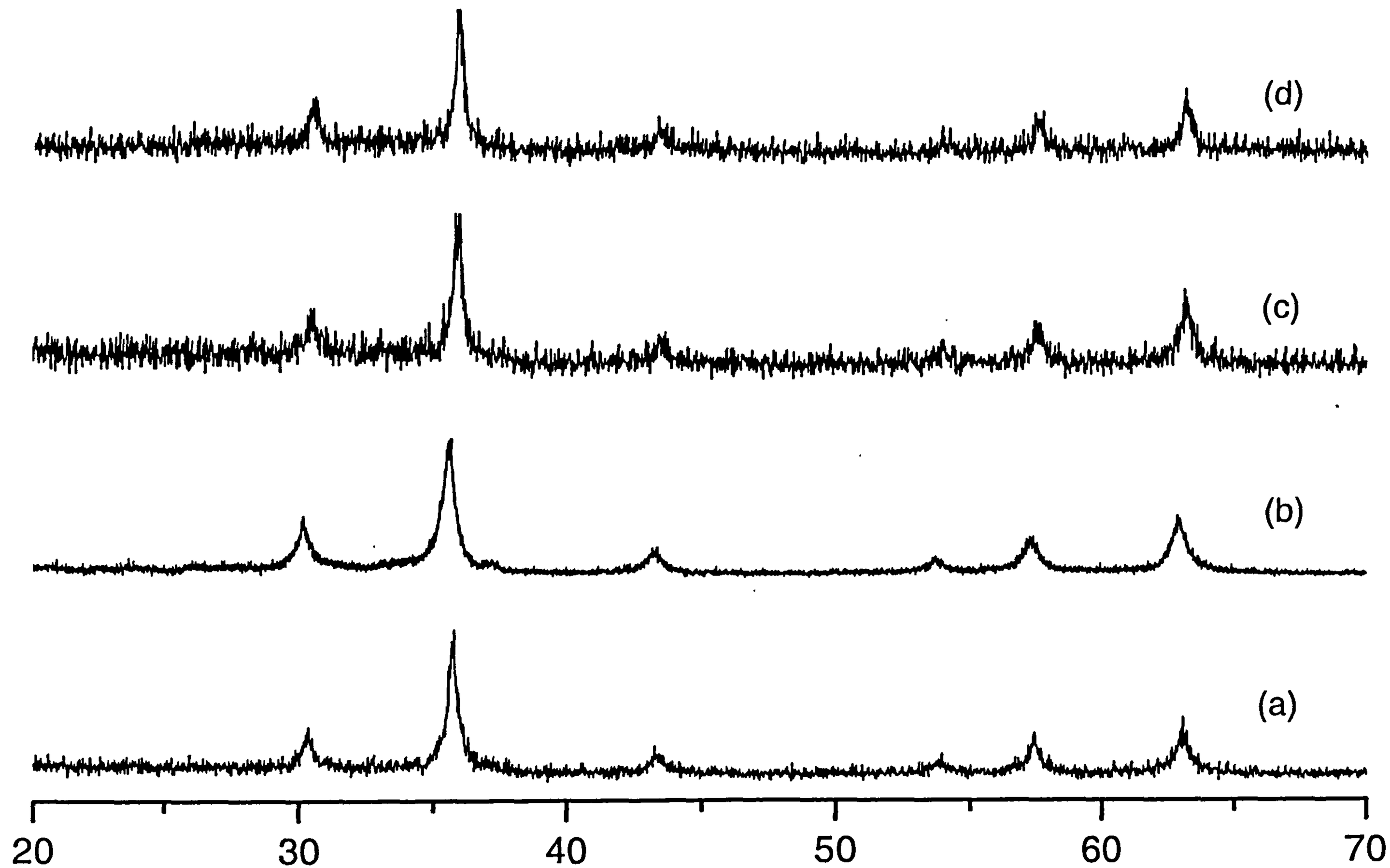

Table 4.11 EDX analysis data and lattice parameters recorded from titanium-doped γ–Fe_2O_3 with different nominal titanium content

Nominal titanium content / mass %	EDX analysis (± 10 %)		Lattice parameter
	Mass %	Atomic %	a/ Å (± 0.01)
5	4.13	3.03	8.353
8	4.89	3.31	8.369
10	7.04	4.76	8.346
20	14.31	10.14	8.346

Given the lack of systematic variation in lattice parameters between materials with increasing titanium content it appears likely that the total titanium incorporation with γ–Fe_2O_3 may not be indicated by the observation of single spinel-related phases in the X-ray powder diffraction patterns. Although the limit of titanium incorporation with γ–Fe_2O_3 has not been accurately determined, it would seem reasonable that it is low and that samples with high titanium content contain appreciable amorphous titanium-containing material.

The ^{57}Fe Mössbauer spectra are shown in Figure 4.27 (a-d), Table 4.12 lists the Mössbauer parameters. For all loadings the spectra showed a sextet pattern corresponding to γ–Fe_2O_3[1,2] and a paramagnetic doublet pattern attributed to small particle iron-containing oxide[3].

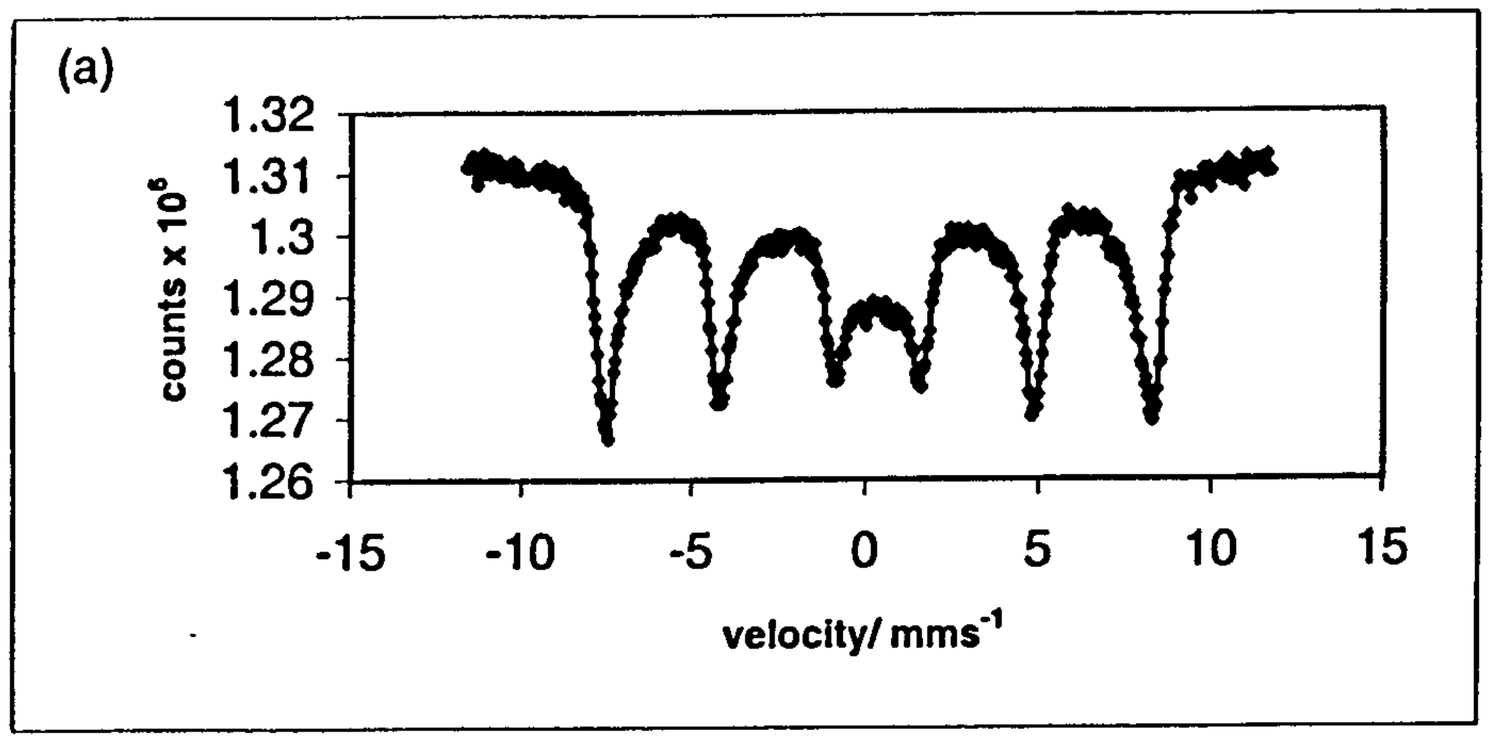

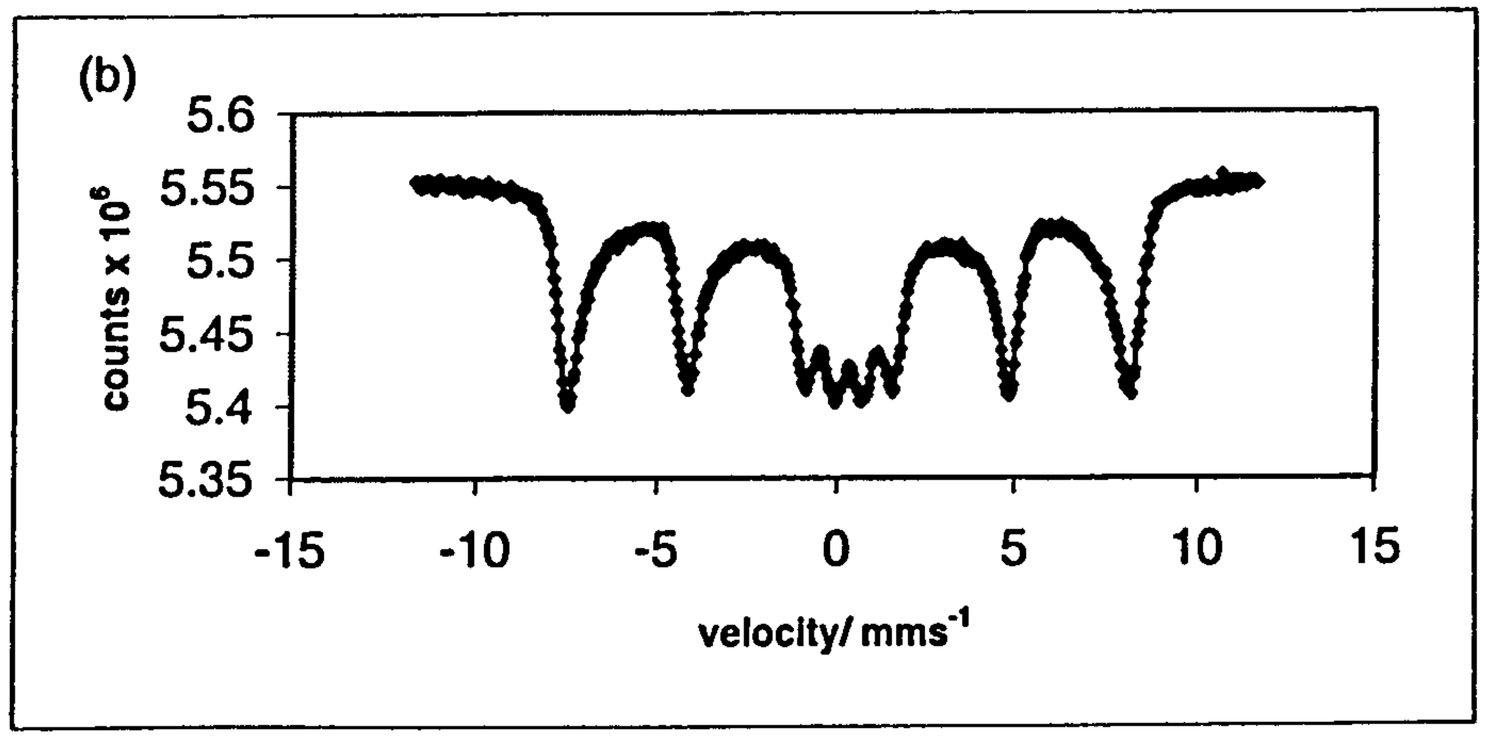

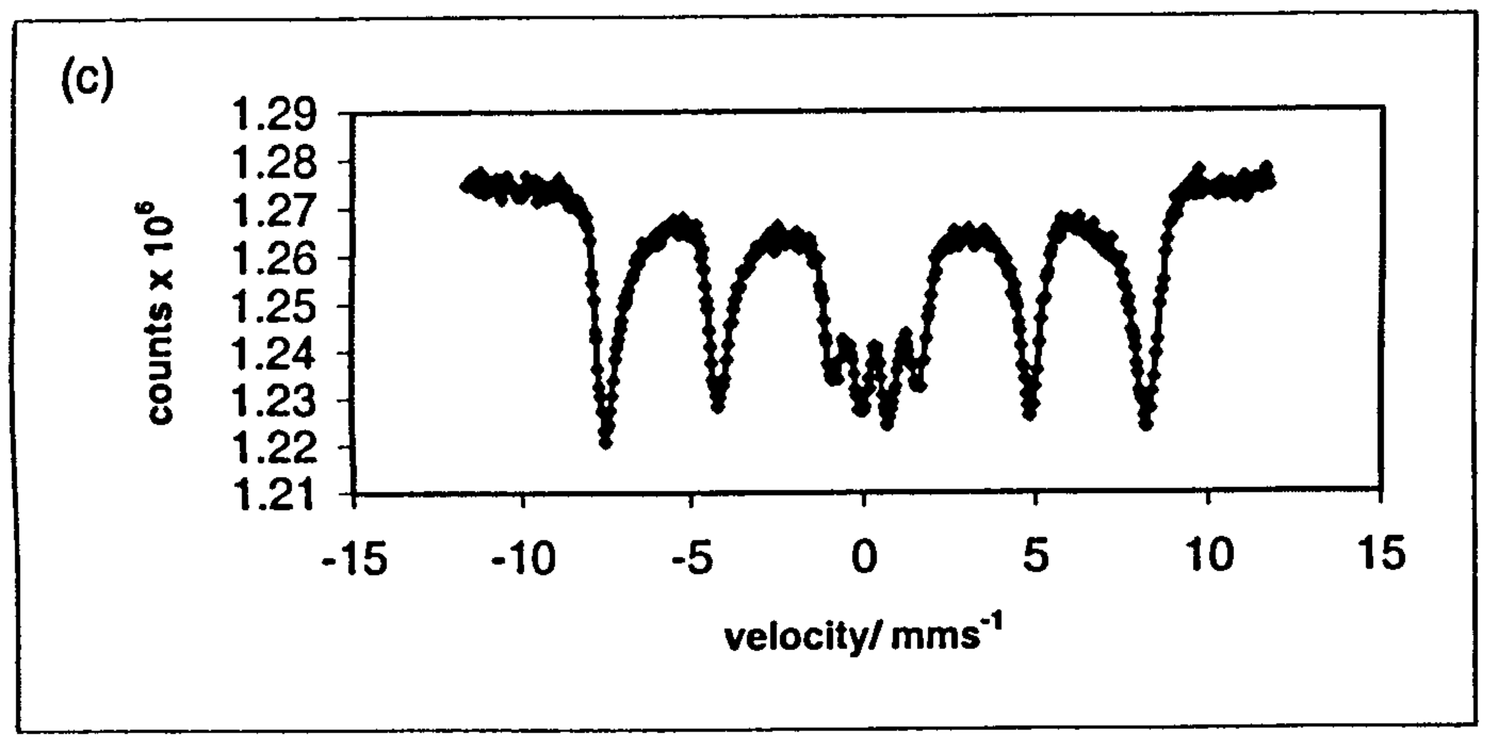

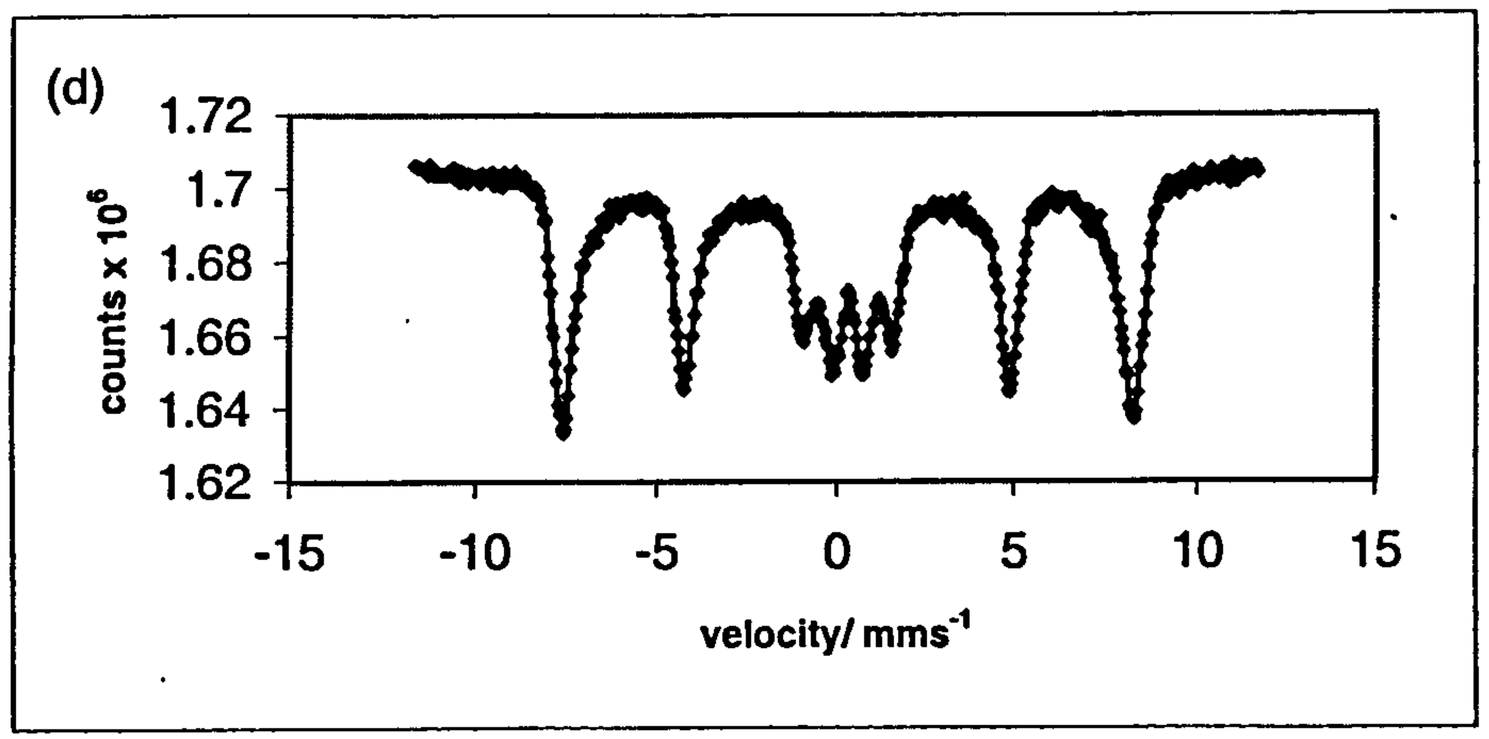

Figure 4.27 ^{57}**Fe Mössbauer spectra recorded from Ti/γ-Fe_2O_3 with nominal loadings of (a) 5, (b) 8, (c) 10 and (d) 20 mass % titanium**

Table 4.12 ^{57}Fe Mössbauer parameters recorded from titanium- doped γ–Fe_2O_3 with different nominal titanium contents

Nominal titanium content / mass %	δ (± 0.02) mms^{-1}	Δ (± 0.02) mms^{-1}	H (± 1) T	Interpretation	Area (± 5) %
5	0.27	0.40	---	Small particle iron oxide	40
	0.35	0.01	48	γ-Fe_2O_3	60
8	0.35	0.17	---	Small particle iron oxide	42
	0.35	0.01	48	γ-Fe_2O_3	58
10	0.35	0.86	---	Small particle iron oxide	28
	0.35	0.01	48	γ-Fe_2O_3	72
20	0.34	0.84	---	Small particle iron oxide	19
	0.35	0.02	49	γ-Fe_2O_3	81

The samples of Ti/γ–Fe_2O_3 with different nominal titanium contents were subjected to heat treatment and the XRD patterns recorded *ex situ* (Figures 4.28 - 4.31) after cooling. The temperatures at which α-Fe_2O_3 appeared and γ–Fe_2O_3 disappeared are shown in Table 4.13. The results suggest some evidence for increased stabilisation of the γ–Fe_2O_3 structure with respect to α-Fe_2O_3 with nominal titanium contents up to 10 mass percent which, given the EDX results (Table 4.11), equates to *ca.* 7.04 mass percent. Taken together it would appear that the limit of titanium- solubility in γ–Fe_2O_3 is less than 8 mass percent and that this induces the maximum stabilisation of the γ–Fe_2O_3 structure with respect to thermal conversion to α-Fe_2O_3. It is interesting that γ–Fe_2O_3 prepared by addition of salt to base and boiling under reflux which had a similar surface area (150 m^2g^{-1}) as Ti/γ–Fe_2O_3 (139 m^2g^{-1}) converted to α-Fe_2O_3 between 400 °C and 450 °C. The results demonstrate that the stabilisation of the spinel-related γ–Fe_2O_3 structure with respect to its thermally- induced conversion

Figure 4.28 XRD patterns recorded *ex situ* from nominal 5 % Ti/γ-Fe_2O_3 prepared by addition of base to salt, boiling under reflux, and heating at 250 °C and then heated from 500 to 700 °C

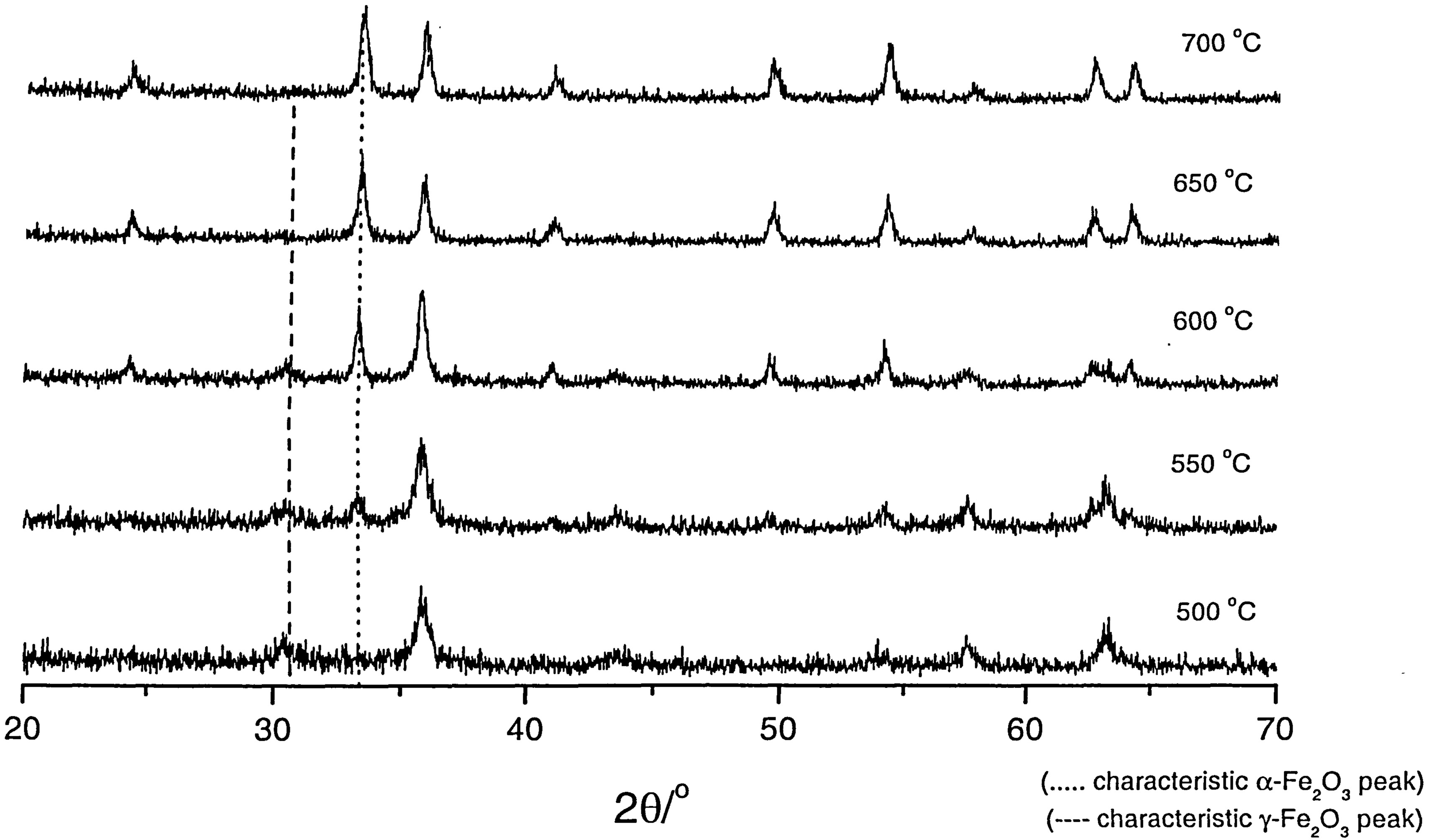

Figure 4.29 XRD patterns recorded *ex situ* from nominal 8 % Ti/γ-Fe_2O_3 prepared by addition of base to salt, boiling under reflux, and heating to 250 °C and then heated from 350 to 700 °C

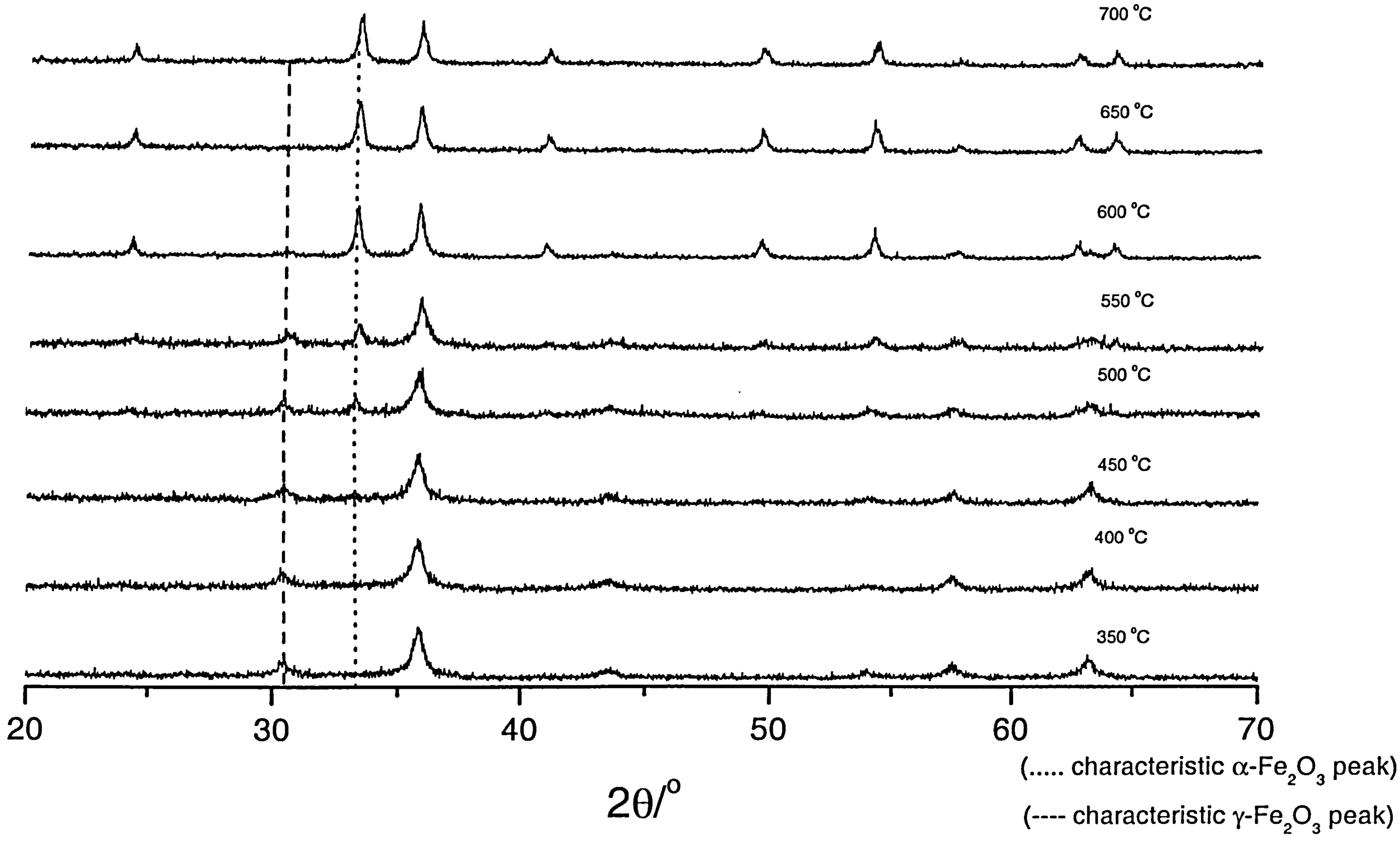

Figure 4.30 XRD patterns recorded *ex situ* from nominal 10 % Ti/γ-Fe_2O_3 prepared by addition of base to salt, boiling under reflux, and heating at 250 °C and then heated from 550 to 700 °C

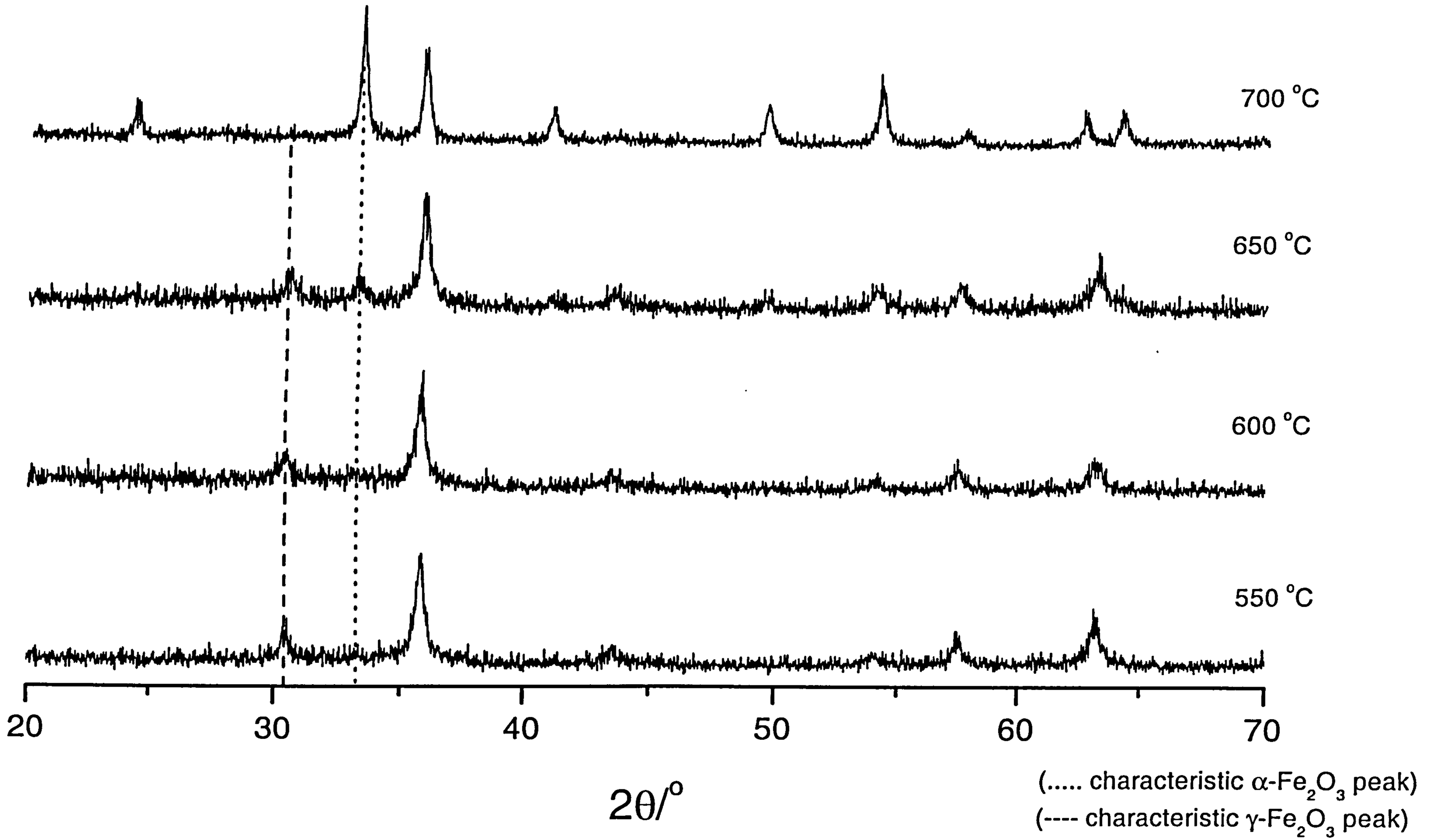

Figure 4.31 XRD patterns recorded *ex situ* from nominal 20 % Ti/γ-Fe_2O_3 prepared by addition of base to salt, boiling under reflux, and heating at 250 °C and then heated from 300 to 700 °C

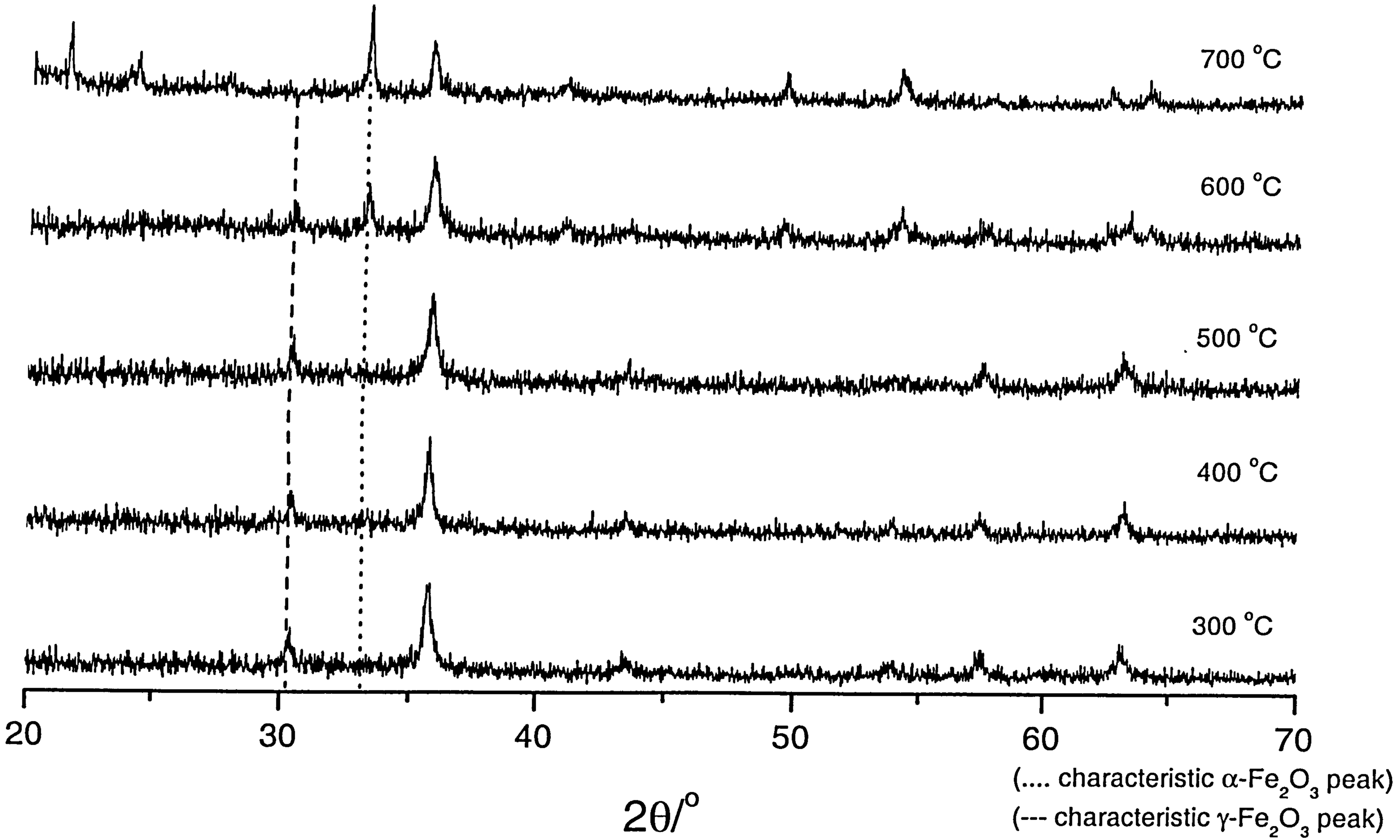

to α-Fe_2O_3 is a result of the presence of titanium as opposed to the small particle size and higher surface area of the γ–Fe_2O_3 phase.

Table 4.13 Temperature of conversion of Ti/γ–Fe_2O_3 to Ti/α-Fe_2O_3 recorded from materials with different titanium contents

Nominal titanium content / mass %	Temperature/ °C (± 25 °C)	
	α-Fe_2O_3 formation	γ-Fe_2O_3 disappearance
5	550	650
8	500	650
10	650	700
20	600	700

Conclusion

Ti/γ-Fe_2O_3 prepared by addition of base to salt, boiling under reflux, and calcination at 250 °C had a significantly higher surface area compared to γ-Fe_2O_3 prepared by a similar method. The surface area was similar to γ–Fe_2O_3 prepared by addition of salt to base, boiling under reflux, and calcination at 250 °C. The *in situ* high temperature Mössbauer spectra and the *ex situ* XRD patterns recorded from Ti/γ–Fe_2O_3 showed an increase in the temperature of conversion to α-Fe_2O_3 compared with undoped γ–Fe_2O_3 samples. The TPR profile recorded from Ti/γ–Fe_2O_3 showed three reduction peaks similar to undoped γ–Fe_2O_3 prepared by a similar method, but with the latter two peaks merged to give a broader peak and indicative of the reduction taking place over a larger temperature range. The Ti/γ–Fe_2O_3 followed a similar reduction pathway as undoped γ–Fe_2O_3 prepared by a similar method but without the formation of FeO. Reduction and reoxidation showed decreases in the surface area and

increases in particle size, with the initial reduction step indicating the greatest change. Titanium doping suppresses the growth of particle size and maintains a high surface area as compared with its undoped counterpart during reduction- reoxidation cycling. The limit of titanium incorporation within the γ–Fe_2O_3 structure appeared to be less than 8 mass percent and this concentration maximises the thermal stability of the γ–Fe_2O_3 phase.

4.2.2 Tin- doped γ–Fe_2O_3 (addition of base to salt, boiling under reflux, and calcination at 250 °C/12 h)

The X-ray powder diffraction pattern (Figure 4.32) recorded from the material, which was shown by ICP analysis to contain 8.06 mass % Sn, showed a single phase spinel-related structure. The lattice parameter of a = 8.375(2) Å compared to a = 8.334 Å for γ–Fe_2O_3[8] and a = 8.354(2) Å for γ–Fe_2O_3 and a = 8.368(2) Å for Ti/γ–Fe_2O_3 prepared here by addition of base to salt, boiling under reflux, and calcination at 250 °C. EXAFS studies[17] of Sn/γ–Fe_2O_3 have indicated that the tin adopts the octahedral site in the spinel-related structure. Given that Sn^{4+} in octahedral co-ordination has a radius of 0.69 Å compared to Fe^{3+}, which has a radius of 0.65 Å in six fold co-ordination[16], the small increase in lattice parameter is quite reasonable.

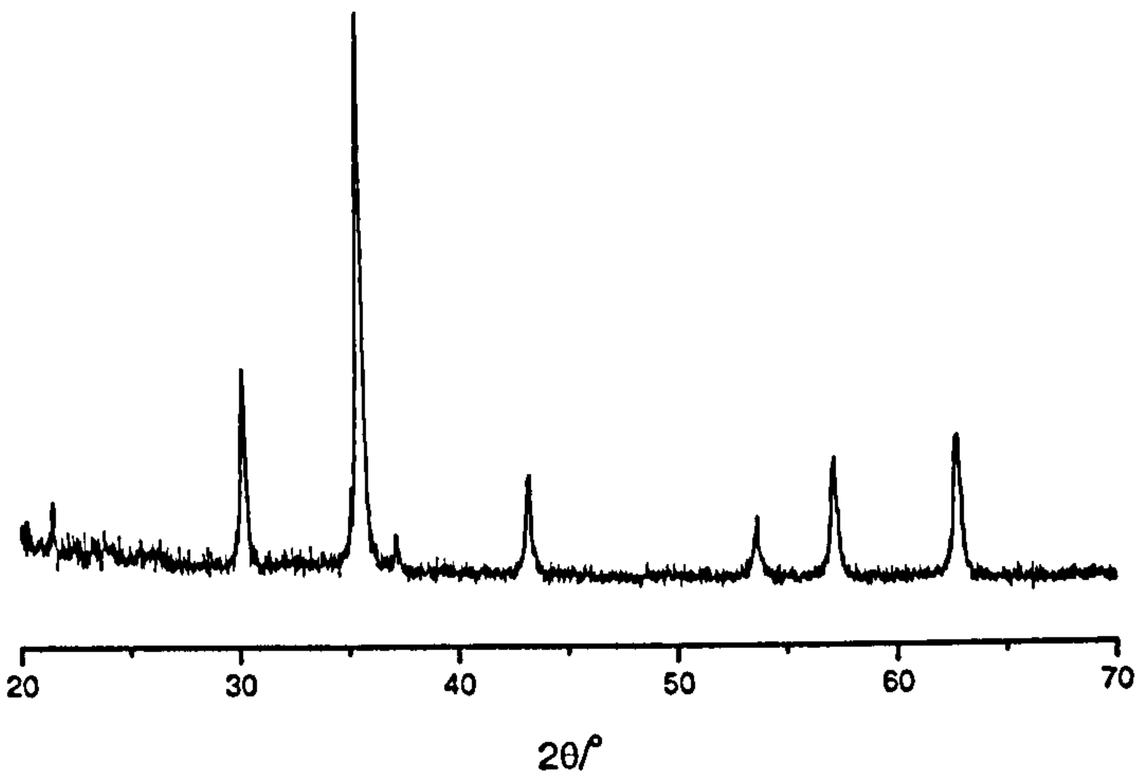

Figure 4.32 XRD pattern recorded from Sn/γ–Fe_2O_3 prepared by addition of base to salt, boiling under refluxed, and calcination at 250 °C

The ^{57}Fe Mössbauer spectrum recorded from Sn/γ–Fe_2O_3 (Figure 4.33) (δ 0.35(2) mms^{-1}, Δ 0.01(2) mms^{-1}, H 48(1) T) was more similar to that of undoped γ–Fe_2O_3 prepared by a similar method (Figure 4.5) and did not contain the broadened central doublet observed in the spectrum recorded from titanium- doped γ–Fe_2O_3 (Figure 4.20) which indicated the additional presence of small particle iron oxide. The particle size determined by the Scherrer method from the X-ray powder diffraction data of *ca.* 33 nm was higher than that of undoped γ–Fe_2O_3 (*ca.* 13 nm) and titanium-doped γ–Fe_2O_3 (*ca.* 12 nm) prepared by similar methods. The surface area of Sn/γ–Fe_2O_3 of 59 m^2g^{-1} was slightly lower than that of undoped γ–Fe_2O_3 (*ca.* 69 m^2g^{-1}) and significantly lower than titanium- doped γ–Fe_2O_3 (*ca.* 139 m^2g^{-1}) prepared by similar methods.

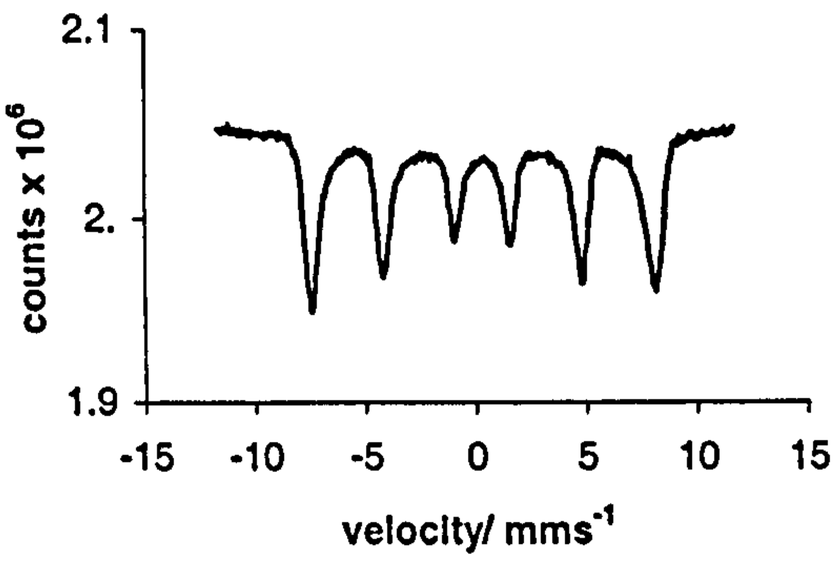

Figure 4.33 ^{57}Fe Mössbauer spectrum recorded from Sn/γ–Fe_2O_3 prepared by addition of base to salt, boiling under refluxed, and calcination at 250 °C

The temperature programmed reduction profile (Figure 4.34) was identical in shape to that of undoped γ–Fe_2O_3 prepared by addition of base to salt, boiling under reflux, and calcination at 250 °C (Figure 4.7) except the that initial peak was of lower intensity. The X-ray powder diffraction patterns (Figure 4.34), together with ^{57}Fe Mössbauer spectra (Figure 4.35, Table 4.14) recorded *ex situ* following each reduction peak showed a similar reduction pathway to operate for the reduction of Sn/γ–Fe_2O_3 as that observed for undoped γ–Fe_2O_3 prepared by a similar method. The material was initially reduced at 350 °C to Fe_3O_4 and then at 720 °C to a mixture of Fe_3O_4, FeO and Fe before, at 1150 °C, to a metallic product. It is interesting to observe in this final product a mixture of iron- tin alloy and metallic iron. In the case of Ti/γ–Fe_2O_3 no FeO or iron- titanium alloy were observed, the latter could be because of the lower content of titanium (4.04 mass %) as compared with tin (8.06 mass %).

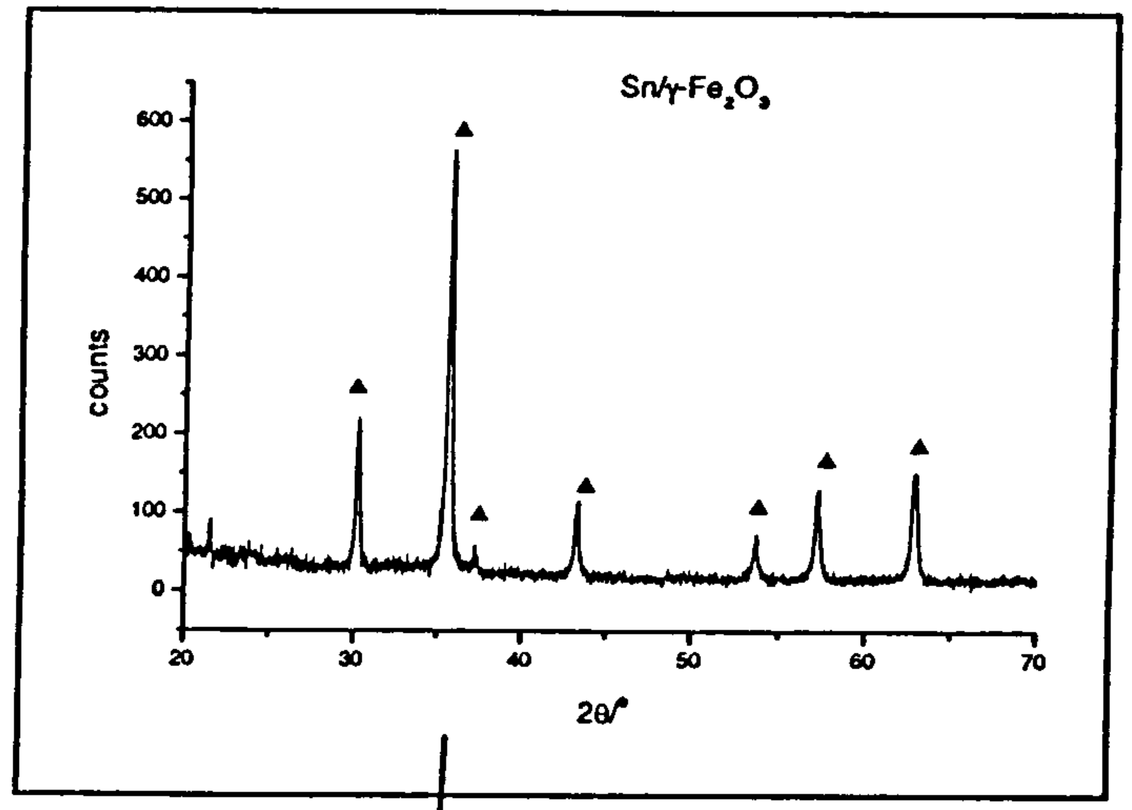

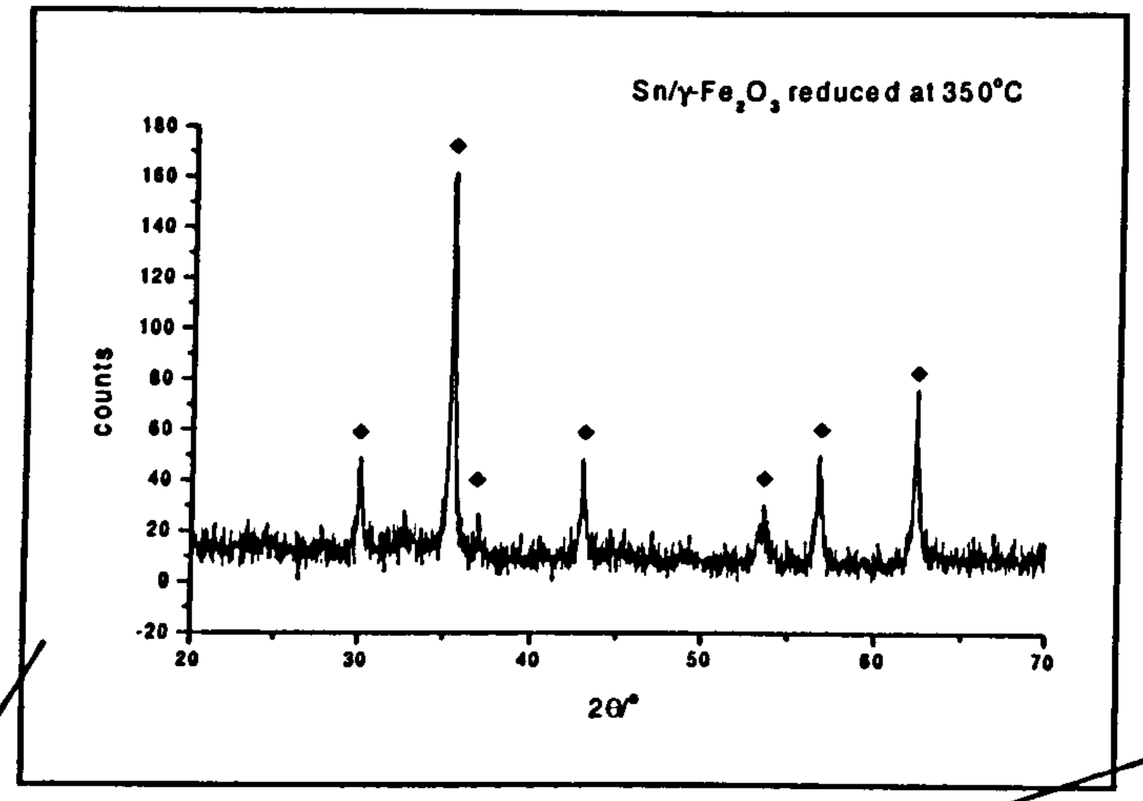

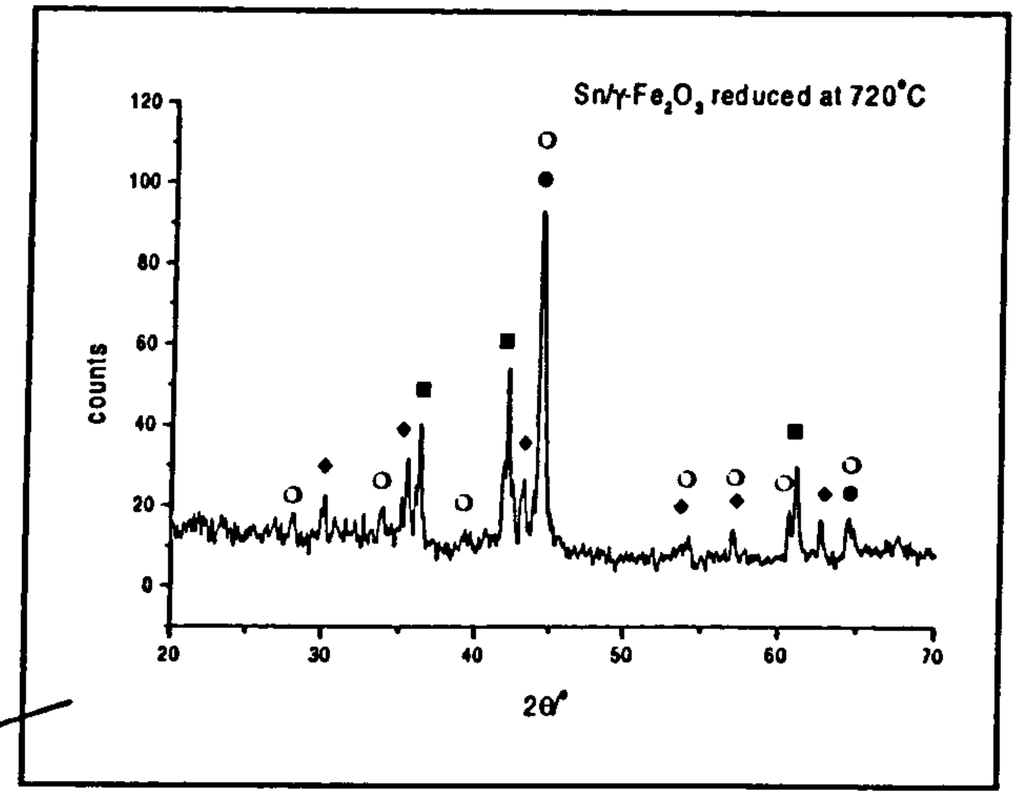

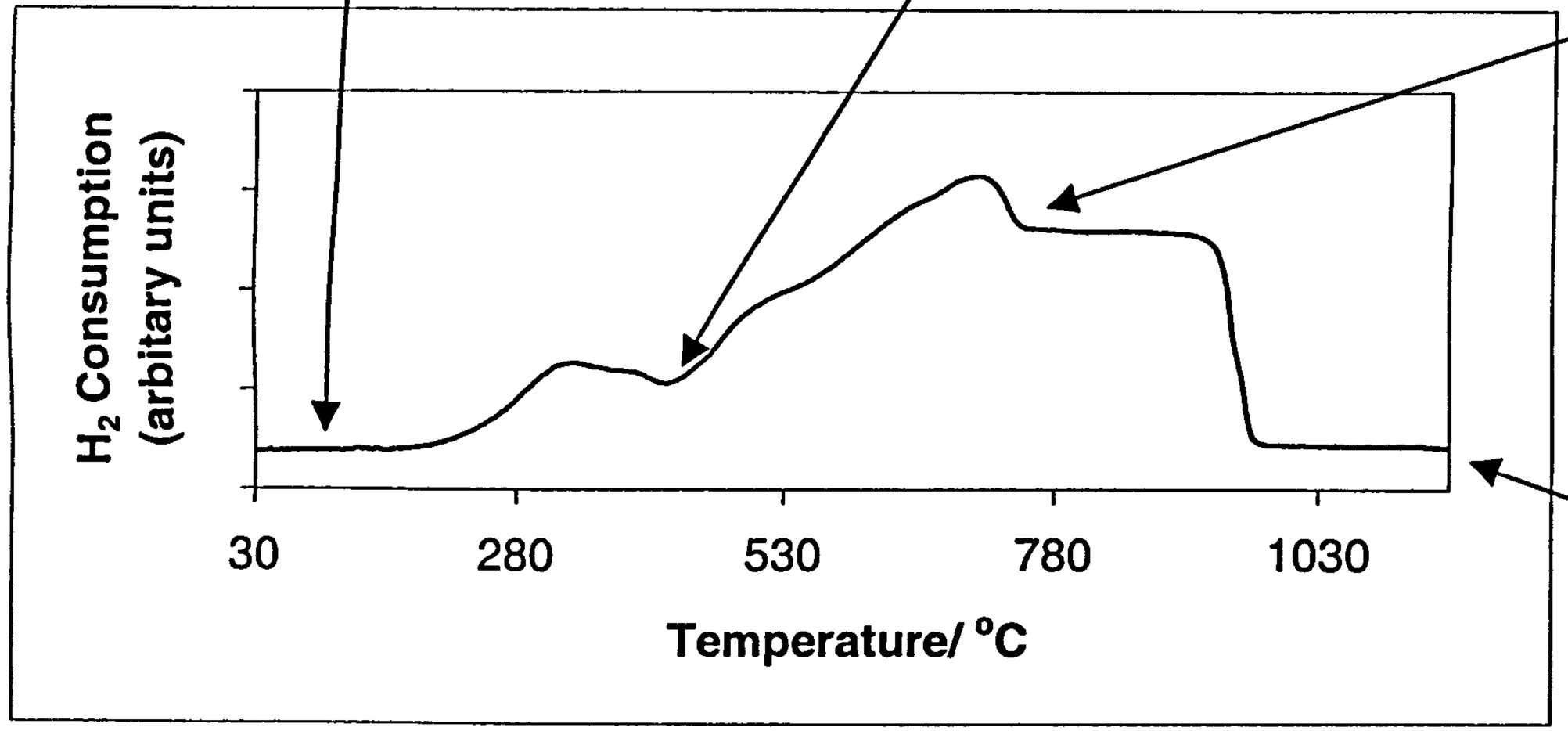

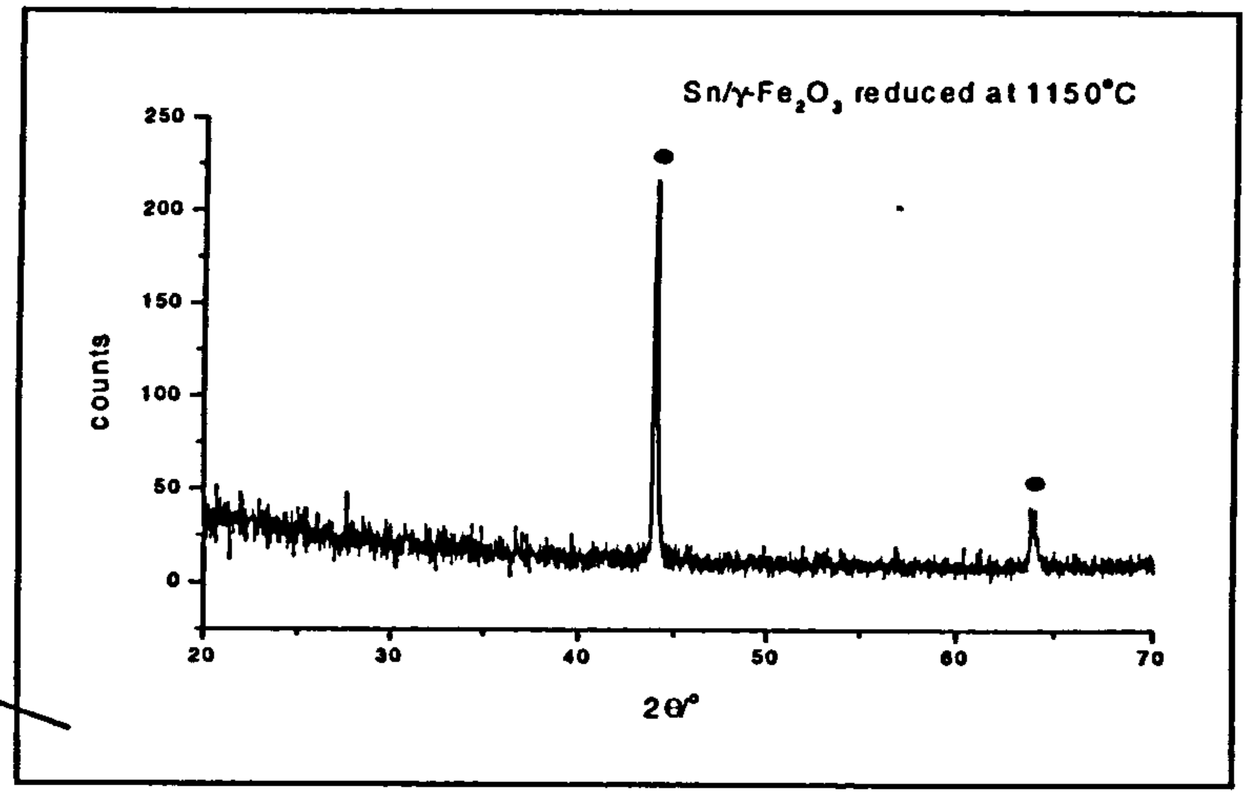

▲ = γ-Fe_2O_3 O = FeSn

◆ = Fe_3O_4

■ = FeO

● = Fe

Figure 4.34 TPR profile recorded from Sn/γ-Fe_2O_3 and XRD patterns recorded following each reduction peak

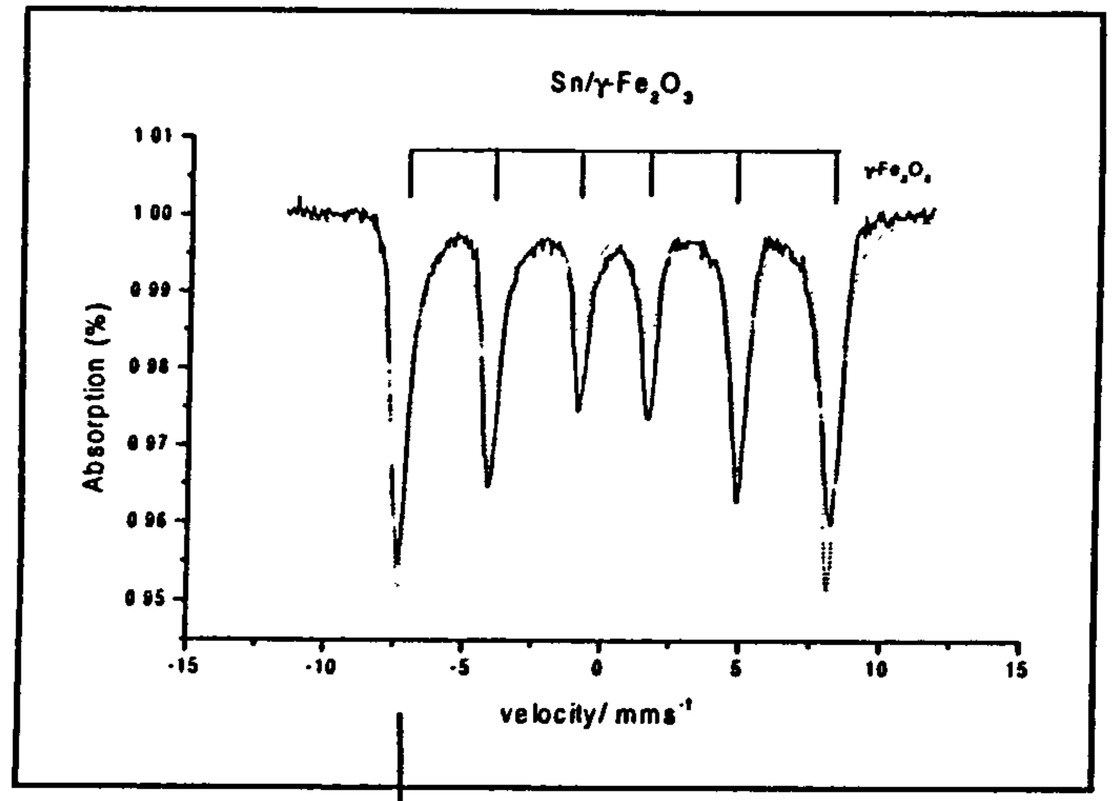

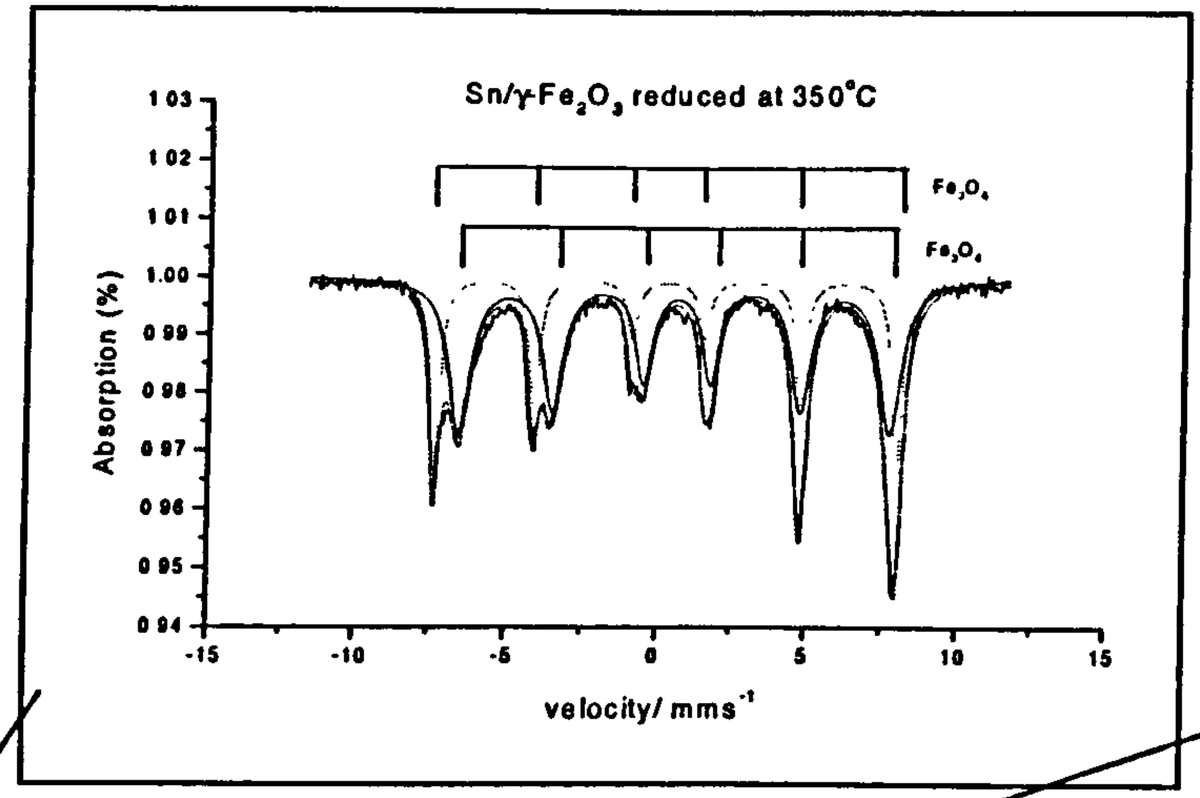

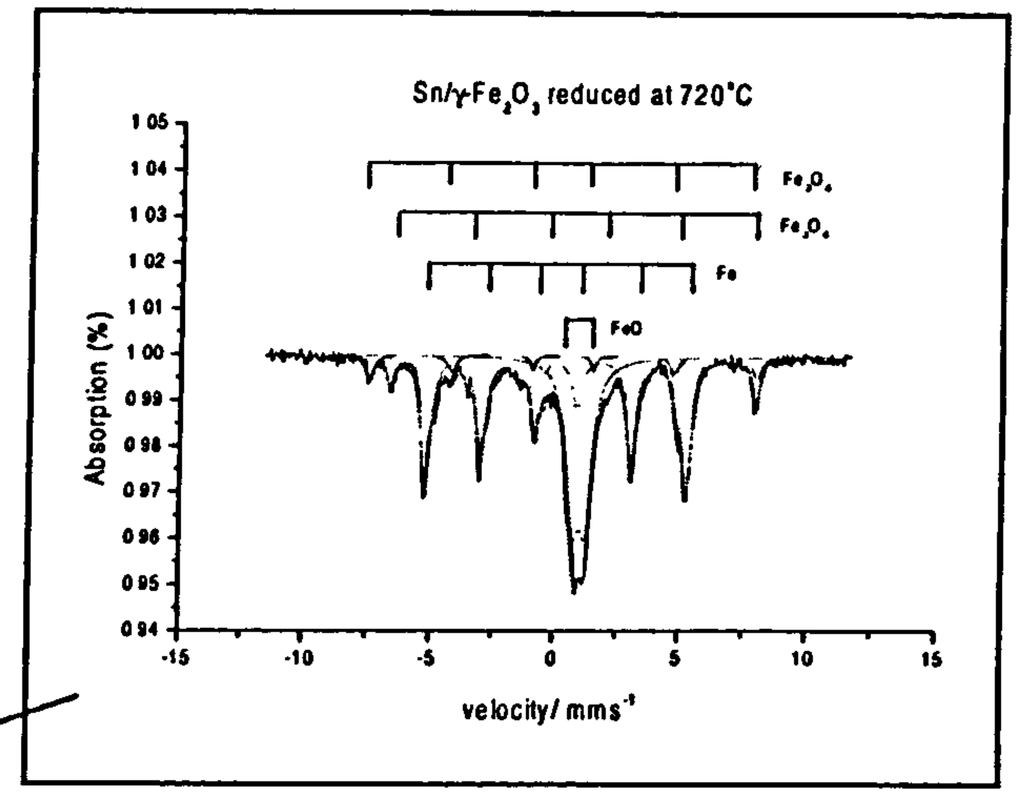

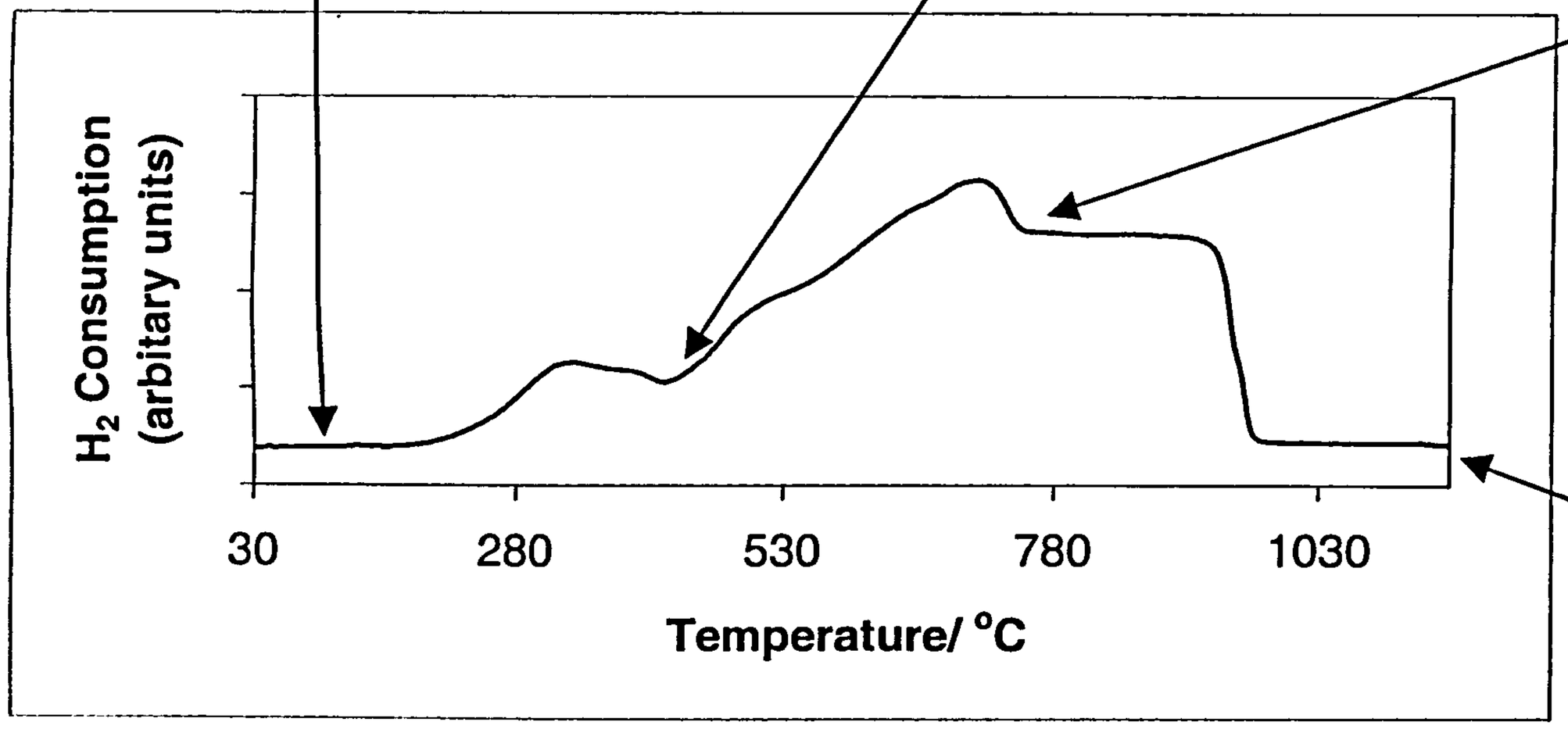

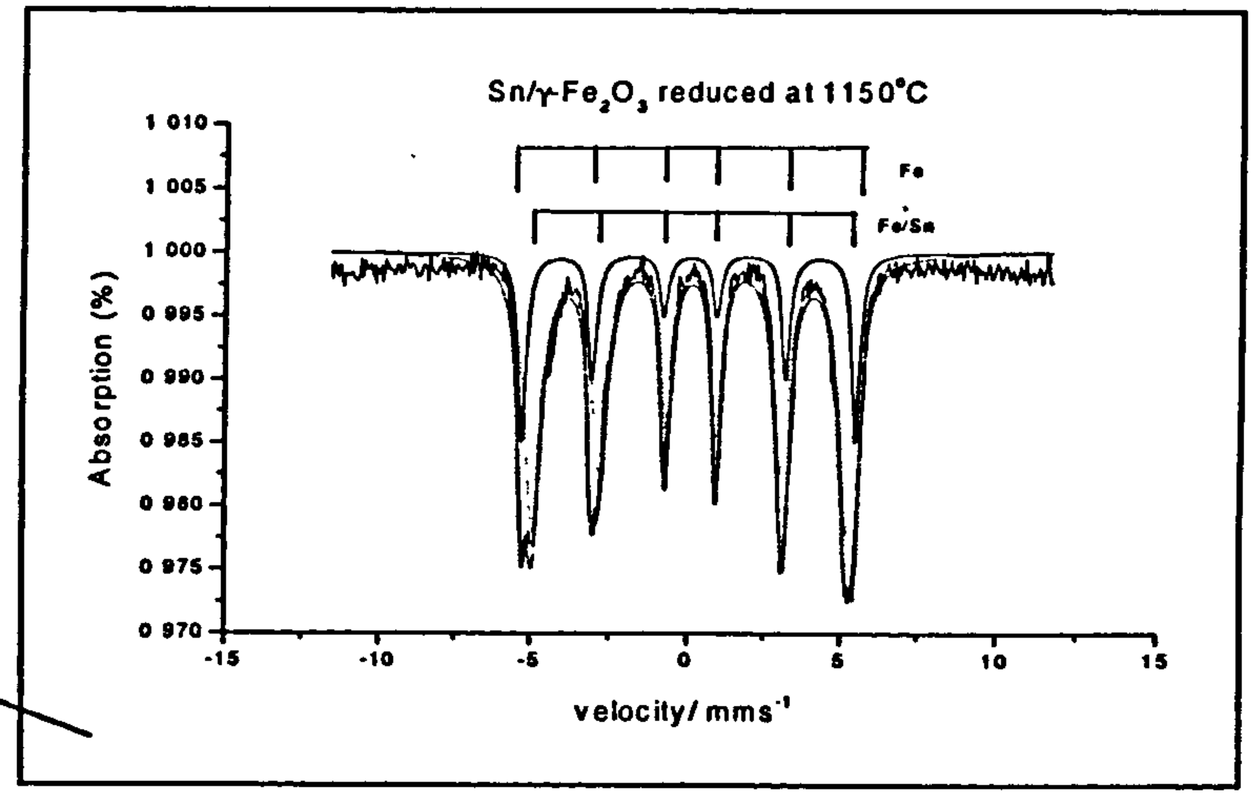

Figure 4.35 TPR profile recorded from Sn/γ-Fe_2O_3 and ^{57}Fe Mössbauer spectra recorded following each reduction peak

Table 4.14 ^{57}Fe Mössbauer parameters recorded from Sn/γ-Fe_2O_3 following reduction in TPR experiment

Sample	δ (± 0.02) mms^{-1}	Δ (± 0.02) mms^{-1}	H (± 1) T	Interpretation	Area (± 5) %
Sn/γ-Fe_2O_3	0.35	0.01	48	γ-Fe_2O_3	100
Sn/γ-Fe_2O_3 reduced at 350 °C	0.63	-0.02	44	Fe_3O_4	100
	0.33	0.0	48	Fe_3O_4	
Sn/γ-Fe_2O_3 reduced at 720 °C	0.70	0.0	45	Fe_3O_4	13
	0.30	0.0	48	Fe_3O_4	
	0.99	0.52	---	FeO	36
	0.05	0.0	32	Fe	51
Sn/γ-Fe_2O_3 reduced at 1150 °C	0.09	0.0	33	Fe	91
	0.19	0.01	29	Sn/Fe	9

Reduction-reoxidation properties

Sn/γ–Fe_2O_3 was subjected to reduction at 350 °C in the 10 % hydrogen- 90 % nitrogen mixture (R1) and reoxidised by heating at 400 °C for 1 h in air (O1). The cycle of reduction and reoxidation was repeated twice (samples R2, O2, R3 and O3). X-ray powder diffraction (Figure 4.36) and ^{57}Fe Mössbauer spectroscopy (Figure 4.37, Table 4.15) were used to identify the products after each step in the reduction-oxidation cycle.

Figure 4.36 XRD patterns recorded *ex situ* from Sn/γ-Fe_2O_3 following reduction and reoxidation cycles

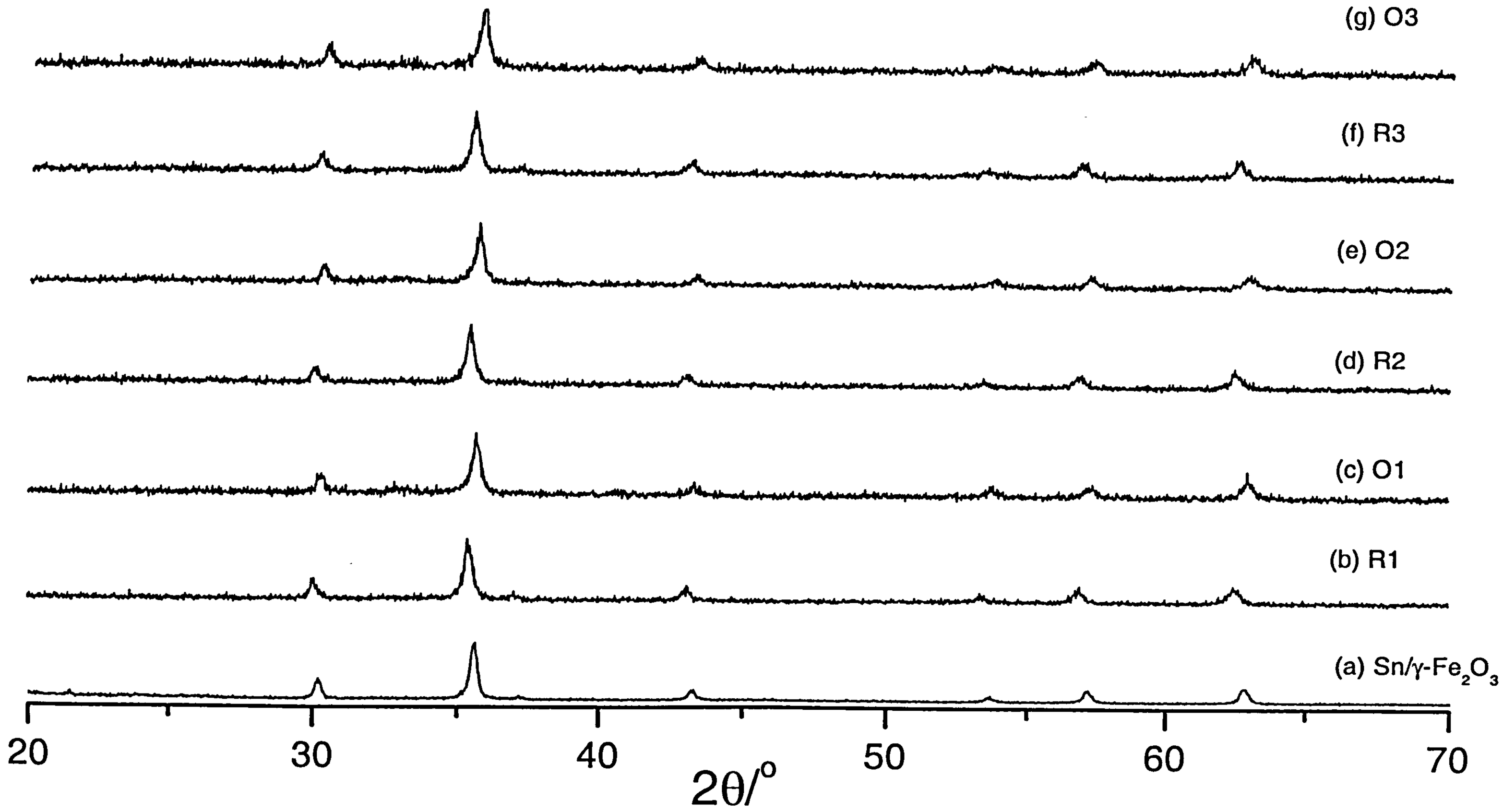

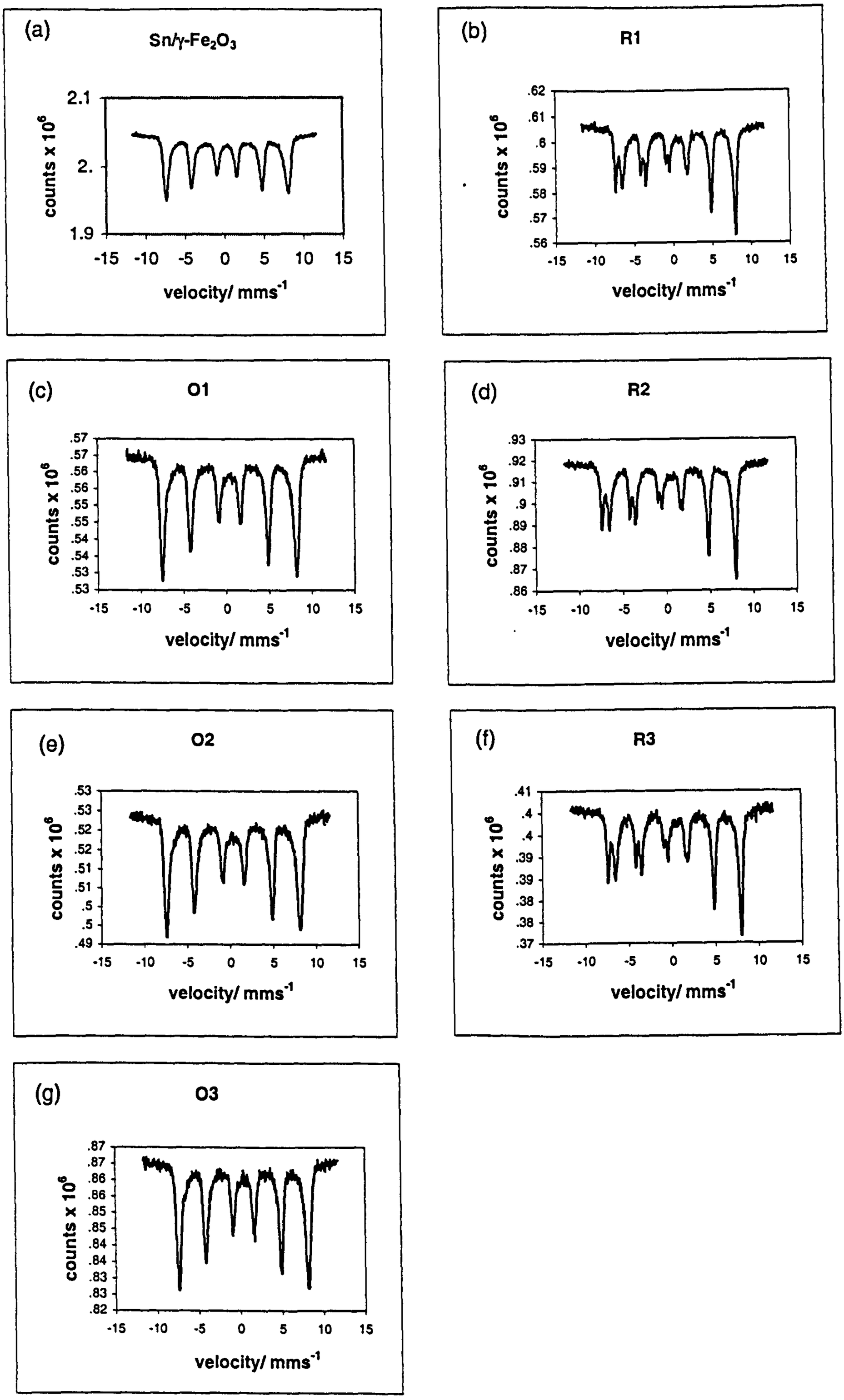

Figure 4.37 ^{57}Fe Mössbauer spectra recorded from Sn/γ-Fe_2O_3 following reduction and reoxidation cycles

Table 4.15 ^{57}Fe Mössbauer parameters recorded from Sn/γ-Fe_2O_3 following treatment in reducing and oxidising environments

Sample	δ (± 0.02) mms^{-1}	Δ (± 0.02) mms^{-1}	H (± 1) T	Interpretation
Sn/γ-Fe_2O_3	0.35	0.01	48	γ-Fe_2O_3
R1	0.65	-0.01	44	Fe_3O_4
	0.29	0.00	48	Fe_3O_4
O1	0.34	0.00	48	γ-Fe_2O_3
R2	0.65	-0.01	44	Fe_3O_4
	0.30	0.00	48	Fe_3O_4
O2	0.34	0.00	48	γ-Fe_2O_3
R3	0.66	0.00	45	Fe_3O_4
	0.29	0.00	48	Fe_3O_4
O3	0.34	0.00	48	γ-Fe_2O_3

The results show that Sn/γ–Fe_2O_3 can be reduced to Sn/Fe_3O_4 and reoxidised to Sn/γ–Fe_2O_3 and the reduction and reoxidation cycle repeated.

The particle size of tin- doped Fe_3O_4 (R1) (*ca.* 34 nm) formed by initial reduction of tin- doped γ–Fe_2O_3 at 350 °C in the 10 % hydrogen- 90 % nitrogen gas mixture was similar to that of tin- doped γ–Fe_2O_3 (*ca.* 33 nm), but the surface area of the tin-doped Fe_3O_4 (R1) (*ca.* 36 m^2g^{-1}) was lower than that of tin- doped γ–Fe_2O_3 (*ca.* 59 m^2g^{-1}). Reoxidation by heating at 400 °C for 1 h in air followed by two further cycles of reduction and reoxidation produced slight changes in particle size and surface area with the finally regenerated tin- doped γ–Fe_2O_3 (O3) having a size of 25 nm and surface area of 29 m^2g^{-1}. The results showed that tin produces similar effect on the particle size and surface area as titanium over a three fold reduction and oxidation cycle, but with titanium maintaining a higher surface area.

In situ ^{57}Fe Mössbauer spectroscopy studies

The ^{57}Fe Mössbauer spectra recorded *in situ* from tin- doped γ–Fe_2O_3 and subsequently heated in the furnace[13] in an oxygen partial pressure of *ca.* 1 Pa are shown in Figure 4.38. The material was heated from 200 - 450 °C (Figure 4.38(b-e)) and gave broad lined spectra best fitted to a distribution of sextet patterns and characteristic of tin- doped γ–Fe_2O_3 together with a paramagnetic doublet. The room temperature spectrum recorded after heating at 450 °C (Figure 4.38(f)) showed little change as compared with the starting material. The material was further heated to 500 °C and then cooled to 200 °C (Figure 4.38(g and h)). The spectrum recorded at 200 °C, showed the onset of α-Fe_2O_3 formation (H = 47(1) T) accounting for *ca.* 5 % of the spectral area. The material was further heated to 530 °C and a room temperature spectrum recorded (Figure 4.38(i and j)) which showed an increases in the spectral area for α-Fe_2O_3 (H = 52(1) T). The material was heated to 550 °C and a final room temperature spectrum recorded (Figure 4.38(k and l)), which showed a sextet corresponding to α-Fe_2O_3 (H = 51(1) T) and a doublet accounting for *ca.* 14 % of the spectral area. The results resemble those recorded from titanium- doped γ–Fe_2O_3 in which the spinel-related structure was stabilised with respect to conversion to the corundum-related phase by the presence of titanium (Section 4.2.1).

Effect of metal loading

γ-Fe_2O_3 was nominally doped with 5, 8, 10 and 20 mass % tin. The XRD patterns are shown in Figure 4.39(a and b) corresponding to a spinel- related phase[5] for

Figure 4.38 ***In situ*** **Mössbauer spectra recorded from Sn/γ-Fe_2O_3**

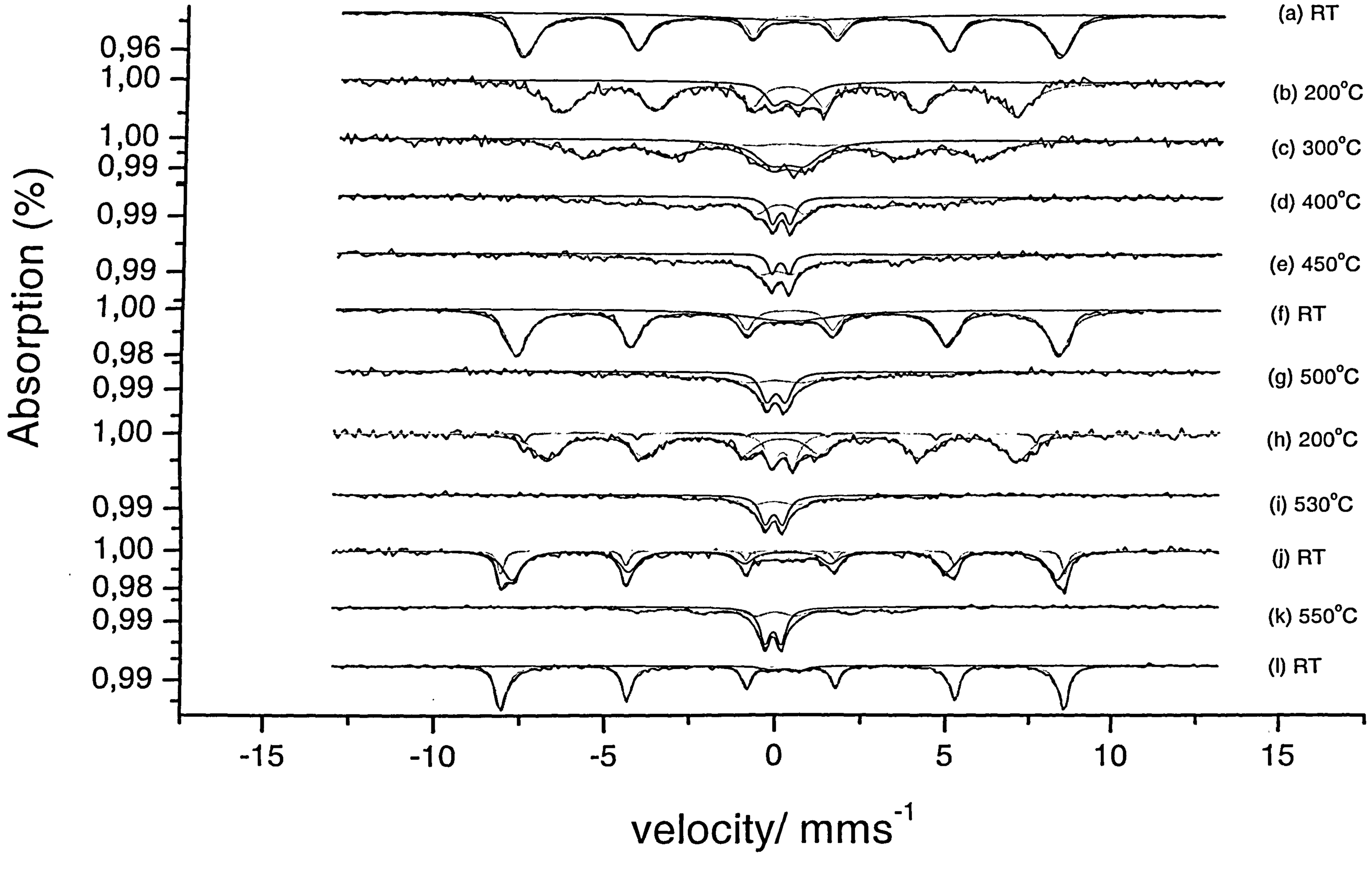

Figure 4.39 XRD patterns recorded from Sn/γ-Fe_2O_3 with nominal loadings of (a) 5, (b) 8, (c) 10 and (d) 20 mass % tin

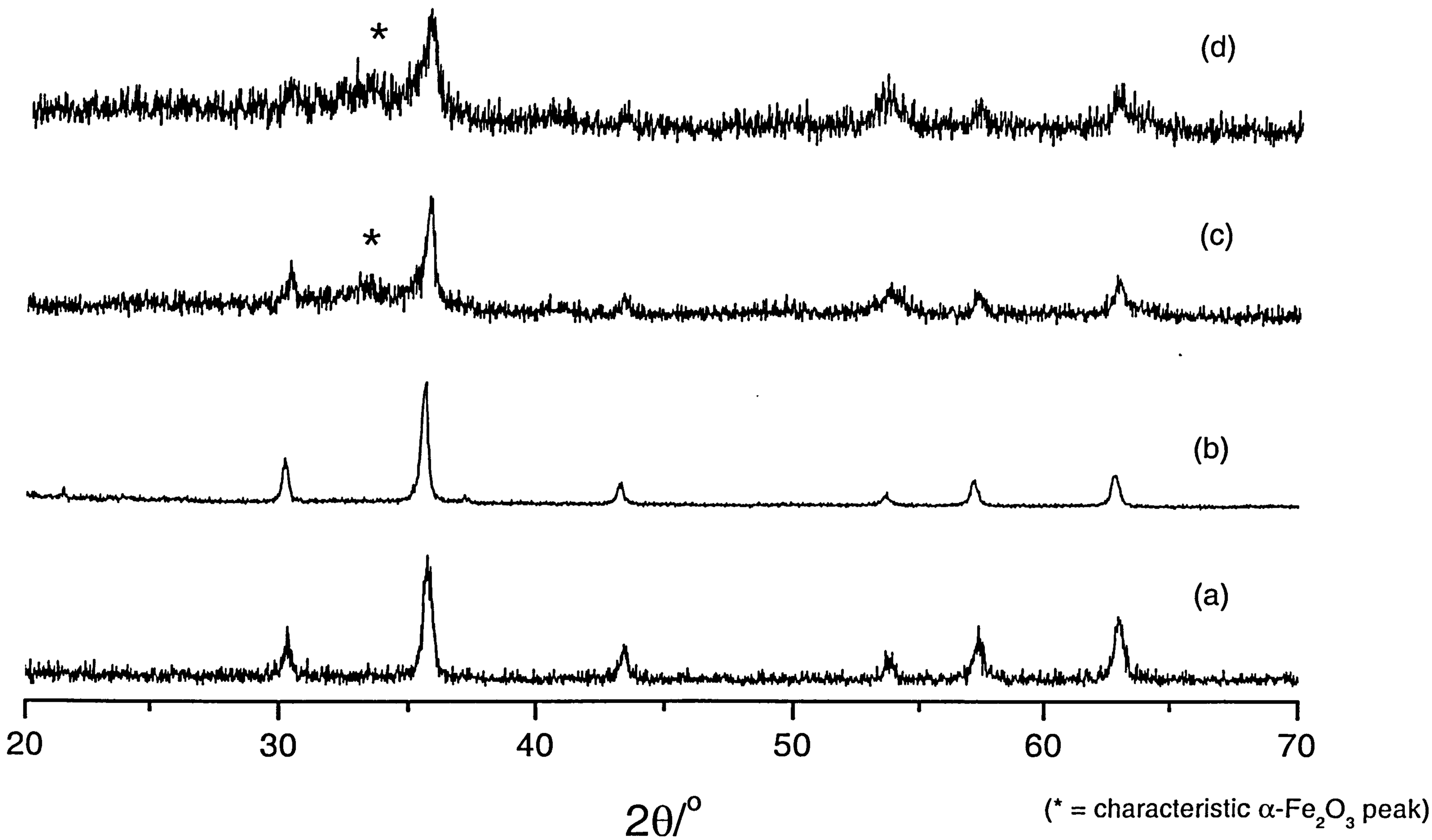

nominally 5 % and 8 % Sn/γ-Fe_2O_3 respectively. The EDX analyses data and lattice parameters are shown in Table 4.16. The XRD patterns recorded from 10% Sn/γ-Fe_2O_3 and 20 % Sn/γ-Fe_2O_3 corresponded to a mixture of γ–Fe_2O_3- and α-Fe_2O_3- related structures[5,6] (Figure 4.39 (c and d) respectively).

Table 4.16 EDX analysis data and lattice parameters calculated from tin- doped γ–Fe_2O_3 with different nominal tin content

Nominal tin content / mass %	EDX analysis (± 10 %)		Lattice parameter
	Mass %	Atomic %	a/Å (± 0.01)
5	7.15	1.99	8.363
8	9.22	2.64	8.375
10	13.63	4.02	-
20	30.43	10.03	-

The results must be considered in the same context as those recorded from Ti/γ–Fe_2O_3 (Section 4.2.1) and it seems that given the low temperature of calcination, appreciable amorphous tin- containing material exist in the samples and that the limit of solubility of tin in γ–Fe_2O_3 is less than *ca.* 10 mass percent.

The ^{57}Fe Mössbauer spectra confirmed the XRD results, showing a sextet corresponding to γ–Fe_2O_3[1,2] for all tin loadings, and an additional sextet pattern corresponding to α-Fe_2O_3[1,2] impurity with higher tin loadings (Figure 4.40, Table 4.17).

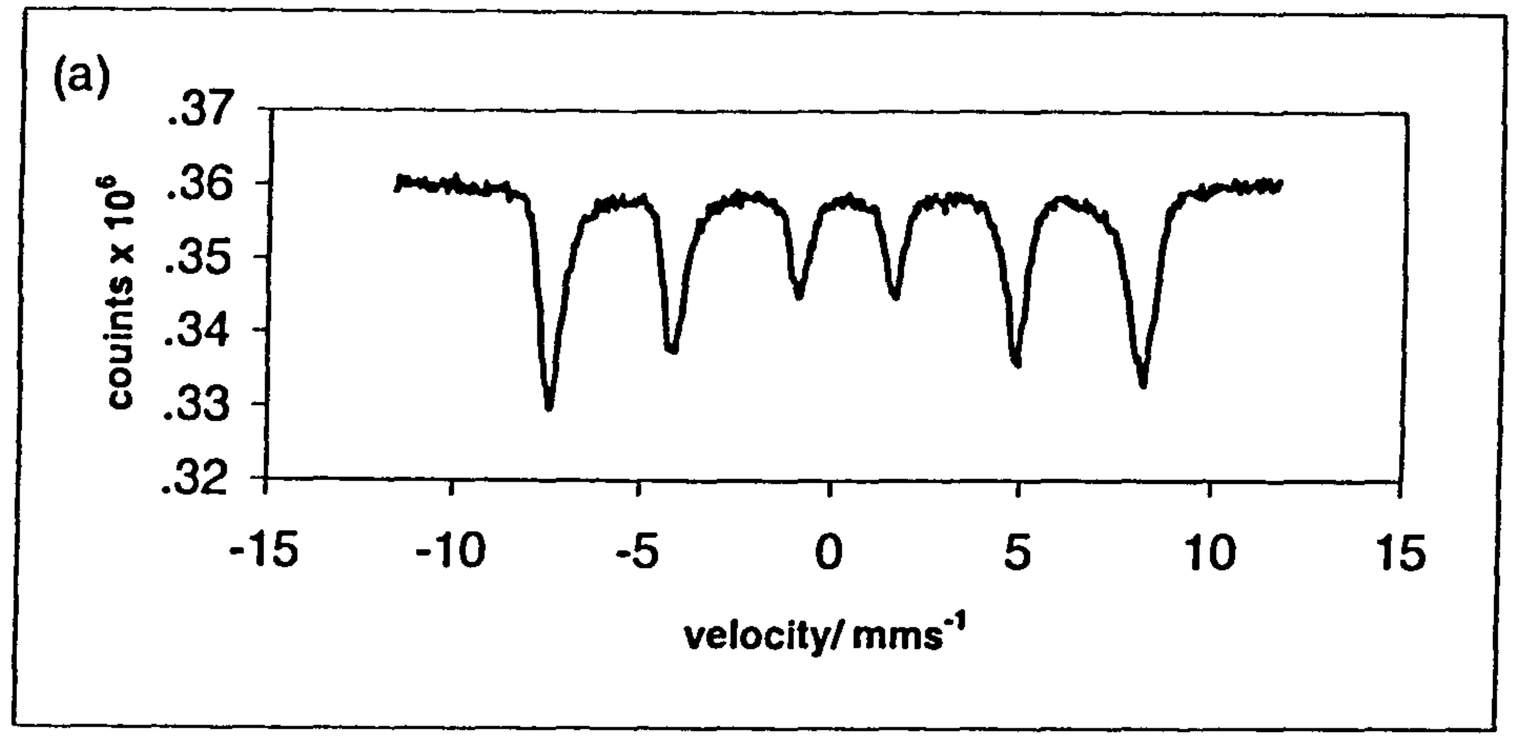

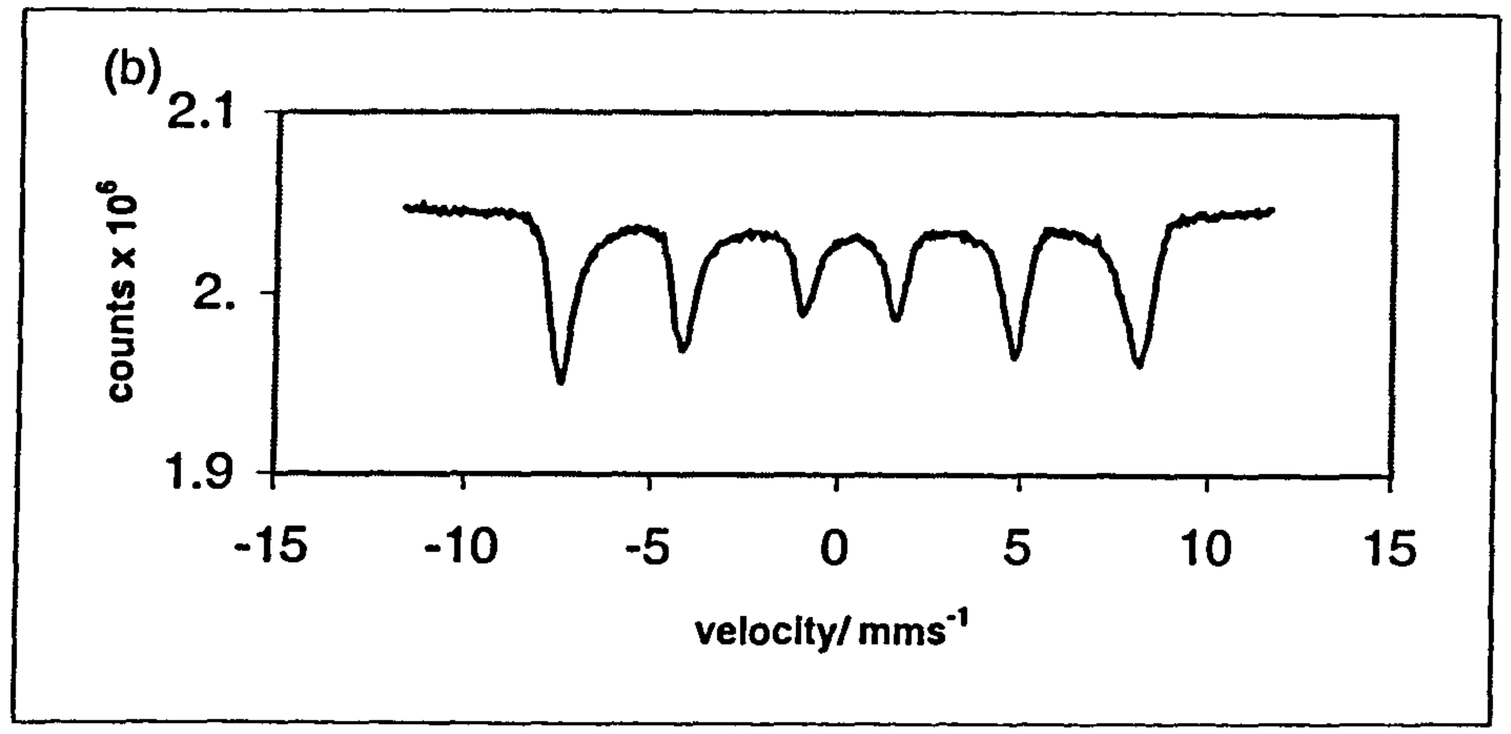

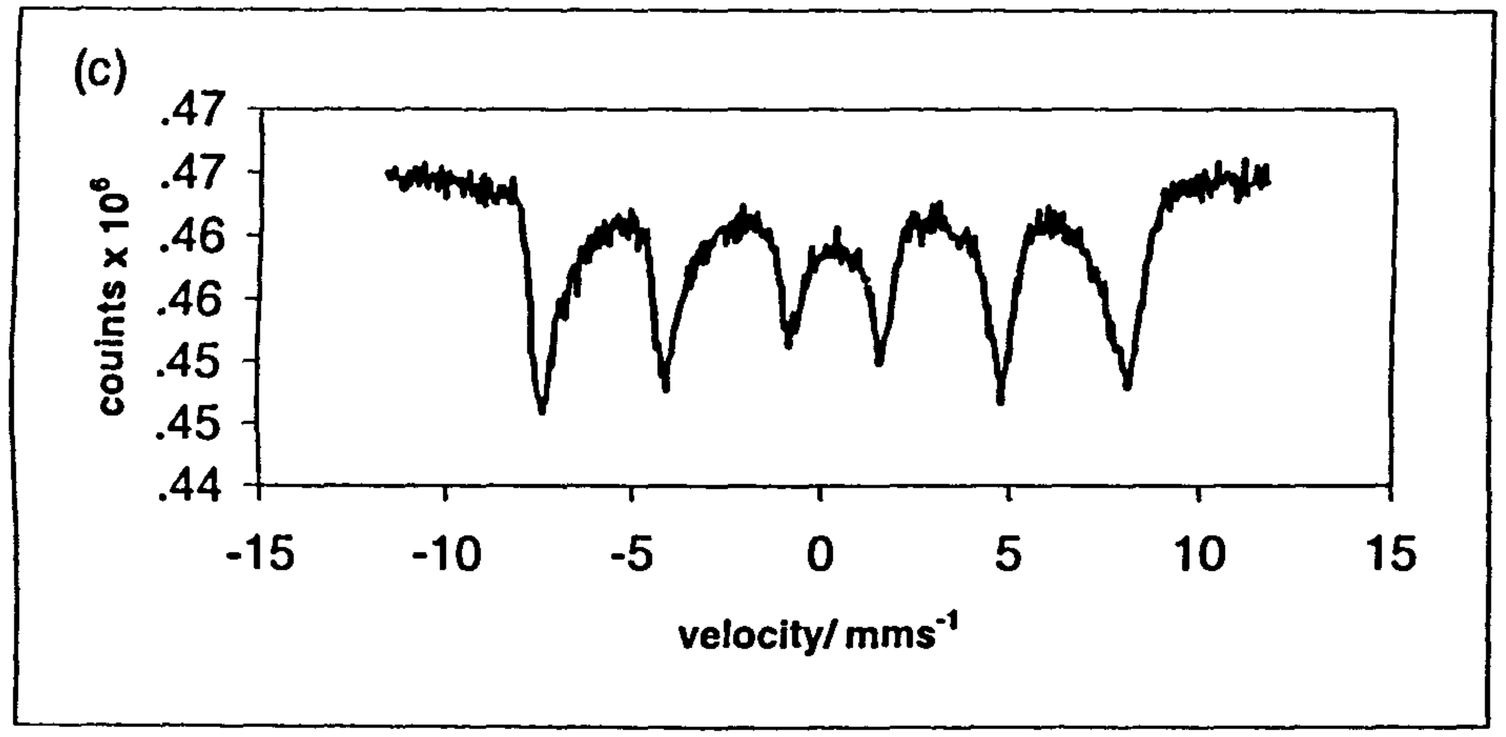

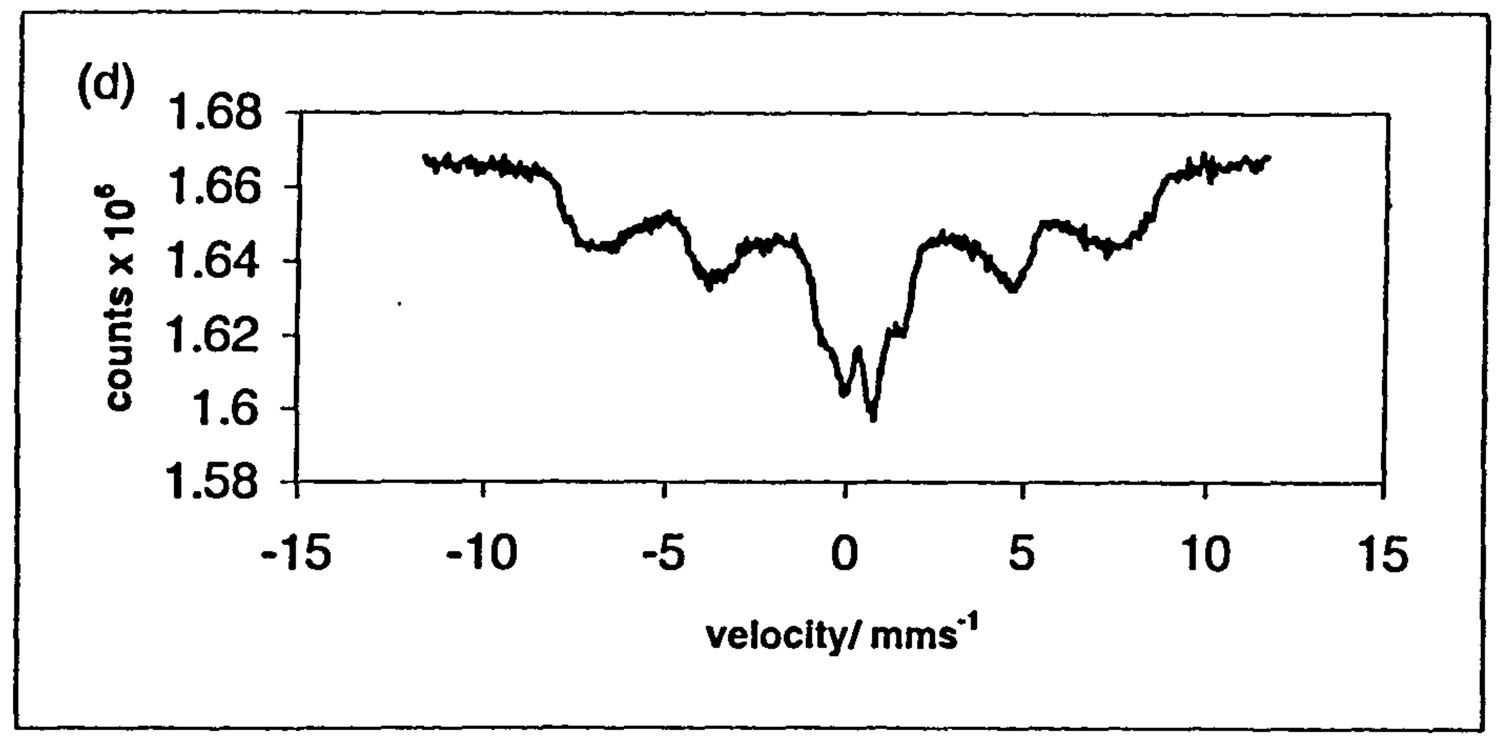

Figure 4.40 ^{57}Fe Mössbauer spectra recorded from Sn/γ-Fe_2O_3 of nominal loadings of (a) 5, (b) 8, (c) 10 and (d) 20 mass % tin

Table 4.17 ^{57}Fe Mössbauer parameters recorded from tin- doped γ–Fe_2O_3 with different nominal tin content

Nominal tin content / mass %	δ (± 0.02) mms^{-1}	Δ (± 0.02) mms^{-1}	H (± 1) T	Interpretation	Area (± 5) %
5	0.33	0.01	48	γ-Fe_2O_3	100
8	0.35	0.01	48	γ-Fe_2O_3	100
10	0.30	0.01	46	γ-Fe_2O_3	85
	0.38	-0.1	48	α-Fe_2O_3	15
20	0.37	0.84	---	Small particle iron oxide	16
	0.34	-0.05	40	γ-Fe_2O_3	57
	0.37	-0.1	46	α-Fe_2O_3	27

The different samples of Sn/γ–Fe_2O_3 with different tin contents were subjected to heat treatment and XRD patterns recorded *ex situ*, Table 4.18 shows the temperature of α-Fe_2O_3 appearance and γ–Fe_2O_3 disappearance. Nominally 5 % Sn/γ-Fe_2O_3 showed complete conversion to an α-Fe_2O_3- related phase by 700 °C (Figure 4.41). Nominally 8 % Sn/γ-Fe_2O_3 (Figure 4.42) showed complete conversion to the α-Fe_2O_3- type structure by 750 °C. The results are similar to those recorded from analogous titanium- doped γ–Fe_2O_3 (Section 4.2.1) and showed that the addition of tin to γ–Fe_2O_3 increases the temperature at which the spinel- related γ–Fe_2O_3 is converted to α-Fe_2O_3.

Table 4.18 γ–Fe_2O_3 to α-Fe_2O_3 conversion temperature recorded from tin-doped γ–Fe_2O_3 with different nominal tin contents

Nominal tin content / mass %	Temperature/ °C (± 25°C)	
	α-Fe_2O_3 formation	γ-Fe_2O_3 disappearance
5	650	700
8	500	750

Figure 4.41 XRD patterns recorded *ex situ* from nominal 5 % Sn/γ-Fe_2O_3 prepared by addition of base to salt, boiling under reflux, and heating at 250 °C and then heated from 550 to 750 °C

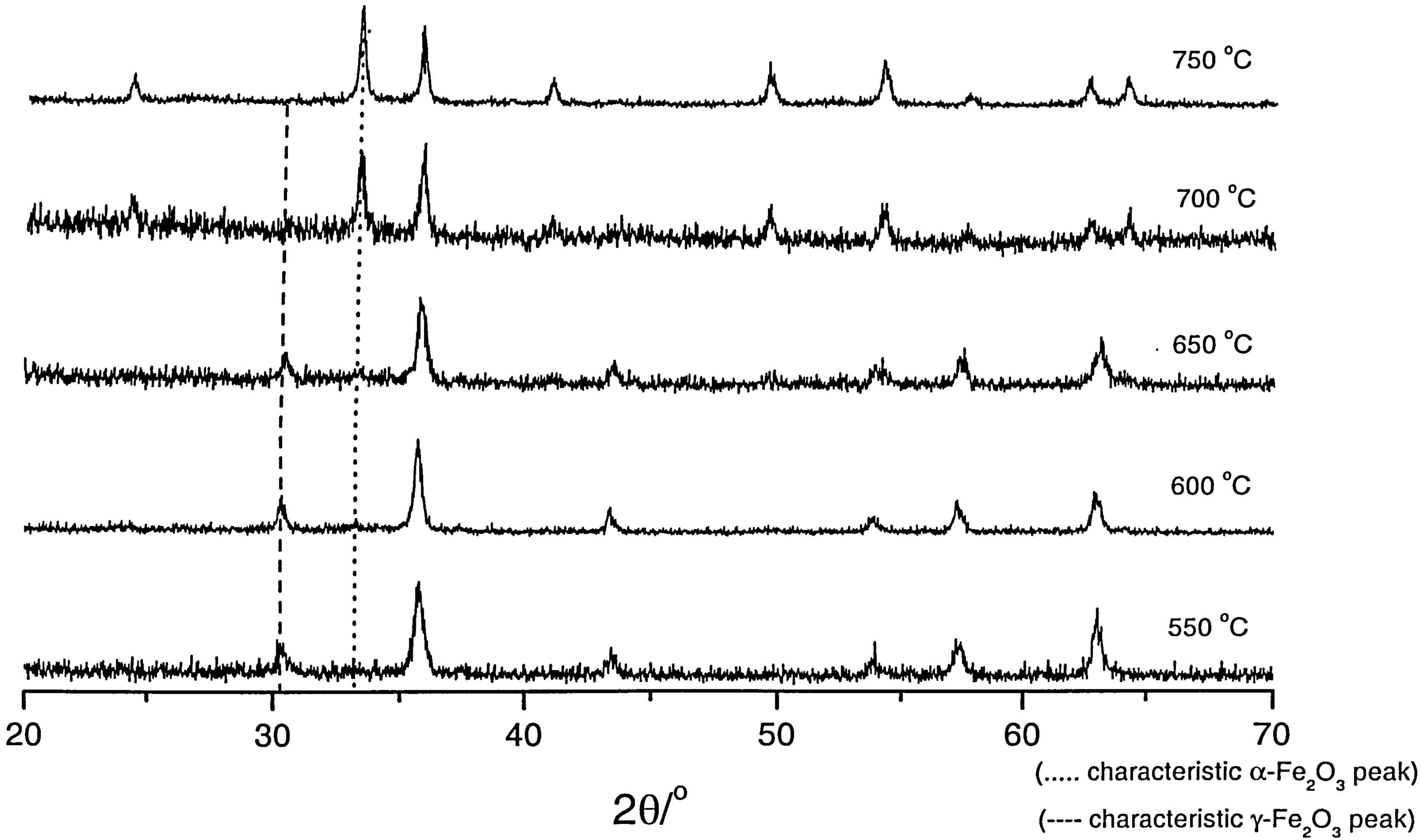

Figure 4.42 XRD patterns recorded *ex situ* from nominal 8 % Sn/γ-Fe_2O_3 prepared by addition of base to salt, boiling under reflux, and heating at 250 °C and then heated from 350 to 750 °C

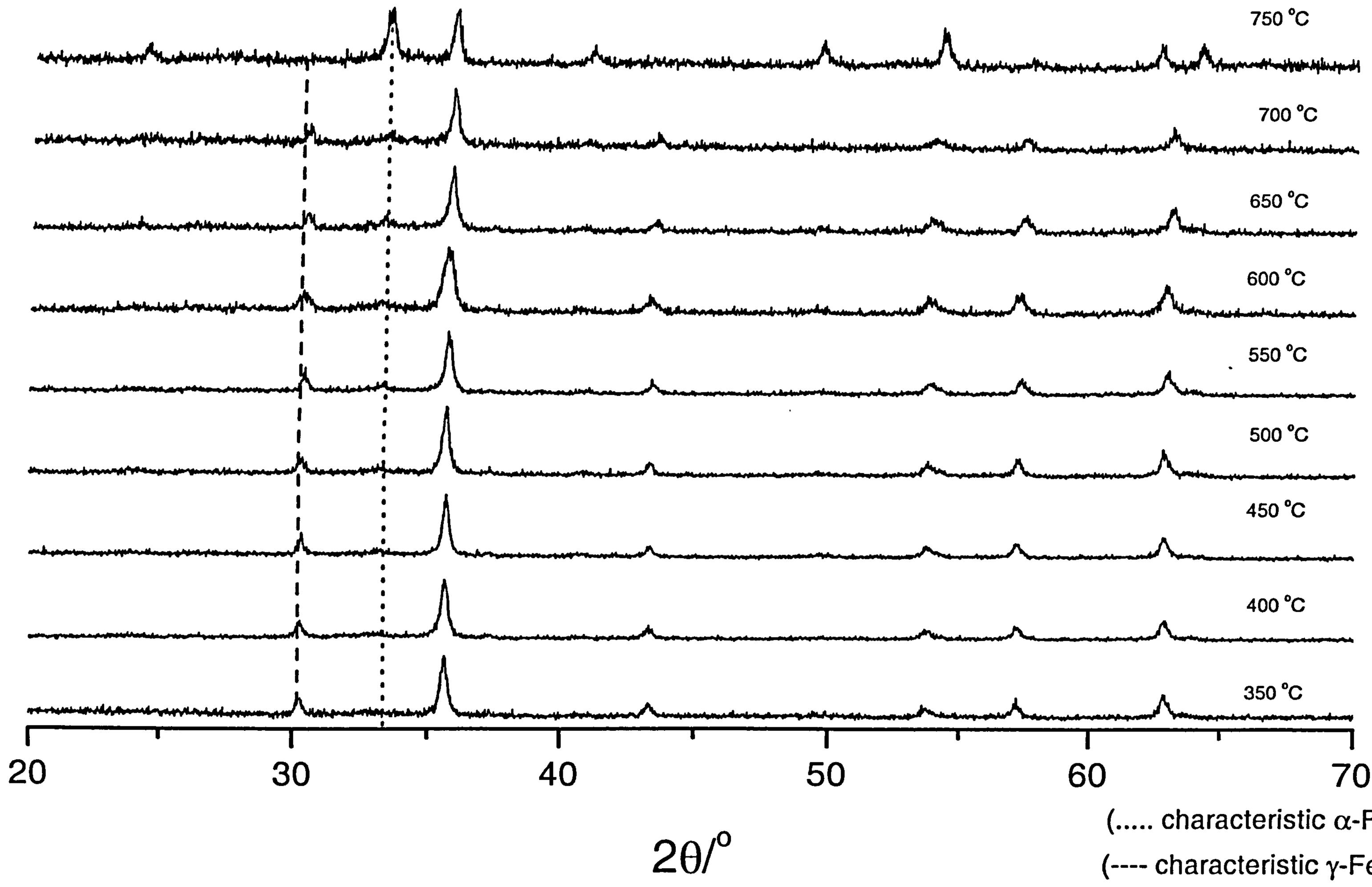

Conclusion

Sn/γ–Fe_2O_3 prepared by the addition of base to salt, boiling under reflux, and calcination at 250 °C/12 h had a lower surface area as compared with undoped γ–Fe_2O_3 and Ti/γ–Fe_2O_3 prepared by a similar method. The TPR profile of Sn/γ–Fe_2O_3 showed the material to follow a similar reduction pathway as undoped γ–Fe_2O_3 prepared by a similar method. The formation of FeO was observed, which was not detected in the reduction pathway of Ti/γ–Fe_2O_3, and an iron- tin alloy was identified as a reduction product. Reduction and reoxidation produced slight changes in the surface area and particle size, with the initial reduction step showing the greatest change in the surface area. It was found that the incorporation of tin maintains the stability of the γ–Fe_2O_3 structure with respect to conversion to the α-Fe_2O_3 structure.

4.2.3 Ruthenium- doped γ–Fe_2O_3 (addition of base to salt, boiling under reflux, and calcination at 250 °C/12 h)

The X-ray powder diffraction pattern (Figure 4.43) recorded from the material which ICP analysis showed to contain 3.12 mass % Ru was characteristic of a single phase spinel-related structure. The lattice parameter a = 8.360(2) Å can be compared to a = 8.334 Å reported for γ–Fe_2O_3[8] and the γ–Fe_2O_3 formed here by addition of base to salt, boiling under reflux, and calcination at 250 °C (a = 8.354(2) Å). Ru^{4+} has a radius[16] of 0.62 Å, similar to Ti^{4+} (0.61 Å), and slightly lower than Fe^{3+} (0.65 Å). The small increase in the lattice parameter observed in both titanium- and ruthenium-doped γ–Fe_2O_3 is unexpected.

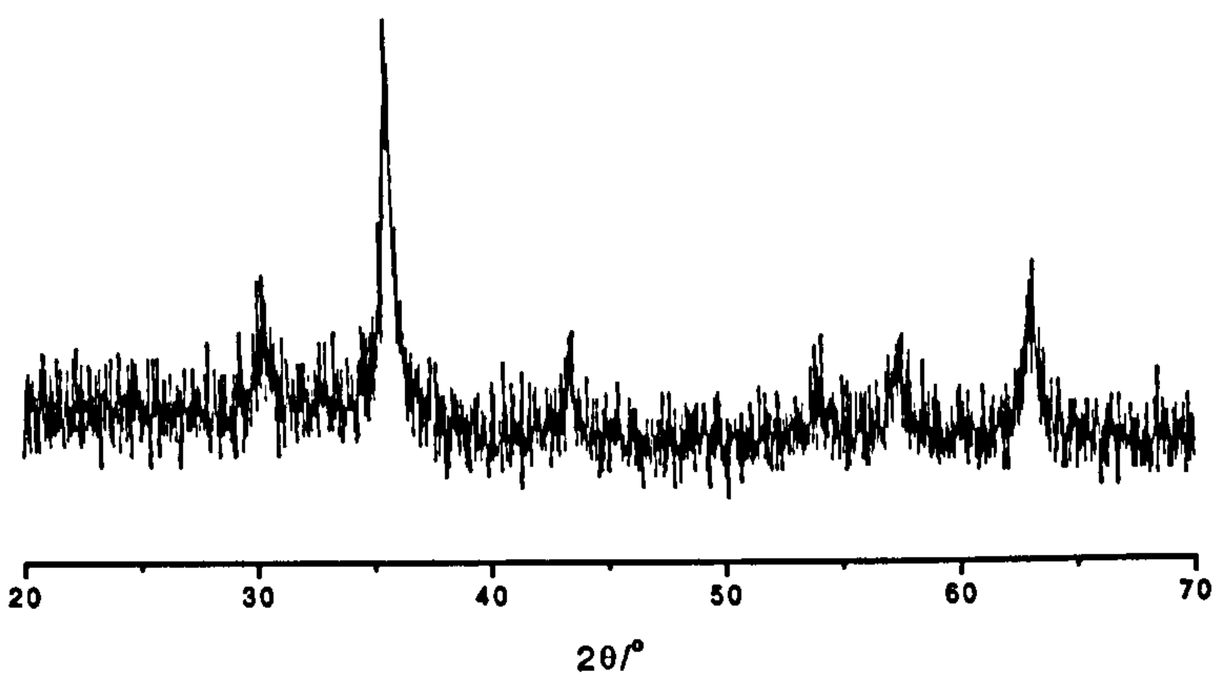

Figure 4.43 XRD pattern recorded from Ru/γ–Fe_2O_3 prepared by addition of base to salt, boiling under reflux, and calcination at 250 °C

The ^{57}Fe Mössbauer spectrum (Figure 4.44) recorded from ruthenium- doped γ–Fe_2O_3 at 298 K was similar to that of titanium- doped γ–Fe_2O_3 prepared by a similar method (Figure 4.20) and showed a sextet pattern (δ 0.33(2) mms^{-1}, Δ 0.02(2) mms^{-1}, H 47(1) T) characteristic[1,2] of a γ–Fe_2O_3-related phase together with a doublet, accounting for *ca.* 46 % of the spectrum and indicative of the presence of Fe^{3+} in small particle iron oxide[3]. The particle size of *ca.* 15 nm obtained from the X-ray powder diffraction linewidth data was similar to that of undoped γ–Fe_2O_3 and titanium doped γ–Fe_2O_3 both prepared by addition of base to salt, boiling under reflux, and calcined at 250 °C. The surface area of *ca.* 131 m^2g^{-1} was similar to that of titanium- doped γ–Fe_2O_3 (139 m^2g^{-1}) and greater than that of undoped γ–Fe_2O_3 (69 m^2g^{-1}) and Sn/γ–Fe_2O_3 (59 m^2g^{-1}) prepared by similar methods.

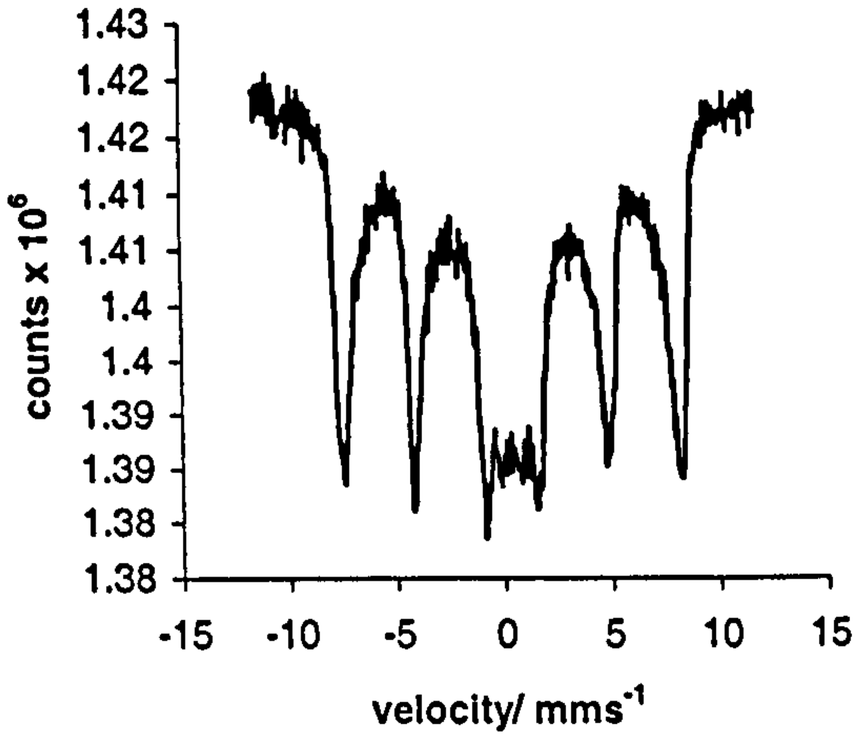

Figure 4.44 ^{57}Fe Mössbauer spectrum recorded from Ru/γ–Fe_2O_3 prepared by addition of base to salt, boiling under reflux, and calcination at 250 °C

The temperature programmed reduction profile is shown in Figure 4.45. *Ex situ* XRD and *ex situ* ^{57}Fe Mössbauer spectroscopy examination of samples retrieved after each reduction peak from the TPR experiment have revealed the identity of the reduced phases (Figures 4.45 and 4.46 respectively). Table 4.19 shows the ^{57}Fe Mössbauer parameters of Ru/γ-Fe_2O_3 after each reduction step.

The TPR profile is more similar in shape to that of undoped γ–Fe_2O_3 (Figure 4.7) and Sn/γ–Fe_2O_3 (Figure 4.34) than to titanium- doped γ–Fe_2O_3 (Figure 4.21) prepared by similar methods. The first reduction peak at *ca.* 175 °C is significantly lower in temperature than that recorded from either undoped γ–Fe_2O_3 or titanium- or tin-doped γ–Fe_2O_3 prepared by addition of base to salt, boiling under reflux, and calcination at 250 °C (*ca.* 350 °C for γ–Fe_2O_3). The subsequent reduction peaks (at *ca.* 680 and 900 °C) are also at lower temperature than that of undoped γ–Fe_2O_3 prepared by a similar method (*ca.* 720 and 990 °C). The results indicate that ruthenium induces reduction at lower temperatures. The presence of a small (*ca.*

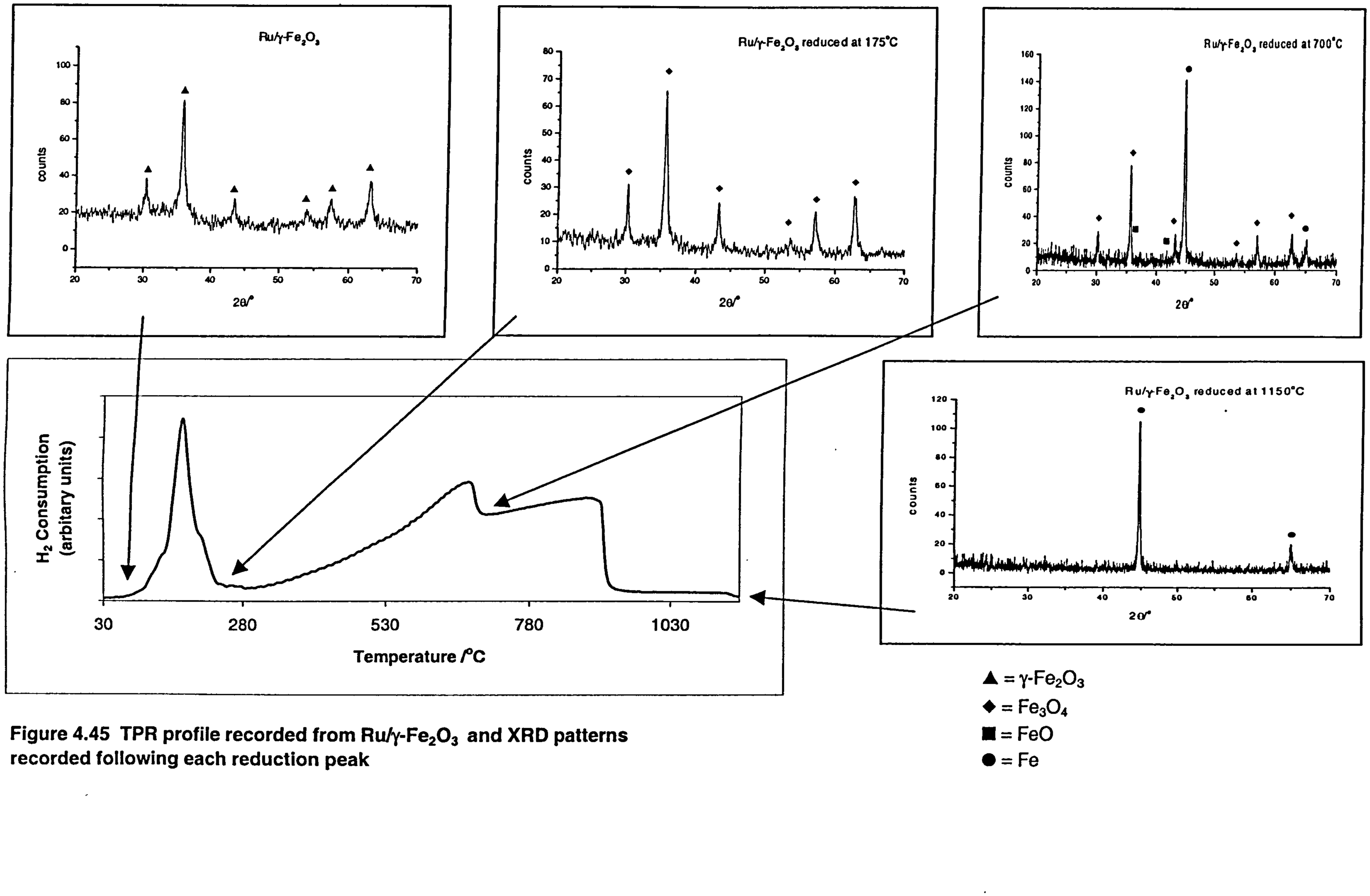

Figure 4.45 TPR profile recorded from Ru/γ-Fe_2O_3 and XRD patterns recorded following each reduction peak

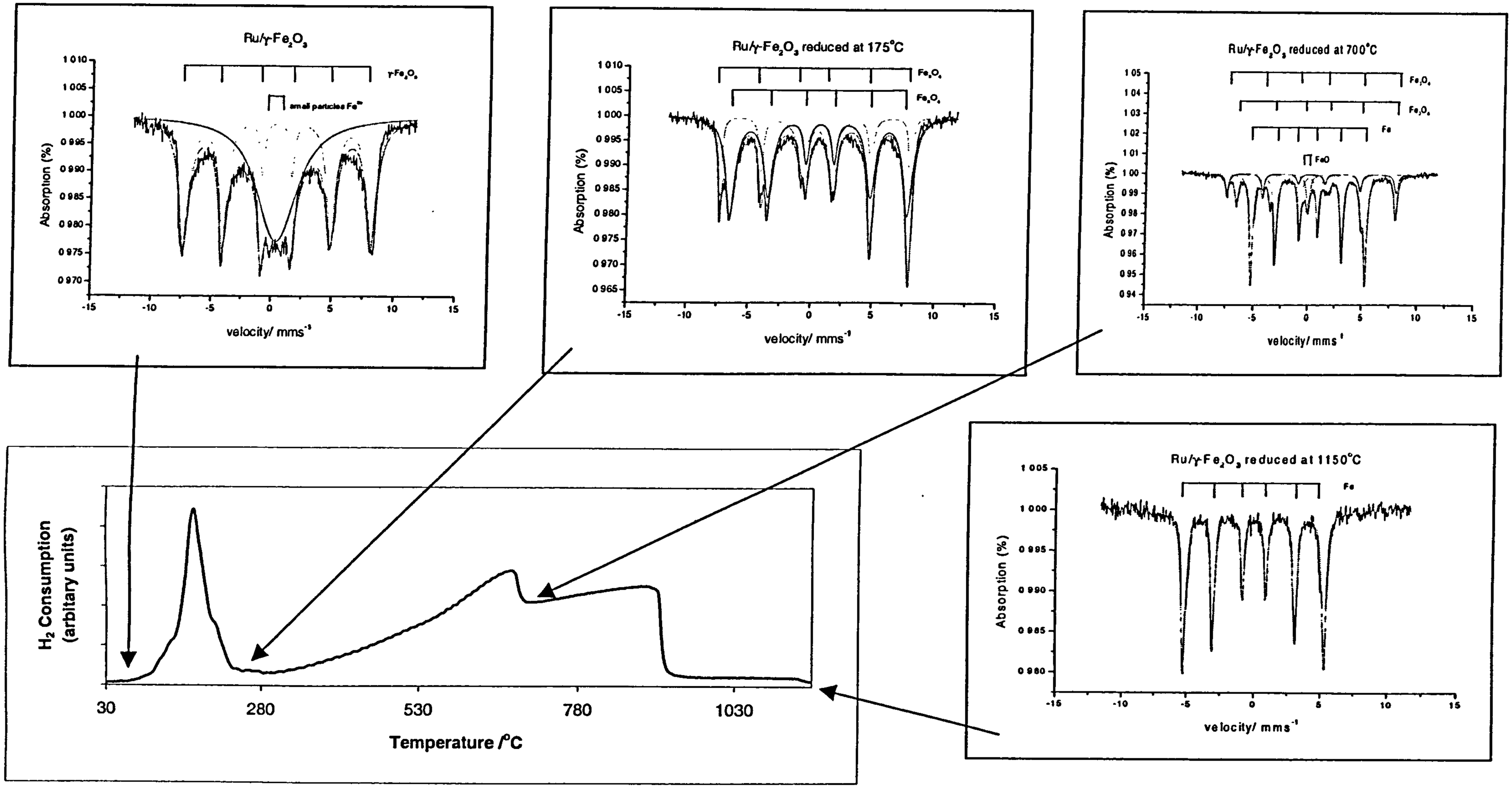

Figure 4.46 TPR profile recorded from Ru/γ-Fe_2O_3 and ^{57}Fe Mössbauer spectra recorded following each reduction peak

5 %) amount of wüstite after the second reduction peak was observed in the Mössbauer spectrum but was not clearly detected in the X-ray powder diffraction pattern (Figure 4.45). The reduction profile followed a similar reduction pathway to that of undoped γ–Fe_2O_3 and Sn/γ–Fe_2O_3 where FeO was observed, but is different from the reduction pathway of Ti/γ–Fe_2O_3 where FeO was not detected. No iron-ruthenium alloy was detected in contrast to the reduction profile for Sn/γ–Fe_2O_3, which is probably due to the low ruthenium content.

Table 4.19 ^{57}Fe Mössbauer parameters recorded from Ru/γ-Fe_2O_3 following reduction in TPR experiment

Sample	δ (± 0.02) mms^{-1}	Δ (± 0.02) mms^{-1}	H (± 1) T	Interpretation	Area (± 5) %
Ru/γ-Fe_2O_3	0.35	1.14	---	Small particle iron oxide	46
	0.33	0.02	47	γ-Fe_2O_3	54
Ru/γ-Fe_2O_3 reduced at 175 °C	0.44	0.03	---	Small particle iron oxide	37
	0.53	0.01	44	Fe_3O_4	63
	0.30	-0.01	48	Fe_3O_4	
Ru/γ-Fe_2O_3 reduced at 700 °C	0.67	0.00	45	Fe_3O_4	32
	0.26	0.01	48	Fe_3O_4	
	-0.07	0.15	---	FeO	5
	0.01	0.01	33	Fe	63
Ru/γ-Fe_2O_3 reduced at 1150 °C	0.01	0.01	33	Fe	100

Reduction-reoxidation properties

Ru/γ–Fe_2O_3 was subjected to reduction at 175 °C in the 10 % hydrogen- 90 % nitrogen mixture (R1) and reoxidised by heating at 250 °C for 1 h in air (O1). The cycle of reduction and reoxidation was repeated twice (samples R2, O2, R3 and O3).

X-ray powder diffraction (Figure 4.47) and ^{57}Fe Mössbauer spectroscopy (Figure 4.48, Table 4.20) were used to identify the materials after each reduction-oxidation step.

Table 4.20 ^{57}Fe Mössbauer parameters recorded from Ru/γ-Fe_2O_3 following treatment in reducing and oxidising environments

Sample	δ (± 0.02) mms^{-1}	Δ (± 0.02) mms^{-1}	H (± 1) T	Interpretation	Area (± 5) %
Ru/γ-Fe_2O_3	0.35	1.14	---	Small particle iron oxide	46
	0.33	0.02	47	γ-Fe_2O_3	54
R1	0.44	0.03	---	Small particle iron oxide	37
	0.53	0.01	44	Fe_3O_4	63
	0.30	-0.01	48	Fe_3O_4	
O1	0.33	0.01	48	γ-Fe_2O_3	100
R2	0.59	0.02	44	Fe_3O_4	100
	0.30	-0.01	48	Fe_3O_4	
O2	0.33	0.01	48	γ-Fe_2O_3	100
R3	0.62	-0.01	45	Fe_3O_4	100
	0.30	0.00	48	Fe_3O_4	
O3	0.33	0.01	48	γ-Fe_2O_3	100

The results show that Ru/γ–Fe_2O_3 can be reduced to Ru/Fe_3O_4 and reoxidised to Ru/γ–Fe_2O_3 and the reduction and reoxidation cycle repeated.

The particle size of ruthenium- doped Fe_3O_4 (R1) (*ca.* 17 nm) formed by initial reduction of the ruthenium- doped γ–Fe_2O_3 at 175 °C in the 10 % hydrogen- 90 % nitrogen gas mixture was similar to that of the precursor ruthenium- doped γ–Fe_2O_3 (*ca.* 15 nm). The surface area of the ruthenium- doped Fe_3O_4 (R1) (*ca.* 70 m^2g^{-1}) was

Figure 4.47 XRD patterns recorded *ex situ* from Ru/γ-Fe_2O_3 following reduction and reoxidation cycles

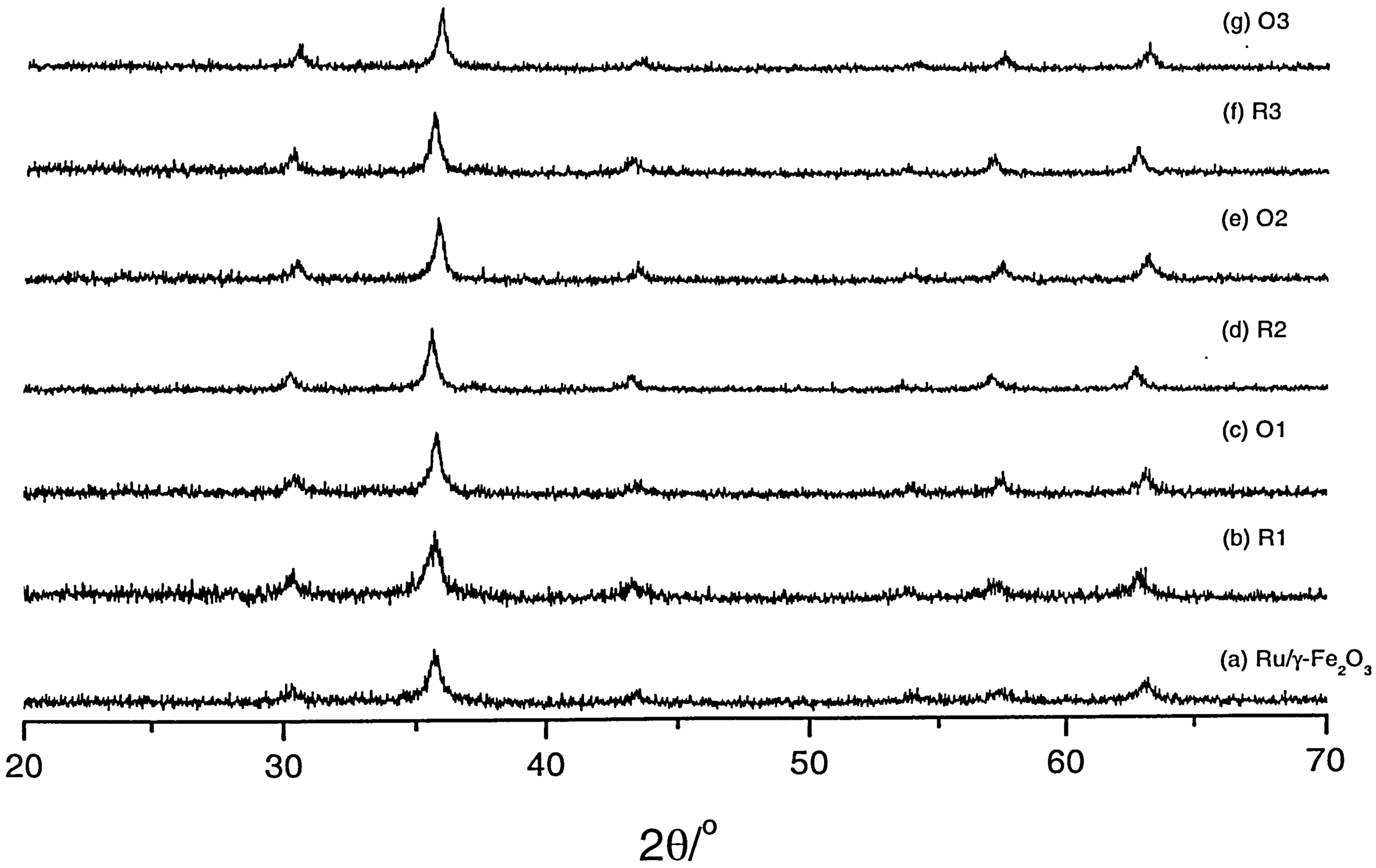

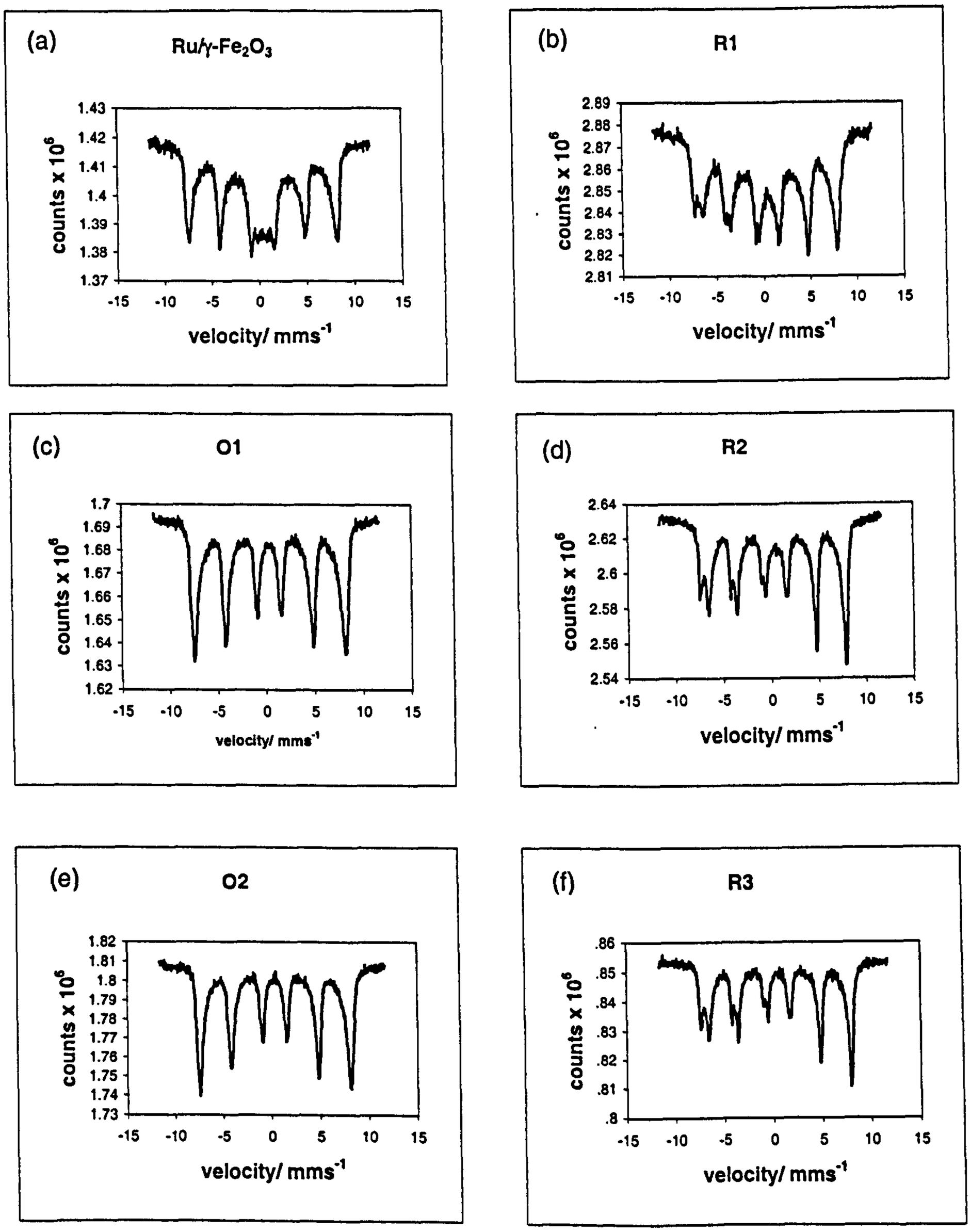

Figure 4.48 ^{57}Fe Mössbauer spectra recorded from Ru/γ-Fe_2O_3 following reduction and reoxidation cycles

lower than that of ruthenium- doped γ–Fe_2O_3 (*ca.* 131 m^2g^{-1}). Reoxidation by heating at 250 °C for 1 h in air followed by two further cycles of reduction and reoxidation produced small variations in particle size and surface area but with the finally regenerated ruthenium- doped γ–Fe_2O_3 (O3) having a size of *ca.* 22 nm and a surface area of *ca.* 44 m^2g^{-1}. Ru/γ–Fe_2O_3 therefore maintains a smaller particle size and higher surface area than that of the undoped γ–Fe_2O_3 prepared by a similar method over a three fold reduction- reoxidation cycle. Most significant is the observation that the initial reduction step results in a nearly 50 % loss of surface area and another *ca.* 50 % loss during the subsequent reduction-reoxidation cycles.

In situ ^{57}Fe Mössbauer spectroscopy studies

The ^{57}Fe Mössbauer spectra recorded *in situ* from ruthenium- doped Fe_3O_4 formed by reduction of ruthenium- doped γ–Fe_2O_3 and subsequent heating in the furnace[13] are shown in Figure 4.49. The material was heated to 250 °C and a room temperature spectrum recorded (Figure 4.49(b and c)), which showed a distribution of sextets that corresponded to the oxidation of Fe_3O_4 to γ-Fe_2O_3 (H = 49(1) T). The material was heated to 350 °C (Figure 4.49(d)), which showed the onset of α-Fe_2O_3 formation accounting for *ca.* 23 % of the spectral area. The material was further heated to 450 °C and a room temperature spectrum recorded (Figure 4.49(e and f)). The results showed an increase in the spectral area for the α-Fe_2O_3 component (H = 51(1) T). The material was heated to 527 °C and a final room temperature spectrum recorded (Figure 4.49(g and h)), which showed a sextet characteristic of only α-Fe_2O_3 (H = 52(1) T). A comparison of the results with those recorded from undoped γ–Fe_2O_3, titanium- and tin- doped γ–Fe_2O_3 prepared by similar methods (Figures 4.11, 4.25

Figure 4.49 *In situ* Mössbauer spectra recorded from Ru/Fe_3O_4 reduced from $Ru/\gamma\text{-}Fe_2O_3$

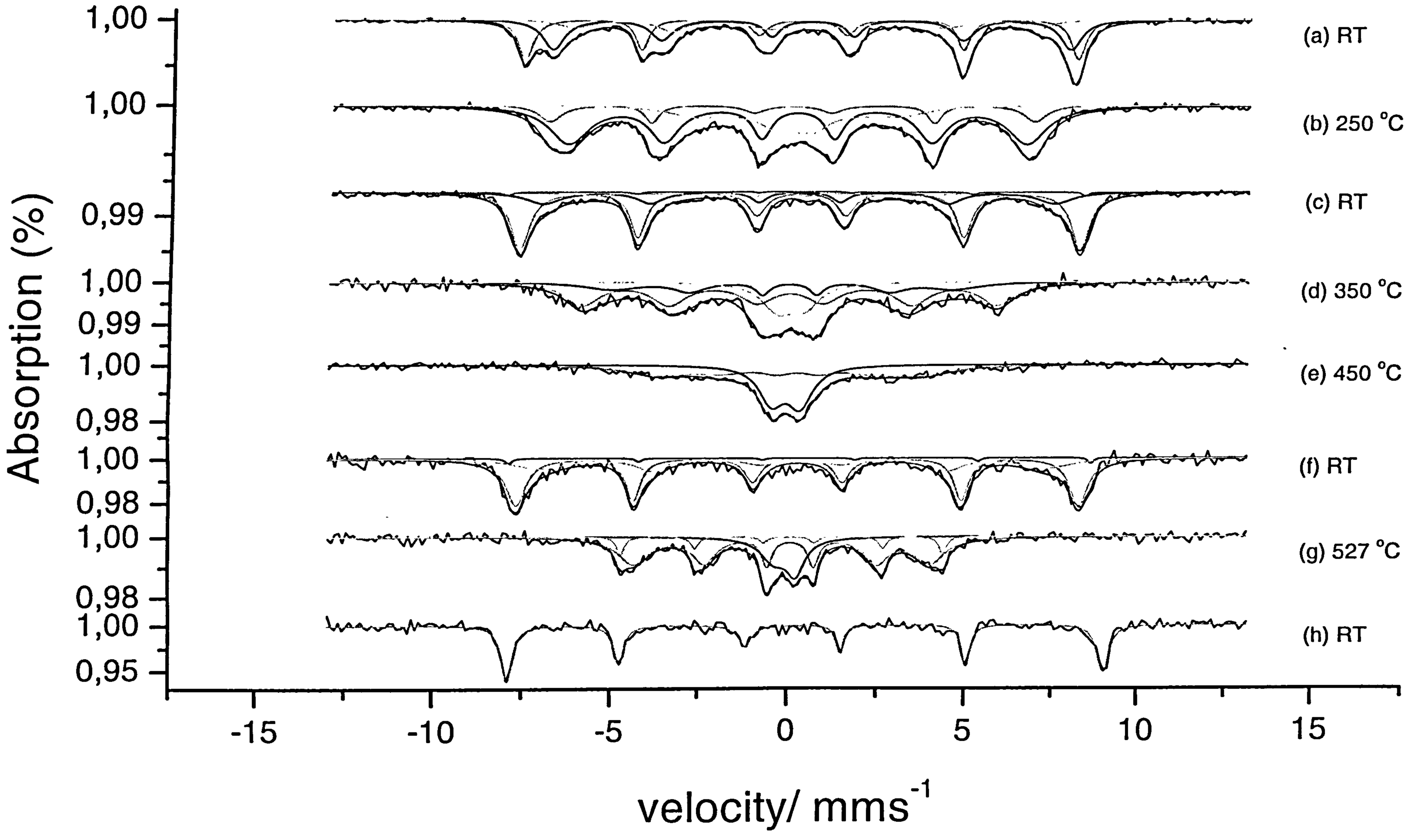

and 4.38 respectively) showed that ruthenium does not induce an equivalent degree of thermal stability in γ–Fe_2O_3 with respect to conversion to α-Fe_2O_3 as was observed in materials doped with titanium and tin.

Ex situ studies on the conversion of γ–Fe_2O_3 to α-Fe_2O_3

The X-ray powder diffraction patterns recorded *ex situ* from ruthenium- doped γ–Fe_2O_3 following heating in air are shown in Figure 4.50. The results showed the conversion of the spinel-related γ–Fe_2O_3 structure to the corundum-related α-Fe_2O_3 structure between 450 and 500 °C. The results are similar to those recorded from undoped γ–Fe_2O_3 prepared by addition of base to salt, boiling under reflux, and calcination at 250 °C (Figure 4.12) and confirm that the incorporation of Ru^{4+} ions does not stabilise the phase transformation of γ–Fe_2O_3 with respect to α-Fe_2O_3 in a way similar to that achieved by the incorporation of titanium or tin.

Conclusion

Ru/γ–Fe_2O_3 prepared by addition of base to salt, boiling under reflux, and calcined at 250 °C/12 h showed an increase in the surface area similar to Ti/γ–Fe_2O_3 prepared by a similar method. The TPR profile showed the reduction peaks at lower temperatures especially the initial reduction peak as compared with undoped γ–Fe_2O_3 prepared by a similar method, indicating that ruthenium promotes reduction. The reduction-reoxidation cycle showed that Ru/γ–Fe_2O_3 could be reduced to Ru/Fe_3O_4 and reoxidised back to Ru/γ–Fe_2O_3. The results showed that Ru/γ–Fe_2O_3 maintains smaller particle size and higher surface area than that of undoped γ–Fe_2O_3, although

Figure 4.50 XRD patterns recorded *ex situ* from Ru/γ-Fe_2O_3 prepared by addition of base to salt, boiling under reflux, and heating at 250 °C and then heated from 300 to 550 °C

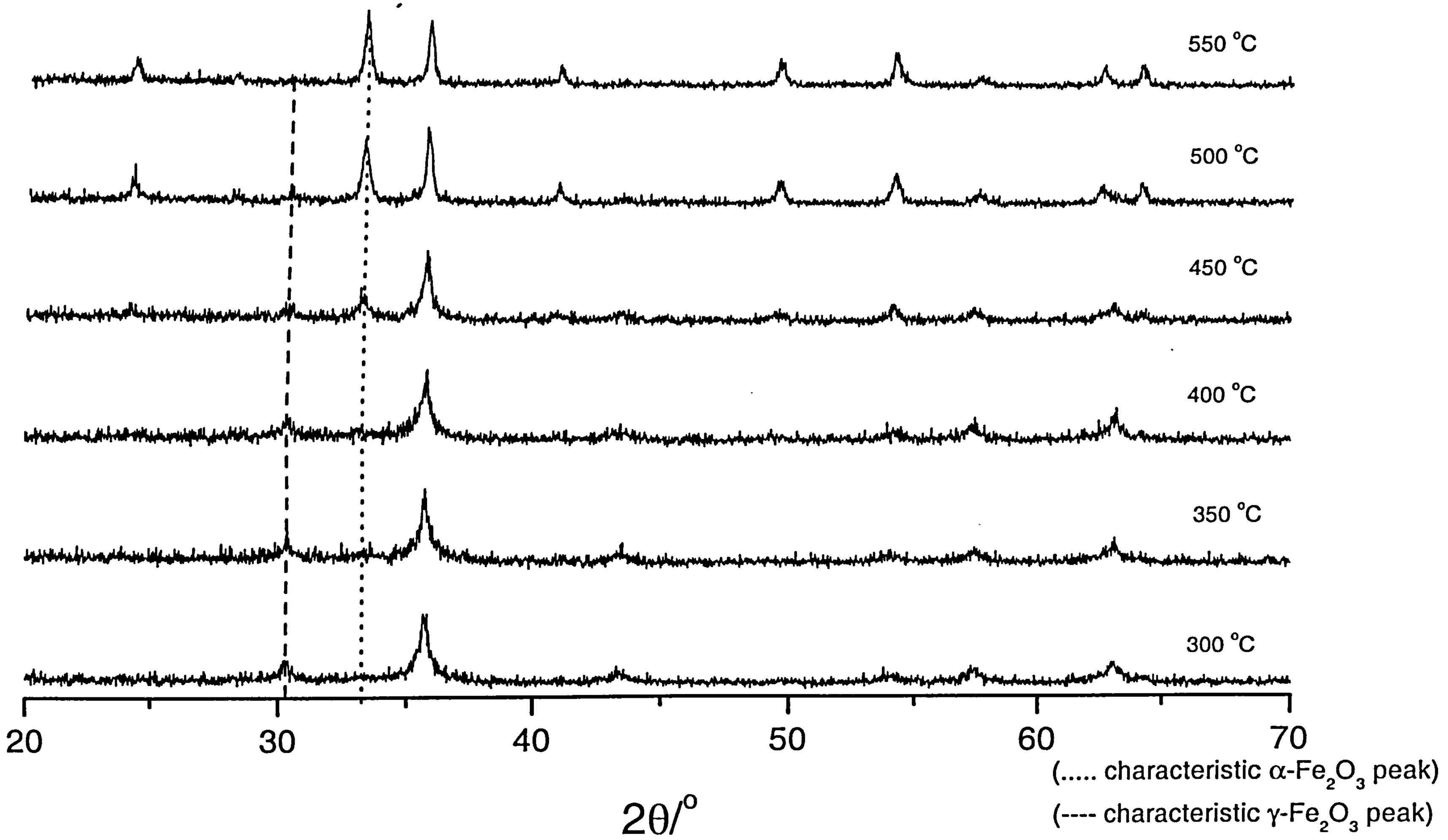

significant reduction in surface area was observed for the initial reduction step and during the subsequent reduction- reoxidation cycle. The *in situ* high temperature Mössbauer spectroscopy studies and *ex situ* XRD studies indicate that ruthenium does not stabilise the γ–Fe_2O_3 structure with respect to the thermal conversion to α-Fe_2O_3 as was observed in the case of titanium- and tin- doped analogous.

4.2.4 Magnesium- doped γ–Fe_2O_3 (addition of base to salt, boiling under reflux, and calcination at 250 °C/12 h)

The X-ray powder diffraction pattern (Figure 4.51) recorded from the material, which was shown by ICP analysis to contain 0.93 mass % Mg, showed a single phase spinel-related structure, a = 8.370(2) Å compared to a = 8.334 Å for γ–Fe_2O_3[8], and a = 8.354 Å for γ–Fe_2O_3 prepared here by a similar method. Mg^{2+} has a radius of 0.72 Å in 6 co-ordination[16], which is larger than that of Fe^{3+} (0.65 Å) and an increase in lattice parameter is quite reasonable.

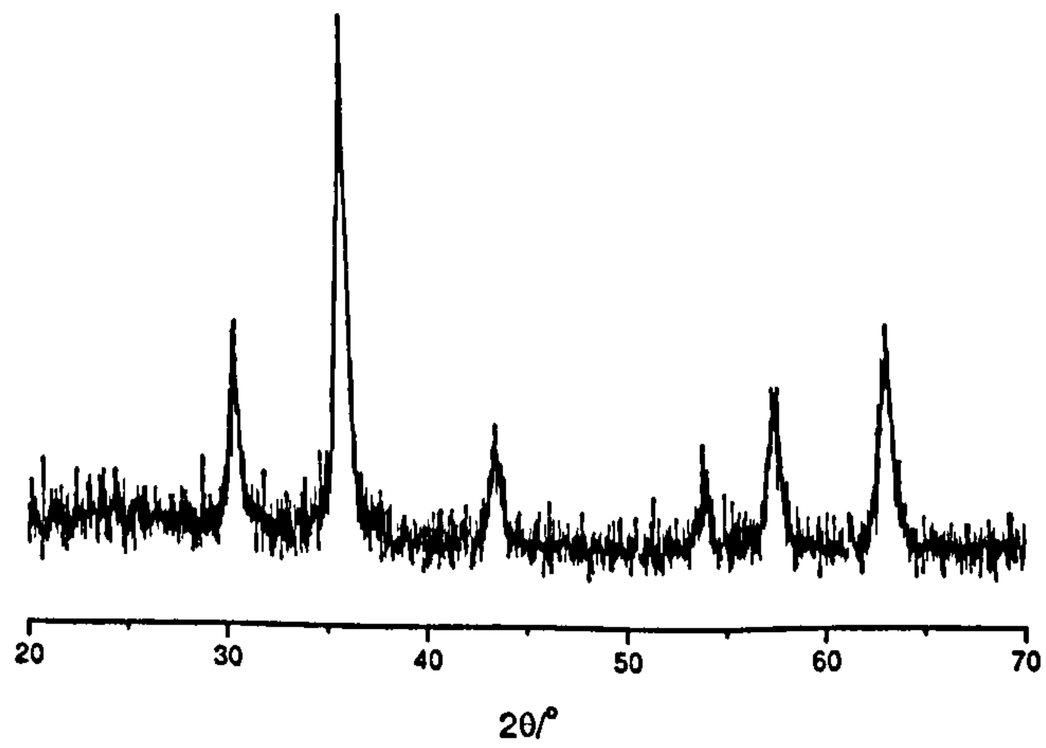

Figure 4.51 XRD pattern recorded from Mg/γ–Fe_2O_3 prepared by addition of base to salt, boiling under reflux, and calcination at 250 °C

The ^{57}Fe Mössbauer spectrum recorded from Mg/γ–Fe_2O_3 (Figure 4.52) (δ 0.34(2) mms^{-1}, Δ 0.01(2) mms^{-1}, H 46(1) T) was more similar to that of undoped γ–Fe_2O_3 and tin- doped γ–Fe_2O_3 prepared by addition of base to salt, boiling under reflux, and calcination at 250 °C (Figures 4.5 and 4.33 respectively) and did not contain the broadened central doublet observed in the spectra recorded from titanium- and ruthenium- doped γ–Fe_2O_3 (Figures 4.20 and 4.44 respectively) which indicated the additional presence of smaller particle material. The particle size of *ca.* 13 nm was similar to that of undoped γ–Fe_2O_3, titanium- and ruthenium- doped γ–Fe_2O_3, all prepared by a similar method. The surface area of 106 m^2g^{-1} was higher then undoped γ–Fe_2O_3 and tin- doped γ–Fe_2O_3 but lower than titanium- and ruthenium-doped γ–Fe_2O_3 prepared by similar methods.

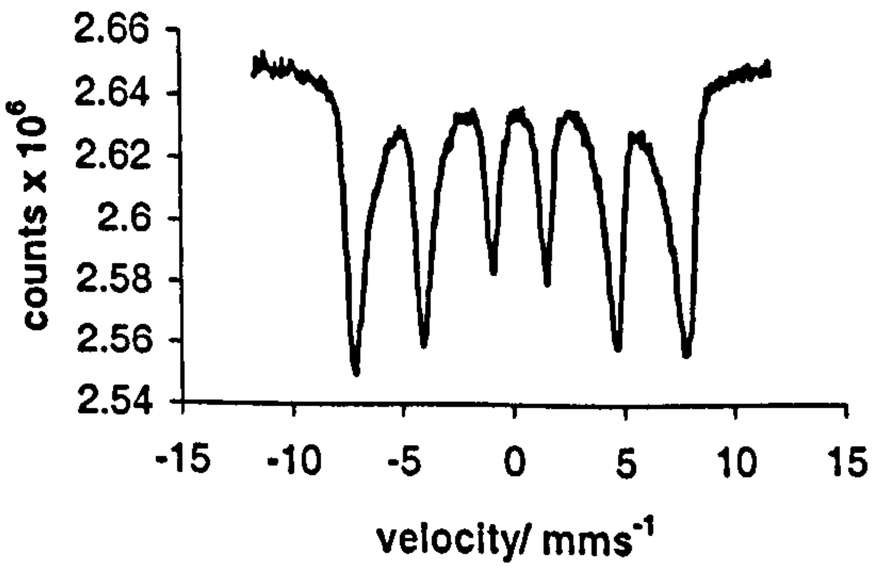

Figure 4.52 ^{57}Fe Mössbauer spectrum recorded from Mg/γ–Fe_2O_3 prepared by addition of base to salt, boiling under reflux, and calcination at 250 °C

The temperature programmed reduction profile (Figure 4.53) was identical in shape to that of undoped γ–Fe_2O_3 prepared by addition of base to salt, boiling under reflux, and calcination at 250 °C (Figure 4.7). X-ray powder diffraction patterns (Figure 4.53) together with ^{57}Fe Mössbauer spectra (Figure 4.54, Table 4.21) recorded *ex situ*

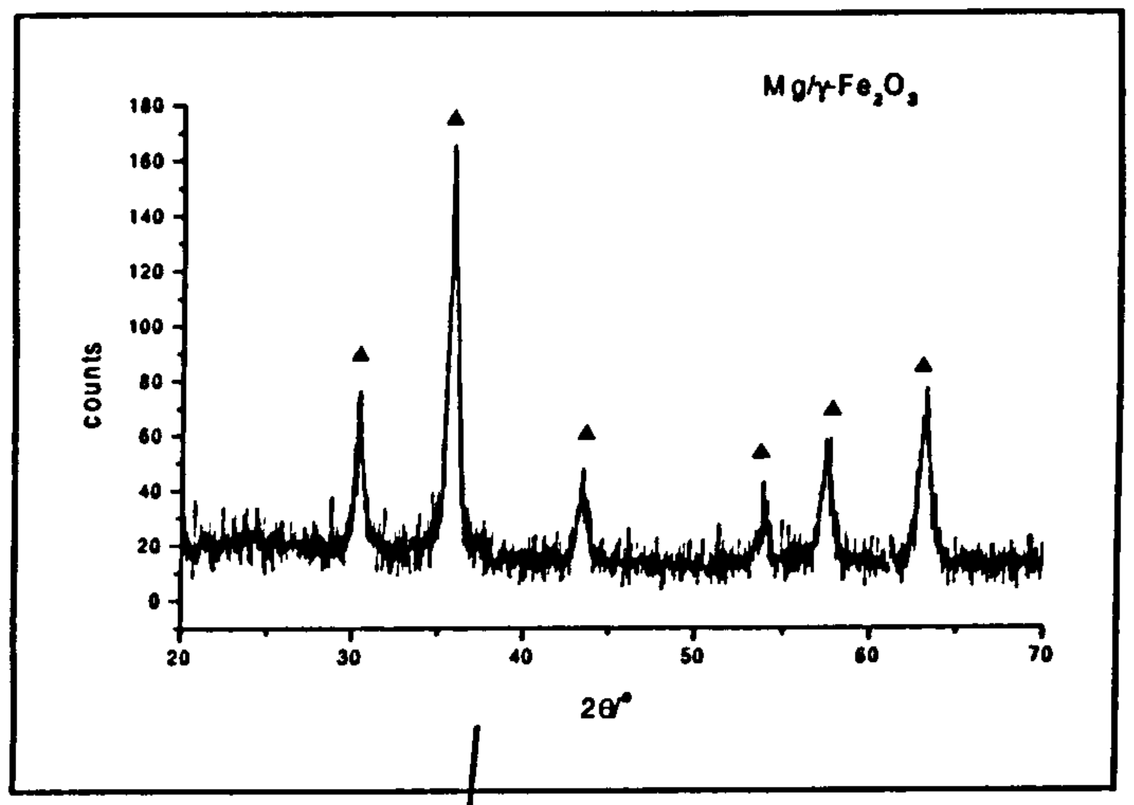

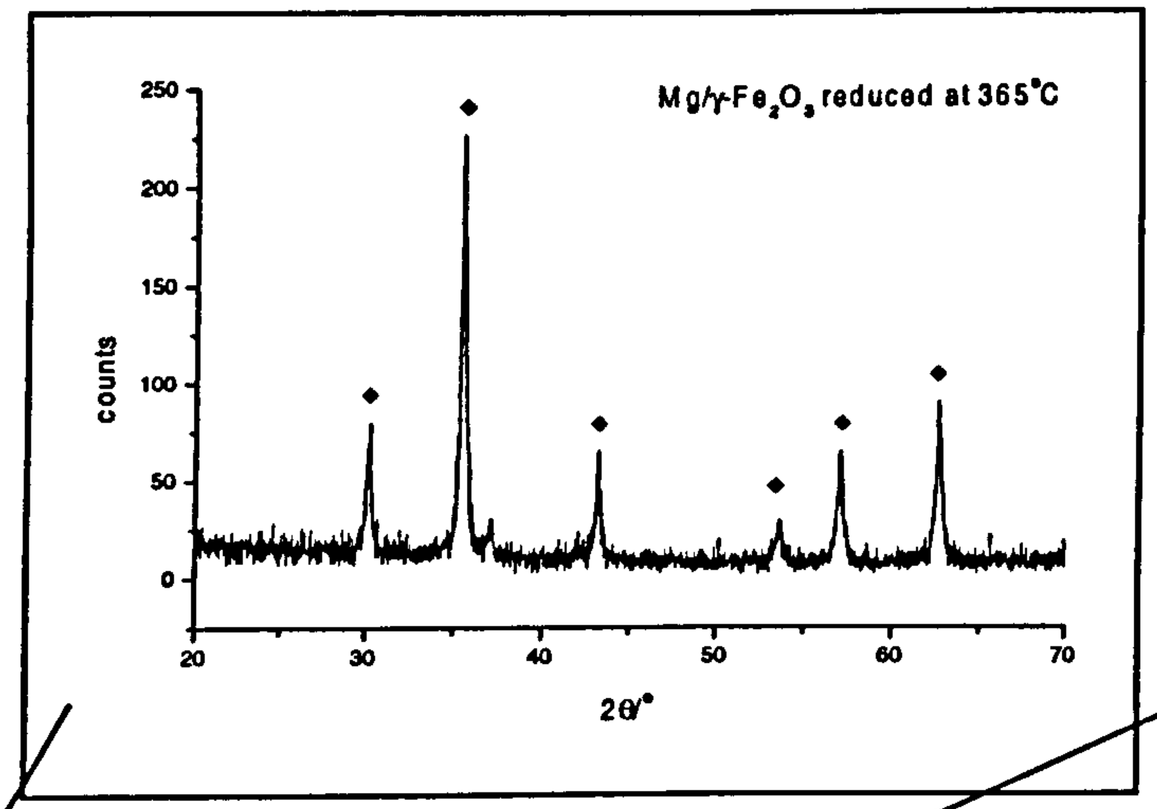

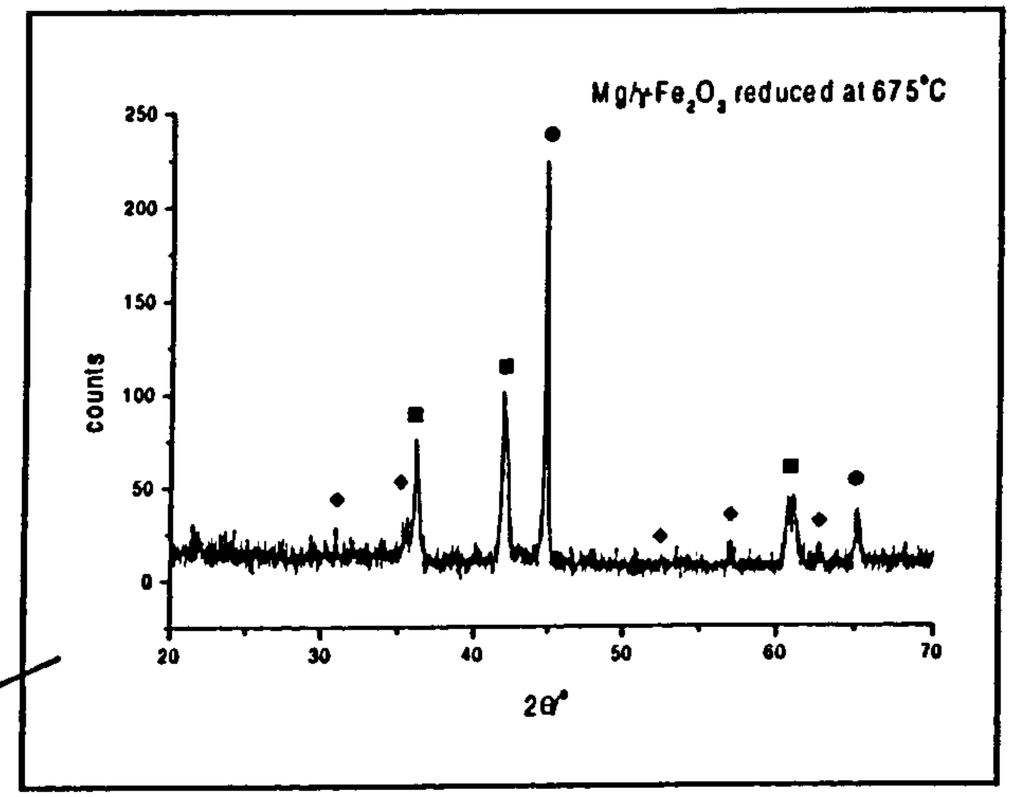

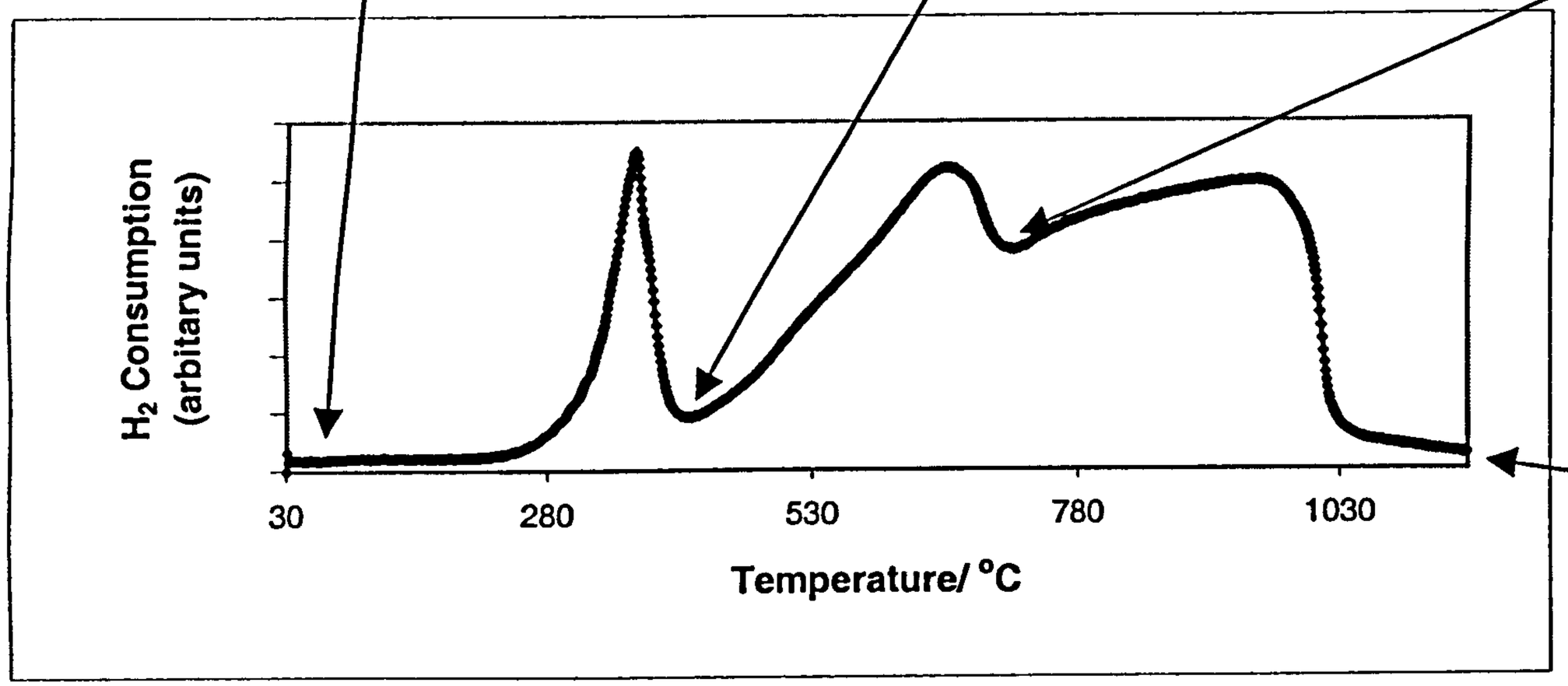

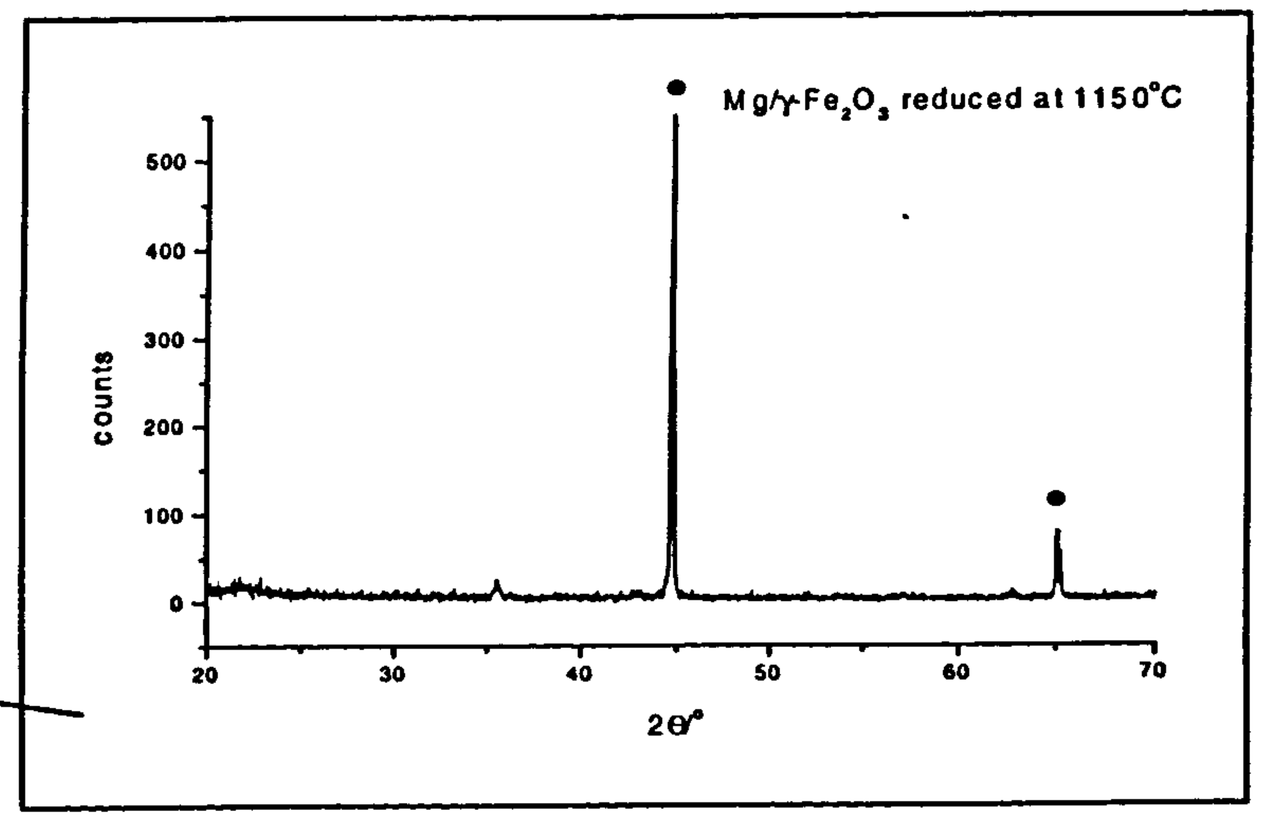

▲ = γ-Fe_2O_3
◆ = Fe_3O_4
■ = FeO
● = Fe

Figure 4.53 TPR profile recorded from Mg/γ-Fe_2O_3 and XRD patterns recorded following each reduction peak

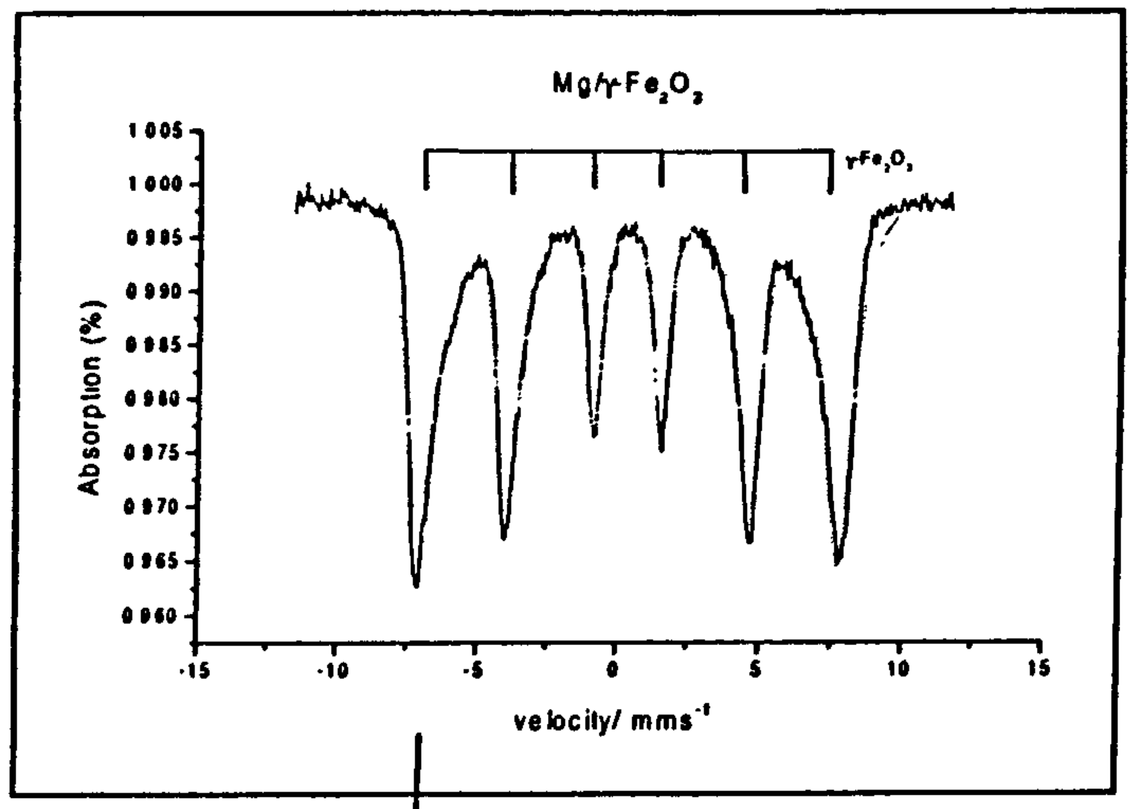

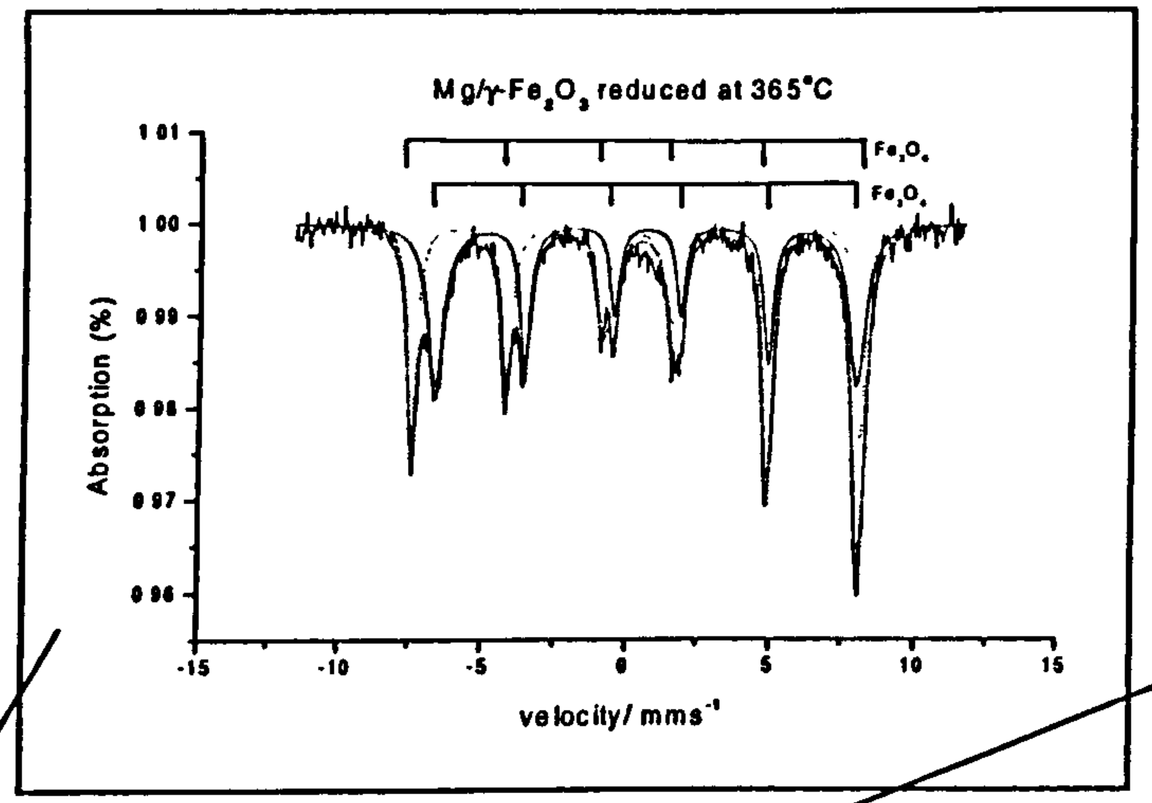

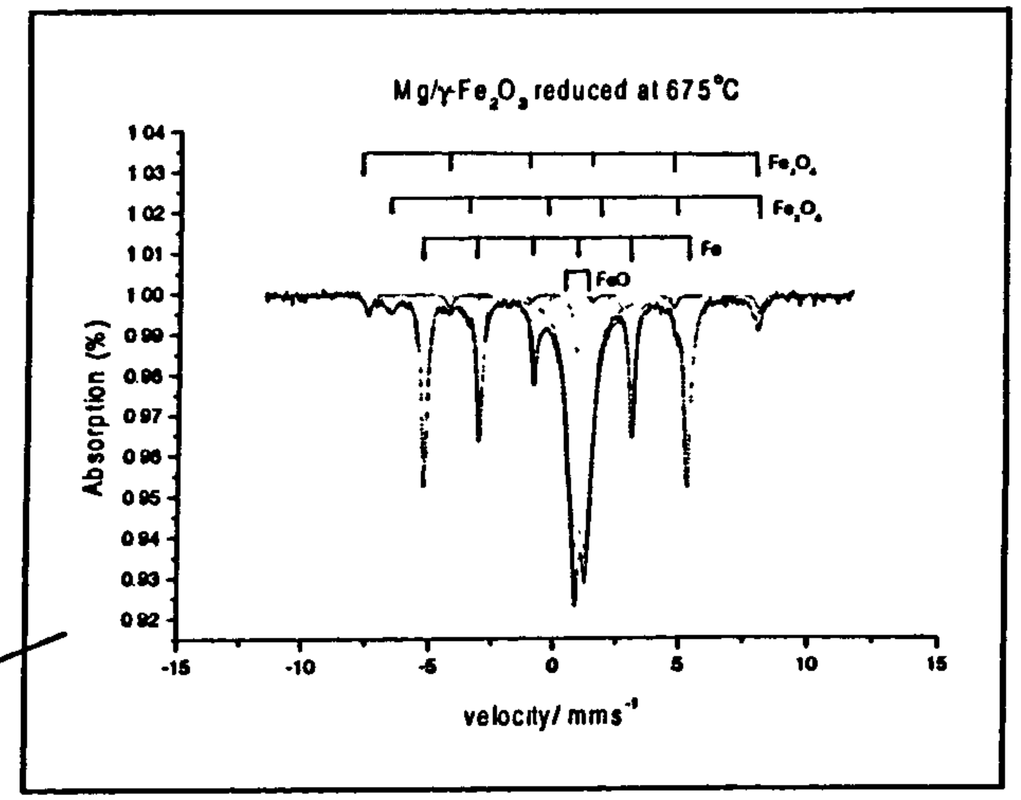

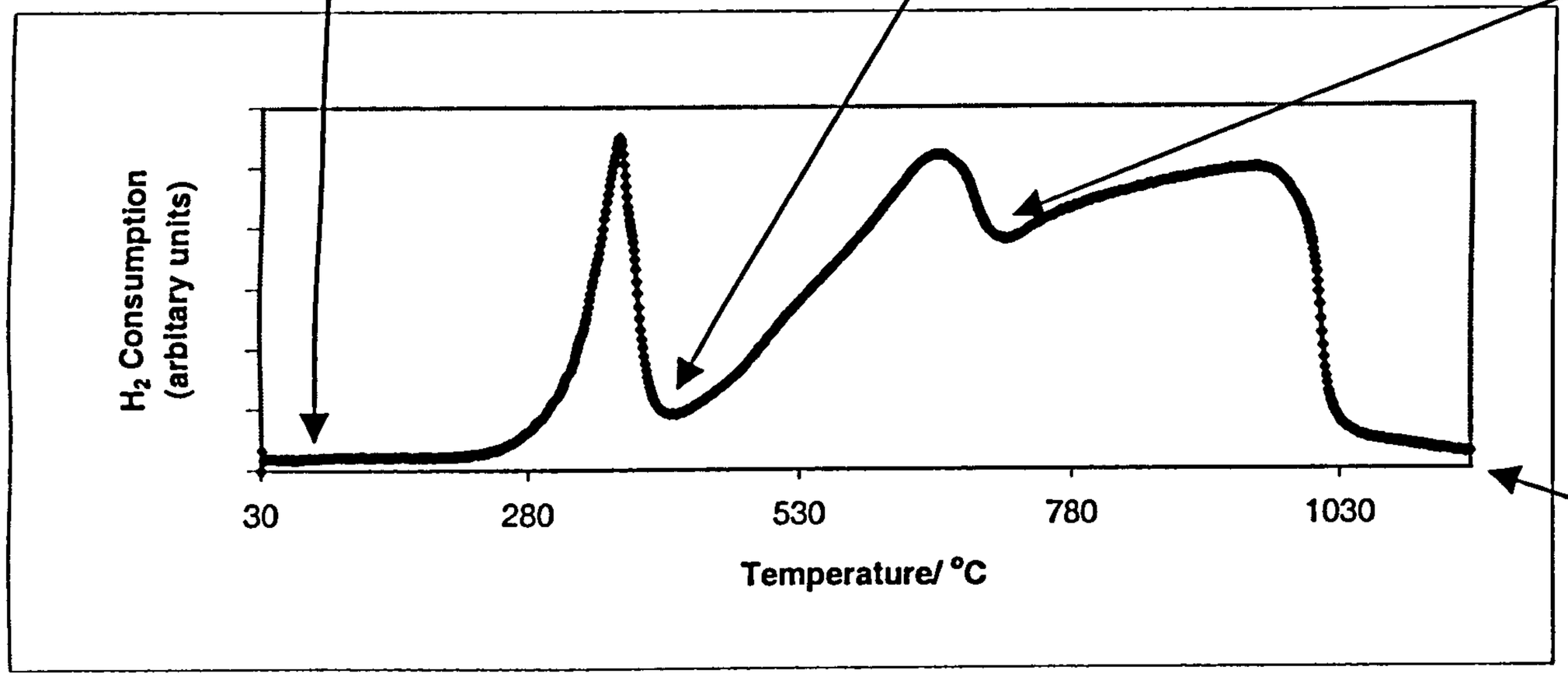

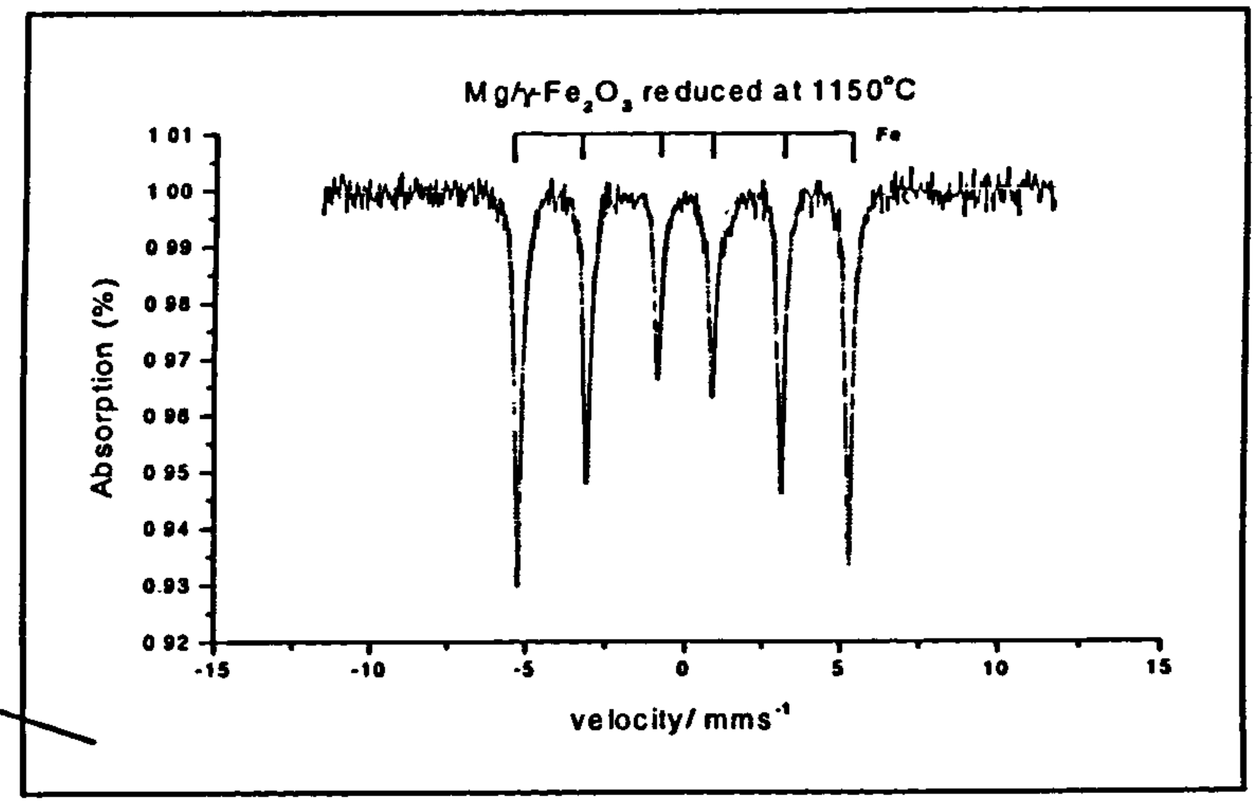

Figure 4.54 TPR profile recorded from Mg/γ-Fe_2O_3 and ^{57}Fe Mössbauer spectra recorded following each reduction peak

following each reduction peak showed a similar reduction pathway to those recorded from undoped γ–Fe_2O_3, tin- and ruthenium- doped γ–Fe_2O_3 prepared by similar methods, including, the formation of wüstite.

Table 4.21 ^{57}Fe Mössbauer parameters recorded from Mg/γ-Fe_2O_3 following reduction in TPR experiment

Sample	δ (± 0.02) mms^{-1}	Δ (± 0.02) mms^{-1}	H (± 1) T	Interpretation	Area (± 5) %
Mg/γ-Fe_2O_3	0.34	0.01	46	γ-Fe_2O_3	100
Mg/γ-Fe_2O_3 reduced at 365 °C	0.67	0.0	45	Fe_3O_4	100
	0.32	0.0	48	Fe_3O_4	
Mg/γ-Fe_2O_3 reduced at 675 °C	0.68	0.0	45	Fe_3O_4	11
	0.29	0.0	48	Fe_3O_4	
	1.02	0.51	---	FeO	48
	0.02	0.0	33	Fe	41
Mg/γ-Fe_2O_3 reduced at 1150 °C	0.02	0.01	33	Fe	100

Reduction-reoxidation properties

Mg/γ–Fe_2O_3 was subjected to reduction at 365 °C in the 10 % hydrogen- 90 % nitrogen mixture (R1) and reoxidation by heating at 400 °C for 1 h in air (O1). The cycle of reduction and reoxidation was repeated twice (samples R2, O2, R3 and O3). X-ray powder diffraction (Figure 4.55) and ^{57}Fe Mössbauer spectroscopy (Figure 4.56, Table 4.22) were used to identify the materials after each reduction-oxidation cycle.

Figure 4.55 XRD patterns recorded *ex situ* from Mg/γ-Fe_2O_3 following reduction and reoxidation cycles

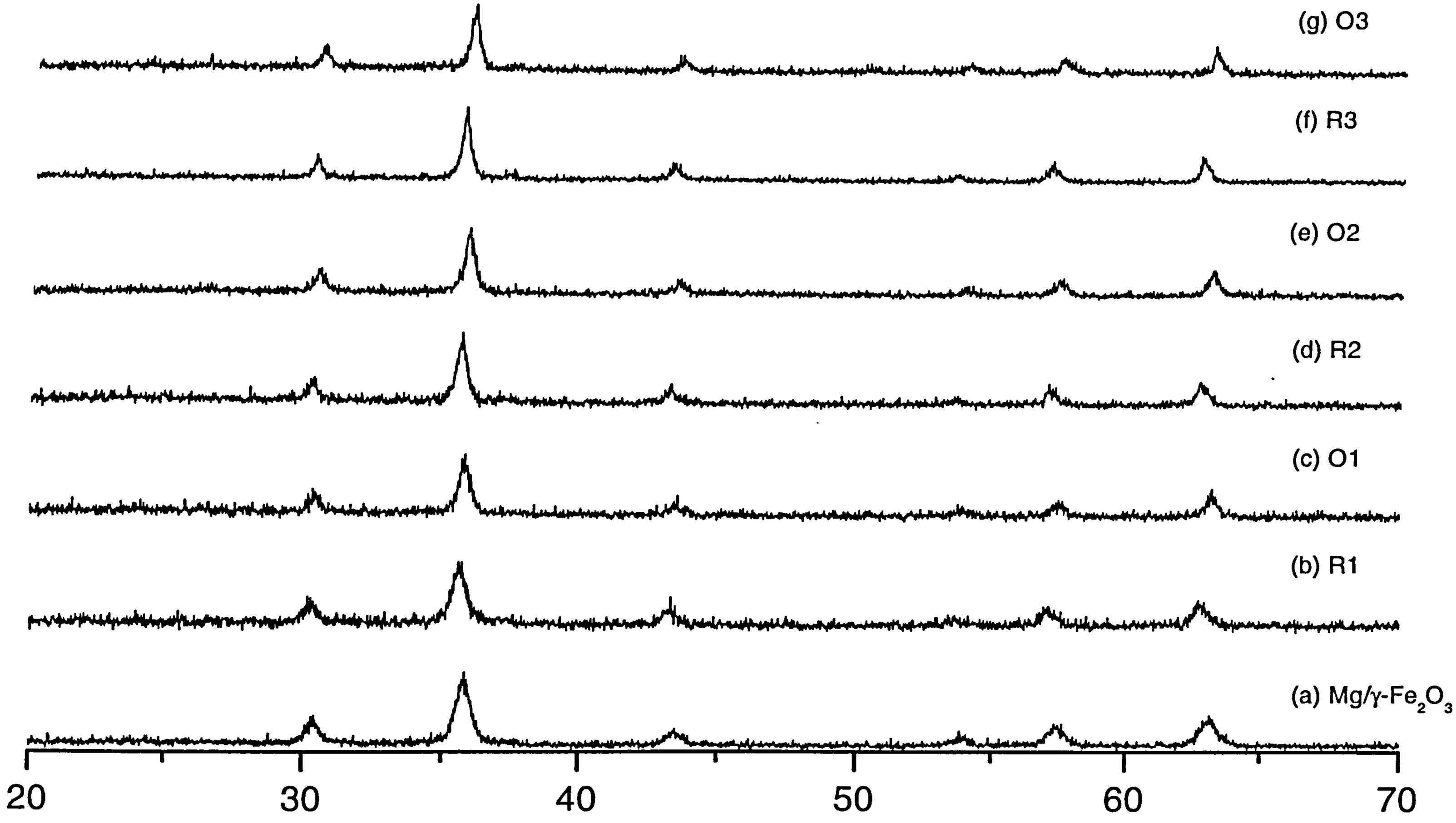

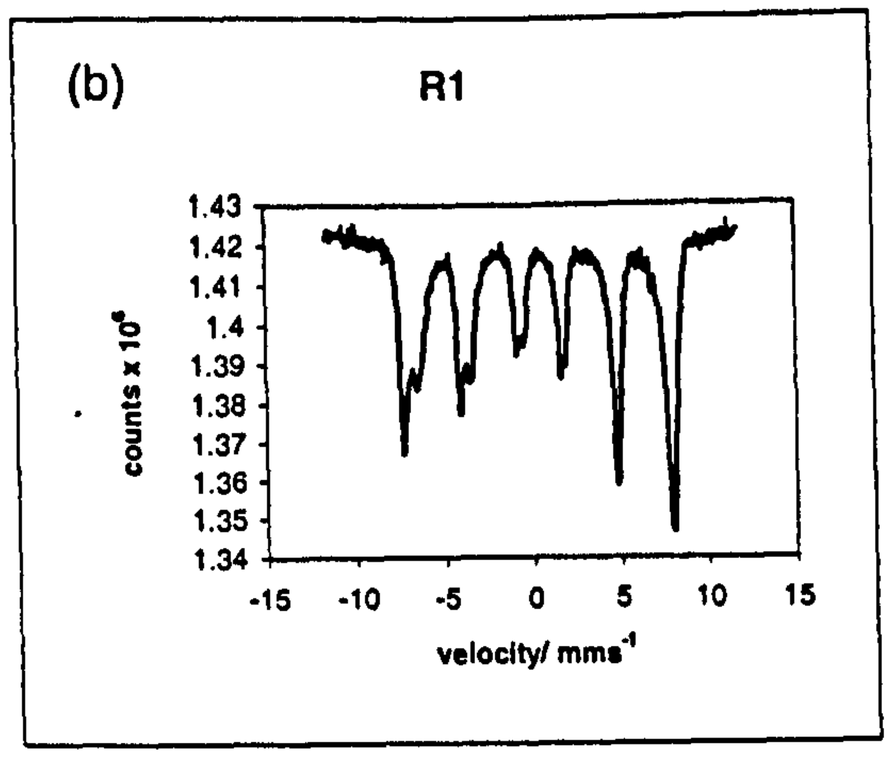

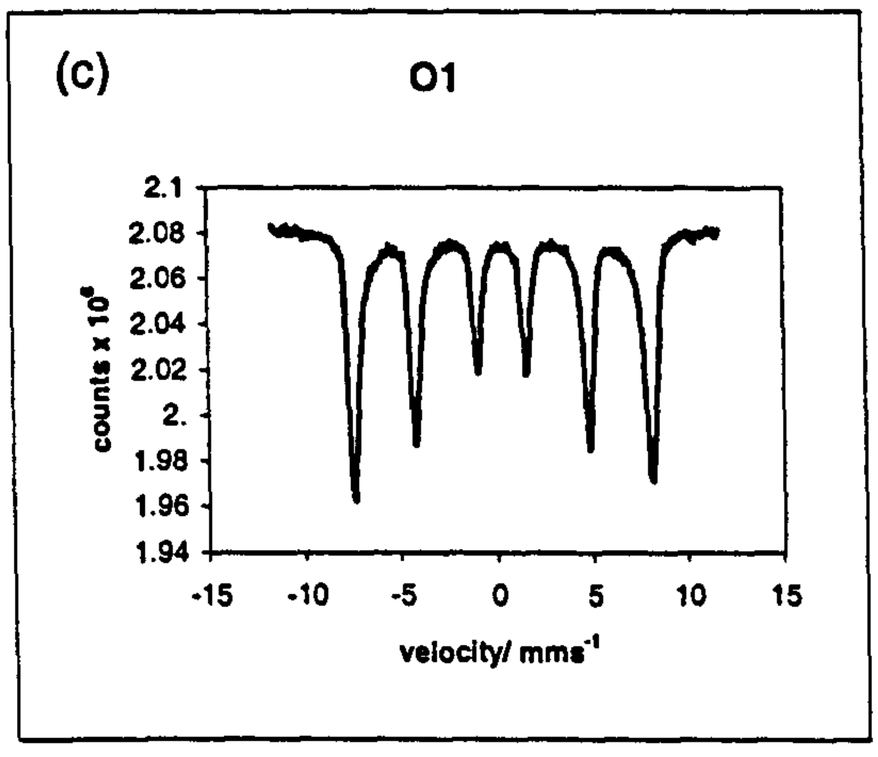

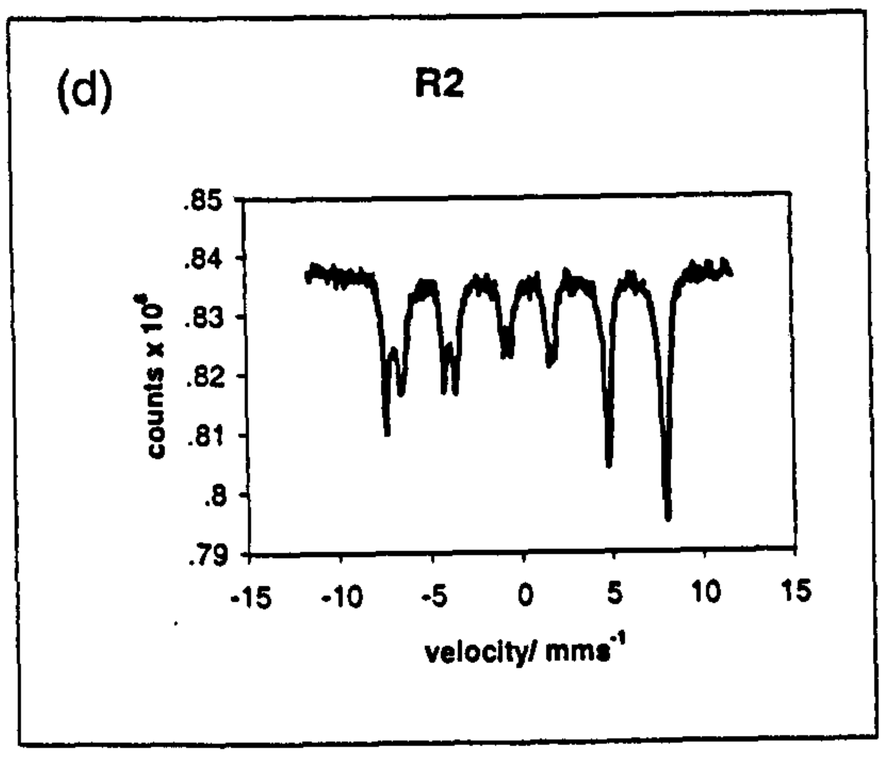

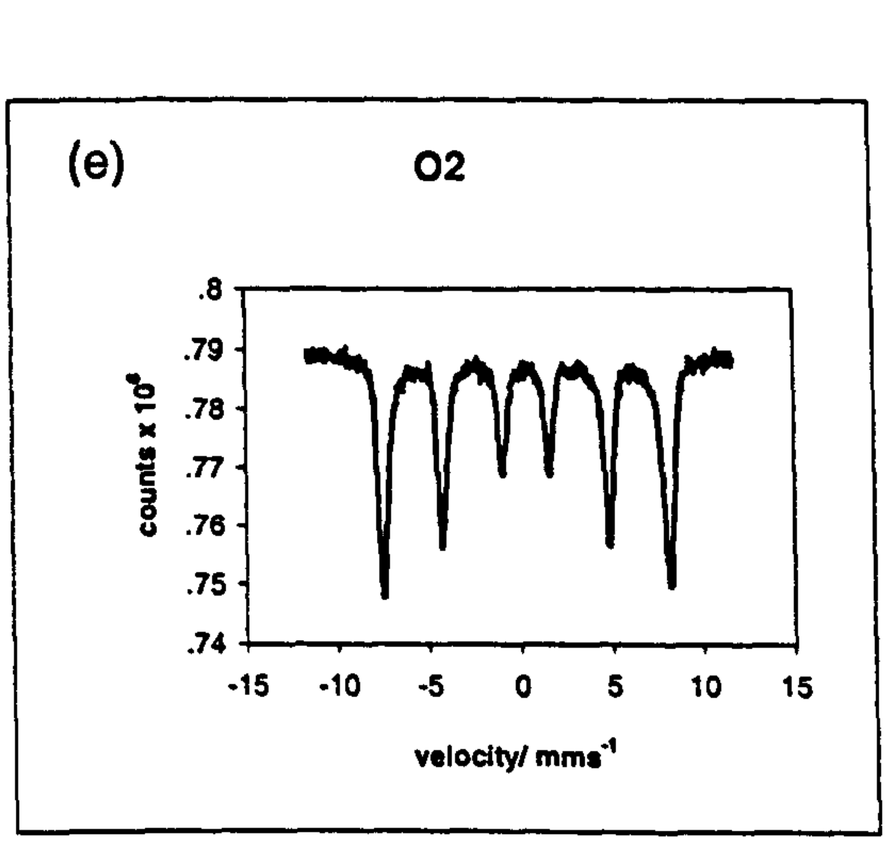

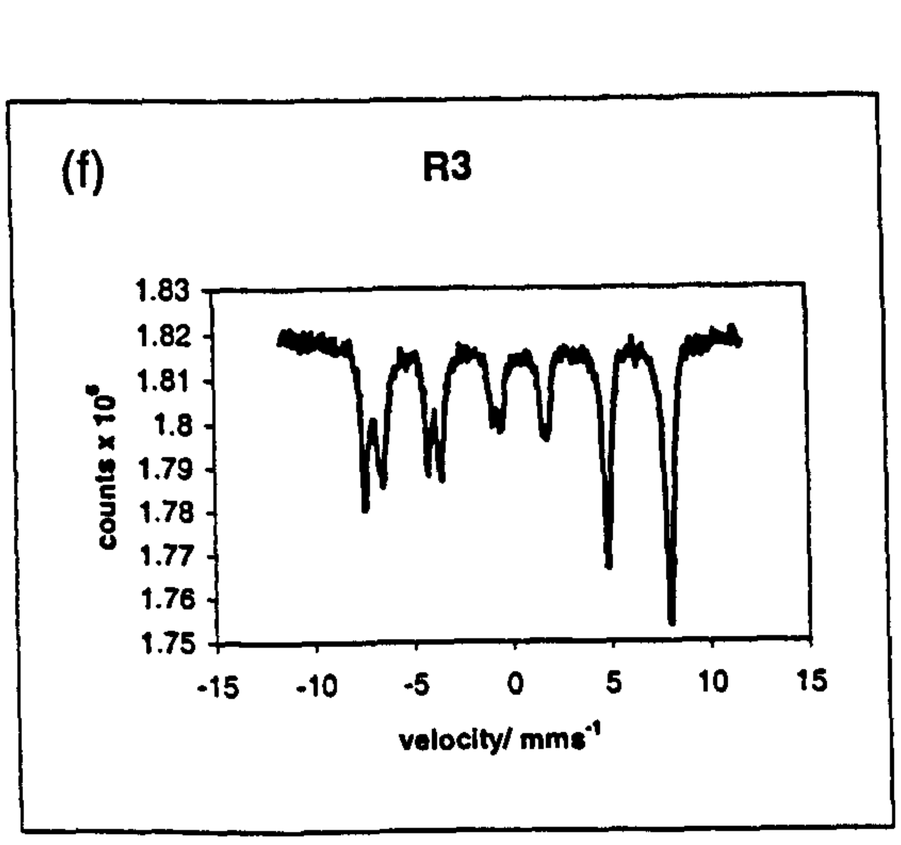

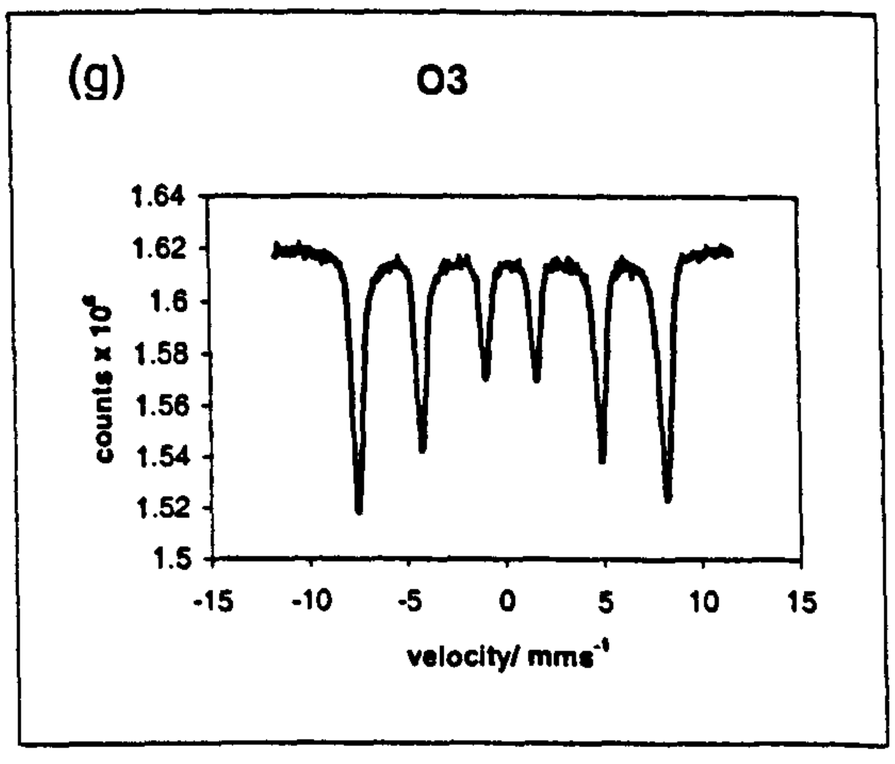

Figure 4.56 ^{57}Fe Mössbauer spectra recorded from Mg/γ-Fe_2O_3 following reduction and reoxidation cycles

Table 4.22 ^{57}Fe Mössbauer parameters recorded from Mg/γ-Fe_2O_3 following treatment in reducing and oxidising environments

Sample	δ (± 0.02) mms^{-1}	Δ (± 0.02) mms^{-1}	H (± 1) T	Interpretation
Mg/γ-Fe_2O_3	0.34	0.01	46	γ-Fe_2O_3
R1	0.59	-0.01	45	Fe_3O_4
	0.31	0.01	48	Fe_3O_4
O1	0.33	0.02	48	γ-Fe_2O_3
R2	0.64	0.02	45	Fe_3O_4
	0.27	0.03	48	Fe_3O_4
O2	0.33	0.01	49	γ-Fe_2O_3
R3	0.65	0.03	45	Fe_3O_4
	0.27	0.02	48	Fe_3O_4
O3	0.33	0.01	49	γ-Fe_2O_3

The results show that Mg/γ–Fe_2O_3 can be reduced to Mg/Fe_3O_4 and reoxidised to Mg/γ–Fe_2O_3 and the reduction and reoxidation cycle repeated.

The particle size of magnesium- doped Fe_3O_4 (R1) (*ca.* 17 nm) formed by initial reduction of magnesium- doped γ–Fe_2O_3 at 365 °C in the 10 % hydrogen- 90 % nitrogen gas mixture was larger than that of magnesium- doped γ–Fe_2O_3 (*ca.* 13 nm). The surface area of the magnesium- doped Fe_3O_4 (R1) (*ca.* 51 m^2g^{-1}) was lower than that of magnesium- doped γ–Fe_2O_3 (*ca.* 106 m^2g^{-1}). Reoxidation by heating at 400 °C for 1 h in air followed by two further cycles of reduction and reoxidation produced variations in particle size and surface area but with the finally regenerated magnesium- doped γ–Fe_2O_3 (O3) having a size of 26 nm and surface area of 29 m^2g^{-1}. The results show that Mg/γ–Fe_2O_3 has smaller particle size and larger

surface area produced over a three fold reduction- reoxidation cycle than that of undoped γ–Fe_2O_3. Most significant is the observation that the initial reduction step results in a nearly 50 % loss of surface area and another *ca.* 50 % loss during the subsequent reduction-reoxidation cycles.

In situ ^{57}Fe Mössbauer spectroscopy studies

The ^{57}Fe Mössbauer spectra recorded *in situ* from magnesium- doped Fe_3O_4 formed by reduction of magnesium- doped γ–Fe_2O_3 and subsequently heated in an oxygen partial pressure of *ca.* 0.2 Pa are shown in Figure 4.57. Heating at 300 °C caused a decrease in the magnitude of the magnetic hyperfine field. After heat treatment at 300 °C (Figure 4.57(b)) the broadened spectrum was best fitted to distribution of magnetic fields characteristic of γ–Fe_2O_3. The sextet characteristic of α-Fe_2O_3 was clearly seen in the spectrum recorded from the material heated at 527 °C (Figure 4.57(c)) with a paramagnetic doublet accounting for *ca.* 28 % of the spectral area. This is similar to those recorded from undoped γ–Fe_2O_3 and ruthenium- doped γ–Fe_2O_3 prepared by a similar method. The ^{57}Fe Mössbauer spectrum recorded at room temperature (Figure 4.57(d)) confirmed the formation of α-Fe_2O_3 (H = 51(1) T). The results contrast strikingly with those recorded from titanium- and tin-doped γ–Fe_2O_3 prepared by similar methods in which the spinel-related structure was stabilised with respect to conversion to the corundum-related phase by the presence of titanium or tin.

Figure 4.57 ***In situ*** **Mössbauer spectra recorded from Mg/Fe_3O_4 reduced from Mg/γ-Fe_2O_3**

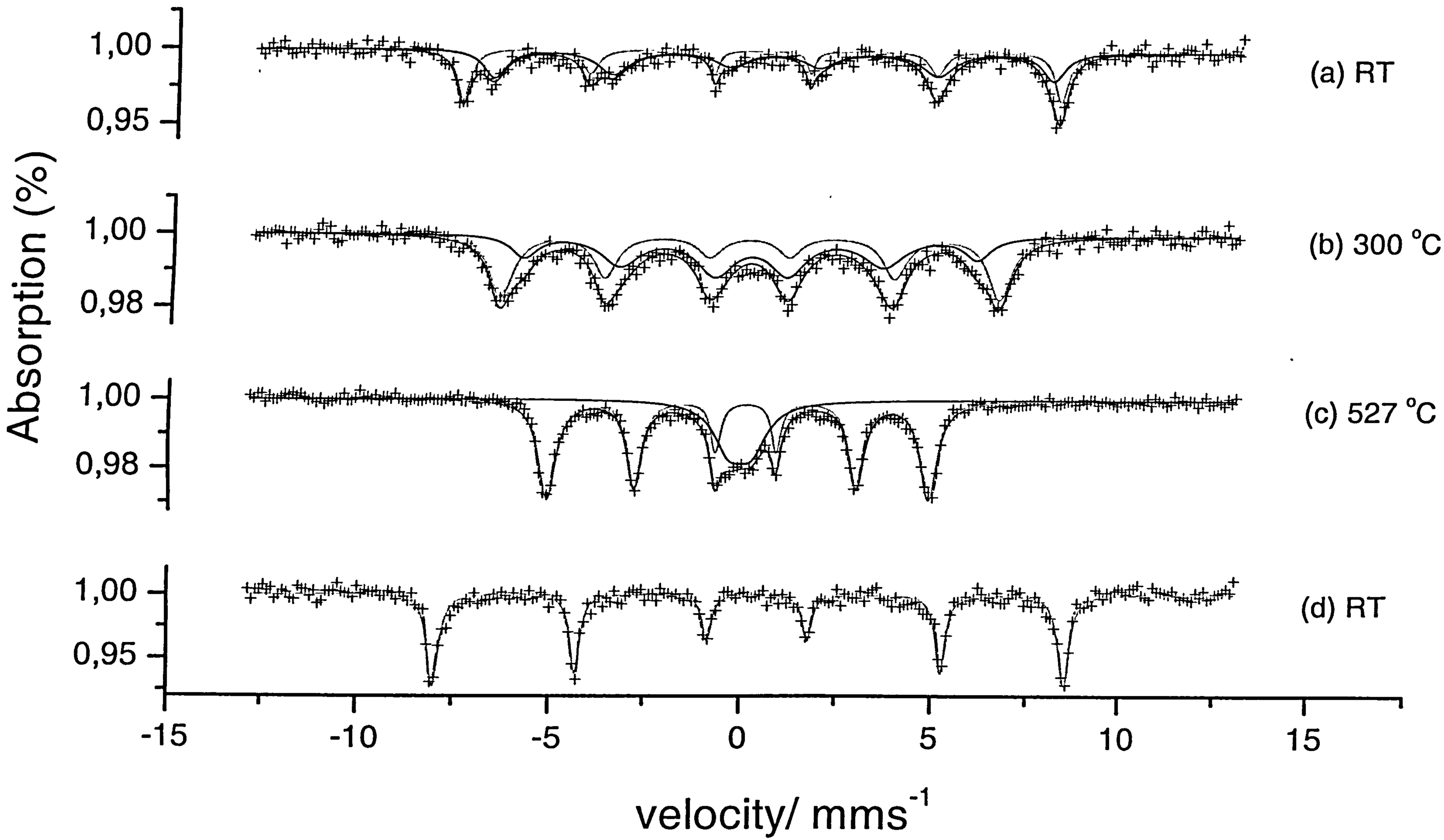

Ex situ studies on the conversion of γ–Fe_2O_3 to α-Fe_2O_3

The X-ray powder diffraction patterns recorded from magnesium- doped γ–Fe_2O_3 confirmed the *in situ* high temperature Mössbauer results showing the conversion of magnesium- doped γ–Fe_2O_3 to the magnesium- doped α-Fe_2O_3 between 450 and 500 °C (Figure 4.58). The results indicate that, like ruthenium, magnesium does not stabilise the γ–Fe_2O_3 structure in the way observed for titanium and tin.

Conclusion

Mg/γ–Fe_2O_3 prepared by addition of base to salt, boiling under reflux and calcination at 250 °C/12 h showed a higher surface area than undoped γ–Fe_2O_3 and Sn/γ–Fe_2O_3 but lower than titanium- or ruthenium- doped γ–Fe_2O_3 prepared by similar methods. Reduction and reoxidation cycling induced changes in the particle size and surface area which has smaller particle size and larger surface area than that of undoped γ–Fe_2O_3. The conversion of γ–Fe_2O_3 to α-Fe_2O_3 occurred over a narrower temperature range as compared to that observed for titanium- and tin- doped γ–Fe_2O_3 prepared by a similar method. The thermal stability of Mg/γ–Fe_2O_3 was more similar to that of undoped γ–Fe_2O_3 and Ru/γ–Fe_2O_3 prepared by a similar method.

Figure 4.58 XRD patterns recorded *ex situ* from Mg/γ-Fe_2O_3 prepared by addition of base to salt, boiling under reflux, and heating at 250 °C and then heated from 350 to 650 °C

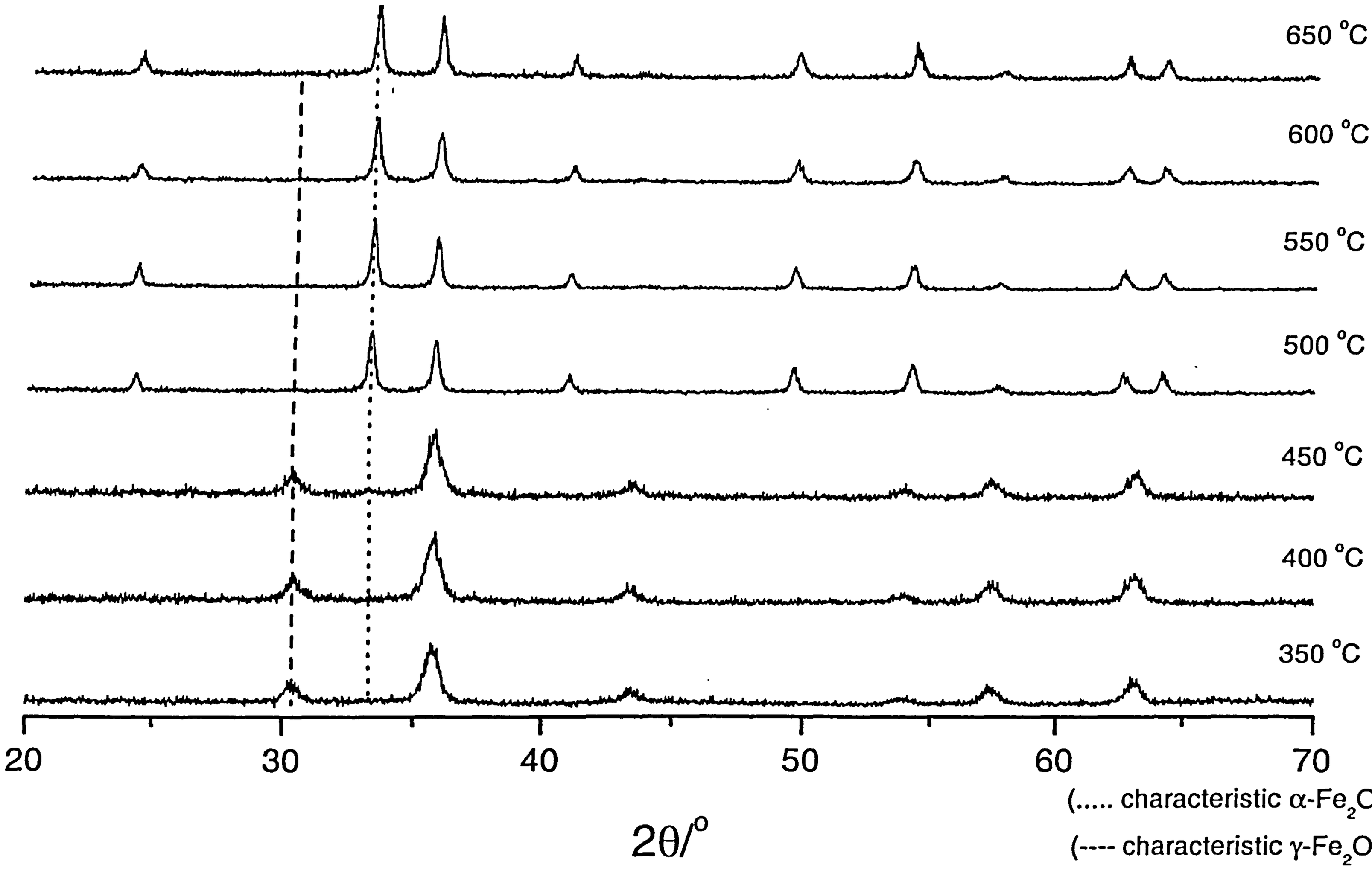

4.3 γ–Fe_2O_3 Doped With Two Metals

γ–Fe_2O_3 was doped with two metals of nominal loading of 4 mass % each, to give materials with the following composition: Sn/Mg/γ–Fe_2O_3, Ti/Mg/γ–Fe_2O_3, and Sn/Ti/γ–Fe_2O_3. All the samples were prepared by addition of base to salt, boiling under reflux, and calcination at 250 °C/12 h.

4.3.1 Sn/Mg/γ-Fe_2O_3 (addition of base to salt, boiling under reflux, and calcination at 250 °C/12 h)

The XRD pattern recorded (Figure 4.59) from the attempted preparation of γ–Fe_2O_3 doped with tin and magnesium corresponded to a spinel- related structure[5] with lattice parameter a = 8.375(2) Å compared to a = 8.334 Å for γ–Fe_2O_3[8] and a = 8.354(2) Å for γ–Fe_2O_3 prepared here by addition of base to salt, boiling under reflux, and calcination at 250 °C. The ^{57}Fe Mössbauer spectrum showed a sextet pattern (δ 0.34(2) mms^{-1}, Δ 0.01(2) mms^{-1}, H 48(1) T) confirming the material to be γ-Fe_2O_3[1,2] (Figure 4.60, Table 4.23). ICP analysis showed a tin content of 5.79 mass % and a magnesium content of 0.81 mass %.

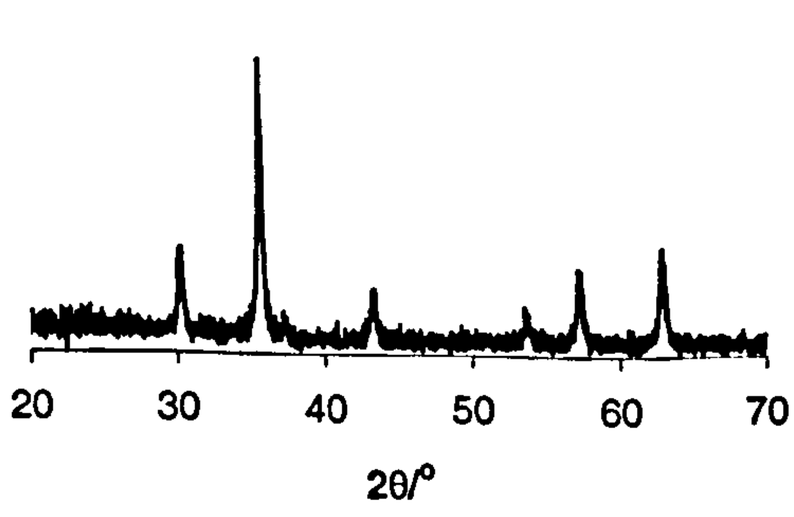

Figure 4.59 XRD pattern recorded from Sn/Mg/γ–Fe_2O_3 prepared by addition of base to salt, boiling under reflux, and calcination at 250 °C

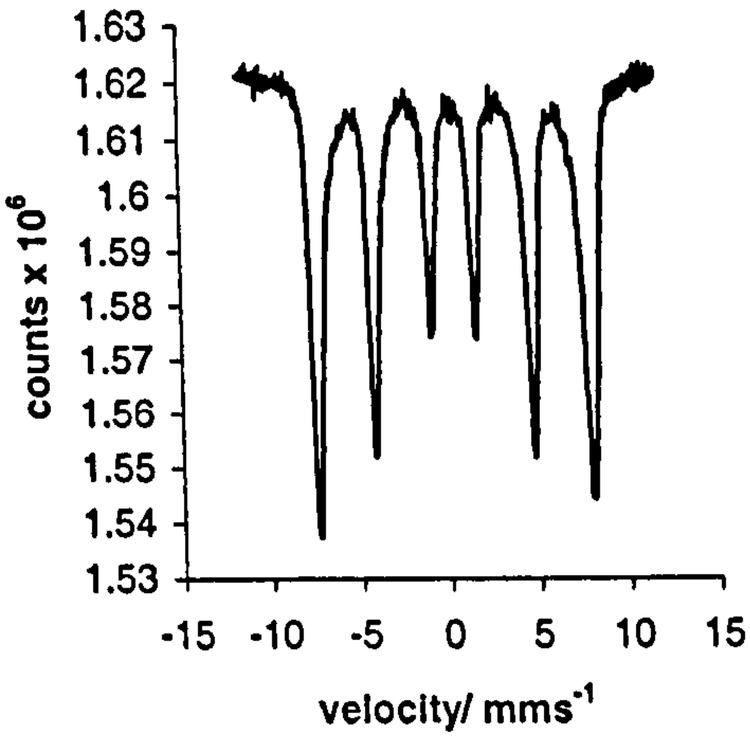

Figure 4.60 ^{57}Fe Mössbauer spectrum recorded from Sn/Mg/γ–Fe_2O_3 prepared by addition of base to salt, boiling under reflux, and calcination at 250 °C

Table 4.23 ^{57}Fe Mössbauer parameters recorded from γ–Fe_2O_3 doped with two metals

Sample	δ (± 0.02) mms^{-1}	Δ (± 0.02) mms^{-1}	H (± 1) T	Interpretation	Area (± 5) %
Sn/Mg/γ-Fe_2O_3	0.34	0.01	48	γ-Fe_2O_3	100
Ti/Mg/γ-Fe_2O_3	0.34	0.01	43	γ-Fe_2O_3	100
Sn/Ti/γ-Fe_2O_3	0.44	0.00	---	Small particle iron oxide	43
	0.34	0.02	48	γ-Fe_2O_3	53
	0.47	-0.10	49	α-Fe_2O_3	<5

The particle size and surface area data are collected in Table 4.24. The surface area calculated from Sn/Mg/γ–Fe_2O_3 was 54 m^2g^{-1}, which is lower than undoped γ-Fe_2O_3 (69 m^2g^{-1}) and Mg/γ-Fe_2O_3 (106 m^2g^{-1}) but similar to Sn/γ-Fe_2O_3 (59 m^2g^{-1}) which were all prepared by a similar method. The particle size obtained from the X-ray powder diffraction linewidth data was calculated as *ca.* 22 nm and electron microscopy showed the particle size to be *ca.* 25nm.

Table 4.24 Particle size and surface area data recorded from γ–Fe_2O_3 doped with two metals

Sample	Average particle size Scherrer method / nm (± 10 %)	Average particle size TEM / nm (± 10 %)	Surface Area / m^2g^{-1} (± 10 %)
Sn/Mg/γ-Fe_2O_3	22	25	54
Ti/Mg/γ-Fe_2O_3	10	8	126
Sn/Ti/γ-Fe_2O_3	27	20	85

The TPR profile (Figure 4.61, Table 4.25) gave three peak maxima similar to undoped γ-Fe_2O_3 prepared by addition of base to salt, boiling under reflux, and calcination at 250 °C (Figure 4.7). The intensity of the initial peak was intermediate between the intensities of the initial peaks for Sn/γ-Fe_2O_3 and Mg/γ-Fe_2O_3, Figures 4.34 and 4.53 respectively.

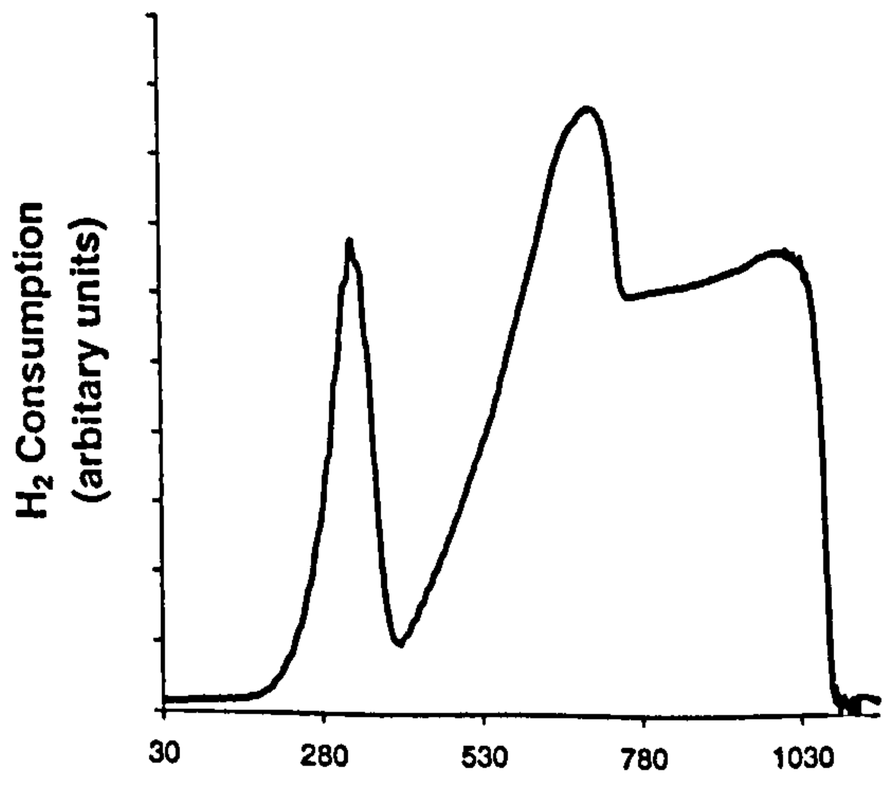

Figure 4.61 TPR profile recorded from Sn/Mg/γ–Fe_2O_3 prepared by addition of base to salt, boiling under reflux, and calcination at 250 °C

Table 4.25 TPR reduction peak data recorded from γ–Fe_2O_3 doped with two metals

Sample	Reduction Peaks (°C) (± 50 °C)			
	Peak 1	Peak 2	Peak 3	Additional peaks
Sn/Mg/γ-Fe_2O_3	335	720	1020	
Ti/Mg/γ-Fe_2O_3	320	800	1000	*600, 1130 (shoulders)*
Sn/Ti/γ-Fe_2O_3	310	760	1000	420, *560, 700 (shoulders)*

In situ ^{57}Fe Mössbauer spectroscopy studies

The ^{57}Fe Mössbauer spectra recorded *in situ* from tin- magnesium- doped γ–Fe_2O_3 and subsequently heated in an oxygen partial pressure of *ca.* 0.2 Pa are shown in Figure 4.62. The material heated from 200 to 300 °C and cooled to room temperature gave spectra (Figure 4.62(b - d)) which were similar to the starting material. The material was further heated to 400 °C and the spectrum (Figure 4.62(e)) showed a paramagnetic doublet accounting for *ca.* 24 % of the spectral area. The material was then cooled to room temperature and the spectrum (Figure 4.62(f)) found to be similar to that of the starting material. The spectrum recorded from the material further heated to 450 °C (Figure 4.62(g)) showed the paramagnetic doublet to have increased to *ca.* 44 % of the spectral area. Cooling the material to room temperature gave a spectrum (Figure 4.62(h)) similar to that of the starting material. The spectrum recorded from the material heated from 500 to 550 °C (Figure 4.62(i - j)) showed the major component to be a paramagnetic doublet. The results confirm that the spinel- related structure of Sn/Mg/γ–Fe_2O_3 is not converted to the α-Fe_2O_3 structure at temperatures below *ca.* 600 °C. The material was heated to 600 °C (Figure 4.62(k)) and the spectrum showed a sextet characteristic of α-Fe_2O_3 which

Figure 4.62 ***In situ*** **Mössbauer spectra recorded from Sn/Mg/γ-Fe_2O_3**

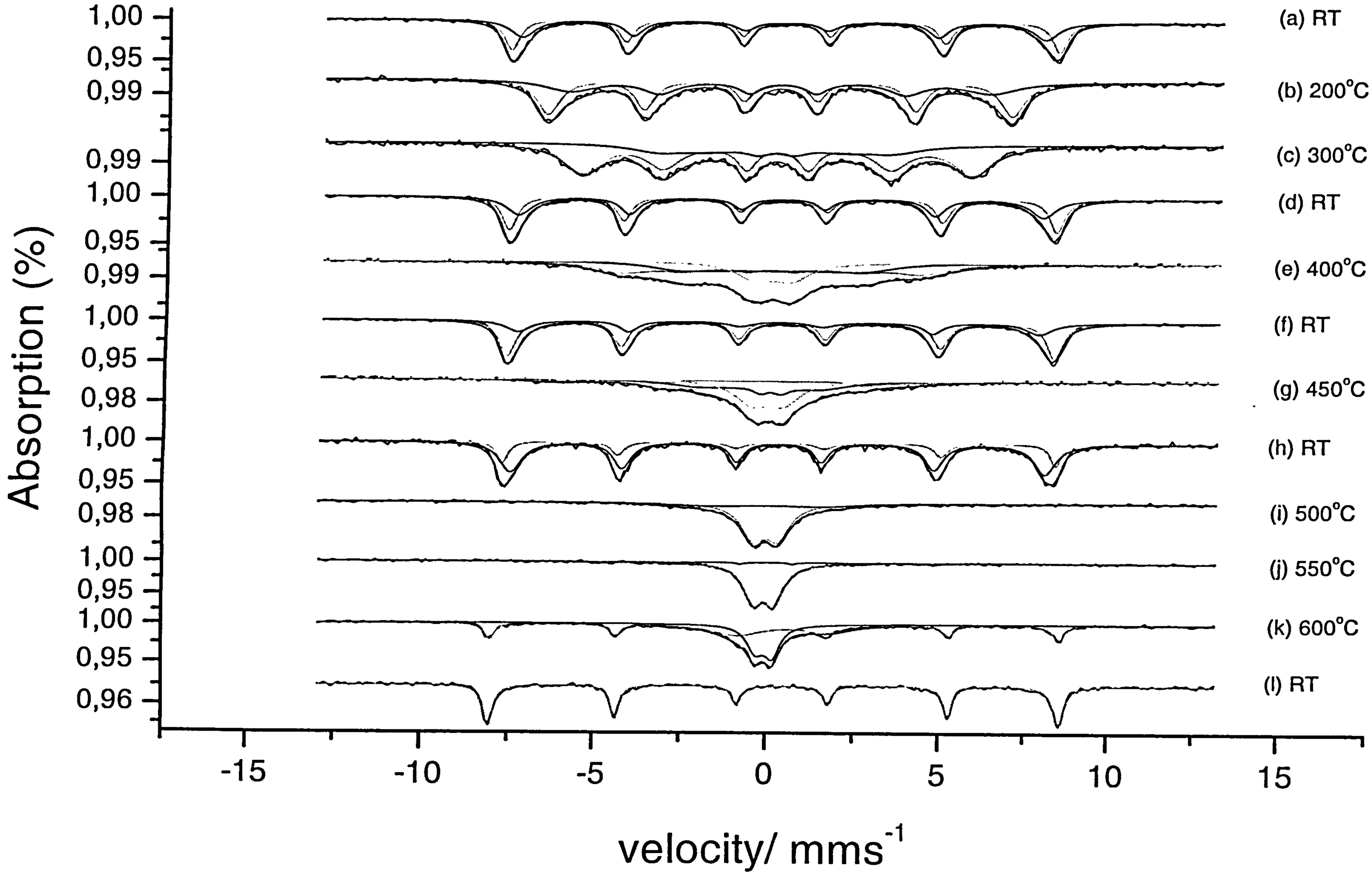

was confirmed at room temperature (Figure 4.62(l)) (H = 52(1) T). Hence Sn/Mg/γ–Fe_2O_3 showed the formation of α-Fe_2O_3 at *ca.* 600 °C, the result is similar to that recorded from Sn/γ–Fe_2O_3, which reflects the higher loading of tin.

Ex situ studies on the conversion of γ–Fe_2O_3 to α-Fe_2O_3

The Sn/Mg/γ–Fe_2O_3 was heated from 300 °C to 700 °C, at 50 °C intervals and XRD patterns recorded *ex situ* (Figure 4.63). Table 4.26 shows the temperature of α-Fe_2O_3 appearance and γ–Fe_2O_3 disappearance. The results show the conversion of Sn/Mg/γ–Fe_2O_3 to a corundum- related structure at *ca.* 650 °C and supports the view that both tin and magnesium combined stabilise the γ–Fe_2O_3 and Mg/γ–Fe_2O_3 (Figures 4.12 and 4.58) structures to conversion to α-Fe_2O_3. Sn/Mg/γ–Fe_2O_3 shows a similar thermal stability as Sn/γ–Fe_2O_3 (Figure 4.42). No evidence was found for the segregation of SnO_2 or MgO.

Table 4.26 Temperature of conversion of and γ–Fe_2O_3 to α-Fe_2O_3

Sample	Temperature/ °C (± 25°C)	
	α-Fe_2O_3 appearance	γ–Fe_2O_3 disappearance
Sn/Mg/γ-Fe_2O_3	650	700
Ti/Mg/γ-Fe_2O_3	550	600
Sn/Ti/γ-Fe_2O_3	300	650

Figure 4.63 XRD patterns recorded *ex situ* from Sn/Mg/γ-Fe_2O_3 prepared by addition of base to salt, boiling under reflux, and heating at 250 °C and then heated from 300 to 700 °C

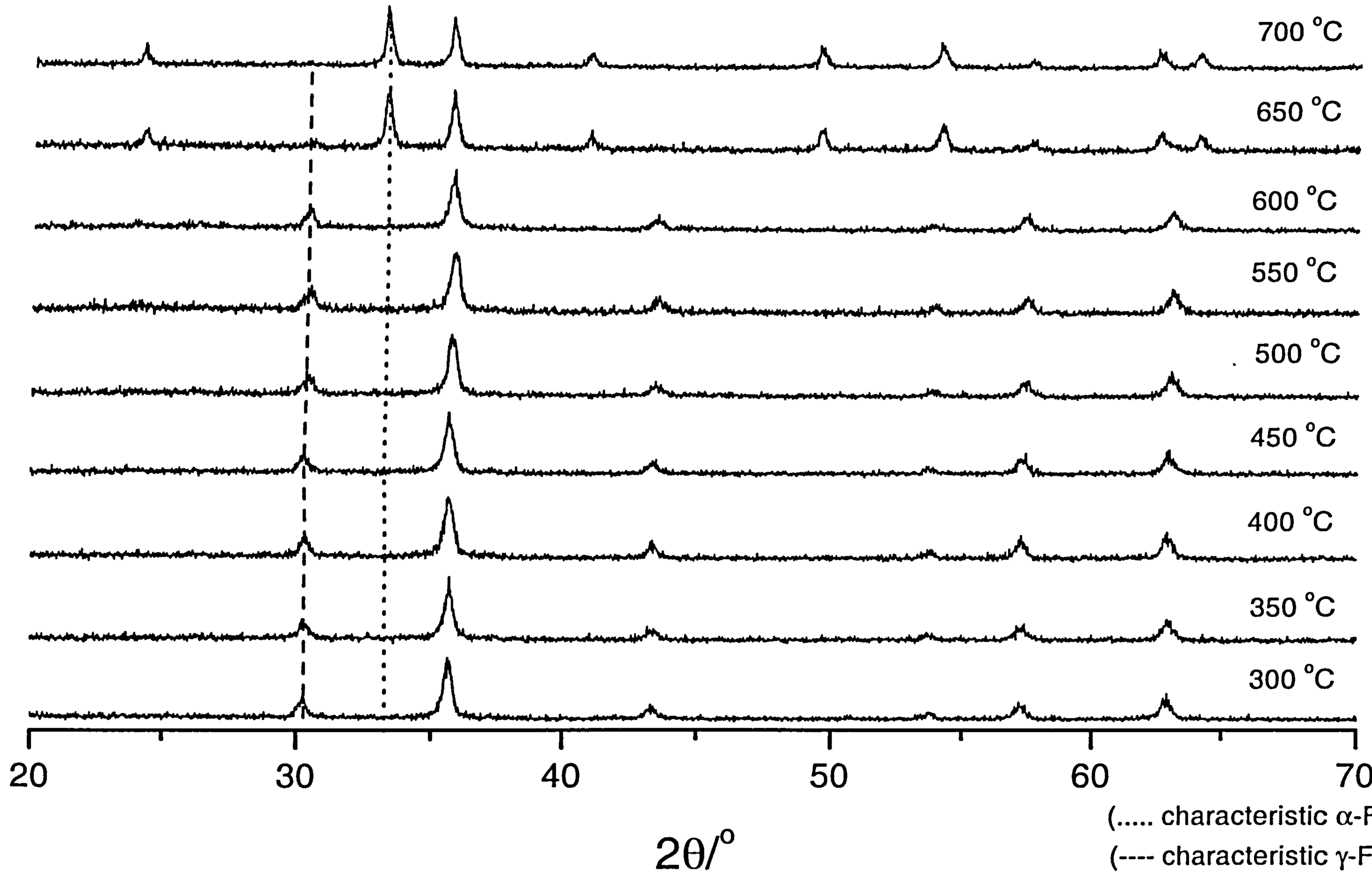

Conclusion

It is possible to synthesise Sn-Mg- doped γ–Fe_2O_3, with properties more similar to those of Sn/γ–Fe_2O_3 than to Mg/γ–Fe_2O_3. The surface area was similar to Sn/γ–Fe_2O_3 but lower than that of Mg/γ–Fe_2O_3. The stabilisation of Sn/Mg/γ–Fe_2O_3 with respect to the thermal conversion to an α-Fe_2O_3 structure was more similar to that of Sn/γ–Fe_2O_3, which may reflect the higher loading of tin.

4.3.2 Ti/Mg/γ-Fe_2O_3 (addition of base to salt, boiling under reflux, and calcination at 250 °C/12 h)

The XRD pattern showed broad peaks suggesting small particle size (Figure 4.64), and corresponded to a spinel- related structure[5] with lattice parameter a = 8.375(2) Å compared to a = 8.334 Å for γ–Fe_2O_3[8] and a = 8.354(2) Å for γ–Fe_2O_3 prepared here by addition of base to salt, boiling under reflux, and calcination at 250 °C. The EDX analysis showed 3.1 mass % of Ti and 1.7 mass % of Mg. The ^{57}Fe Mössbauer spectrum showed a broad sextet pattern (δ 0.34(2) mms^{-1}, Δ 0.01(2) mms^{-1}, H 43(1) T) confirming the material to be γ-Fe_2O_3 (Figure 4.65, Table 4.23). The hyperfine field is lower than the literature[1,2] value due to the presence of small particles.

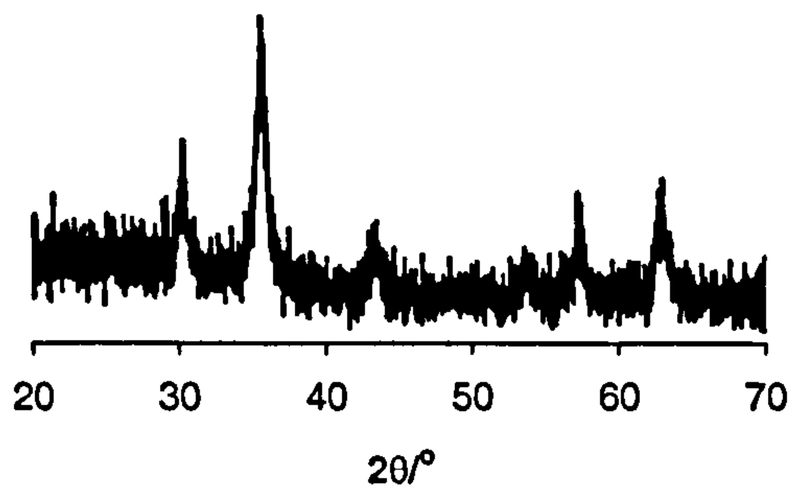

Figure 4.64 XRD pattern recorded from Ti/Mg/γ–Fe_2O_3 prepared by addition of base to salt, boiling under reflux, and calcination at 250 °C

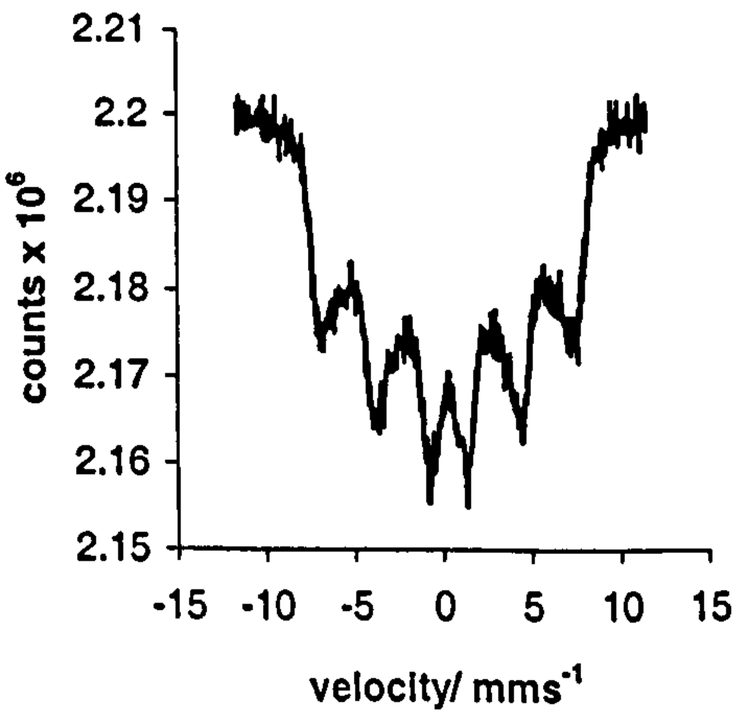

Figure 4.65 ^{57}Fe Mössbauer spectrum recorded from Ti/Mg/γ–Fe_2O_3 prepared by addition of base to salt, boiling under reflux, and calcination at 250 °C

The surface area of Ti/Mg/γ–Fe_2O_3 of 126 m^2g^{-1} (Table 4.24) was higher than undoped γ-Fe_2O_3 (69 m^2g^{-1}) and Mg/γ-Fe_2O_3 (106 m^2g^{-1}) but similar to Ti/γ-Fe_2O_3 (139 m^2g^{-1}), all prepared by addition of base to salt, boiling under reflux, and calcination at 250 °C.

The TPR profile (Figure 4.66, Table 4.25) gave three peak maxima with the latter two peaks merged, albeit to a lesser extent as compared to Ti/γ-Fe_2O_3 prepared by addition of base to salt, boiling under reflux, and calcination at 250 °C (Figure 4.21).

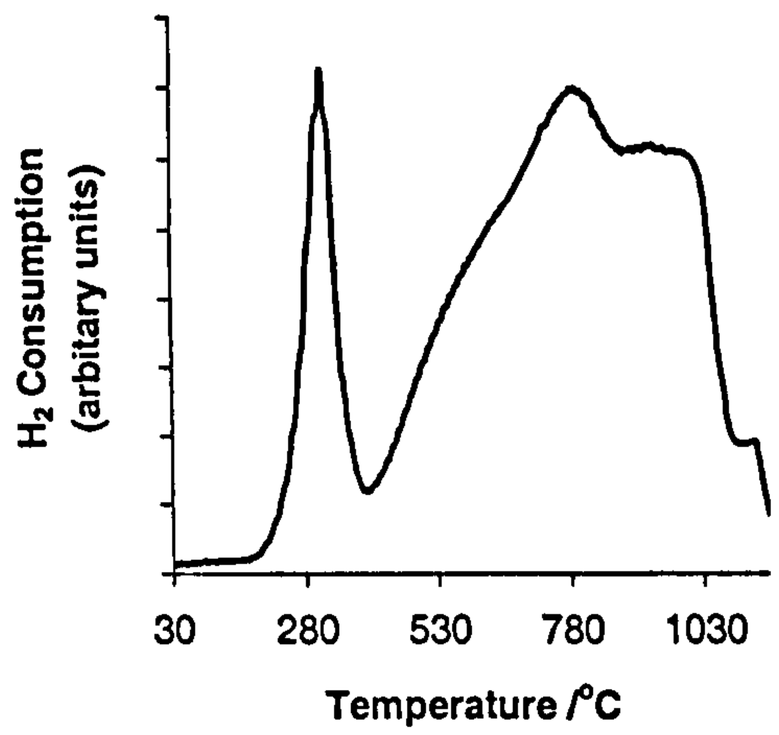

Figure 4.66 TPR profile recorded from Ti/Mg/γ–Fe_2O_3 prepared by addition of base to salt, boiling under reflux, and calcination at 250 °C

In situ ^{57}Fe Mössbauer spectroscopy studies

The ^{57}Fe Mössbauer spectra recorded *in situ* from titanium- magnesium- doped γ–Fe_2O_3 and subsequently heated in an oxygen partial pressure of *ca.* 0.2 Pa are shown in Figure 4.67. The material was heated to 300 °C and a spectrum recorded (Figure 4.67(b)) which showed a paramagnetic doublet accounting for *ca.* 52 % of the spectral area. A room temperature spectrum was then recorded (Figure 4.67(c)) which was similar to the Mössbauer spectrum recorded from the starting material. The spectrum recorded from the material heated to 400 °C (Figure 4.67(d)) showed a paramagnetic doublet accounting for *ca.* 37 % of the spectral area. The spectrum recorded from the subsequent cooling to room temperature (Figure 4.67(e)) showed little change from that of the starting material. Similar results were recorded from the solid heated to 450 °C and cooled to room temperature (Figure 4.67(f and g)). The results showed no evidence for the spinel to corundum transition. The material was further heated to 500 °C and the spectrum (Figure 4.67(h)) showed *ca.* 42 % of the spectral area was constituted by a paramagnetic doublet together with a sextet

Figure 4.67 *In situ* Mössbauer spectra recorded from Ti/Mg/γ-Fe_2O_3

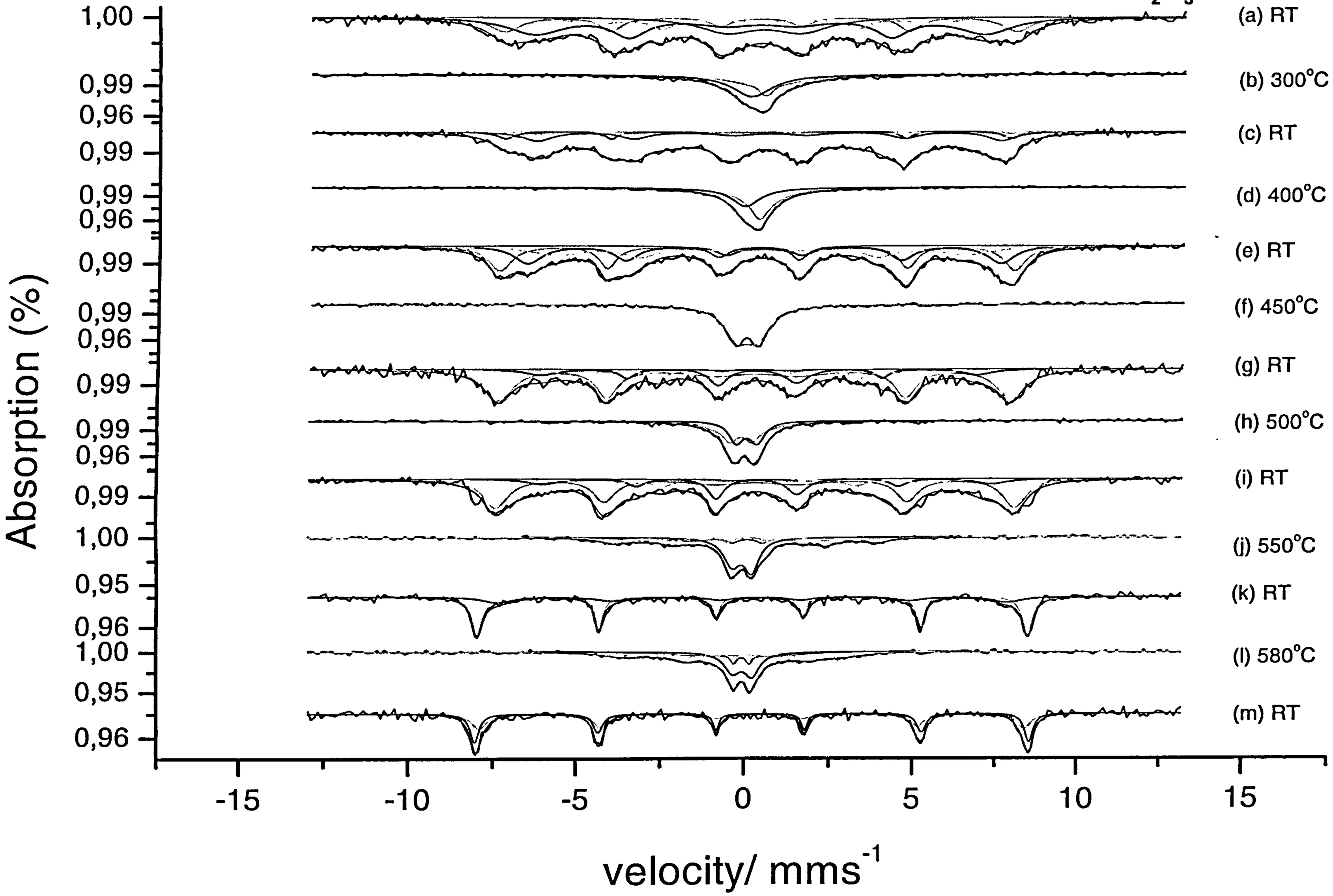

corresponding to γ–Fe_2O_3. On cooling the material to room temperature the spectrum (Figure 4.67(i)) was best interpreted in terms of a distribution of sextets corresponding to a γ–Fe_2O_3– related phase (H = 48(1) T). Further heating to 550 °C (Figure 4.67(j)) showed that *ca.* 47 % of the spectral area corresponded to the paramagnetic doublet, *ca.* 28 % was characteristic of α-Fe_2O_3 and the remaining 25 % characteristic of γ–Fe_2O_3. Cooling to room temperature (Figure 4.67(k)) was fitted to a distribution of sextets characteristic of α-Fe_2O_3 (H = 51(1) T). The material following heating to 580 °C (Figure 4.67(l)) showed a paramagnetic doublet accounting for ca. 35 % and a distribution of sextets characteristic of α-Fe_2O_3. The final room temperature spectrum (Figure 4.67(m)) showed a distribution of sextets characteristic of α-Fe_2O_3 (H = 51(1) T). Hence Ti/Mg/γ–Fe_2O_3 showed the onset of conversion to an α-Fe_2O_3 type structure at 500 °C and its completion at *ca.* 550 °C. The results are similar to those recorded from Ti/γ–Fe_2O_3, and reflect the higher loading of titanium.

Ex situ studies on the conversion of γ–Fe_2O_3 to α-Fe_2O_3

The Ti/Mg/γ–Fe_2O_3 was heated from 300 °C to 700 °C at 50 °C intervals and XRD patterns recorded *ex situ* (Figure 4.68). Table 4.26 shows the temperature of α-Fe_2O_3 appearance and γ–Fe_2O_3 disappearance. The combination of titanium and magnesium stabilised the temperature of spinel to corundum conversion to between 500-580 °C. The stability was greater than that of undoped γ-Fe_2O_3 and Mg/γ–Fe_2O_3, Figures 4.12 and 4.58 respectively but was similar to that of Ti/γ–Fe_2O_3 (Figure 4.29).

Figure 4.68 XRD patterns recorded *ex situ* from Ti/Mg/γ-Fe_2O_3 prepared by addition of base to salt, boiling under reflux, and heating at 250 °C and then heated from 300 to 700 °C

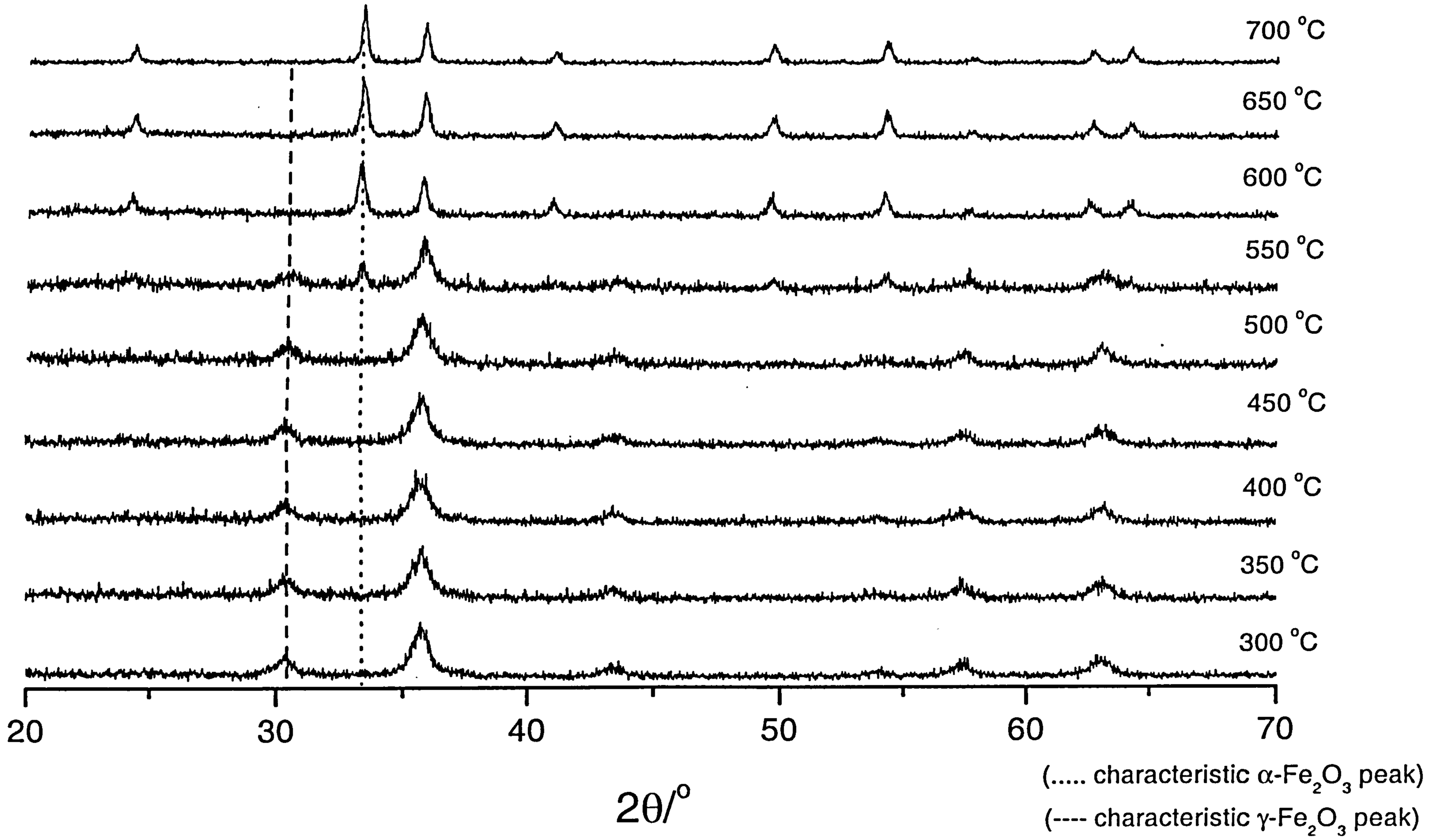

Conclusion

Ti-Mg- doped γ–Fe_2O_3 had higher surface area than undoped γ–Fe_2O_3 and Mg/γ–Fe_2O_3 but was similar to that of Ti/γ–Fe_2O_3, all prepared by addition of base to salt, boiling under reflux, and calcination at 250 °C. The TPR profile showed three reduction peaks similar to that of undoped γ–Fe_2O_3 and titanium- and magnesium-doped γ–Fe_2O_3 prepared by similar methods. The latter two peaks were coalesced but to a lesser extent than Ti/γ–Fe_2O_3. Both titanium and magnesium combined stabilised the temperature of γ–Fe_2O_3 to α-Fe_2O_3 conversion compared to undoped γ-Fe_2O_3 and Mg/γ–Fe_2O_3, the thermal stability was more similar to that of Ti/γ–Fe_2O_3.

Overall, materials of the type MgM/γ–Fe_2O_3 (M = Sn, Ti) showed the properties to be more similar to the M/γ–Fe_2O_3 than the Mg/γ–Fe_2O_3 phase, reflecting the higher loading of M.

4.3.3 Sn/Ti/γ-Fe_2O_3 (addition of base to salt, boiling under reflux, and calcination at 250 °C/12 h)

The XRD pattern (Figure 4.69) corresponded to γ-Fe_2O_3[5] with a minor impurity of α-Fe_2O_3[6]. The EDX analysis showed 5.5 mass % of Sn and 2.4 mass % of Ti. ^{57}Fe Mössbauer spectroscopy confirmed the material to contain γ-Fe_2O_3[1,2] and α-Fe_2O_3[1,2] (Figure 4.70, Table 4.23).

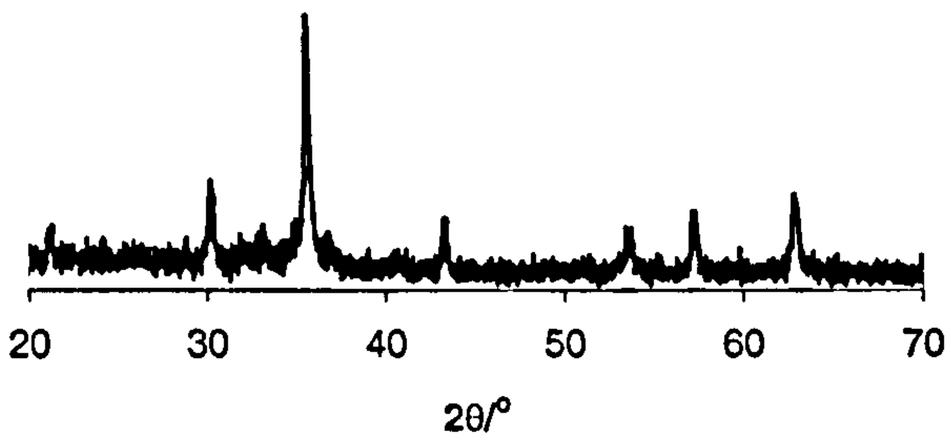

Figure 4.69 XRD pattern recorded from Sn/Ti/γ–Fe_2O_3 prepared by addition of base to salt, boiling under reflux, and calcination at 250 °C

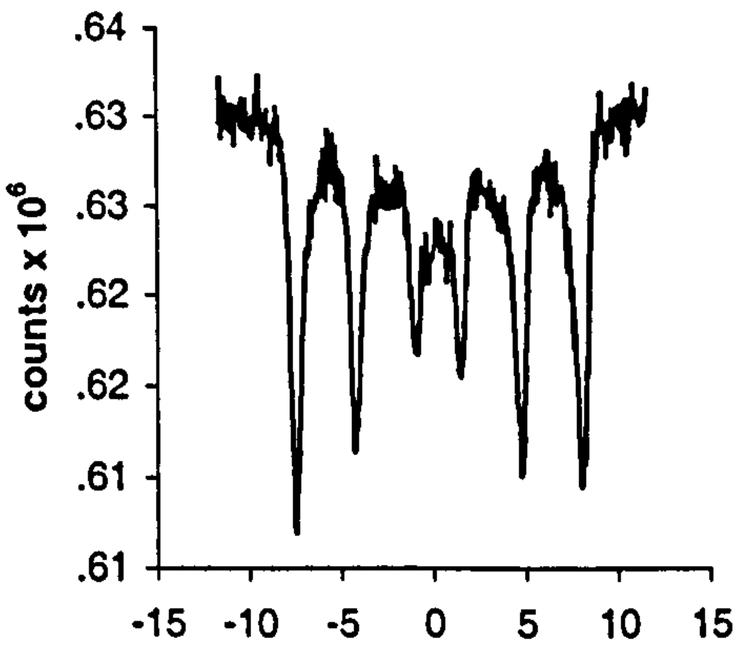

Figure 4.70 ^{57}Fe Mössbauer spectrum recorded from Sn/Ti/γ–Fe_2O_3 prepared by addition of base to salt, boiling under reflux, and calcination at 250 °C

The surface area of Sn/Ti/γ–Fe_2O_3 was found to be 85 m^2g^{-1}, slightly higher than undoped γ-Fe_2O_3 (69 m^2g^{-1}) and between that of Sn/γ-Fe_2O_3 (59 m^2g^{-1}) and Ti/γ-Fe_2O_3 (139 m^2g^{-1}), all prepared by addition of base to salt, boiling under reflux, and calcination at 250 °C.

The TPR profile (Figure 4.71, Table 4.25) gave four peak maxima. The peak at *ca.* 420 °C may be attributed to the α-Fe_2O_3 impurity. The intensity of the initial peak was between the intensities of the initial peaks of Ti/γ-Fe_2O_3 and Sn/γ-Fe_2O_3, Figures 4.21 and 4.34 respectively.

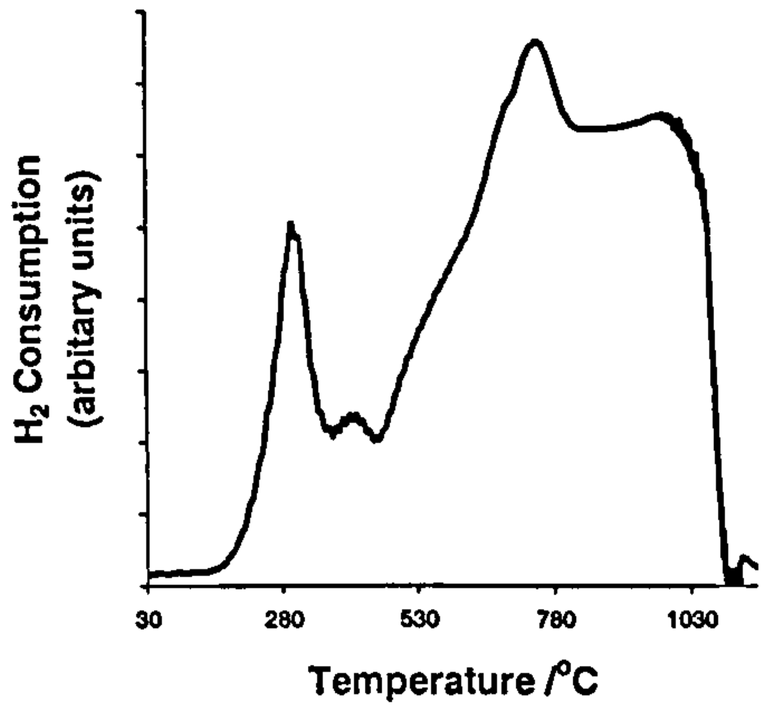

Figure 4.71 TPR profile recorded from Sn/Ti/γ–Fe_2O_3 prepared by addition of base to salt, boiling under reflux, and calcination at 250 °C

Ex situ studies on the conversion of γ–Fe_2O_3 to α-Fe_2O_3

The Sn/Ti/γ–Fe_2O_3 was heated from 300 °C to 700 °C and XRD patterns recorded *ex situ* (Figure 4.72). Table 4.26 shows the temperature of α-Fe_2O_3 appearance and γ–Fe_2O_3 disappearance. Sn/Ti/γ–Fe_2O_3 stabilised the temperature of conversion of the γ–Fe_2O_3 structure to α-Fe_2O_3 to between *ca.* 300 to 650 °C. This is higher then that of undoped γ-Fe_2O_3 (Figures 4.12) and is similar to the thermal stability of titanium- and tin- doped γ–Fe_2O_3 prepared by similar methods (Figures 4.29 and 4.42).

Conclusion

The preparation of single phase Sn/Ti/γ–Fe_2O_3 was unsuccessful, an α-Fe_2O_3 impurity was observed. Sn/Ti/γ–Fe_2O_3 has a surface area intermediate between those

Figure 4.72 XRD patterns recorded *ex situ* from Sn/Ti/γ-Fe_2O_3 prepared by addition of base to salt, boiling under reflux, and heating at 250 °C and then heated from 300 to 700 °C

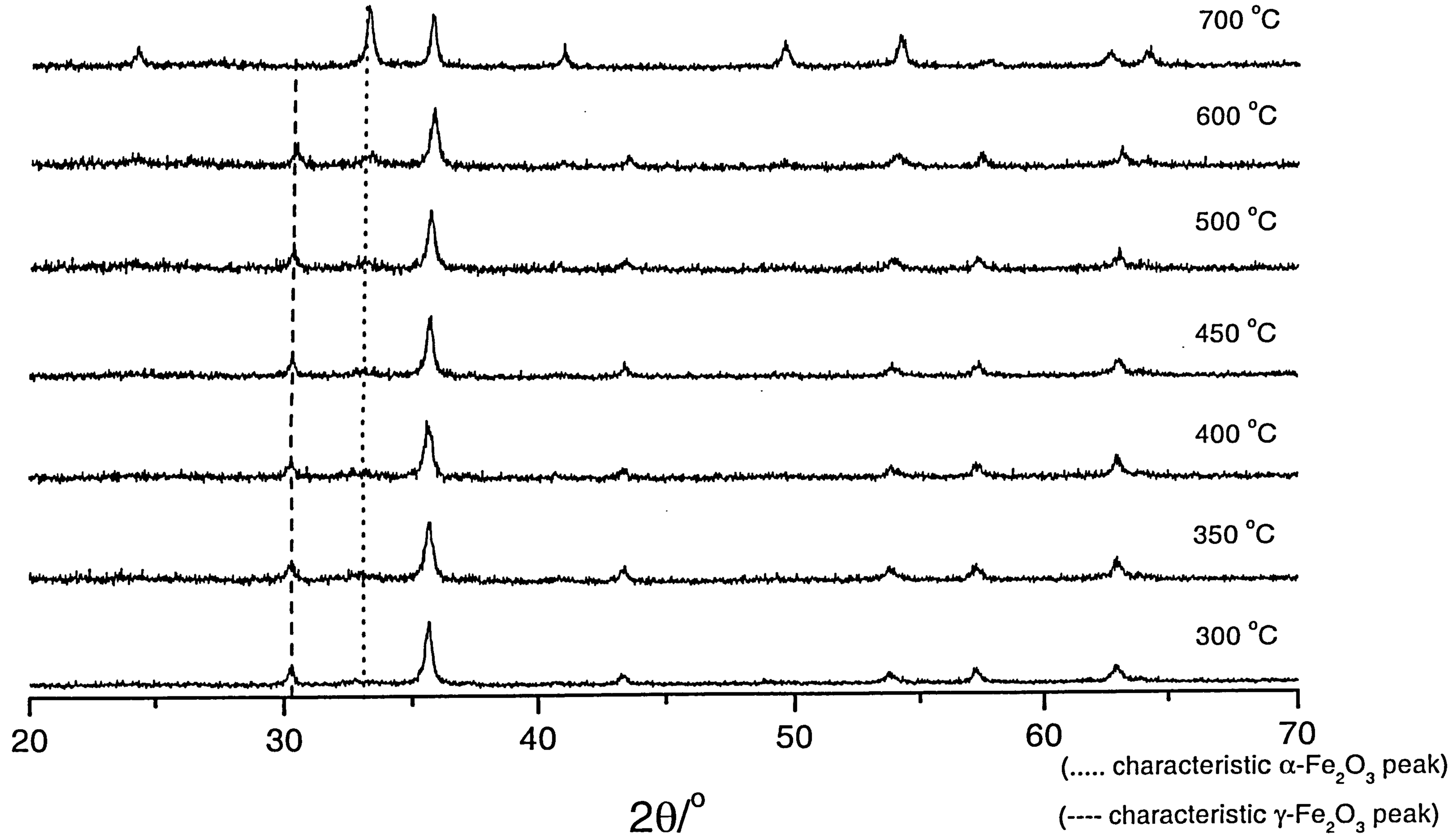

of Sn/γ–Fe_2O_3 and Ti/γ–Fe_2O_3, both prepared by addition of base to salt, boiling under reflux, and calcination at 250 °C. The TPR profile showed four reduction peaks, the peak at *ca.* 420 °C being associated with the α-Fe_2O_3 impurity. Sn/Ti/γ–Fe_2O_3 showed a similar thermal stability with respect to the conversion to a corundum α-Fe_2O_3 structure as Ti/γ–Fe_2O_3 and Sn/ γ–Fe_2O_3.

4.4 Pd/γ-Fe_2O_3 and metal- doped variants

The XRD patterns recorded from Pd impregnated γ-Fe_2O_3 and Ti-, Sn- and Mg-doped variants (all mixed oxides were prepared by addition of base to salt, boiling under reflux, and calcination at 250 °C and impregnated using $Pd(NO_3)_2$), corresponded to γ-Fe_2O_3[5] and are shown in Figure 4.73 (a-d). The samples made by impregnation with Pd(DNDA), and $Pd(acac)_2$ gave identical results. The Sn- doped sample showed a minor impurity of α-Fe_2O_3. No palladium- containing phase was observed in the XRD patterns suggesting that the palladium loading was too low or highly dispersed or amorphous.

Table 4.27 gives the average particle size (i) calculated from the XRD pattern using the Scherrer equation and (ii) estimated from the histograms of TEM micrographs for the Pd impregnated γ-Fe_2O_3 and Ti-, Sn- and Mg- doped variants prepared using the $Pd(NO_3)_2$ precursor. The BET surface area measurements are also shown in Table 4.27. Impregnating with palladium has little effect on the total surface area of γ-Fe_2O_3 samples, except for the Sn- doped γ-Fe_2O_3 where a decrease in the surface area was observed, which is probably due to the α-Fe_2O_3 impurity.

Figure 4.73 XRD patterns recorded from Pd impregnated γ-Fe_2O_3 and metal- doped variants

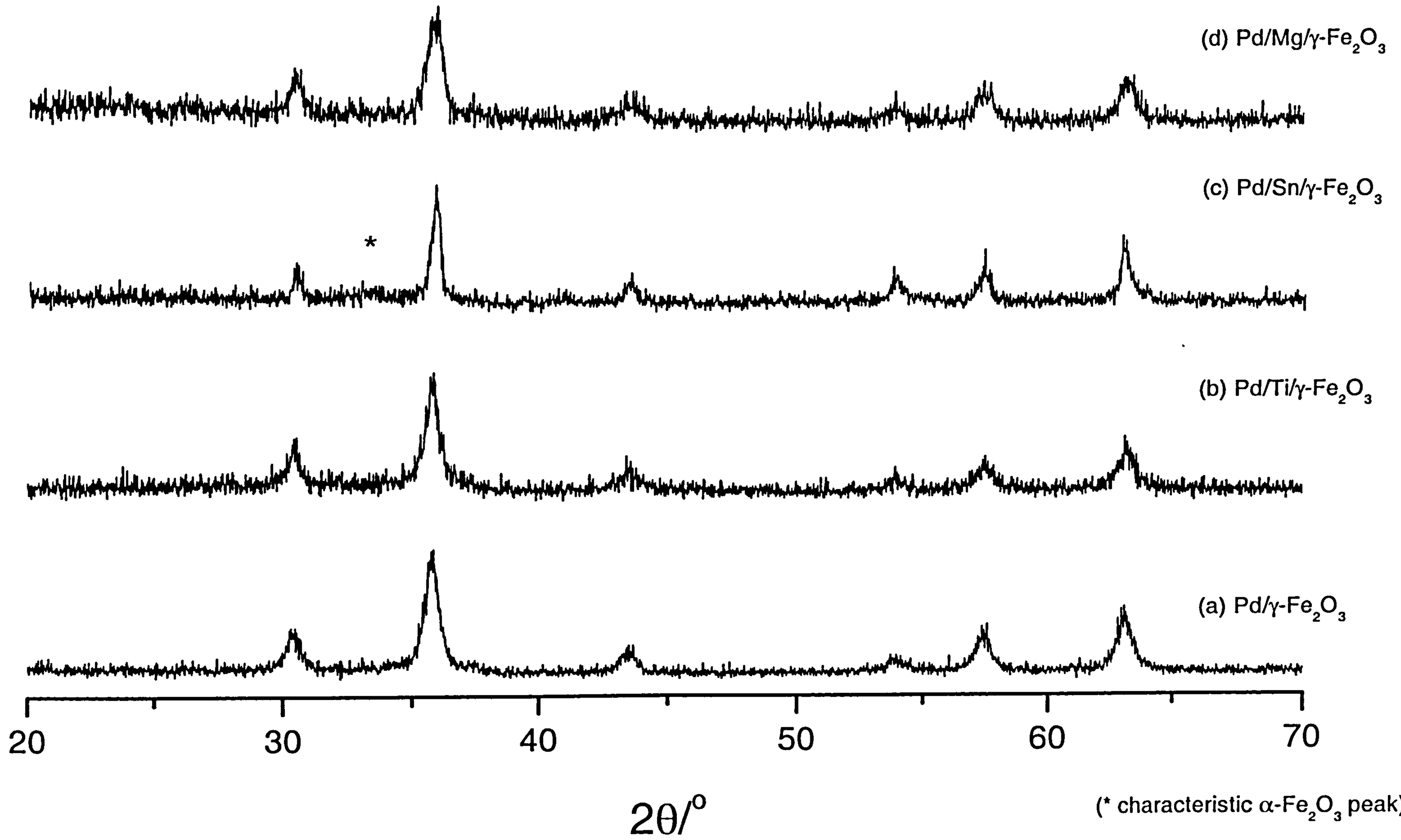

(* characteristic α-Fe_2O_3 peak)

Table 4.27 Particle size and surface area measurements for Pd/γ-Fe_2O_3 and metal-doped variants.

Sample ($Pd(NO_3)_2$)	Average particle size Scherrer method / nm (± 10 %)	Average particle size TEM / nm (± 10 %)	Surface Area / m^2g^{-1} (± 10 %)
Pd/γ-Fe_2O_3	13	14	71
Pd/Ti/γ-Fe_2O_3	14	7	122
Pd/Sn/γ-Fe_2O_3	24	55	41
Pd/Mg/γ-Fe_2O_3	12	7	99

The TPR profiles for Pd impregnated γ-Fe_2O_3 and Ti-, Sn-, and Mg- doped variants using ($Pd(NO_3)_2$, Pd(DNDA), and $Pd(acac)_2$ are shown in Figures 4.74 – 4.77 (a-d) respectively. The reduction temperatures are shown in Table 4.28. In all cases the patterns showed three main reduction peaks, similar to the non-impregnated samples. The addition of Pd resulted in a decrease in the reduction temperature of all the peaks, in particular the initial reduction peak (for example 350, 716, 1013 °C, for γ-Fe_2O_3 and 100, 690, 910 °C, for Pd/γ-Fe_2O_3 prepared using $Pd(NO_3)_2$) suggesting that there is some interaction between Pd and the iron oxides. Pd may have a high affinity for H_2, which dissociates and gives rise to more facile reduction of iron in iron oxide.

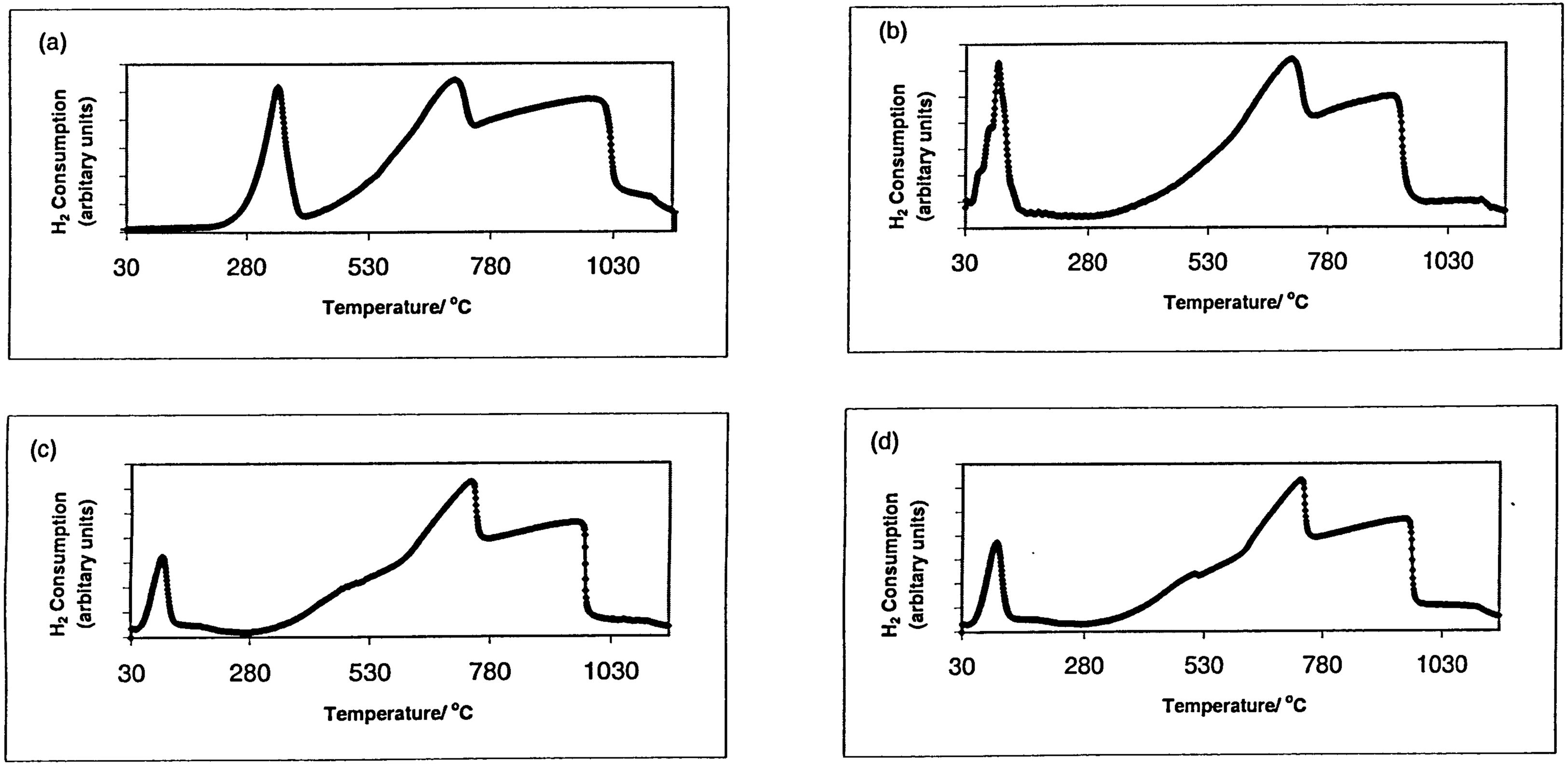

Figure 4.74 TPR profiles recorded from (a) γ-Fe_2O_3 and Pd impregnated samples using (b) $Pd(NO_3)_2$, (c) Pd(DNDA) and (d) $Pd(acac)_2$ precursors

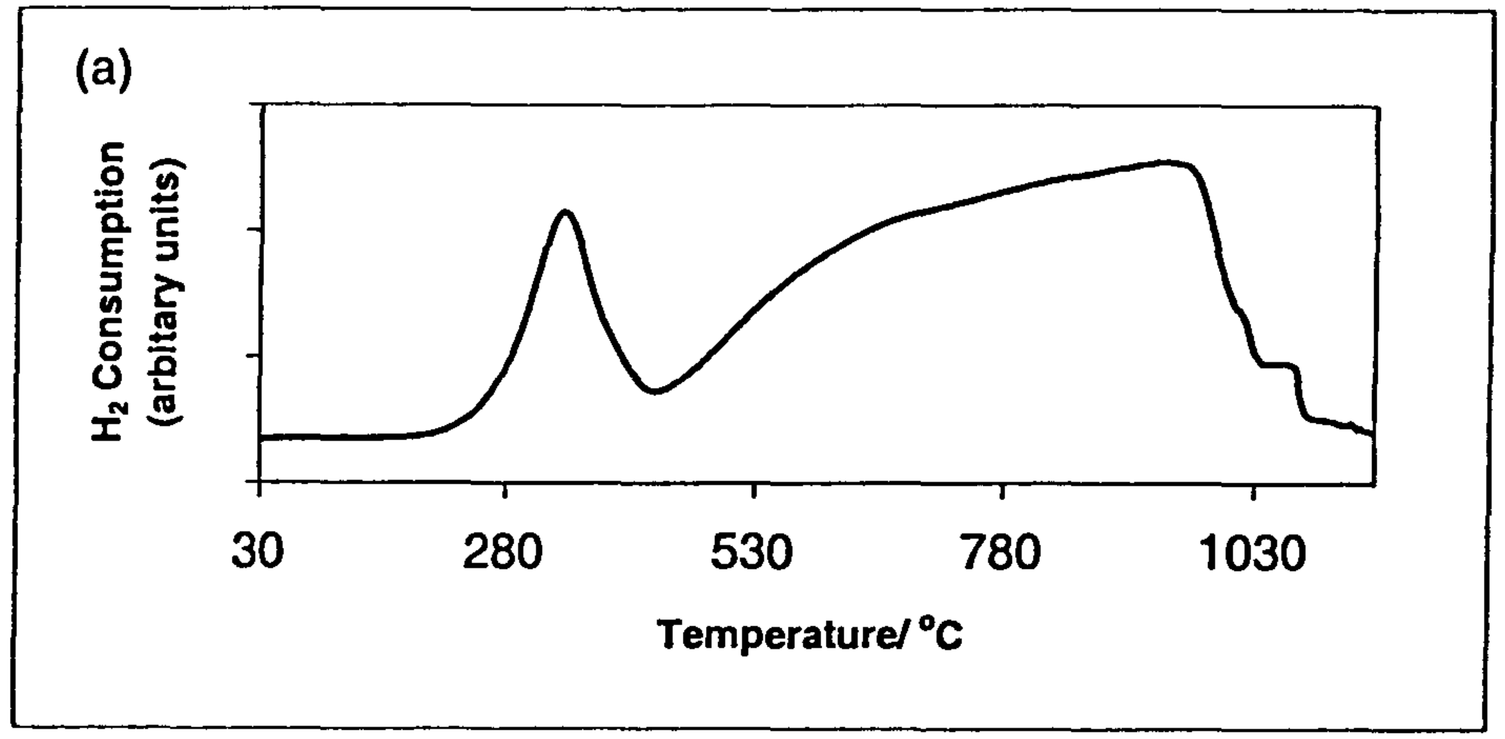

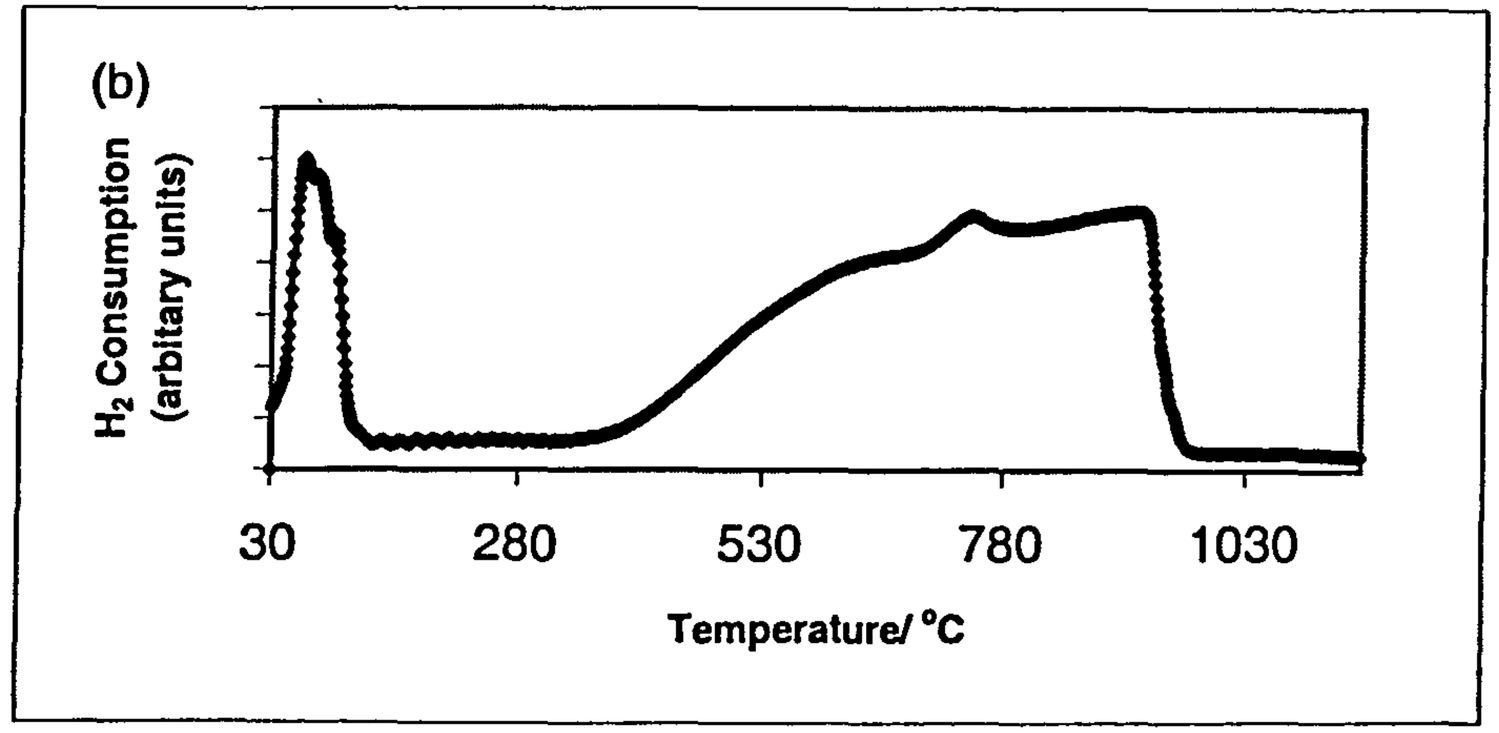

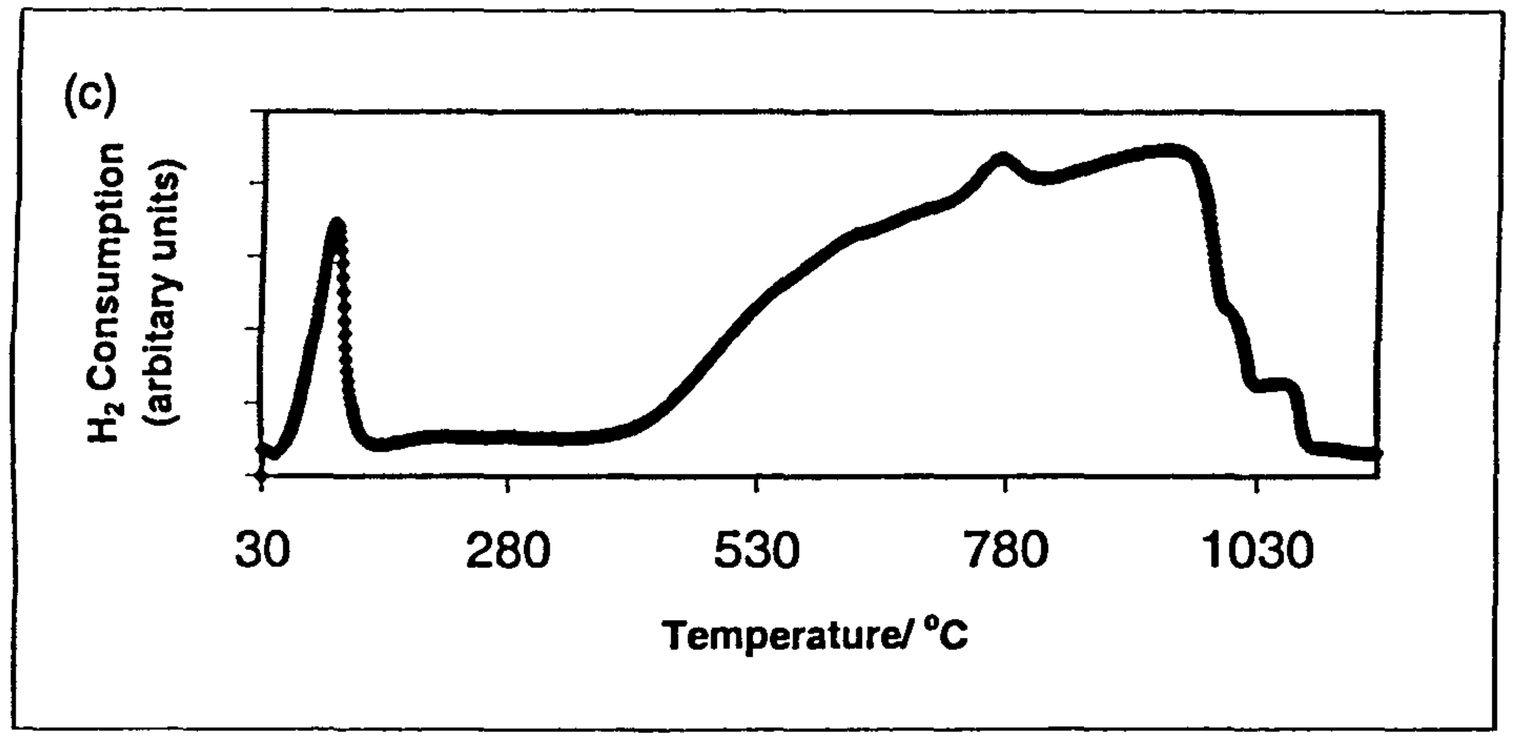

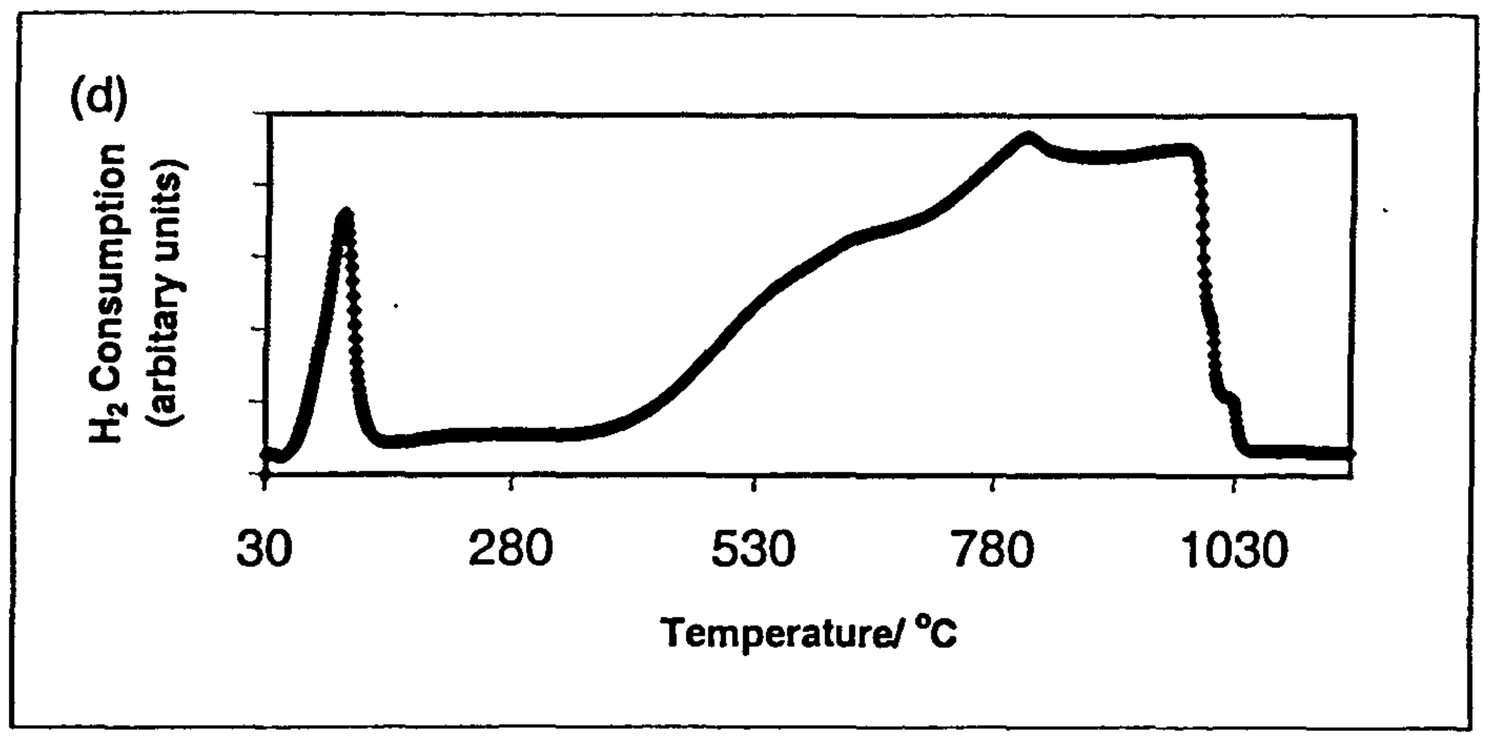

Figure 4.75 TPR profiles recorded from (a) Ti/γ-Fe_2O_3 and Pd impregnated samples using (b) $Pd(NO_3)_2$, (c) Pd(DNDA) and (d) $Pd(acac)_2$ precursors

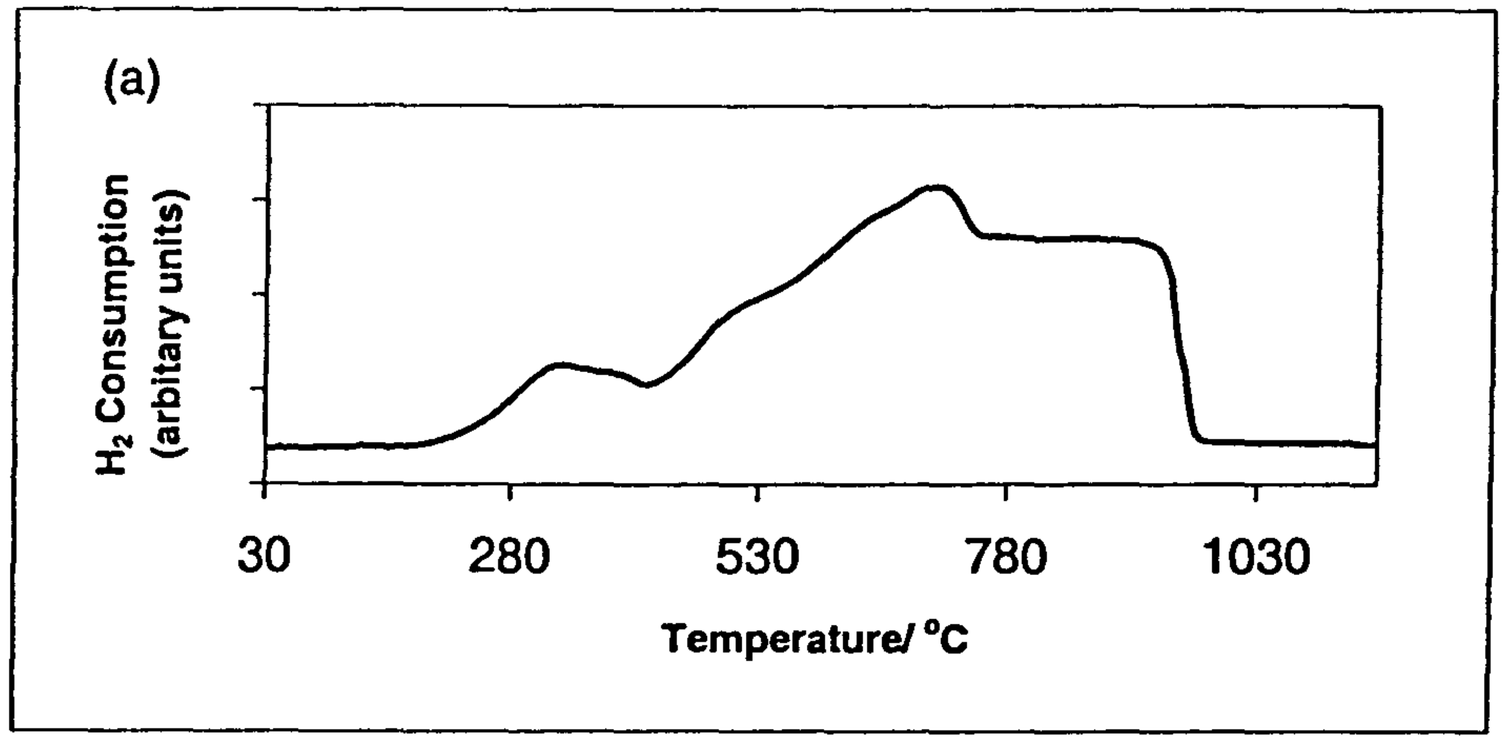

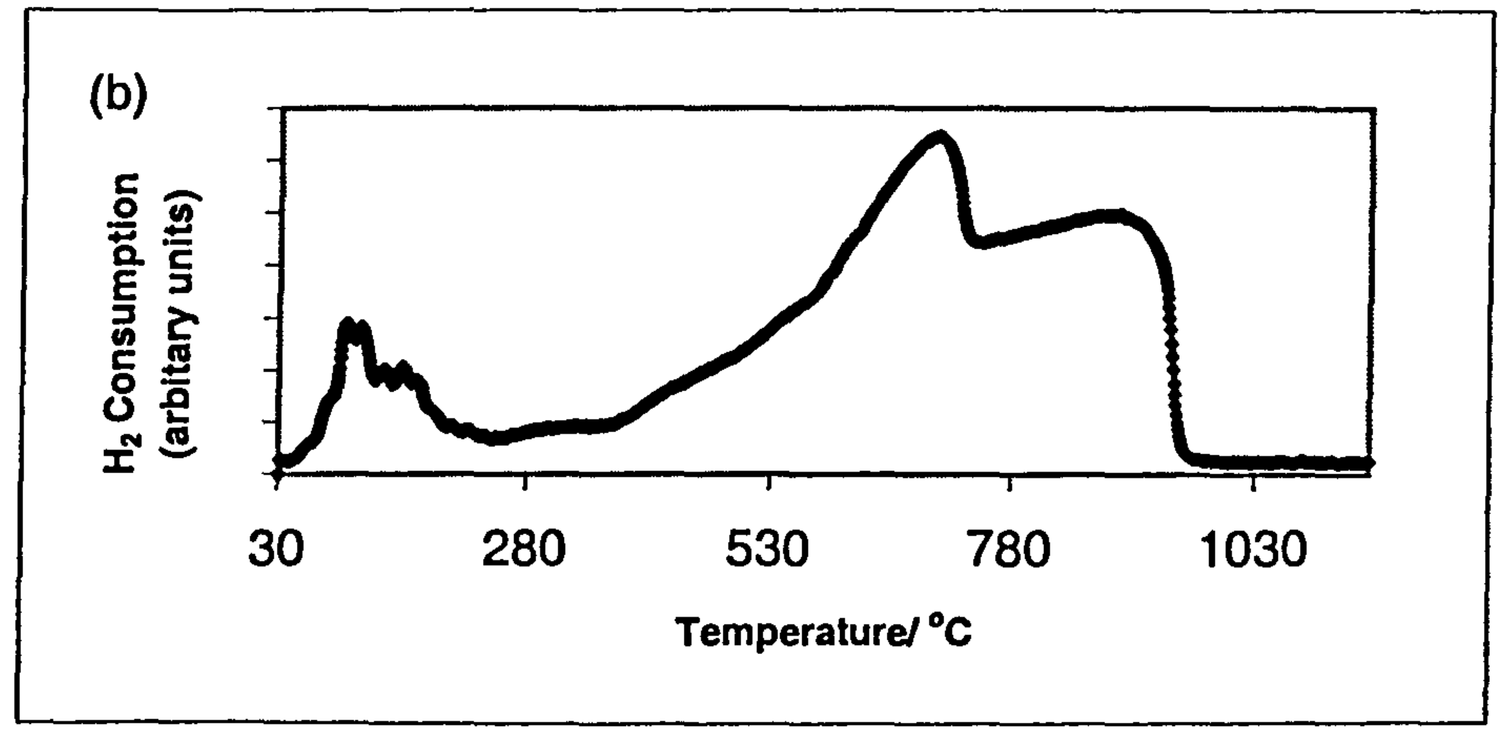

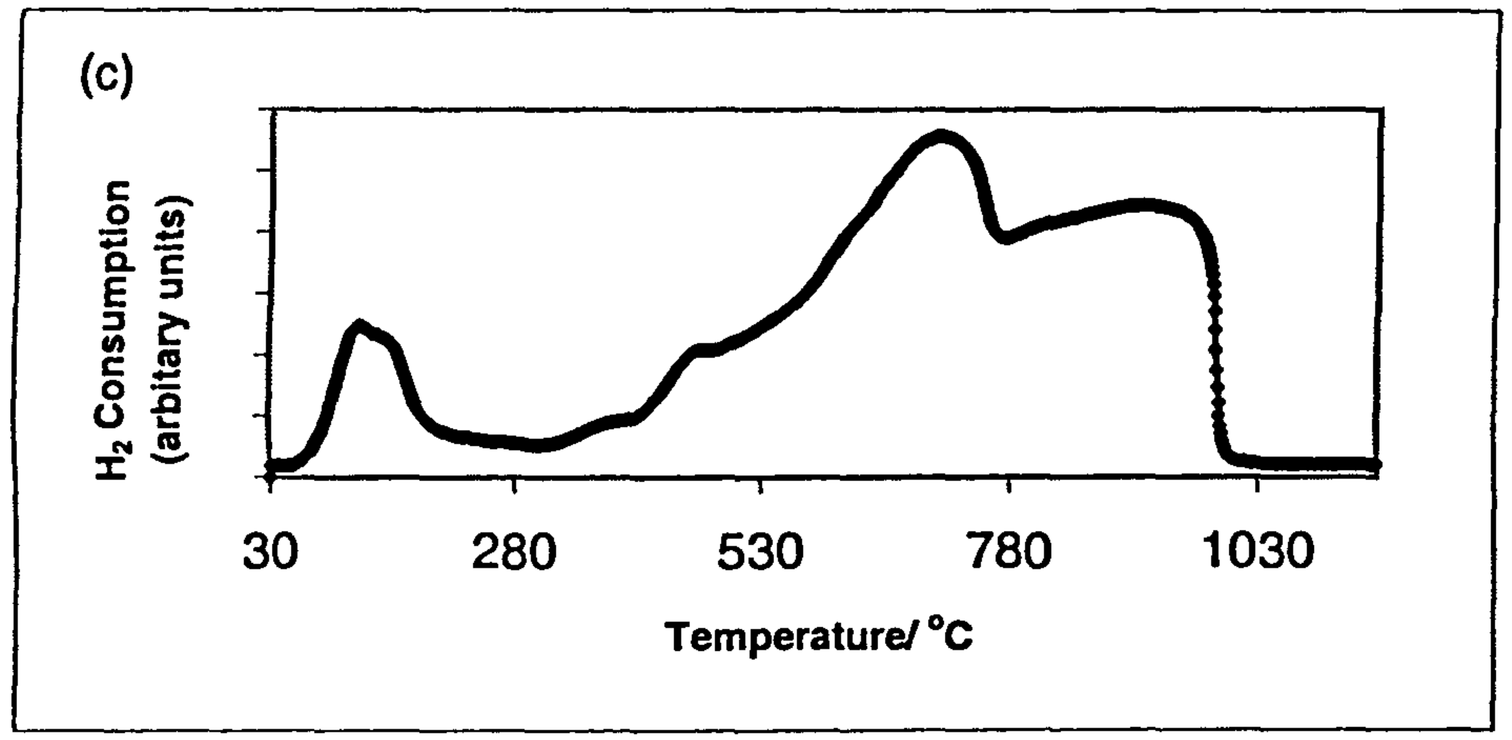

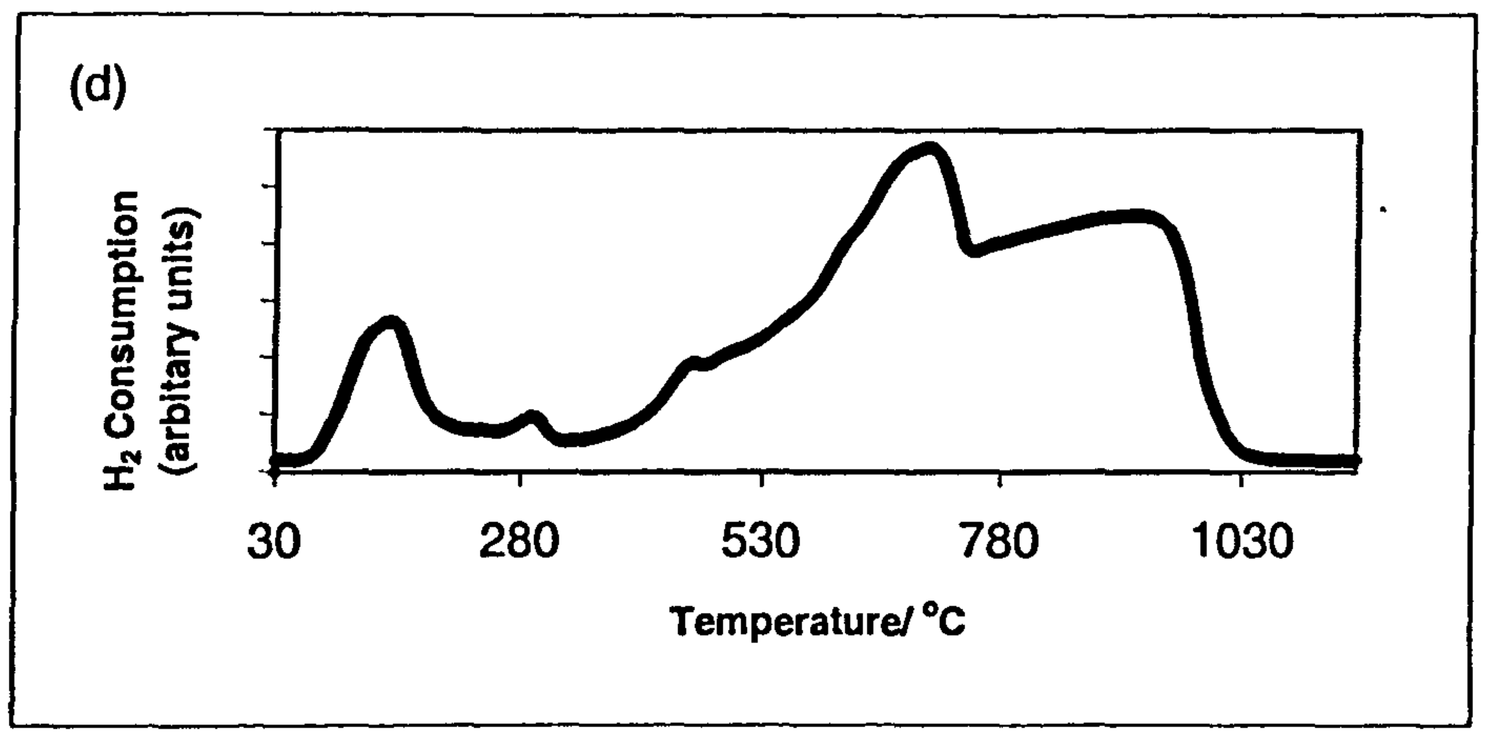

Figure 4.76 TPR profiles recorded from (a) Sn/γ-Fe_2O_3 and Pd impregnated samples using (b) $Pd(NO_3)_2$, (c) Pd(DNDA) and (d) $Pd(acac)_2$ precursors

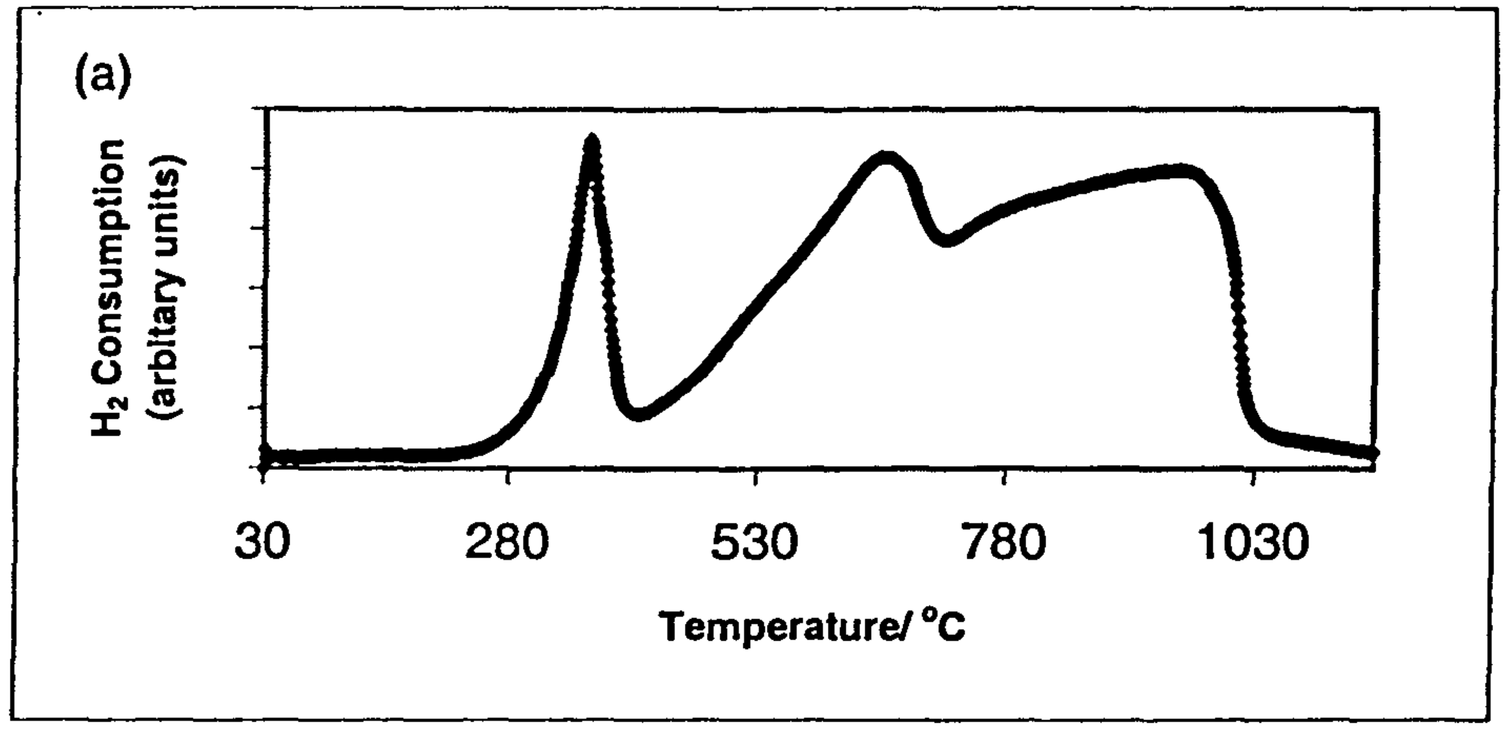

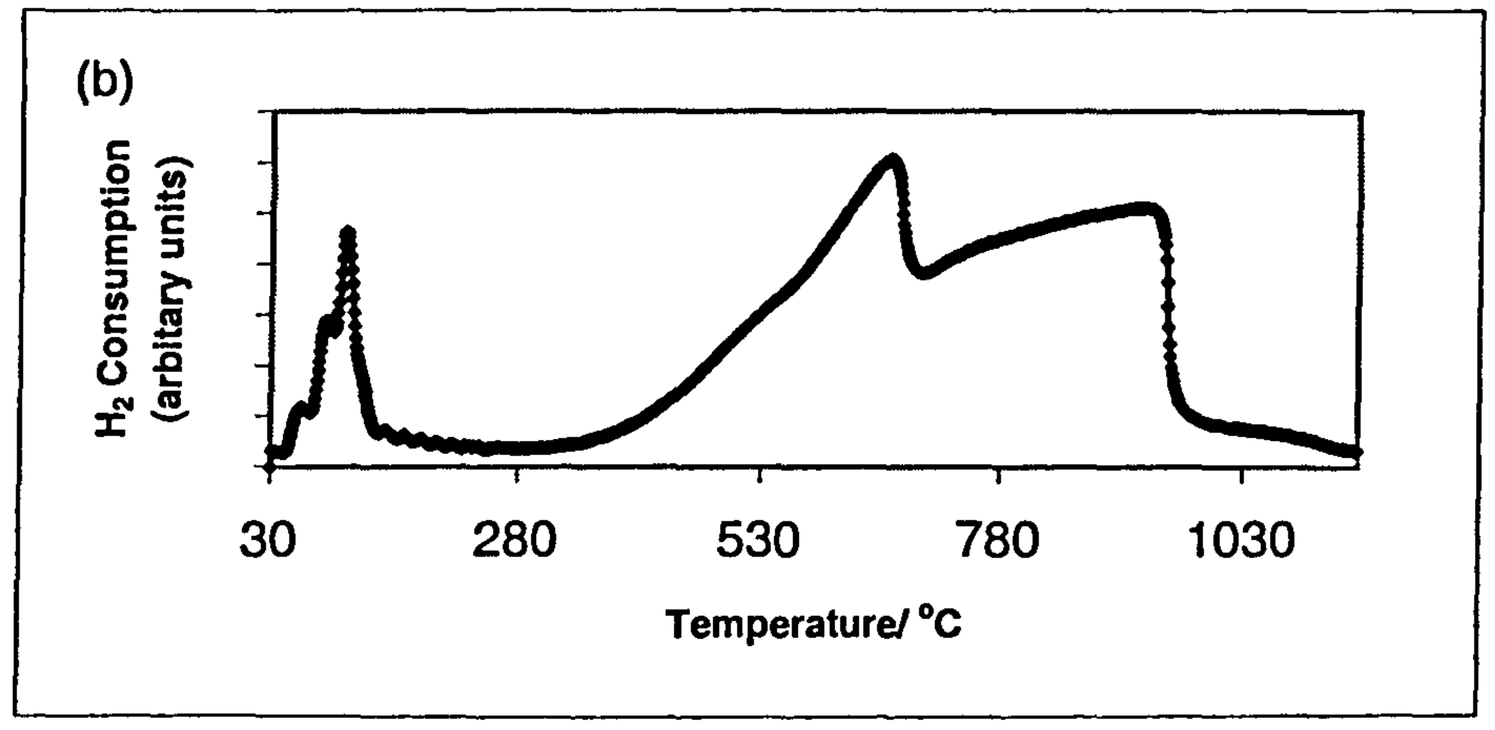

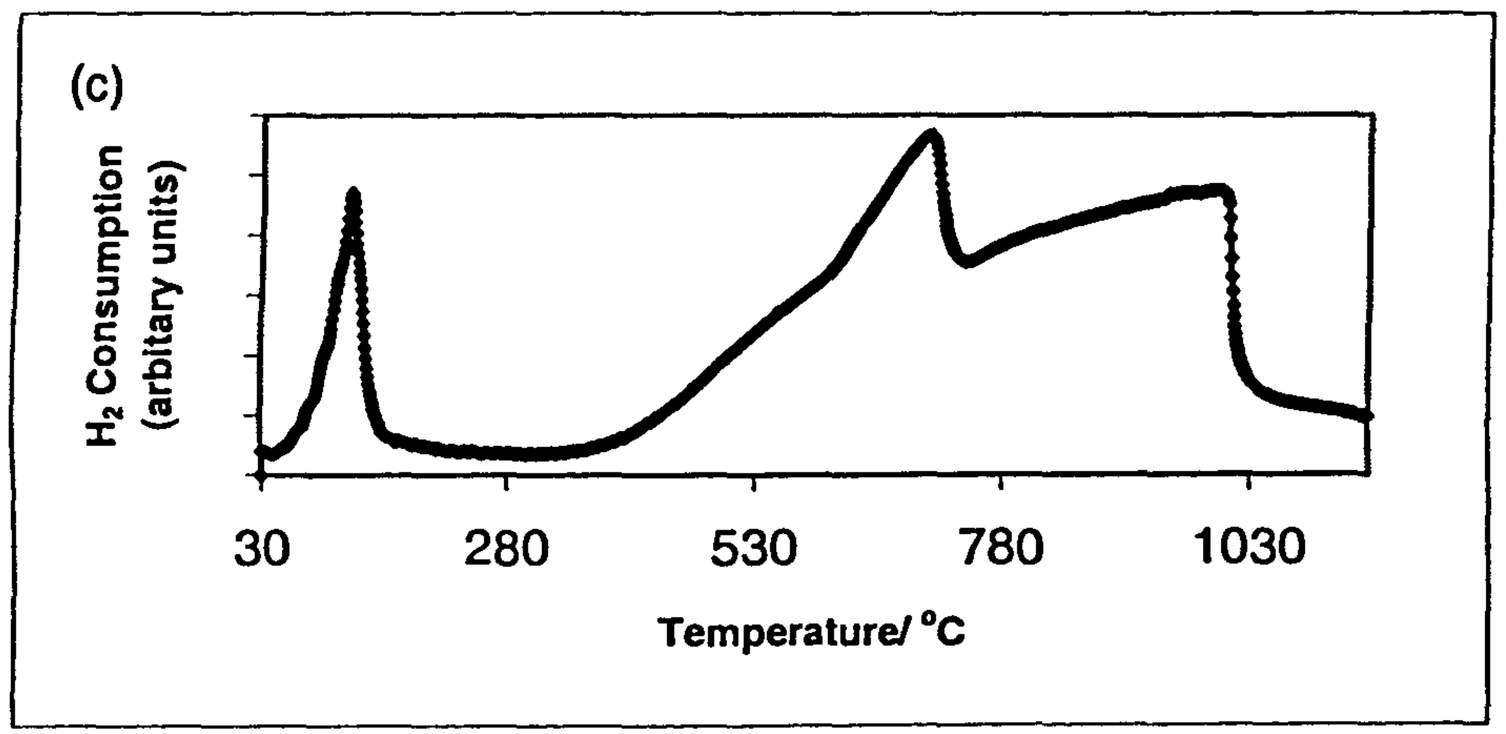

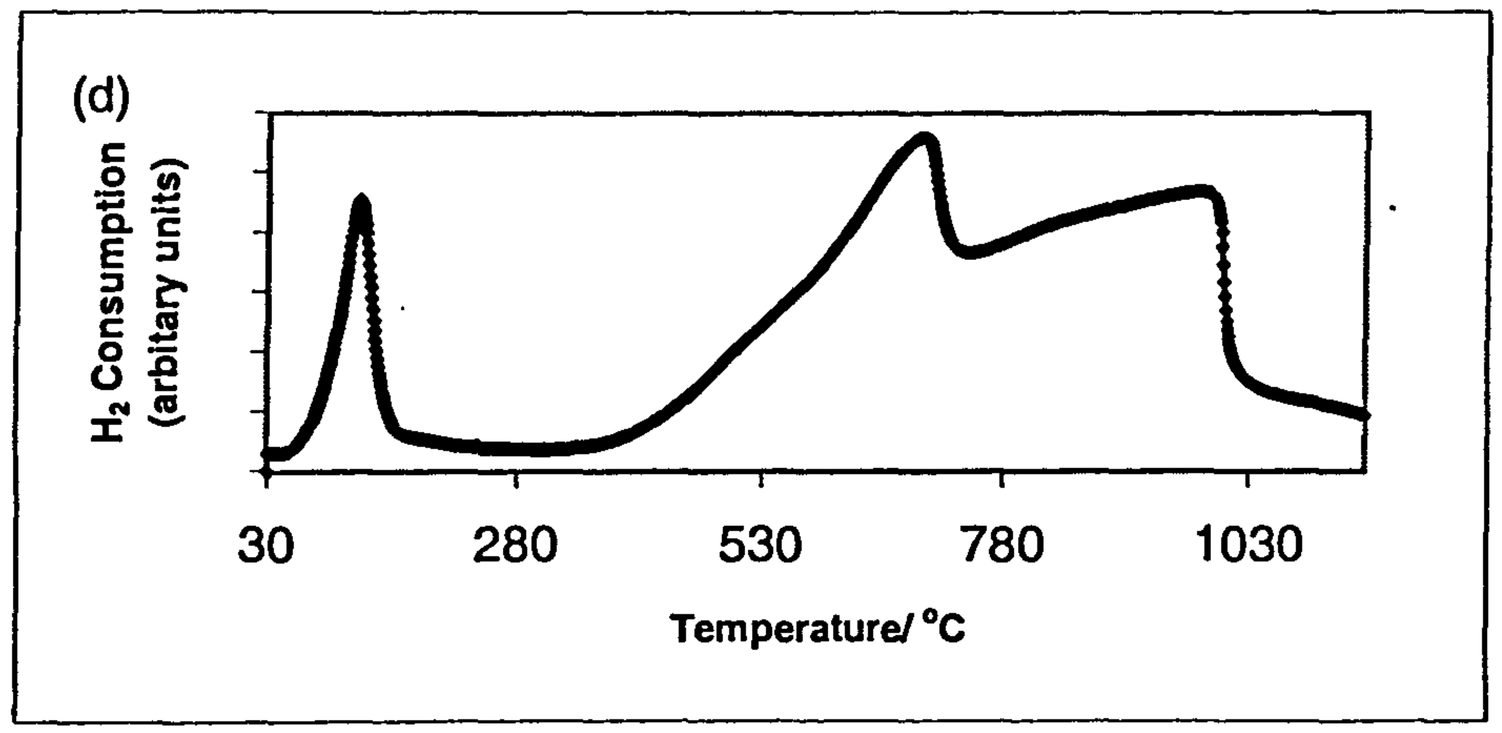

Figure 4.77 TPR profiles recorded from (a) Mg/γ-Fe_2O_3 and Pd impregnated samples using (b) $Pd(NO_3)_2$, (c) Pd(DNDA) and (d) $Pd(acac)_2$ precursors

Table 4.28 TPR data from Pd impregnated γ-Fe_2O_3 and metal- doped variants (major peaks in bold)

Sample	Reduction Peaks / °C (± 50 °C)		
	($Pd(NO_3)_2$)	(Pd(DNDA))	($Pd(acac)_2$)
Pd/γ-Fe_2O_3,	**100, 690, 910**	**100,** *500 (shoulder),* **750, 970**	**100,** 500, **720, 950**
Pd/Ti/γ-Fe_2O_3,	**75,** 650 (shoulder), **750 – 920** (broad)	**110,** *620 (shoulder),* **780-950** (broad), *1000 (shoulder)*	**110,** *620 (shoulder),* **810-980** (broad), *1000 (shoulder)*
Pd/Sn/γ-Fe_2O_3,	**110,** *150 (shoulder),* **700, 890**	**110,** *460 (shoulder),* **700,910**	**140,** 290, *450 (shoulder),* **700, 920**
Pd/Mg/γ-Fe_2O_3,	*50, 90 (shoulders)* **100, 660, 930**	**110, 700, 1000**	**120, 700, 980**

Catalyst Testing

The oxidation of CO to CO_2 was used as a test for the catalytic activity of the Pd impregnated samples. The temperatures at which 50 % conversion (T_{50}) of CO to CO_2 was achieved are collected in Table 4.29. The lower the temperature of CO conversion the more active the catalyst.

Table 4.29 Conversion temperatures of CO to CO_2 from Pd impregnated γ-Fe_2O_3 and metal- doped variants.

Sample	Temperature at 50% CO conversion / °C (± 25 °C)		
	($Pd(NO_3)_2$)	**(Pd(DNDA))**	**($Pd(acac)_2$)**
Pd/γ-Fe_2O_3 (base to salt)	140	130	119
Pd/γ-Fe_2O_3 (salt to base)	149	159	173
Pd/Ti/γ-Fe_2O_3	70	50	47
Pd/Sn/γ-Fe_2O_3	162	162	161
Pd/Mg/γ-Fe_2O_3	128	144	232

The lowest temperatures are achieved with Pd/Ti/γ–Fe_2O_3. Figure 4.78 shows the dependence of CO oxidation on temperature over Pd/γ-Fe_2O_3 prepared by addition of base to salt and boiling under reflux, impregnated using $Pd(NO_3)_2$. The shape of the graph is typical for catalytic performance. Until the incoming gases have heated the catalyst, the activity of the catalyst is low. This temperature, at which the efficiency of the catalyst rapidly increases is known as the light-off temperature. Until this temperature is reached, the catalyst does not work at full efficiency, and so CO will be emitted from the exhaust in significant amounts. This problem is known as cold start. Ideally the light-off temperature should be as low as possible.

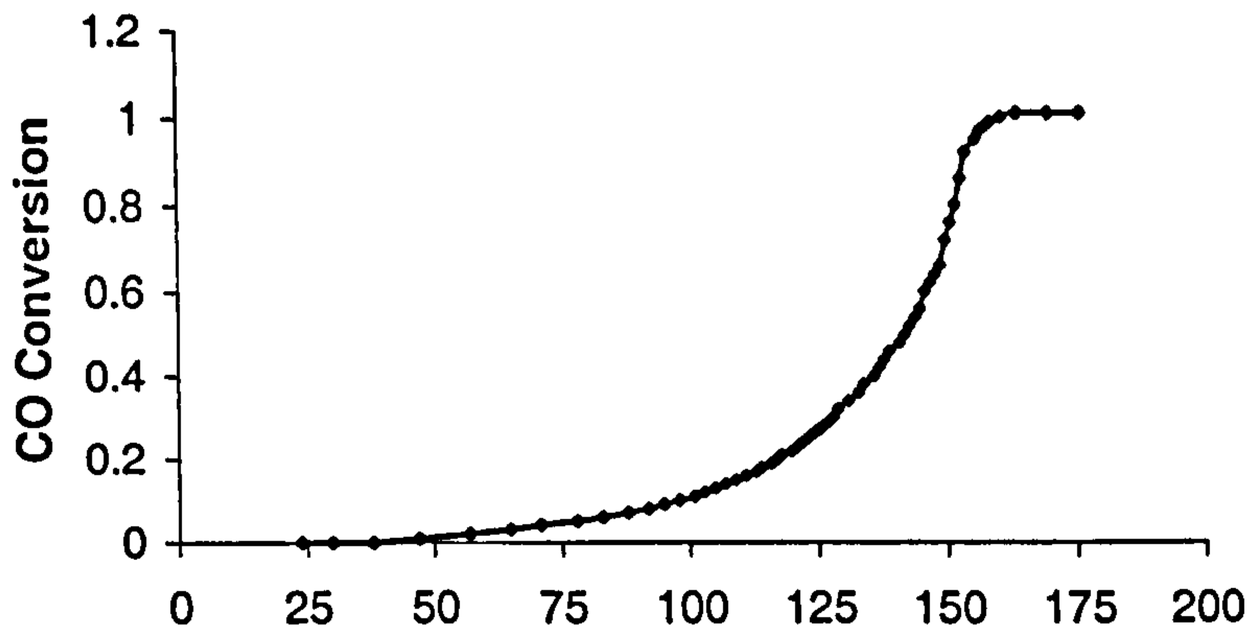

Figure 4.78 Dependence of CO oxidation on temperature for Pd/γ–Fe_2O_3 using $Pd(NO_3)_2$

Pd impregnated Ti- doped γ-Fe_2O_3 appeared to induce a lowering of the temperature of 50 % CO conversion as compared with the Pd impregnated undoped γ-Fe_2O_3, which may be due to smaller particle size and higher surface area of the support. The remaining dopants appeared to induce little difference in the temperature of 50 % CO conversion compared to Pd impregnated undoped γ-Fe_2O_3. The different palladium precursors also showed little differences ranging by *ca.* 30 °C for the different precursors, which may be due to different palladium loading or dispersion. Pd/γ–Fe_2O_3 prepared by addition of salt to base, boiling under reflux, and calcination at 250 °C which has a particle size and surface area comparable with Pd/Ti/γ–Fe_2O_3, had a 50 % CO conversion temperature which was significantly higher than Pd/Ti/γ–Fe_2O_3, suggesting that the presence of titanium as opposed to particle size or surface area effects the catalytic activity.

Oxygen storage capacity (OSC)

One of the most important components of an automobile exhaust catalyst is an oxygen storage material, which is able to store excess oxygen when the exhaust gas from the engine is lean and release oxygen to enable conversion of CO and hydrocarbons when the exhaust gas is rich.

Pd impregnated- γ–Fe_2O_3, Ti/γ–Fe_2O_3 and Sn/γ–Fe_2O_3, all prepared by addition of base to salt, boiling under reflux, and calcination at 250 °C were tested for oxygen storage capacity (OSC), the results are shown in Figure 4.79 (a-c) respectively. The material should have a high OSC value *ca.* 1000 μmol $[O]g^{-1}$ and be maintained at high temperatures up to *ca.* 1000 °C. Pd/γ–Fe_2O_3 showed a maximum OSC of *ca.* 1200 μmol $[O]g^{-1}$ at temperatures ranging between 300 and 500 °C. Pd/Ti/γ–Fe_2O_3 showed a maximum OSC of *ca.* 2000 μmol $[O]g^{-1}$ at temperatures ranging between 300 and 550 °C. Pd/Sn/γ–Fe_2O_3 showed a maximum OSC as high as *ca.* 700 μmol $[O]g^{-1}$ in the temperature range between 500 and 650 °C. All the samples show high OSC but unfortunately not maintained at high temperatures as the samples are converted to the α phase.

Overall, the results showed that palladium impregnated titanium- doped γ–Fe_2O_3 has the greatest oxygen storage capacity.

Conclusion

The different palladium precursors have similar effects on the TPR profiles and lower the temperature of the initial reduction peak. CO oxidation and OSC studies showed that Pd impregnated titanium γ–Fe_2O_3 gave significantly better results as

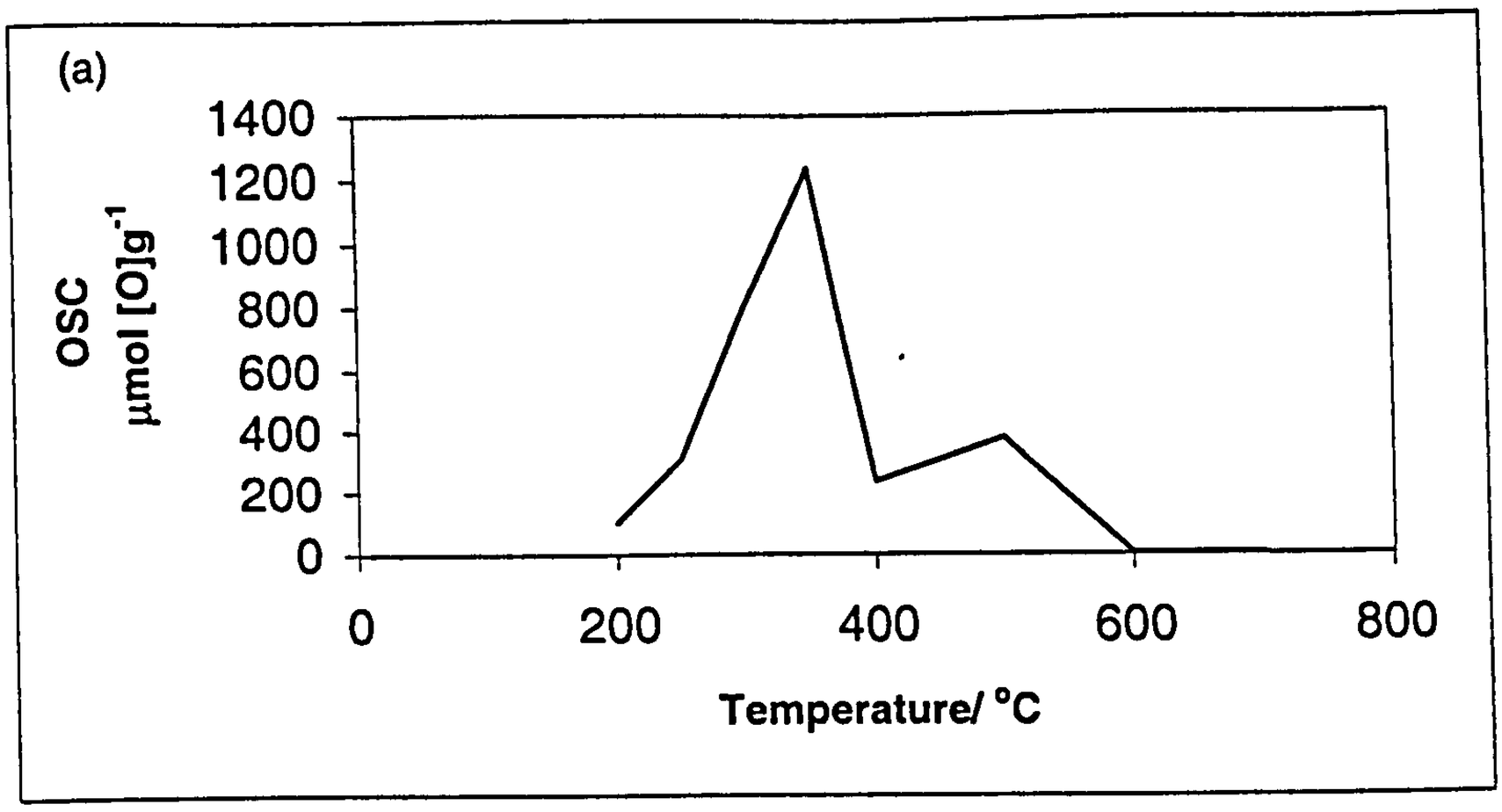

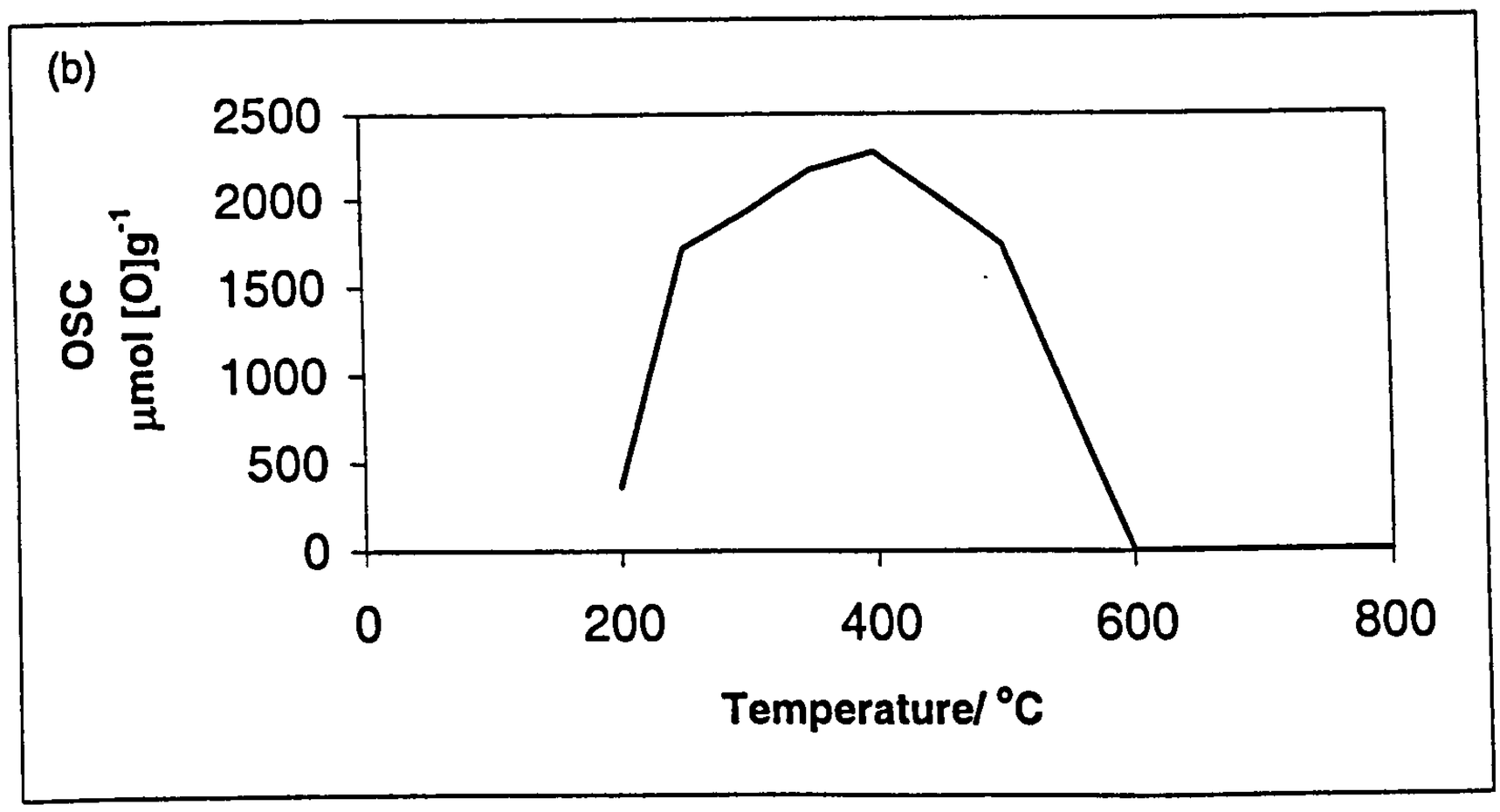

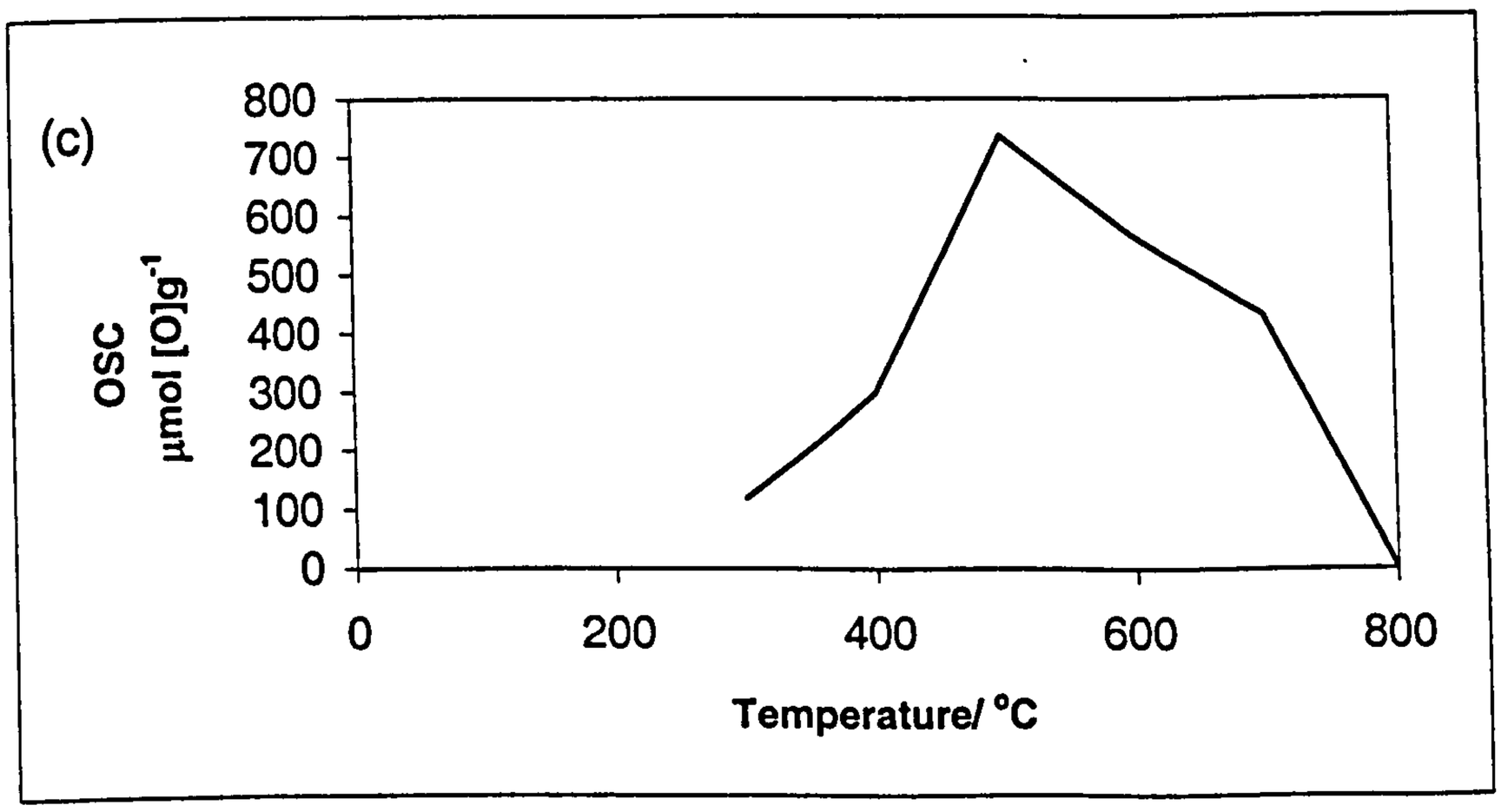

Figure 4.79 OSC measurement recorded from (a) Pd/γ-Fe_2O_3, (b) Pd/Ti/γ-Fe_2O_3 and (c) Pd/Sn/γ-Fe_2O_3

compared with Pd impregnated undoped γ–Fe_2O_3 and Pd impregnated tin- doped γ–Fe_2O_3 all prepared by addition of base to salt, boiling under reflux, and calcination at 250 °C. Pd/γ–Fe_2O_3 prepared by addition of salt to base and boiling under reflux which had a particle size and surface area comparable with Pd/Ti/γ–Fe_2O_3 prepared by addition of base to salt and boiling under reflux, showed higher 50 % CO conversion temperature than Pd/Ti/γ–Fe_2O_3. The results indicate that the presence of titanium as opposed to particle size or surface area effects the catalytic activity.

Taken together the results showed that the higher surface area Ti/γ–Fe_2O_3 has enhanced properties of stability, catalytic activity, and OSC, which are essential for an automobile catalyst component.

References

1. C.W. Childs and J.G. Baker-Sherman, "Mössbauer Spectra and Parameters of standard samples.1", New Zealand Scientific Report 66, 1984.
2. N.N Greenwood and T.C Gibb, "Mössbauer Spectroscopy", Chapman and Hall, London, 1971.
3. F.J. Berry "The Mössbauer Effect in Supported Microcrystallites", Advances in Inorganic Chemistry and Radichemistry, vol. 21, Ed. H.J. Emeleus and A.G. Sharpe, Academic Press, 1978.
4. JCPDS Index Card No. 19-0629 (Fe_3O_4).
5. JCPDS Index Card No. 39-1346 (γ–Fe_2O_3).
6. JCPDS Index Card No. 33-0664 (α-Fe_2O_3).

7. G. Svehla (Editor) "Vogel's Textbook of Macro and Semimicro Qualitative Inorganic Analysis", 5th edition, Longman Group Ltd, London, 1979.

8. C. Greaves, *J. Solid State Chem.*, 1983, 49, 325.

9. D.H. Lindsley in "Oxide Minerals", Ed. P.H Ribbe, Mineralogical Society of America, Washington DC, 1976, pL1.

10. D.P. Johnson, *Solid State Commun.*, 1969, 7, 1785.

11. JCPDS Index Card No. 06-0615 (FeO).

12. JCPDS Index Card No. 06-0696 (Fe).

13. Ö. Helgason, H.P. Gunnlaugsson, K. Jonsson and S. Steinthorsson, *Hyperfine Interact.*, 1994, 91, 595.

14. R.M. Taylor and U. Schwertmann, *Clay Mineral*, 1974, 10, 299.

15. F.J. Berry, Ö. Helgason, J. M. Greneche, F. Mosselmans and S. Mørup, unpublished results.

16. R.D. Shannon, *Acta Crystallogr.*, A, 32, 1976, 751.

17. F. J. Berry, C. Greaves, Ö. Helgason and J. McManus. *J. Mater. Chem.*, 1999, 9, 223.

Chapter 5

RESULTS AND DISCUSSION: Fe_3O_4, α–Fe_2O_3 AND RELATED PHASES

Chapter 5

RESULTS AND DISCUSSION:

Fe_3O_4, α-Fe_2O_3 AND RELATED PHASES

5.1. Fe_3O_4

5.1.1 Fe_3O_4 (addition of base to salt, heated hydrothermally and dried under an infrared lamp)

The XRD pattern recorded from the sample prepared hydrothermally and dried under an infrared lamp (Figure 5.1) was similar to that reported for a spinel-related structure[1], with lattice parameter a = 8.378(2) Å which compares with the reported[1] value of a = 8.396 Å for Fe_3O_4. The average particle size calculated from the XRD data was *ca.* 16 nm. Both Fe_3O_4 and γ-Fe_2O_3 have inverse spinel-related structures and are difficult to distinguish by X-ray powder diffraction alone. The ^{57}Fe Mössbauer spectrum (Figure 5.2) showed two sextet patterns with Mössbauer parameters (δ 0.49(2) mms^{-1}, Δ 0.00(2) mms^{-1}, H 44(1) T, δ 0.34(2) mms^{-1}, Δ 0.00(2) mms^{-1}, H 48(1) T) characteristic of Fe_3O_4[2,3].

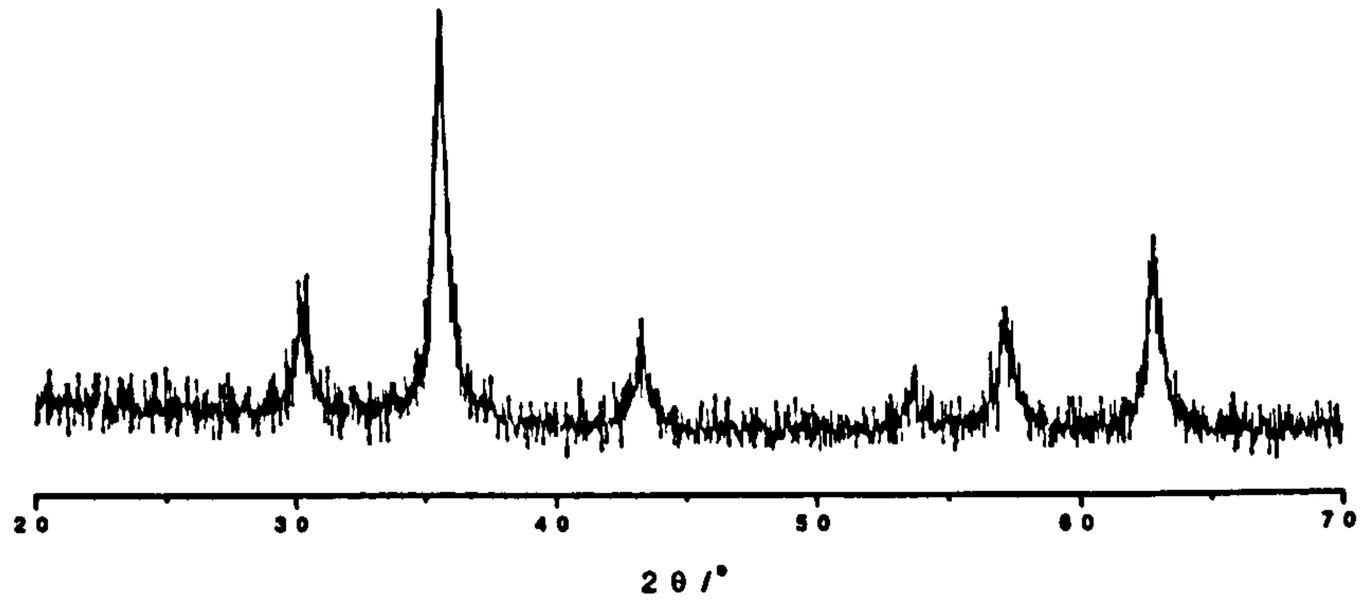

Figure 5.1 XRD pattern recorded from Fe_3O_4 prepared by addition of base to salt, heated hydrothermally and dried under an infrared lamp

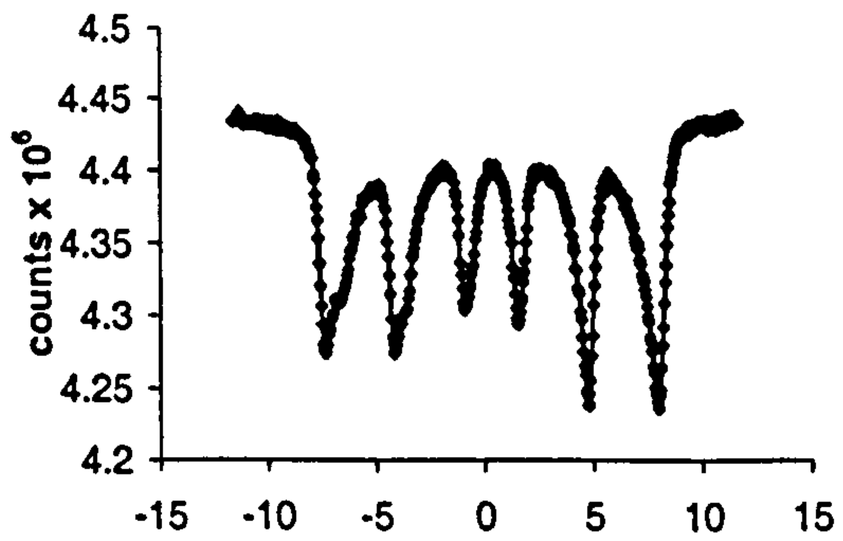

Figure 5.2 ^{57}Fe Mössbauer spectrum recorded from Fe_3O_4 prepared by addition of base to salt, heated hydrothermally and dried under an infrared lamp

The surface area of Fe_3O_4 prepared by addition of base to salt and heated hydrothermally was 99 m^2g^{-1}.

The TPR profile showed three main reduction peaks (310, 700 and 975 °C) (Figure 5.3). The XRD patterns and ^{57}Fe Mössbauer spectra of samples retrieved after each reduction peak from the TPR experiment were recorded *ex situ* and are shown in Figures 5.3 and 5.4 respectively. The ^{57}Fe Mössbauer parameters are summarised in Table 5.1. The XRD pattern and ^{57}Fe Mössbauer spectrum recorded after the first

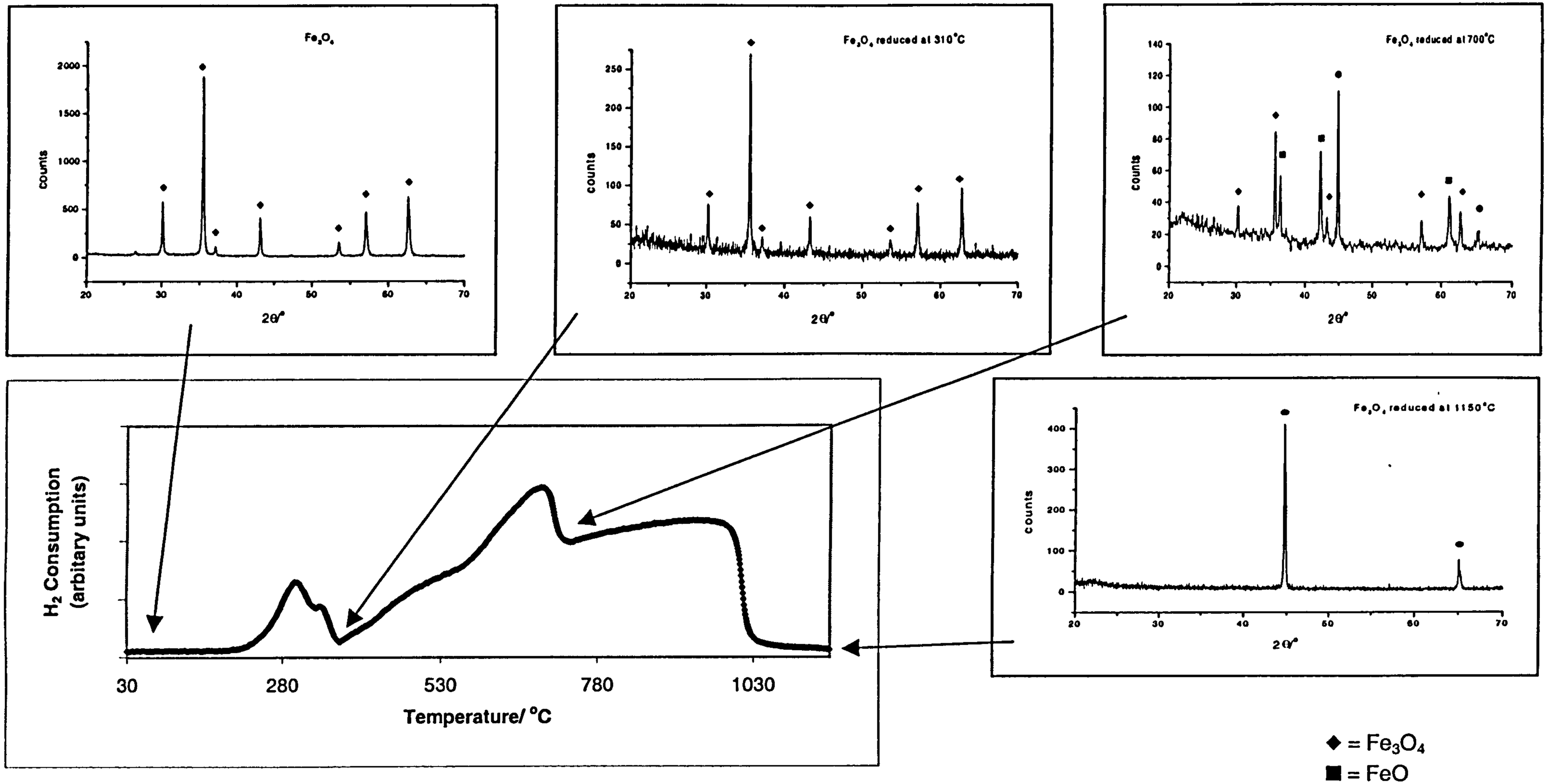

Figure 5.3 TPR profile recorded from Fe_3O_4 prepared by addition of base to salt, heated hydrothermally and dried under an infrared lamp and XRD patterns recorded following each reduction peak

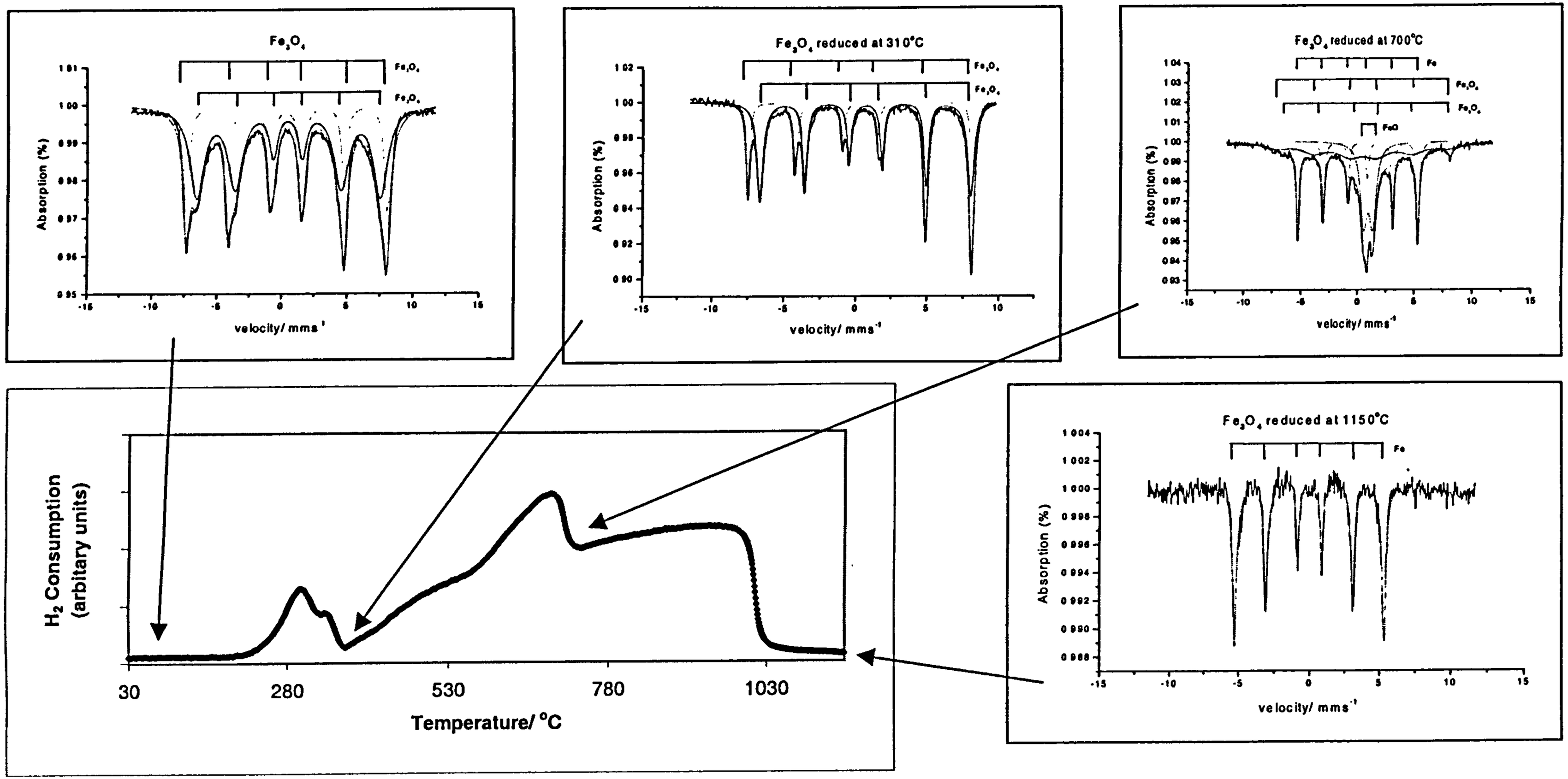

Figure 5.4 TPR profile recorded from Fe_3O_4 prepared by addition of base to salt, heated hydrothermally and dried under an infrared lamp and ^{57}Fe Mössbauer spectra recorded following each reduction peak

reduction peak at *ca.* 310 °C were characteristic of Fe_3O_4. It was shown in Section 4.1.2 that γ–Fe_2O_3 has a reduction peak at *ca.* 350 °C corresponding to its reduction to Fe_3O_4. This may suggests that the first reduction peak is likely to result from a small amount of γ–Fe_2O_3 impurity which is below the level of detectability by XRD and Mössbauer spectroscopy. The Mössbauer spectra of the starting material and the initial reduction product have similar hyperfine fields, but the starting material has broader peaks. The second reduction peak at *ca.* 700 °C corresponded to the partial reduction of magnetite (Fe_3O_4)[1,2,3] to wüstite (FeO)[3,4] and metallic iron (Fe)[3,5]. The complexity of the ^{57}Fe Mössbauer spectra recorded from wüstite has already been discussed (Section 4.1.2). However, the X-ray powder diffraction pattern recorded *ex situ* from Fe_3O_4 after the second reduction peak at *ca.* 700 °C (Figure 5.3) showed the three peaks at *ca.* 37°, 42° and 61° 2θ, which were characteristic of wüstite[4] together with those at *ca.* 30°, 35°, 43°, 57° and 62° 2θ characteristic of Fe_3O_4[1] and at *ca.* 45°, and 65° 2θ, characteristic of metallic iron[5].

The Mössbauer spectrum recorded after the final reduction peak at *ca.* 1150 °C, corresponded to complete reduction of Fe_3O_4 and FeO to metallic iron.

The results show that the reduction of Fe_3O_4 follows two steps:

Step 1		*Step 2*	
Fe_3O_4	**→**	**Fe_3O_4 + FeO + Fe**	**→** **Fe**

Fe_3O_4 therefore follows a similar reduction pathway as that observed for the last two reduction steps of γ–Fe_2O_3 (Section 4.1.2).

Table 5.1 ^{57}Fe Mössbauer parameters recorded from Fe_3O_4 prepared by addition of base to salt, heated hydrothermally, and dried under an infrared lamp following reduction in TPR experiment

Sample	δ (± 0.02) mms^{-1}	Δ (± 0.02) mms^{-1}	H (± 1) T	Interpretation	Area (± 5) %
Fe_3O_4	0.49	0.00	44	Fe_3O_4	100
	0.34	0.00	48	Fe_3O_4	
Fe_3O_4 Reduced at 310 °C	0.68	0.00	46	Fe_3O_4	100
	0.30	0.01	48	Fe_3O_4	
Fe_3O_4 Reduced at 700 °C	0.69	0.01	45	Fe_3O_4	23
	0.29	0.01	48	Fe_3O_4	
	0.94	0.82	---	FeO	41
	0.01	0.01	33	Fe	36
Fe_3O_4 Reduced at 1150 °C	0.02	0.01	33	Fe	100

Conclusion

Fe_3O_4 was prepared hydrothermally by addition of aqueous ammonia to a 1:2 ratio of aqueous Fe(II): Fe(III) solution. The surface area was found to be 99 m^2g^{-1}. The TPR profile showed three reduction peaks. The initial peak is probably due to the reduction of a small amount of γ–Fe_2O_3 impurity to Fe_3O_4. This is followed by further reduction to FeO and metallic iron, similar to the results observed in the TPR profile of γ–Fe_2O_3.

5.1.2 Fe_3O_4 (addition of salt to base, heated hydrothermally and dried under an infrared lamp)

The broad lined XRD pattern recorded from the product formed by the addition of salt to base, heating hydrothermally, and drying under an infrared lamp (Figure 5.5) was similar to that reported for a spinel-related structure, with lattice parameter a = 8.345(2) Å which can be compared with the reported[1] value for Fe_3O_4 a = 8.396 Å and a = 8.378(2) Å for Fe_3O_4 prepared hydrothermally following addition of base to salt formed here. The average particle size calculated from the X-ray powder diffraction linewidth data of *ca.* 17 nm was similar to that for Fe_3O_4 prepared by addition of base to salt and heated hydrothermally (*ca.* 16 nm). The ^{57}Fe Mössbauer spectrum (Figure 5.6) was somewhat different in shape from that which would be expected from Fe_3O_4. The values of the magnetic hyperfine fields were smaller (which would reflect the smaller particle size) and the two sextet patterns, which characterise Fe_3O_4 could not be satisfactorily fitted. It seems likely that the material contains an appreciable amount of γ–Fe_2O_3 and is therefore a mixture of Fe_3O_4 and γ–Fe_2O_3.

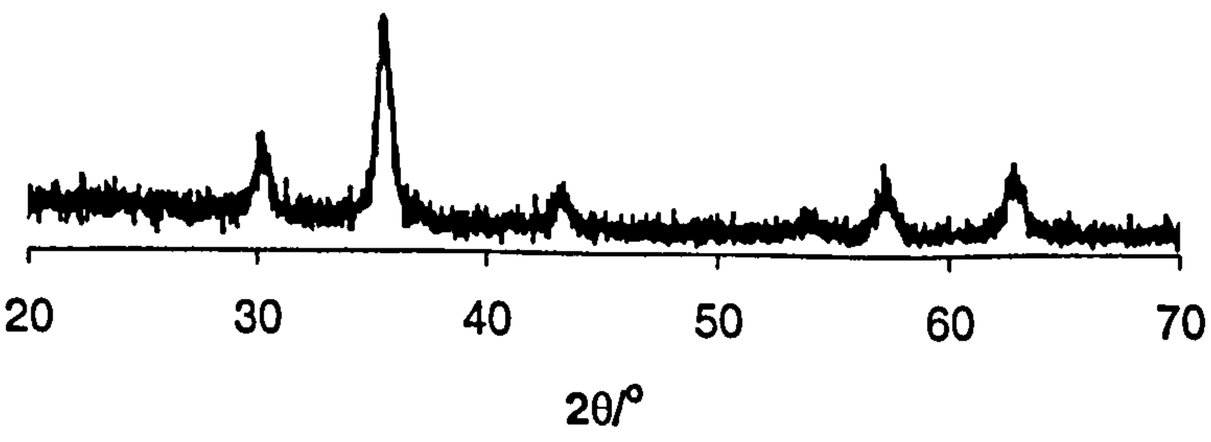

Figure 5.5 XRD pattern recorded from the solid prepared by addition of salt to base, heated hydrothermally, and dried under an infrared lamp

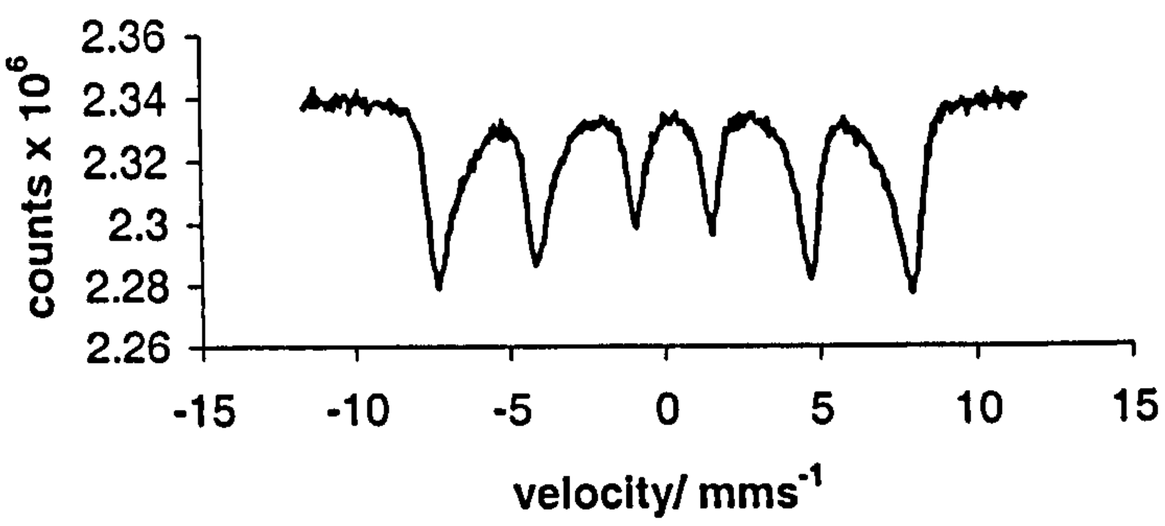

Figure 5.6 ^{57}Fe Mössbauer spectrum recorded from the solid prepared by addition of salt to base, heated hydrothermally, and dried under an infrared lamp

The surface area of the material (79 m^2g^{-1}) was slightly lower than that of Fe_3O_4 prepared by addition of base to salt and heated hydrothermally (99 m^2g^{-1}).

The TPR profile recorded from the material showed three main reduction peaks (320, 690 and 910 °C) (Figure 5.7) and was of similar shape to that recorded from Fe_3O_4 prepared by addition of base to salt, heated hydrothermally, and dried under an infrared lamp (Figure 5.3). The similarity to the TPR profile recorded from γ–Fe_2O_3 prepared by a similar method (Section 4.1.5), especially the enhanced nature of the peak at *ca.* 320 °C, would endorse the notion of a larger amount of γ–Fe_2O_3 impurity in the material. No XRD patterns and ^{57}Fe Mössbauer spectra were recorded after each reduction peak.

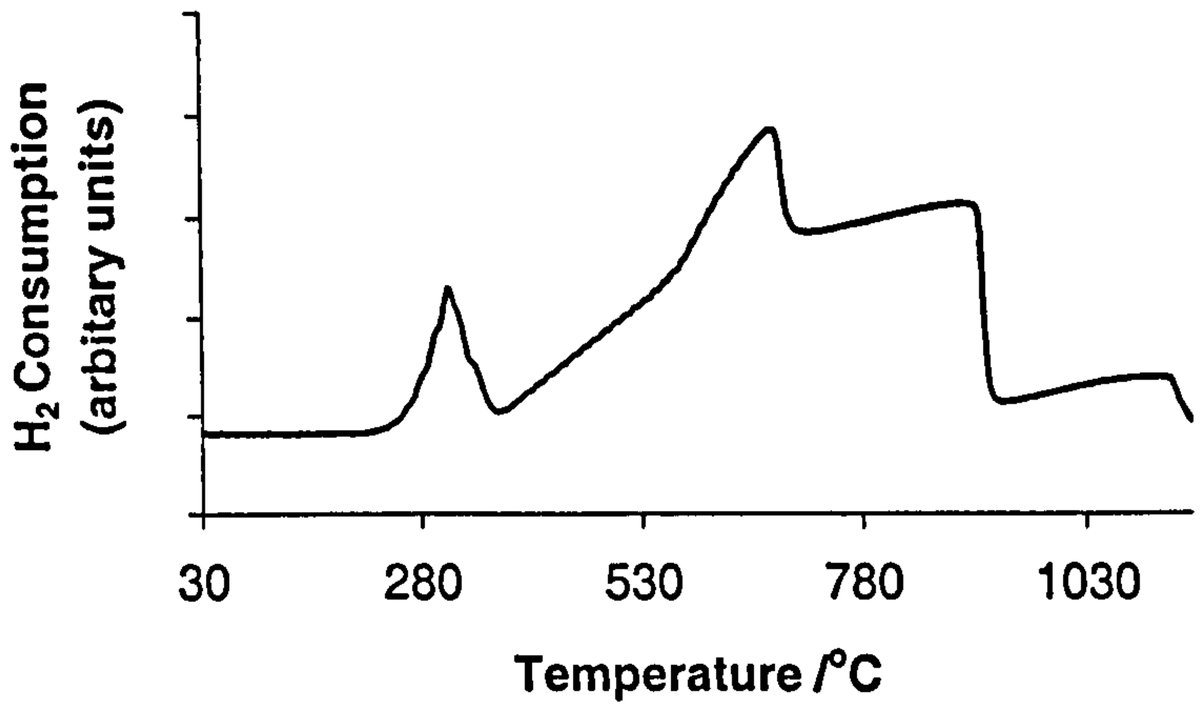

Figure 5.7 TPR profile recorded from the solid prepared by addition of salt to base, heated hydrothermally and dried under an infrared lamp

Conclusion

Fe_3O_4 prepared by addition of salt to base, heated hydrothermally, and dried under an infrared lamp was shown by Mössbauer spectroscopy to contain significant γ–Fe_2O_3 impurity. This was confirmed by an increase in intensity of the initial reduction peak in the TPR profile as compared with the TPR profile of Fe_3O_4 prepared by addition of base to salt.

The metal- doped variants of Fe_3O_4 were prepared hydrothermally by addition of base to salt and dried under an infrared lamp as this method appeared to give higher purity Fe_3O_4 with a high surface area.

5.2. Metal- doped Fe_3O_4

Fe_3O_4 was nominally doped with 8 mass % titanium, tin, ruthenium and magnesium and prepared by addition of base to salt and heated hydrothermally.

5.2.1 Titanium- doped Fe_3O_4 (addition of base to salt, heated hydrothermally, and dried under an infrared lamp)

The X-ray powder diffraction pattern recorded from Ti/Fe_3O_4 nominally prepared with 8 mass % titanium (Figure 5.8) corresponded to a spinel-related structure with lattice parameter a = 8.326(2) Å which compares with the reported[1] value a = 8.396 Å for Fe_3O_4 and a = 8.378(2) Å for Fe_3O_4 prepared here by addition of base to salt and heated hydrothermally. No evidence for a discrete titanium- containing phase was evident in the XRD pattern. Given that, Ti^{4+} has an ionic radius of 0.61 Å, smaller than that of Fe^{3+} (0.65 Å) in octahedral coordination[6], it would be reasonable to observe a decrease in the lattice parameters, although other workers[7,8] have observed an increase in the lattice parameters.

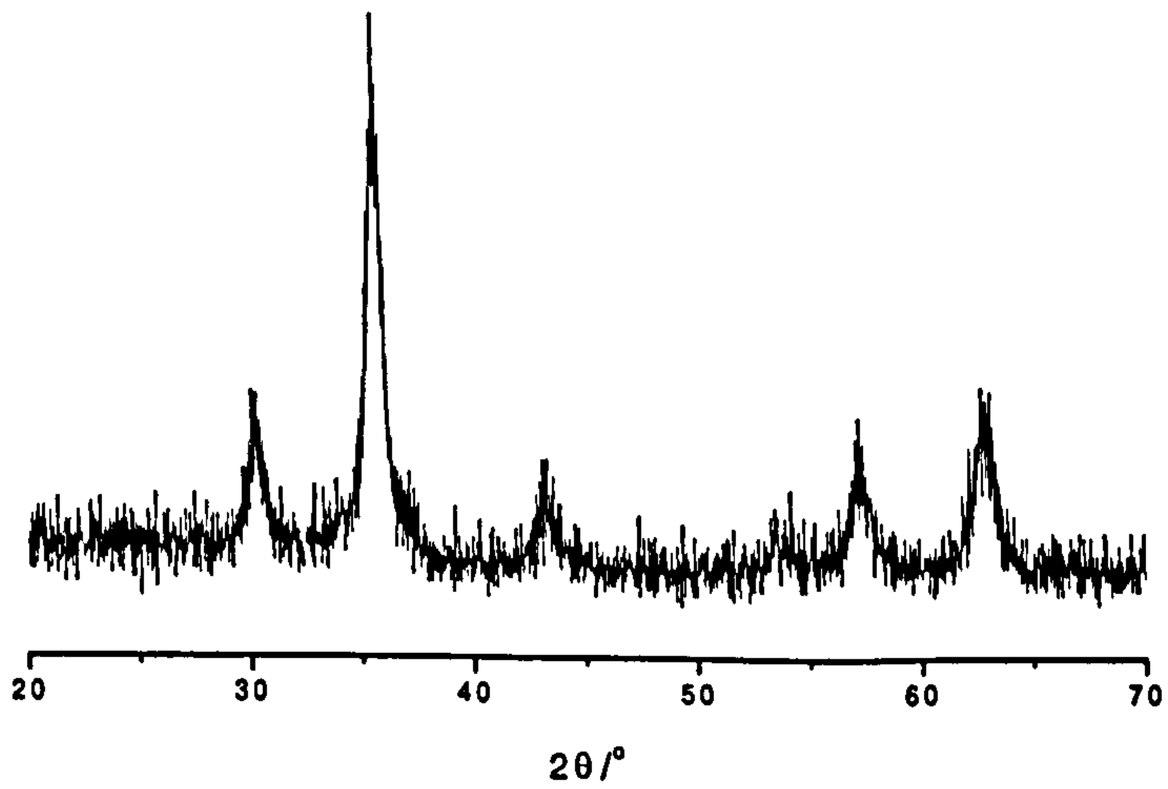

Figure 5.8 XRD pattern recorded from Ti/Fe_3O_4 prepared by addition of base to salt, heated hydrothermally, and dried under an infrared lamp

The ^{57}Fe Mössbauer spectrum (Figure 5.9) showed two sextet patterns with Mössbauer parameters (δ 0.53(2) mms^{-1}, Δ 0.03(2) mms^{-1}, H 43(1) T, δ 0.38(2) mms^{-1}, Δ -0.04(2) mms^{-1}, H 47(1) T) attributed to Fe_3O_4[2,3], and a doublet (δ 0.36(2)

mms^{-1}, Δ 1.05(2) mms^{-1}) accounting for *ca.* 15 % of the spectral area, which was attributed to small particles of iron oxide[9]. The hyperfine field of the sextet component is lower than the literature value[2,3] and the peaks are broad, which reflects the small particle size.

Previous work by Moore et al[10] has shown that M^{4+} (M = Ti and Sn) occupies the octahedral sites in Fe_3O_4 with charge balance being achieved by reduction of Fe^{3+} to Fe^{2+} on a site adjacent to M^{4+}.

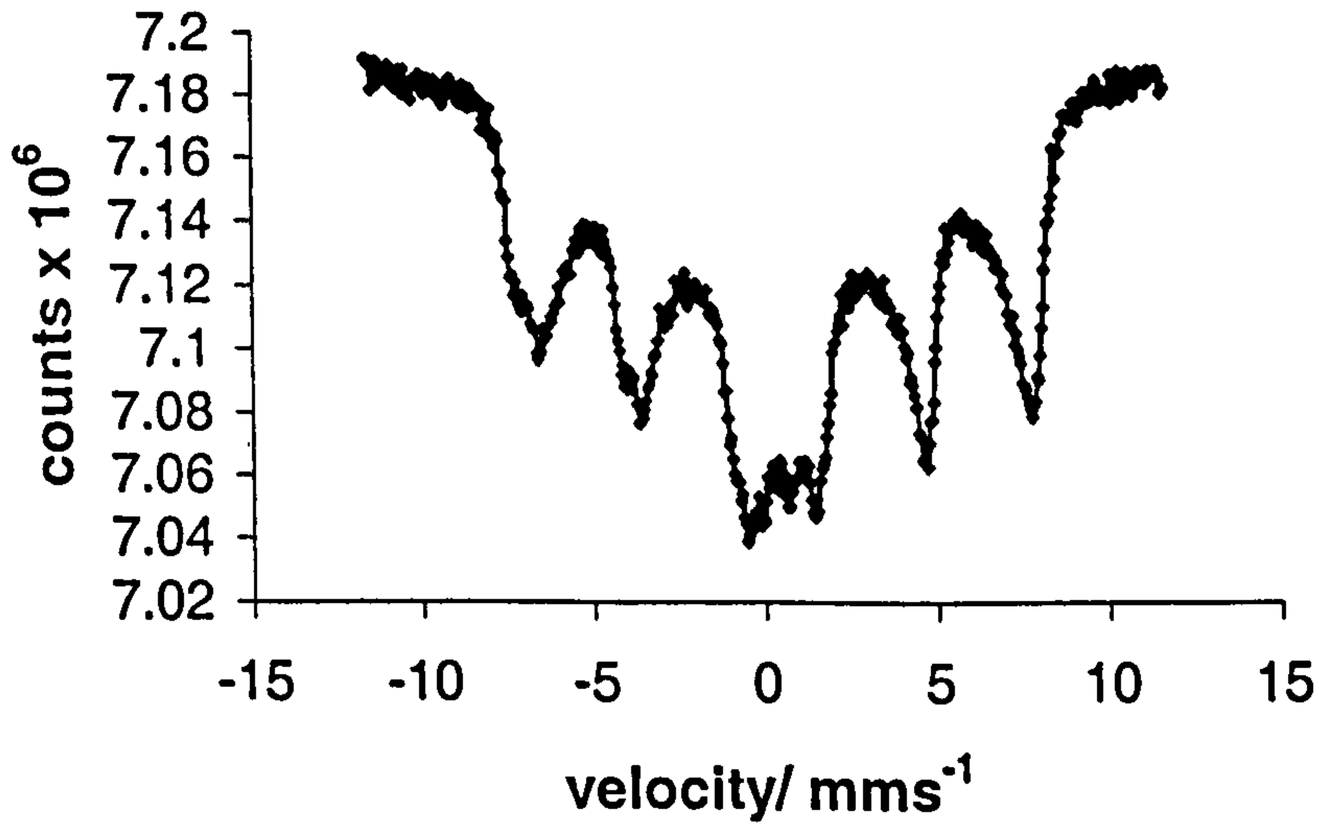

Figure 5.9 ^{57}Fe Mössbauer spectrum recorded from Ti/Fe_3O_4 prepared by addition of base to salt, heated hydrothermally and dried under an infrared lamp

The surface area of Ti/Fe_3O_4 of 120 m^2g^{-1}, was higher then that of Fe_3O_4 prepared by a similar method. The results are consistent with the broad-lined XRD pattern, the doublet observed in the Mössbauer spectrum, and the particle size of 13 nm.

The TPR profile (Figure 5.10) recorded from Ti/Fe_3O_4 showed three main reduction peaks, with the coalescence of the two higher temperature peaks (420, 650-960 °C). The coalescence of the higher temperature peaks suggests that titanium induces

reduction over a larger temperature range. XRD patterns (Figure 5.10) and ^{57}Fe Mössbauer spectra (Figure 5.11, Table 5.2) were recorded *ex situ* after each reduction peak. The results indicate that Ti/Fe_3O_4 follows a similar reduction pathway to that observed for undoped Fe_3O_4 prepared by addition of base to salt and heated hydrothermally and impying the initial reduction of an impurity γ–Fe_2O_3 phase at *ca.* 420 °C. The presence of FeO was not observed in the reduction profile. The final reduction product was metallic iron. The overall result is similar to that recorded from Ti/γ–Fe_2O_3 (Section 4.2.1) and indicates that Ti/Fe_3O_4 is reduced over a larger temperature range.

Table 5.2 ^{57}Fe Mössbauer parameters recorded from Ti/Fe_3O_4 following reduction in TPR experiment

Sample	δ (± 0.02) mms^{-1}	Δ (± 0.02) mms^{-1}	H (± 1) T	Interpretation	Area (± 5) %
Ti/Fe_3O_4	0.36	1.05	---	Small particle iron oxide	15
	0.53	0.03	43	Fe_3O_4	85
	0.38	-0.04	47	Fe_3O_4	
Ti/Fe_3O_4 Reduced at 420 °C	0.42	0.88	---	Small particle iron oxide	43
	0.58	-0.03	44	Fe_3O_4	57
	0.30	0.01	48	Fe_3O_4	
Ti/Fe_3O_4 Reduced at 1150 °C	0.01	0.01	33	Fe	100

Conclusion

Titanium- doped Fe_3O_4 showed a higher surface area (120 m^2g^{-1}) than pure Fe_3O_4 (99 m^2g^{-1}) prepared by a similar method. The effect of titanium on the surface area was similar to that observed when γ–Fe_2O_3 was doped with titanium. The TPR

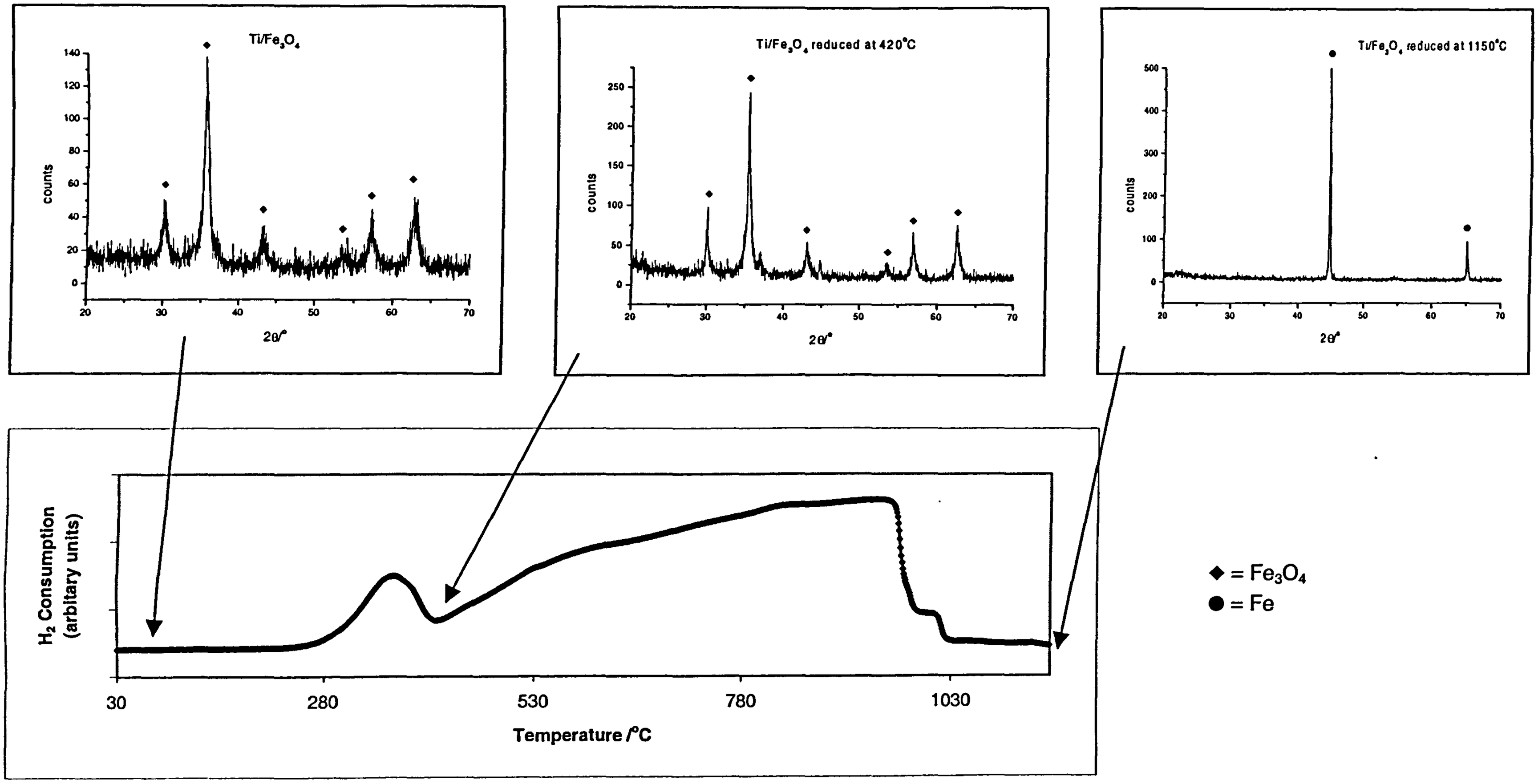

Figure 5.10 TPR profile recorded from Ti/Fe_3O_4 and XRD patterns recorded following each reduction peak

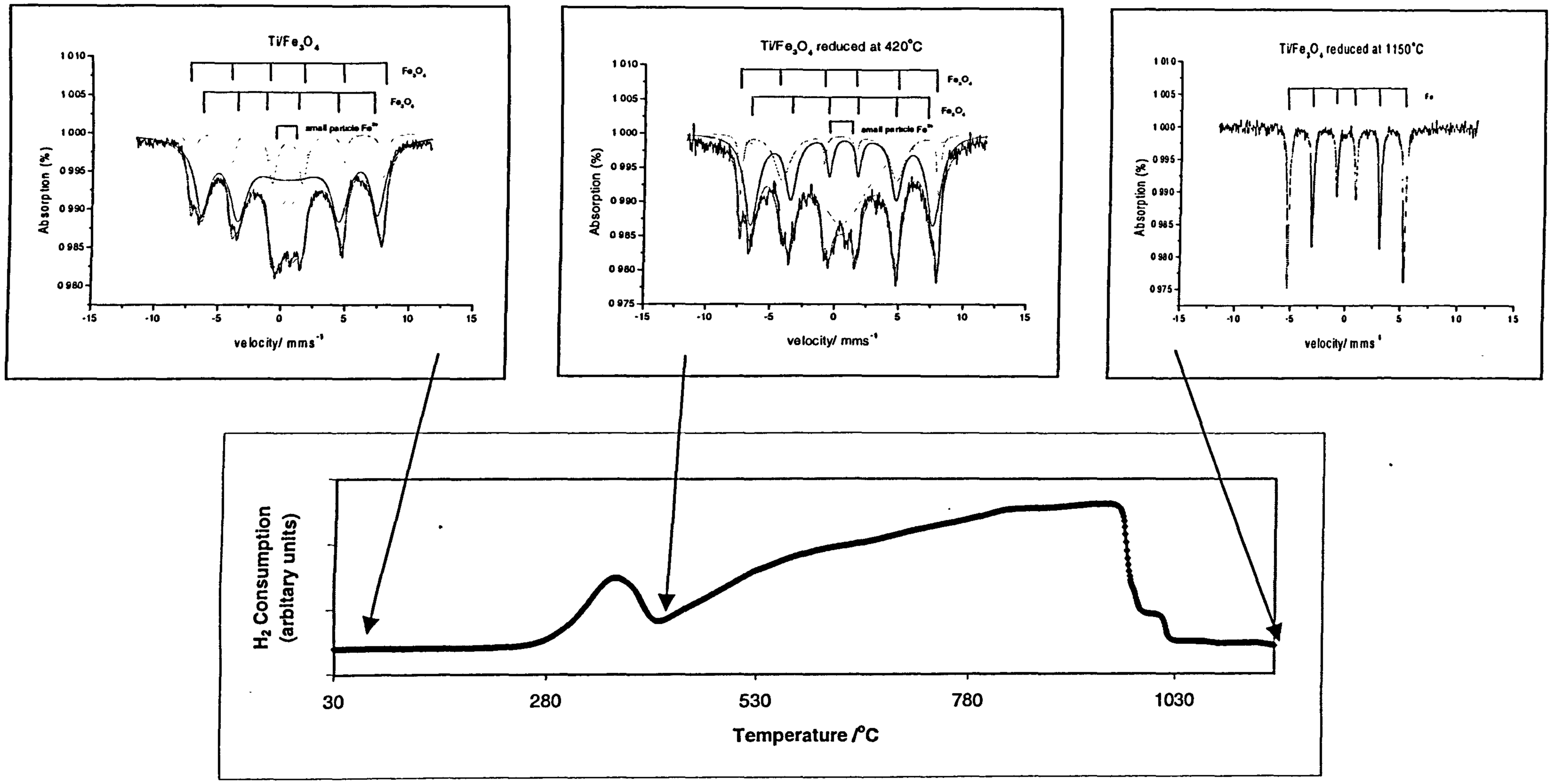

Figure 5.11 TPR profile recorded from Ti/Fe_3O_4 and ^{57}Fe Mössbauer spectra recorded following each reduction peak

profile showed three reduction peaks similar to Fe_3O_4 with the latter two peaks merged, similar to Ti/γ–Fe_2O_3 (Section 4.2.1). No formation of FeO was detected in the reduction pathway.

5.2.2 Tin- doped Fe_3O_4 (addition of base to salt, heated hydrothermally and dried under an infrared lamp)

The X-ray powder diffraction pattern recorded from the material of nominal 8 mass % tin (Figure 5.12) corresponded to that of a spinel-related structure. There was no evidence of a separate tin- containing phase. The lattice parameter of a = 8.452(2) Å was larger than that reported[1] a = 8.396 Å for Fe_3O_4 and a = 8.378(2) Å for Fe_3O_4 prepared here by addition of base to salt and heated hydrothermally.

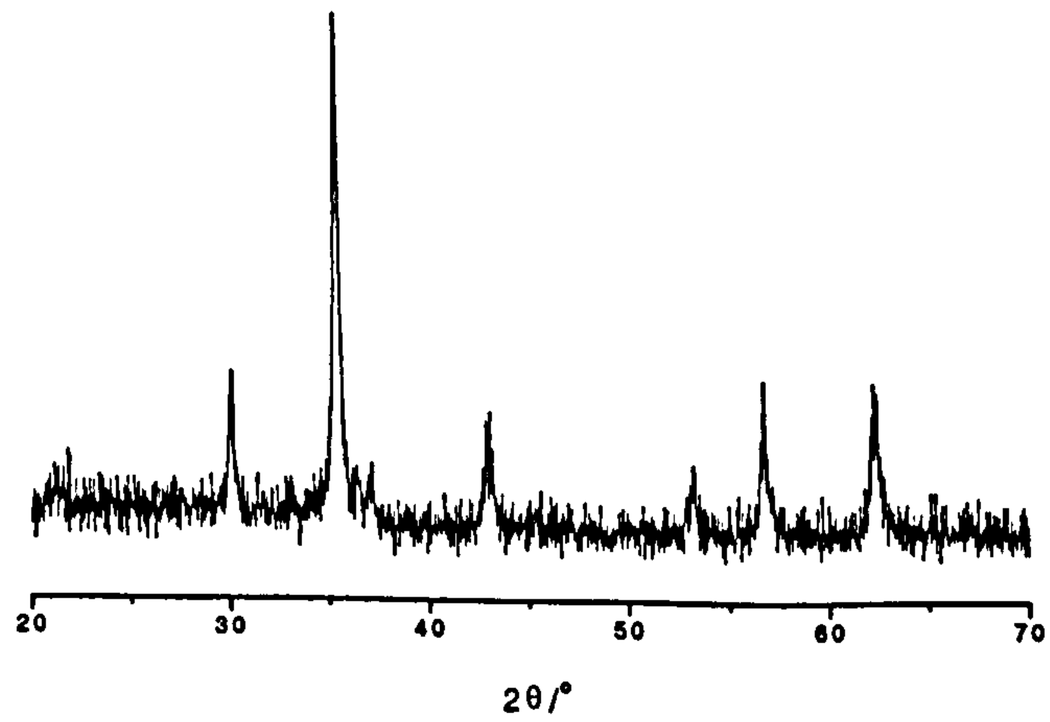

Figure 5.12 XRD pattern recorded from Sn/Fe_3O_4 prepared by addition of base to salt, heated hydrothermally and dried under an infrared lamp

Berry et al[11] showed that the peak positions in the XRD pattern recorded from $Fe_{3-x}Sn_xO_4$ shifted to lower 2θ values indicating an increase in the unit cell size, with increasing incorporation of tin within the Fe_3O_4 structure. The results are consistent with Sn^{4+} ion having a radius of 0.69 Å, as compared to Fe^{3+} (0.65 Å) in six-fold coordination[6].

Tin K-edge Extended X-ray Absorption Fine Structure (EXAFS) has shown that low concentrations of tin in compounds of composition $Fe_{3-x}Sn_xO_4$ ($x < 0.3$) are coordinated by six oxygen atoms[12]. This suggests that tin adopts the octahedral, as opposed to the tetrahedral, sites of the inverse spinel-related structure. X-ray photoelectron spectroscopy (XPS) showed that the incorporation of tin was accompanied by the partial reduction of Fe^{3+} to Fe^{2+} [12].

The ^{57}Fe Mössbauer spectrum (Figure 5.13) showed two sextet patterns with parameters (δ 0.66(2) mms^{-1}, Δ -0.04(2) mms^{-1}, H 45(1) T, δ 0.32(2) mms^{-1}, Δ 0.01(2) mms^{-1}, H 48(1) T). In addition there was a doublet (δ 0.39(2) mms^{-1}, Δ 0.58(2) mms^{-1}) accounting for *ca.* 10 % of the spectral area, which corresponds to small particles of iron- containing oxide[9].

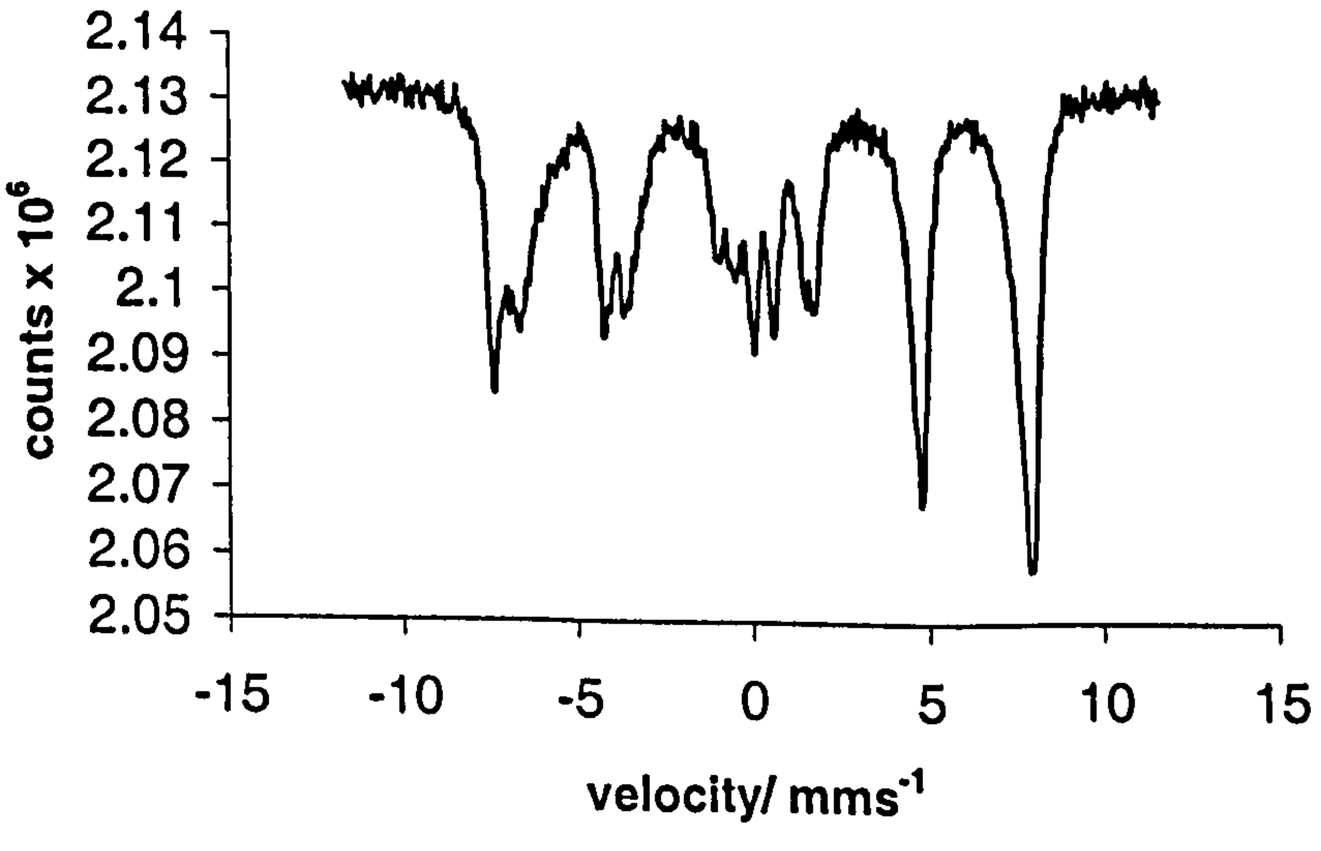

Figure 5.13 ^{57}Fe Mössbauer spectrum recorded from Sn/Fe_3O_4 prepared by addition of base to salt, heated hydrothermally and dried under an infrared lamp

The surface area of Sn/Fe_3O_4 was calculated to be 32 m^2g^{-1}, which is significantly lower than the surface area of undoped Fe_3O_4 (99 m^2g^{-1}) and Ti/Fe_3O_4 (120 m^2g^{-1})

prepared by a similar method. A similar result in terms of the lowering of the surface area was observed when tin was doped into γ–Fe_2O_3 (Section 4.2.2). The surface area measurement is in agreement with the larger particle size of 35 nm calculated from the XRD linewidth data. It is interesting that although Ti^{4+} and Sn^{4+} ions carry the same charge, clearly they have very different effects on the surface area with Ti^{4+} promoting a significant increase in the surface area. The result is similar to that observed in the situation with γ–Fe_2O_3 (Section 4.2) where Ti^{4+} was found to increase the surface area of γ–Fe_2O_3.

The TPR profile (Figure 5.14) recorded from Sn/Fe_3O_4 showed three main reduction peaks (420, 766 and 960 °C), similar to that recorded from undoped Fe_3O_4 prepared by addition of base to salt and heated hydrothermally. The initial peak was broader and was of lower intensity and similar to that observed in the TPR profile of Sn/γ–Fe_2O_3. XRD patterns (Figure 5.14) and ^{57}Fe Mössbauer spectra (Figure 5.15 and Table 5.3) were recorded *ex situ* after each reduction peak. Sn/Fe_3O_4 was found to follow a similar reduction pathway as undoped Fe_3O_4 prepared by addition of base to salt and heated hydrothermally with the formation of FeO being observed after the second reduction peak and which accounted for *ca.* 5 % of the Mössbauer spectral area. Interestingly, FeO was not observed during the reduction of Ti/Fe_3O_4 (Section 5.2.1). Also, the formation of an iron-tin alloy was observed (Figure 5.15, Table 5.3) in the material following reduction at 1150 °C which also contrasts with the final reduction product of Ti/Fe_3O_4. It seems therefore that, despite the similarities of the +4 charge on tin and titanium, the two ions have very different effects on the surface area and reducibility of Fe_3O_4.

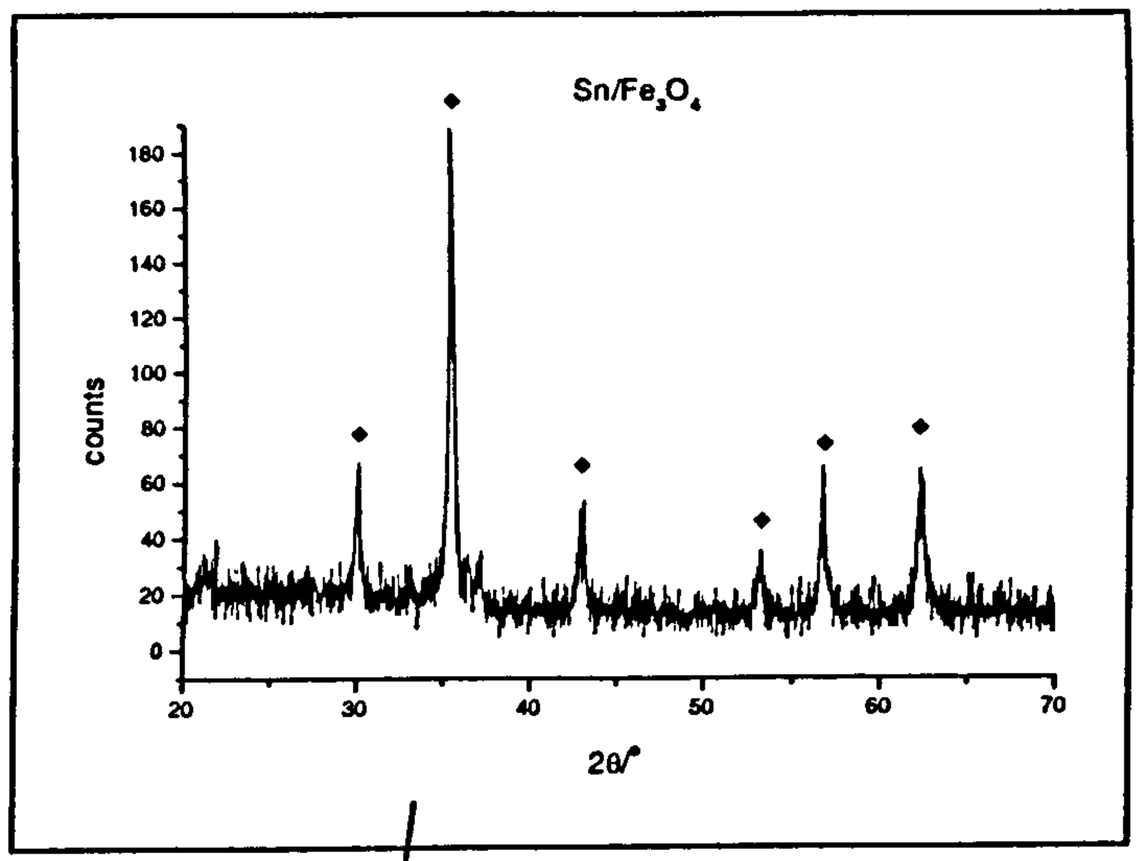

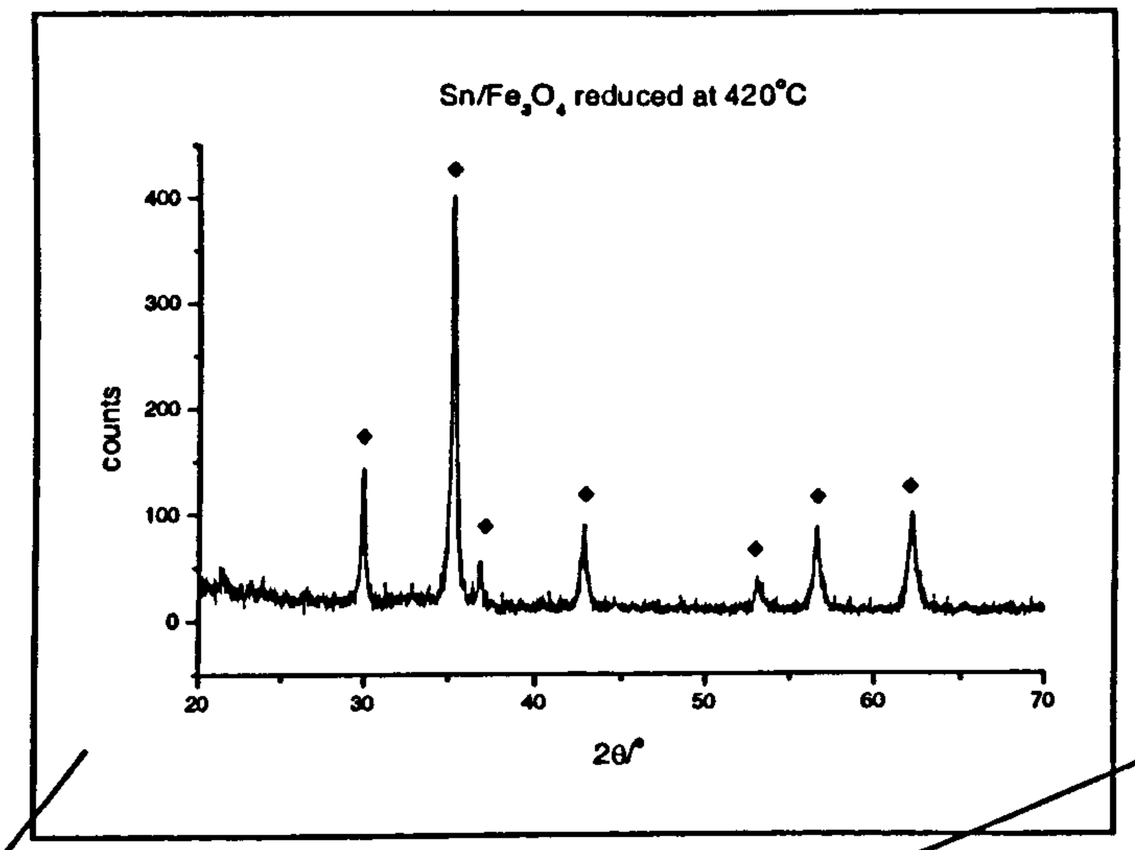

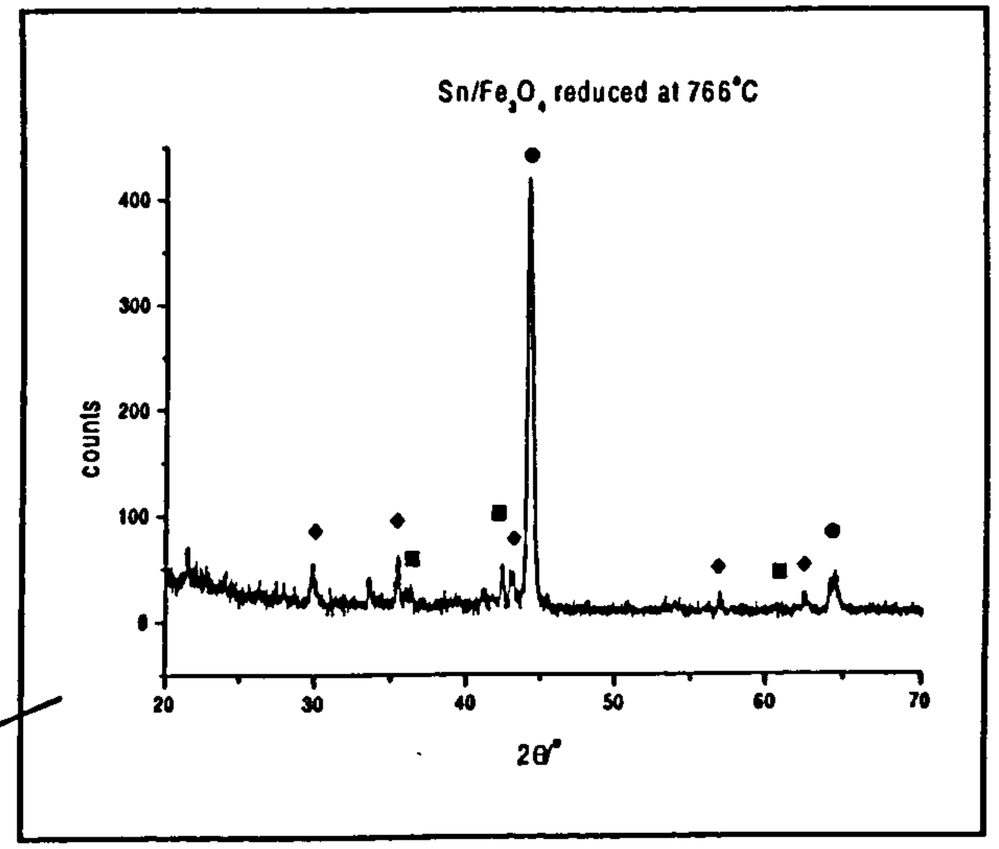

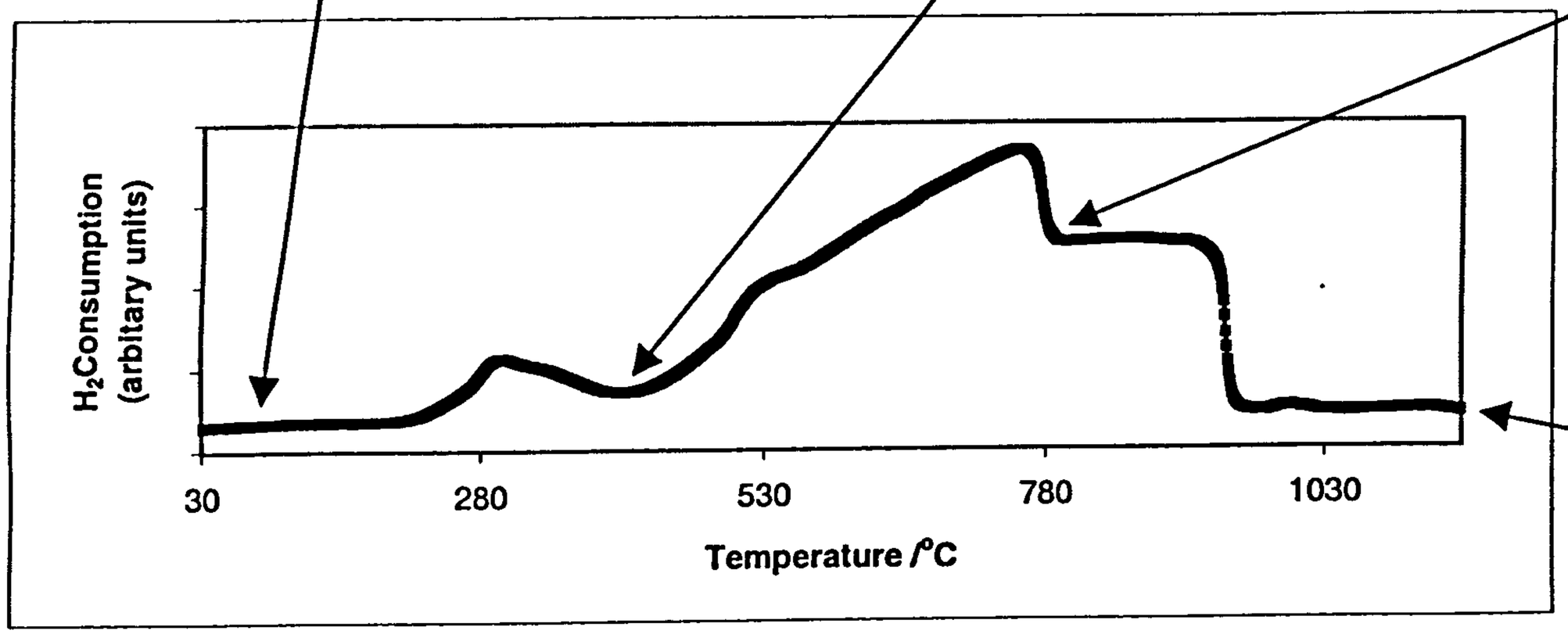

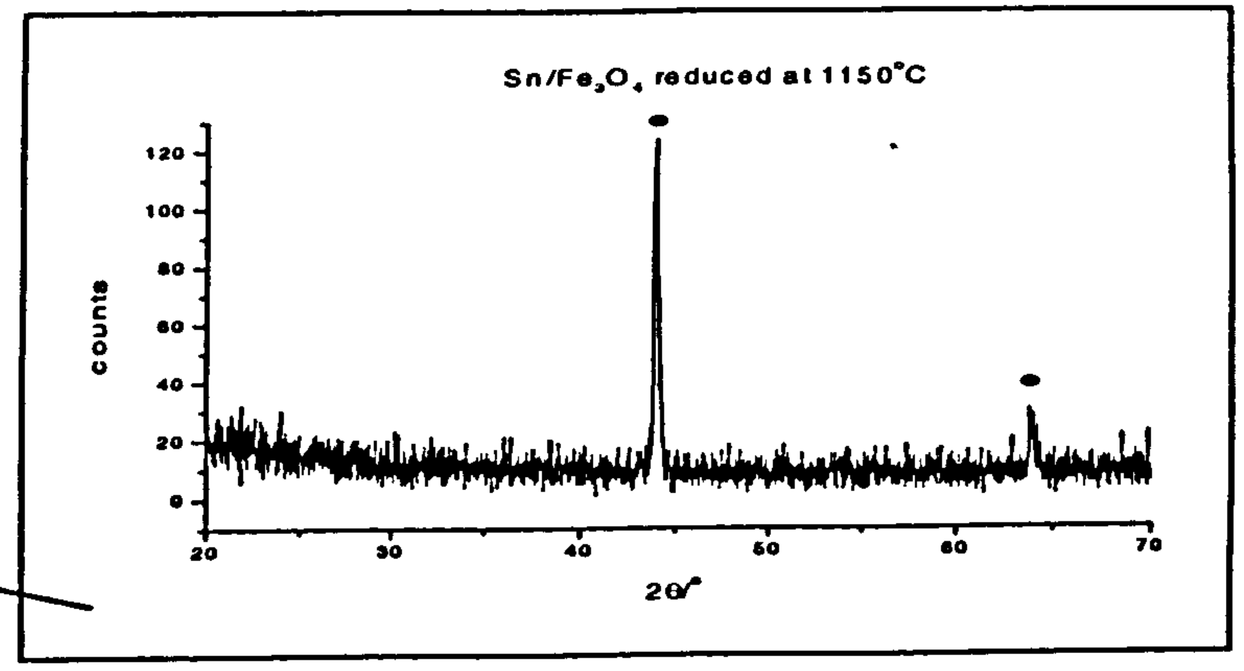

◆ = Fe_3O_4
■ = FeO
● = Fe

Figure 5.14 TPR profile recorded from Sn/Fe_3O_4 and XRD patterns recorded following each reduction peak

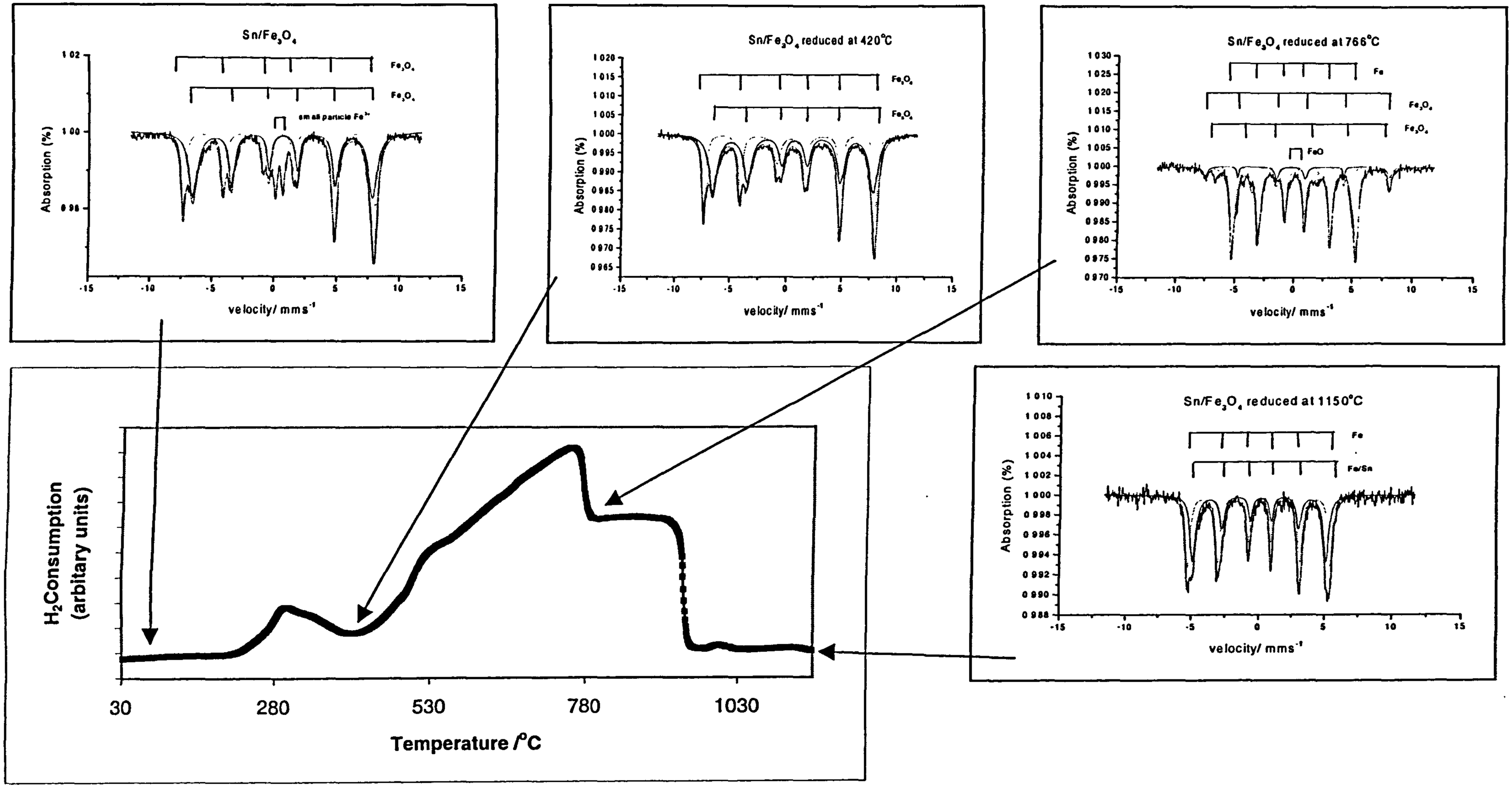

Figure 5.15 TPR profile recorded from Sn/Fe_3O_4 and ^{57}Fe Mössbauer spectra recorded following each reduction peak

Table 5.3 ^{57}Fe Mössbauer parameters recorded from Sn/Fe_3O_4 following reduction in TPR experiment

Sample	δ (± 0.02) mms^{-1}	Δ (± 0.02) mms^{-1}	H (± 1) T	Interpretation	Area (± 5) %
Sn/Fe_3O_4	0.39	0.58	---	Small particle iron oxide	10
	0.66	-0.04	45	Fe_3O_4	90
	0.32	0.01	48	Fe_3O_4	
Sn/Fe_3O_4 Reduced at 420 °C	0.63	-0.03	44	Fe_3O_4	100
	0.31	0.00	48	Fe_3O_4	
Sn/Fe_3O_4 Reduced at 766 °C	0.67	0.05	46	Fe_3O_4	20
	0.29	-0.05	48	Fe_3O_4	
	1.53	0.79	---	FeO	5
	0.03	0.00	33	Fe	75
Sn/Fe_3O_4 Reduced at 1150 °C	0.06	0.01	33	Fe	93
	0.28	0.01	29	Fe/Sn	7

Conclusion

Tin- doped Fe_3O_4 showed an increase in the lattice parameters, due to Sn^{4+} having a larger radius (0.69 Å) than Fe^{3+} (0.65 Å). The surface area was found to be 32 m^2g^{-1}, significantly lower than Fe_3O_4 (99 m^2g^{-1}) and titanium- doped Fe_3O_4 (120 m^2g^{-1}) prepared by a similar method. The TPR profile showed three reduction peaks similar to Fe_3O_4. The formation of FeO and iron-tin alloy was detected in the reduction profile, similar to the situation observed following reduction of Sn/γ–Fe_2O_3 (Section 4.2.2).

5.2.3 Ruthenium- doped Fe_3O_4 (addition of base to salt, heated hydrothermally and dried under an infrared lamp)

The X-ray powder diffraction pattern recorded from the material nominally containing 8 mass % ruthenium (Figure 5.16) corresponded to a single spinel-related phase with lattice parameter a = 8.375(2) Å which compared with the reported[1] value a = 8.396 Å for Fe_3O_4 and a = 8.378(2) Å for Fe_3O_4 prepared by addition of base to salt formed here. There was no evidence in the XRD pattern for a separate ruthenium- containing phase. Ru^{4+} has a radius[6] of 0.62 Å, slightly smaller than Fe^{3+} (0.65 Å), hence a small lowering of the lattice parameters would be expected.

The ^{57}Fe Mössbauer spectrum (Figure 5.17) showed two sextet patterns with Mössbauer parameters (δ 0.42(2) mms^{-1}, Δ 0.02(2) mms^{-1}, H 43(1) T, δ 0.34(2) mms^{-1}, Δ 0.01(2) mms^{-1}, H 48(1) T) related to Fe_3O_4[2,3] (H = 46 T, 49 T). In addition there was a doublet (δ 0.33(2) mms^{-1}, Δ 0.78(2) mms^{-1}) accounting for *ca.* 9 % of the spectral area, which corresponds to small particles of iron oxide[9]. The hyperfine magnetic field is slightly lower than the literature values[2,3] and the peaks are broad, which is probably due to the small particles.

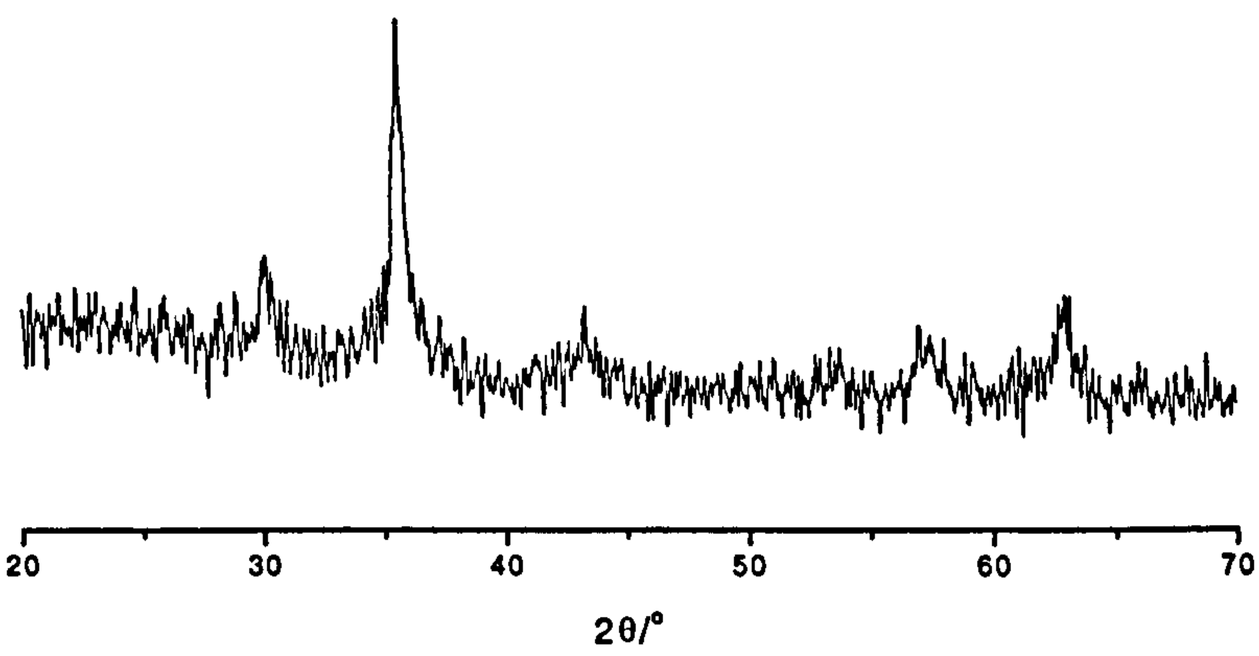

Figure 5.16 XRD pattern recorded from Ru/Fe_3O_4 prepared by addition of base to salt, heated hydrothermally and dried under an infrared lamp

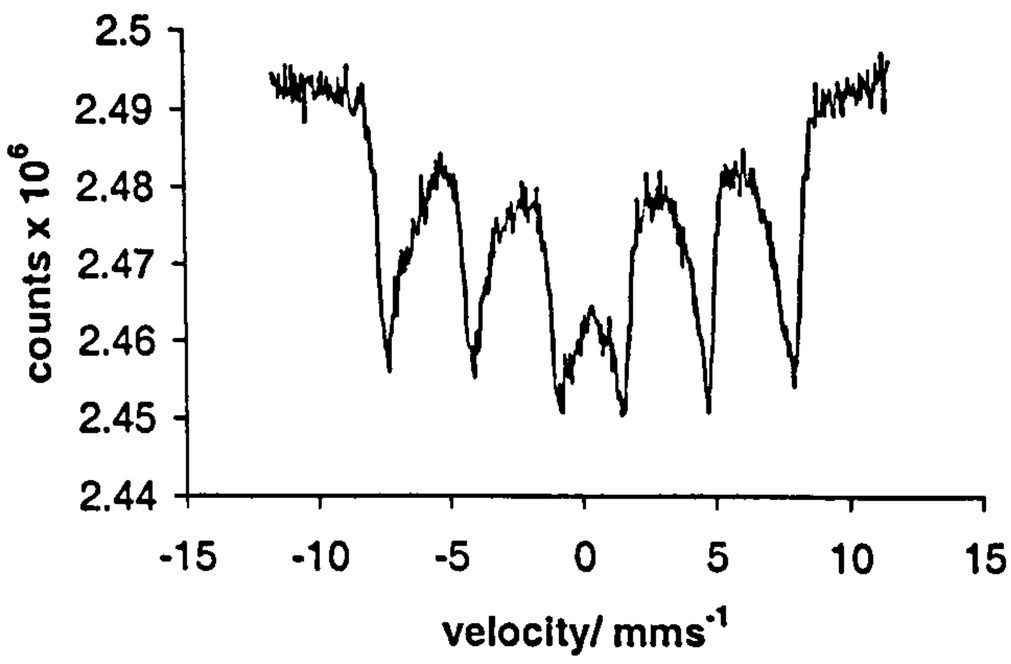

Figure 5.17 ^{57}Fe Mössbauer spectrum recorded from Ru/Fe_3O_4 prepared by addition of base to salt, heated hydrothermally and dried under an infrared lamp

The surface area of Ru/Fe_3O_4 of 112 m^2g^{-1}, was slightly higher than the surface area of undoped Fe_3O_4 prepared by a similar method (99 m^2g^{-1}) and higher than Sn/Fe_3O_4 (32 m^2g^{-1}), but smaller than that of Ti/Fe_3O_4 (120 m^2g^{-1}). An increase in surface area was also observed for Ru/γ–Fe_2O_3. The particle size was found to be *ca.* 27 nm from XRD linewidth data. The increase in surface area does not agree with the particle size measurement which also increased as compared to undoped Fe_3O_4. The increase

in surface area may be due to amorphous RuO_2 which was not detected in the XRD pattern.

The TPR profile (Figure 5.18) recorded from Ru/Fe_3O_4 showed three main reduction peaks (300, 740 and 850 °C), similar to that recorded from undoped Fe_3O_4 and tin- and titanium- doped Fe_3O_4 prepared by addition of base to salt, heated hydrothermally, and dried under an infrared lamp. An additional peak at *ca.* 190 °C was also observed probably due to RuO_2 reduction. XRD patterns (Figure 5.18) and ^{57}Fe Mössbauer spectra (Figure 5.19 and Table 5.4) have been recorded *ex situ* after each reduction peak and the results show that the material follows a similar reduction pathway to that for undoped Fe_3O_4 prepared by addition of base to salt and heated hydrothermally. Ru/Fe_3O_4 showed the production of FeO after the second reduction peak which accounted for less than 5% of the spectral area of the Mössbauer spectrum, and which was not observed for titanium- doped Fe_3O_4. The small amount of FeO was not detected in the XRD pattern. The formation of iron-ruthenium alloy was not detected as observed in the reduced product of Sn/Fe_3O_4 which contain an iron-tin alloy.

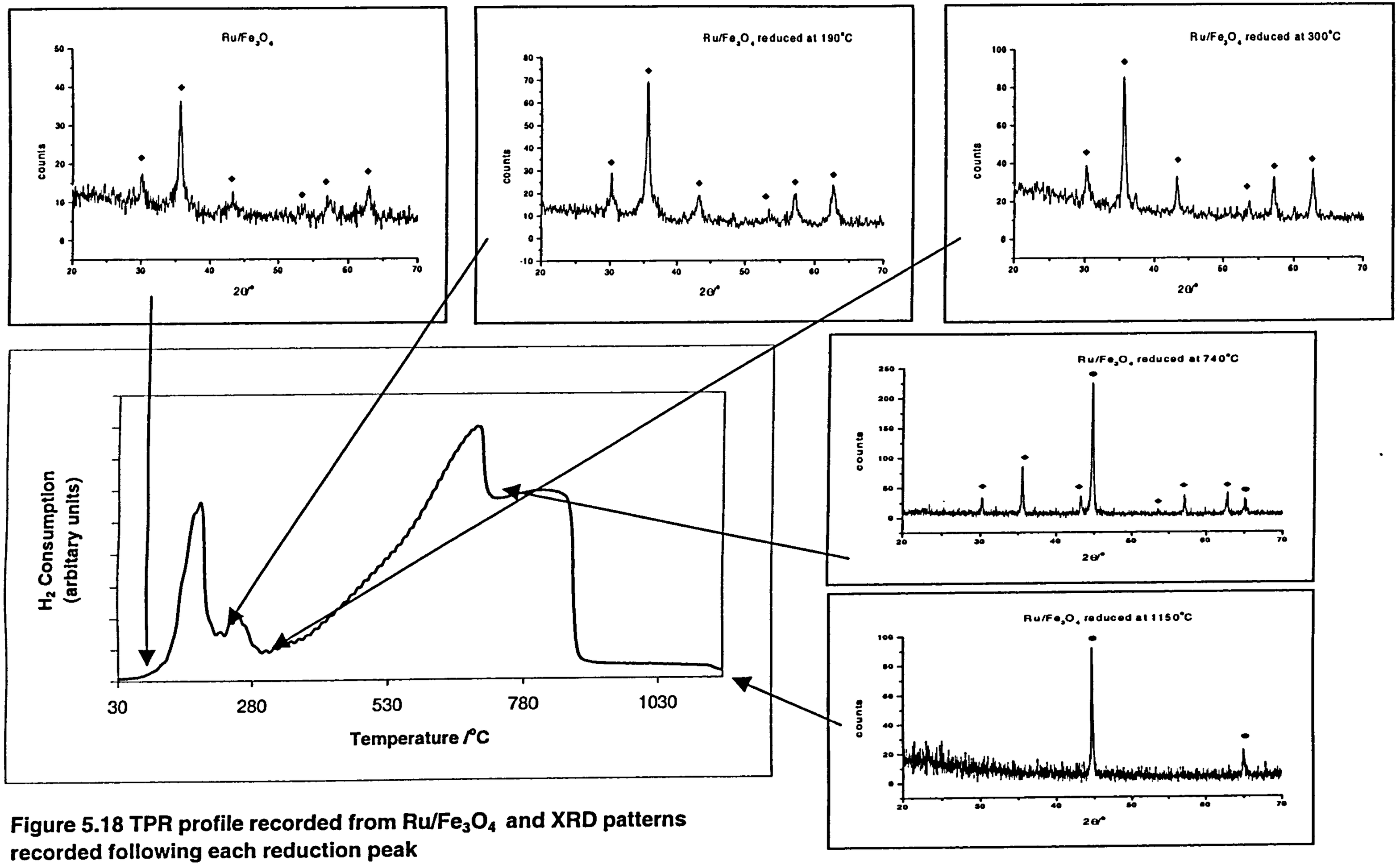

Figure 5.18 TPR profile recorded from Ru/Fe_3O_4 and XRD patterns recorded following each reduction peak

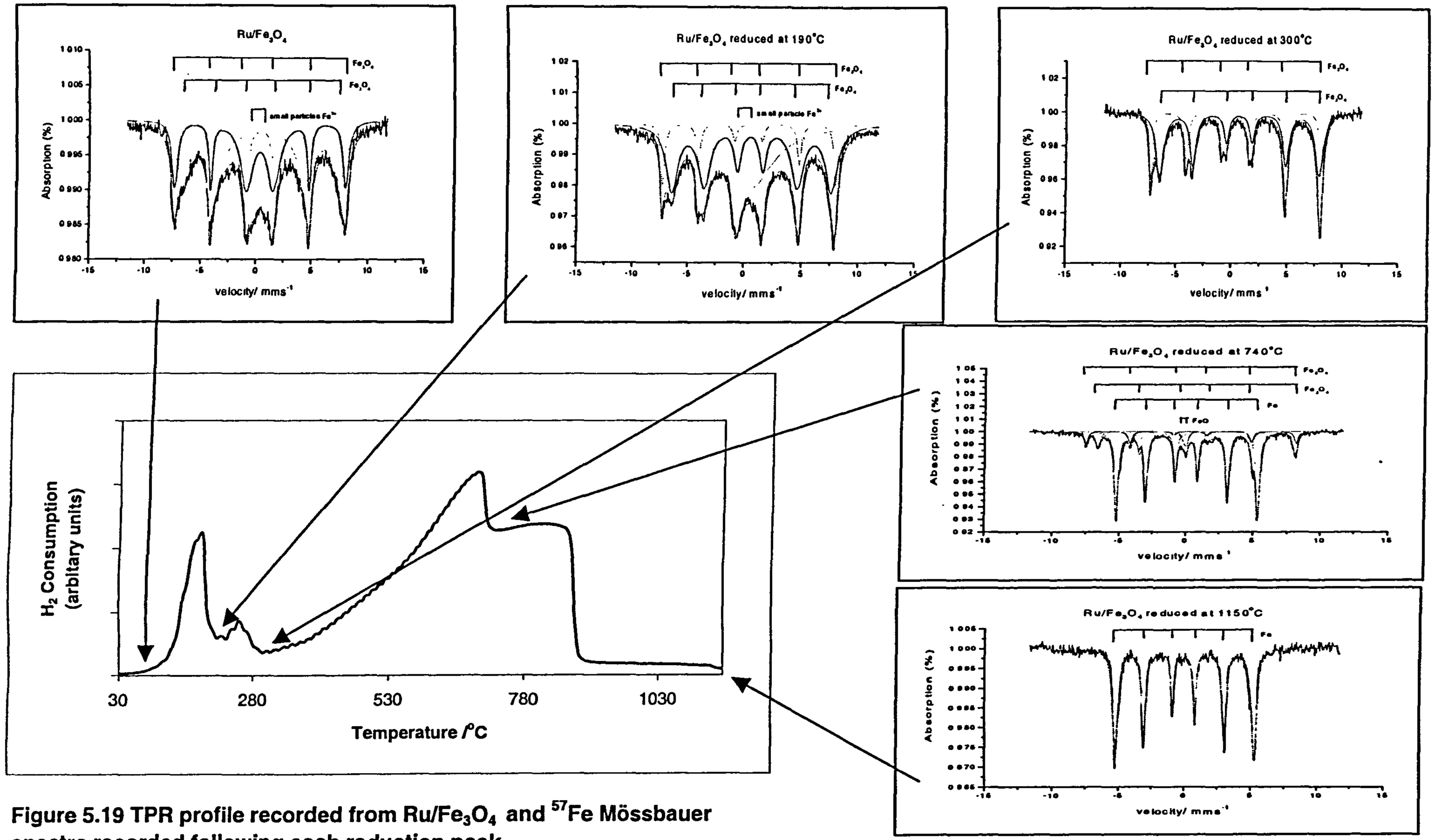

Figure 5.19 TPR profile recorded from Ru/Fe_3O_4 and ^{57}Fe Mössbauer spectra recorded following each reduction peak

Table 5.4 ^{57}Fe Mössbauer parameters recorded from Ru/Fe_3O_4 following reduction in TPR experiment

Sample	δ (± 0.02) mms^{-1}	Δ (± 0.02) mms^{-1}	H (± 1) T	Interpretation	Area (± 5) %
Ru/Fe_3O_4	0.33	0.78	---	Small particle iron oxide	9
	0.42	0.02	43	Fe_3O_4	91
	0.34	0.01	48	Fe_3O_4	
Ru/Fe_3O_4 Reduced at 190 °C	0.37	0.87	---	Small particle iron oxide	39
	0.52	0.02	43	Fe_3O_4	61
	0.31	-0.01	47	Fe_3O_4	
Ru/Fe_3O_4 Reduced at 300 °C	0.62	-0.01	45	Fe_3O_4	100
	0.30	0.00	48	Fe_3O_4	
Ru/Fe_3O_4 Reduced at 740 °C	0.67	0.00	45	Fe_3O_4	29
	0.29	0.00	49	Fe_3O_4	
	-0.09	0.18	---	FeO	<5
	0.01	0.01	33	Fe	68
Ru/Fe_3O_4 Reduced at 1150 °C	0.02	0.01	33	Fe	100

Conclusion

Ruthenium- doped Fe_3O_4 showed an increase in the surface area (112 m^2g^{-1}) similar to Ti/Fe_3O_4 (120 m^2g^{-1}). The TPR profile showed four reduction peaks, the initial peak is probably due to the reduction of ruthenium dioxide, which may have been present as an amorphous phase, and therefore not detected by XRD. Ruthenium has a +4 charge as does Ti^{4+} and Sn^{4+}. Although Ru/Fe_3O_4 has a surface area more similar to that of Ti/Fe_3O_4, its reduction pathway is more similar to Sn/Fe_3O_4.

5.2.4 Magnesium- doped Fe_3O_4 (addition of base to salt, heated hydrothermally and dried under an infrared lamp)

The X-ray powder diffraction pattern recorded from the material nominally containing 8 mass % magnesium (Figure 5.20) corresponded to that of a spinel-related structure with lattice parameter a = 8.388(2) Å which compared with the reported[1] value a = 8.396 Å for Fe_3O_4 and a = 8.378(2) Å for Fe_3O_4 prepared here by addition of base to salt. There was no evidence of a separate magnesium- containing phase. The lattice parameter was slightly larger than that of undoped Fe_3O_4 prepared by a similar method and reflects the larger size of Mg^{2+} of 0.72 Å in six-fold coordination[6], as compared to a radius of 0.65 Å for Fe^{3+}, but smaller then Fe^{2+} (0.78 Å). $MgFe_2O_4$ [13] also has a spinel- related structure with lattice parameter a = 8.375 Å.

The ^{57}Fe Mössbauer spectrum (Figure 5.21) showed two sextet patterns with Mössbauer parameters (δ 0.52(2) mms^{-1}, Δ -0.01(2) mms^{-1}, H 43(1) T, δ 0.32(2) mms^{-1}, Δ 0.01(2) mms^{-1}, H 46(1) T) which can be associated with a spinel- related structure of Fe_3O_4[2,3] (H = 46 T, 49 T). $MgFe_2O_4$ gives a ^{57}Fe Mössbauer spectrum containing only one sextet with magnetic hyperfine field H = 50 T [3].

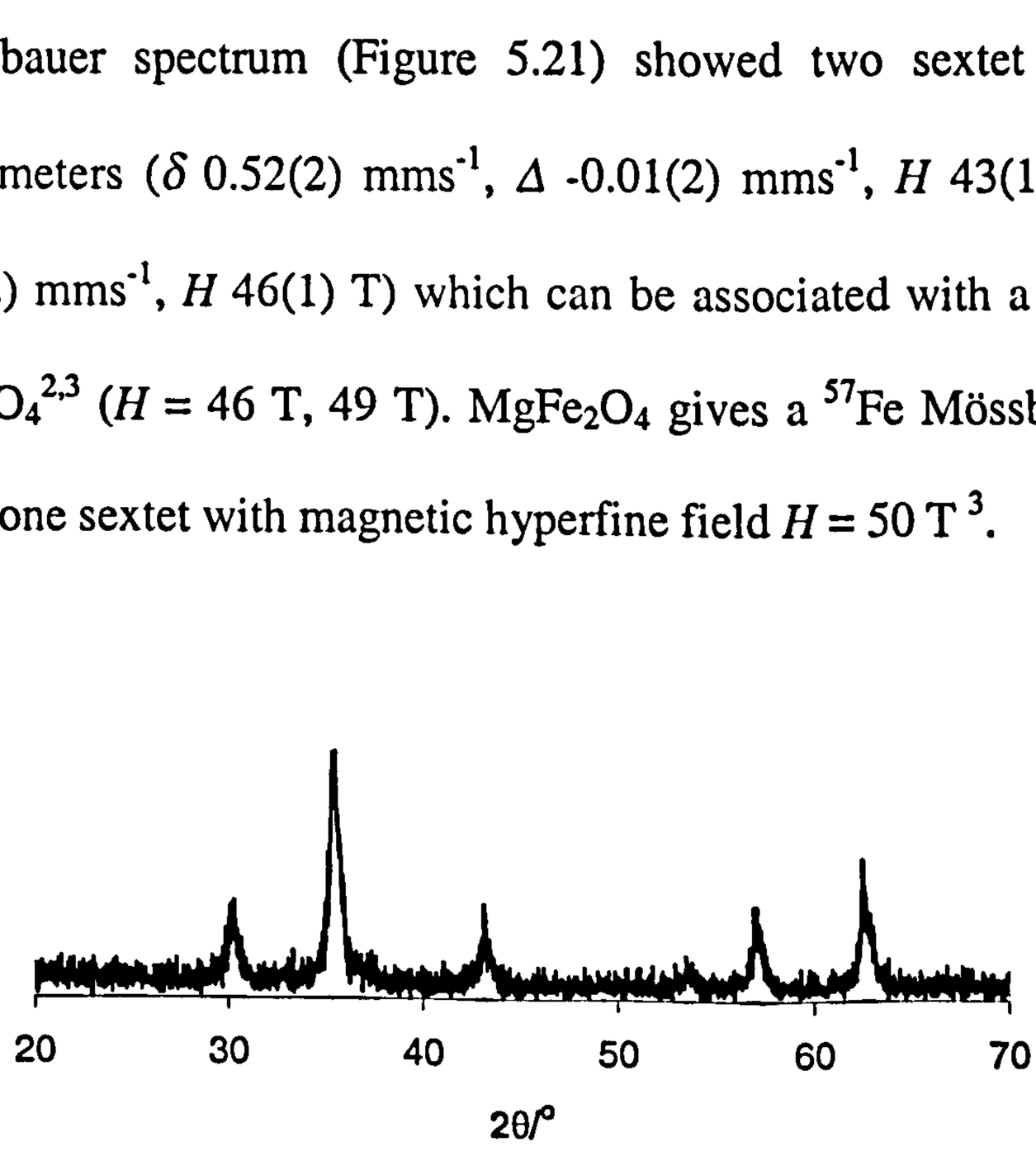

Figure 5.20 XRD pattern recorded from Mg/Fe_3O_4 prepared by addition of base to salt, heated hydrothermally and dried under an infrared lamp

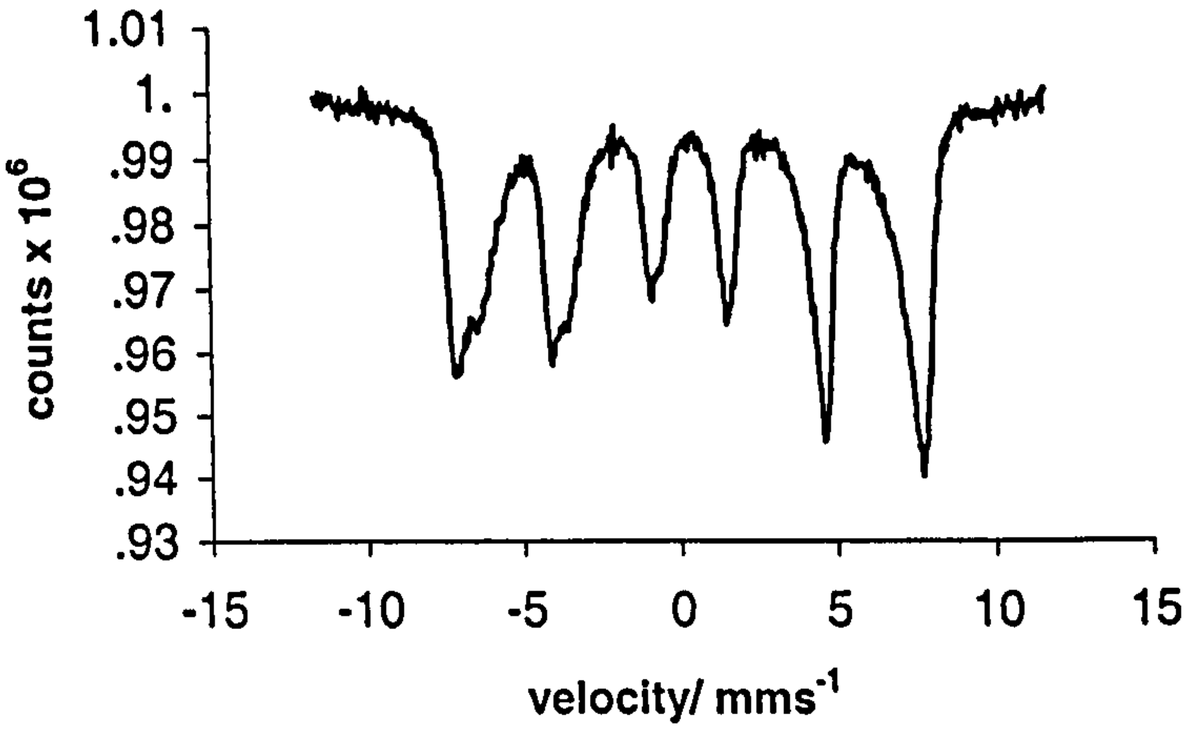

Figure 5.21 ^{57}Fe Mössbauer spectrum recorded from Mg/Fe_3O_4 prepared by addition of base to salt, heated hydrothermally and dried under an infrared lamp

The surface area of Mg/Fe_3O_4 of 72 m^2g^{-1}, was lower than the surface area of Fe_3O_4 (99 m^2g^{-1}), titanium- and ruthenium- doped Fe_3O_4 (120 and 112 m^2g^{-1}), but higher then Sn/Fe_3O_4 (32 m^2g^{-1}).

The TPR profile (Figure 5.22) recorded from Mg/Fe_3O_4 showed three main reduction peaks (300, 740 and 870 °C), similar to that recorded from undoped Fe_3O_4 and tin-doped Fe_3O_4. The XRD patterns (Figure 5.22) and ^{57}Fe Mössbauer spectra (Figure 5.23 and Table 5.5) recorded *ex situ* after each reduction peak showed that Mg/Fe_3O_4 follows a similar reduction pathway to Fe_3O_4 and their metal- doped variants. Mg/Fe_3O_4 showed the formation of FeO after the second reduction peak, similar to undoped Fe_3O_4 and tin- and ruthenium- doped Fe_3O_4, but which was not observed in titanium- doped Fe_3O_4. It is also notable that, after the reduction at 740 °C their was no evidence of a spinel- related phase and it seems that Fe_3O_4 reduces completely to FeO (*ca.* 62 %) and metallic iron (*ca.* 38 %) at 740 °C in hydrogen. The final reduction product is to metallic iron.

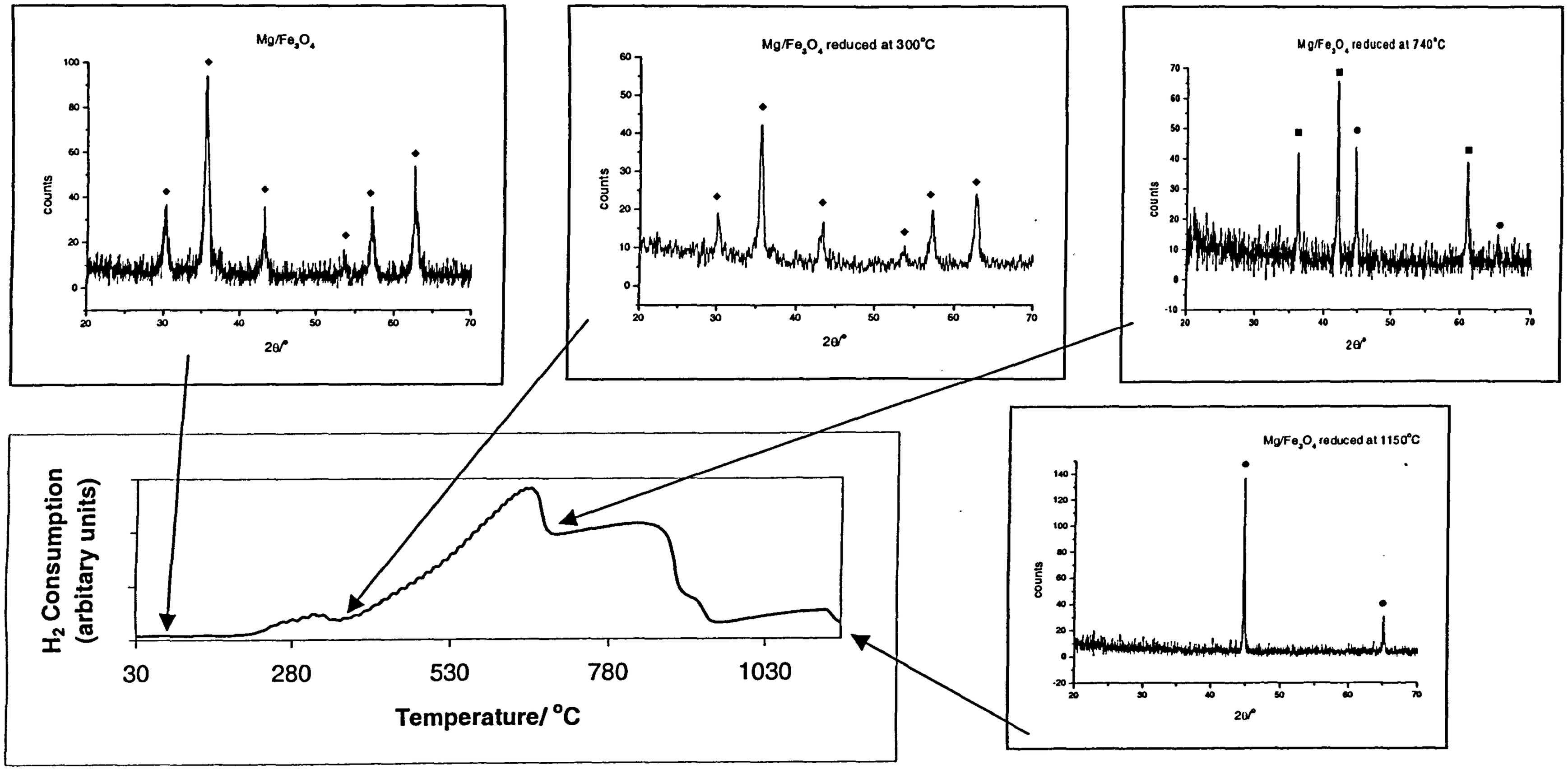

Figure 5.22 TPR profile recorded from Mg/Fe_3O_4 and XRD patterns recorded following each reduction peak

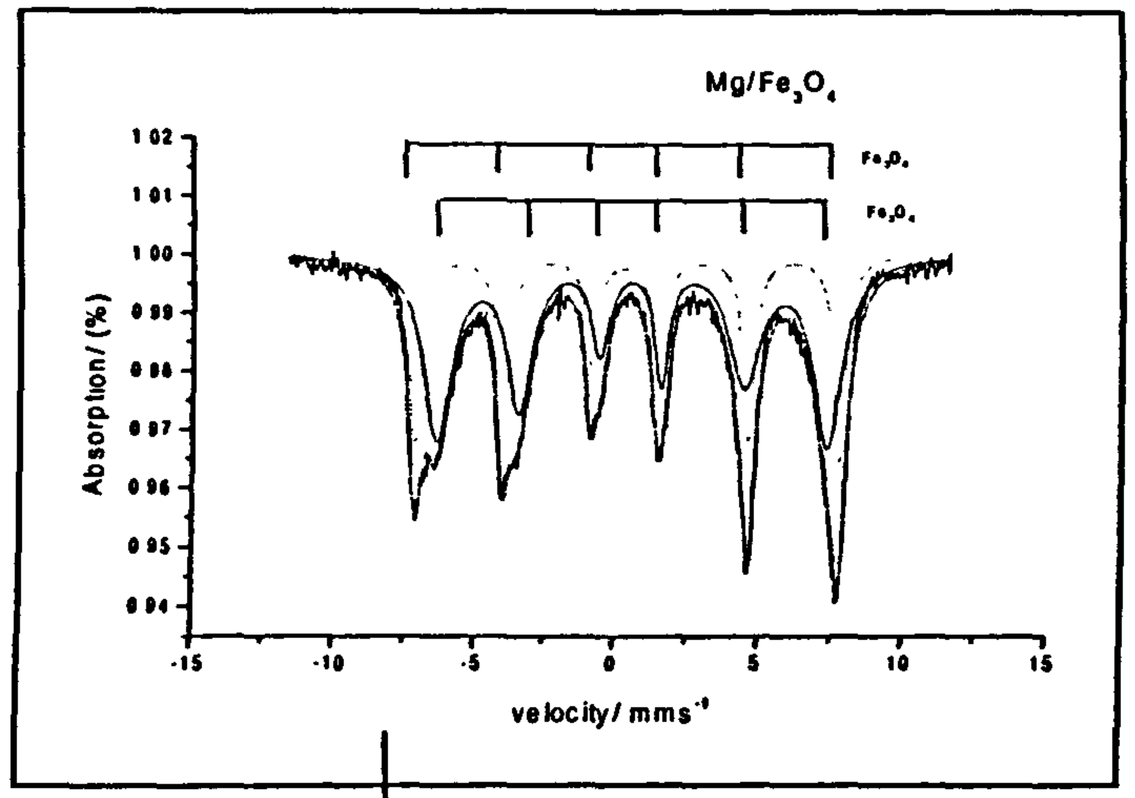

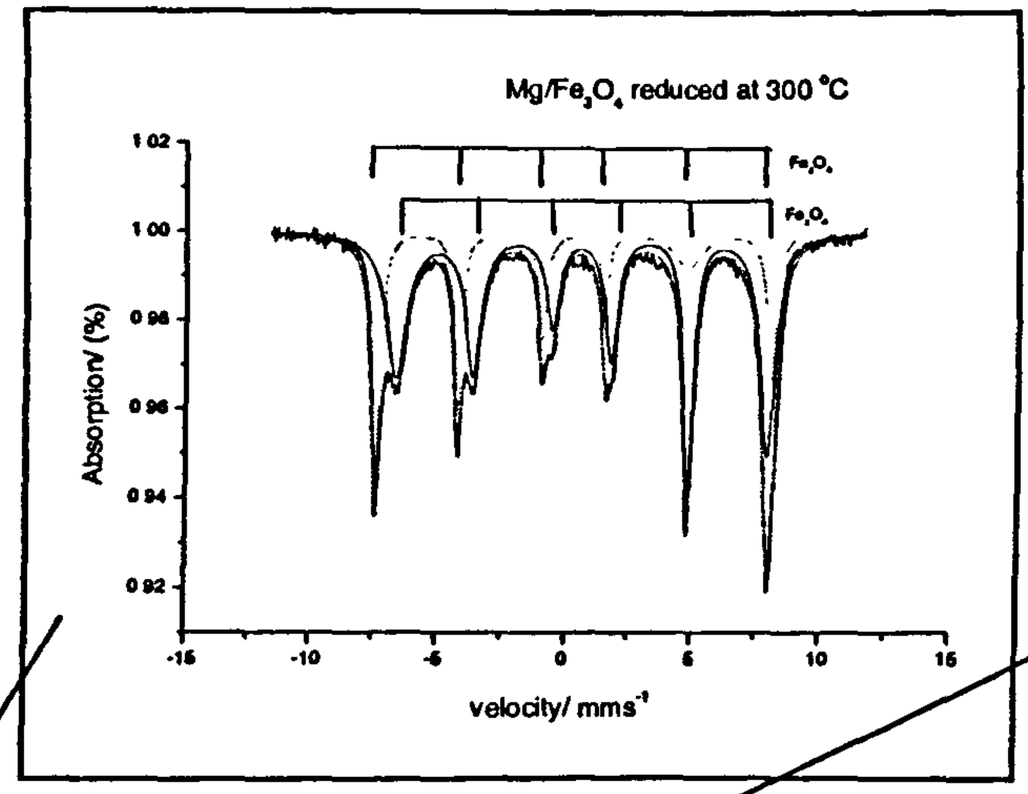

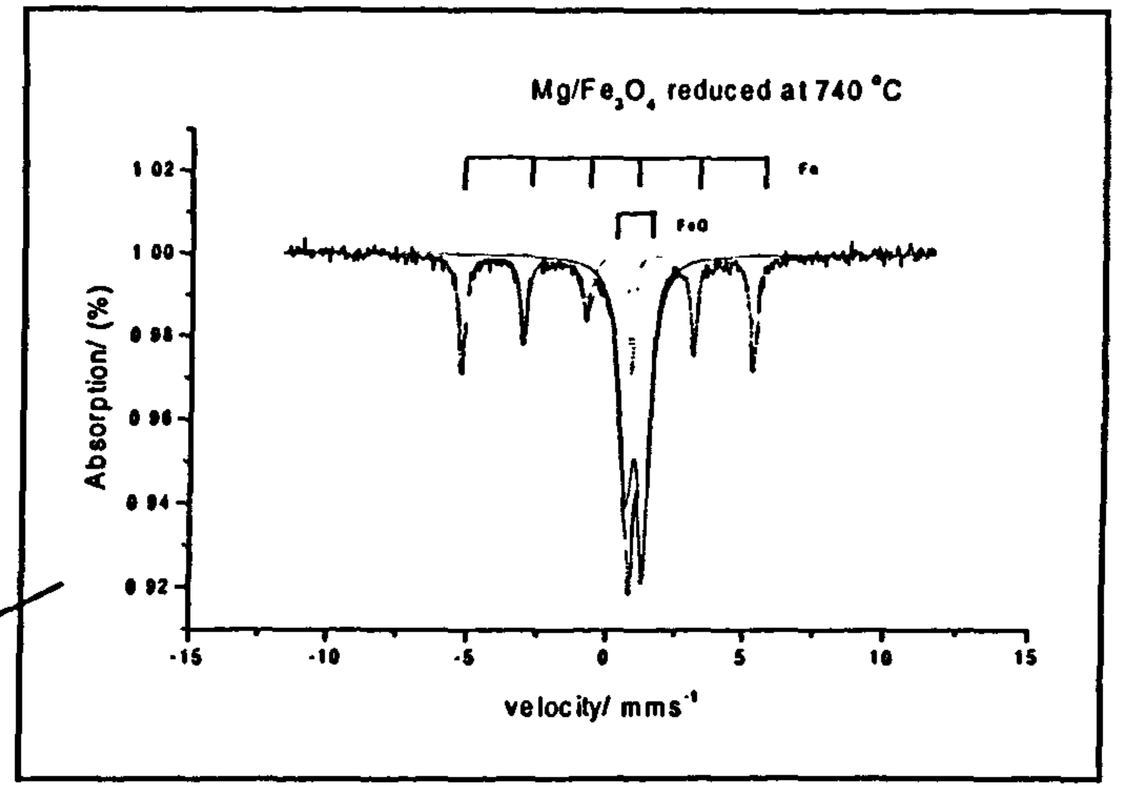

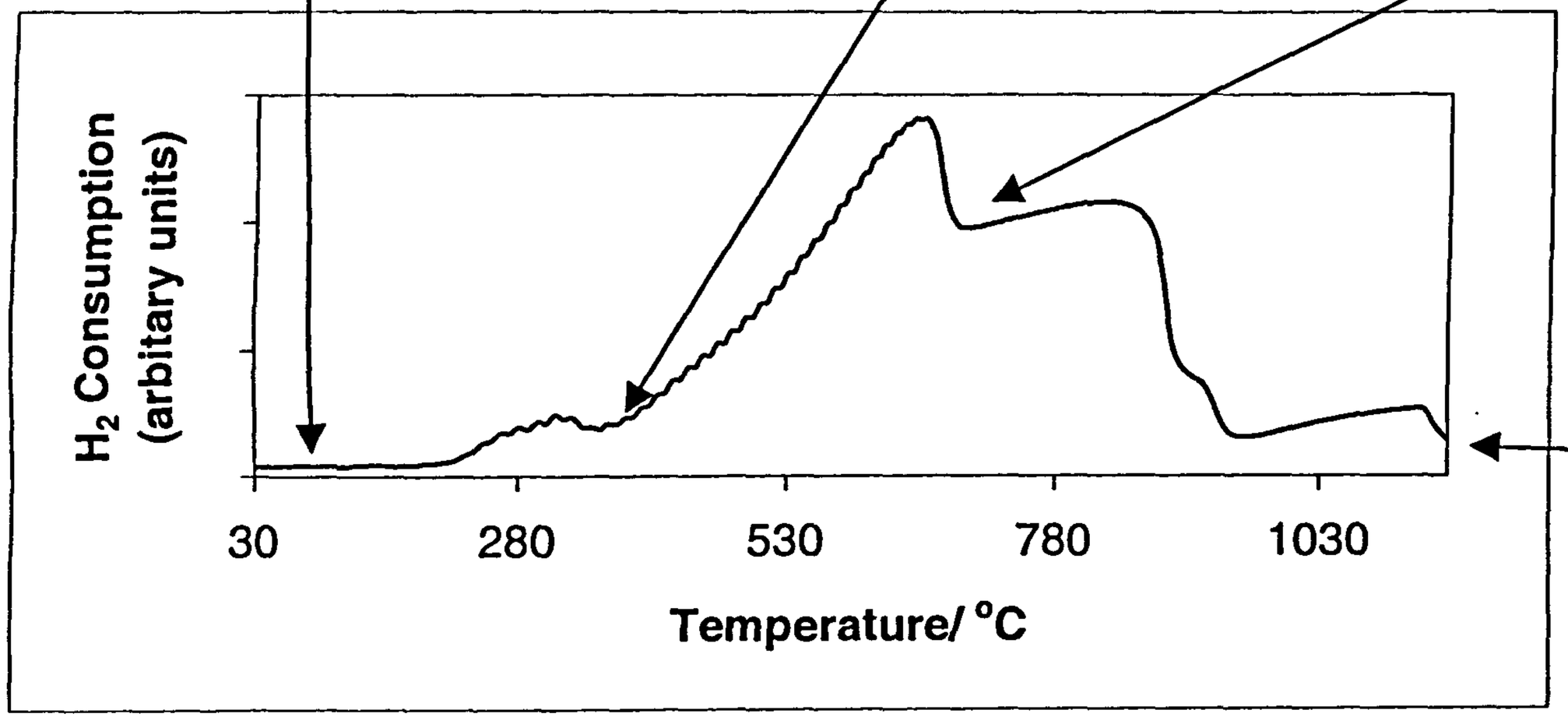

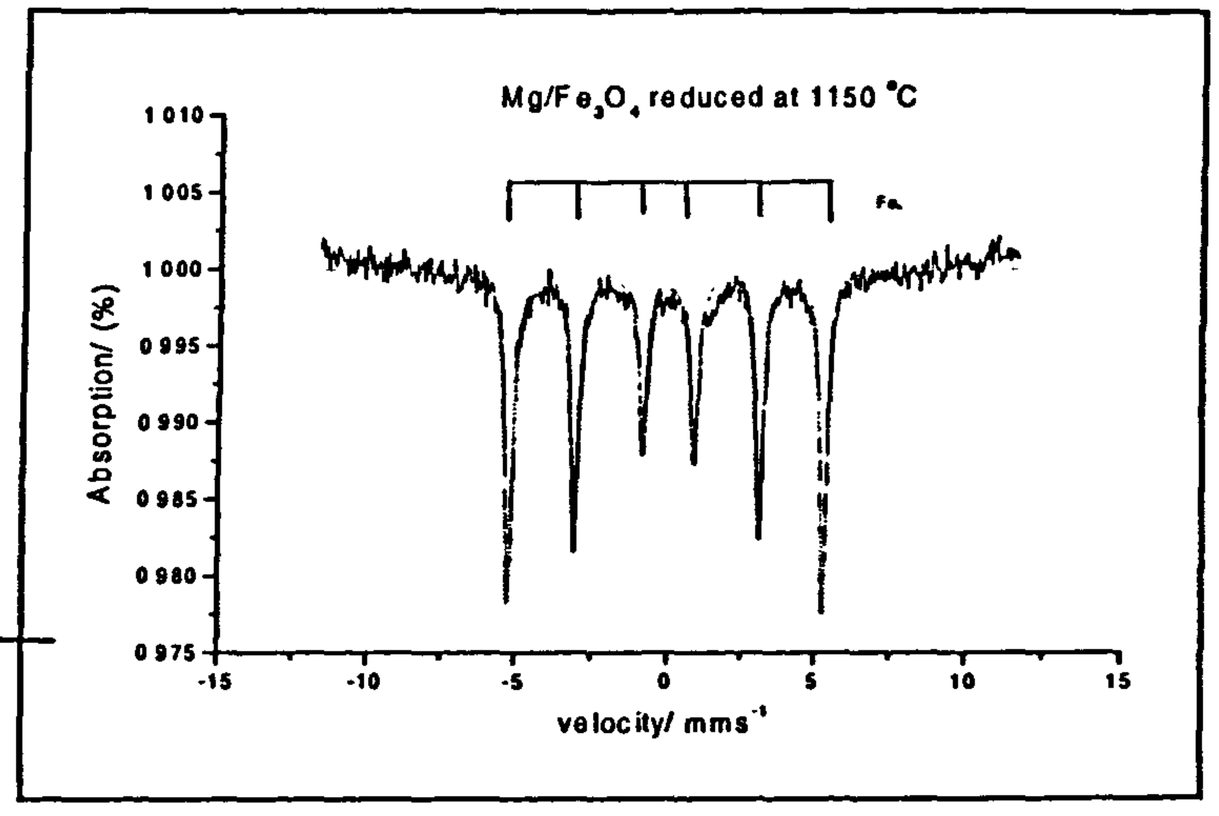

Figure 5.23 TPR profile recorded from Mg/Fe_3O_4 and ^{57}Fe Mössbauer spectra recorded following each reduction peak

Table 5.5 ^{57}Fe Mössbauer parameters recorded from Mg/Fe_3O_4 following reduction in TPR experiment

Sample	δ (± 0.02) mms^{-1}	Δ (± 0.02) mms^{-1}	H (± 1) T	Interpretation	Area (± 5) %
Mg/Fe_3O_4	0.52	-0.01	43	Fe_3O_4	100
	0.32	0.01	46	Fe_3O_4	
Mg/Fe_3O_4 Reduced at 300 °C	0.62	0.02	45	Fe_3O_4	100
	0.30	0.03	48	Fe_3O_4	
Mg/Fe_3O_4 Reduced at 740 °C	0.99	0.65	---	FeO	62
	0.02	0.00	33	Fe	38
Mg/Fe_3O_4 Reduced at 1150 °C	0.00	0.01	33	Fe	100

Conclusion

Magnesium- doped Fe_3O_4 showed a lower surface area (72 m^2g^{-1}) compared with Fe_3O_4 (99 m^2g^{-1}), Ti/Fe_3O_4 (120 m^2g^{-1}) and Ru/Fe_3O_4 (112 m^2g^{-1}) but higher then that of Sn/Fe_3O_4 (32 m^2g^{-1}) all prepared by a similar method. The TPR profile showed three reduction peaks similar to Fe_3O_4, Ti/Fe_3O_4 and Sn/Fe_3O_4. However the spinel- related phase was not observed after the second reduction peak, indicating that Fe_3O_4 reduces completely to FeO and metallic iron by 740 °C. No iron-magnesium alloy was detected.

5.3 Palladium impregnated Fe_3O_4 (addition of base to salt, heated hydrothermally and dried under an infrared lamp)

Fe_3O_4 prepared by addition of base to salt, heated hydrothermally, and dried under an infrared lamp was impregnated with nominal 2 mass % Pd using $Pd(NO_3)_2$ solution. The XRD pattern corresponded to a spinel-related structure (Figure 5.24). There was no indication of palladium oxide. The ^{57}Fe Mössbauer spectrum (Figure 5.25) showed a sextet pattern with magnetic hyperfine field 47 (1) T corresponding to the spinel-related structure γ–Fe_2O_3[2,3]. One of the preparation steps of Pd impregnated Fe_3O_4 is calcination at 300 °C/2 h. At this temperature Fe_3O_4 is oxidised to γ–Fe_2O_3.

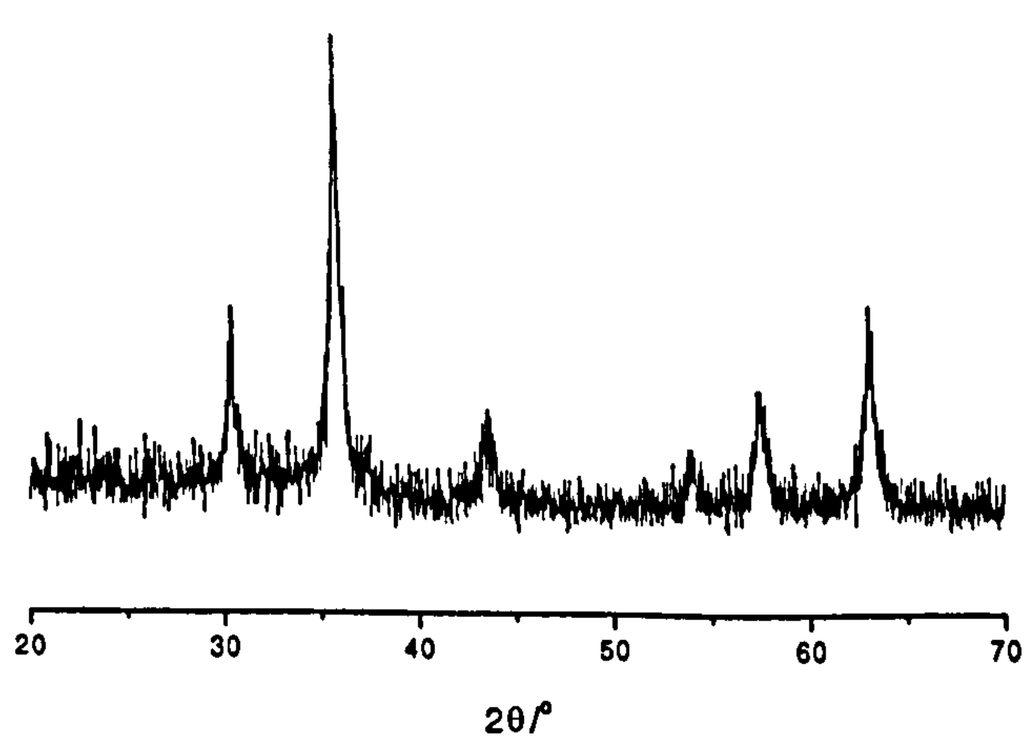

Figure 5.24 XRD pattern recorded from attempted preparation of Pd/Fe_3O_4

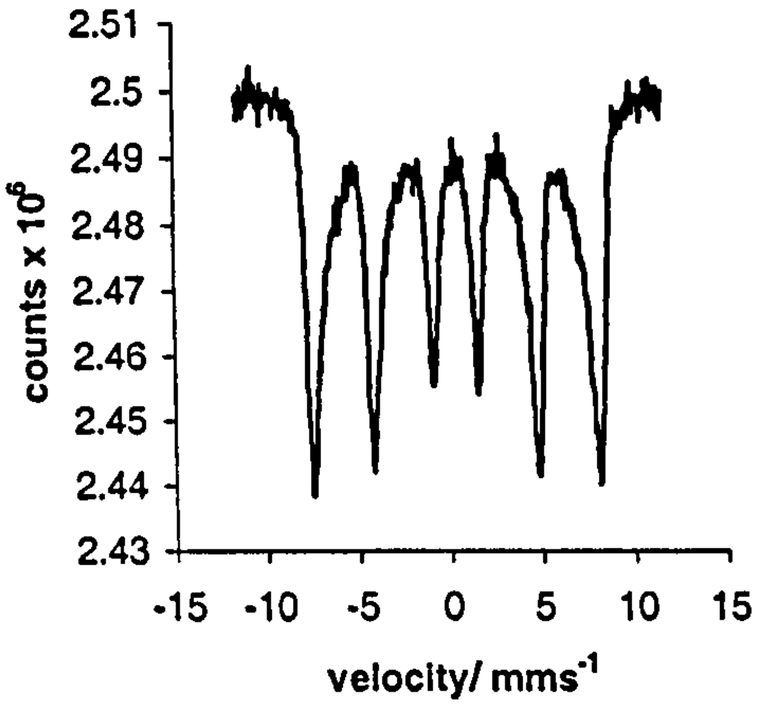

Figure 5.25 ^{57}Fe Mössbauer spectrum recorded from attempted preparation of Pd/Fe_3O_4

5.4 α–Fe_2O_3

5.4.1 α-Fe_2O_3 (addition of base to salt, boiling under reflux, and calcination at 600 °C/12 h)

The X-ray powder diffraction pattern (Figure 5.26) recorded from the material prepared from the iron (III)- salt showed a single-phase corundum-related structure[14] with lattice parameters a = 5.034(2) Å, c = 13.755(2) Å which compare with the reported[14] values a = 5.035 Å, c = 13.749 Å for α-Fe_2O_3. The ^{57}Fe Mössbauer spectrum recorded at 298 K (Figure 5.27) showed a sextet pattern (δ 0.40(2) mms^{-1}, Δ -0.10(2) mms^{-1}, H 51(1) T) characteristic[2,3] of α–Fe_2O_3.

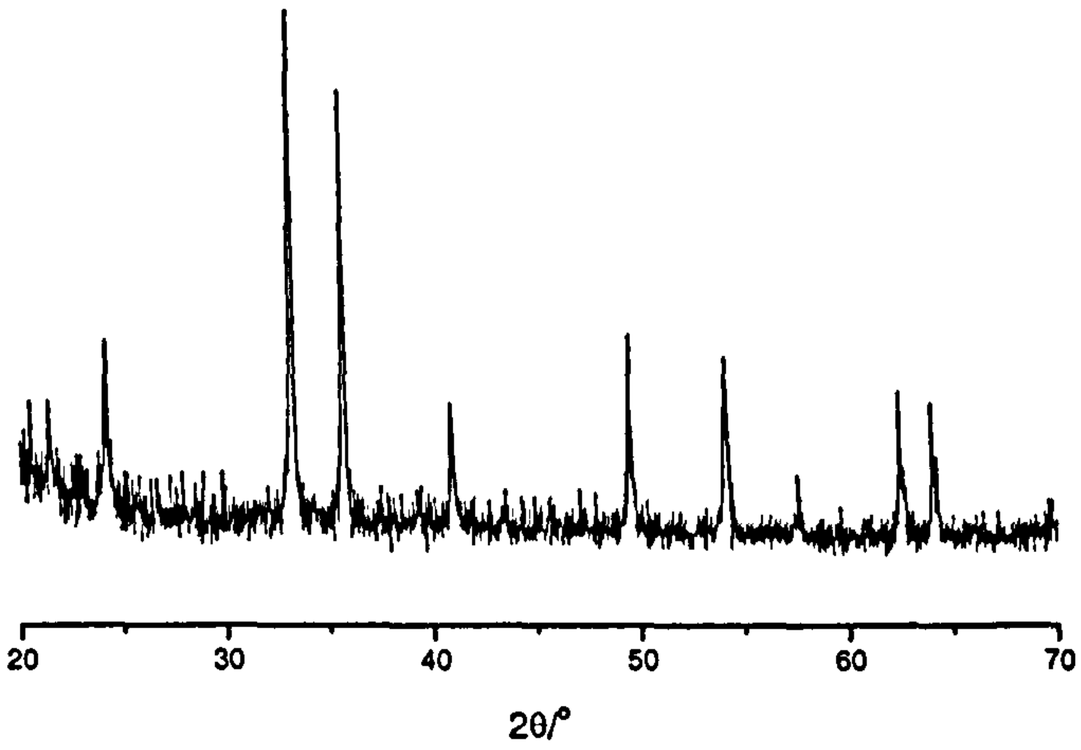

Figure 5.26 XRD pattern recorded from α-Fe_2O_3 prepared by addition of base to salt, boiling under reflux, and calcination at 600 °C

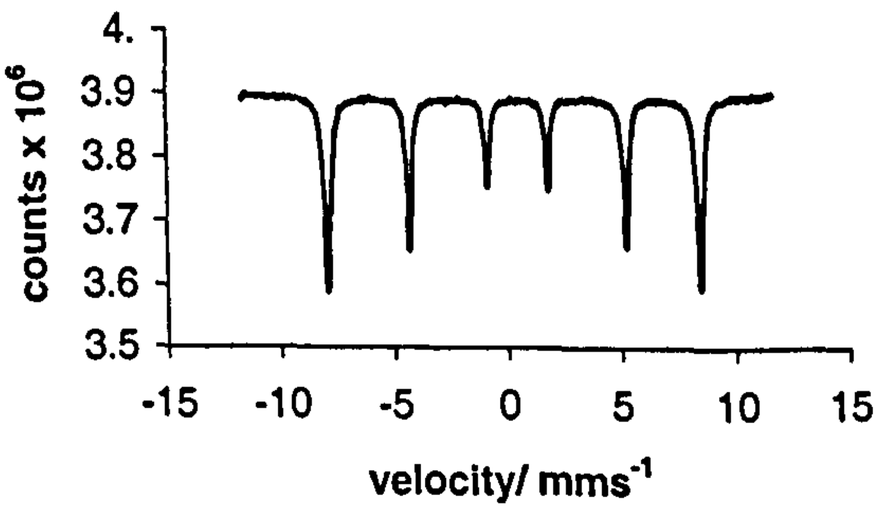

Figure 5.27 ^{57}Fe Mössbauer spectrum recorded from α-Fe_2O_3 prepared by addition of base to salt, boiling under reflux, and calcination at 600 °C

α–Fe_2O_3 prepared by addition of base to salt and boiling under reflux had a particle size of *ca.* 57 nm which was deduced from the X-ray powder diffraction linewidth data and *ca.* 45 nm from TEM. The surface area of *ca.* 10 m^2g^{-1} was determined by nitrogen adsorption methods. The surface area of α-Fe_2O_3 is much smaller than that of γ–Fe_2O_3.

The temperature programmed reduction profile recorded from α–Fe_2O_3 prepared by addition of base to salt, boiling under reflux and calcination at 600 °C/12 h is shown in Figure 5.28 and showed three reduction peaks (*ca.* 432, 727 and 1050 °C). It follows a similar reduction pathway as γ-Fe_2O_3 prepared by a similar method and calcined at 250 °C/12 h. *Ex situ* XRD and *ex situ* ^{57}Fe Mössbauer spectroscopy studies of samples retrieved after each reduction peak from the TPR experiment are shown in Figures 5.28 and 5.29 respectively. Table 5.6 shows the ^{57}Fe Mössbauer parameters of α-Fe_2O_3 after each reduction step.

The ^{57}Fe Mössbauer spectra recorded *ex situ* after each reduction step (Figure 5.29) showed the initial reduction of α–Fe_2O_3 to Fe_3O_4 at 350 °C with a small amount of Fe (< 5 %). This was followed by partial reduction to wüstite (FeO) and metallic iron at *ca.* 720 °C. The identification of FeO during the reduction of iron oxide has been disscussed in Section 4.1.2. The X-ray powder diffraction pattern recorded *ex situ* from α–Fe_2O_3 after the second reduction peak at *ca.* 720 °C (Figure 5.28) showed the three peaks at *ca.* 37°, 42° and 61° 2θ, characteristic of wüstite[4] together with peaks at *ca.* 30°, 35°, 43°, 57° and 62° 2θ characteristic of Fe_3O_4[1] and at *ca.* 45°, and 65° 2θ, characteristic of metallic iron[5].

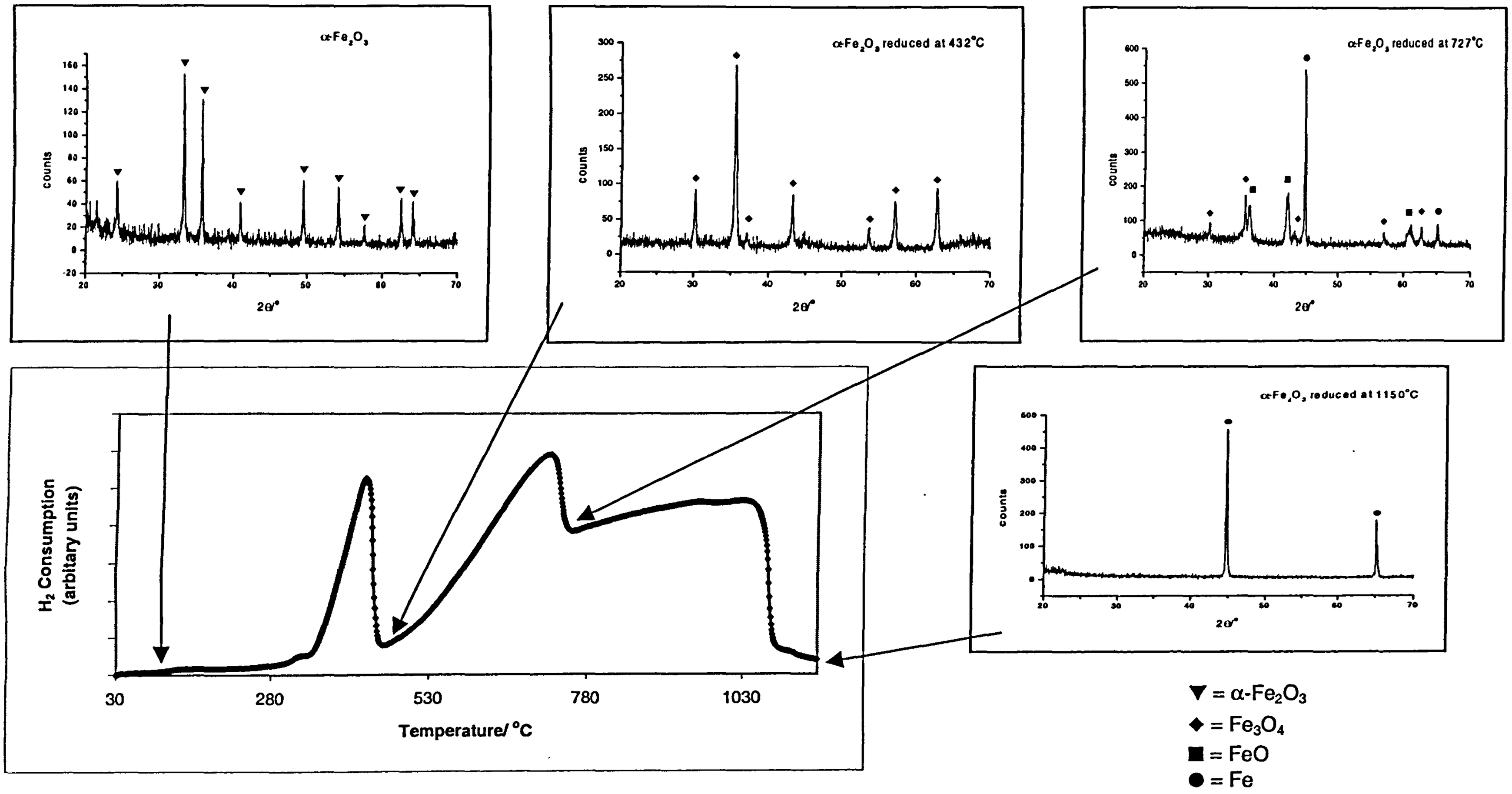

Figure 5.28 TPR profile recorded from α-Fe_2O_3 and XRD patterns recorded following each reduction peak

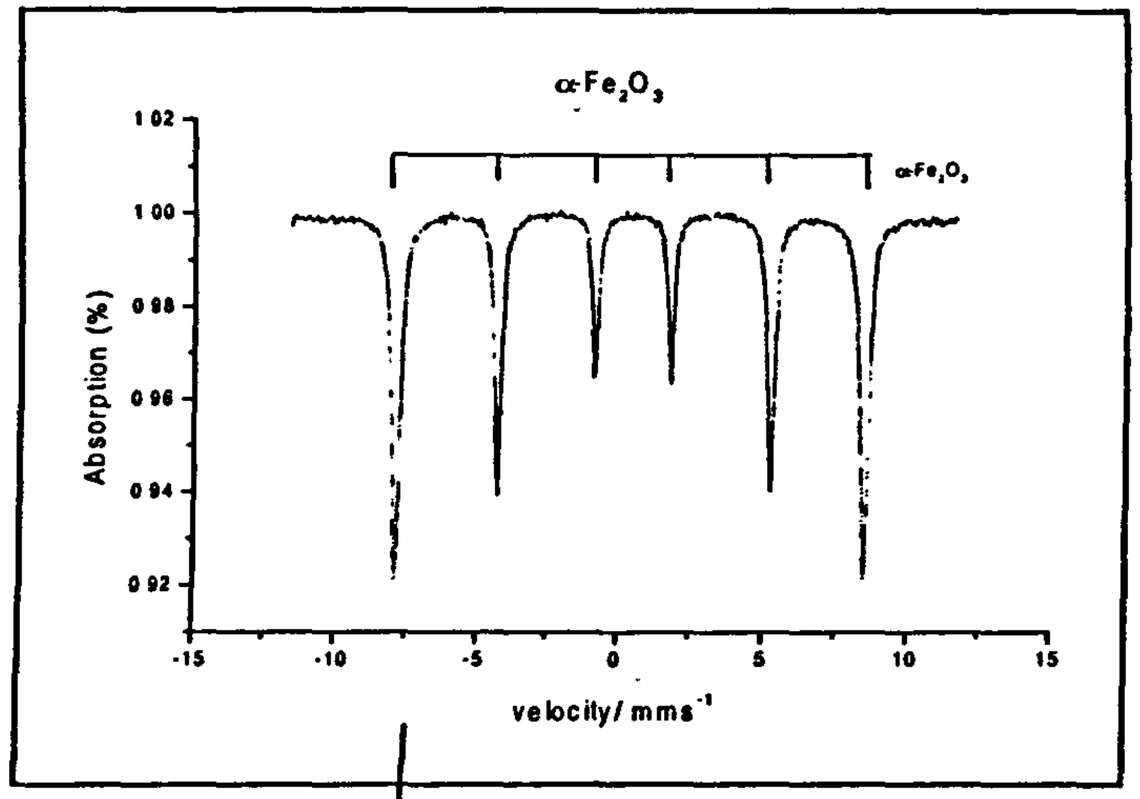

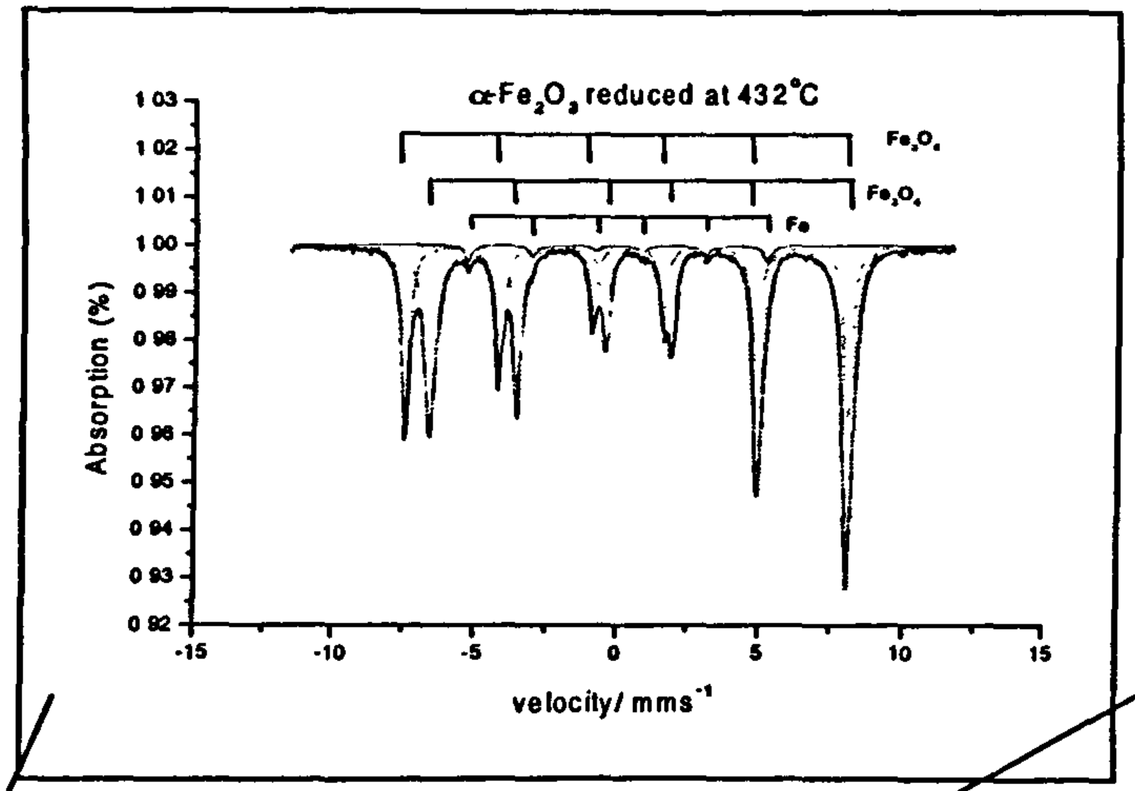

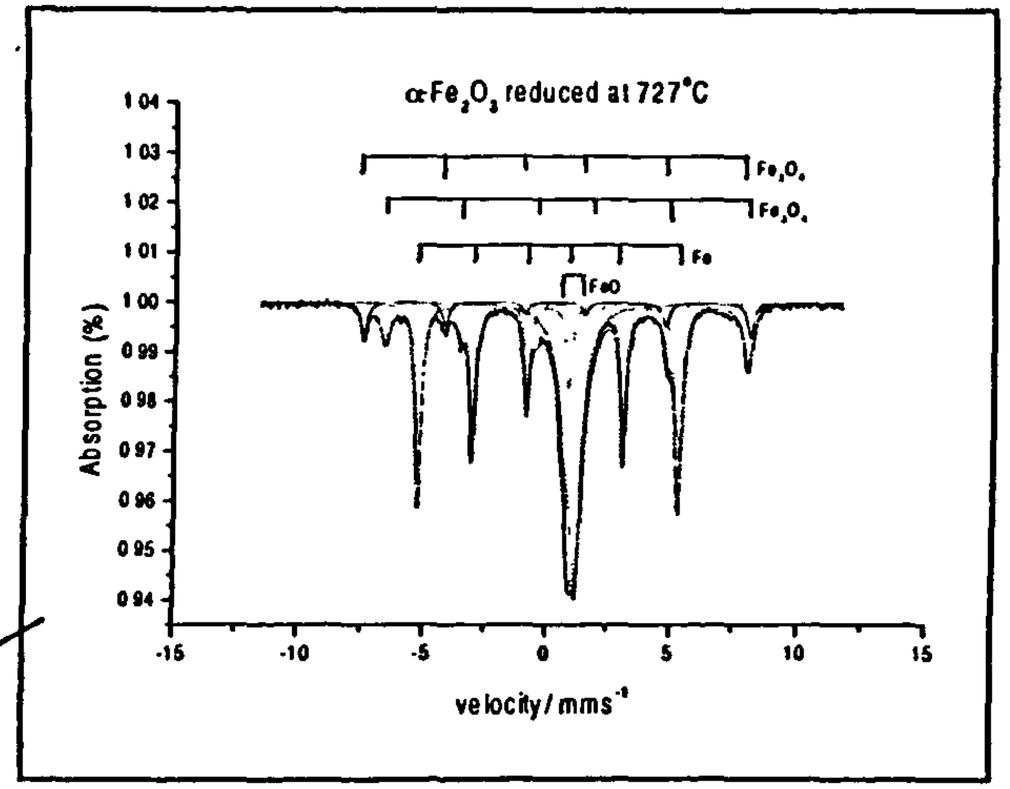

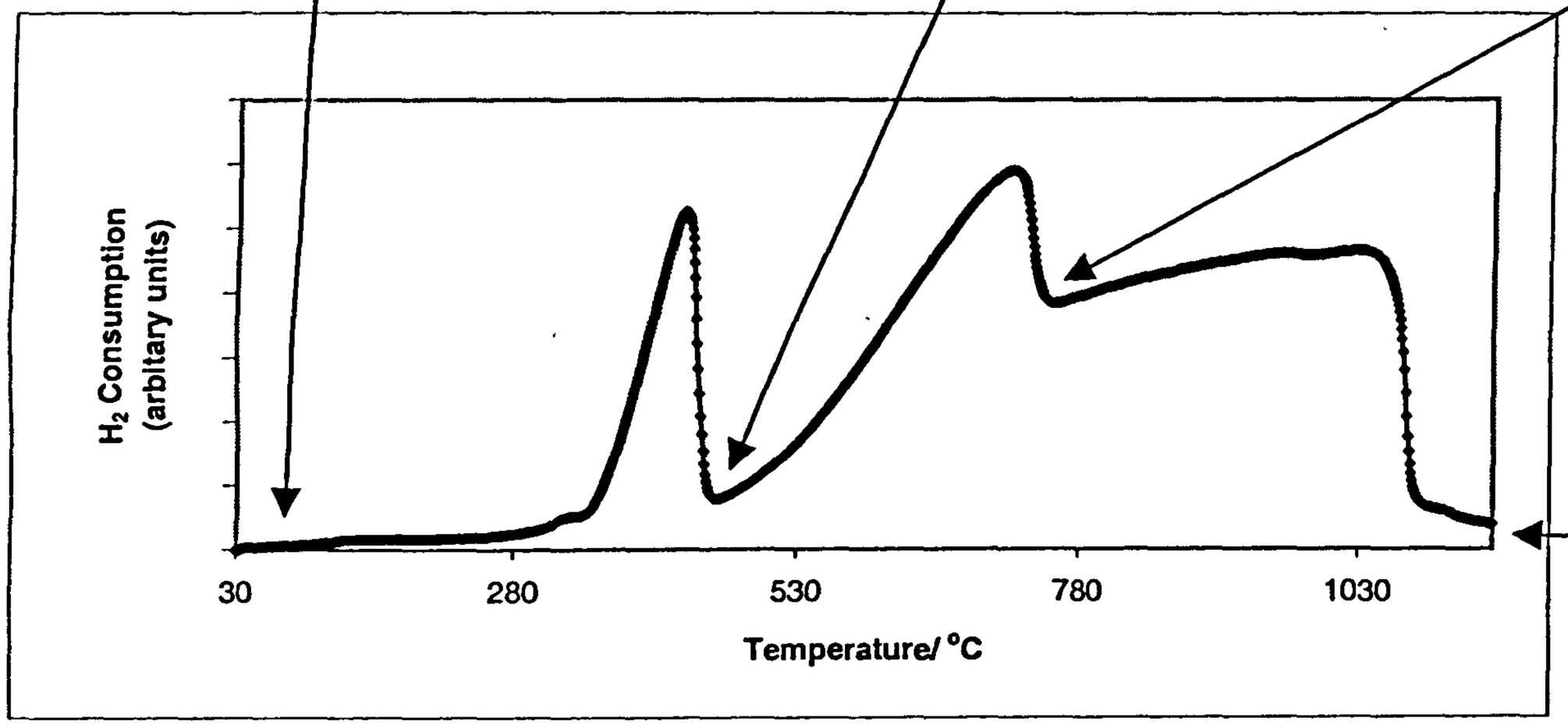

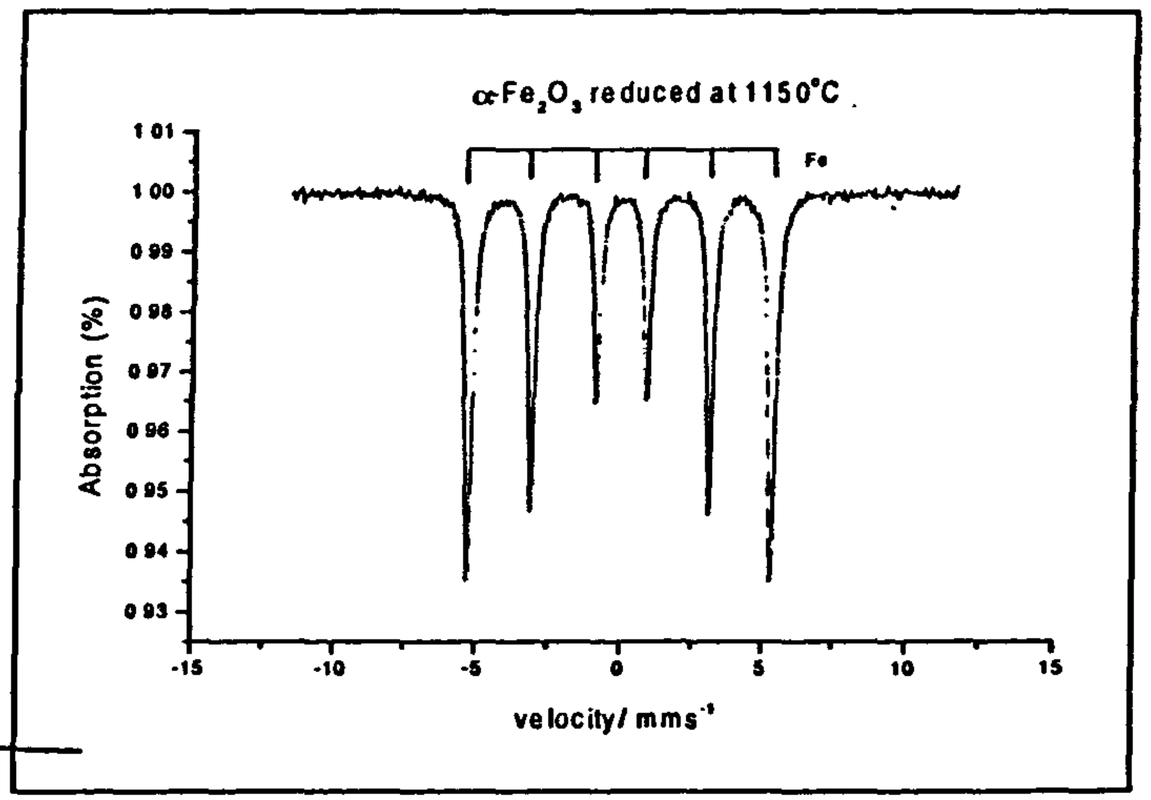

Figure 5.29 TPR profile recorded from α-Fe_2O_3 and ^{57}Fe Mössbauer spectra recorded following each reduction peak

Table 5.6 ^{57}Fe Mössbauer parameters recorded from α-Fe_2O_3 prepared by addition of base to salt, boiling under reflux, and calcination at 600 °C

Sample	δ (± 0.02) mms^{-1}	Δ (± 0.02) mms^{-1}	H (± 1) T	Interpretation	Area (± 5) %
α-Fe_2O_3	0.40	-0.10	51	α-Fe_2O_3	100
α-Fe_2O_3 reduced at 432 °C	0.69	0.02	45	Fe_3O_4	97
	0.29	0.0	48	Fe_3O_4	
	-0.04	-0.05	32	Fe	<5
α-Fe_2O_3 reduced at 727 °C	0.69	0.0	45	Fe_3O_4	20
	0.29	0.0	48	Fe_3O_4	
	1.05	0.34	---	FeO	37
	0.02	0.0	33	Fe	43
α-Fe_2O_3 reduced at 1150 °C	0.02	0.01	33	Fe	100

The ^{57}Fe Mössbauer spectrum recorded *ex situ* after the final reduction peak in the TPR profile (Figure 5.29) was characteristic of metallic iron. This was endorsed by the X-ray powder diffraction pattern recorded from the reduced phase (Figure 5.28).

The results show that the reduction of α–Fe_2O_3 follows three steps:

Step 1 *Step 2* *Step 3*

$$\alpha\text{–}Fe_2O_3 \rightarrow Fe_3O_4 \rightarrow Fe_3O_4 + FeO + Fe \rightarrow Fe$$

The results show that α-Fe_2O_3 follows a similar reduction pathway as γ–Fe_2O_3 (Section 4.1.2).

Reduction-reoxidation properties

α–Fe_2O_3 was subjected to reduction at 400 °C in the 10 % hydrogen- 90 % nitrogen mixture (R1) and reoxidation by heating at 400 °C for 1 h in air (O1). The cycle of reduction and reoxidation was repeated twice (samples R2, O2, R3 and O3). X-ray powder diffraction (Figure 5.30) and ^{57}Fe Mössbauer spectroscopy (Figure 5.31, Table 5.7) were used to identify the materials after each reduction-reoxidation step.

Table 5.7 ^{57}Fe Mössbauer parameters recorded from α-Fe_2O_3 following treatment in reducing and oxidising environments

Sample	δ (± 0.02) mms^{-1}	Δ (± 0.02) mms^{-1}	H (± 1) T	Interpretation
α-Fe_2O_3	0.40	-0.10	51	α-Fe_2O_3
R1	0.68	0.01	46	Fe_3O_4
	0.31	0.0	48	Fe_3O_4
O1	0.35	0.0	49	γ-Fe_2O_3
R2	0.69	0.01	46	Fe_3O_4
	0.29	0.0	48	Fe_3O_4
O2	0.35	0.01	49	γ-Fe_2O_3
R3	0.62	0.02	46	Fe_3O_4
	0.29	0.0	48	Fe_3O_4
O3	0.35	0.0	50	γ-Fe_2O_3

The results show that α–Fe_2O_3 can be reduced to Fe_3O_4 and reoxidised to γ–Fe_2O_3 and the reduction and reoxidation cycle repeated.

Figure 5.30 XRD patterns recorded *ex situ* from α-Fe_2O_3 following reduction and reoxidation cycles

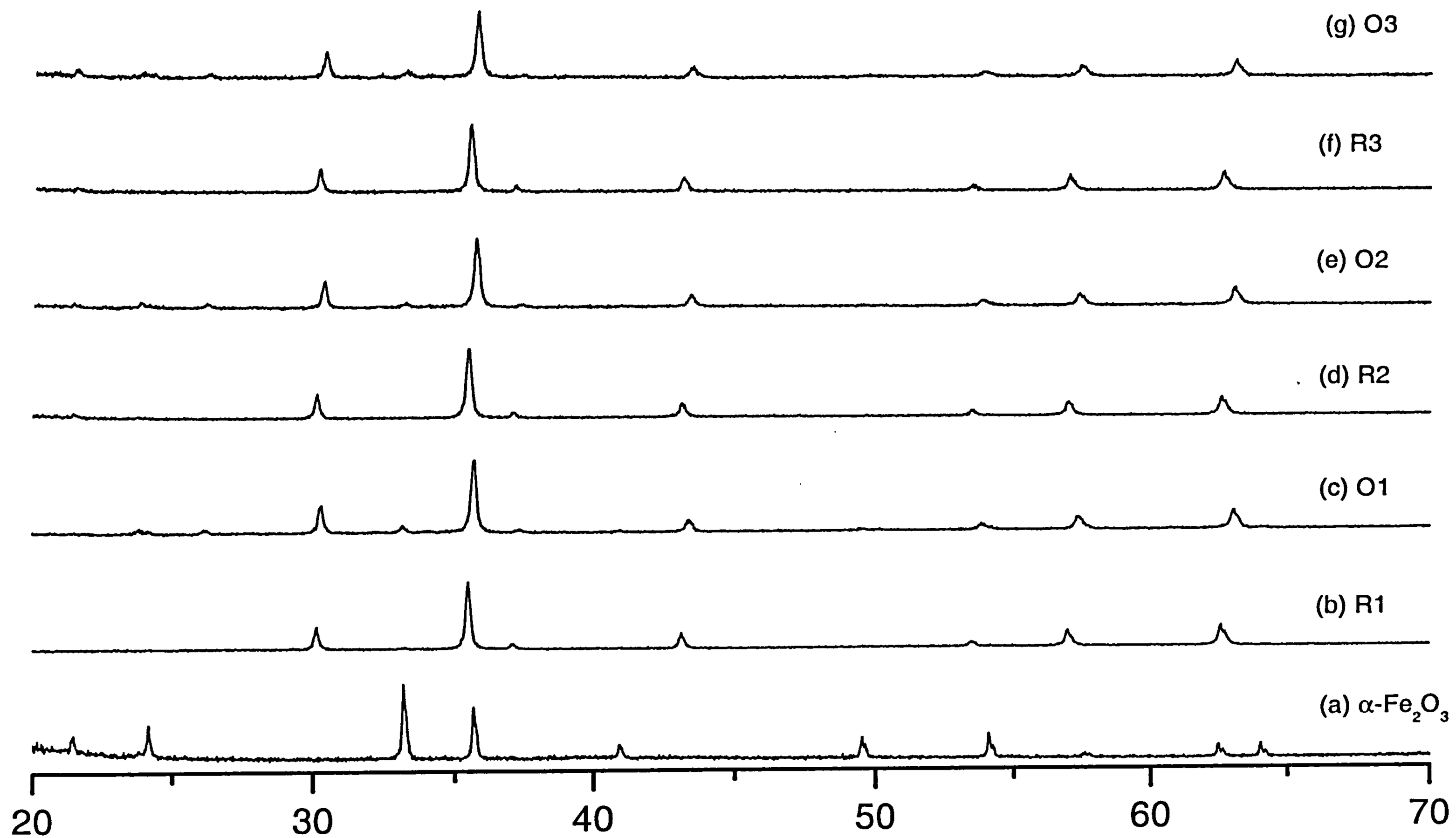

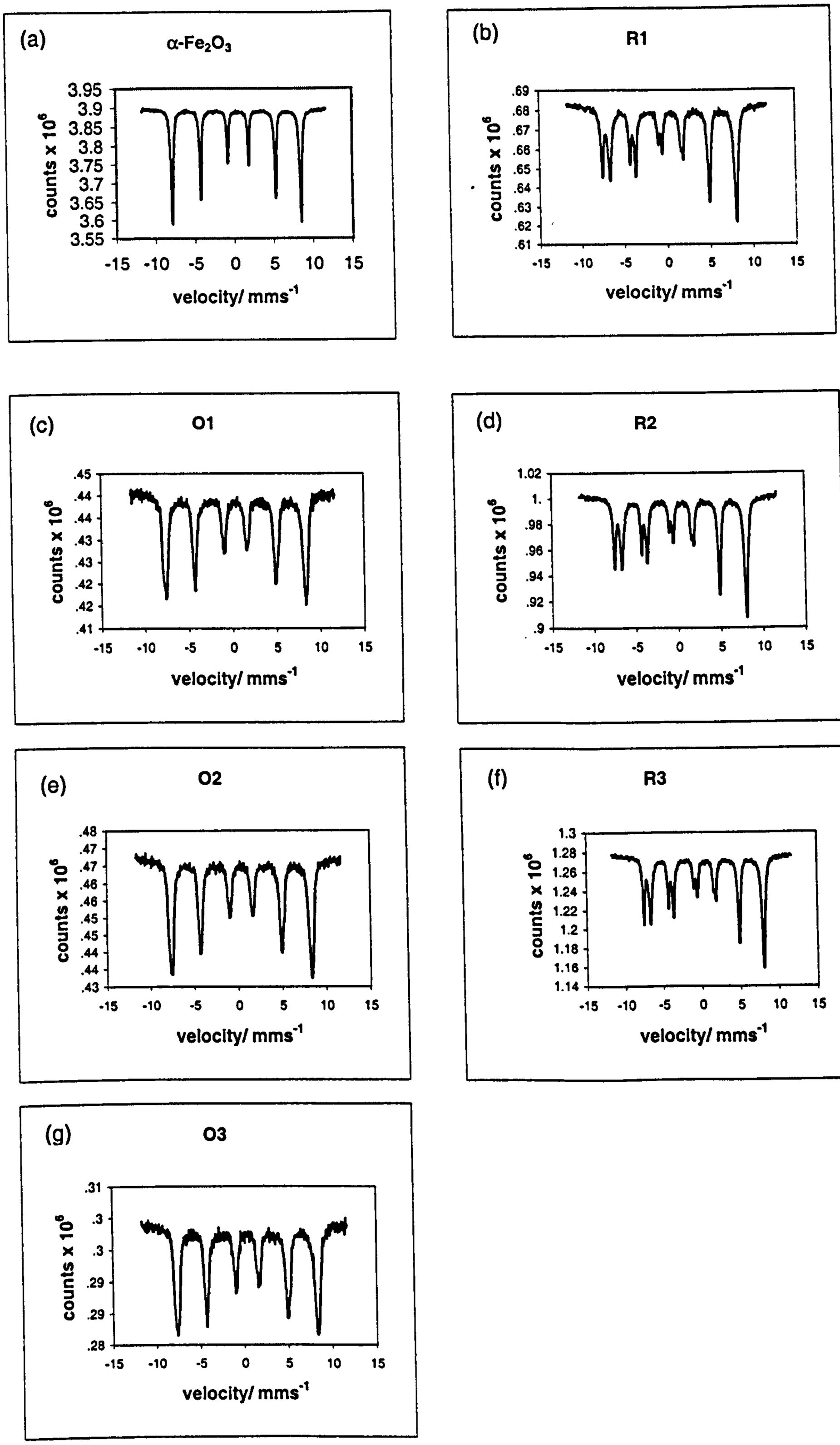

Figure 5.31 ^{57}Fe Mössbauer spectra recorded from α-Fe_2O_3 following reduction and reoxidation cycles

The particle size of α–Fe_2O_3 of *ca.* 57 nm was found to decrease slightly to 48 nm for Fe_3O_4 formed by initial reduction (R1). The surface area showed a slight increase from *ca.* 10 m^2g^{-1} for α–Fe_2O_3 to *ca.* 15 m^2g^{-1} for Fe_3O_4 (R1). This was followed by reoxidation to γ–Fe_2O_3 (O1) with similar particle size (*ca.* 54 nm), and surface area (14 m^2g^{-1}). The reduction-oxidation process was repeated on the same sample for a further two cycles with changes in particle size and surface area being within the errors. The finally regenerated γ–Fe_2O_3 (O3) had a particle size of *ca.* 48 nm and surface area of *ca.* 12 m^2g^{-1}.

Conclusion

α-Fe_2O_3 prepared by addition of base to salt, boiling under reflux, and calcination at 600 °C/12 h has a surface area of 10 m^2g^{-1}, compared to 69 m^2g^{-1} for γ–Fe_2O_3 prepared by addition of base to salt, boiling under reflux, and calcination at 250 °C/12 h. The TPR profile showed three reduction peaks, similar to γ–Fe_2O_3. The initial reduction peak is at slightly higher temperature compared with γ–Fe_2O_3. α-Fe_2O_3 follows a similar reduction pathway as γ–Fe_2O_3. The reduction- reoxidation results show that α–Fe_2O_3 can be reduced to Fe_3O_4 and reoxidised to γ–Fe_2O_3 and the reduction and reoxidation cycle repeated with little variation in the particle size and surface area.

5.4.2 α-Fe_2O_3 (addition of salt to base, boiling under reflux, and calcination at 600 °C/12 h)

The XRD pattern recorded from α-Fe_2O_3 prepared by addition of salt to base, boiling under reflux, and calcination at 600 °C/12 h corresponded to α–Fe_2O_3[14] with lattice parameters a = 5.035(2) Å, c = 13.749(2) Å which compare with the reported[14] values a = 5.035 Å, c = 13.749 Å for α-Fe_2O_3.

The ^{57}Fe Mössbauer spectrum showed a sextet pattern (δ 0.40(2) mms^{-1}, Δ -0.09(2) mms^{-1}, H 51(1) T) corresponding to α–Fe_2O_3[2,3].

The BET surface area was calculated to be 15 m^2g^{-1}, slightly higher than the surface area of α-Fe_2O_3 prepared by addition of base to salt, boiling under reflux, and calcination at 600 °C/12 h (10 m^2g^{-1}).

The particle size from the X-ray powder diffraction linewidth data was found to be *ca.* 55 nm and *ca.* 45 nm from TEM, similar to that of α–Fe_2O_3 prepared by addition of base to salt, boiling under reflux, and calcination at 600 °C/12 h.

The TPR profile showed three reduction peaks (*ca.* 400, 740 and 1000 °C) similar to α-Fe_2O_3 prepared by addition of base to salt, boiling under reflux, and calcination at 600 °C/12 h.

Conclusion

α-Fe_2O_3 prepared by addition of salt to base, boiling under reflux, and calcination at 600 °C/12 h had a slightly higher surface area than α-Fe_2O_3 prepared by addition of base to salt, boiling under reflux, and calcination at 600 °C/12 h. The TPR profile recorded from α-Fe_2O_3 prepared by addition of salt to base, boiling under reflux, and calcination at 600 °C/12 h was similar to that of α-Fe_2O_3 prepared by addition of base to salt, boiling under reflux, and calcination at 600 °C/12 h.

5.4.3 α-Fe_2O_3 (addition of base to salt, heated hydrothermally and dried under an infrared lamp)

The XRD pattern recorded from the hydrothermally prepared sample formed by addition of base to salt corresponded to α-Fe_2O_3[14], with lattice parameters a = 5.035(2) Å, c = 13.750(2) Å which compared with the reported[14] values a = 5.035 Å, c = 13.749 Å for α-Fe_2O_3.

The ^{57}Fe Mössbauer spectrum showed a sextet pattern (δ 0.40(2) mms^{-1}, Δ -0.09(2) mms^{-1}, H 51(1) T) which is similar to the literature values reported for α–Fe_2O_3[2,3].

The surface area was calculated to be 17 m^2g^{-1}, higher than the surface area of α-Fe_2O_3 prepared by addition of base to salt, boiling under reflux, and calcination at 600 °C (10 m^2g^{-1}), but similar to α-Fe_2O_3 prepared by addition of salt to base, boiling under reflux, and calcination at 600 °C (15 m^2g^{-1}).

The particle size of *ca.* 65 nm which was deduced from the X-ray powder diffraction linewidth data was similar to that of α–Fe_2O_3 prepared by addition of base to salt or salt to base, boiling under reflux and calcination at 600 °C/12 h.

The TPR profile showed three reduction peaks (*ca.* 400, 680 and 860 °C) similar to that of α-Fe_2O_3 prepared by addition of base to salt or salt to base, boiling under reflux, and calcined at 600 °C/12 h. Shoulders at *ca.* 430 and 1100 °C, were also observed.

Conclusion

α-Fe_2O_3 prepared by addition of base to salt and heated hydrothermally has a higher surface area as compared with α-Fe_2O_3 prepared by addition of base to salt, boiling under reflux, and calcination at 600 °C/12 h. The TPR profile recorded from α-Fe_2O_3 prepared by addition of base to salt and heated hydrothermally showed three reduction peaks similar to α-Fe_2O_3 prepared by addition of base to salt or salt to base, boiling under reflux, and calcination at 600 °C/12 h.

5.4.4 α-Fe_2O_3 (addition of salt to base, heated hydrothermally and dried under an infrared lamp)

The XRD pattern recorded from the sample prepared by addition of salt to base and heated hydrothermally corresponded to an α-Fe_2O_3 structure[14] with lattice parameters a = 5.034(2) Å, c = 13.752(2) Å which compare with the reported[14]

values a = 5.035 Å, c = 13.749 Å for α-Fe_2O_3, and the α–Fe_2O_3 prepared here by addition of base to salt and heated hydrothermally (a = 5.035(2) Å, c = 13.750(2) Å).

The ^{57}Fe Mössbauer spectrum showed a sextet pattern (δ 0.40(2) mms^{-1}, Δ -0.09(2) mms^{-1}, H 51(1) T) corresponding to α-Fe_2O_3[2,3], similar to α–Fe_2O_3 prepared by addition of base to salt and heated hydrothermally and α-Fe_2O_3 prepared by addition of base to salt or salt to base, boiling under reflux, and calcination at 600 °C/12 h.

The BET surface area was calculated to be 20 m^{2}g^{-1}, similar to the surface area of α-Fe_2O_3 prepared by addition of base to salt and heated hydrothermally and higher than the surface area of α-Fe_2O_3 prepared by addition of base to salt, boiling under reflux, and calcination at 600 °C.

The particle size calculated from the X-ray powder diffraction linewidth data of *ca.* 62 nm was similar to that of α–Fe_2O_3 prepared by addition of base to salt and heated hydrothermally and also to that prepared by addition of base to salt or salt to base and boiling under reflux and calcination at 600 °C.

The TPR profile showed three reduction peaks (383, 679 and 877 °C) similar to that of α-Fe_2O_3 prepared by addition of base to salt and heated hydrothermally and that of α-Fe_2O_3 prepared by addition of base to salt or salt to base, boiling under reflux, and calcination at 600 °C/12 h. A shoulder at *ca.* 1000 °C was also observed.

Conclusion

α-Fe_2O_3 prepared by addition of salt to base, heated hydrothermally, and dried under an infrared lamp had a similar surface area as α-Fe_2O_3 prepared by addition of base to salt and heated hydrothermally and higher than α-Fe_2O_3 prepared by addition of base to salt, boiling under reflux, and calcination at 600 °C/12 h. The TPR profile showed three reduction peaks similar to α-Fe_2O_3 prepared by addition of base to salt and heated hydrothermally.

5.5 Metal- doped α–Fe_2O_3

α–Fe_2O_3 was nominally doped with 8 mass % titanium, tin, and magnesium all prepared by adding excess aqueous ammonia to an iron (III)- containing solution, boiling under reflux, and calcined at 600 °C/12 h. Nominal 8 mass % ruthenium-doped α-Fe_2O_3 was prepared by addition of base to salt and subsequent hydrothermal heating.

5.5.1 Titanium- doped α–Fe_2O_3 (addition of base to salt, boiling under reflux, and calcination at 600 °C/12 h)

The X-ray powder diffraction pattern (Figure 5.32) recorded from the material which EDX analysis showed to contain 5.73 mass % Ti was characteristic of a single phase corundum-related structure[14]. The lattice parameters a = 5.034(2) Å, c = 13.746(2) Å compare with the reported values for Ti/α-Fe_2O_3[15] (a = 5.029 Å, c = 13.765 Å) and

α–Fe_2O_3 prepared here by addition of base to salt, boiling under reflux, and calcination at 600 °C/12 h, (a = 5.034(2) Å, c = 13.755(2) Å).

Materials of the type M/α-Fe_2O_3 (M = Ti, Sn) prepared by hydrothermal methods have been investigated[16] by Rietveld structure refinement of the X-ray powder diffraction data. The analysis revealed that the dopant ions adopt two distinct sites, in addition to partially substituting at the octahedral Fe sites, they also occupy the interstitial octahedral sites which are vacant in the α-Fe_2O_3 structure. The results were confirmed by neutron diffraction studies[15].

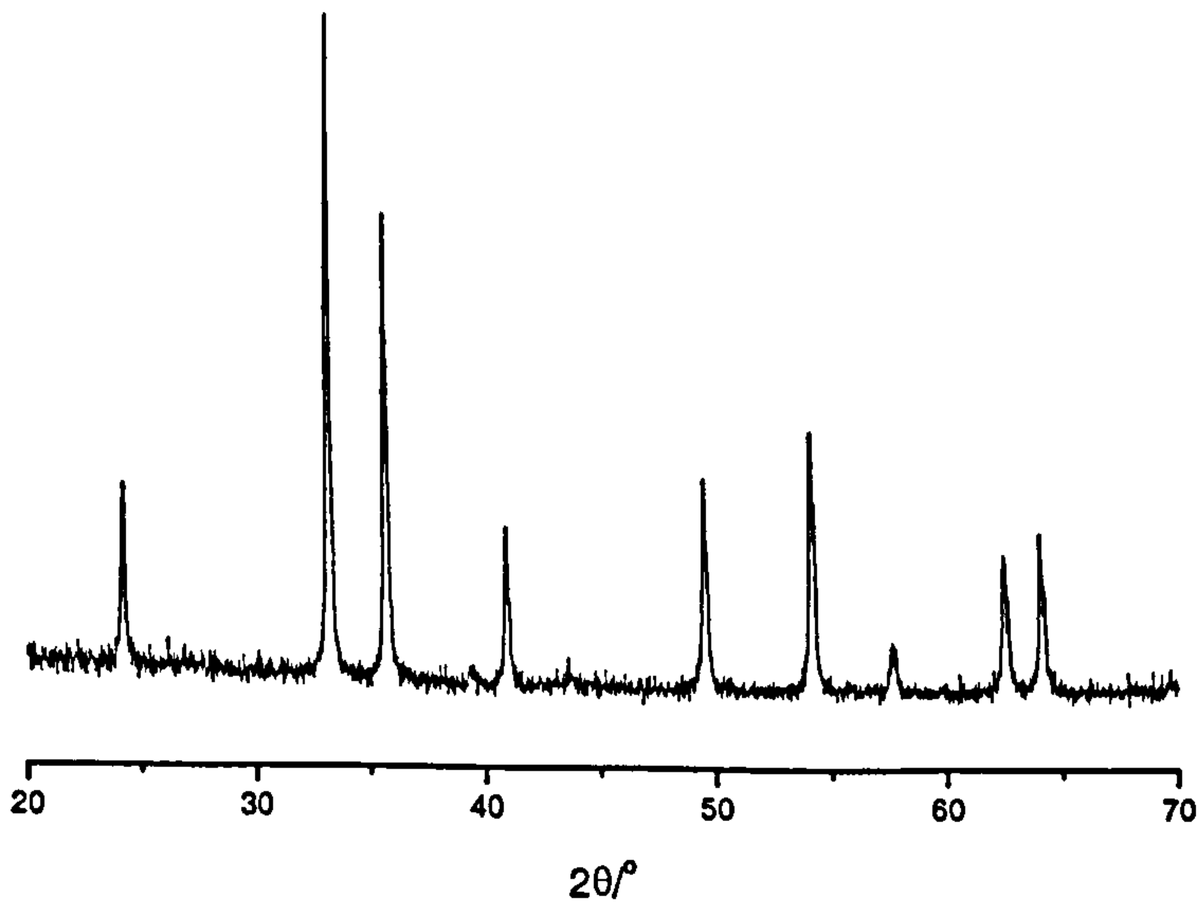

Figure 5.32 XRD pattern recorded from Ti/α–Fe_2O_3 prepared by addition of base to salt, boiling under reflux and calcination at 600 °C

The ^{57}Fe Mössbauer spectrum (Figure 5.33) recorded at 298 K showed a sextet pattern (δ 0.40(2) mms^{-1}, Δ -0.10(2) mms^{-1}, H 50(1) T) characteristic[2,3] of an α–Fe_2O_3- related phase together with a doublet (δ 0.40(2) mms^{-1}, Δ 0.69(2) mms^{-1}) characteristic of the additional presence of small particle iron oxide[9] accounting for *ca.* 6 % of the spectral area. The particle size of *ca.* 57 nm, obtained from the X-ray powder diffraction linewidth data, was similar to that of undoped α–Fe_2O_3 prepared

by addition of base to salt, boiling under reflux, and calcination at 600 °C/12 h. The surface area of *ca.* 29 m^2g^{-1} was however larger than that of undoped α–Fe_2O_3 prepared by a similar method.

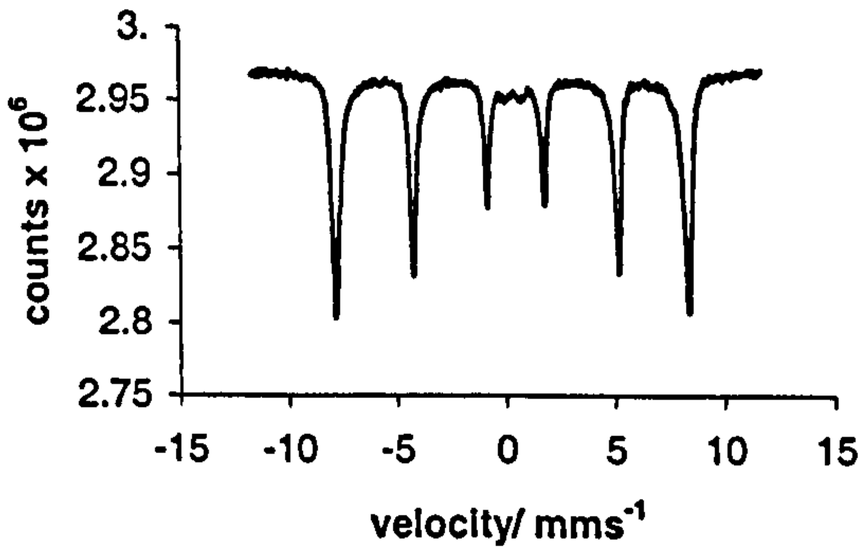

Figure 5.33 ^{57}Fe Mössbauer spectrum recorded from Ti/α–Fe_2O_3 prepared by addition of base to salt, boiling under reflux and calcination at 600 °C

The temperature programmed reduction profile recorded from titanium- doped α–Fe_2O_3 is shown in Figure 5.34. The profile showed three reduction peaks with the latter two peaks merged (519 °C, 800-940 °C). A similar effect was observed in the TPR profiles of Ti/γ–Fe_2O_3 prepared by addition of base to salt, boiling under reflux, and calcination at 250 °C/12 h and Ti/Fe_3O_4 prepared hydrothermally (Sections 4.2.1 and 5.2.1 respectively). *Ex situ* XRD and *ex situ* ^{57}Fe Mössbauer spectroscopy studies of samples retrieved after each reduction peak from the TPR experiment have revealed the identity of the reduced phases (Figures 5.34 and 5.35 respectively). Table 5.8 shows the ^{57}Fe Mössbauer parameters of Ti/α-Fe_2O_3 after each reduction step.

The first reduction step at *ca.* 519 °C can, as in the case of undoped α–Fe_2O_3 prepared by a similar method (Figure 5.28), be associated with the reduction of titanium- doped α–Fe_2O_3 to titanium- doped Fe_3O_4 and a small amount of metallic iron. The temperature of the initial reduction peak was higher than that of undoped α-Fe_2O_3 prepared by a similar method (432 °C), indicating that the presence of

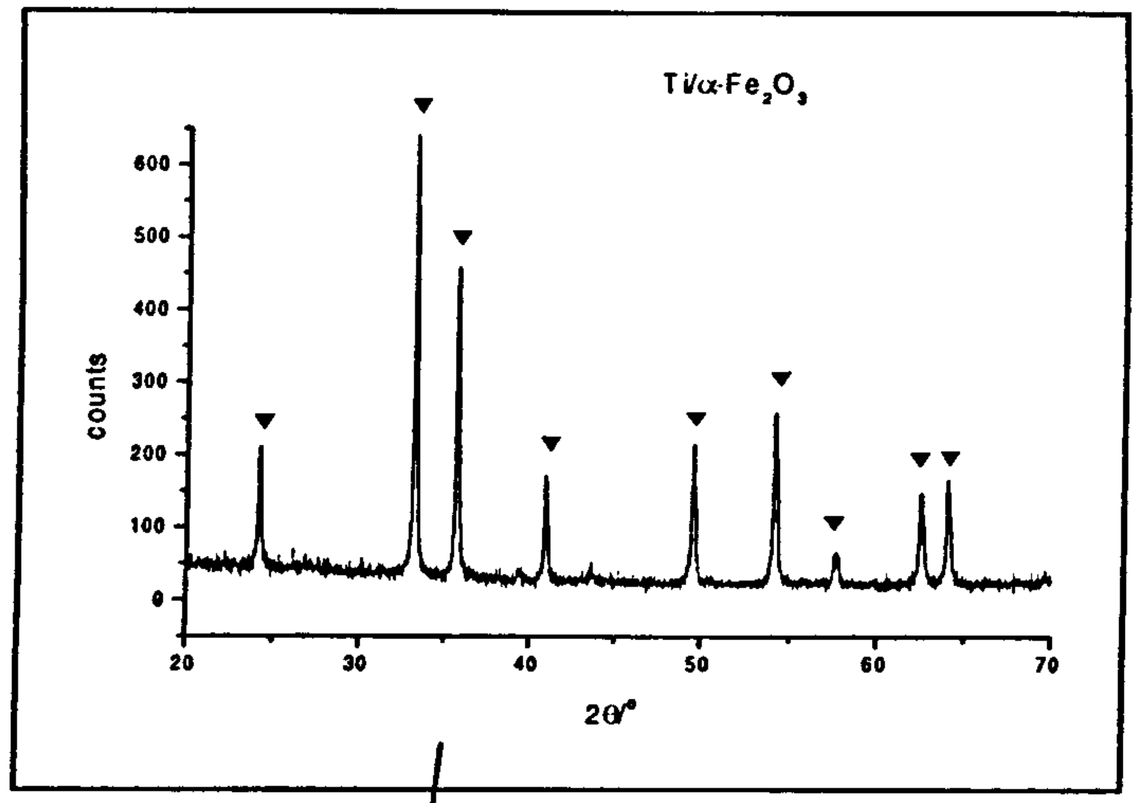

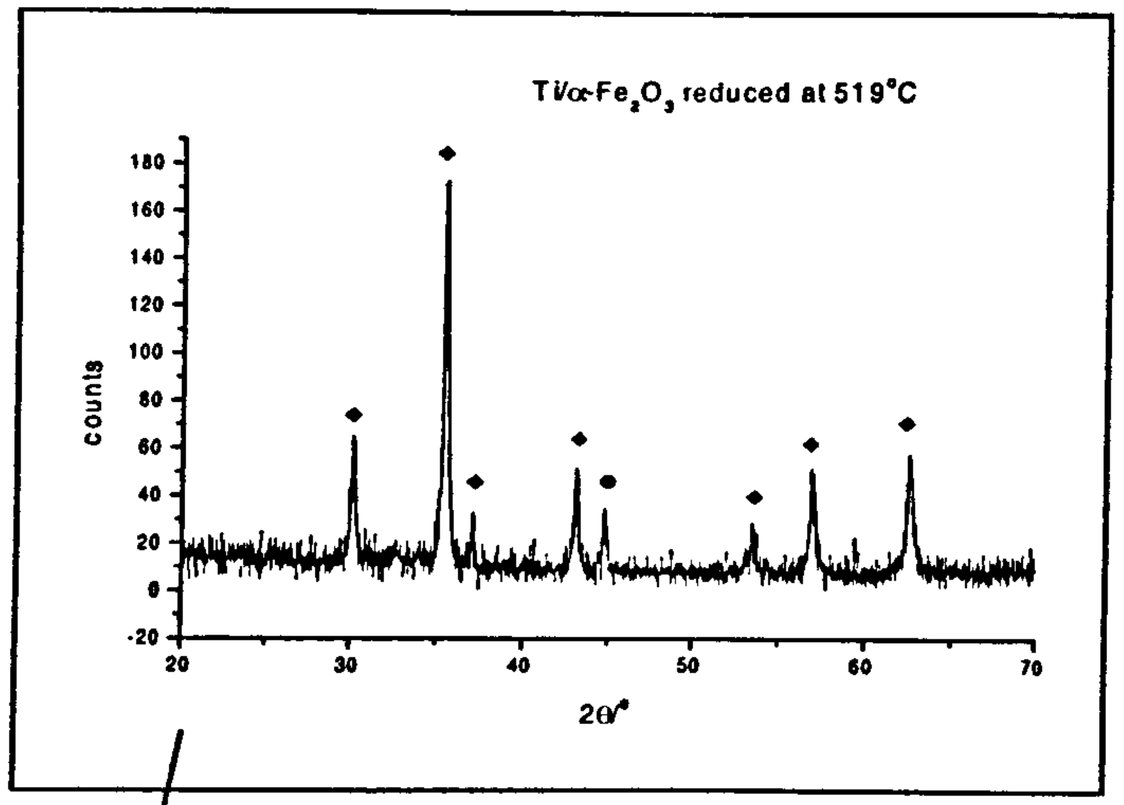

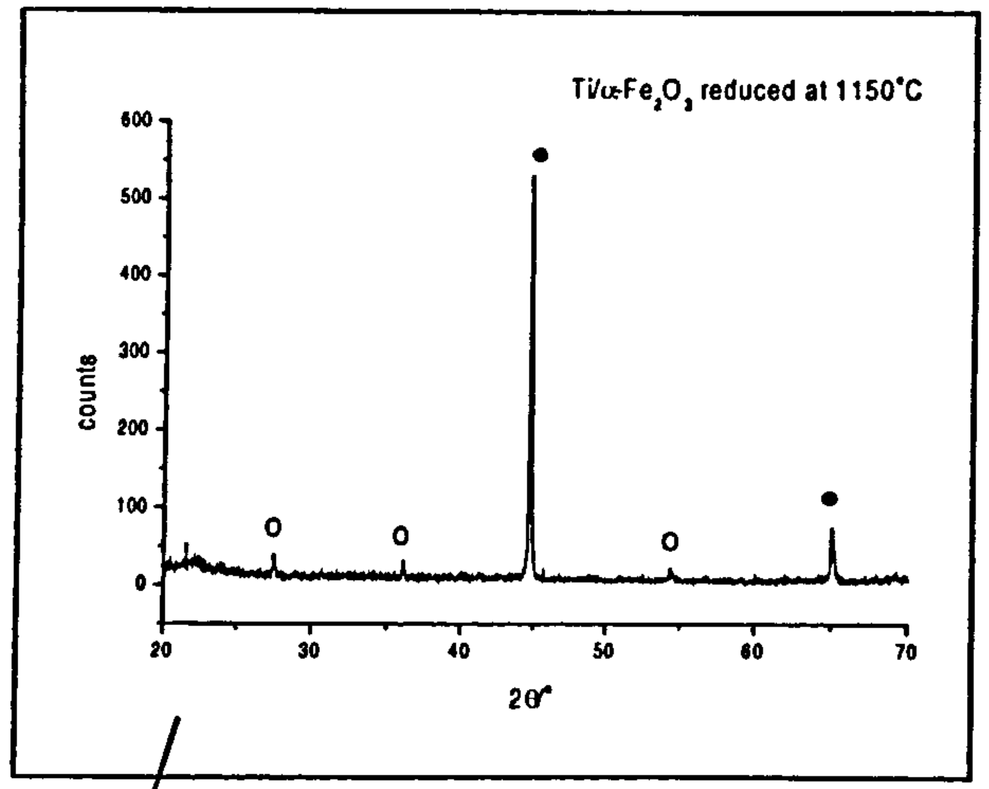

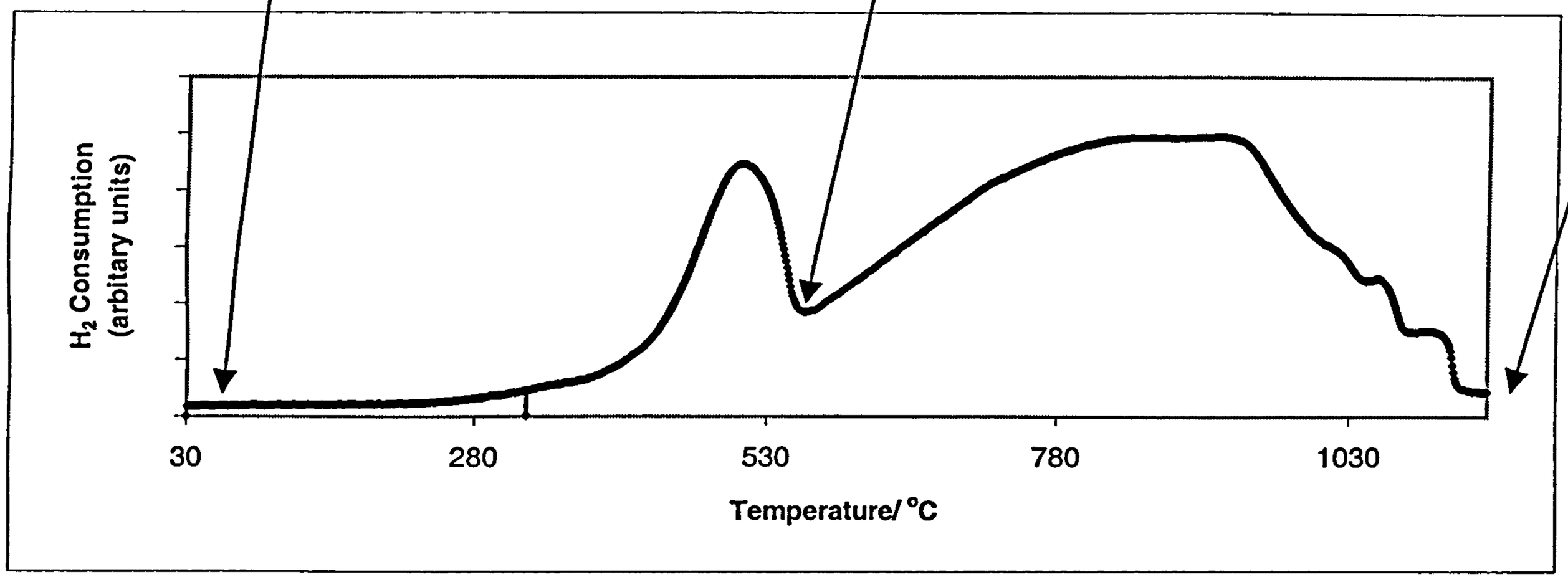

▼ = α-Fe_2O_3
◆ = Fe_3O_4
● = Fe
O = TiO_2

Figure 5.34 TPR profile recorded from Ti/α-Fe_2O_3 and XRD patterns recorded following each reduction peak

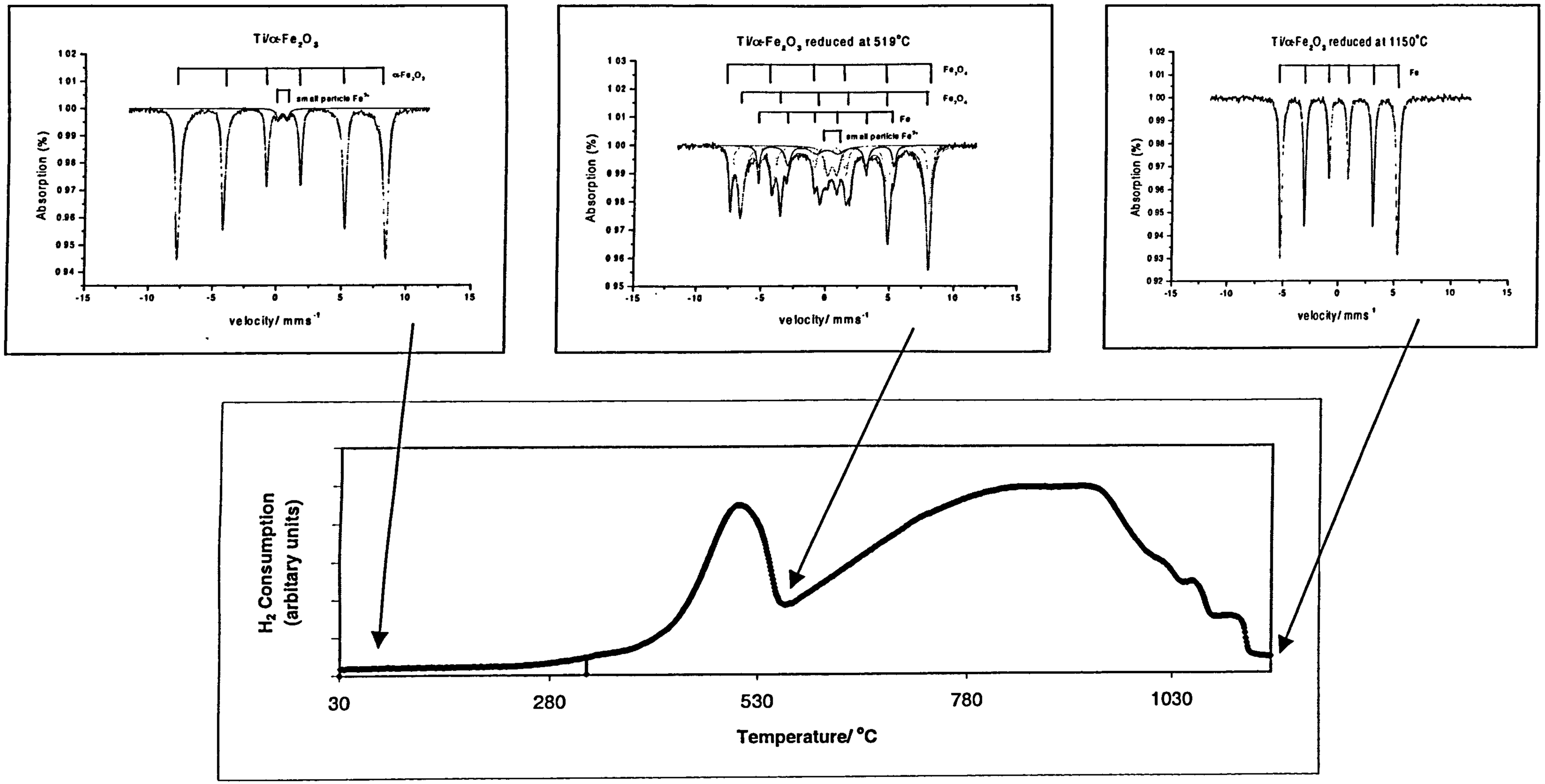

Figure 5.35 TPR profile recorded from Ti/α-Fe_2O_3 and ^{57}Fe Mössbauer spectra recorded following each reduction peak

titanium suppresses reduction of α-Fe_2O_3 to Fe_3O_4. The ^{57}Fe Mössbauer spectrum also showed that *ca.* 8 % of the material remained in small particle form following the initial reduction step. In contrast to the results recorded from undoped α–Fe_2O_3 prepared by addition of base to salt and boiling under reflux (Figure 5.28) subsequent reduction proceeded over a large temperature range reaching completion at *ca.* 1030 °C where the ^{57}Fe Mössbauer spectrum showed the formation of metallic iron.

The XRD pattern also showed peaks for TiO_2 after the final reduction.

Table 5.8 ^{57}Fe Mössbauer parameters recorded from Ti/α-Fe_2O_3 following reduction in TPR experiment

Sample	δ (± 0.02) mms^{-1}	Δ (± 0.02) mms^{-1}	H (± 1) T	Interpretation	Area (± 5) %
Ti/α-Fe_2O_3	0.40	0.69	---	Small particle iron oxide	6
	0.40	-0.10	50	α-Fe_2O_3	94
Ti/α-Fe_2O_3 reduced at 519 °C	0.43	0.73	---	Small particle iron oxide	8
	0.65	-0.01	45	Fe_3O_4	77
	0.31	0.01	48	Fe_3O_4	
	0.02	-0.01	33	Fe	15
Ti/α-Fe_2O_3 reduced at 1150 °C	0.02	0.01	33	Fe	100

No evidence for the formation of wüstite was observed. The result is similar to that recorded from Ti/γ–Fe_2O_3 prepared by addition of base to salt, boiling under reflux, and calcination at 250 °C/12 h (Section 4.2.1).

Reduction-reoxidation properties

Ti/α–Fe_2O_3 was subjected to reduction at 500 °C in the 10 % hydrogen- 90 % nitrogen mixture (R1) and reoxidation by heating at 400 °C for 1 h in air (O1). The

cycle of reduction and reoxidation was repeated twice (samples R2, O2, R3 and O3). X-ray powder diffraction (Figure 5.36) and ^{57}Fe Mössbauer spectroscopy (Figure 5.37, Table 5.9) were used to identify the materials after each reduction-reoxidation step.

Table 5.9 ^{57}Fe Mössbauer parameters recorded from Ti/α-Fe_2O_3 following treatment in reducing and oxidising environments

Sample	δ (± 0.02) mms^{-1}	Δ (± 0.02) mms^{-1}	H (± 1) T	Interpretation	Area (± 5) %
Ti/α-Fe_2O_3	0.40	0.69	---	Small particle iron oxide	6
	0.40	-0.10	50	α-Fe_2O_3	94
R1	0.43	0.56	---	Small particle iron oxide	5
	0.67	0.01	45	Fe_3O_4	95
	0.32	-0.02	48	Fe_3O_4	
O1	0.38	0.70	---	Small particle iron oxide	6
	0.35	0.0	49	γ-Fe_2O_3	94
R2	0.45	0.57	---	Small particle iron oxide	6
	0.69	0.01	45	Fe_3O_4	94
	0.30	-0.01	49	Fe_3O_4	
O2	0.37	0.69	---	Small particle iron oxide	6
	0.36	-0.01	49	γ-Fe_2O_3	94
R3	0.44	0.56	---	Small particle iron oxide	6
	0.67	0.02	45	Fe_3O_4	94
	0.31	-0.01	48	Fe_3O_4	
O3	0.42	0.74	---	Small particle iron oxide	5
	0.35	0.01	49	γ-Fe_2O_3	95

The results show that Ti/α–Fe_2O_3 can be reduced to Ti/Fe_3O_4 and reoxidised to Ti/γ–Fe_2O_3 and the reduction and reoxidation cycle repeated.

Figure 5.36 XRD patterns recorded *ex situ* from Ti/α-Fe_2O_3 following reduction and reoxidation cycles

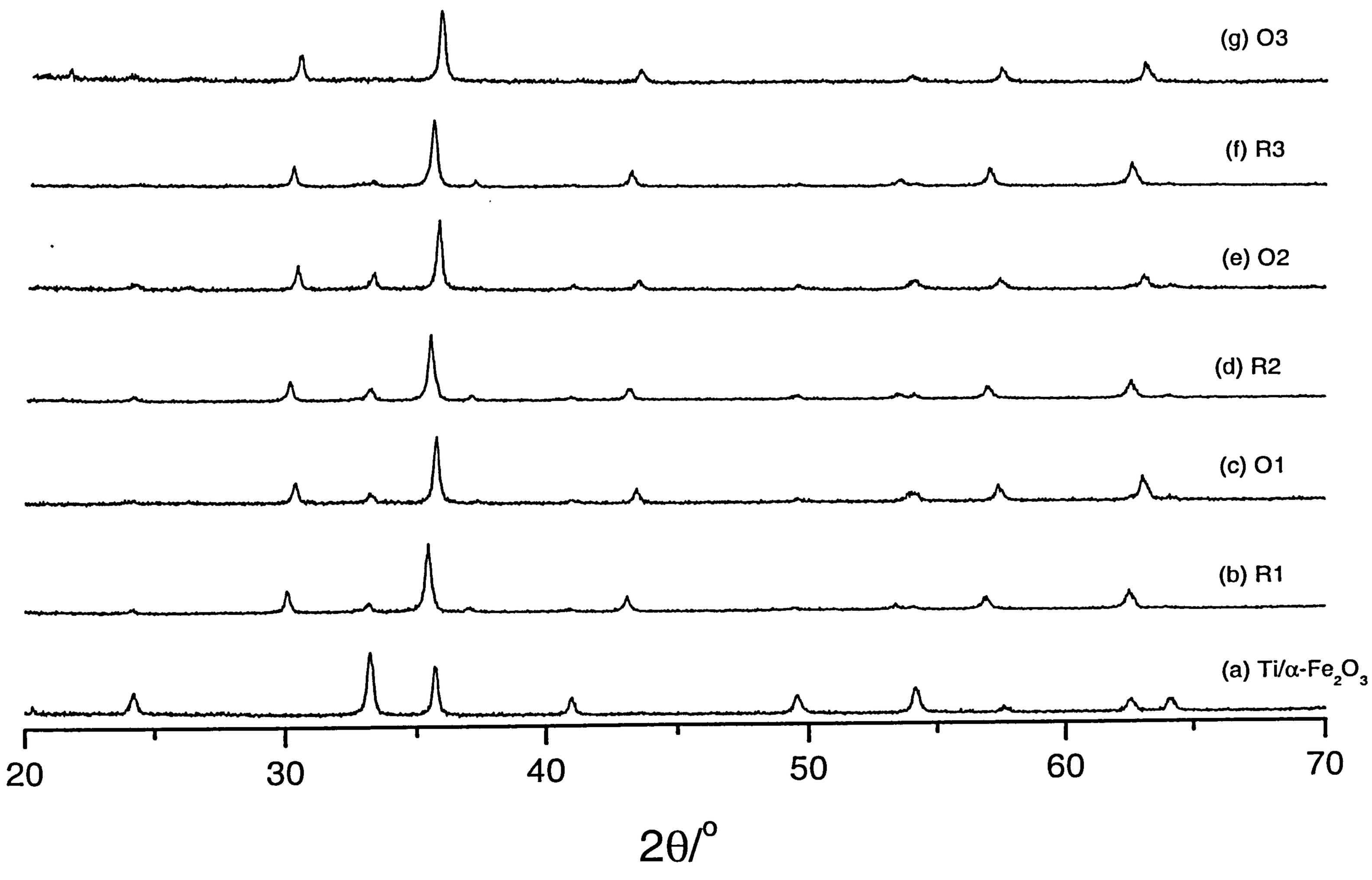

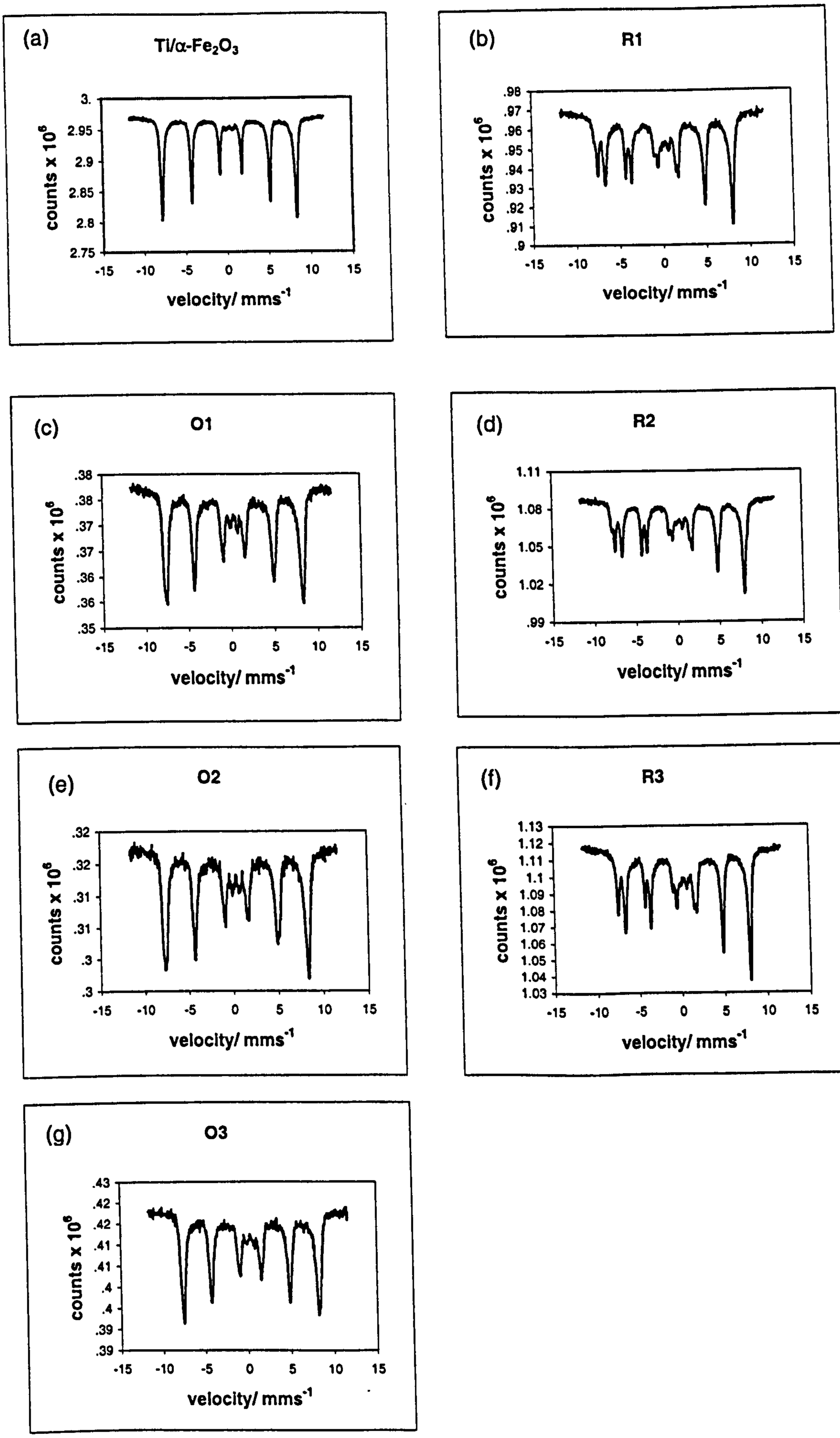

Figure 5.37 ^{57}Fe Mössbauer spectra recorded from Tl/α-Fe_2O_3 following reduction and reoxidation cycles

The particle size of titanium- doped Fe_3O_4 (R1) (*ca.* 53 nm) formed by initial reduction of titanium- doped α–Fe_2O_3 was only slightly smaller than that of the precursor titanium- doped α–Fe_2O_3 (*ca.* 57 nm). The surface area of the titanium-doped Fe_3O_4 (R1) (*ca.* 23 m^2g^{-1}) was slightly lower than titanium- doped α–Fe_2O_3 (*ca.* 29 m^2g^{-1}). Reoxidation by heating at 400 °C for 1 h in air followed by reduction and reoxidation for a further two cycles produced small changes in particle size and surface area but with the finally regenerated titanium- doped γ–Fe_2O_3 (O3) having a particle size of *ca.* 46 nm and surface area of *ca.* 18 m^2g^{-1}. The results show that titanium- doped- γ–Fe_2O_3 and - Fe_3O_4 are of similar particle size and slightly higher surface area as compared to their undoped counterparts.

Conclusion

Ti/α-Fe_2O_3 prepared by addition of base to salt, boiling under reflux, and calcination at 600 °C/12 h had a higher surface area than undoped α-Fe_2O_3 prepared by a similar method. The TPR profile showed three reduction peaks with the latter two peaks merged and the initial reduction peak being at a higher temperature than that of undoped α-Fe_2O_3 prepared by a similar method. The second reduction step did not show the formation of FeO in contrast to α-Fe_2O_3 prepared by a similar method. The TPR profile showed similar characteristics as Ti/γ–Fe_2O_3 prepared by addition of base to salt, boiling under reflux, and calcination at 250 °C/12 h with the only difference being the higher reduction temperature for the initial peak. The reduction-reoxidation treatment induced little variation in the particle size and surface area, with a higher surface area being maintained as compared with the undoped counterpart.

5.5.2 Tin- doped α–Fe_2O_3 (addition of base to salt, boiling under reflux, and calcination at 600 °C/12 h)

The X-ray powder diffraction pattern (Figure 5.38) recorded from the material which EDX analysis showed to contain 14.5 mass % Sn was characteristic of a single phase corundum-related structure[14]. Given the high content of tin it is reasonable to assume that not all the tin is incorporated into the α-Fe_2O_3- related structure and an appreciable amount may be on the surface of the iron oxide in an amorphous state. The lattice parameters a = 5.063(2) Å, c = 13.809(2) Å compare with the reported values for Sn/α-Fe_2O_3[15] (a = 5.037 Å, c = 13.752 Å), and for α–Fe_2O_3 formed here by a similar method a = 5.034(2) Å, c = 13.755(2) Å. The increase in lattice parameters can be associated with the larger size of Sn^{4+} in octahedral coordination (0.69 Å)[6] as compared to Fe^{3+} (0.65 Å). The peaks at *ca.* 33 and 36 ° 2θ showed an inversion of intensities as compared with those of pure α-Fe_2O_3 as has been observed previously[16].

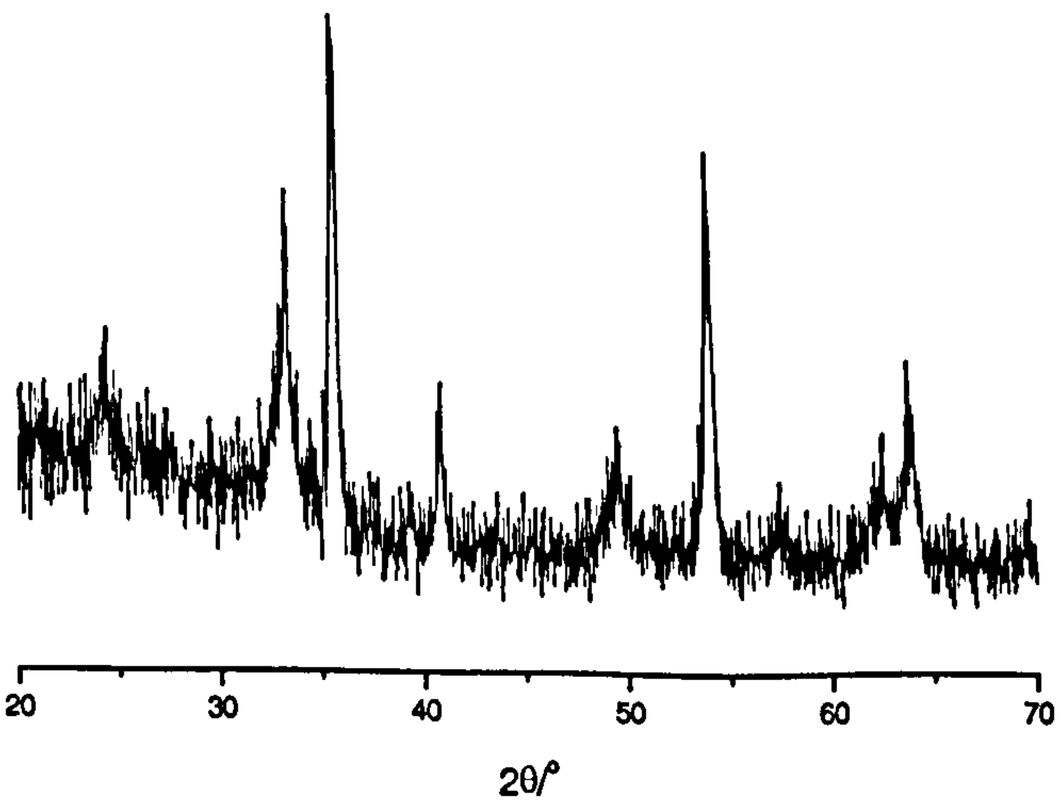

Figure 5.38 XRD pattern recorded from Sn/α–Fe_2O_3 prepared by addition of base to salt, boiling under reflux, and calcination at 600 °C

The ^{57}Fe Mössbauer spectrum (Figure 5.39) recorded at 298 K showed a sextet pattern (δ 0.39(2) mms^{-1}, Δ -0.09(2) mms^{-1}, H 49(1) T) characteristic[2,3] of an α–Fe_2O_3 related phase together with a doublet (δ 0.46(2) mms^{-1}, Δ 0.00(2) mms^{-1}) characteristic of the additional presence of small particle iron oxide[9] accounting for *ca.* 36 % of the spectral area. The particle size of *ca.* 16 nm obtained from the X-ray powder diffraction linewidth data, was lower than that of undoped α–Fe_2O_3 and Ti/α-Fe_2O_3 prepared by a similar method. The surface area of *ca.* 35 m^{2}g^{-1} was greater than that of undoped α–Fe_2O_3, but similar to Ti/α-Fe_2O_3 prepared by a similar method.

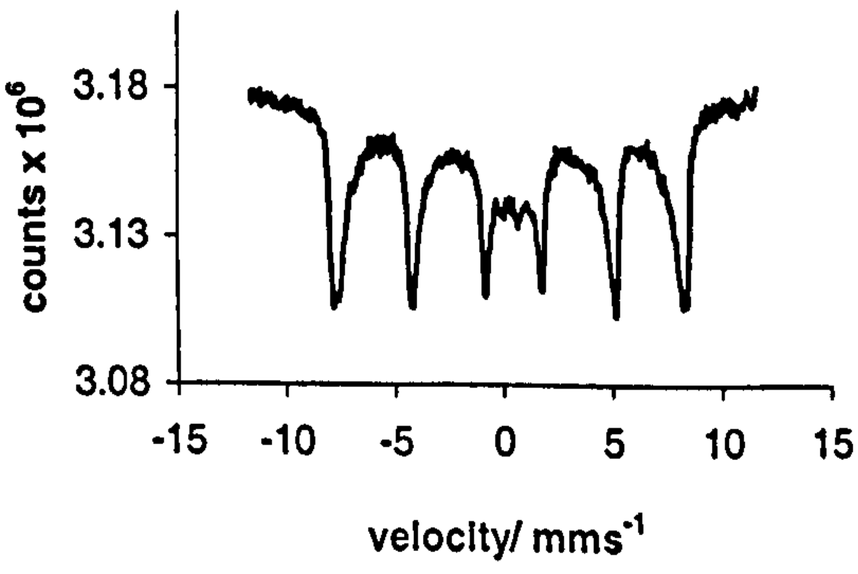

Figure 5.39 ^{57}Fe Mössbauer spectrum recorded from Sn/α–Fe_2O_3 prepared by addition of base to salt, boiling under reflux, and calcination at 600 °C

The temperature programmed reduction profile recorded from tin- doped α–Fe_2O_3 is shown in Figure 5.40. The profile showed three reduction peaks (342, 774, 946 °C), and a shoulder at *ca.* 500 °C. The intensity of the initial peak was smaller than that of undoped α-Fe_2O_3 prepared by a similar method. The lowering of the intensity of the first peak was also observed in the TPR profiles of Sn/γ–Fe_2O_3 prepared by addition of base to salt, boiling under reflux, and calcination at 250 °C/12 h (Section 4.2.2) and Sn/Fe_3O_4 prepared by a hydrothermal process (Section 5.2.2). *Ex situ* XRD and *ex situ* ^{57}Fe Mössbauer spectroscopy studies of samples retrieved after each reduction

peak from the TPR experiment have revealed the identity of the reduced phases (Figures 5.40 and 5.41 respectively). Table 5.10 shows the ^{57}Fe Mössbauer parameters of Sn/α-Fe_2O_3 after each reduction step.

The first reduction step at *ca.* 342 °C can, as in the case of undoped α–Fe_2O_3 prepared by addition of base to salt, boiling under reflux, and calcination at 600 °C/12 h (Figure 5.28), be associated with the partial reduction of tin- doped α–Fe_2O_3 to tin- doped Fe_3O_4. This was followed by partial reduction at *ca.* 774 °C, to FeO and metallic iron, (and an iron- tin alloy and SnO observed in the XRD pattern (Figure 5.40)). Reduction at 1150 °C showed the formation of metallic iron and an iron- tin alloy (Figures 5.40, 5.41 and Table 5.10).

Table 5.10 ^{57}Fe Mössbauer parameters recorded from Sn/α-Fe_2O_3 following reduction in TPR experiment

Sample	δ (± 0.02) mms^{-1}	Δ (± 0.02) mms^{-1}	H (± 1) T	Interpretation	Area (± 5) %
Sn/α-Fe_2O_3	0.46	0.00	---	Small particle iron oxide	36
	0.39	-0.09	49	α-Fe_2O_3	64
Sn/α-Fe_2O_3 reduced at 342 °C	0.51	0.00	45	Fe_3O_4	74
	0.29	0.00	48	Fe_3O_4	
	0.39	-0.10	50	α-Fe_2O_3	26
Sn/α-Fe_2O_3 reduced at 774 °C	0.68	0.00	45	Fe_3O_4	30
	0.30	0.00	48	Fe_3O_4	
	1.09	0.27	---	FeO	32
	0.05	0.0	33	Fe	38
Sn/α-Fe_2O_3 reduced at 1150 °C	0.18	0.00	21	Sn/Fe	8
	0.13	0.00	33	Fe	92

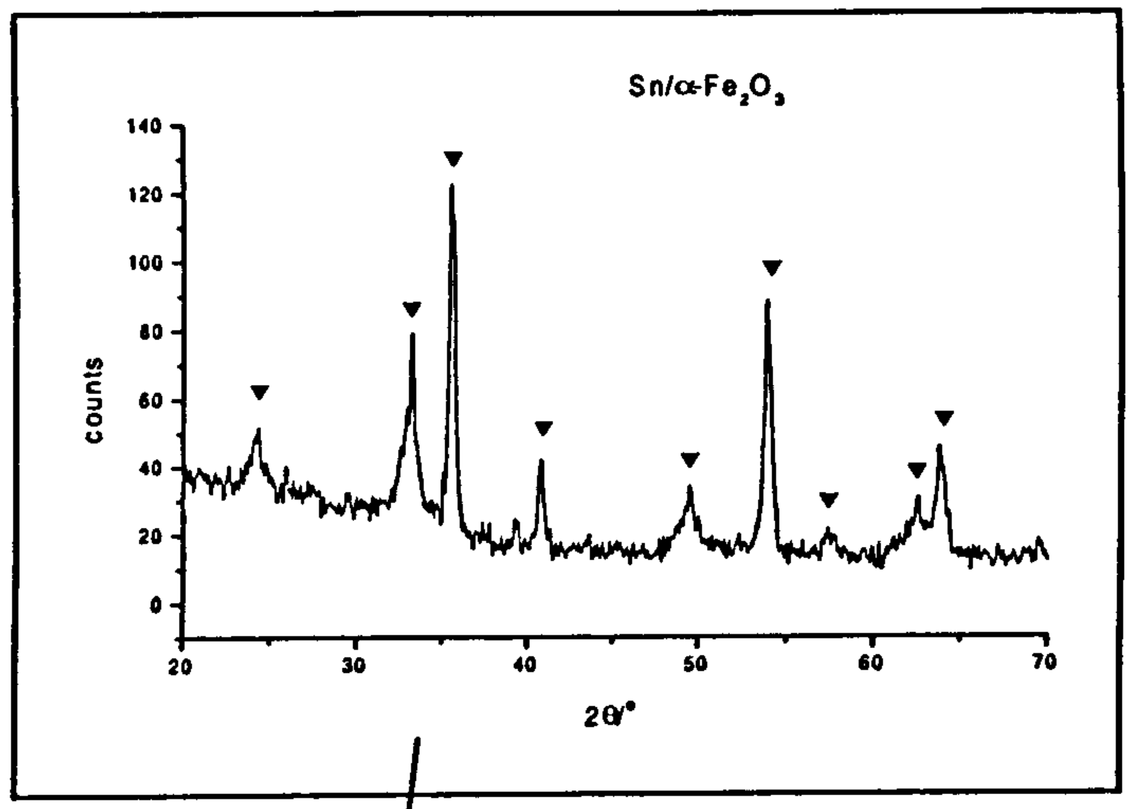

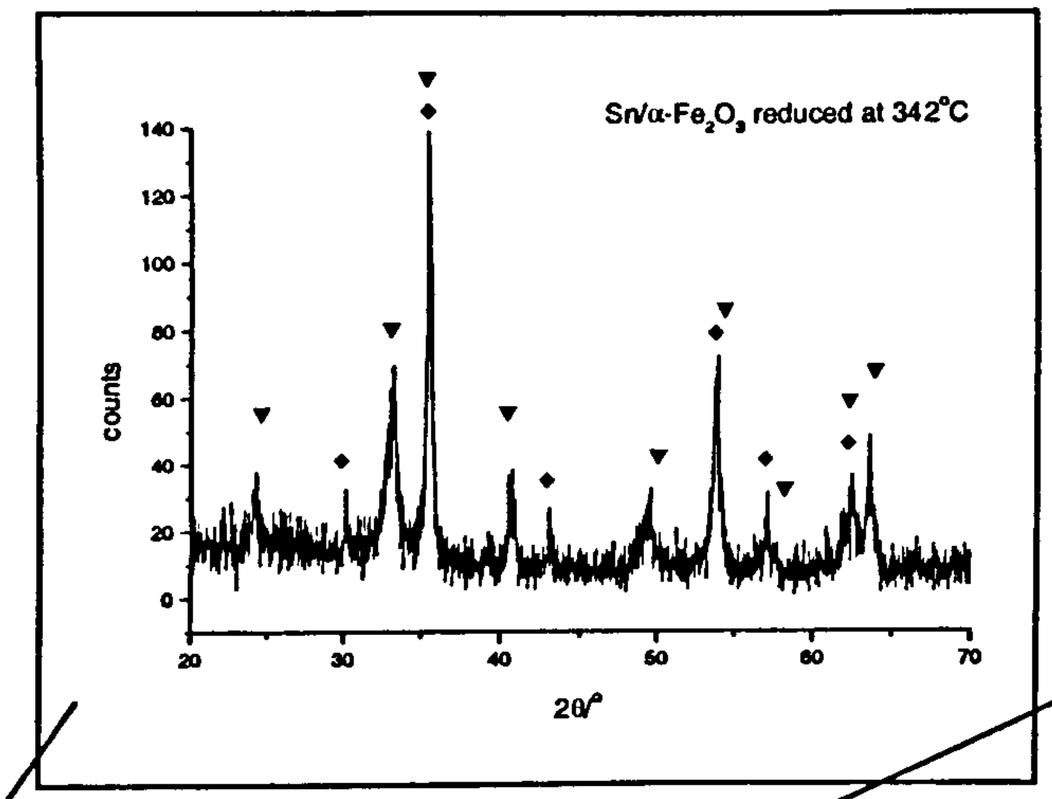

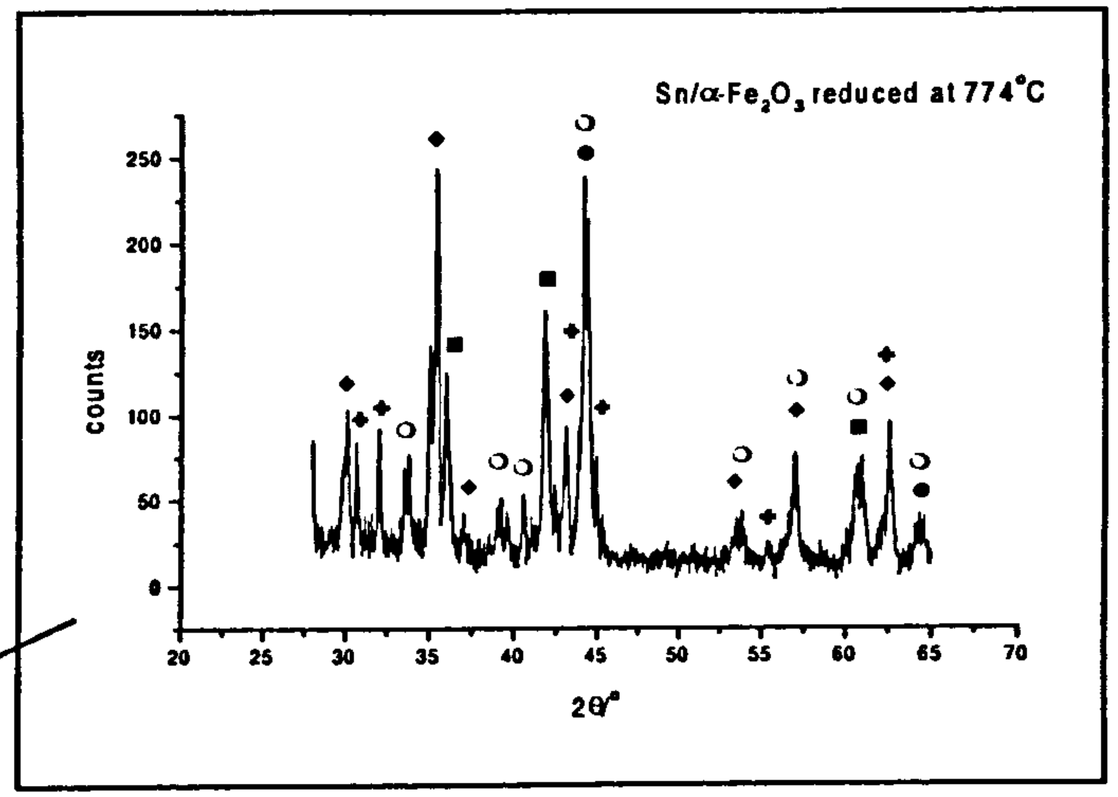

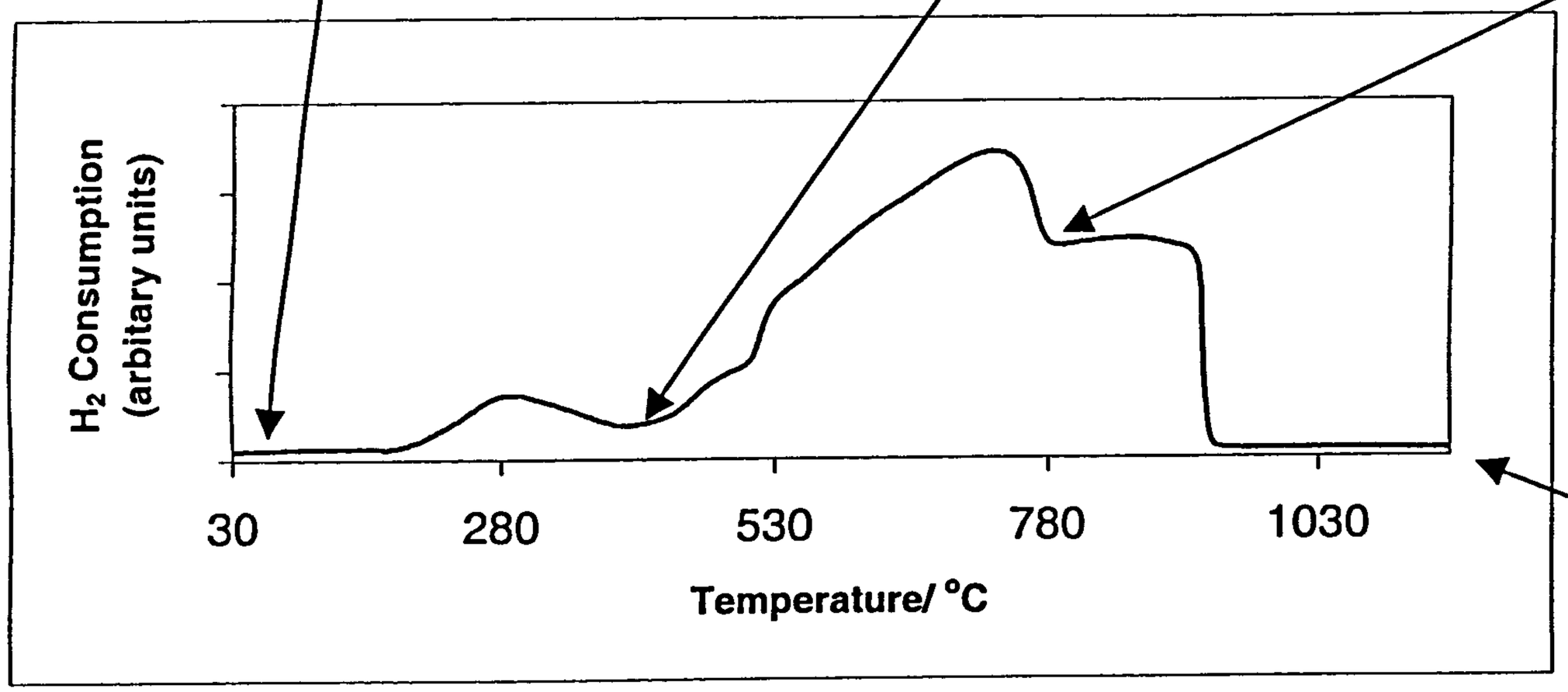

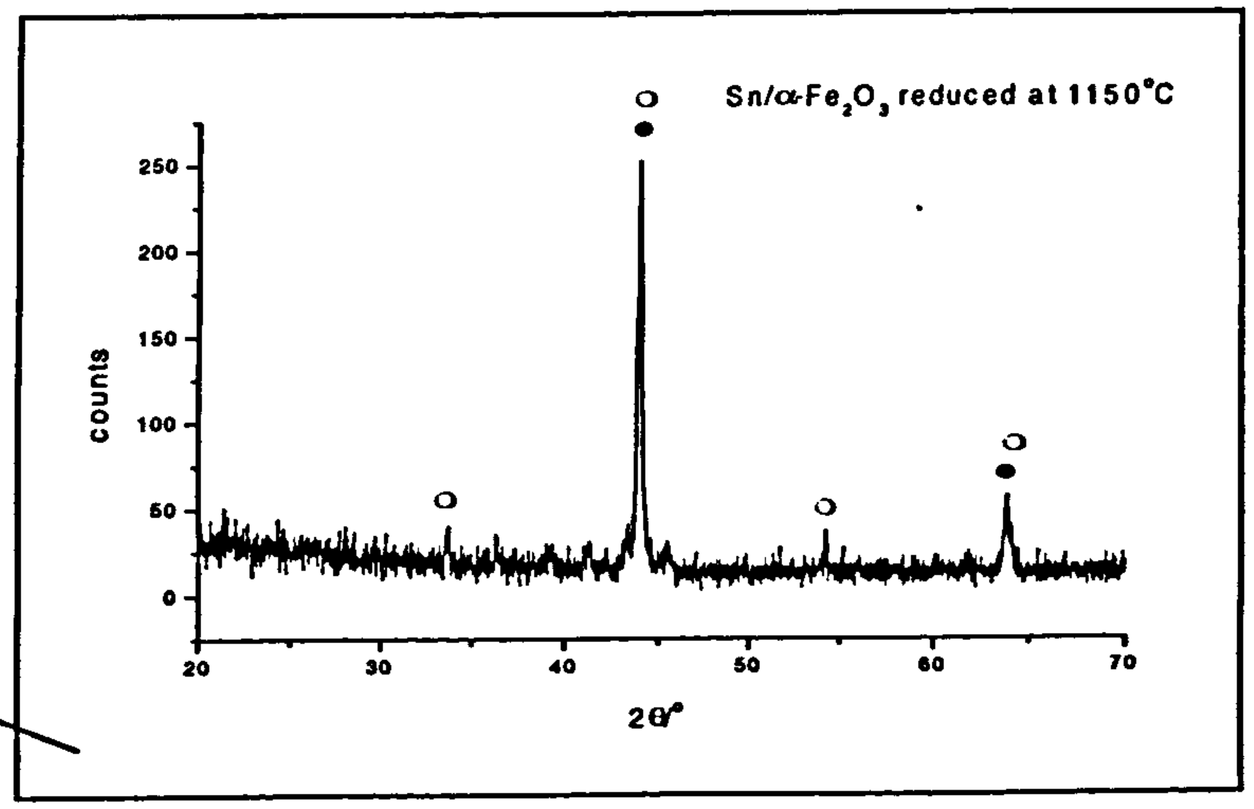

▼ = α-Fe_2O_3
◆ = Fe_3O_4
■ = FeO
● = Fe
O = SnFe
✣ = SnO

Figure 5.40 TPR profile recorded from Sn/α-Fe_2O_3 and XRD patterns recorded following each reduction peak

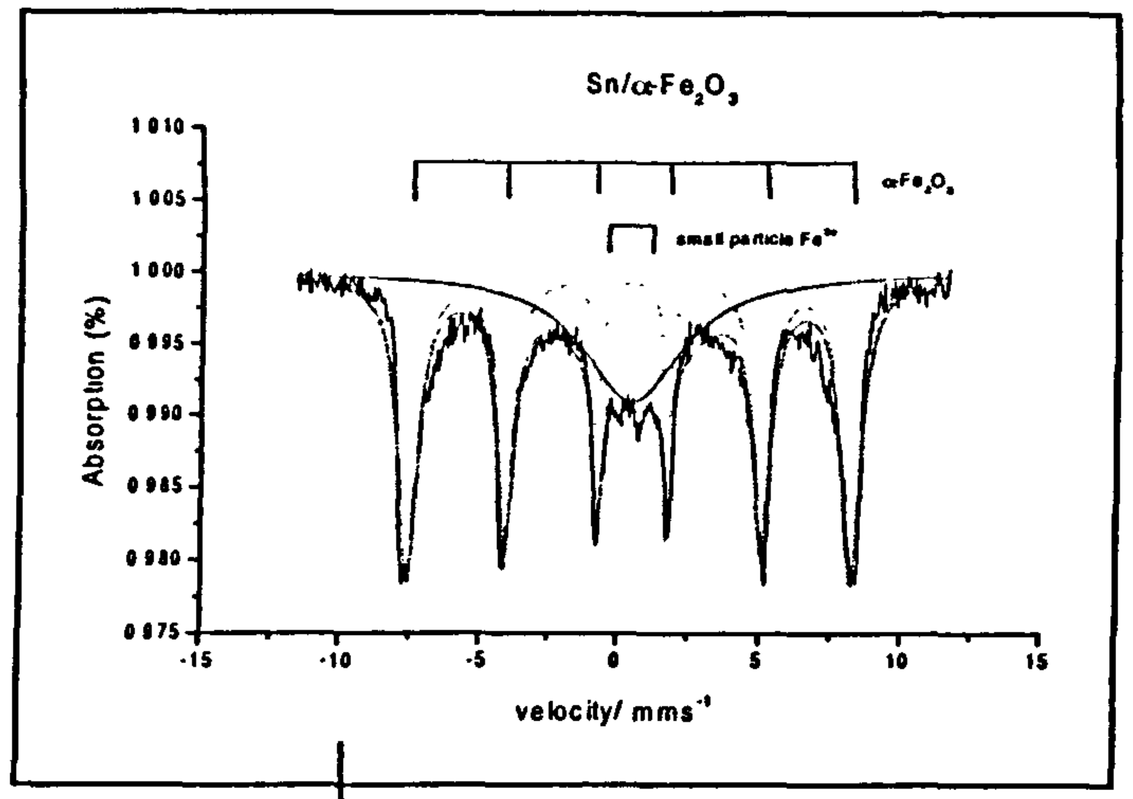

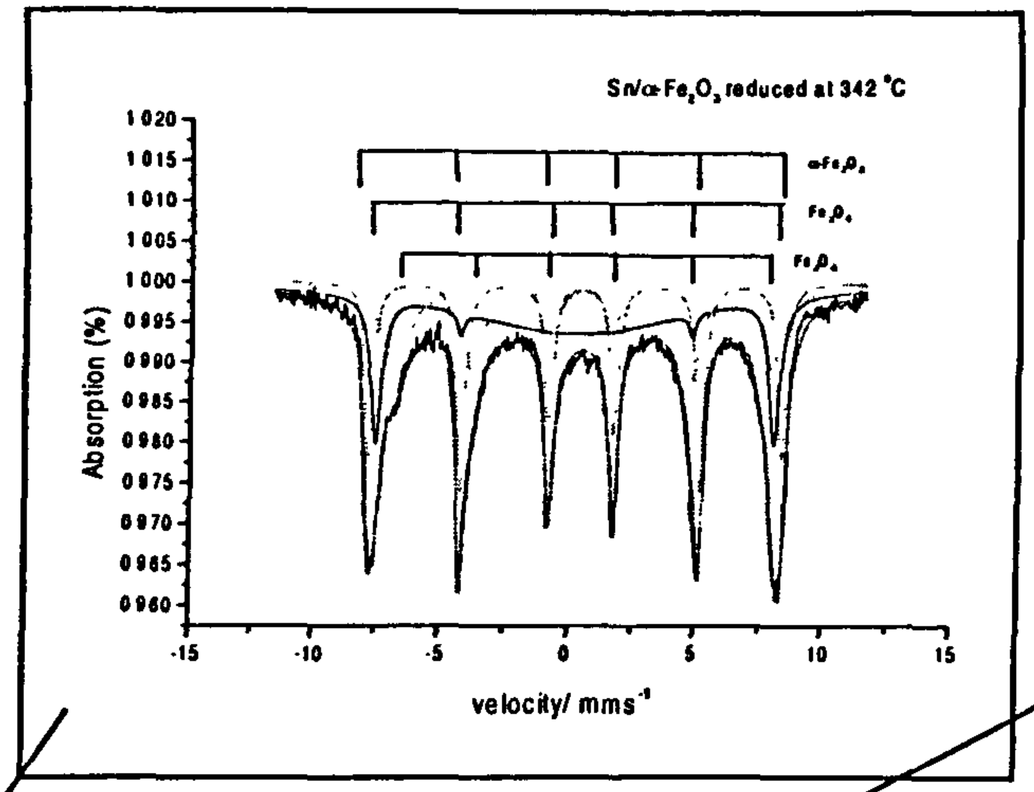

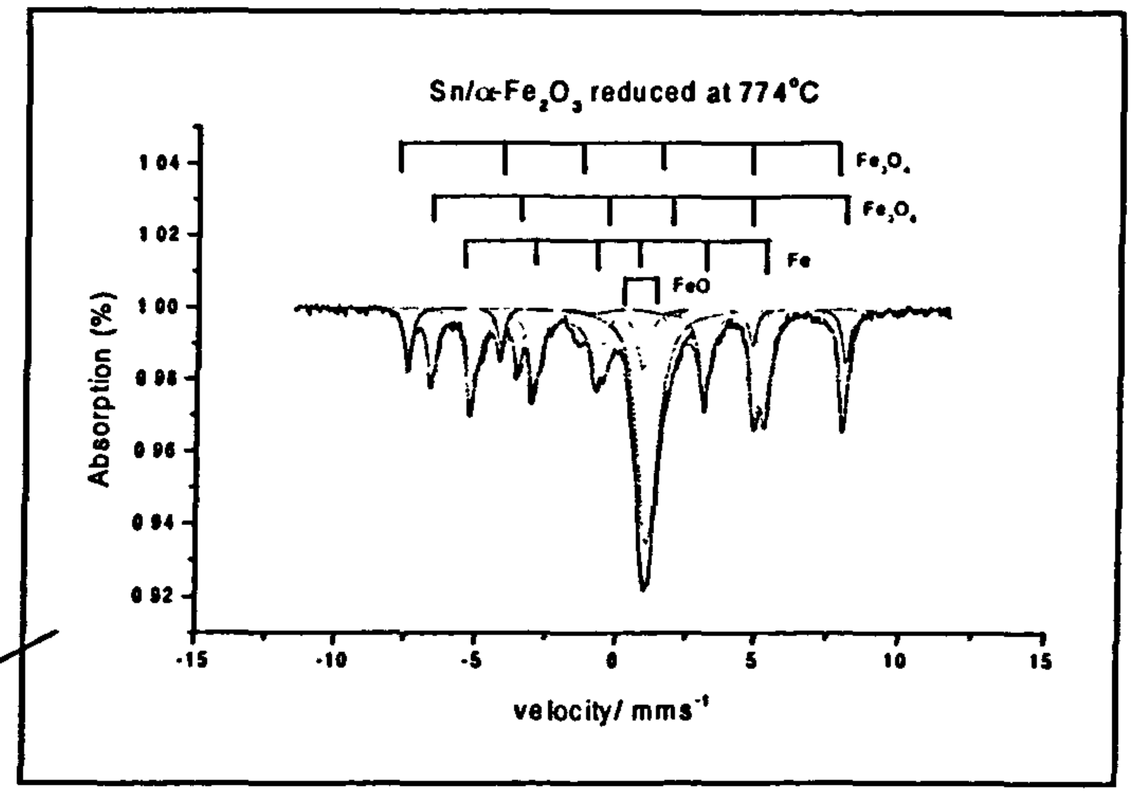

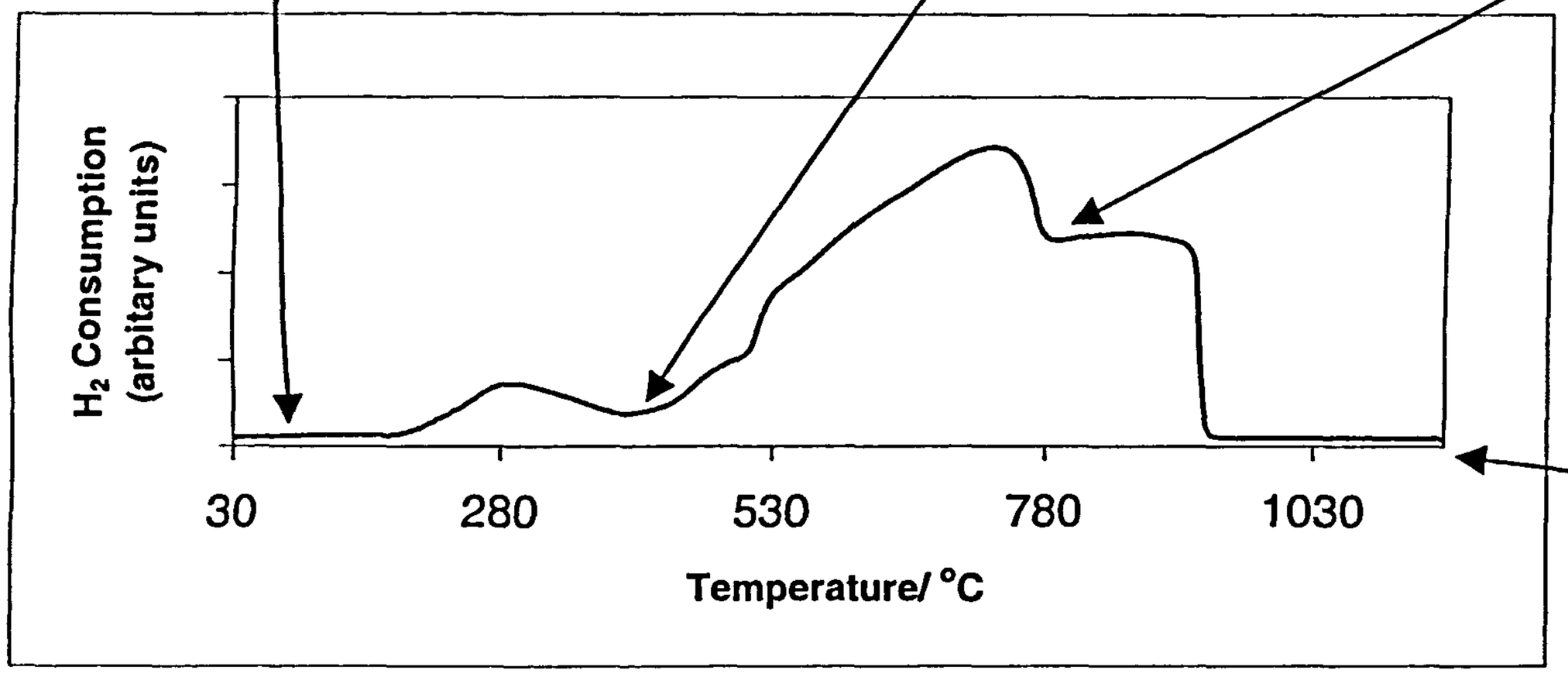

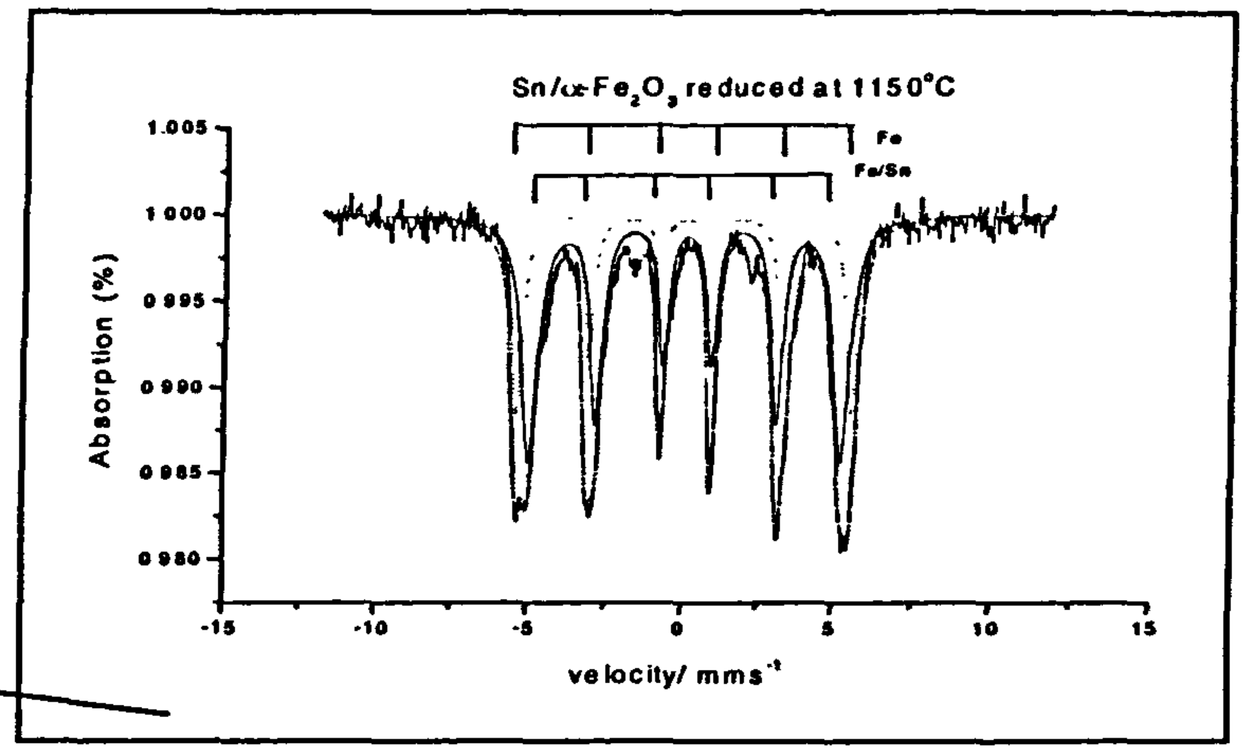

Figure 5.41 TPR profile recorded from Sn/α-Fe_2O_3 and ^{57}Fe Mössbauer spectra recorded following each reduction peak

Reduction-reoxidation properties

Sn/α–Fe_2O_3 was subjected to reduction at 400 °C in the 10 % hydrogen- 90 % nitrogen mixture (R1) and reoxidation by heating at 400 °C for 1 h in air (O1). The cycle of reduction and reoxidation was repeated twice (samples R2, O2, R3 and O3). X-ray powder diffraction (Figure 5.42) and ^{57}Fe Mössbauer spectroscopy (Figure 5.43, Table 5.11) were used to identify the materials after each reduction-reoxidation step. The initial reduction process did not completely eliminate α-Fe_2O_3 as a small amount (*ca.* 15 %) remained.

Table 5.11 ^{57}Fe Mössbauer parameters recorded from Sn/α-Fe_2O_3 following treatment in reducing and oxidising environments

Sample	δ (± 0.02) mms^{-1}	Δ (± 0.02) mms^{-1}	H (± 1) T	Interpretation	Area (± 5) %
Sn/α-Fe_2O_3	0.46	0.00	---	Small particle iron oxide	36
	0.39	-0.09	49	α-Fe_2O_3	64
R1	0.57	-0.02	44	Fe_3O_4	85
	0.32	-0.05	48	Fe_3O_4	
	0.36	-0.09	50	α-Fe_2O_3	15
O1	0.34	0.69	---	Small particle iron oxide	26
	0.34	-0.02	48	γ-Fe_2O_3	52
	0.37	-0.08	50	α-Fe_2O_3	22
R2	0.60	-0.01	44	Fe_3O_4	91
	0.30	-0.03	48	Fe_3O_4	
	0.34	-0.08	50	α-Fe_2O_3	9
O2	0.34	0.01	48	γ-Fe_2O_3	95
	0.39	-0.09	50	α-Fe_2O_3	5
R3	0.62	-0.04	45	Fe_3O_4	90
	0.30	0.01	48	Fe_3O_4	
	0.38	-0.09	49	α-Fe_2O_3	10
O3	0.33	0.01	48	γ-Fe_2O_3	91
	0.39	-0.09	50	α-Fe_2O_3	9

Figure 5.42 XRD patterns recorded *ex situ* from Sn/α-Fe_2O_3 following reduction and reoxidation cycles

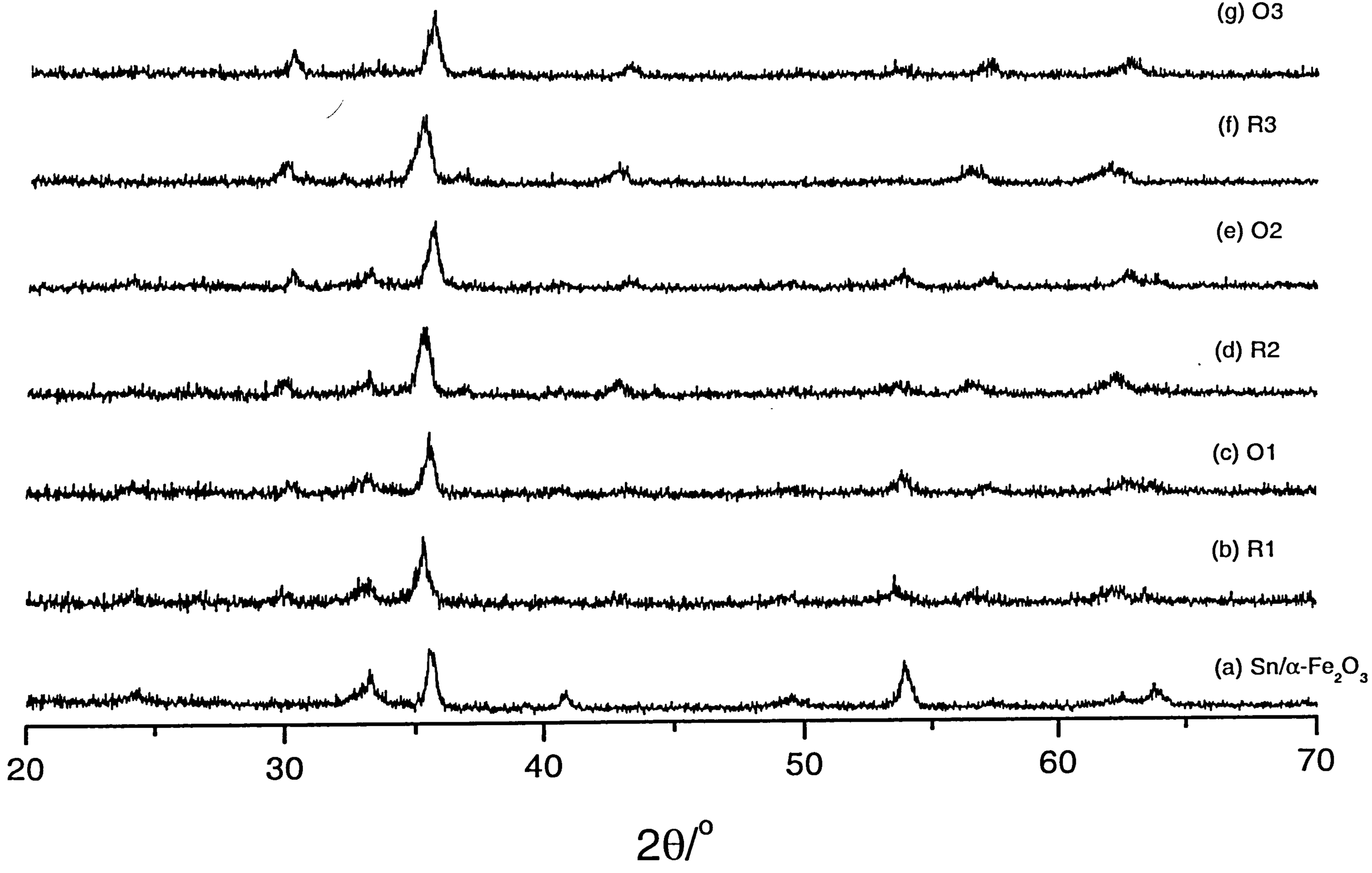

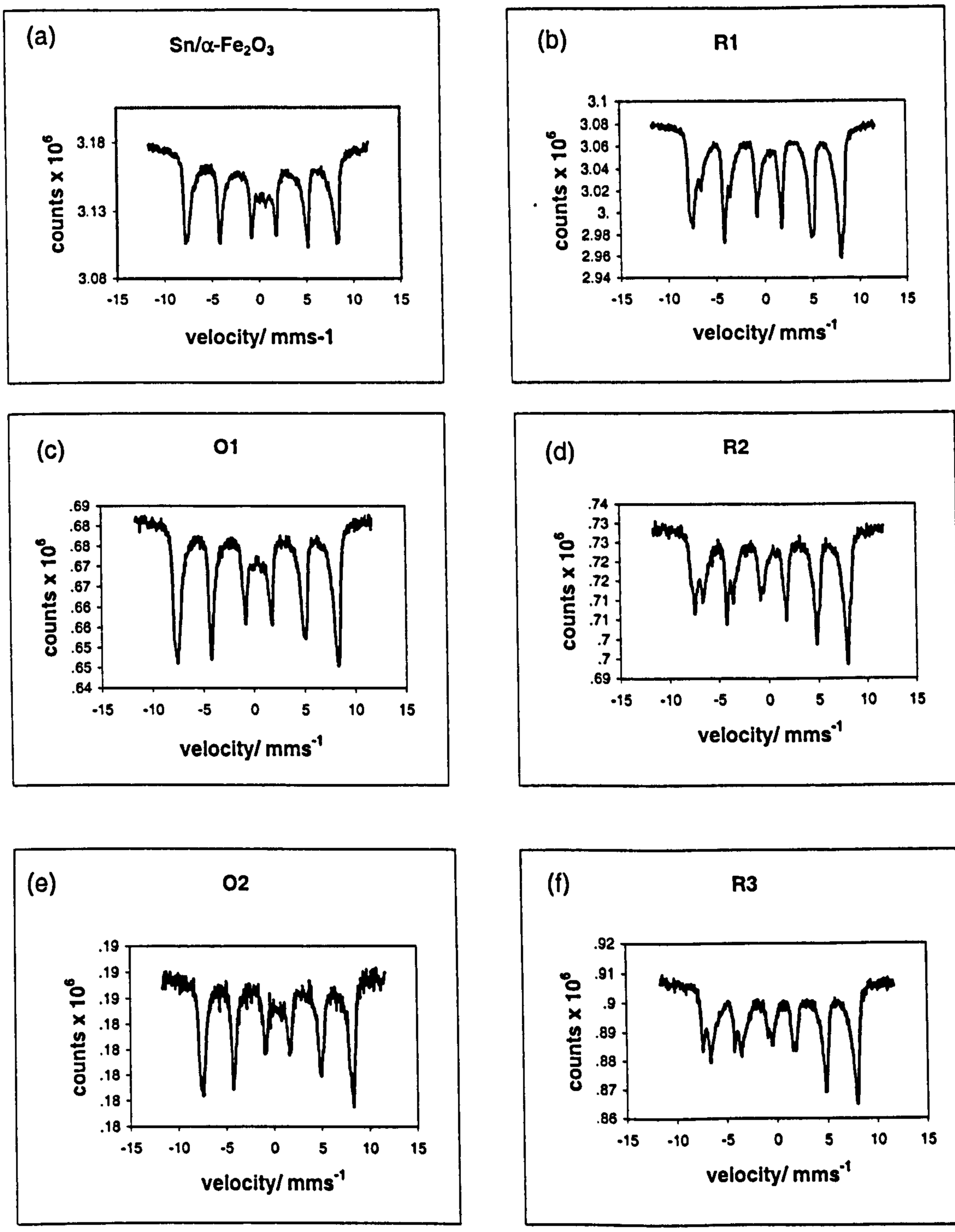

Figure 5.43 ^{57}Fe Mössbauer spectra recorded from Sn/α-Fe_2O_3 following reduction and reoxidation cycles

The results show that Sn/α–Fe_2O_3 can be reduced to Sn/Fe_3O_4 and reoxidised to Sn/γ–Fe_2O_3 and the reduction and reoxidation cycle repeated. A small amount of α-Fe_2O_3 remained throughout the reduction- oxidation cycling.

The particle size of tin- doped Fe_3O_4 (R1) (*ca.* 32 nm) formed by initial reduction of tin- doped α–Fe_2O_3 was larger than that of the precursor tin- doped α–Fe_2O_3 (*ca.* 16 nm). The surface area of the tin- doped Fe_3O_4 (R1) (*ca.* 24 m^2g^{-1}) was lower than tin-doped α–Fe_2O_3 (*ca.* 35 m^2g^{-1}). Reoxidation by heating at 400 °C for 1 h in air followed by reduction and reoxidation for a further two cycles produced variations in particle size and surface area, with the finally regenerated tin- doped γ–Fe_2O_3 (O3), having a size of *ca.* 19 nm and surface area of *ca.* 19 m^2g^{-1}. The results showed that tin- doped -γ–Fe_2O_3 and -Fe_3O_4 (reduced and reoxidised products) are of smaller particle size than undoped α-Fe_2O_3 and Ti/α-Fe_2O_3 counterparts.

Conclusion

Sn/α-Fe_2O_3 prepared by addition of base to salt, boiling under reflux, and calcination at 600 °C/12 h showed a higher surface area than α-Fe_2O_3, but similar to Ti/α-Fe_2O_3 prepared by a similar method. The TPR profile showed three reduction peaks similar to α-Fe_2O_3 prepared by a similar method, with the formation of FeO, which was not observed in the reduction process of Ti/α-Fe_2O_3. The reduction- reoxidation results show that Sn/α–Fe_2O_3 can be reduced to Sn/Fe_3O_4 and reoxidised to Sn/γ–Fe_2O_3 and the reduction and reoxidation cycle repeated, with the maintenance of a smaller particle size than that of undoped α-Fe_2O_3 and Ti/α-Fe_2O_3 prepared by a similar method.

5.5.3.1 Ruthenium- doped α–Fe_2O_3 (addition of base to salt, or salt to base, boiling under reflux, and calcination at 600 °C/12 h)

The attempted preparation of ruthenium- doped α-Fe_2O_3 by the addition of base to salt or salt to base, boiling under reflux, and calcination at 600 °C/12 h gave a bi-phasic mixture of α-Fe_2O_3 and RuO_2. The formation of α-Fe_2O_3 and RuO_2 was also observed when ruthenium- doped γ–Fe_2O_3 was heated at elevated temperatures (Section 4.2.3). It therefore seems that high temperature calcination induces the segregation of ruthenium from the iron oxide.

5.5.3.2 Ruthenium- doped α–Fe_2O_3 (addition of base to salt, heated hydrothermally, and dried under an infrared lamp)

The X-ray powder diffraction pattern (Figure 5.44) recorded from the material which EDX analysis showed to contain 9.69 mass % Ru was characteristic of single phase corundum-related structure[14]. The high content of ruthenium may be due to an appreciable amount of amorphous RuO_2 on the surface of the iron oxide, not detected by XRD. The lattice parameters a = 5.039(2) Å, c = 13.780(2) Å were larger then the reported[14] values for α-Fe_2O_3 a = 5.035 Å, c = 13.749 Å, and the α–Fe_2O_3 prepared here by addition of base to salt and heated hydrothermally, (a = 5.035(2) Å, c = 13.750(2) Å). This was unexpected since Ru^{4+} in octahedral coordination has a radius of 0.62 Å[6] as compared to Fe^{3+} (0.65 Å).

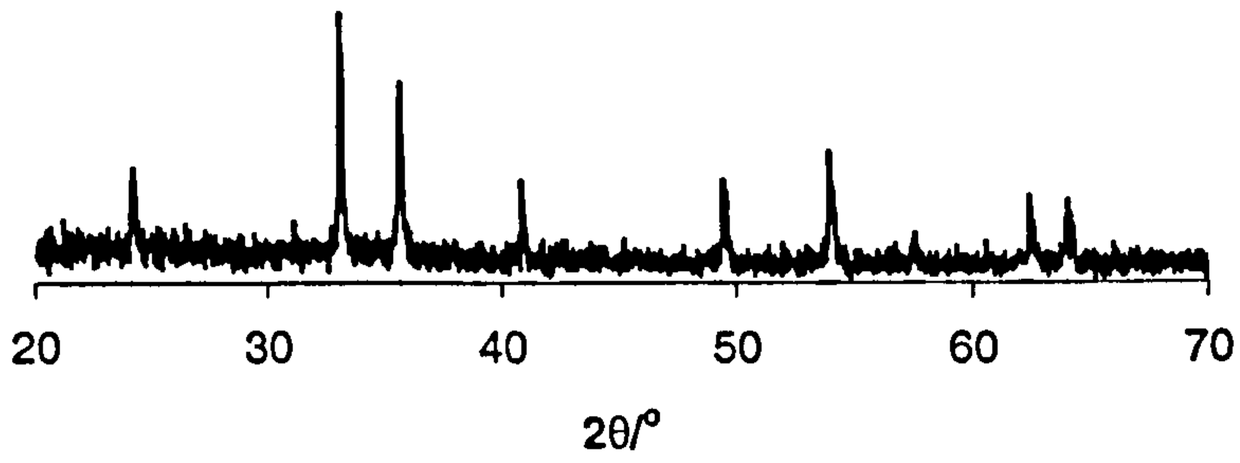

Figure 5.44 XRD pattern recorded from Ru/α–Fe_2O_3 prepared by addition of base to salt, heated hydrothermally and dried under an infrared lamp

The ^{57}Fe Mössbauer spectrum (Figure 5.45) recorded at 298 K showed a sextet pattern (δ 0.38(2) mms^{-1}, Δ -0.08(2) mms^{-1}, H 50(1) T) characteristic[2,3] of an α–Fe_2O_3- related phase together with a doublet (δ 0.34(2) mms^{-1}, Δ 0.68(2) mms^{-1}) characteristic of the additional presence of small particle iron oxide[9] which accounted for *ca.* 11 % of the spectral area. The particle size of *ca.* 48 nm, obtained from the X-ray powder diffraction linewidth data, was lower than that of undoped α–Fe_2O_3 prepared by addition of base to salt and heated hydrothermally and Ti/α-Fe_2O_3 prepared by addition of base to salt, boiling under reflux and calcination at 600 °C/12 h, but higher that that of Sn/α-Fe_2O_3 prepared by addition of base to salt, boiling under reflux and calcination at 600 °C. The surface area of *ca.* 75 m^2g^{-1} was significantly higher than that of undoped α–Fe_2O_3 prepared by addition of base to salt and heated hydrothermally and titanium- and tin- doped α-Fe_2O_3 prepared by addition of base to salt, boiling under reflux and calcination at 600 °C/12 h. The higher surface area may be due to appreciable amounts of amorphous RuO_2 on the surface of the iron oxide, not detected by XRD.

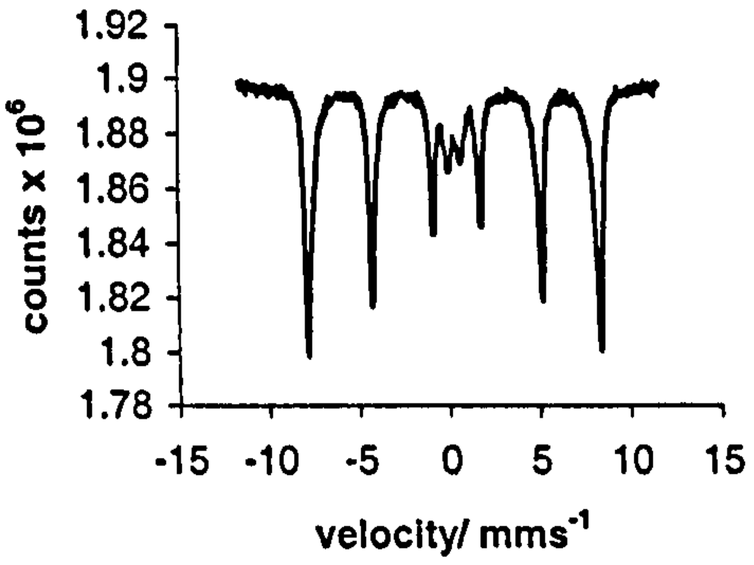

Figure 5.45 ^{57}Fe Mössbauer spectrum recorded from Ru/α–Fe_2O_3 prepared by addition of base to salt, heated hydrothermally and dried under an infrared lamp

The temperature programmed reduction profile recorded from ruthenium- doped α–Fe_2O_3 is shown in Figure 5.46. The profile showed four reduction peaks (220, 270, 718, 873°C) compared to three observed from undoped α-Fe_2O_3, titanium- and tin- doped α-Fe_2O_3. The initial reduction peak was assigned to the reduction of amorphous ruthenium dioxide not detected by the X-ray powder diffraction pattern. The reduction peaks were at lower temperature than that of undoped α-Fe_2O_3 prepared by addition of base to salt and heated hydrothermally and probably reflect the presence of ruthenium which promotes reduction. *Ex situ* XRD and *ex situ* ^{57}Fe Mössbauer spectroscopy studies of samples retrieved after each reduction peak from the TPR experiment have revealed the identity of the reduced phases (Figures 5.46 and 5.47). Table 5.12 shows the ^{57}Fe Mössbauer parameters of Ru/α-Fe_2O_3 after each reduction step.

The initial reduction peak was assigned to the reduction of amorphous ruthenium dioxide. The second reduction step at *ca.* 270 °C can be associated with the reduction of ruthenium- doped α–Fe_2O_3 to ruthenium- doped Fe_3O_4. This is followed by partial reduction to FeO and metallic iron at *ca.* 718 °C. The final reduction product was

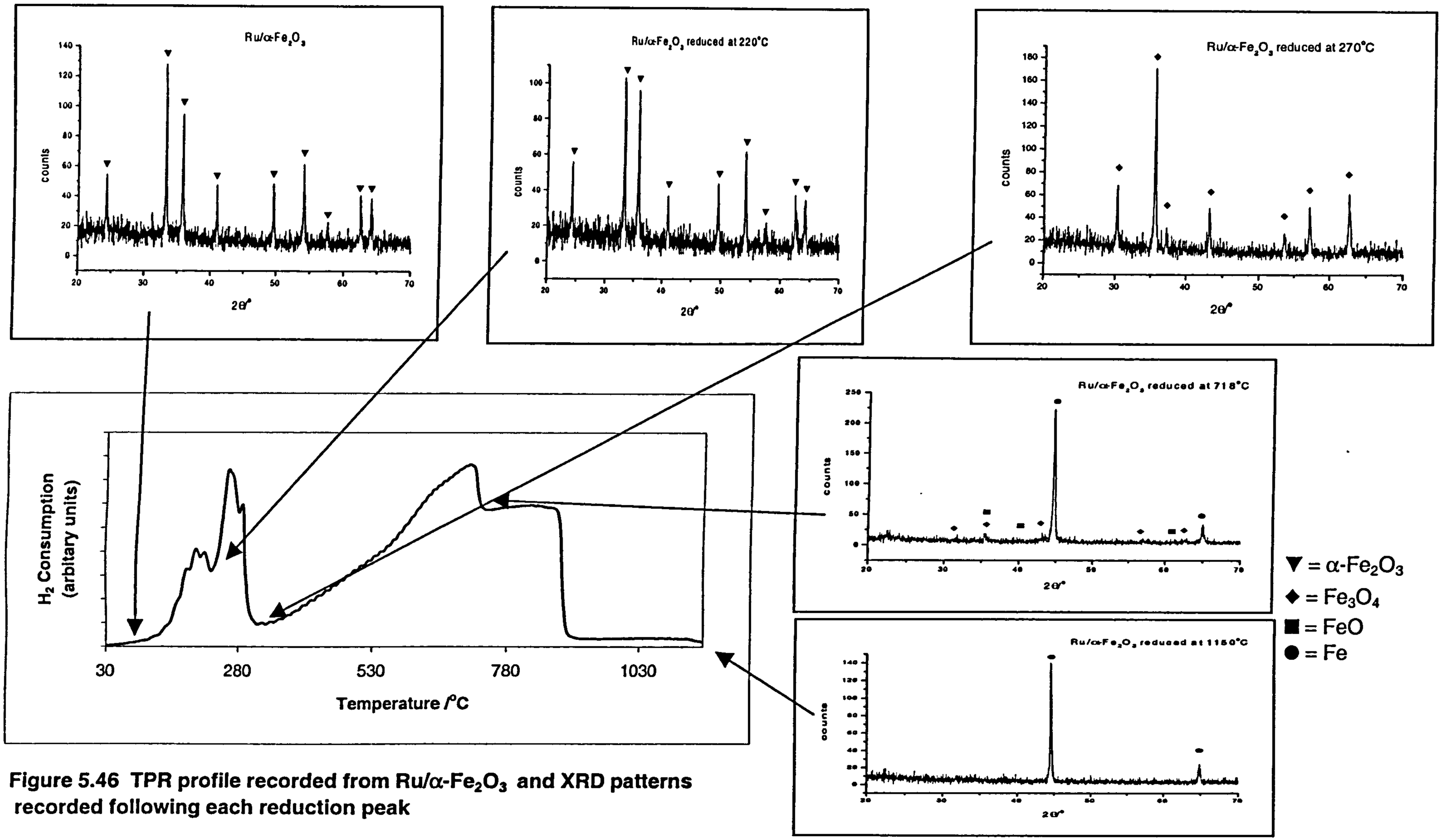

Figure 5.46 TPR profile recorded from Ru/α-Fe_2O_3 and XRD patterns recorded following each reduction peak

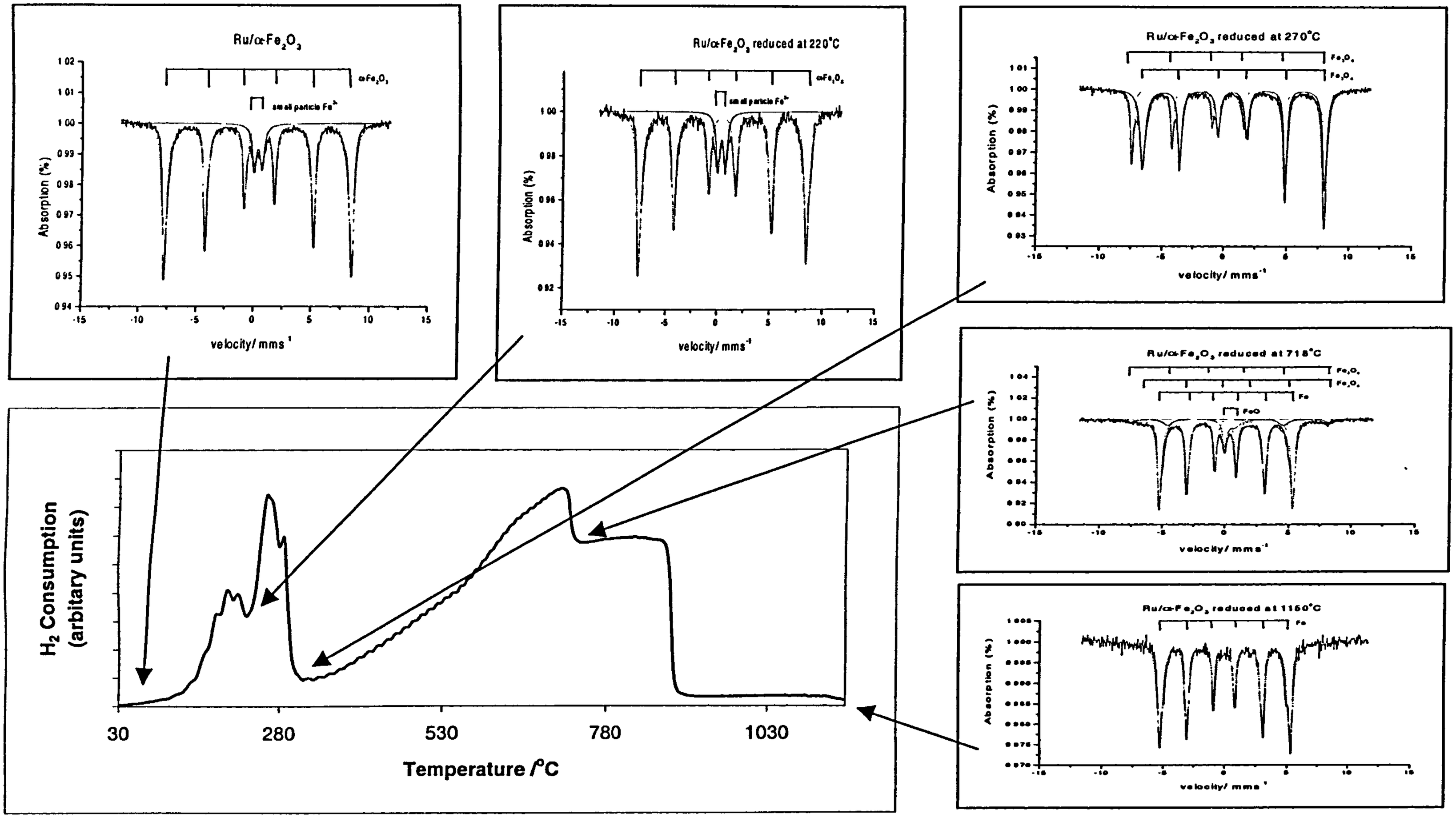

Figure 5.47 TPR profile recorded from Ru/α-Fe_2O_3 and ^{57}Fe Mössbauer spectra recorded following each reduction peak

confirmed to be metallic iron. No evidence for the formation of an iron-ruthenium alloy was observed.

Table 5.12 ^{57}Fe Mössbauer parameters recorded from Ru/α-Fe_2O_3 following reduction in TPR experiment

Sample	δ (± 0.02) mms^{-1}	Δ (± 0.02) mms^{-1}	H (± 1) T	Interpretation	Area (± 5) %
Ru/α-Fe_2O_3	0.34	0.68	---	Small particle iron oxide	11
	0.38	-0.08	51	α-Fe_2O_3	89
Ru/α-Fe_2O_3 reduced at 220 °C	0.33	0.73	---	Small particle iron oxide	11
	0.38	-0.02	50	α-Fe_2O_3	89
Ru/α-Fe_2O_3 reduced at 270 °C	0.66	0.04	45	Fe_3O_4	100
	0.23	0.02	48	Fe_3O_4	
Ru/α-Fe_2O_3 reduced at 718 °C	0.65	-0.02	43	Fe_3O_4	14
	0.09	0.15	49	Fe_3O_4	
	0.30	0.74	---	FeO	10
	0.02	0.00	33	Fe	76
Ru/α-Fe_2O_3 reduced at 1150 °C	0.02	0.01	33	Fe	100

Reduction-reoxidation properties

Ru/α–Fe_2O_3 was subjected to reduction at 270 °C in the 10 % hydrogen- 90 % nitrogen mixture (R1) and reoxidation by heating at 300 °C for 1 h in air (O1). The cycle of reduction and reoxidation was repeated twice (samples R2, O2, R3 and O3). X-ray powder diffraction (Figure 5.48) and ^{57}Fe Mössbauer spectroscopy (Figure 5.49, Table 5.13) were used to identify the materials after each reduction- reoxidation step.

Figure 5.48 XRD patterns recorded *ex situ* from Ru/α-Fe_2O_3 following reduction and reoxidation cycles

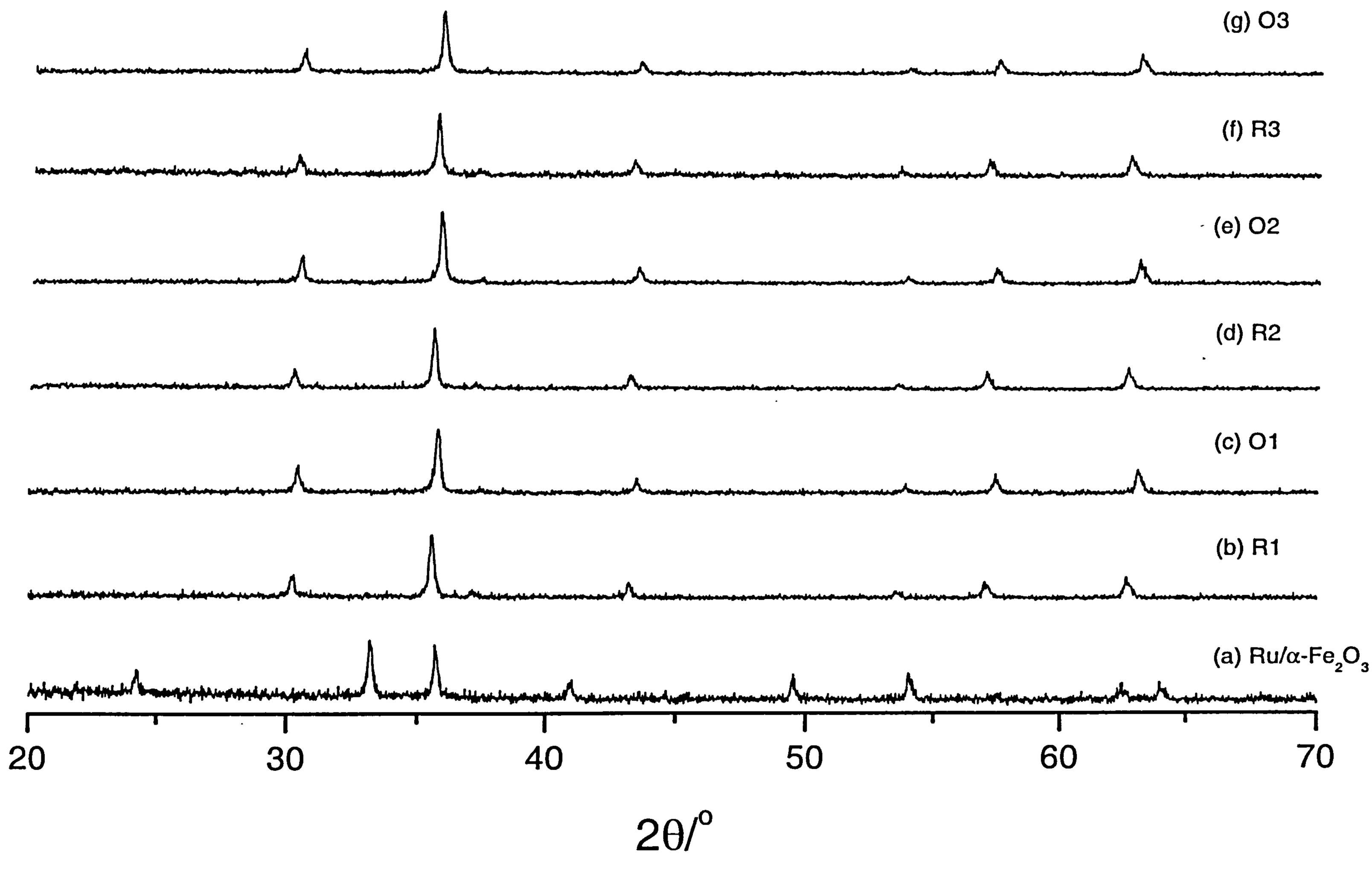

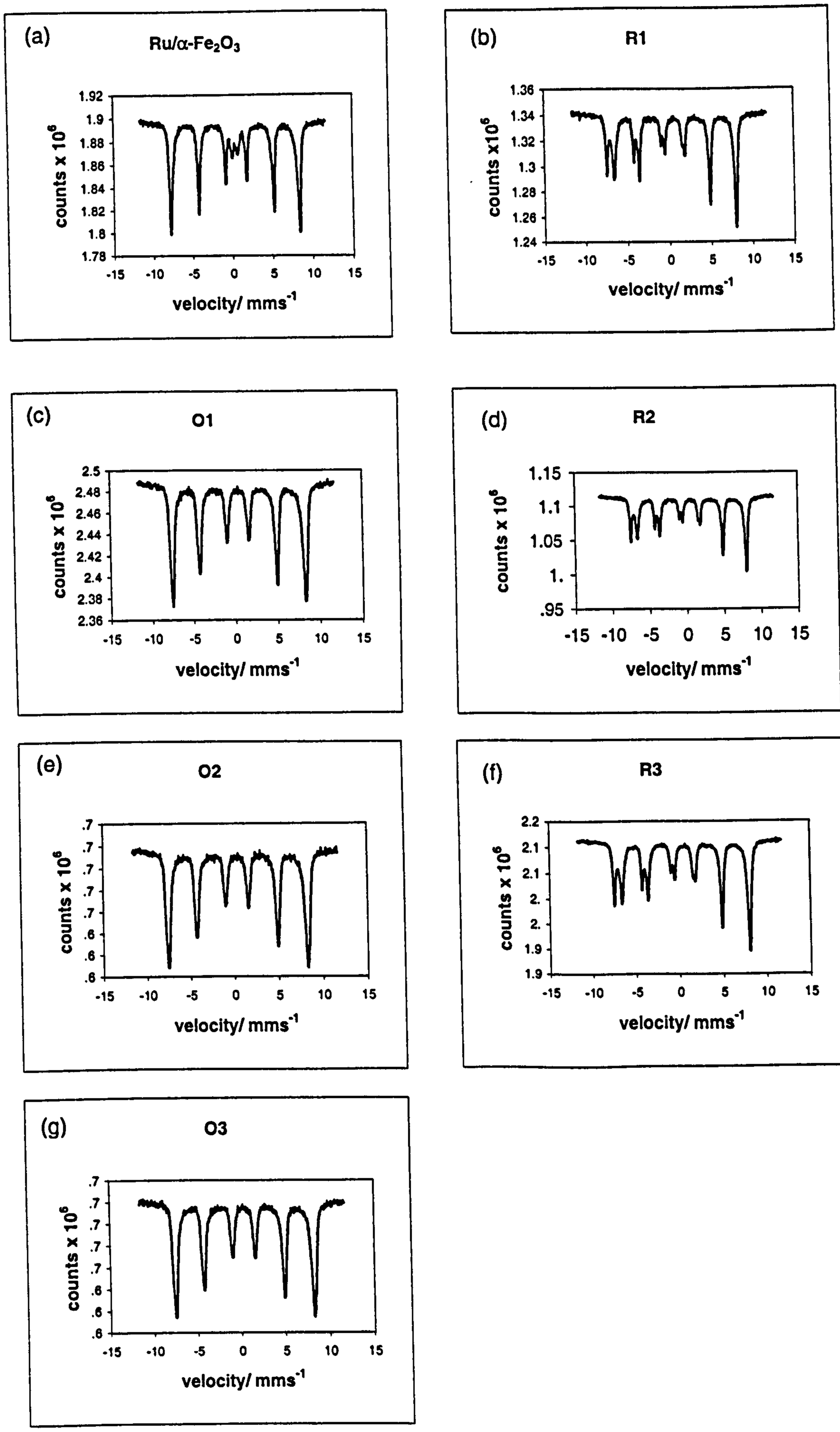

Figure 5.49 ^{57}Fe Mössbauer spectra recorded from Ru/α-Fe_2O_3 following reduction and reoxidation cycles

Table 5.13 ^{57}Fe Mössbauer parameters recorded from Ru/α-Fe_2O_3 following treatment in reducing and oxidising environments

Sample	δ (± 0.02) mms^{-1}	Δ (± 0.02) mms^{-1}	H (± 1) T	Interpretation	Area (± 5) %
Ru/α-Fe_2O_3	0.34	0.68	---	Small particle iron oxide	11
	0.38	-0.08	51	α-Fe_2O_3	89
R1	0.66	0.04	45	Fe_3O_4	100
	0.23	0.02	48	Fe_3O_4	
O1	0.34	0.02	49	γ-Fe_2O_3	100
R2	0.66	0.02	45	Fe_3O_4	100
	0.27	0.02	48	Fe_3O_4	
O2	0.33	0.01	49	γ-Fe_2O_3	100
R3	0.66	0.03	45	Fe_3O_4	100
	0.26	0.02	48	Fe_3O_4	
O3	0.33	0.01	49	γ-Fe_2O_3	100

The results show that Ru/α–Fe_2O_3 can be reduced to Ru/Fe_3O_4 and reoxidised to Ru/γ–Fe_2O_3 and the reduction and reoxidation cycle repeated.

The particle size of ruthenium- doped Fe_3O_4 (R1) (*ca.* 53 nm) formed by initial reduction of ruthenium- doped α–Fe_2O_3 was slightly larger than that of the precursor ruthenium- doped α–Fe_2O_3 (*ca.* 48 nm). The surface area of the ruthenium- doped Fe_3O_4 (R1) (*ca.* 17 m^2g^{-1}) was significantly lower than ruthenium- doped γ–Fe_2O_3 (*ca.* 75 m^2g^{-1}). Reoxidation by heating at 300 °C for 1 h in air followed by reduction and reoxidation for a further two cycles produced little differences in particle size and surface area but with the finally regenerated ruthenium- doped γ–Fe_2O_3 (O3) having a size of *ca.* 51 nm and surface area of *ca.* 12 m^2g^{-1}. The significant feature of

these results is that the initial reduction step showed the greatest change in surface area. Thereafter ruthenium- doped -γ–Fe_2O_3 and -Fe_3O_4 showed similar particle size and surface area to the undoped α-Fe_2O_3 prepared by addition of base to salt, boiling under reflux, and calcination at 600 °C/12 h.

Conclusion

The attempted preparation of ruthenium- doped α-Fe_2O_3 by the addition of base to salt or salt to base, boiling under reflux and calcination at 600 °C/12 h gave a bi-phasic mixture of α-Fe_2O_3 and RuO_2, which was due to the high calcination temperature. Ru/α-Fe_2O_3 prepared by addition of base to salt, heated hydrothermally, and dried under an infrared lamp gave a single phase material with a significantly higher surface area than undoped α-Fe_2O_3 prepared by a similar method, and titanium- and tin- doped counterparts prepared by addition of base to salt, boiling under reflux, and calcination at 600 °C. The higher surface area may be due to an appreciable amount of amorphous RuO_2 on the surface of the iron oxide, not detected by XRD. The TPR profile showed four reduction peaks compared with three for undoped α-Fe_2O_3, and titanium- and tin- doped α-Fe_2O_3. The initial step was attributed to the reduction of amorphous ruthenium dioxide. The presence of ruthenium lowered the temperatures of the reduction peaks, particularly that of the initial reduction peak. Reduction and reoxidation cycling induced little difference in particle size and surface area, with the initial reduction step showing the greatest change in surface area.

5.5.4 Magnesium- doped α–Fe_2O_3 (addition of base to salt, boiling under reflux, and calcination at 600 °C/12 h)

The X-ray powder diffraction pattern (Figure 5.50) recorded from the material which EDX analysis showed to contain 2.32 mass % magnesium was characteristic of a single phase corundum-related structure[14]. The lattice parameters a = 5.033(2) Å, c = 13.751(2) Å were similar to the reported[14] values for α-Fe_2O_3 a = 5.035 Å, c = 13.749 Å, and the α–Fe_2O_3 prepared here by addition of base to salt and boiling under reflux, (a = 5.034(2) Å, c = 13.755(2) Å). Mg/α-Fe_2O_3 prepared by Berry et al[15] with 10 % magnesium had lattice parameter values a = 5.050 Å, c = 13.792 Å reflecting the Mg^{2+}, having a radius of 0.72 Å in six coordination[6] as compared with Fe^{3+} of 0.65 Å. The sample prepared here does not show an increase in the lattice parameters probably because of the low loading of magnesium.

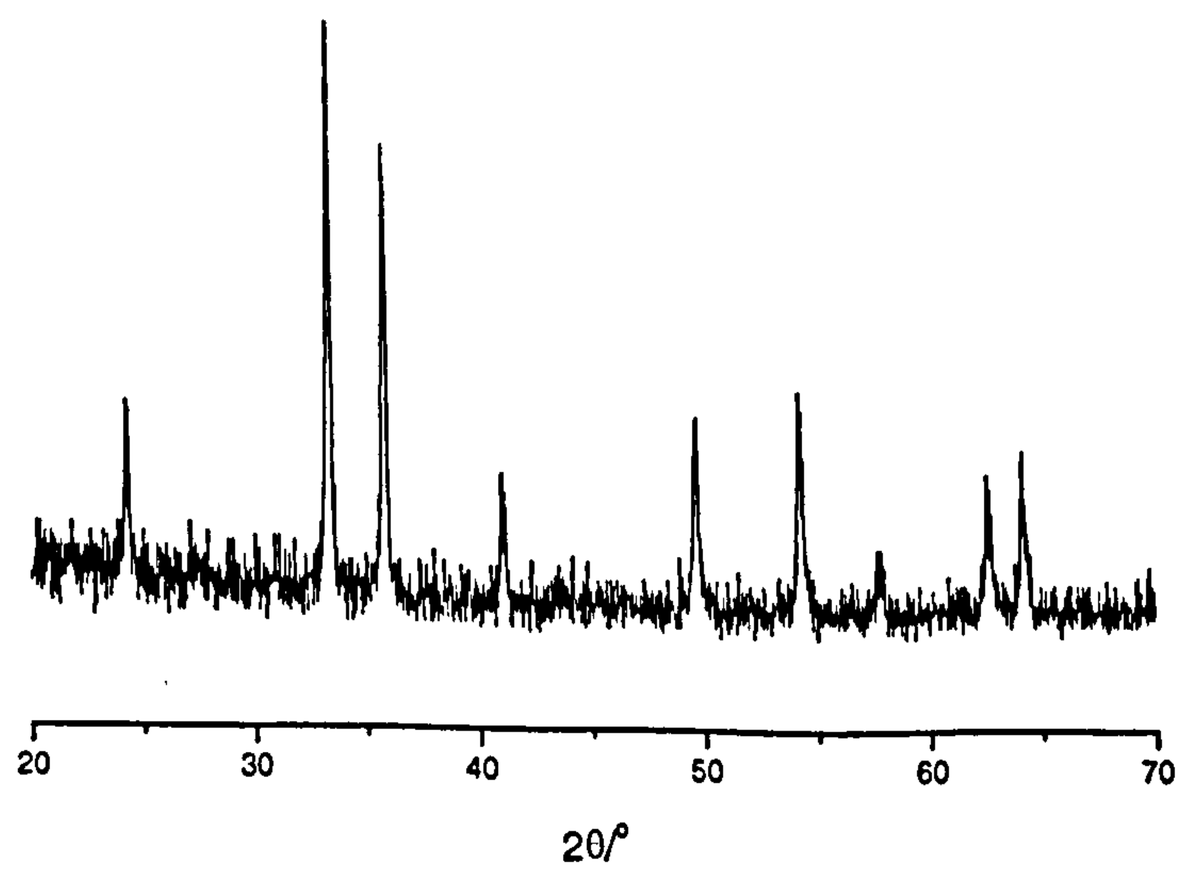

Figure 5.50 XRD pattern recorded from Mg/α–Fe_2O_3 prepared by addition of base to salt, boiling under reflux, and calcination at 600 °C

The ^{57}Fe Mössbauer spectrum (Figure 5.51) recorded at 298 K showed a sextet pattern (δ 0.40(2) mms^{-1}, Δ -0.09(2) mms^{-1}, H 51(1) T) characteristic[2,3] of an α–Fe_2O_3 related phase. The particle size of *ca.* 45 nm, obtained from the X-ray powder diffraction linewidth data, was lower than that of undoped α–Fe_2O_3 and Ti/α-Fe_2O_3, similar to Ru/α-Fe_2O_3 (prepared by hydrothermal process) but higher than Sn/α-Fe_2O_3 prepared by a similar method. The surface area of *ca.* 31 m^2g^{-1} was greater than that of undoped α–Fe_2O_3, similar to that of titanium- and tin- doped α-Fe_2O_3 but lower than that of Ru/α-Fe_2O_3.

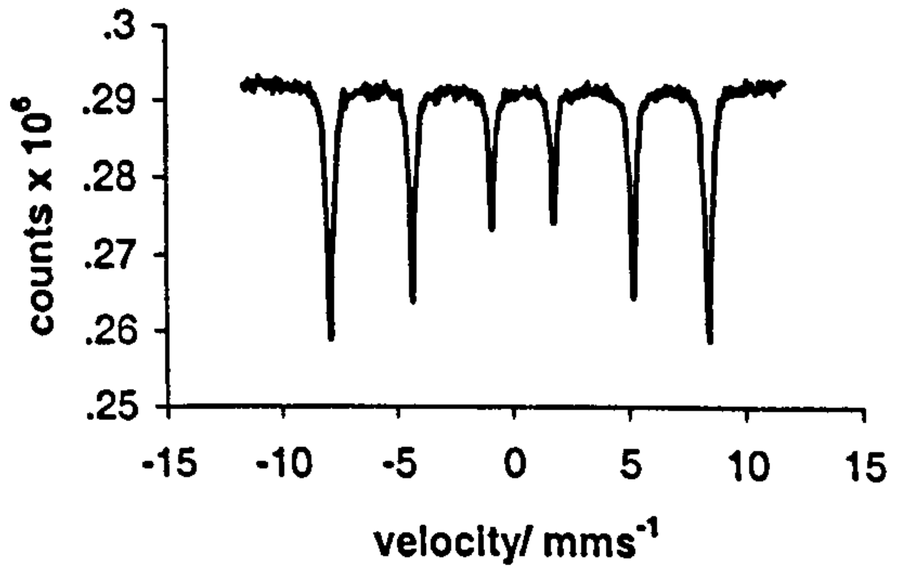

Figure 5.51 ^{57}Fe Mössbauer spectrum recorded from Mg/α–Fe_2O_3 prepared by addition of base to salt, boiling under reflux, and calcination at 600 °C

The temperature programmed reduction profile recorded from magnesium- doped α–Fe_2O_3 is shown in Figure 5.52. The profile showed three reduction peaks (415, 681, 960 °C) similar to undoped α-Fe_2O_3 and tin- doped α–Fe_2O_3. *Ex situ* XRD and *ex situ* ^{57}Fe Mössbauer spectroscopy studies of samples retrieved after each reduction peak from the TPR experiment have revealed the nature of the reduced phases (Figures 5.52 and 5.53 respectively). Table 5.14 shows the ^{57}Fe Mössbauer parameters of Mg/α-Fe_2O_3 after each reduction step.

The first reduction step at *ca.* 415 °C can, as in the case of undoped α–Fe_2O_3 prepared by a similar method (Figure 5.28), be associated with the reduction of

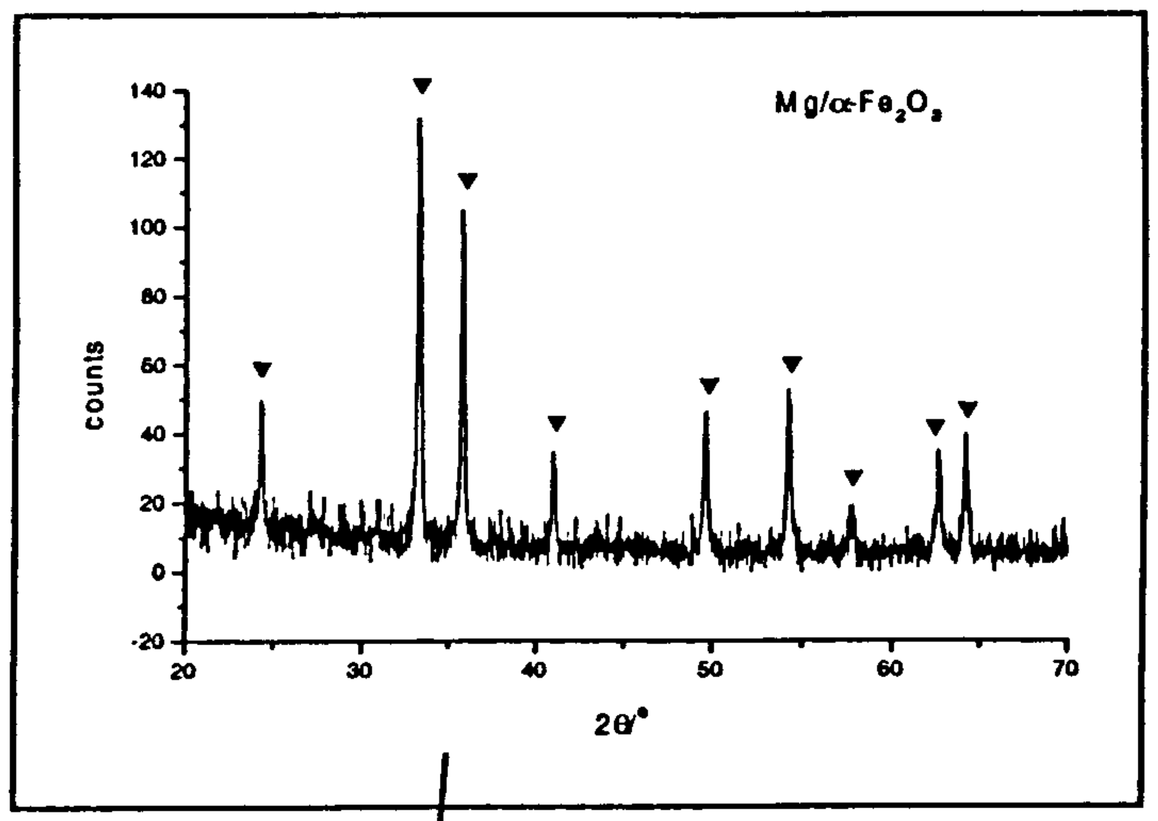

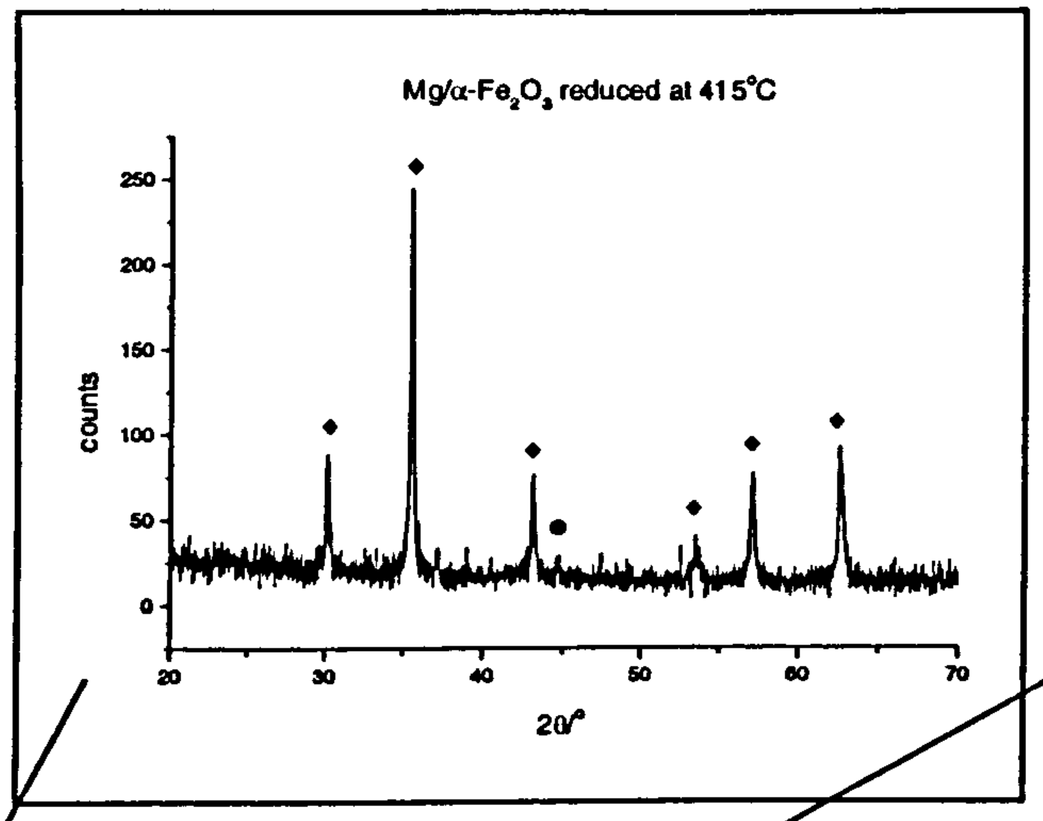

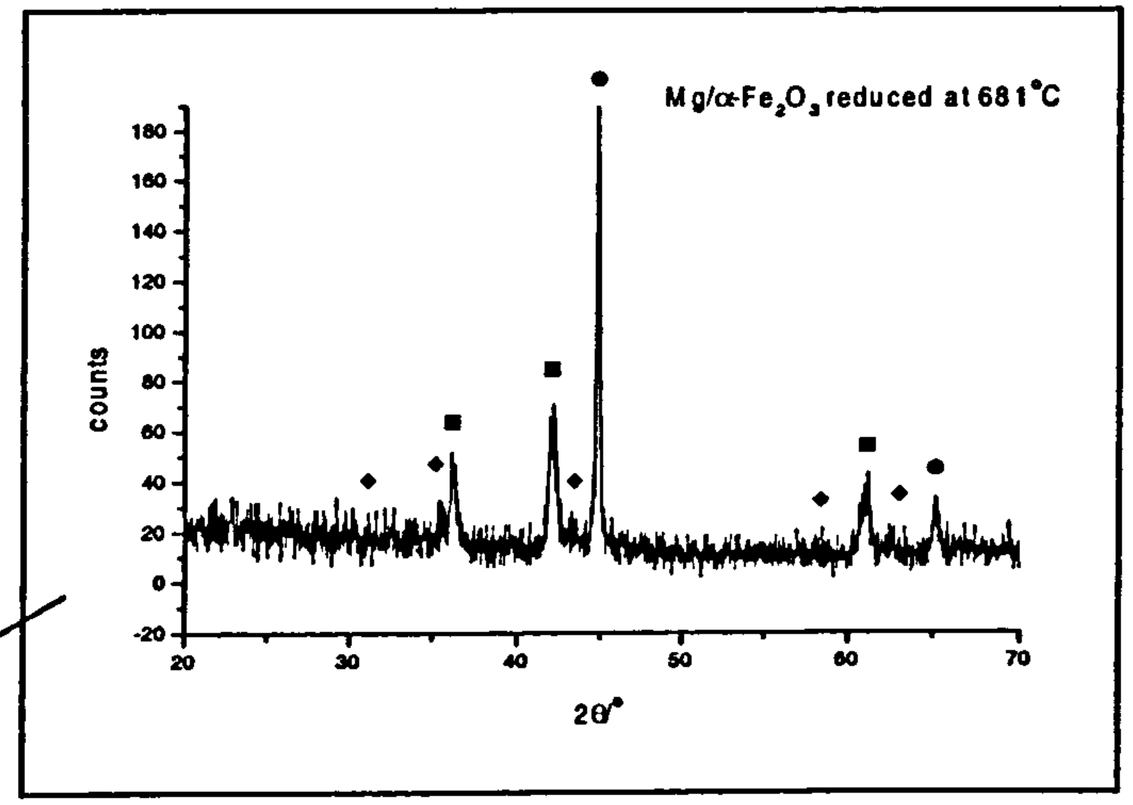

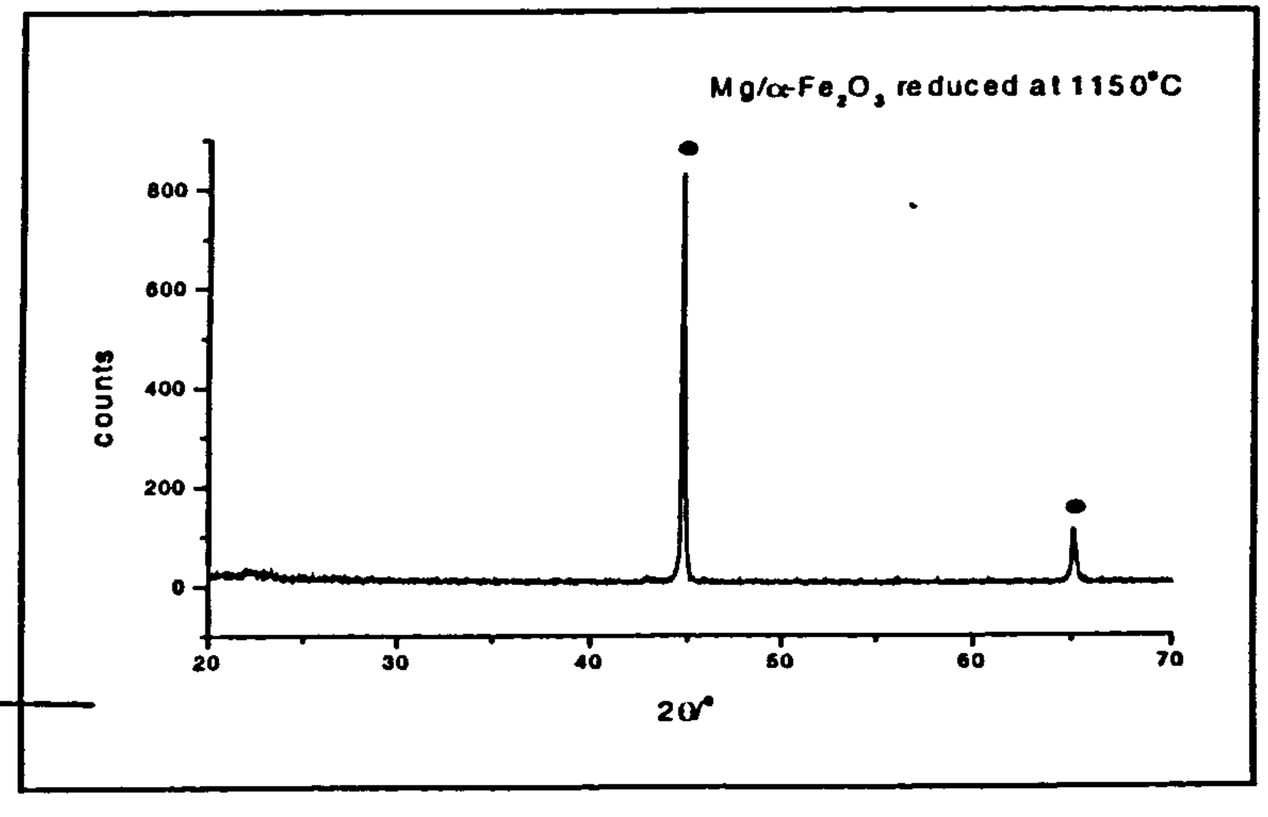

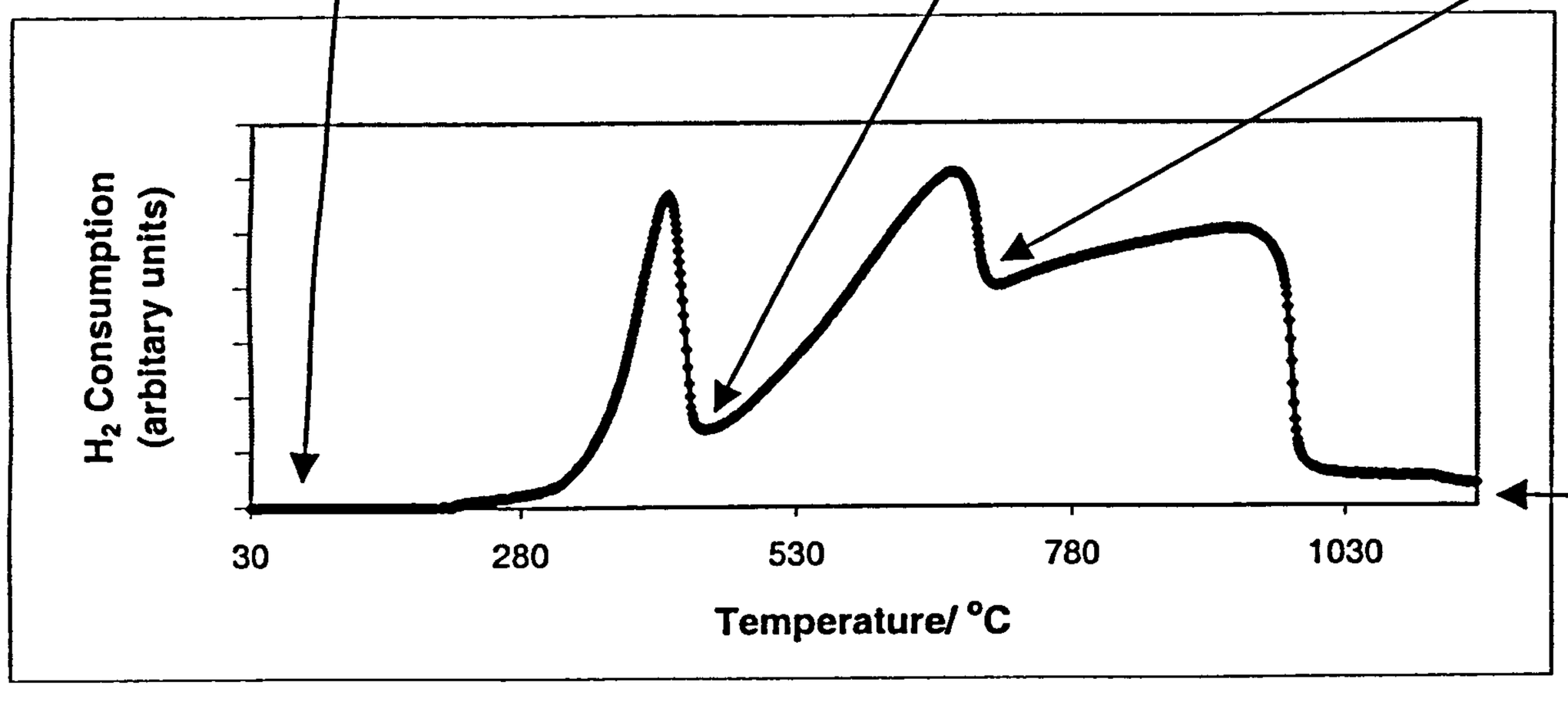

▼ = α-Fe_2O_3
◆ = Fe_3O_4
■ = FeO
● = Fe

Figure 5.52 TPR profile recorded from Mg/α-Fe_2O_3 and XRD patterns recorded following each reduction peak

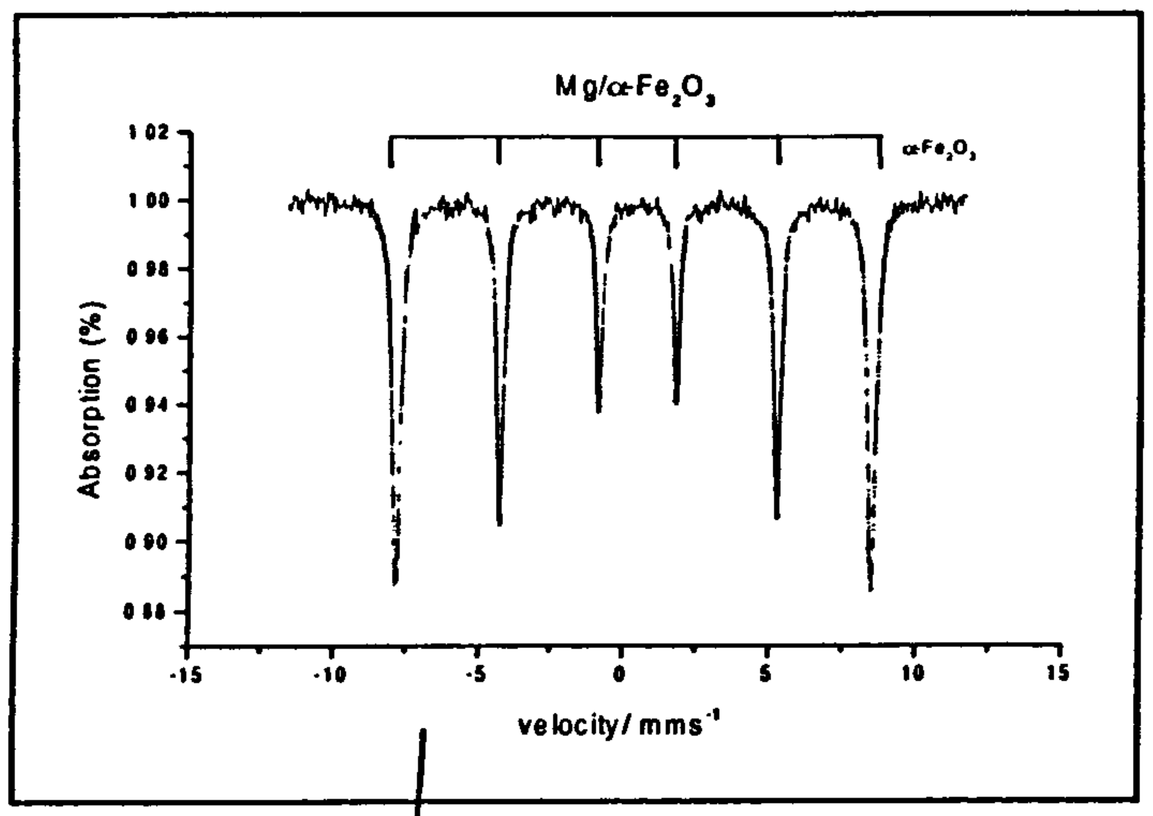

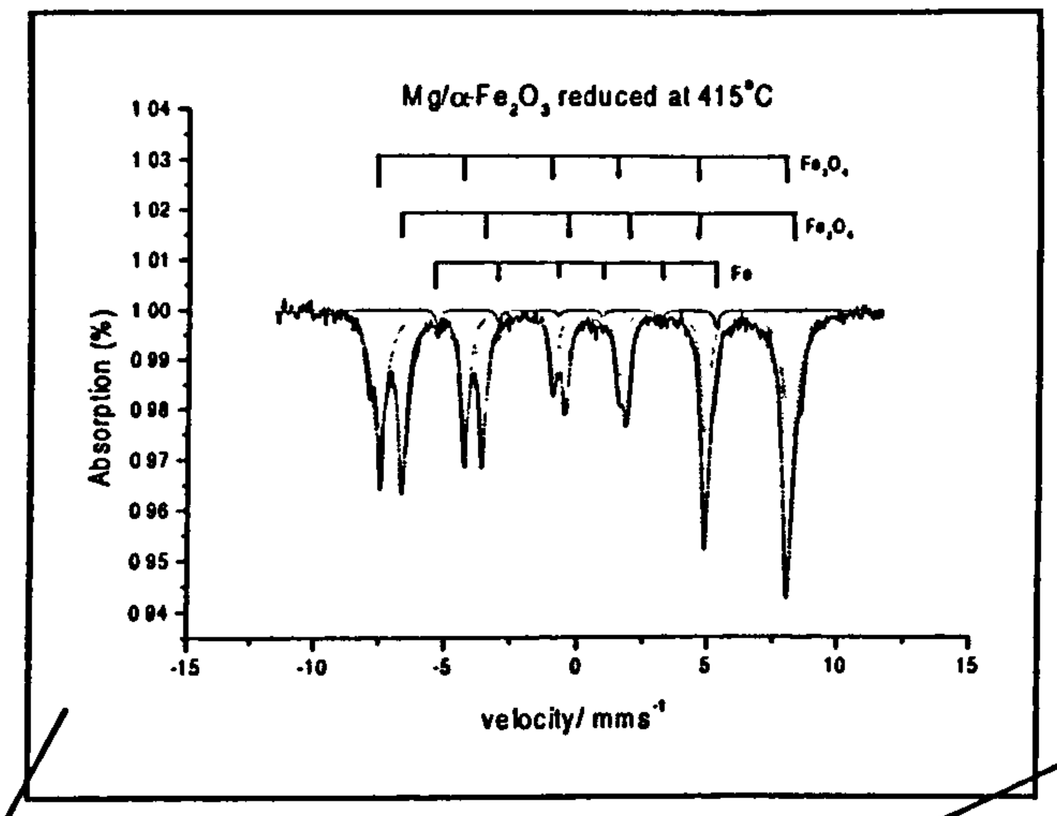

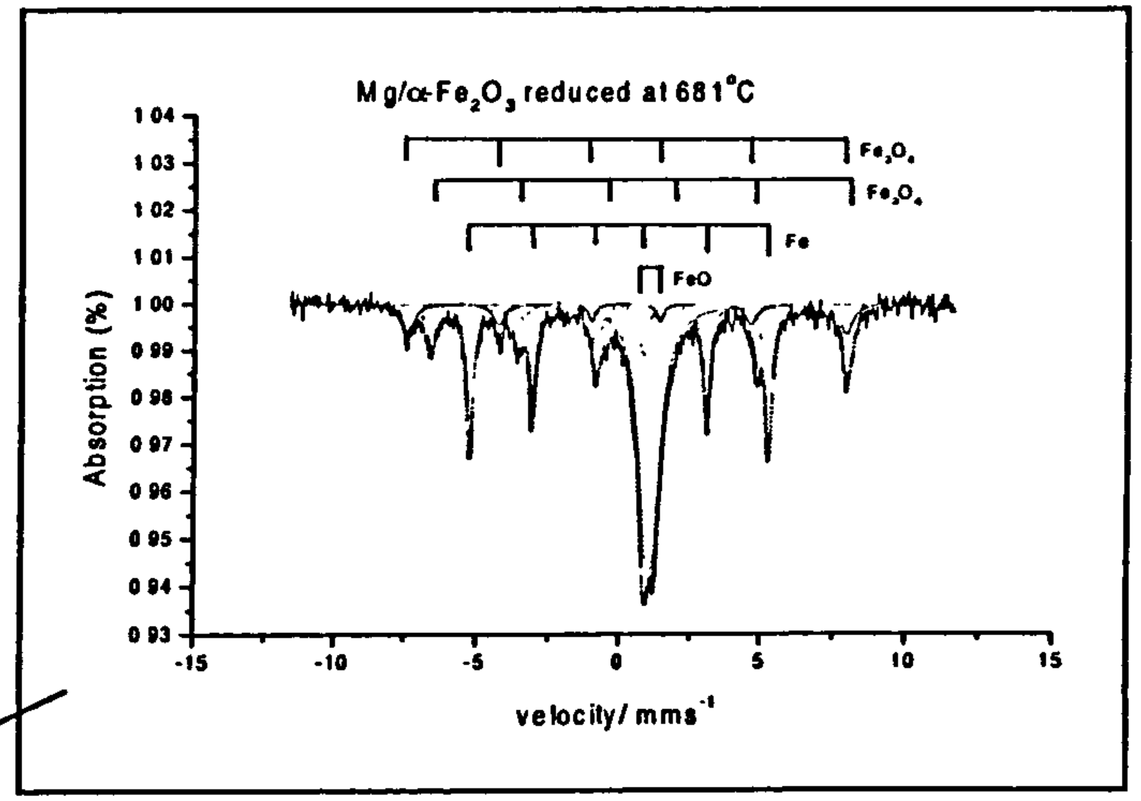

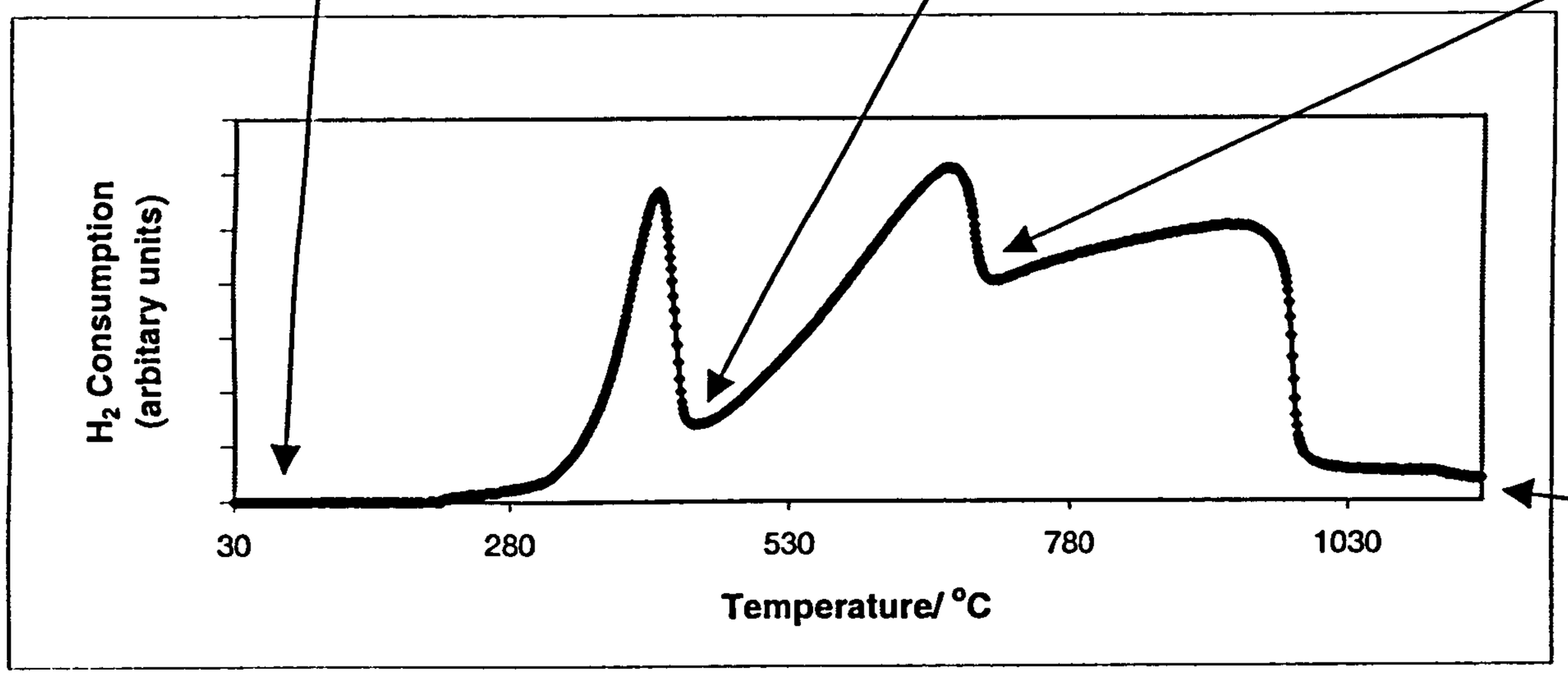

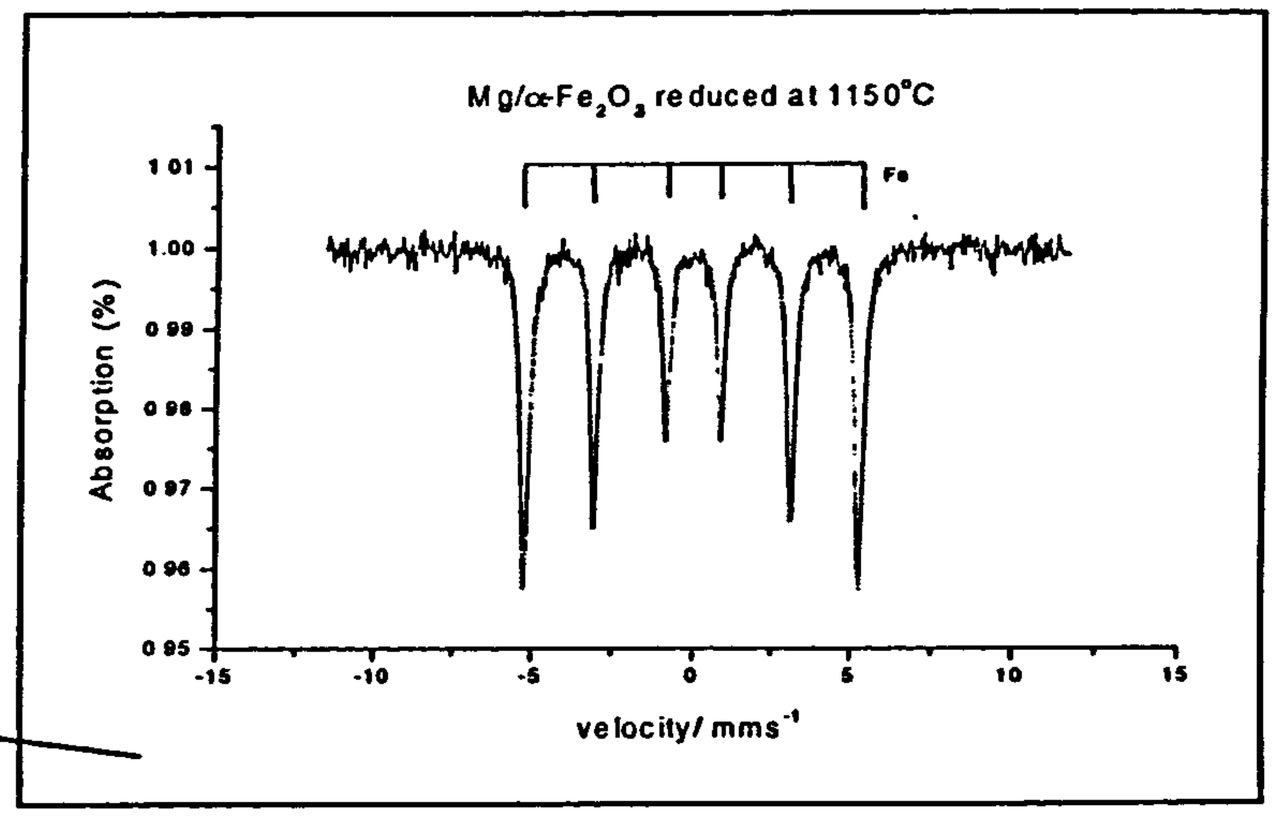

Figure 5.53 TPR profile recorded from Mg/α-Fe_2O_3 and ^{57}Fe Mössbauer spectra recorded following each reduction peak

magnesium- doped α–Fe_2O_3 to magnesium- doped Fe_3O_4, with the detection of a small amount of metallic iron. This was followed by partial reduction to FeO and metallic iron at *ca.* 681 °C, and finally reduction to metallic iron.

Table 5.14 ^{57}Fe Mössbauer parameters recorded from Mg/α-Fe_2O_3 following reduction in TPR experiment

Sample	δ (± 0.02) mms^{-1}	Δ (± 0.02) mms^{-1}	H (± 1) T	Interpretation	Area (± 5) %
Mg/α-Fe_2O_3	0.40	-0.09	51	α-Fe_2O_3	100
Mg/α-Fe_2O_3 reduced at 415 °C	0.69	0.0	45	Fe_3O_4	97
	0.30	0.0	49	Fe_3O_4	
	0.08	-0.07	32	Fe	<5
Mg/α-Fe_2O_3 reduced at 681 °C	0.56	0.0	45	Fe_3O_4	26
	0.28	0.0	48	Fe_3O_4	
	1.06	0.35	---	FeO	40
	0.02	0	33	Fe	34
Mg/α-Fe_2O_3 reduced at 1150 °C	0.02	0.01	33	Fe	100

Reduction-reoxidation properties

Mg/α–Fe_2O_3 was subjected to reduction at 400 °C in the 10 % hydrogen- 90 % nitrogen mixture (R1) and reoxidation by heating at 400 °C for 1 h in air (O1). The cycle of reduction and reoxidation was repeated twice (samples R2, O2, R3 and O3). X-ray powder diffraction (Figure 5.54) and ^{57}Fe Mössbauer spectroscopy (Figure 5.55, Table 5.15) were used to identify the materials after each reduction-reoxidation step.

Figure 5.54 XRD patterns recorded *ex situ* from Mg/α-Fe_2O_3 following reduction and reoxidation cycles

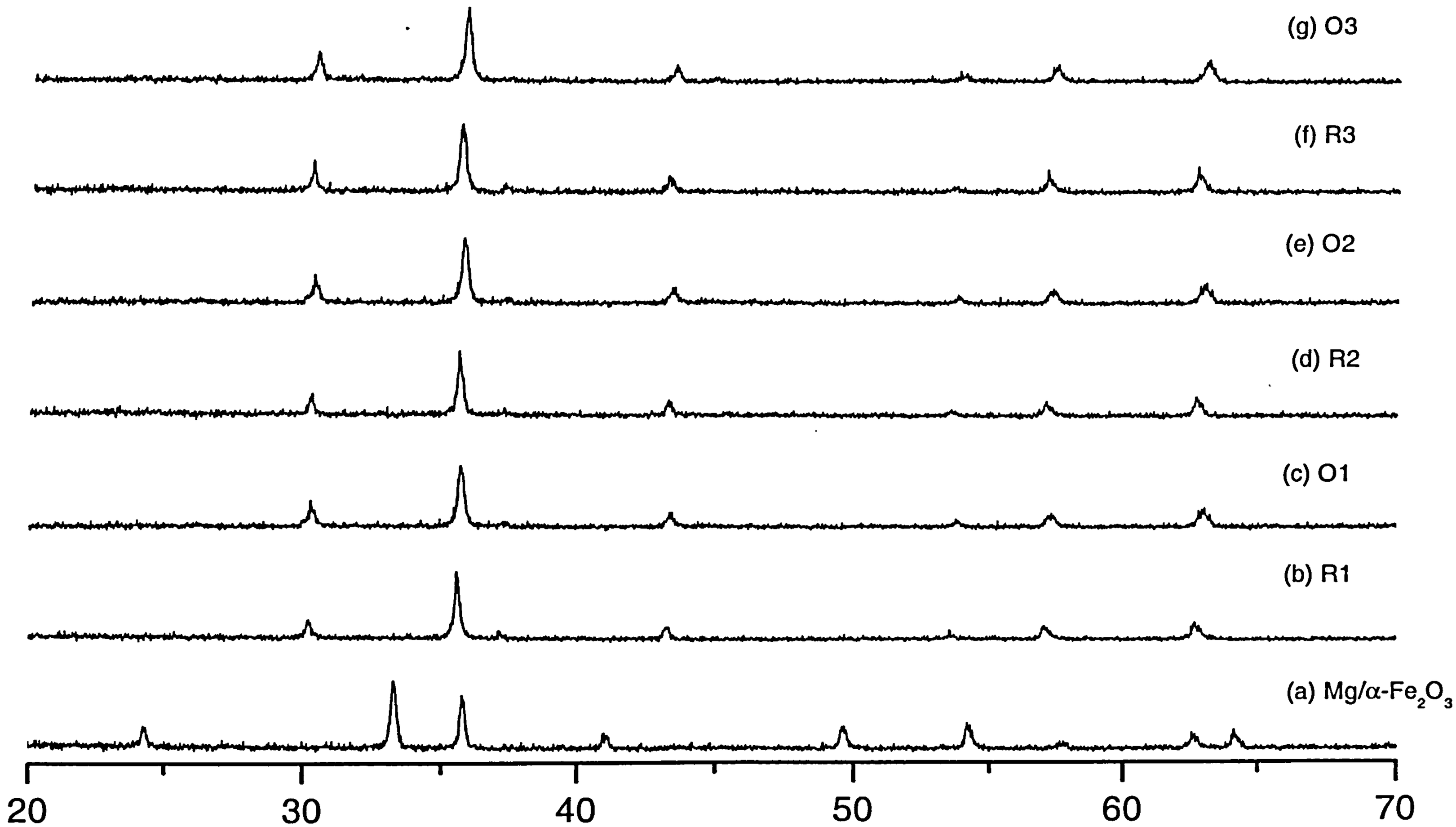

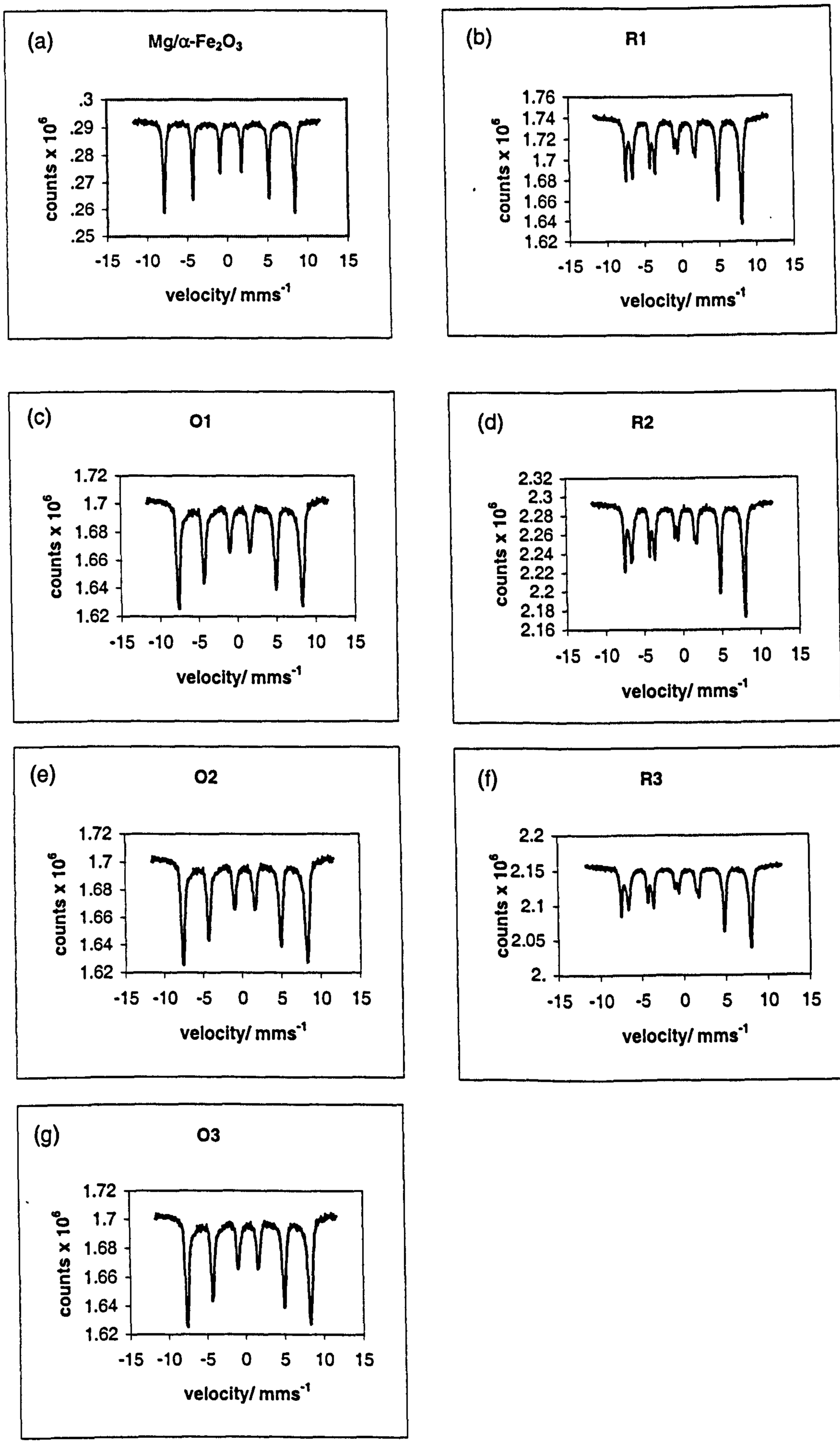

Figure 5.55 ^{57}Fe Mössbauer spectra recorded from Mg/α-Fe_2O_3 following reduction and reoxidation cycles

Table 5.15 ^{57}Fe Mössbauer parameters recorded from Mg/α-Fe_2O_3 following treatment in reducing and oxidising environments

Sample	δ (± 0.02) mms^{-1}	Δ (± 0.02) mms^{-1}	H (± 1) T	Interpretation
Mg/α-Fe_2O_3	0.40	-0.09	51	α-Fe_2O_3
R1	0.67	0.02	46	Fe_3O_4
	0.28	0.00	48	Fe_3O_4
O1	0.34	0.02	49	γ-Fe_2O_3
R2	0.67	0.02	45	Fe_3O_4
	0.29	0.00	48	Fe_3O_4
O2	0.34	-0.01	49	γ-Fe_2O_3
R3	0.67	0.01	45	Fe_3O_4
	0.29	0.00	48	Fe_3O_4
O3	0.33	0.00	49	γ-Fe_2O_3

The results show that Mg/α–Fe_2O_3 can be reduced to Mg/Fe_3O_4 and reoxidised to Mg/γ–Fe_2O_3 and the reduction and reoxidation cycle repeated.

The particle size of magnesium- doped Fe_3O_4 (R1) (*ca.* 49 nm) formed by initial reduction of magnesium- doped α–Fe_2O_3 was only slightly larger than that of the precursor magnesium- doped α–Fe_2O_3 (*ca.* 45 nm). The surface area of the magnesium- doped Fe_3O_4 (R1) (*ca.* 20 m^2g^{-1}) was also lower than magnesium-doped α–Fe_2O_3 (*ca.* 31 m^2g^{-1}). Reoxidation by heating at 400 °C for 1 h in air followed by reduction and reoxidation for a further two cycles produced small changes in particle size and surface area, with the finally regenerated magnesium-doped γ–Fe_2O_3 (O3) having a size of *ca.* 37 nm and surface area of *ca.* 17 m^2g^{-1}. The results show that magnesium- doped- γ–Fe_2O_3 and - Fe_3O_4 are of similar particle size to that of undoped α-Fe_2O_3.

Conclusion

Mg/α-Fe_2O_3 prepared by addition of base to salt, boiling under reflux, and calcination at 600 °C/12 h showed a higher surface area than the undoped α-Fe_2O_3, similar to titanium- and tin- doped α-Fe_2O_3 prepared by a similar method, but lower than that of Ru/α-Fe_2O_3 prepared by hydrothermal processing. The TPR profile showed three reduction steps similar to undoped α-Fe_2O_3, and tin- doped α-Fe_2O_3 prepared by addition of base to salt and boiling under refluxed. Reduction and reoxidation cycling induced little difference in particle size and surface area.

5.6 α–Fe_2O_3 Doped With Two Metals

α–Fe_2O_3 was doped with two metals of nominal loading of 4 mass % each, to give materials of the type: Sn/Mg/α–Fe_2O_3, Ti/Mg/α–Fe_2O_3, and Sn/Ti/α–Fe_2O_3. All were prepared by addition of base to salt, boiling under reflux, and calcination at 600 °C/12 h.

5.6.1 Sn/Mg/α-Fe_2O_3 (addition of base to salt, boiling under reflux, and calcination at 600 °C/12 h)

The XRD pattern recorded (Figure 5.56) corresponded to α-Fe_2O_3[14] with lattice parameters a = 5.051(2) Å, c = 13.775(2) Å which were larger than the reported[14] values for α-Fe_2O_3 a = 5.035 Å, c = 13.749 Å. The inversion of the intensity of peaks at *ca.* 33 ° and 36 ° 2θ is similar to Sn/α-Fe_2O_3 prepared by a similar method. The EDX analysis showed a tin content of 7.3 mass % and a magnesium content of 0.7

mass %. Given the high content of tin it is reasonable to assume that not all the tin is incorporated into the α-Fe_2O_3- related structure and an appreciable amount may be on the surface of the iron oxide in an amorphous state. The ^{57}Fe Mössbauer spectrum (Figure 5.57) showed a sextet pattern (δ 0.40(2) mms^{-1}, Δ -0.09(2) mms^{-1}, H 49(1) T) characteristic[2,3] of α–Fe_2O_3 together with a doublet pattern (δ 0.45(2) mms^{-1}, Δ 0.42(2) mms^{-1}) characteristic of the additional presence of small particle iron oxide[9] accounting for *ca.* 41 % of the spectral area.

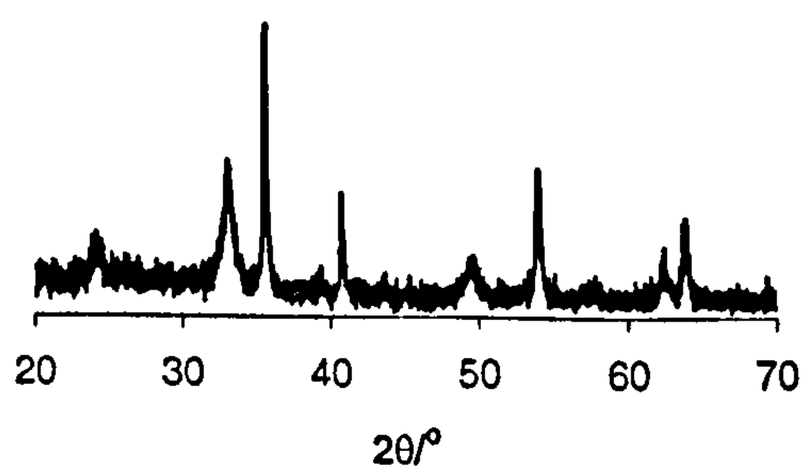

Figure 5.56 XRD pattern recorded from Sn/Mg/α-Fe_2O_3 prepared by addition of base to salt, boiling under reflux, and calcination at 600 °C

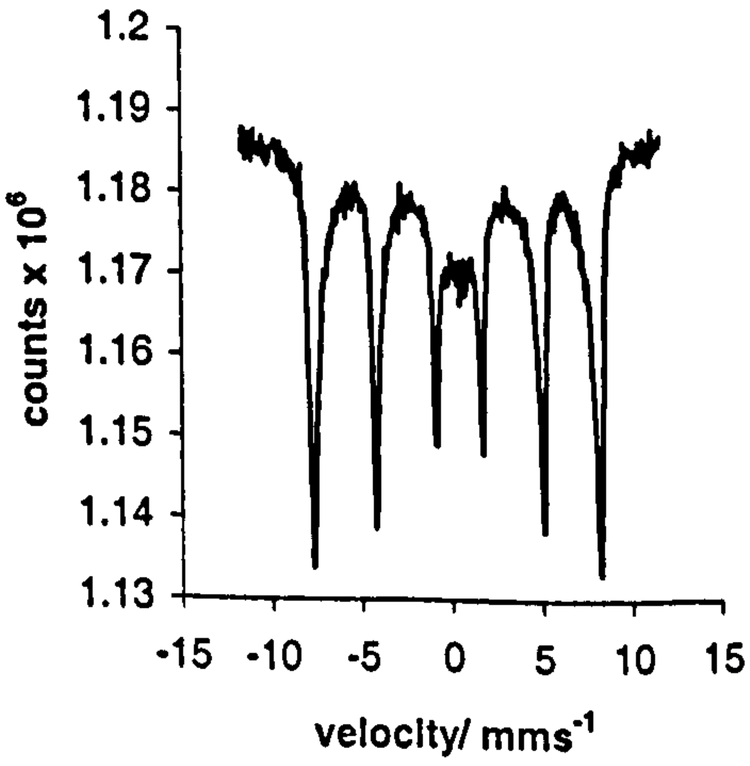

Figure 5.57 ^{57}Fe Mössbauer spectrum recorded from Sn/Mg/α-Fe_2O_3 prepared by addition of base to salt, boiling under reflux, and calcination at 600 °C

The surface area was found to be 36 m^2g^{-1}, higher than that of undoped α-Fe_2O_3 (10 m^2g^{-1}) but similar to Sn/α-Fe_2O_3 (35 m^2g^{-1}) and Mg/α-Fe_2O_3 (31 m^2g^{-1}), all prepared by a similar method. The particle size calculated from the XRD linewidth was found to be *ca.* 21 nm and *ca.* 30 nm from TEM, compared with *ca.* 16 nm for Sn/α-Fe_2O_3 and *ca.* 45 nm from Mg/α-Fe_2O_3, calculated from the XRD linewidth data.

The TPR profile (Figure 5.58) gave three peak maxima (550, 780 and 1050 °C) similar to undoped α-Fe_2O_3, and Sn/α-Fe_2O_3 and Mg/α-Fe_2O_3 prepared by a similar method. The position of the first peak had shifted to higher temperatures compared to undoped α-Fe_2O_3, and Sn/α-Fe_2O_3 and Mg/α-Fe_2O_3, indicating that both tin and magnesium combined stabilise the material with respect to the reduction to Fe_3O_4.

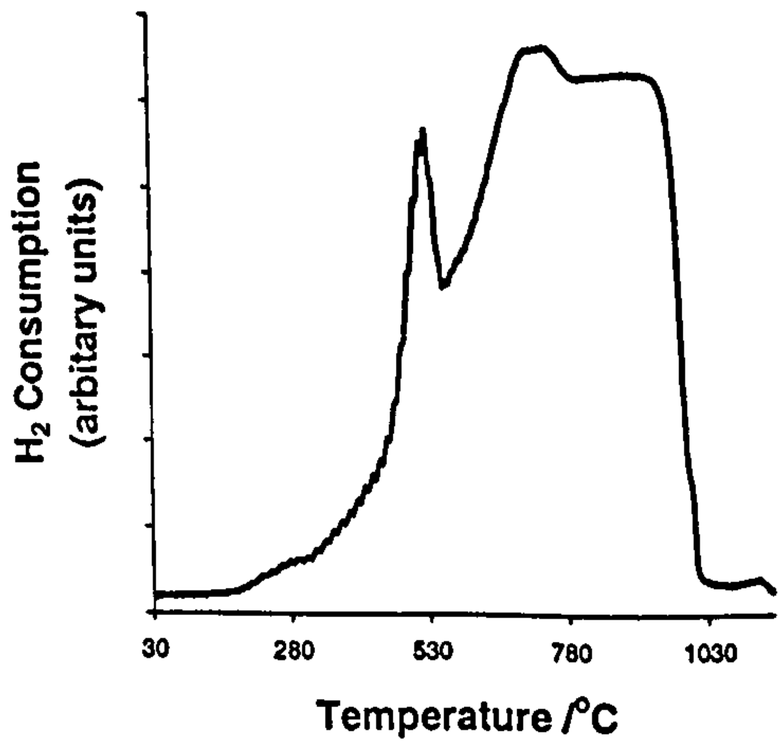

Figure 5.58 TPR profile recorded from Sn/Mg/α-Fe_2O_3 prepared by addition of base to salt, boiling under reflux, and calcination at 600 °C

Conclusion

Sn/Mg/α-Fe_2O_3 had a higher surface area than undoped α-Fe_2O_3, but similar to those of Sn/α-Fe_2O_3 and Mg/α–Fe_2O_3 prepared by addition of base to salt, boiling under

reflux, and calcination at 600 °C/12 h. The TPR profile showed three reduction peaks, with the initial reduction peak located at higher temperature compared with undoped α-Fe_2O_3, and Sn/α-Fe_2O_3 and Mg/α-Fe_2O_3, indicating that the presence of both tin and magnesium combined suppresses the reduction of α-Fe_2O_3 to Fe_3O_4.

5.6.2 Ti/Mg/α-Fe_2O_3 (addition of base to salt, boiling under reflux, and calcination at 600 °C/12 h)

The XRD pattern (Figure 5.59) corresponded to α-Fe_2O_3[14] with lattice parameters *a* = 5.033(2) Å, *c* = 13.751(2) Å similar to those of reported[14] value *a* = 5.035 Å, *c* = 13.749 Å for α-Fe_2O_3. The EDX analysis showed 3.2 mass % of Ti and 1.3 mass % of Mg. The ^{57}Fe Mössbauer spectrum showed a sextet pattern (δ 0.40(2) mms^{-1}, Δ -0.09(2) mms^{-1}, *H* 51(1) T) confirming the material to be α-Fe_2O_3[2,3] (Figure 5.60).

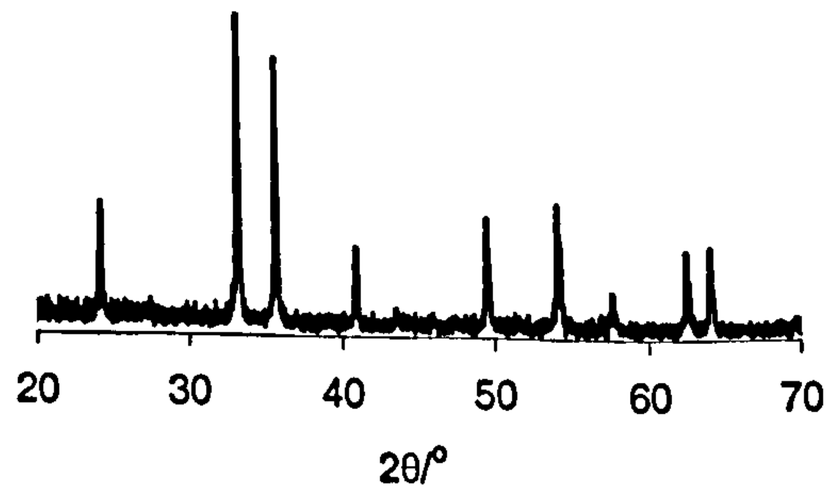

Figure 5.59 XRD pattern recorded from Ti/Mg/α-Fe_2O_3 prepared by addition of base to salt, boiling under reflux, and calcination at 600 °C

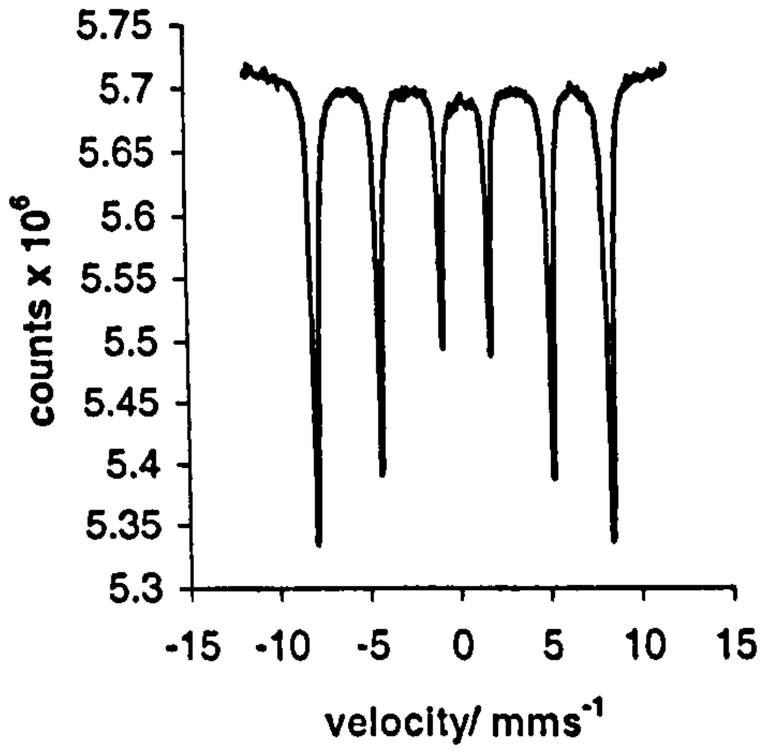

Figure 5.60 ^{57}Fe Mössbauer spectrum recorded from Ti/Mg/α-Fe_2O_3 prepared by addition of base to salt, boiling under reflux, and calcination at 600 °C

The surface area was found to be 19 m^2g^{-1}, higher than undoped α-Fe_2O_3 (10 m^2g^{-1}) but lower than Ti/α-Fe_2O_3 (29 m^2g^{-1}) and Mg/α-Fe_2O_3 (31 m^2g^{-1}), all prepared by a similar method. The particle size was found to be *ca.* 58 nm calculated from the XRD linewidth and *ca.* 60 nm from TEM, compared with *ca.* 57 nm for Ti/α-Fe_2O_3 and *ca.* 45 nm from Mg/α-Fe_2O_3, calculated from the XRD linewidth data.

The TPR profile (Figure 5.61) gave three peak maxima (515, 800 and 1100 °C), with the latter two peaks merging, but to a lesser extent compared to Ti/α-Fe_2O_3 prepared by a similar method, this may reflect the lower loading of titanium.

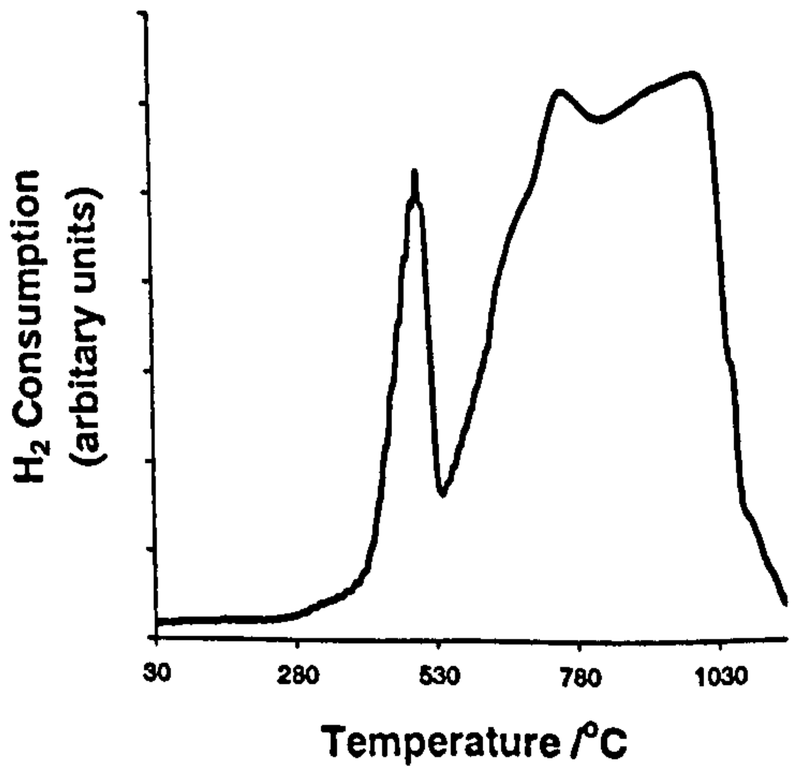

Figure 5.61 TPR profile recorded from Ti/Mg/α-Fe_2O_3 prepared by addition of base to salt, boiling under reflux, and calcination at 600 °C

Conclusion

Ti/Mg/α-Fe_2O_3 had a higher surface area than that of undoped α-Fe_2O_3, but lower than Ti/α-Fe_2O_3 and Mg/α-Fe_2O_3 prepared by addition of base to salt, boiling under reflux, and calcination at 600 °C/12 h. The TPR profile showed three reduction steps with the latter two peak coalesced but to a lesser extent compared to that of pure Ti/α-Fe_2O_3 prepared by a similar method.

Overall, materials of the type Mg/M/α–Fe_2O_3 (M = Sn, Ti) showed properties more similar to the M/α–Fe_2O_3 phases than to the Mg/α–Fe_2O_3 phase, reflecting the lower magnesium content.

5.6.3 Sn/Ti/α-Fe_2O_3 (addition of base to salt, boiling under reflux, and calcination at 600 °C/12 h)

The XRD pattern (Figure 5.62) corresponded to α-Fe_2O_3[14] with impurity of γ-Fe_2O_3[17]. The EDX analysis showed 9 mass % of Sn and 1.1 mass % of Ti. Given the high content of tin it is reasonable to assume that not all the tin is incorporated into the α-Fe_2O_3- related structure and an appreciable amount may be on the surface of the iron oxide in an amorphous state. The ^{57}Fe Mössbauer spectrum showed two sextet patterns (Figure 5.63) corresponding to α–Fe_2O_3[2,3] pattern (δ 0.39(2) mms^{-1}, Δ -0.08(2) mms^{-1}, H 51(1) T) and γ–Fe_2O_3[2,3] pattern (δ 0.34(2) mms^{-1}, Δ -0.01(2) mms^{-1}, H 49(1) T) together with a doublet pattern (δ 0.37(2) mms^{-1}, Δ 0.90(2) mms^{-1}) characteristic of the additional presence of small particle iron oxide[9] accounting for *ca.* 21 % of the spectral area.

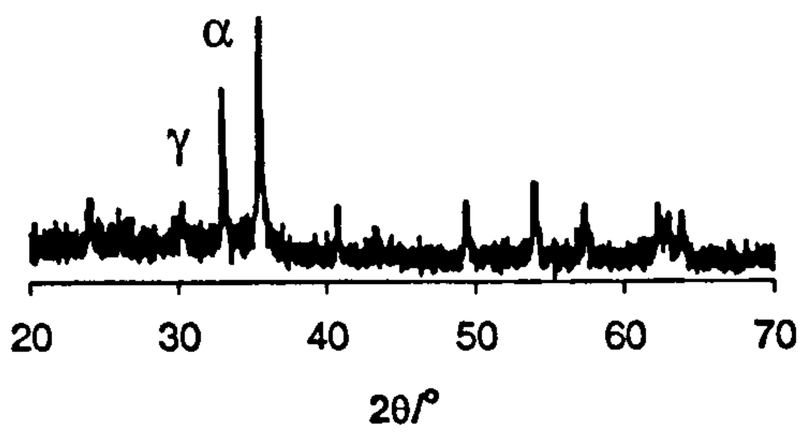

Figure 5.62 XRD pattern recorded from Sn/Ti/α-Fe_2O_3 prepared by addition of base to salt, boiling under reflux, and calcination at 600 °C

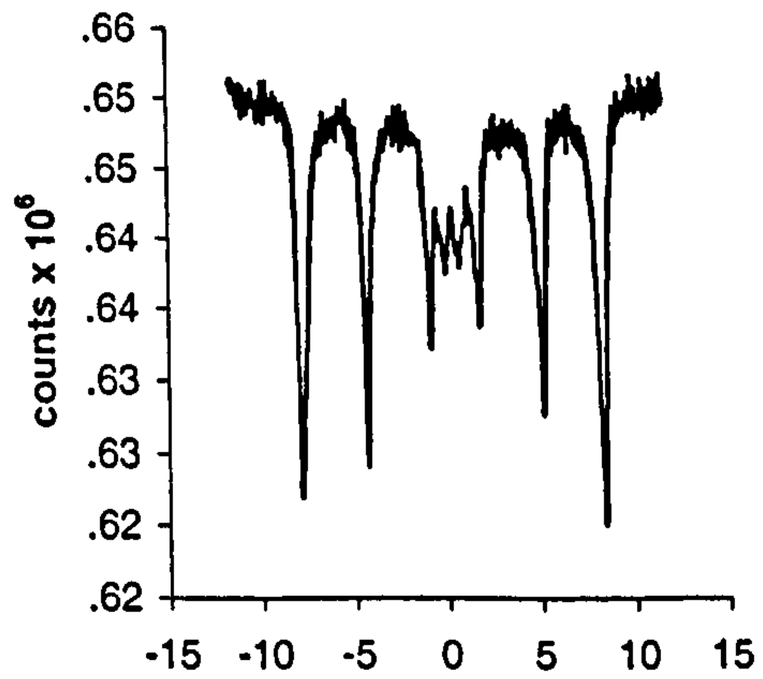

Figure 5.63 ^{57}Fe Mössbauer spectrum recorded from Sn/Ti/α-Fe_2O_3 prepared by addition of base to salt, boiling under reflux, and calcination at 600 °C

The surface area was calculated to be 61 m^2g^{-1}, significantly higher than undoped α-Fe_2O_3 (10 m^2g^{-1}), Sn/α-Fe_2O_3 (35 m^2g^{-1}) and Ti/α-Fe_2O_3 (29 m^2g^{-1}), all prepared by a similar method. The increase in surface area may be due to the γ–Fe_2O_3 impurity as the gamma phases have a higher surface area compared with the alpha counterparts. The particle size calculated from the XRD linewidth was found to be *ca.* 32 nm and *ca.* 18 nm from TEM, compared with *ca.* 16 nm for Sn/α-Fe_2O_3 and *ca.* 57 nm from Ti/α-Fe_2O_3, calculated from the XRD linewidth data.

The TPR profile (Figure 5.64) gave four peak maxima (350, 460, 720 and 1040 °C). The peak at *ca.* 350 °C was due to γ-Fe_2O_3 impurity. The intensities of the initial two peaks were low, a similar effect was observed for the initial peak of pure Sn/α-Fe_2O_3 prepared by a similar method.

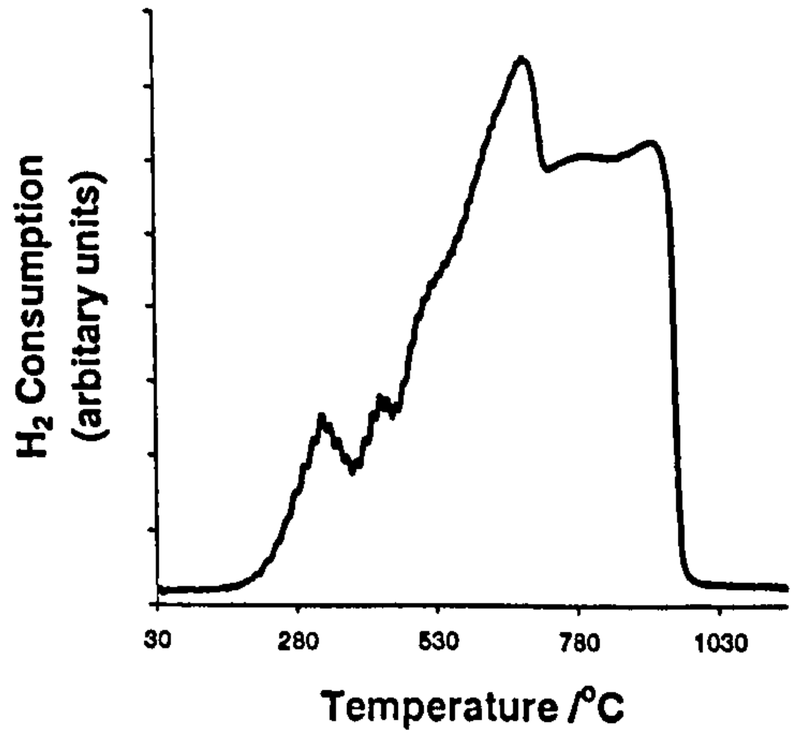

Figure 5.64 TPR profile recorded from Sn/Ti/α-Fe_2O_3 prepared by addition of base to salt, boiling under reflux, and calcination at 600 °C

Conclusion

The preparation of single phase Sn/Ti/α–Fe_2O_3 was unsuccessful, γ-Fe_2O_3 impurity was observed. Sn/Ti/α-Fe_2O_3 can be prepared with a much high surface area than undoped α-Fe_2O_3, Sn/α-Fe_2O_3 and Ti/α-Fe_2O_3 all prepared by a similar method. The increase in the surface area is probably due to γ–Fe_2O_3 impurity, which has a higher surface area than the alpha- counterparts. The TPR profile showed four reduction steps. The initial step was probably due to γ–Fe_2O_3 impurity.

5.7 Pd/α-Fe_2O_3 and metal- doped variants

The XRD patterns for Pd impregnated α-Fe_2O_3 and Ti-, Sn-, and Mg- doped variants using ($Pd(NO_3)_2$, are shown in Figure 5.65 (a-d) respectively and corresponded to α-Fe_2O_3[14]. The samples made by impregnation with Pd(DNDA), and $Pd(acac)_2$) gave identical results. No palladium- containing phase was observed suggesting that the palladium loading was too low or that the palladium was highly dispersed or amorphous.

Table 5.16 Particle size and surface area measurements for Pd impregnated α-Fe_2O_3 and metal- doped variants

Sample	Average particle size Scherrer method / nm (± 10 %)	Average particle size TEM / nm (± 10 %)	Surface Area / m^2g^{-1} (± 10 %)
Pd/α-Fe_2O_3, ($Pd(NO_3)_2$)	37	68	8
Pd/Ti/α-Fe_2O_3, ($Pd(NO_3)_2$)	32	40	36
Pd/Sn/α-Fe_2O_3, ($Pd(NO_3)_2$)	15	36	41
Pd/Mg/α-Fe_2O_3, ($Pd(NO_3)_2$)	42	56	31

Table 5.16 gives the mean crystalline size (i) calculated from the XRD pattern using the Scherrer equation and (ii) estimated from the histograms of TEM micrographs for the Pd impregnated α-Fe_2O_3 and Sn-, Ti-, and Mg- doped variants using $Pd(NO_3)_2$ precursor. The BET surface area measurements obtained from nitrogen physisorption are also shown. The results showed that palladium impregnation had little effect on the total surface area of the non-impregnated samples.

Figure 5.65 XRD patterns recorded from Pd impregnated α-Fe_2O_3 and metal- doped variants

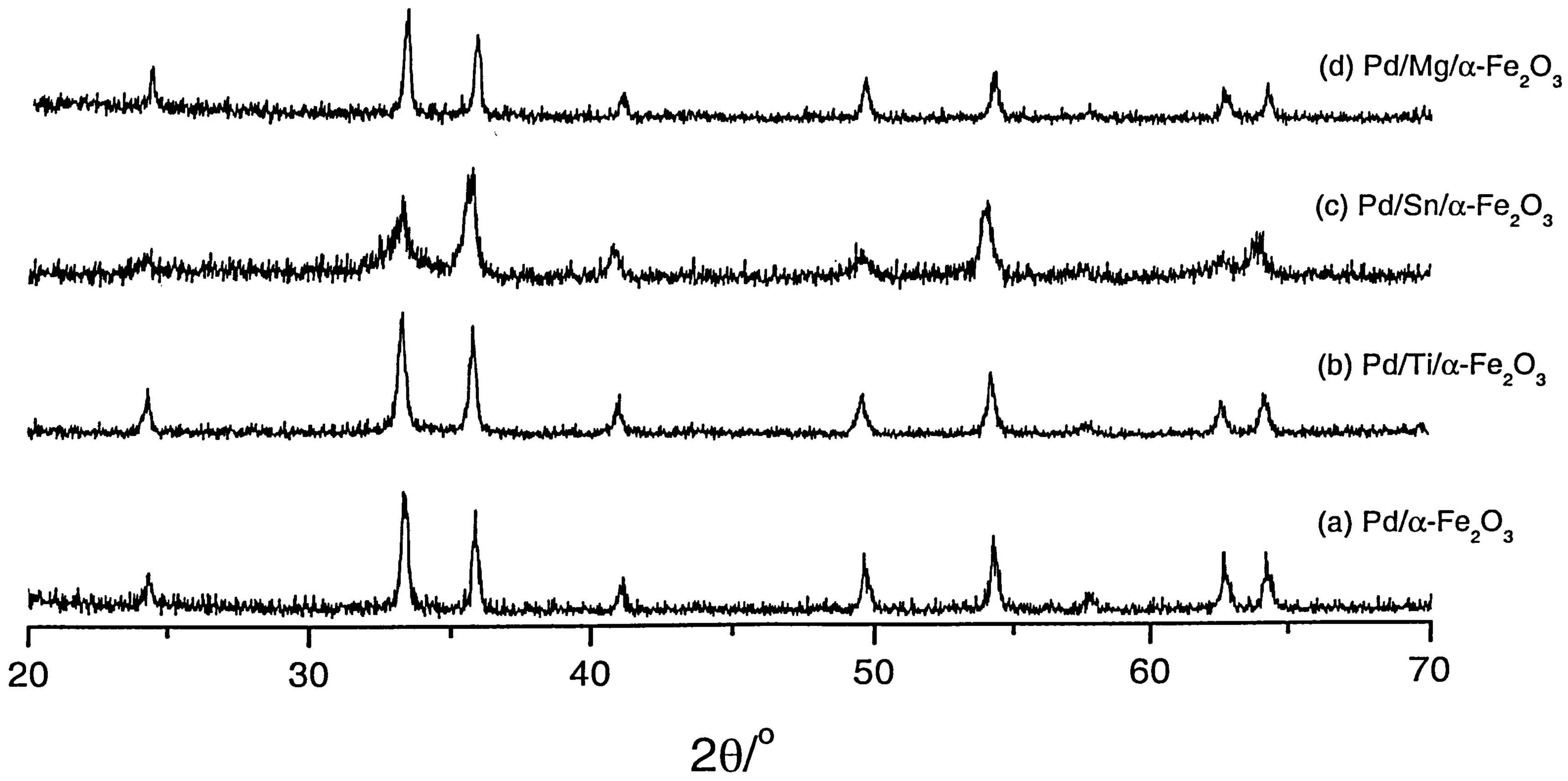

The TPR patterns for Pd impregnated α-Fe_2O_3 and Ti-, Sn-, and Mg- doped variants using ($Pd(NO_3)_2$, Pd(DNDA), and $Pd(acac)_2$ are shown in Figures 5.66 – 5.69 (a-d) respectively. The reduction peak temperatures are shown in Table 5.17. In all cases the patterns showed three main reduction peaks, similar to the non-impregnated samples. The addition of Pd resulted in a decrease in the reduction temperature of the initial peak, suggesting that there is some interaction between Pd and the iron oxides. The decrease of the reduction temperature may be due to Pd having a high affinity for H_2, which dissociates and gives rise to more facile reduction of iron in the iron oxide.

The different palladium precursors all have similar effects on the TPR profiles and lower the temperature of the initial reduction peak.

Table 5.17 TPR reduction peaks (major peaks in bold) of Pd impregnated α-Fe_2O_3 and metal-doped variants

Sample	Reduction Peaks / °C (± 50 °C)		
	($Pd(NO_3)_2$)	**(Pd(DNDA))**	**($Pd(acac)_2$)**
Pd/α-Fe_2O_3,	80, **280, 750, 940**	80, **290, 730, 980**	80, **280, 720, 1000**
Pd/Ti/α-Fe_2O_3,	110, 250, 320 - 410, **820 – 1000** (broad)	120, 250, **500, 830-1000** (broad)	110, 260, **490, 820-1010** (broad)
Pd/Sn/α-Fe_2O_3,	175, **280**, 490, **730, 920**	**220**, 300, 500, **720, 900**	**220**, 300, 510, **740, 900**
Pd/Mg/α-Fe_2O_3,	**280, 680, 965**	50, 100, **290, 670, 1020**	120, **290, 680, 1020**

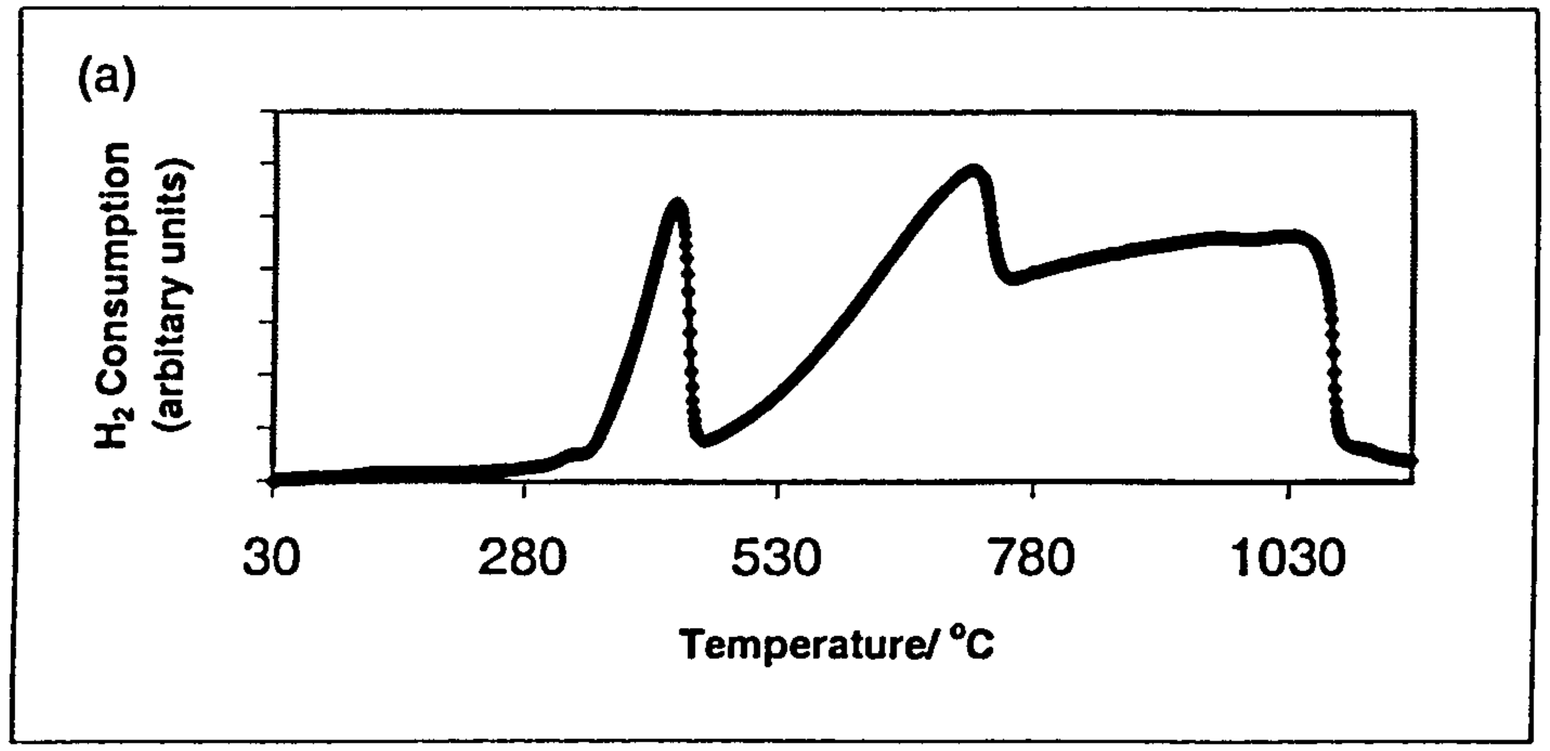

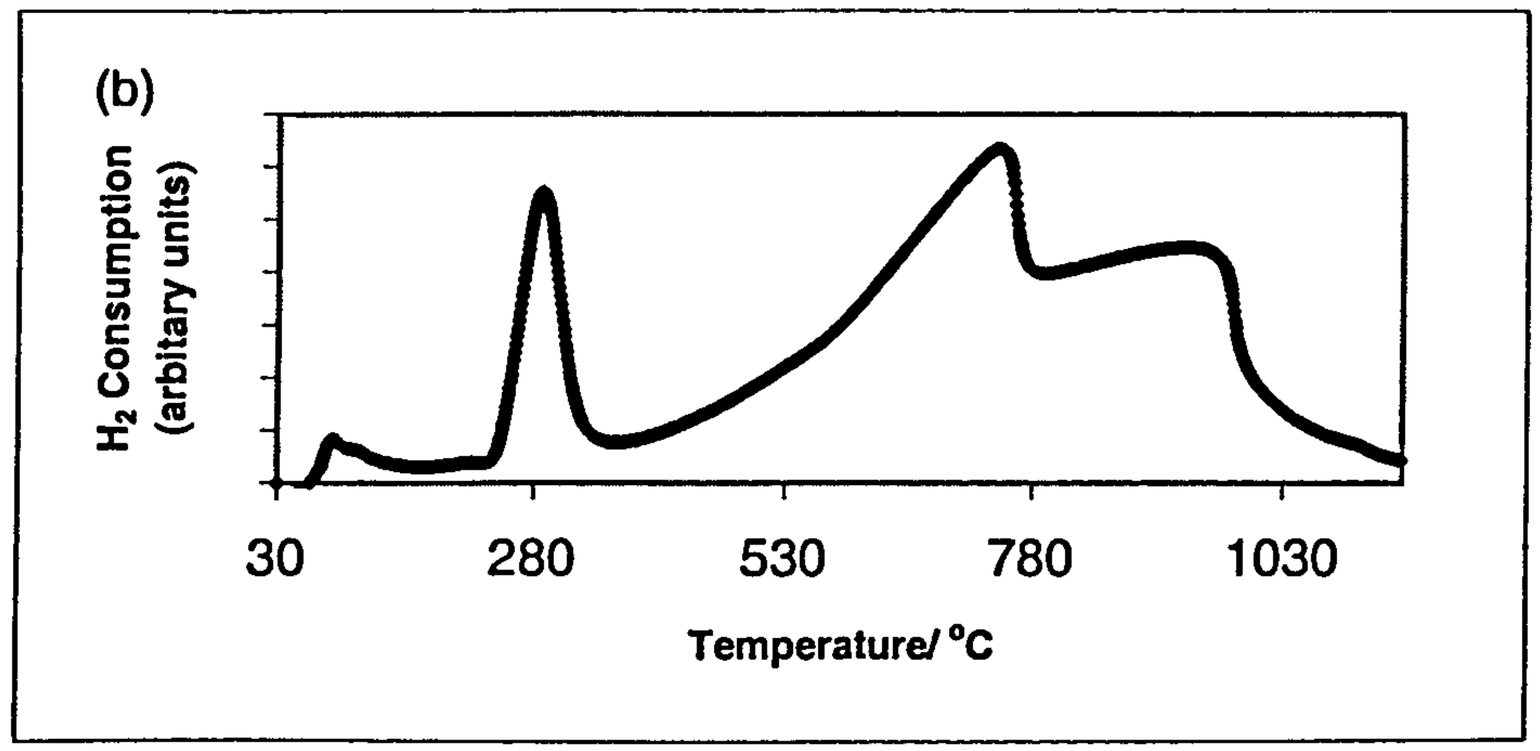

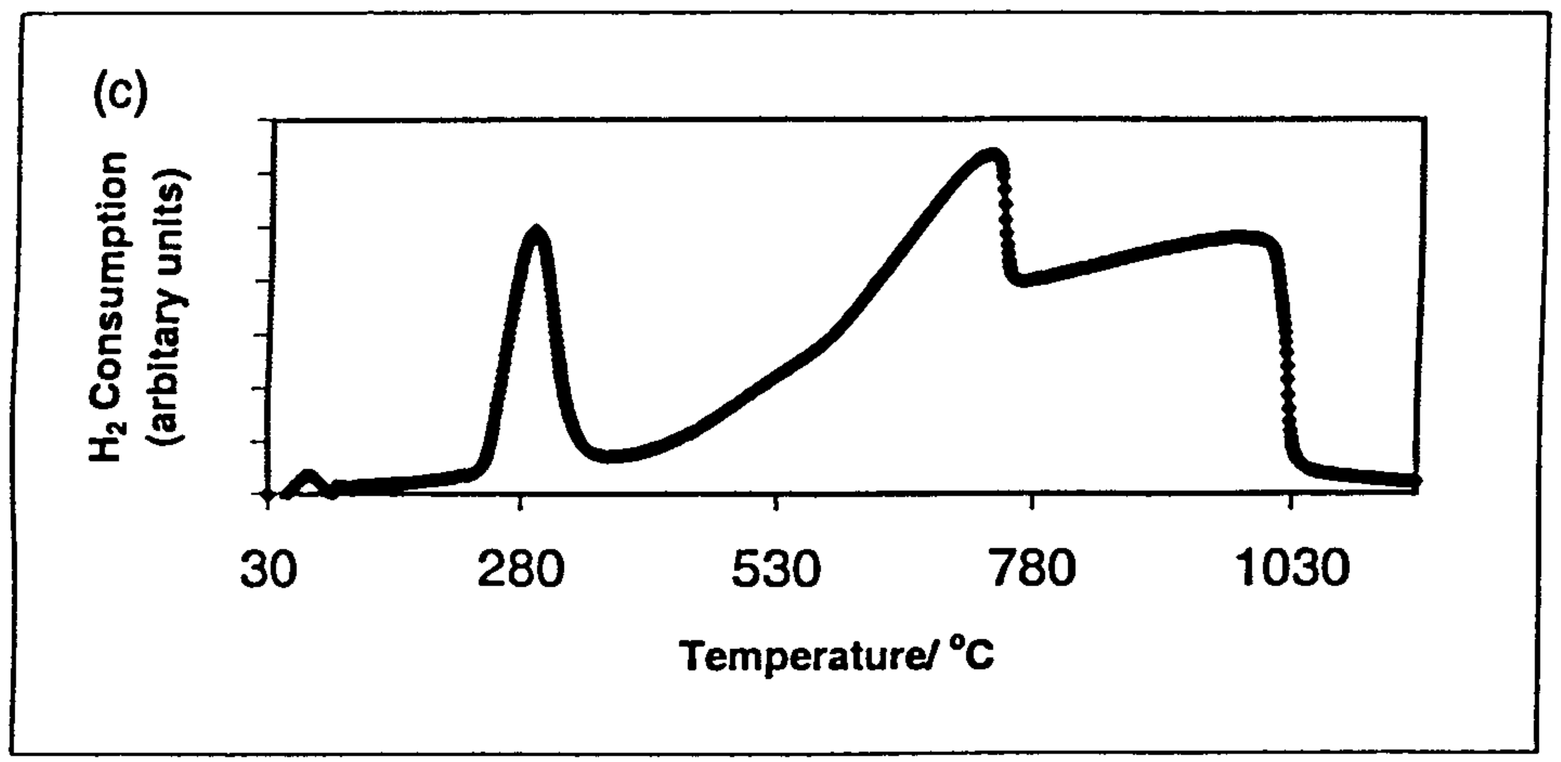

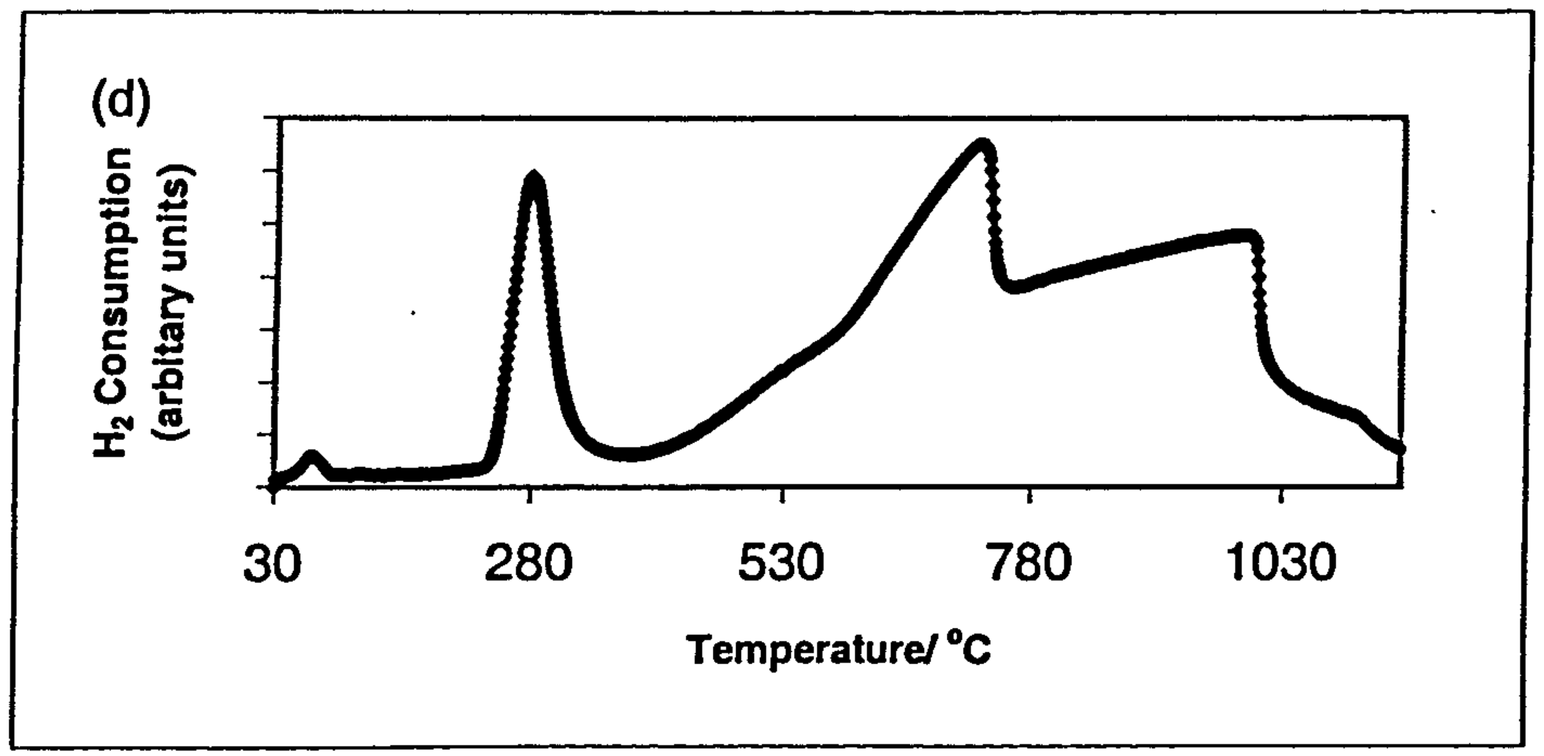

Figure 5.66 TPR profiles recorded from (a) α-Fe_2O_3 and Pd impregnated samples using (b) $Pd(NO_3)_2$, (c) Pd(DNDA) and (d) $Pd(acac)_2$ precursors

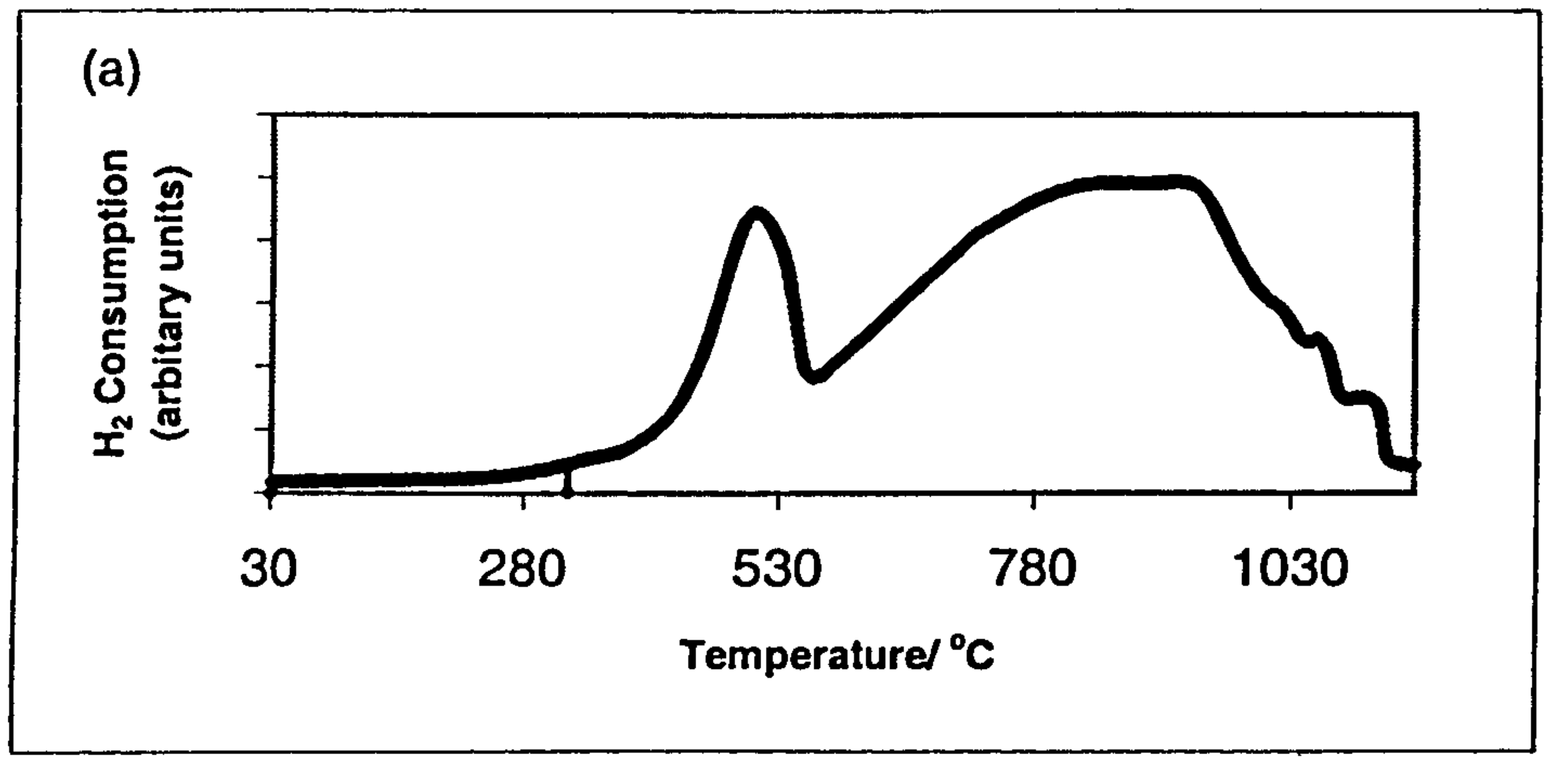

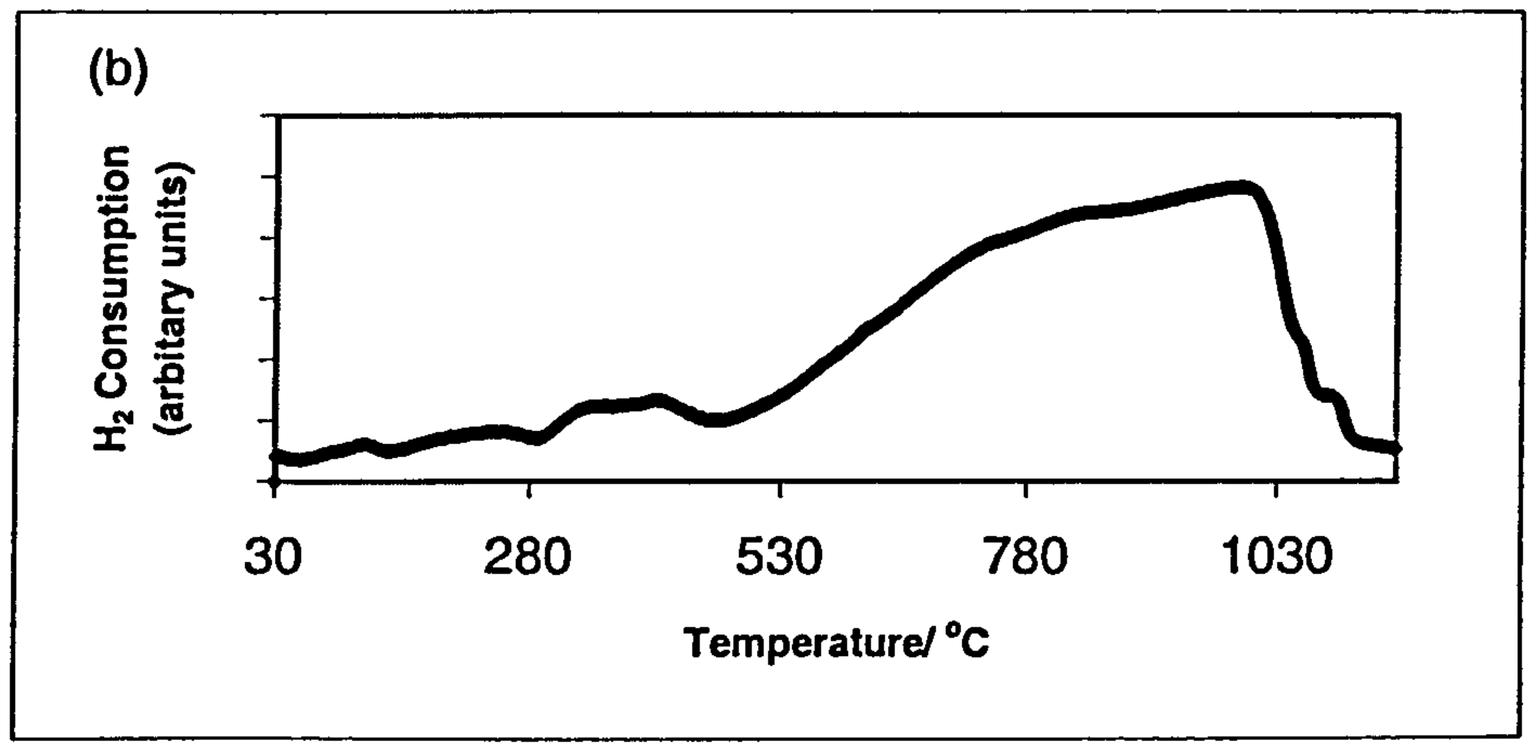

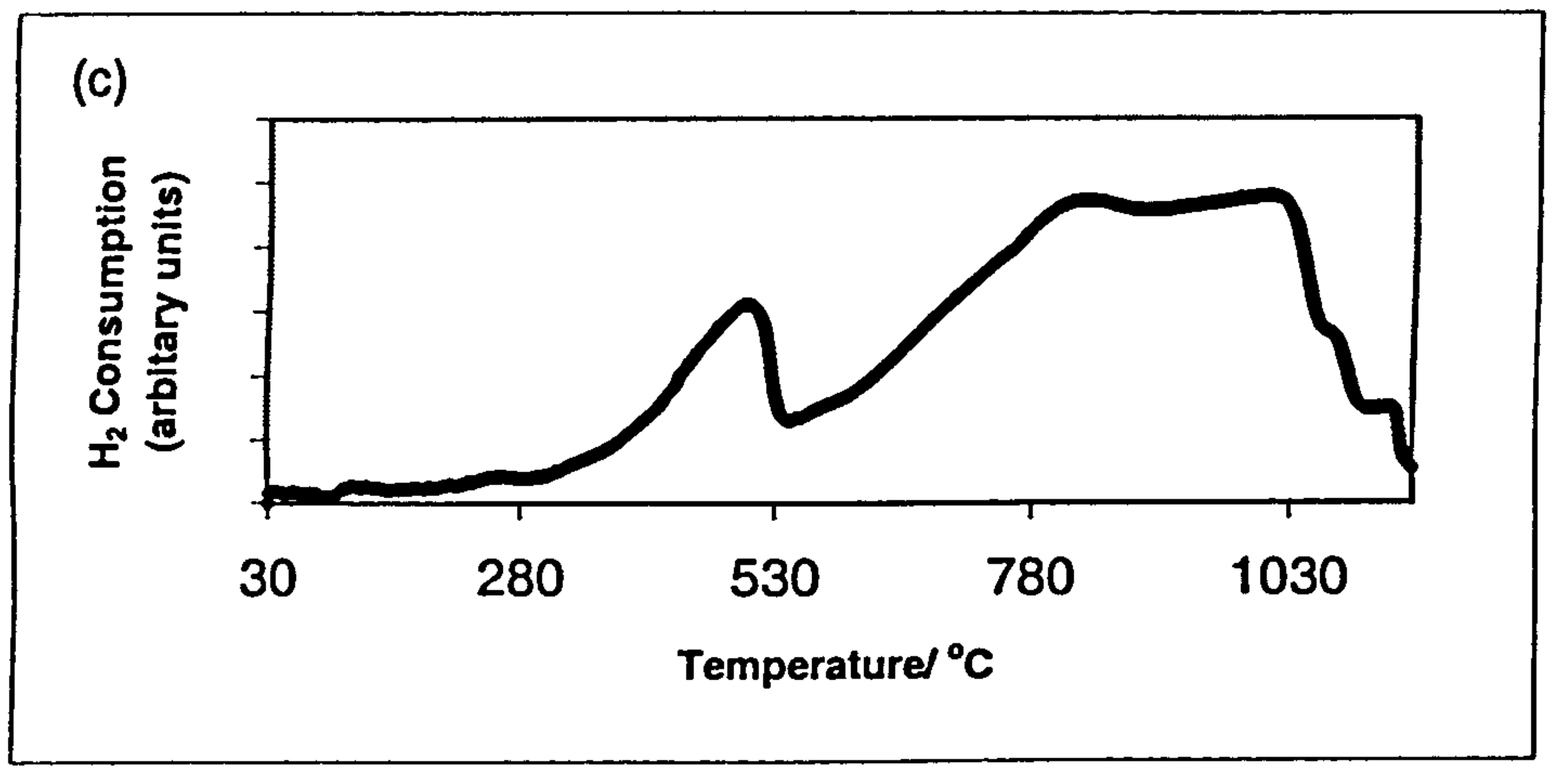

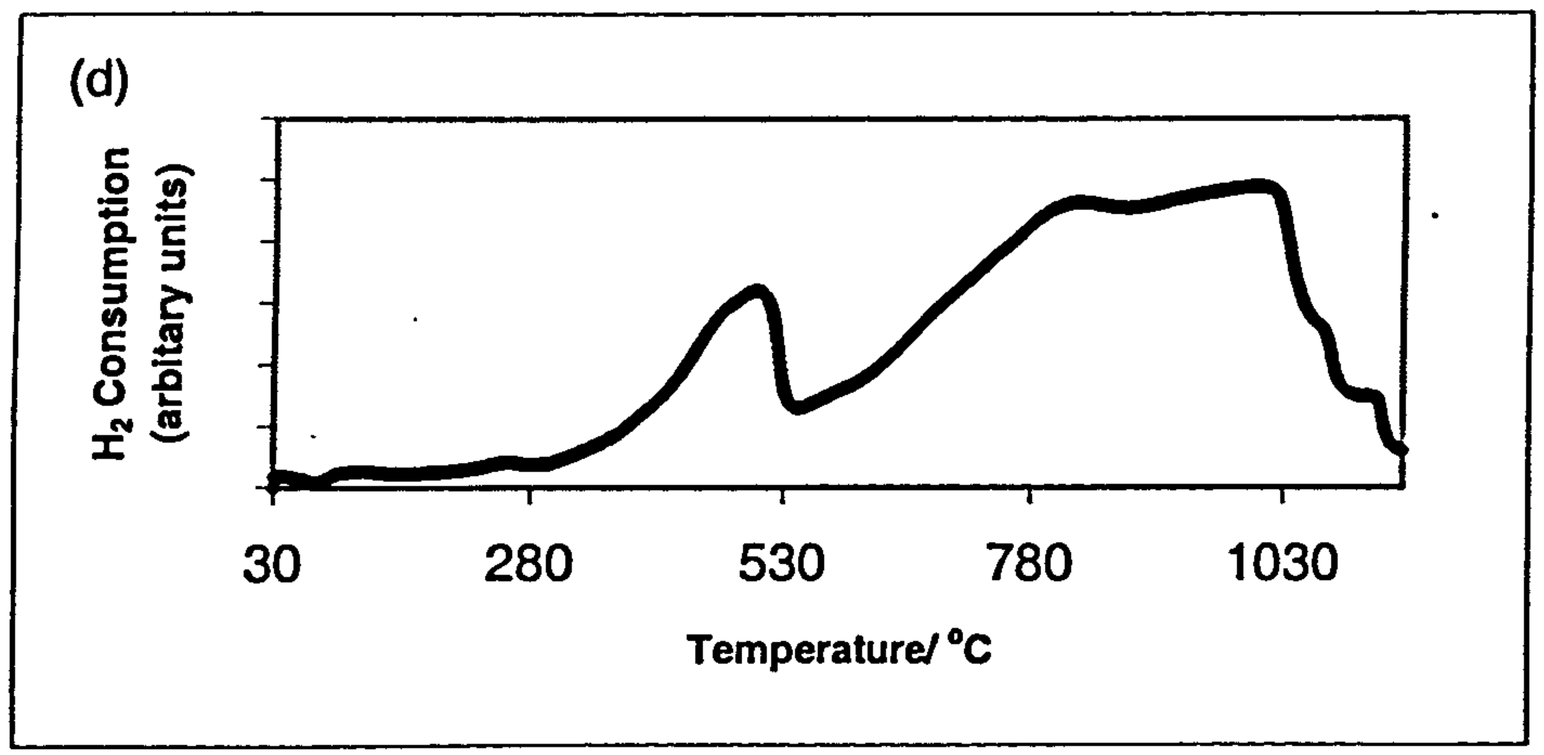

Figure 5.67 TPR profiles recorded from (a) Ti/α-Fe_2O_3 and Pd impregnated samples using (b) $Pd(NO_3)_2$, (c) Pd(DNDA) and (d) $Pd(acac)_2$ precursors

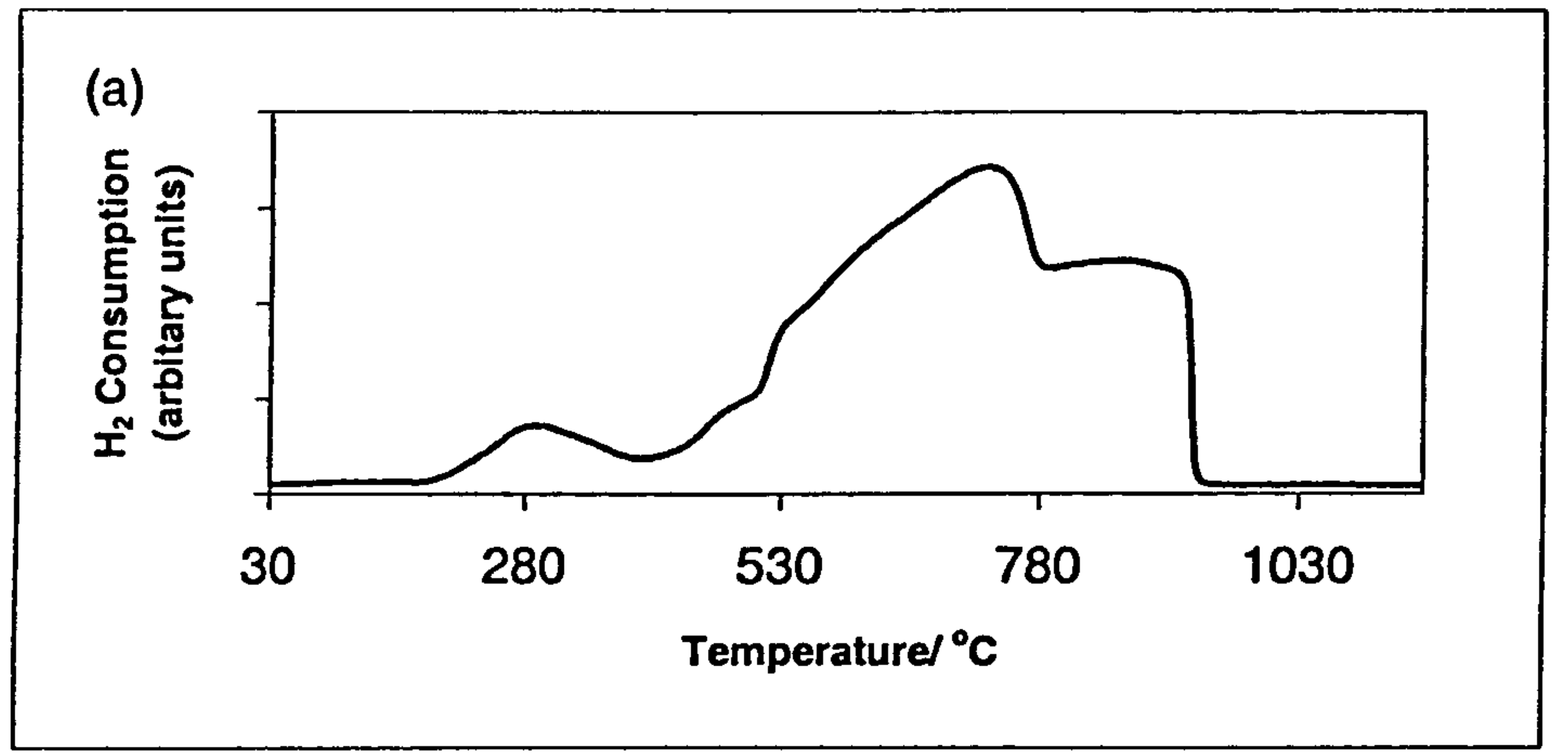

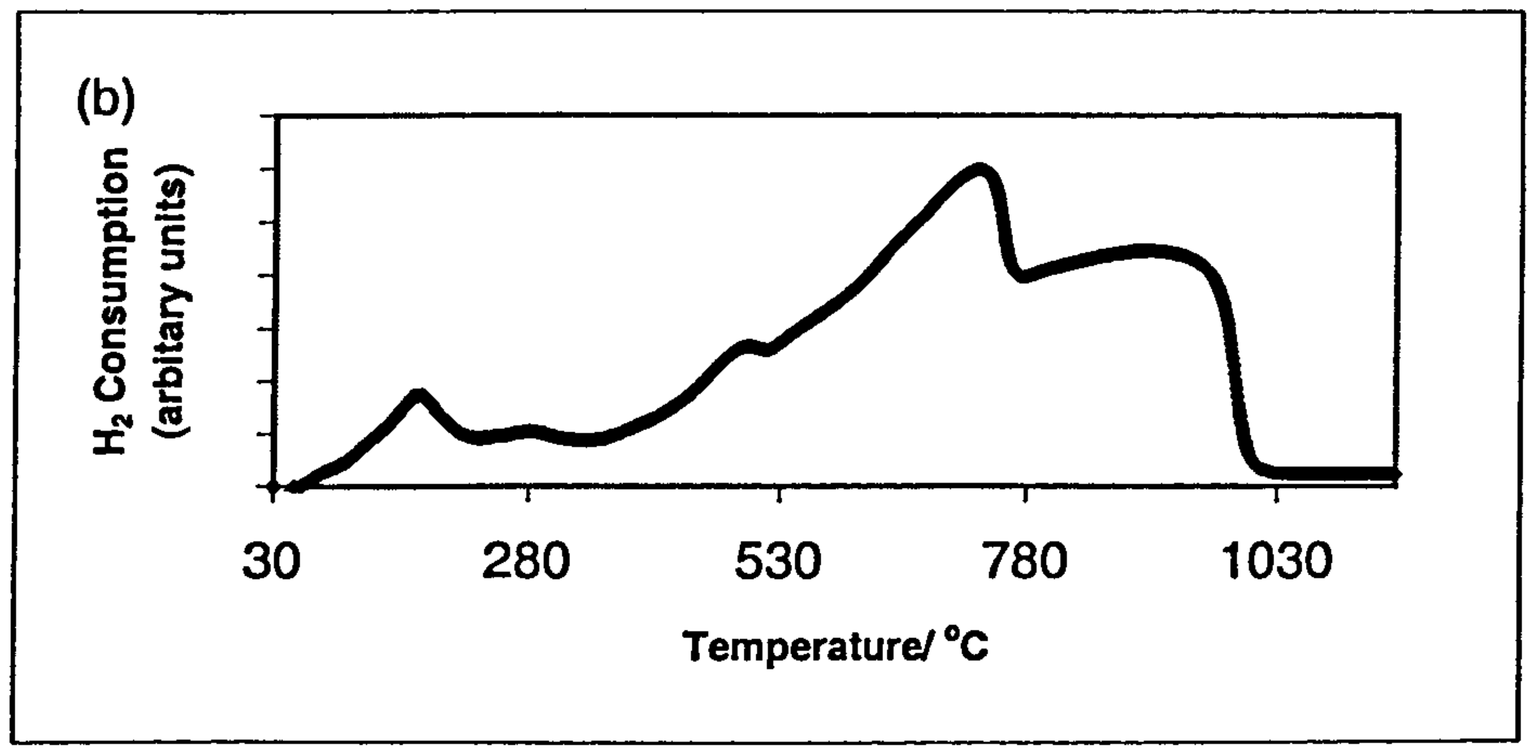

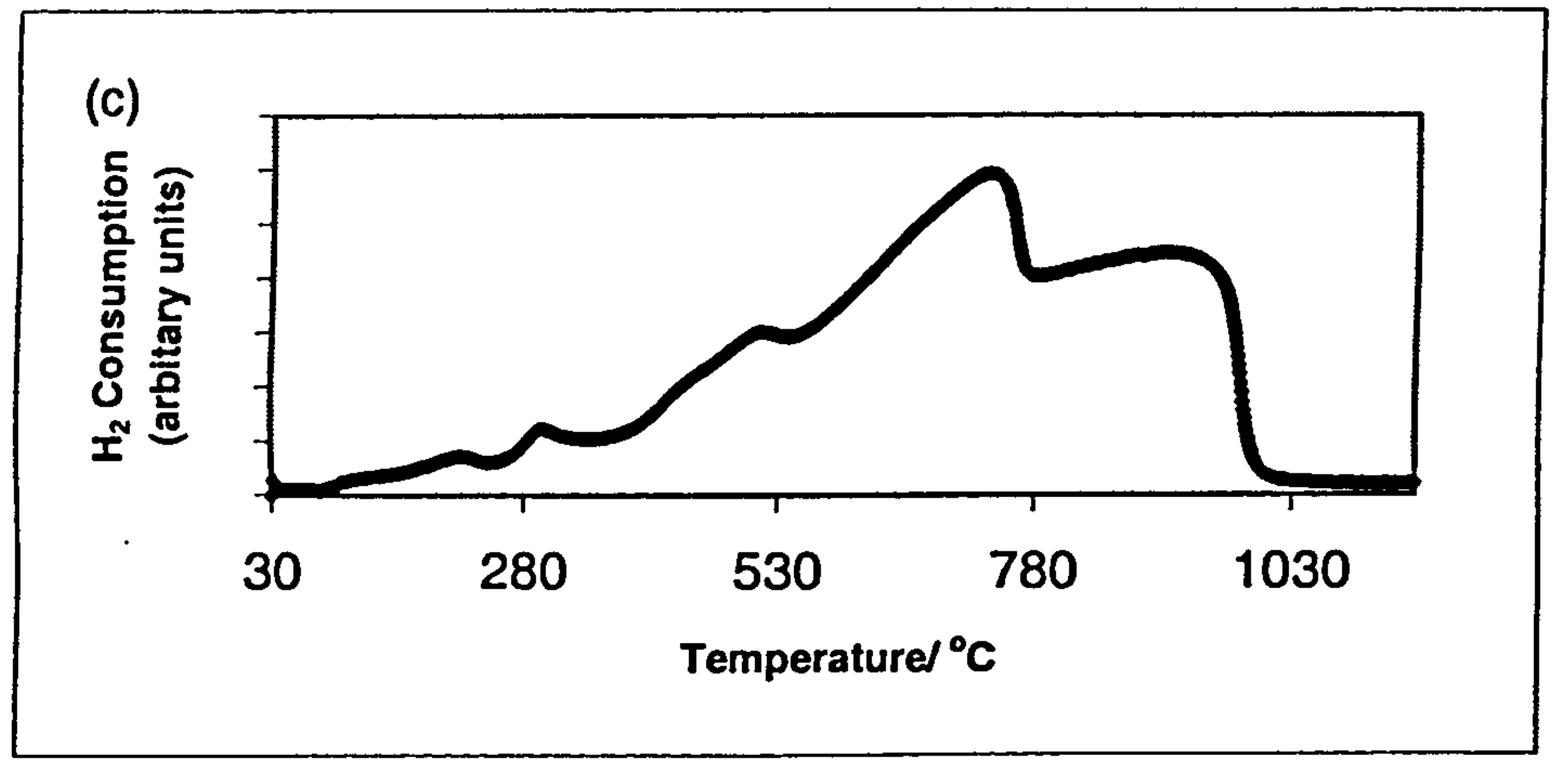

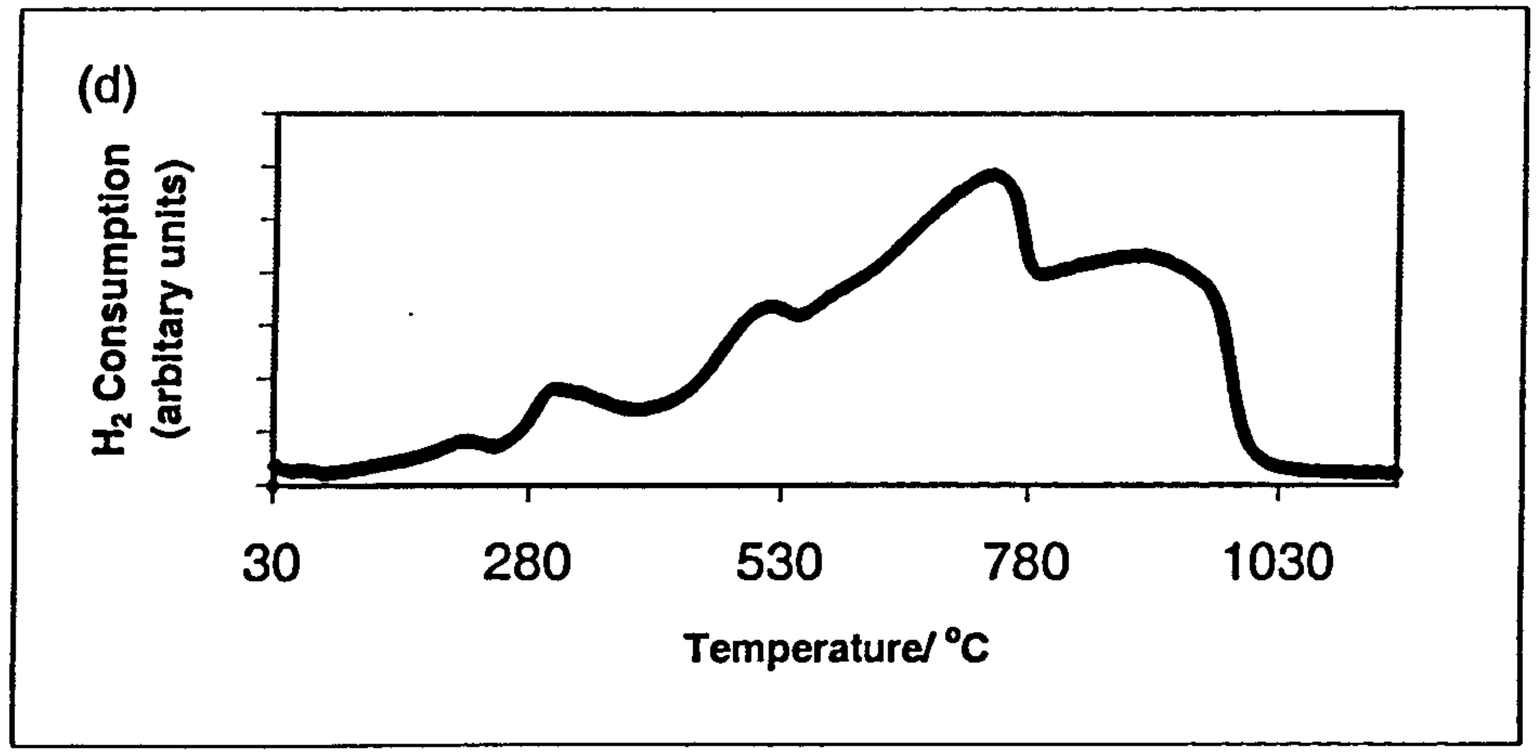

Figure 5.68 TPR profiles recorded from (a) Sn/α-Fe_2O_3 and Pd impregnated samples using (b) $Pd(NO_3)_2$, (c) Pd(DNDA) and (d) $Pd(acac)_2$ precursors

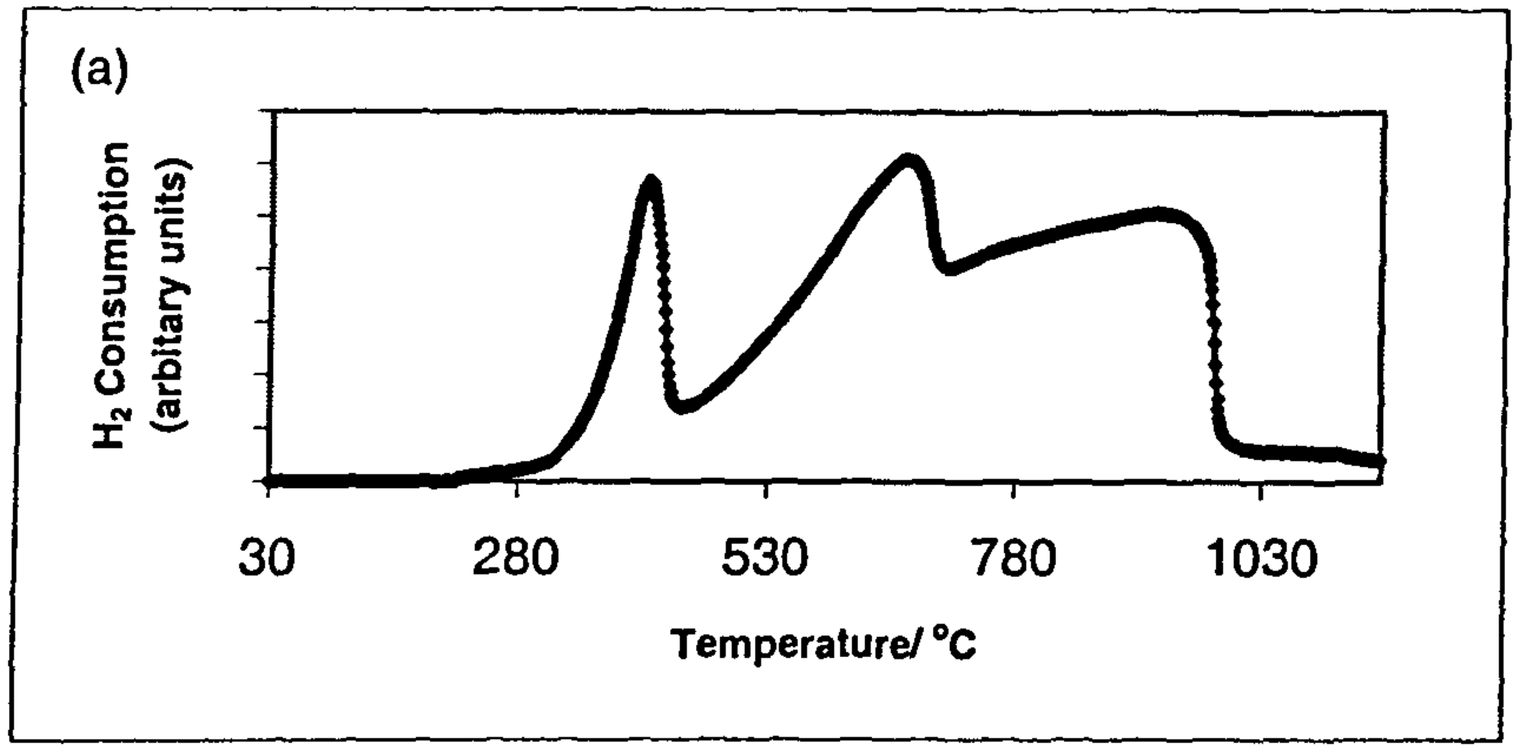

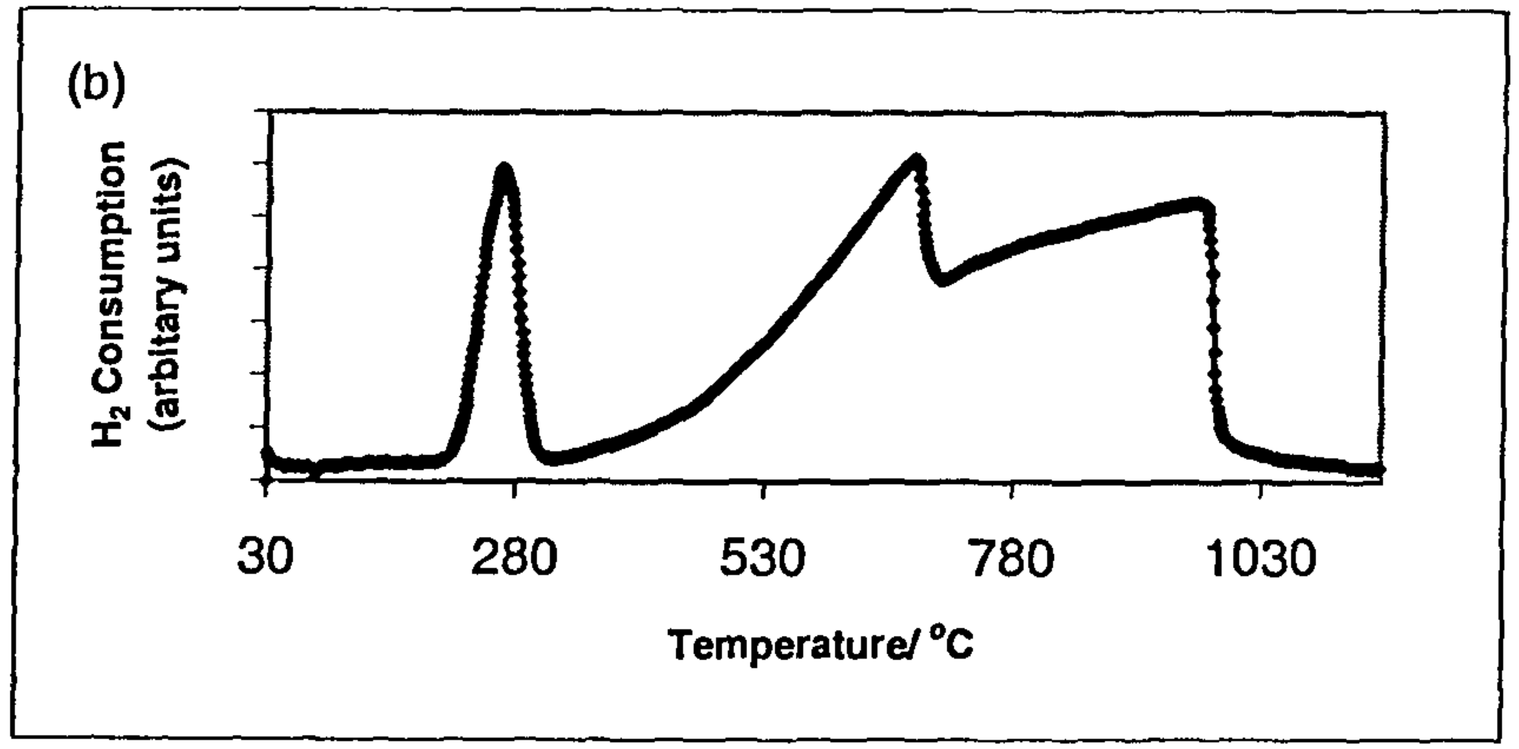

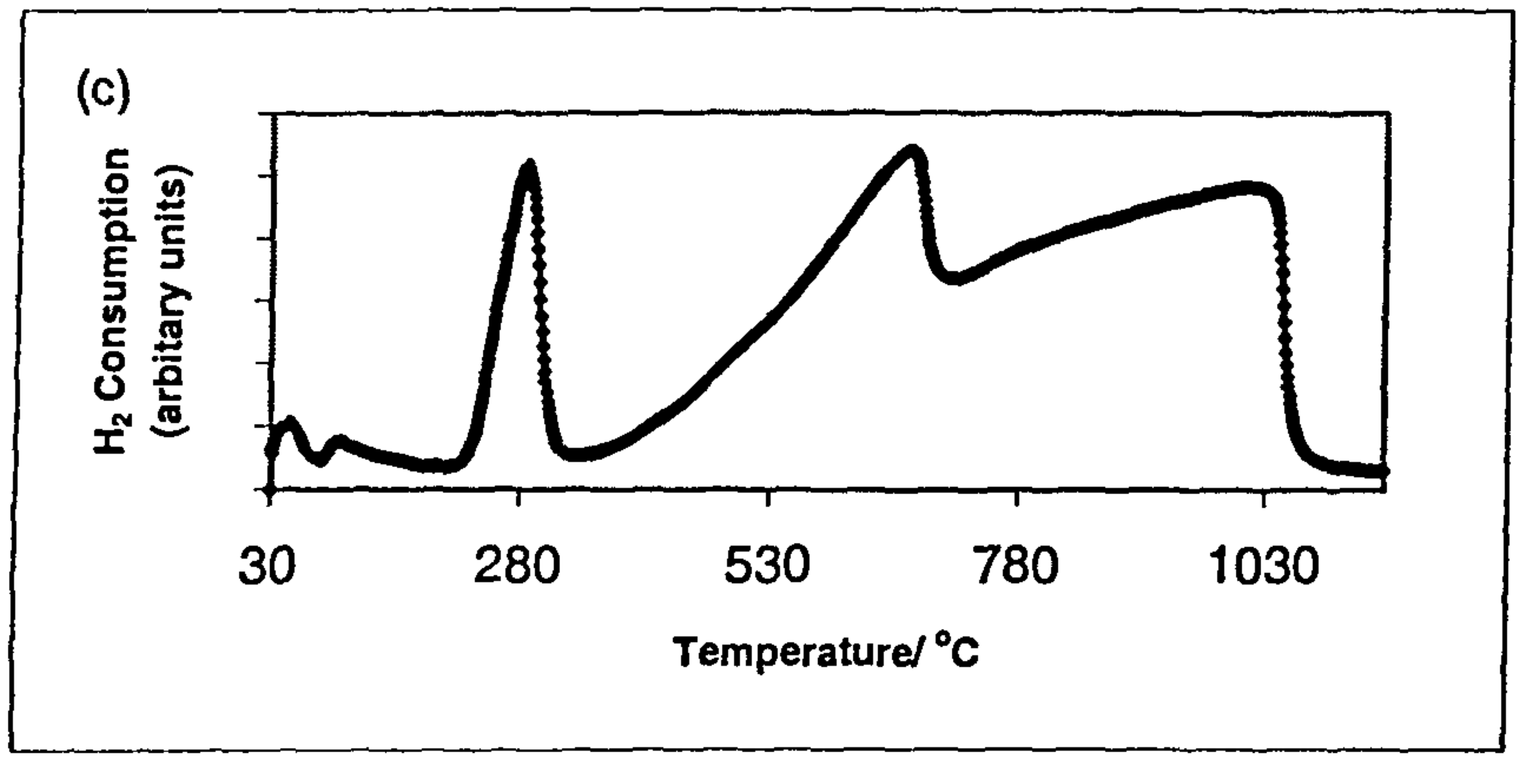

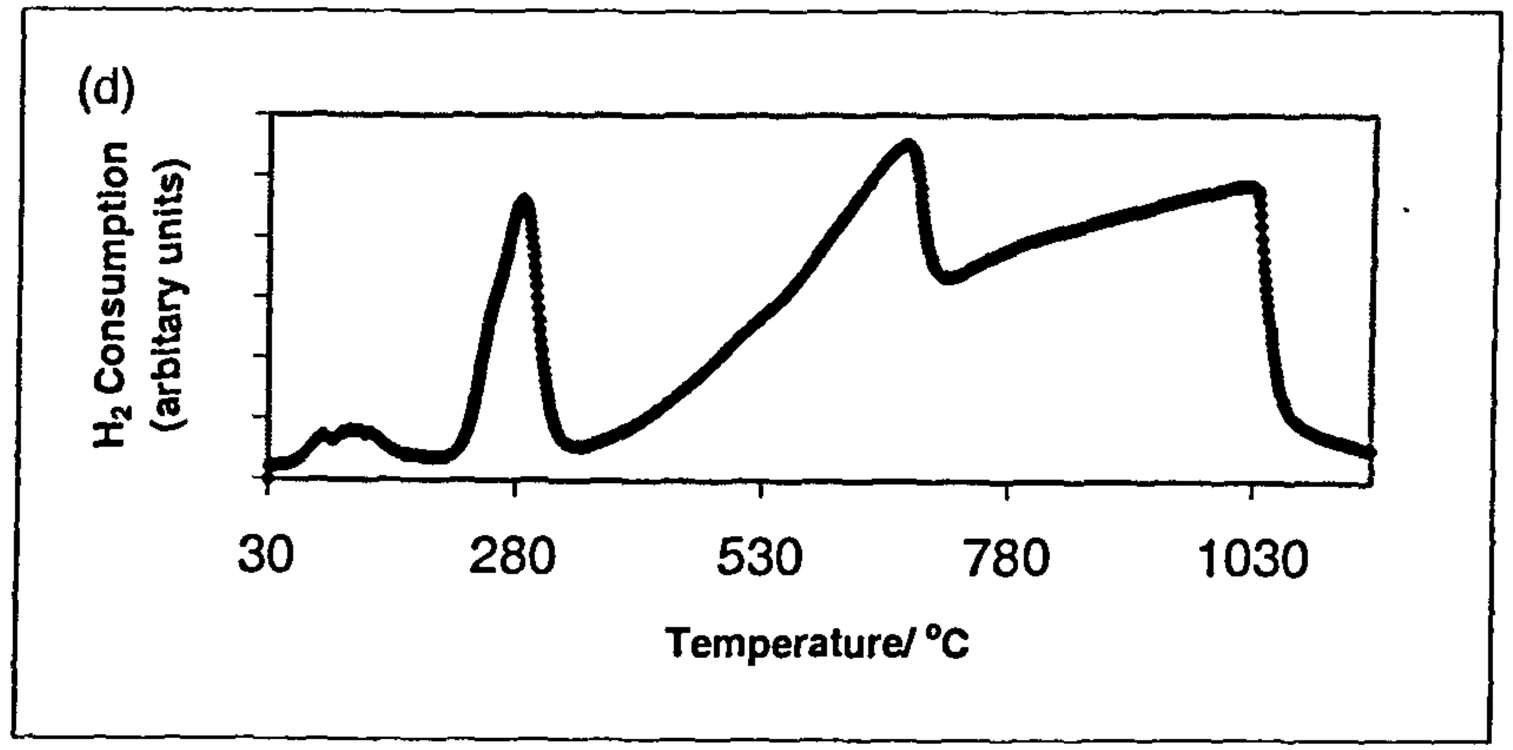

Figure 5.69 TPR profiles recorded from (a) Mg/α-Fe_2O_3 and Pd impregnated samples using (b) $Pd(NO_3)_2$, (c) Pd(DNDA) and (d) $Pd(acac)_2$ precursors

Catalyst Testing

The oxidation of CO to CO_2 was used as a test for the catalytic activity of the Pd impregnated samples. The temperatures at which 50 % conversion (T_{50}) of CO to CO_2 was achieved are collected in Table 5.18. The lower the temperature of CO conversion the more active the catalyst.

Table 5.18 Conversion temperatures of CO to CO_2 from Pd impregnated α-Fe_2O_3 and metal-doped variants.

Sample	Temperature at 50% CO conversion / °C (± 25 °C)		
	($Pd(NO_3)_2$)	(Pd(DNDA))	($Pd(acac)_2$)
Pd/α-Fe_2O_3	193	205	211
Pd/Ti/α-Fe_2O_3	154	125	103
Pd/Sn/α-Fe_2O_3	164	137	167
Pd/Mg/α-Fe_2O_3	189	182	202

The lowest temperatures are achieved with Pd/Ti/α–Fe_2O_3. Figure 5.70 shows the dependence of CO oxidation with temperature over Pd/α-Fe_2O_3 prepared by addition of base to salt and boiling under reflux, impregnated with $Pd(NO_3)_2$. The shape of the graph is typical for catalytic performance. Until the incoming gases have heated the catalyst, the activity of the catalyst is low. This temperature, at which the efficiency of the catalyst rapidly increases is known as the light-off temperature. Until this temperature is reached, the catalyst does not work at full efficiency, and so CO will be emitted from the exhaust in significant amounts. This problem is known as cold start. Ideally the light-off temperature should be as low as possible.

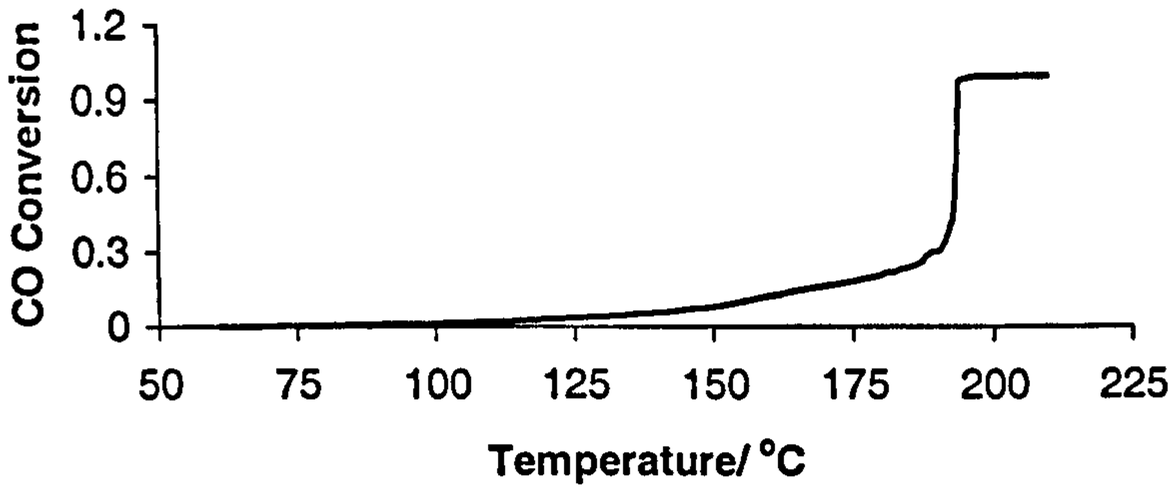

Figure 5.70 Dependence of CO oxidation on temperature for Pd/α-Fe_2O_3 using $Pd(NO_3)_2$

Pd impregnated Ti- doped α-Fe_2O_3 appeared to induce a lowering of the temperature of 50 % CO conversion as compared with the Pd impregnated undoped α-Fe_2O_3. The impregnation of Ti/α-Fe_2O_3 using $Pd(acac)_2$ precursor showed the best activity probably due to better metal dispersion compared with $Pd(NO_3)_2$ and Pd(DNDA) precursors. The Pd/Sn/α-Fe_2O_3 showed better catalytic activity than Pd/α-Fe_2O_3 but lower than the titanium- containing samples. Pd/Mg/α-Fe_2O_3 appeared to induce little difference in the temperature of 50 % CO conversion compared to Pd impregnated α-Fe_2O_3. The different palladium precursors also showed little difference in performance, which may be due to different palladium loading or dispersion. Pd/Ti/α-Fe_2O_3 showed the highest catalytic activity for the conversion of CO to CO_2.

Oxygen storage capacity (OSC)

Pd impregnated- α–Fe_2O_3, Ti/α–Fe_2O_3 and Sn/α–Fe_2O_3, all prepared by addition of base to salt and boiling under reflux were tested for oxygen storage capacity (OSC). The results are shown in Figure 71 (a-c) respectively. Pd/α–Fe_2O_3 showed a

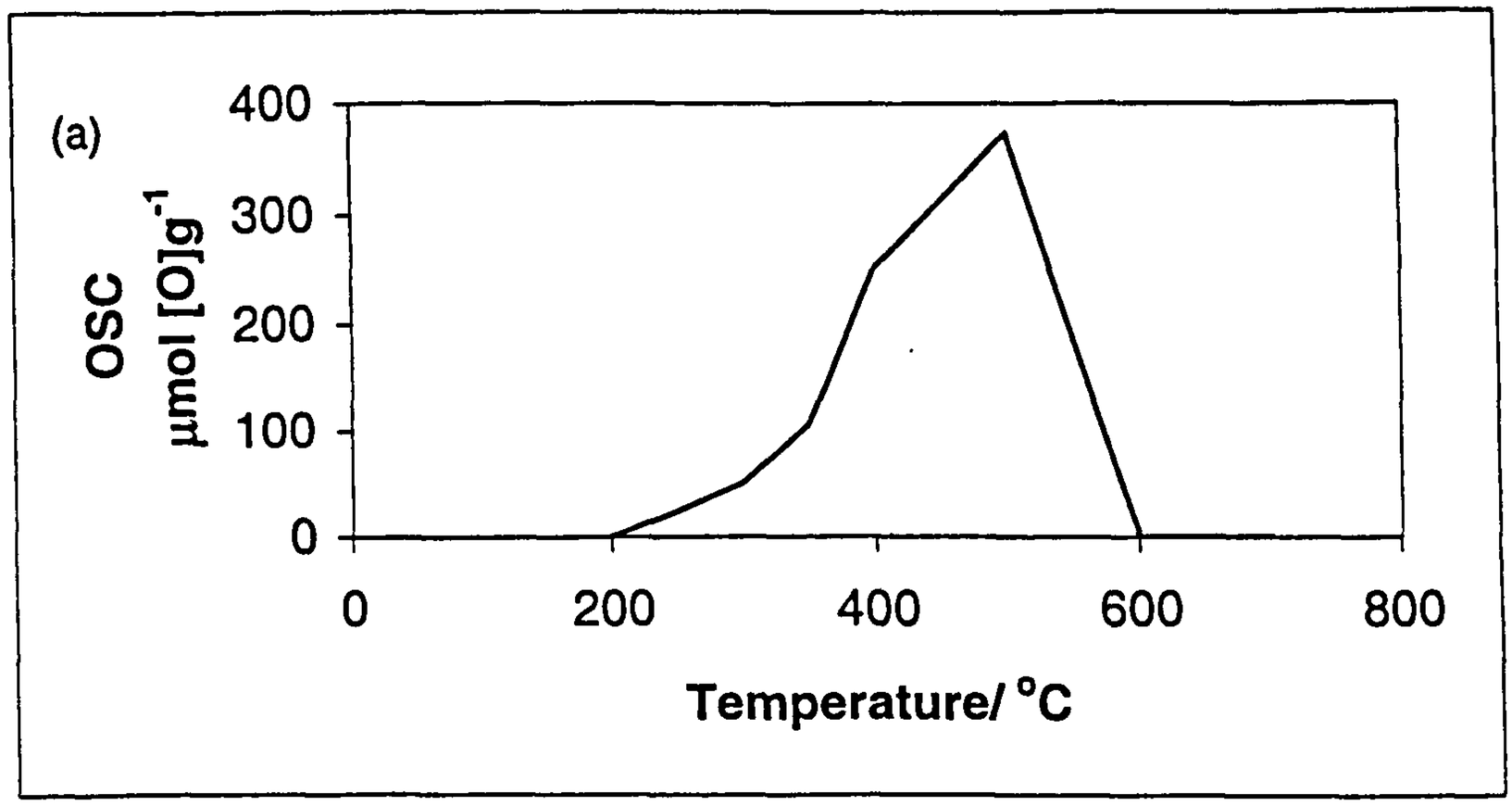

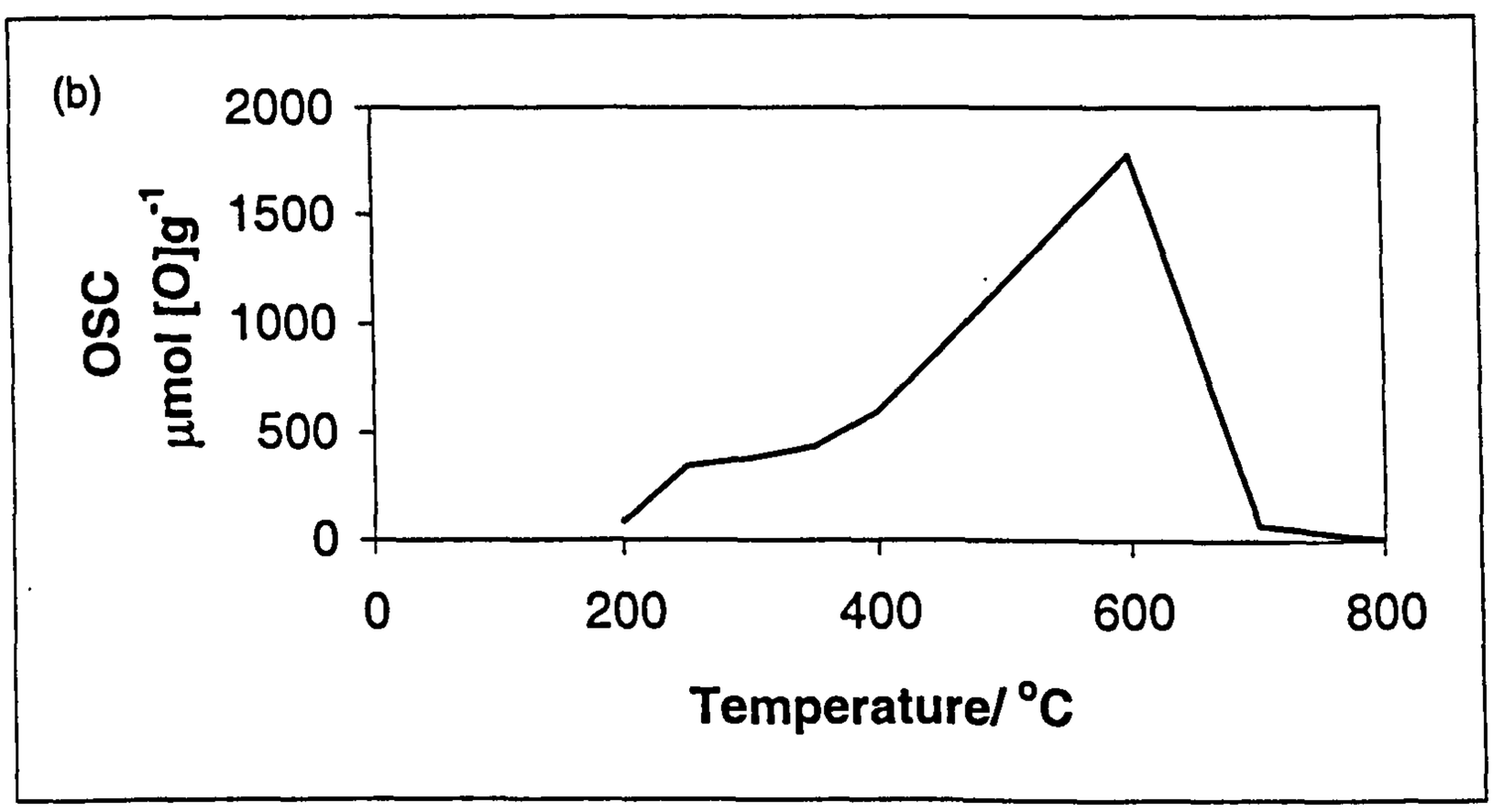

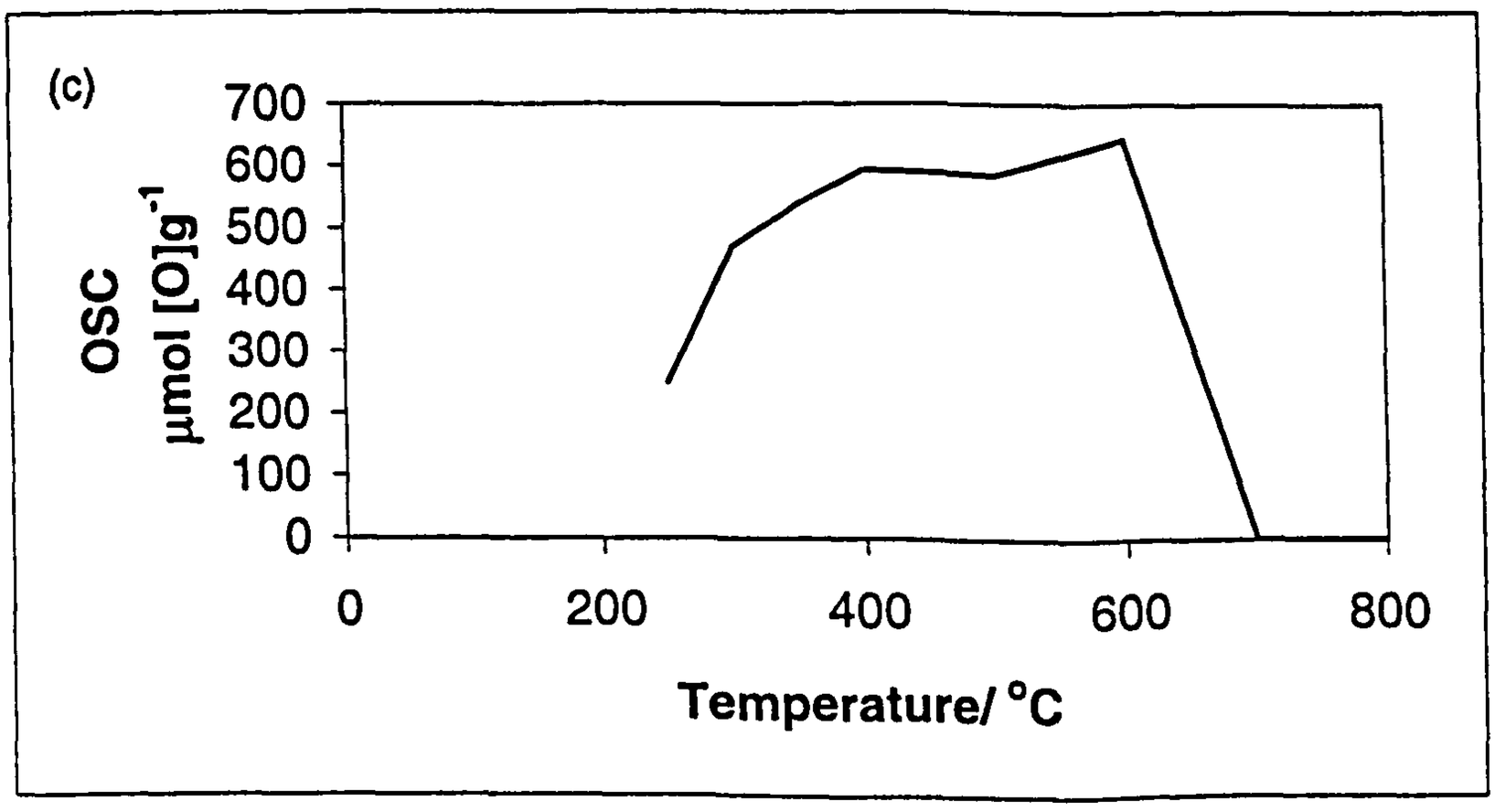

Figure 5.71 OSC measurement recorded from (a) Pd/α-Fe_2O_3, (b) Pd/Ti/α-Fe_2O_3 and (c) Pd/Sn/α-Fe_2O_3

maximum OSC of *ca.* 400 μmol $[O]g^{-1}$ in the temperature range between 450 and 550 °C. Pd/Ti/α–Fe_2O_3 showed a maximum OSC of *ca.* 1800 μmol $[O]g^{-1}$ in the temperature range between 550 and 650 °C. Pd/Sn/α–Fe_2O_3 showed a maximum OSC of *ca.* 600 μmol $[O]g^{-1}$ over a wider temperature range between 350 and 600 °C. At higher temperatures the samples sintered and the OSC decreased. The metal dopants induced a similar effect on the OSC as they did in their γ–Fe_2O_3 counterparts.

Overall, the results showed that the titanium-containing sample had the greatest oxygen storage capacity.

Conclusion

The different palladium precursors all had similar effects on the TPR profiles and lowered the temperature of the initial reduction peak. CO oxidation and OSC studies showed that Pd/Ti/α–Fe_2O_3 gave significantly better results as compared with Pd impregnated undoped α–Fe_2O_3 and the other Pd impregnated metal- doped α–Fe_2O_3.

References

1. JCPDS Index Card No. 19-0629 (Fe_3O_4).
2. C.W. Childs and J.G. Baker-Sherman, "Mössbauer Spectra and Parameters of standard samples.1", New Zealand Scientific Report 66, 1984.
3. N.N Greenwood and T.C Gibb, "Mössbauer Spectroscopy", Chapman and Hall, London, 1971.
4. JCPDS Index Card No. 06-0615 (FeO).

5. JCPDS Index Card No. 06-0696 (Fe).

6. R.D. Shannon, *Acta Crystallogr. Sect. A*, 1976, 32, 751.

7. B.A. Wechsler, D.H. Lindslay and C.T. Prewitt, *Am. Mineral*, 1984, 69, 754.

8. F.J. Berry, Ö. Helgason, K. Jonsson and S.J. Skinner, *J. Solid State Chem.*, 1996, 122, 353.

9. F.J. Berry "The Mössbauer Effect in Supported Microcrystallites", Advances in Inorganic Chemistry and Radichemistry, vol. 21, Ed. H.J. Emeleus and A.G. Sharpe, Academic Press, 1978.

10. E.A. Moore, A. Bohorquez, F.J. Berry, Ö. Helgason and J.F. Marco, *J. Phys. Chem. Solids,* 2001, 62, 1277.

11. F. J. Berry, C. Greaves, Ö. Helgason and J. McManus, *J. Mater. Chem.*, 1999, 9, 223.

12. F.J. Berry, S.J. Skinner, Ö. Helgason, R. Bilsborrow and J.F. Marco, *Polyhedron,* 1998, 17, 149.

13. JCPDS Index Card No. 17-0464 ($MgFe_2O_4$).

14. JCPDS Index Card No. 33-0664 (α-Fe_2O_3).

15. F.J. Berry, C. Greaves, Ö. Helgason, J. McManus, H.M. Palmer and R.T. Williams, *J. Solid State Chem.*, 2000, 151, 157.

16. F.J. Berry, C. Greaves, J. McManus, M. Mortimer and G. Oates, *J. Solid State Chem.*, 1997, 130, 272.

17. JCPDS Index Card No. 39-1346 (γ–Fe_2O_3).

Chapter 6

CONCLUSION

Chapter 6

CONCLUSION

One of the aims of the project was to investigate the potential of iron oxides as alternative materials for use as oxygen storage and release components in automobile exhaust catalysts. Such materials require high surface area for high surface contact with reactants, reductive and oxidative properties for oxygen storage and release, and stability at high temperatures to maintain structure and activity.

Iron oxides and their metal- doped variants of formulation M/Fe_3O_4, $M/\gamma–Fe_2O_3$, M/α-Fe_2O_3 (M = Ti, Sn, Ru and Mg) were prepared by the calcination of solids formed by the boiling of precipitates under reflux and by hydrothermal processing. These iron oxides were characterised using X-ray powder diffraction, ^{57}Fe Mössbauer spectroscopy, temperatured programme reduction, BET surface area measurement and transmission electron microscopy. Fe_2O_3 samples were impregnated with palladium and the catalytic properties for the oxidation of carbon monoxide examined.

$\gamma–Fe_2O_3$ and its metal- doped variants were subjected to special investigation and the influence of the dopants on the surface area, particle size, reduction properties, stability to conversion to α-Fe_2O_3- related structures, and oxidation- reduction cycling were examined. Titanium- doped $\gamma–Fe_2O_3$ prepared by the calcination of a solid formed by the addition of base to salt and boiling the precipitate under reflux was formed with a smaller particle size and higher surface area than the other counterparts. These properties remained superior to those of the other materials when

Ti/γ–Fe_2O_3 was subjected to a three-fold reduction- oxidation cycle. The stabilisation of a spinel- related γ–Fe_2O_3 structure with respect to thermally induced conversion to a corundum- related α-Fe_2O_3 phase was related to the presence of titanium as opposed to particle size or surface area effects. The oxygen storage capacity and the performance of palladium- impregnated Ti/γ–Fe_2O_3 for the oxidation of carbon monoxide to carbon dioxide was good. Although generally similar behaviour was observed in γ–Fe_2O_3 doped with tin, ruthenium, and magnesium, and in palladium impregnated variants, Ti/γ–Fe_2O_3 and palladium impregnated Ti/γ–Fe_2O_3 showed the most favourable properties in terms of their potential use as oxygen-storage components in automobile exhaust catalysts.

A comparison of the results with those recorded from materials derived from Fe_3O_4 and α-Fe_2O_3 confirmed the superior properties of Ti/γ–Fe_2O_3 and palladium impregnated Ti/γ–Fe_2O_3 for use as catalysts in automobile exhaust systems.

Further work is needed to either enhance the stability of Ti/γ–Fe_2O_3 to temperatures up to *ca.* 1000 °C and without the loss of desirable properties essential for an automobile catalyst component or to improve the properties of the more stable Ti/α-Fe_2O_3 phase.